Tenth International Symposium on Long Range Sound Propagation

September 12-13, 2002

Centre Scientifique et Technique du Bâtiment CTSB Grenoble, France

Supported by:
Department of the Army
Army Research Office
Research Triangle Park, NC USA

NCPA Report Number JC 1003-01

TABLE OF CONTENTS

COMPUTATIONAL ISSUES

PREFACE

The first Long Range Sound Symposia or LRSP was held over 20 years ago in Mississippi with the idea of allowing scientists with a common interest in long range atmospheric acoustics a forum to exchange ideas. The 10th Long Range Sound Propagation Symposium (LRSP) was Held on September 12-13, 2002 in Grenoble France and was hosted by Drs. Jerome Defrance and Eric Premat of the Centre Scientifique et Technique du Bâtiment (CSTB). The meeting had 29 presentations as well as group discussions separated into 4 categories: Ground and Meteorological Effects (9); Turbulence (6); Infrasound, Signal Processing and Experimental Techniques (8); Computational Issues (6). There was a continued consensus that the state of the art for long range sound propagation has grown from 100's of meters (from the early symposia) to kilometers and beyond now -especially with the growing emphasis on infrasound.

The hosts would like to express their appreciation to the participants for their attendance and contributions whether through presentations or lively group discussions. The hosts would also like to thank the personnel of the Centre Scientifique et Technique du Bâtiment (CSTB), especially the symposium secretary Ms. Catherine Mandon, for their support of the conference as well as the Army Research Laboratory for their support of the conference and these proceedings.

James P. Chambers and Henry E. Bass
National Center for Physical Acoustics
University of Mississippi
University, MS 38677
USA

Keith Attenborough
School of Engineering
University of Hull
HU6 7RX
East Yorkshire
GREAT BRITAIN

Eric Premat and Jerome Defrance
Centre Scientifique et Technique du Bâtiment
Environmental Acoustics
24, rue Joseph Fourier
38400 saint Martin-d'Heres
FRANCE

Tenth International Symposium on Long Range Sound Propagation 12-13 September 2002

Centre Scientifique et Technique du Bâtiment

CSTB

le futur en construction

Grenoble, France

ABALLÉA François
Centre Scientifique et Technique du Bâtiment (CSTB)
Environmental Acoustics
24, rue Joseph Fourier
38400 Saint-Martin-d'Hères
France
faballea@cstb.fr

ATTENBOROUGH Keith
Department of Engineering
University of Hull
Hull HU6 7RX
United Kingdom
K.Attenborough@hull.ac.uk

BASS Henry E.
National Center for Physical Acoustics
University of Mississippi
University, MS 38677
USA
pabass@olemiss.edu

BLAIRON Nicolas
Centre Acoustique
LMFA/UMR CNRS 5509
Ecole Centrale de Lyon
36, avenue Guy de Collongue
BP 163
69131 Ecully
France
nicolas.blairon@ec-lyon.fr

BLANC-BENON Philippe
Centre Acoustique
LMFA/UMR CNRS 5509
Ecole Centrale de Lyon
36, avenue Guy de Collongue
BP 163
69131 Ecully
France
Philippe.Blanc-Benon@ec-lyon.fr

BLUMRICH Reinhard
DLR
Institut fuer Physik der Atmosphaere
Oberpfaffenhofen
D-82234 Wessling
Germany
reinhard.blumrich@dlr.de

BOULANGER Patrice
Department of Engineering
University of Hull
Hull HU6 7RX
United Kingdom
patriceboulanger@hotmail.com

CHAMBERS James P.
National Center for Physical Acoustics
University of Mississippi
University, MS 38677
USA
chambers@olemiss.edu

COLLIER Sandra L.
U.S. Army Research Laboratory
ATTN: AMSRL-CI-EE
2800 Powder Mill Rd.
Adelphi, MD 20783-1197
USA
scollier@arl.army.mil

COULOUVRAT François
Laboratoire de Modélisation en Mécanique
(UMR CNRS 7607)
Université Pierre et Marie Curie
8, rue du Capitaine Scott
75015 Paris
France
coulouvr@moka.ccr.jussieu.fr

DALLOIS Laurent
Centre Acoustique
LMFA/UMR CNRS 5509
Ecole Centrale de Lyon
36, avenue Guy de Collongue
BP 163
69131 Ecully
France
Laurent.Dallois@ec-lyon.fr

DEFRANCE Jérôme
Centre Scientifique et Technique du Bâtiment (CSTB)
Environmental Acoustics
24, rue Joseph Fourier
38400 Saint-Martin-d'Hères
France
j.defrance@cstb.fr

OSTASHEV Vladimir
NOAA
Environmental Technology Laboratory
325 Broadway, Boulder CO 80305
USA
Vladimir.Ostashev@noaa.gov

PREMAT Eric
Centre Scientifique et Technique du Bâtiment (CSTB)
Environmental Acoustics
24, rue Joseph Fourier
38400 Saint-Martin-d'Hères
France
e.premat@cstb.fr

PRIOUR Maud
Centre Scientifique et Technique du Bâtiment (CSTB)
Environmental Acoustics
24, rue Joseph Fourier
38400 Saint-Martin-d'Hères
France
maud.priour@cstb.fr

TALMADGE Carrick
National Center for Physical Acoustics
University of Mississippi
University, MS 38677
USA
clt@olemiss.edu

THORSSON Pontus
Applied Acoustics
Chalmers University of Technology
SE-41296 Göteborg
Sweden
Pontus@ta.chalmers.se

WAGSTAFF Ronald A.
National Center for Physical Acoustics
University of Mississippi
University, MS 38677
USA
rwagstaf@sunset.olemiss.edu

WANG Qiang
Department of Engineering
University of Hull
Hull HU6 7RX
United Kingdom
Q.Wang@hull.ac.uk

WAXLER Roger
National Center for Physical Acoustics
University of Mississippi
University, MS 38677
USA
rwax@olemiss.edu

WEST Martin
Acoustical Software Limited
Bury
United Kingdom
acoustical@cwcom.net

WILSON Keith
US Army Research Laboratory
2800 Powder Mill Road
Adelphi, MD 20783-1197
USA
d.keith.wilson@erdc.usace.army.mil

EFFECTIVE IMPEDANCE OF ROUGH SEA SURFACES

Patrice Boulanger and Keith Attenborough
Department of Engineering, The University of Hull, Hull HU6 7RX, United Kingdom

ABSTRACT

Sonic boom characteristics are likely to be modified during near-grazing propagation above a rough sea surface. The derivation of effective impedance spectra for rough seas is a convenient way of allowing for such propagation effects. Two methods for the calculation of the effective impedance spectra of acoustically-hard, randomly-rough, two-dimensional surfaces have been developed. The first method uses the complex excess attenuation spectrum predicted by a Boundary Element Method (BEM) input to the classical expression for the sound field due to a point source above a smooth impedance plane which is solved subsequently for effective impedance roots identified by a winding number integral method. The second method is based on Twersky's theory which sums the contributions from random distributions of surface scatterers to obtain the total scattered field. Measured data for the complex excess attenuation above 2-D randomly-rough surfaces formed by semi-cylinders and wedges have been used to deduce effective impedance spectra that are compared to theories. BEM-deduced effective impedance spectra have been fitted with simple polynomials, and their coefficients have been found corresponding to sea states from 2 to 7 for five incidence angles. The general coefficients trends are consistent with the expected decrease in effective impedance with increasing grazing incidence angles and with decreasing roughness scale.

I. INTRODUCTION

The main effect of surface impedance on sonic boom propagation is on each side of the carpet edge and in the shadow zone[1]. There are less important effects in the primary carpet, where the incidence angle varies quite significantly. This work is focused on the shadow zone region that involves grazing incidence on the ground corresponding to the series of creeping waves diffracting into the shadow zone. The effective impedance of the ground is influenced by its roughness and, therefore, it is likely that boom characteristics are modified during near-grazing propagation above a rough sea surface. It is important therefore to describe the acoustical properties of a rough sea surface in a way that can be incorporated into sonic boom propagation models. The objective of this work is to develop models for the effective impedance spectra of rough-hard surfaces corresponding to different sea states. The specific impedance of seawater is greater than that of air by four orders of magnitude, therefore the sea surface is considered to be acoustically hard for atmospheric sound propagation. Although, in reality, the scattered field is not constant because the boundary is continuously in motion associated with winds and currents, the roughness is considered to be static so that the effect of the diffraction of sound waves by roughness may be modelled as an effective admittance. Several theories have been developed to describe the effective impedance of rough surfaces when the roughness scale is small compared to the acoustic wavelength. The boss theory due to Biot and Tolstoy models rough surfaces of finite impedance but does not account for incoherent scattering that was found necessary when comparing predicted results with measurements[2]. Twersky[3] developed a theory that incorporates an incoherent scattering term and his results were applied to model 2-D periodic and random hard

roughness which gave reasonable agreement with measured ground effect[4]. This model was heuristically extended to finite impedance roughness and gave good agreement with ground effect measured over rough indoor sand surfaces and outdoor ground[5]. This work shows that the impedance real part obtained from Twersky's theory for hard rough surfaces does not predict the low frequency limit that is expected from physical considerations. The method of effective impedance derivation from excess attenuation (EA) measurements is well established[6], and this work presents the novelty of identifying the impedance roots of the classical expression for the sound field due to a point source above a smooth impedance plane by a winding number integral method[7]. A Boundary Element Method (BEM) is used also to predict EA spectra that are compared with Twersky's theory and measurements. As with measured data, effective impedance spectra are deduced by the winding number integral method and the results are compared to Twersky's theory and measurements. The BEM has proved in the past to be an accurate model of sound pressure level prediction when compared to past experiments involving mixed impedance[8] and rough ground[4]. In this work, it proves again to be more versatile than the Twersky analytical model for effective impedance evaluation when a large range of parabolically shaped roughness sizes is considered together with a variety of incidence angles. Intersecting parabolas are chosen as the most realistic roughness profile to model a sea surface. The impedance real part obtained by varying Twersky's theory parameters to fit the BEM or measured data does not predict the low frequency limit that is measured and predicted by the BEM in the case of small roughness. As a result, empirical frequency dependent polynomial fits of BEM-deduced spectra are derived for the effective impedance evaluations corresponding to roughness profiles formed by intersecting parabolas and intended to model sea-waves. Four 6x5 matrices of coefficients are reported to model the effective impedance of six rough sea states in five cases of acoustic wave incident angle.

This paper is organized such that section II presents the geometry of the sonic boom propagation in shadow zones to justify the grazing incidence angles used in this work. Section III states relationships between wind speed and sea states as well as between sea wave-lengths and wave amplitudes. It also motivates the use of parabolically shaped roughness profiles. The two models that are used to estimate the attenuation of sound above hard rough surfaces are described in section IV. The Boundary Element Method is presented first and Twersky's boss theory that incorporates an effective impedance formulation is described next. The EA measurements as well as the Boundary Element calculations are used to derive effective impedances by searching for complex roots of the equation for the EA spectra due to a point source above an impedance plane. Section V describes the method to obtain the effective impedance for rough surfaces using a winding number integral with the measured or Boundary Element predicted EA. Section VI tests the validity of the model's predictions by comparing results with measured data for semi-cylindrical and wedge roughness. Polynomial fits of the BEM-deduced effective impedance are also presented. Sections VII.A-F show BEM EA and deduced effective impedance for six parabolically shaped roughness scales with five different grazing angles. The effective impedance fit-coefficients are shown to be dependent on both average roughness sizes and incidence angles and an interpretation is presented in section VIII.A-B. Section VIII.C gives a brief analysis of the inaccuracies in the effective impedance fit-coefficient estimations as well as an explanation for unexpected coefficient behaviour in the case <H>=1.5m. Section IX.A establishes the variation of the effective impedance plane height with average roughness height. and section IX.B, shows that

the computed effective impedance is very sensitive to excess attenuation fluctuations at low frequencies. Section IX.C shows that the fluctuations may be due to surface waves. Conclusions are drawn in section X.

II. GEOMETRY OF SONIC BOOM PROPAGATION

The boundaries of the primary sonic boom carpet are defined by the touch down of the direct grazing rays. This occurs because of refraction that can be caused by the effective sound speed decrease with altitude in the lower atmosphere. Beyond this boundary, the rays of secondary booms may touch the ground at any angle as illustrated in Figure 1. However, on the edge of the primary sonic boom carpet, some creeping waves may enter the shadow zone with an angle of incidence close to grazing.
Pierce[9] presents relationships between the half width $W_{1/2}$ of the sonic boom carpet, the Mach number M_g, the radius of curvature R_g of the grazing ray, the speed of sound at ground level c_g, the aircraft speed V_f and the flight altitude z_f.

$$W_{1/2} = \{(2 R_g z_f - z_f^2)[1-(1/M_g)^2]\}^{1/2} \quad (1)$$

with $M_g = V_f/c_g$. The expression is presented here with an extra factor z_f^2 that is missing in Pierce's paper. The radius of curvature R_g is equal to the height of apparent top of atmosphere Z_{top} based on a linear extrapolation of the sound speed beyond flight altitude. Let's compute a rough estimate of the half width of the sonic boom carpet. For a US standard Atmosphere without winds, Z_{top}= 88400m. Assuming a low flight altitude z_f=1000m, a Mach number M_g = 2, a speed of sound at ground level c_g=340m/s, the half-width of the sonic boom carpet is $W_{1/2}$ =11500m. For comparison, a flight altitude z_f=10000m, closer to a standard cruise altitude, implies a half width sonic boom carpet $W_{1/2}$=35400m.

III. SEA WAVES

We are seeking to characterise the acoustical properties of a rough air water interface by means of an effective impedance spectrum. To specify the physical profile of this water surface it is necessary to investigate some results from the field of oceanography. In this section, relationships between atmospheric conditions and the sea states and between wavelengths and wave heights are presented.

A. Relationships between wind speed and sea state

The generation of sea waves is a complex process that is not completely understood but two main mechanisms have been identified[10]:

1. The deflection of the wind as it blows over the wave profile causing dynamic pressure difference which can feed energy into waves
2. The wind-generated turbulence causes a moving pattern of pressure fluctuations, which, in turn, can generate waves.

Water waves are of great interest in underwater acoustics for sonar performance modelling[11] and Table 1 summarizes the measured root mean square (rms) wave heights with respect to the wind speed.
If the wave rms (m) and the wind speed (m/s) are denoted by h and w respectively, reference 11 presents the empirical relation $h = 0.019w^2$. This is plotted as the green

line in Figure 2 that summarises the various relationships between wind speed and wave heights available in the literature. The measured rms sea-wave heights are plotted as the red dots. The relation $H = 4.18\ 10^{-3}w^{5/2}$ is a metric version of the expression given by Fortuin[12] where H is the wave height. This expression, plotted as the blue line in Figure 2, is deduced from a Neumann-Pierson surface wave spectrum for a fully risen sea. Additional data reported by Thurman[13] for the highest 10% sea-waves are plotted as the yellow dots.

B. Relationships between water wave-lengths and wave heights

Another important aspect for the modelling of sea waves is the dependence between the wave heights and the wave-lengths. In addition to the highest 10% sea-waves plotted in Figure 2, Thurman[13] reports data on wave-lengths. It is important also to consider the shape of the water wave profile. Assuming a sinusoidal water wave of amplitude a, an empirical relation[14,15] between wave heights and wave-lengths gives the maximum limit $2a/\lambda \sim 0.14$ beyond which the waves break. In general the sea surface is irregular and does not undergo simple sinusoidal variations[16]. The wave crests are sharper and the wave troughs are flatter than in a true sinusoid. For the larger amplitude waves this effect becomes more marked with crests reaching a limiting 120deg angle corresponding to a wave slope of about 1/7 beyond which the waves break. The wave heights increase with distance from offshore (fetch). As fetch increases, the spectra become more narrow and more of the wave energy becomes concentrated in fewer frequencies. The wind feeds energy into the waves, and when energy is dissipated at the same rate, the spectra are then in a steady state. There are theories to predict the spectra of water wave-lengths with respect to weather conditions but they are not applicable to purely sinusoidal wave profiles. Other ocean surface profiles such as trochoids[17] have been used in the modelling of sonic boom penetration in the ocean, but they are basically a sum of sinusoids and have very rounded crests. Trochoids are far from realistic fully developed sea profiles with sharp crests.
On the basis of this brief summary of knowledge about water waves from the field of oceanography, profiles formed from randomly intersecting parabolas are chosen to model acoustically rough random surfaces. The resulting wave crests are sharper and the wave troughs flatter in parabolic waves than in sinusoidal profiles.

IV. THE ACOUSTIC MODELS

A. The Boundary Element model

The Boundary Element Method calculates the sound field at the boundaries of the volume that is considered, under the assumption of a homogeneous atmosphere. With the solution known at the arbitrary boundary, the sound field can be calculated at any point using analytical formulas for sound propagation in homogeneous air.
Chandler-Wilde[18,19] has developed a boundary integral equation method to evaluate the solution of the Helmholtz equation for the pressure at the receiver as:

$$P(\mathbf{r},\mathbf{r}_0)=G_\beta(\mathbf{r}_0,\mathbf{r})+\int_\gamma\left\{\frac{\partial G_\beta(\mathbf{r}_s,\mathbf{r})}{\partial n(\mathbf{r}_s)}-ik\beta(\mathbf{r}_s)G_\beta(\mathbf{r}_s,\mathbf{r})\right\}P(\mathbf{r}_s,\mathbf{r}_0)ds(\mathbf{r}_s) \quad (2)$$

where $P(\mathbf{r},\mathbf{r}_0)$ is the pressure at the point $\mathbf{r}$ when the source is at $\mathbf{r}_0$. The integral extends over the ground surface γ which is either the part of the surface lying above the horizontal or the part of the boundary with a normalized surface admittance $\beta(\mathbf{r}_s)$ different from β. $G_\beta(\mathbf{r}_0,\mathbf{r})$, the Green's function for the Helmholtz equation in a half plane with impedance boundary condition, can be calculated analytically and represents the pressure at $\mathbf{r}$ when the source is at $\mathbf{r}_0$ with the boundary in a horizontal plane of constant admittance β. $G_\beta(\mathbf{r},\mathbf{r}_0)=G_0(\mathbf{r},\mathbf{r}_0)+P_\beta(\mathbf{r},\mathbf{r}_0)$ is expressed in terms of the Green's function corresponding to a flat hard surface (β=0) $G_0(\mathbf{r},\mathbf{r}_0)=-(i/4)H_0^{(1)}(kR)-(i/4)H_0^{(1)}(kR')$, with R = $|\mathbf{r}-\mathbf{r}_0|$, R' = $|\mathbf{r}-\mathbf{r}_0'|$ and in terms of an additional expression for a surface of general admittance β, $P_\beta(\mathbf{r},\mathbf{r}_0)=\frac{i\beta}{2\pi}\int_{-\infty}^{+\infty}\frac{\exp\left(ik\left((y+y_0)(1-s^2)^{1/2}-(x-x_0)s\right)\right)}{(1-s^2)^{1/2}\left((1-s^2)^{1/2}+\beta\right)}ds$. The Green's function for cylindrical wave source giving the pressure above the horizontal plane with constant admittance β=0 (hard ground) is the Hankel function of first kind and order zero of the distance. The Green's function for the general case (non-zero admittance β) is evaluated asymptotically in the far field (kr>>1) using a steepest descent method. The boundary integral equation is solved approximately by assuming a constant pressure value in each boundary element of the ground surface using the (point) collocation method. This consists in approximating the solution by weighted residuals and setting the residual function to zero at a series of points. These equations for each point plus the discretization of the integral equation give a system of equations whose dimension is the number of collocation points. It is possible to model either a flat or profiled ground surface since the discretizing points can be chosen out of the horizontal plane. An equivalent two-dimensional problem can be solved in order to save computation time. The code is two-dimensional in the sense that only ground and sound sources can be modelled that show no variation along one axis. Source, receiver and specular point are assumed to be in a vertical plane perpendicular to the roughness axis, and a line integral is solved instead of a surface integral. The acoustic impedance can be chosen independently for each surface element of the profile.

The BEM is used to predict sound levels over rough surfaces by including the roughness profile in the form of node coordinates input to the program. To model the rough surface correctly, it is necessary to use boundary element lengths that are smaller than the smallest segment between two nodes. A second constraint, for accurate use of the boundary element technique, is the need to choose boundary element lengths no more than one fifth of the wave-length. The first and second constraints govern computation times at low frequencies and high frequencies respectively. In all of the acoustical models used in this work, the hard surfaces are modelled with an admittance β=0.

In this work, the BEM is considered as the reference to which other model's results are compared. The draw back of such a numerical model is that it may not give much insight into the physical phenomena involved in the sound reflection or scattering process.

B. Twersky's theory

Twersky has developed a boss model[3] to describe coherent reflection from a hard (or pressure release) surface containing semi-cylindrical or semi-elliptical roughness in which the contributions of the scatterers are summed to obtained the total scattered field. Sparse and closely-packed distributions of bosses have been considered and interactions between neighbouring scatterers have been included. His results lead to a real part of the effective admittance of the rough hard surface which may be attributed to incoherent scattering.

Consider a plane wave incident on an array of semi-cylinders of radius a and mean centre-to-centre spacing b on an otherwise plane hard boundary (See Figure 3 and Figure 4). The angle of incidence with respect to the normal is α and the azimuthal angle between the wave vector and the roughness axes is φ.

Twersky's result for the effective admittance β relative to air of a rough hard surface (zero admittance of the rough material) containing randomly spaced 2-D circular semi-cylinders is

$$\beta = \eta - i\xi. \tag{3}$$

where

$$\xi(\alpha,\varphi) \approx kV\left[-1+\left(\delta\cos^2(\varphi)+\sin^2(\varphi)\right)\sin^2(\alpha)\right]+O(k^3) \tag{4}$$

$$\eta(\alpha,\varphi) \approx \frac{nk^3\pi^2a^4}{8}(1-W)^2\left\{\left(1-\sin^2\alpha\sin^2\varphi\right)\left[1+\left(\frac{\delta^2}{2}\cos^2\varphi-\sin^2\varphi\right)\sin^2\alpha\right]\right\}+O(k^5) \tag{5}$$

Note that the expression for η in reference 4 presents a typo, the square is applied to the term W instead of being applied to the term $(1-W)$ as shown above. The term $V = n\pi a^2/2$ is the raised cross sectional area per unit length, n is the number of semi-cylinders per unit length (= $1/b$), $\delta = \dfrac{2}{1+I}$ is a measure of the dipole coupling between the semi-cylinders, $I = \dfrac{a^2}{b^{*2}}I_2$ (note that the definition of I in reference 4 presents the typo of showing b in the denominator rather than the correct b^*) where

$$I_2 \cong 2W\left(1+0.307W+0.137W^2\right) \qquad \text{for } W<0.8,$$

$$I_2 \cong \frac{\pi^2}{3}\left[1-\frac{2(1-W)}{W}\right]+6\frac{(1-W)^2}{W^2}\left[\frac{\pi^2}{6}+1.202\right] \qquad \text{for } W \geq 0.8$$

$$I \cong \frac{(\pi a)^2}{3b^2} \qquad \text{for } W = 1 \text{ (periodic)},$$

$(1-W)^2$ is a packing factor introduced for random distributions, $W = nb^* = \dfrac{b^*}{b}$, b^* is the minimum (centre-to-centre) separation between two cylinders and $k=2\pi f$ is the wave number with f the frequency.

According to Lucas and Twersky[3], for semi-elliptical cylinders with ratio K of the major (Ka) and minor (a) axes (note that K is erroneously defined as the eccentricity

in reference 4), such that $V = n\pi a^2 K / 2$, the dipole coupling between the semi-cylinders is $\delta = \dfrac{1+K}{1+I\dfrac{K(1+K)}{2}}$.

In this work, the source height h_s, n, Ka, a and b^* are varied to obtain the best least square fit with the effective impedance obtained from BEM predictions or from measured data.

The frequency dependence of the admittance, $\beta = \mathrm{Re}(\beta) + i\,\mathrm{Im}(\beta)$, is given by $\mathrm{Re}(\beta) = \chi f^3 + O(f^5)$ and $\mathrm{Im}(\beta) = \gamma f + O(f^3)$ where χ is a positive coefficient and the sign of the coefficient γ depends on the semi-width/height of the semi-elliptical cylinders but is mostly negative for roughness close to semi-cylindrical shape. When f goes to zero, $\mathrm{Re}(\beta)$ decreases much faster than $\mathrm{Im}(\beta)$ and Z tends to ∞ as $-i/(\gamma f)$. This implies that, when f goes to zero, $\mathrm{Re}(Z)$ tends towards the x-axis and $-\mathrm{Im}(Z)$ goes to $-\infty$. This result is confirmed by the effective impedance graphs presented in section VI. In order to obtain the expected asymptotic behaviour of Z (Infinite Re(Z)), one needs to have the first term of the $\mathrm{Re}(\beta)$ expansion dominating the first term of the $\mathrm{Im}(\beta)$ expansion. Therefore, a more general version of Twersky's work that includes absorption of acoustic energy in porous roughness will be presented in future work. This more achieved version of the theory will allow modelling of ground surfaces with finite impedance roughness by introducing a term proportional to f in the $\mathrm{Re}(\beta)$ expansion.

V. EFFECTIVE IMPEDANCE OBTAINED FROM MEASURED AND BEM-BASED EXCESS ATTENUATION

A. Computation method for excess attenuation

The excess attenuation (EA), which is the attenuation of the sound wave in excess of that from spherical spreading, is defined from both models and from measurements by:

$$EA = 20\log\left|\frac{P}{P_1}\right| \tag{6}$$

where the direct wave is estimated for both models by

$$P_1 = P_0\frac{\exp(ikR_1)}{R_1} \tag{7}$$

The total pressure P for the model based on Twersky's theory is computed from

$$P = P_0\frac{\exp(ikR_1)}{R_1} + QP_0\frac{\exp(ikR_2)}{R_2} \tag{8}$$

The total pressure P for the BEM is computed from equation (2) and the distances R_1 and R_2 are shown in Figure 5. The model based on Twersky's theory incorporates the spherical wave reflection coefficient defined by: $Q = R + B[1-R]F(w)$ where the coefficient B takes into account the phase changes upon reflection from a complex impedance surface. $B \sim 1$ for a locally reacting surface that is typical of outdoors. B has a more complex form[20] in the case of extended reaction and depends on the

incidence angle. The plane wave reflection coefficient is defined by: $R = \frac{\cos(\theta) - \beta}{\cos(\theta) + \beta}$

and $F(w) = 1 + i\sqrt{\pi} w e^{-w^2} erfc(-iw)$ with $w = \sqrt{\frac{1}{2} ikR_2} \left(\beta + \cos\theta\right)$

where $F(w)$ is the sphericity factor arising from the need to match the curved wave front to a plane boundary. w is often referred as the "numerical distance", and represents the propagation distance scaled by the impedance Z. As w increases, the wave front becomes more planar and $F(w)$ decreases. w has a more complex form in the extended reaction case. In the case of Twersky's theory for semi-cylindrical rough surfaces, the effective admittance β relative to air used in the above expressions for R and w is obtained from equations (3)-(5) for hard roughness.

B. Effective impedance from BEM-computed or measured excess attenuation

1. The admittance root equation

The excess attenuation evaluated from the BEM with equations (2),(6) and (7) or from measurements with equations (6) corresponds to the attenuation due to the interference between the direct wave, the rough surface reflected wave and a possible surface wave. The method used here to estimate the effective impedance relative to air of such a rough surface is to consider that the EA predicted by the BEM (or measured) is produced by a flat surface of effective admittance relative to air β_{ef}. Use is made of the classical expression for the sound field due to a point source above an impedance boundary. This expression is sometimes referred to as the Weyl van der Pol expression after the originators of the equivalent formula for electromagnetic wave propagation. The problem becomes a search for complex β_{ef} roots of the following equation (9)

$$1 + \frac{R_1}{R_2} e^{ik(R_2 - R_1)} \left\{ \frac{\cos\theta - \beta}{\cos\theta + \beta} + \left(1 - \frac{\cos\theta - \beta}{\cos\theta + \beta}\right) \left(1 + i\sqrt{\pi} \sqrt{ikR_2/2} (\beta + \cos\theta) e^{-\left(\sqrt{ikR_2/2}(\beta + \cos\theta)\right)^2} erfc(-iw(\beta)) \right) \right\} - \frac{P}{P_1} = 0$$

This equation is to be solved for each frequency point, for input values of R_1, R_2, $\cos\theta$, P and P_1, but does not have a readily available analytical solution, so numerical methods have to be sought. Two widely used numerical methods for root finding of complex variables equations have been implemented in this work. The Newton Raphson method may be one of the most popular in the literature but produces only one root per frequency point. It has been reported[6] previously in effective impedance estimations and was tested in this work. The second common method based on Müller's work is found in the IMSL library routine "ZANLY" and is limited to two roots for each frequency point. The weakness of these two methods which is true also for all methods of this type is that, if several existing roots are in the same complex admittance neighbourhood for a given frequency, the single-root methods may pick up a root belonging to another root spectrum and follow that other set for subsequent frequencies, giving therefore mixed root spectra in the end. This was observed in several test cases. To avoid this problem, a third more thorough root search method based on winding number integral was developed.

2. *The winding number integral method*

This root search method, seldom implemented in the acoustical literature, uses the winding number integral, which is a contour integral around a closed path in the complex plane, to determine the presence of zeros and poles in the enclosed area. Having determined that a closed area in the complex plane contains roots, the location of those roots can be deduced with a high degree of accuracy by using higher moments of the winding integral. The method is described by Brazier –Smith et al.[7] where it is applied to the determination of the roots of dispersion equations. A summary of the method follows.

Let's assume that the roots of a function F, analytic everywhere inside a closed contour Γ, are sought. The difference between the number of zeros n_Z and the number of poles n_P of F inside Γ can be computed from the winding integral.

$$\frac{1}{2\pi i}\oint_{\Gamma}\frac{F'}{F}dz = n_z - n_p \tag{10}$$

where the complex integral can be evaluated by the winding number of F(Γ) around the origin in an anticlockwise path noted by

$$n_Z - n_P = \mathrm{Wnd}(F(\Gamma),0). \tag{11}$$

Once the image of the closed contour Γ is computed by the function F it is simple to divide the path into a series of chords and examine whether each cord takes Ln(F) across the negative real axis. If it crosses from above, the winding number is increased by 1, and, if from below, reduced by 1.

When the number of zeros inside a contour is established, the roots need to be identified. This study will consider the search of roots two at a time in a contour, therefore only the first two moments of the winding integral are required. The moment of order n is given by:

$$I_n = -\frac{1}{2\pi i}\left\{\left[z^n \ln F\right] - n\oint_{\Gamma} z^{n-1}\ln F dz\right\} = \sum_i \left(z_z^i\right)^n - \sum_j \left(z_p^j\right)^n \tag{12}$$

where z_z^i is the location of the ith zero and where z_p^j is the location of the jth pole. Equation () shows only one pole for $\beta = -cos(\theta)$ therefore the expressions for the moments are simplified and contain only z_z^i in most of the complex plane. When the winding number is equal to 1, the single zero is given by I_1 and when the winding number is equal to 2, the two zeros are determined by the roots of the quadratic equation

$$z^2 - I_1 z + 0.5(I_1^2 - I_2) = 0 \tag{13}$$

Let's note that when 3 roots are sought at a time, the third moment of the winding number integral is needed. The cubic equation given in equation (9) of reference 7 presents an error, the constant term $-(I_1^2)/6$ should really be $-(I_1^3)/6$.

The integral shown in equation (12) is computed numerically with a Riemann sum. Great care has to be exercised when computing the function $Ln(F)$ because Ln is not analytical across the negative real axis and the argument F of Ln might cross this branch cut. This potential discontinuity problem with $Ln(F(z))$ is solved using an analytical continuation of Ln across the branch cut. Thus instead of considering Ln as a simple function, it is viewed as a family of Ln functions each defined on a separate Riemannian sheet. This allows the continuity of the $Ln(F(z))$ family function at each branch cut. A branch cut is then viewed as a seam between two successive Riemannian sheets. Practically, this means that instead of considering $Ln(F)$ as the

function with argument θ only such that $-\pi<\theta<\pi$ (as FORTRAN does) and getting a discontinuity when θ increases beyond π (because FORTRAN comes back to $-\pi$), one requires that the argument of *Ln* increases by 2π. Therefore, when $\mathrm{Arg}(F(z))=\theta$ increases n times beyond π, $\mathrm{Arg}(F(z))=\theta + 2n\pi$, and $Ln(F(Z)) = Ln|F(z)| + i\mathrm{Arg}\{F(z)\} + 2n\pi i$. When applied to a function F of known roots the relative error of the winding integral method is found to be on the order of 10^{-6} for the real and imaginary parts of the first moments I_1 in single precision. The relative error of the winding integral method is greater and on the order of 10^{-3} for the second moments I_2. In general, the relative calculation errors of the moments I_n increase with the order n. When applied to the admittance root equation (9), the method uses a series of square contours Γ in which the roots are searched. The square is the most convenient and efficient geometrical shape with which to cover the β-plane in the areas of interest. If more than 2 roots are detected with the winding number count inside each square contour Γ, a smaller contour must be chosen.

An important constraint to the method's computer time is the number of points N used to discretize a given contour size. This number is crucial as it determines also the relative error of the numerical integration used to evaluate the first and second moments I_1 and I_2 of the winding integral on which are based the calculation of the roots. If N is too small, the estimation of the root values is so approximate that they do not verify the conditions of a root $F(z)=0$. It was found that 2^N points with N=12 for a square contour 2x2 would give a relative error of 0.01 on known roots of a test function. As a consequence, a series of small 2x2 square contours is chosen to cover the search area. As an example of computer run time, on a 800MHz processor it takes 10 minutes to run a root search for one frequency point in an array 1000x100 using 2x2 square contours. A frequency loop to search for admittance roots over the whole frequency spectrum was implemented in the code.

The winding number integral method is more computationally intensive than the usual Newton-Raphson or Müller's method but is more powerful as it computes all the roots in a chosen complex plane area. It allows complete root searches when the classical methods fail to converge and it leads us to conclude that for some roughness profiles there are frequency ranges with only negative real effective impedance roots. Possible reasons for this unphysical behaviour are presented in section IX.B-C. The method chosen to avoid this difficulty consists in computing several BEM EA spectra corresponding to various roughness profiles and to evaluate the effective impedance relative to air from the averaged complex EA above a raised smooth ground plane. The following section will develop the details of the method and the results will be compared to measurements made above arrays of 2-D random hard semi-cylinders and above wedge roughness profiles.

VI. RESULTS FOR HARD RANDOMLY SPACED 2-D ROUGHNESS

In the following, d denotes the source-receiver separation distance, h represents the (equal) source and receiver heights, h_{eff} is the effective source and receiver height, l is the semi-cylinder diameter and Z is the impedance. The experimental procedure has been described in detail in other work[4] and results only are reported here.

A. Excess attenuation and effective impedance results for small hard

randomly spaced semi-cylinders

The measurements and BEM predictions concern profiles formed by 20 hard semi-cylinders with l=0.0135m, d=1m and h=0.1m. Since the measured data and BEM predictions of excess attenuation spectra are rather sensitive to the roughness condition at the point of specular reflection between source and receiver, data and predictions are averaged over several random distributions. The averaging process can be justified by the fact that the roughness profile at the specular reflection point will vary with time during the propagation of the boom and will vary also with location due to randomness of the sea surface. The averaged BEM prediction (Figure 6.b) compares favourably with averaged measured data (Figure 6.a) for the excess attenuation spectra. It should be noted that the measured data are unreliable below 700Hz as a result of the limited frequency response of the loudspeaker used in the measurements.

The winding number integral method results in only unphysical negative real impedance roots to equation (9) for some frequency points when using the nominal ground plane height with BEM predictions. The results are improved when the effective impedance is computed with a ground plane effective height set to the top of the random roughness (h_{eff}=0.093m). Raising the effective impedance plane above the lowest point in the roughness profile has been suggested before[21,22] and is applied in all effective impedance calculations from BEM predictions. Subsequently, any negative Re(Z) is set to zero. The latter step produces very little discrepancy between the nominal and deduced EA. The effective impedances deduced from measured data and BEM predictions are shown in Figure 7.a and Figure 7.b respectively. The predictions resulting from a 5-parameter least-square fit with the Twersky's theory (relations (4)-(5)) are shown as the dashed cyan and continous magenta lines for Re(Z_{eff}) and Im(Z_{eff}) respectively. Polynomial fits $\alpha f^{-1}+\delta$ and $\alpha' f^{-1/2}+\delta'$ are shown also as the black-dashed and black-solid lines for Re(Z_{eff}) and Im(Z_{eff}) respectively. The forms of these polynomial expressions are empirical. They resemble the 2-parameter model for the surface impedance of rigid porous ground in which the porosity decreases with depth[23,24,25]. In the two-parameter model the real part is proportional to $1/\sqrt{f}$ and the imaginary part contains terms proportional to $1/\sqrt{f}$ and $1/f$. The form of the fit-polynomials for the effective impedance of hard rough surfaces were chosen to be as simple as possible and to ensure that the real part dominates at low frequency consistent with the BEM results and as expected from physical considerations.
The effective impedance obtained from measured data agrees fairly well with the BEM results in the frequency range 700Hz-7000Hz for the real part and in the frequency range 2000Hz-7000Hz for the imaginary part. Note that an unexpected resonance is obtained from measurements at 8000Hz. Such high frequency resonance is seen frequently in measured complex EA available for small roughness and in BEM predictions of the effective impedance for surfaces with parabolically-shaped roughness. The resonance magnitude in BEM predictions is found to depend on the location of the effective impedance plane but no clear explanation of their cause is available at this point. As mentioned in section IV.B.1, the low frequency Twersky theory predictions of the real part of effective impedance tend toward zero although infinitely increasing values are expected and predicted by the BEM. The values of the Twersky least square fit parameters found for the BEM predictions and measured data are summarized in Table 3. The values of the polynomial fit coefficients for the small semi-cylinder cases studied are summarized in Table 4.

B. Excess attenuation and effective impedance results for larger hard randomly spaced semi-cylinders

The measurements and BEM predictions in Figure 8 are for a hard surface profile including twelve randomly-spaced semi-cylinders with l=0.04m, d=1m and h=0.1m. There is good agreement between the BEM-calculated EA magnitude and measured data.

The effective impedance computed from the measured and BEM Excess Attenuation data are shown in Figure 9.a and Figure 9.b respectively. The results of a 5-parameter least-square fit using Twersky's theory for hard roughness is shown as the cyan-dashed and magenta-solid line. Polynomial fits $\alpha f^{-1}+\delta$ and $\alpha f^{-1/2}+\delta$ are shown also as the black-dashed and black-solid lines for $\mathrm{Re}(Z_{eff})$ and $\mathrm{Im}(Z_{eff})$ respectively. The effective impedance obtained from measured data agrees fairly well with the BEM results in the frequency range 1000Hz-3000Hz for the real part, and in the frequency range 1000Hz-6000Hz for the imaginary part. The measured data are not reliable below 700Hz, and an unexpected resonance is obtained from measurements at 7000Hz. The polynomial fits for imaginary parts do not appear close to the data they are fitting. This is due to the frequency dependence that seems under-predicted by the one half power of the fit in this case. As mentioned in section IV.B.1, the low frequency predictions of the Twersky effective impedance real part are seen to tend toward zero although infinitely increasing values are expected and predicted by the BEM. The values of the Twersky least square fit parameters found for the two roughness sizes and from the BEM prediction and measured data are summarized in Table 5. The values of the polynomial fit coefficients for the large semi-cylinder cases studied are summarized in Table 6.

C. Excess attenuation and effective impedance results for triangular wedge roughness

The measurements and BEM predictions are for profiles formed by random distributions of 15 hard rods with triangular cross section. The base and height of the triangle are 0.03m and 0.015m respectively. The source receiver geometry are given by d=1m and h=0.1m. The averaged excess attenuation spectrum from BEM prediction (Figure 10.b) compares favourably with averaged measured data (Figure 10.a). It should be noted that the measured data are unreliable below 400 Hz

The effective impedance computed from the measured and BEM Excess Attenuation data are shown in Figure 11.a and Figure 11.b respectively. A polynomial fit is shown also as the black-dashed and black-solid line. The results of a 5-parameter least-square fit using Twersky's theory is shown as the cyan-dashed and magenta-solid line. The agreement between effective impedance obtained from measured and predicted data is good for frequencies in the range 400-8000Hz. The values of the Twersky least square fit parameters found for the two roughness sizes and from the BEM prediction and measured data are summarized in Table 7. The values of the polynomial fit coefficients for the measured and predicted wedge roughness cases are summarized in Table 8. Due to the poor results obtained with Twersky's theory effective impedance for hard roughness at low frequency, only the BEM is used to predict sound levels over larger parabolic rough profiles (modelling sea waves) from which effective impedance spectra are deduced and fitted with polynomials.

VII. PARABOLIC ROUGHNESS RESULTS

As discussed in section III, random parabolic profiles are chosen to model acoustically-hard, rough random surfaces corresponding to the various sea states. The height H and wavelength λ of the parabolic roughness are related by the ratio H/λ=0.1 chosen to be below the upper value 0.14, beyond which the water waves break.
The following random parabolic wave surfaces are generated using a random number generator constraining the height of the parabolas in a chosen range. The method chosen in this section to evaluate effective impedance spectra and their dependence on geometrical and roughness profile parameters is summarised as a flow chart in Figure 12. The excess attenuation and effective impedance fit results are presented in increasing order of average roughness height.

A. Average roughness height <H>=0.25m

Examples of random-height parabolic roughness profiles are generated with roughness heights in the range [0.1m-0.4m] in Figure 13. The source-receiver separation distance is 8m (as in all of the simulations presented in section VII.A). The discretization step of the parabolic roughness is chosen to be one-third of the smallest roughness wave-length, i.e. 0.3m. Let's recall that the parabolic roughness length is chosen to be 10 times the roughness height. The length of rough ground modelled is limited to wr=20m to keep BEM run time for the whole spectrum under 20 minutes on a Pentium III processor. The rough surface is extended on each side of source and receiver by a 90m flat hard surface to avoid edge effect, so that the total modelled surface length is w=200m.
For each average roughness height, the excess attenuation and effective impedance fit results are ordered by increasing grazing angle measured from the horizontal in radian. First it is necessary to consider the meaning of angle of incidence on a randomly-rough surface. It should be noted that the choice of horizontal plane from which the incident angle is evaluated is arbitrary as the surface is rough. The apparent angle of incidence depends on the points of the profile being considered. The reference plane from which the incidence angle is evaluated in this work is chosen at the average roughness height. For example, the incidence angle for the source height h=0.93m, the average roughness height <H>=0.25m and the propagation distance d=8m is obtained using arctan(2(0.93-0.25)/8)=0.17rad. All geometries used with the various roughness profiles studied in this work require that the source and receiver are in line of sight in order to obtain a non-zero direct wave since the excess attenuation is based on the ratio of total pressure wave over direct pressure wave. Note that the lowest incident angle of the series (for h=0.3m) is already below the lowest limit (h=0.4m) that would ensure, with any random profile 0.1m<H<0.4m, that no roughness could be higher than the source-receiver and prevent line-of-sight. Despite this, the case is reported anyway because, in the five roughness profiles used for the average, no roughness greater than the source was found to shadow the receiver from the source. The source height limitation explains why no grazing angle smaller than 0.012 rad is reported with the chosen randomly generated roughness profiles heights. BEM excess attenuation spectra are predicted for grazing incidence angles 0.012, 0.04, 0.065, 0.17 and 0.23 radians The example of grazing incidence angle 0.012 radian (h=0.3m) is presented in Figure 15(a) while the corresponding effective impedance spectrum and associated polynomial fit is shown in Figure 15(b). Comprehensive reports on EA and effective impedance spectra for all the roughness

scales and geometries studied in this work are published elsewhere[26, 27] and only the main results are presented here. When δ is not shown in the legend of the impedance graph, it indicates that the fit for the real part of effective impedance is obtained with αf^{1} only. Even if negative δ would give a better fit it is not permitted since it would lead to negative real impedance at high frequencies. The frequency range used for the polynomial impedance fit computation is shown in the legend. The angle dependence of the fit coefficients α (or α') and δ (or δ') are represented by circles and error bars in Figures 16 and 17 respectively. The error bars indicate the inaccuracies inherent to the method. The sources of inaccuracies are presented and estimated in section VIII.C. The angle dependent fit-coefficients $\alpha(\theta)$, $\alpha'(\theta)$, $\delta(\theta)$, $\delta'(\theta)$ and their error bars are visually fitted with Gaussians (continuous lines) of the type $\gamma+\gamma_m\exp[-\theta^2/\sigma]$ where γ, γ_m and σ are parameters varied for best fit. Figure 16 shows the particular case of a Gaussian fit with semi-width $\sigma=\infty$ indicating that the best fit is an horizontal straight line. Figure 15(b) reports results obtained from both the real (α, δ) and imaginary part (α', δ') of the effective impedance. Because of the definition of the polynomials used in the effective impedance fits, the coefficients α for $\mathrm{Re}(Z_{eff})$ have units of Hz^{-1}, the coefficients α' for $\mathrm{Im}(Z_{eff})$ have units of $\mathrm{Hz}^{-1/2}$, while δ and δ' are dimensionless. α and α' do not have homogeneous units and can not be compared directly, indeed, α has to be divided by $f^{1/2}$ to be compared to α'. Using the 100Hz lower frequency bound of most of the fits for this roughness size, a conversion factor 1/10 applied to α allows comparison with α', and the resulting value $\alpha/10$ appears to be of the same magnitude as α'. Both α and α' show constant values around $2500\mathrm{Hz}^{-1}$ and $175\mathrm{Hz}^{-1/2}$ respectively for varying incidence angle. Using f=100Hz to compare αf^{1} with δ results in a value $\alpha f^{1}\sim 25$ about two times greater than the highest values of δ or δ'. The fit coefficients $\delta(\theta)$ and $\delta'(\theta)$ show a general decrease with increasing incidence angle

B. Average roughness height <H>=0.4m

BEM excess attenuation spectra are computed along with effective impedance and polynomial fits for incidence angles 0.02, 0.04, 0.065, 0.17 and 0.23 rad. The angle dependence of the fit coefficients α (or α') and δ (or δ') are presented (circles and error bars) in Figures 18 and 19 respectively together with Gaussian fits (continuous lines). These results show that the coefficients α and α' decrease with incidence angle. The coefficients δ tend to decrease with increasing incidence angle, while the coefficients δ' show values 0 ± 2. Note that the fitted horizontal line y=0 does not intersect the small error bars that have been assumed proportional to the coefficient values (see section VIII.C). These results may indicate that this assumption may not be appropriate for small values of coefficients.

C. Average roughness height <H>=0.6m

BEM predicted excess attenuation are computed along with effective impedance and polynomial fit results for incidence angles 0.02, 0.04, 0.065, 0.17 and 0.23 rad. The angle dependence of the fit coefficients α and δ are presented (circles and error bars) in Figures 20 and 21 respectively together with corresponding Gaussian fits (continuous lines). The coefficients α are seen to decrease with increasing incidence angle while the coefficients α' are fairly constant. The coefficients δ and δ' present an overall decrease with increasing incidence angle.

D. Average roughness height <H>=1.5m

BEM predicted excess attenuation is presented in Figures 22(a)-26(a) along with effective impedance and polynomial fit results in Figure 22(b)-26(b) for incidence angles 0.02, 0.04, 0.065, 0.17 and 0.23 rad respectively. The imaginary parts of effective impedances in Figures 25(b) and 26(b) give unrealistic high-frequency asymptotic behaviour when fitted with coefficients δ'. The range 100-300Hz is dominant in these fits and δ' is unrealistically highly negative, therefore $\delta'=0$ is imposed. The angle dependence of the impedance fit coefficients α (or α') and δ (or δ') are presented (circles and error bars) in Figures 27 and 28 respectively together with corresponding Gaussian fits (continuous lines). The fit-coefficients α are seen to increase with the first three angles and decrease afterward while the fit-coefficients α' are fairly constant. Both δ and δ' are found to decrease with increasing angle except for the lowest angle in the case of δ'.

E. Average roughness height <H>=3.5m

BEM predicted excess attenuation spectra are computed along with effective impedance and polynomial fit for average roughness height <H>=3.5m and for incidence angles 0.02, 0.04, 0.065, 0.17 and 0.23 rad. The imaginary part fits of the effective impedance for angles 0.04rad and 0.065rad give unrealistic high-frequency asymptotic behaviour as a result of the apparent resonance. Fits that avoid highly negative values for δ', i.e. $\delta'=0$ are chosen. The angle dependence of the fit coefficients α (or α') and δ (or δ') for <H>=3.5m is presented (circles and error bars) in Figures 29 and 30 respectively together with Gaussian fits (continuous lines). These results show coefficients α, α', δ and δ' decreasing overall with increasing incidence angle.

F. Average roughness height <H>=7.5m

BEM predicted excess attenuation are computed along with effective impedance and polynomial fit for average roughness height <H>=7.5m and incidence angles 0.02, 0.04, 0.065, 0.17 and 0.23 rad. The angle dependence of the fit coefficients α (or α') and δ (or δ') for <H>=7.5m are presented (circles and error bars) in Figure 31 and 32 respectively together with Gaussian fits (continuous lines). Generally, the coefficients α, α' and δ are seen to decrease with increasing incidence angle while δ' is constant.

G. Impedance-fit-coefficient values and Gaussian angle dependence parameters

The matrices of the fit coefficients α, α', δ and δ'obtained for the five incidence angles and six roughness scales are summarized in Tables 9-12 respectively.
As only five angle dependent values are obtained for each of the fit-coefficients $\alpha(\theta)$, $\alpha'(\theta)$, $\delta(\theta)$ and $\delta'(\theta)$, the data points and their error bars are successfully fitted by Gaussians of the type $\gamma+\gamma_m\exp[-\theta^2/\sigma]$, where γ, γ_m and σ are the Gaussian fit parameters varied to obtain the best visual fit with the 'data' points, and their values for best fit are summarized in tables 13-15. Note that the Gaussian fits allow extrapolation of the fit coefficients to angle values near to zero, and that in few cases,

the best fit is obtained with a straight horizontal line ($y=\gamma_m$) i.e. a Gaussian with infinite semi-width ($\sigma=\infty$).

VIII INTERPRETATION AND DISCUSSIONS

A. Angle dependence of fit coefficients at constant average roughness height

The incidence angle and roughness size dependence of fit coefficients α and α' are summarized in the 3-D Figures 33(a) and 33(b) respectively. These results based on the Gaussian best fits show (as expected from the Gaussian angle dependence) that the coefficients $\alpha(\theta)$ and $\alpha'(\theta)$ are either nearly constant or decrease with increasing incidence angle. The incidence angle and roughness size dependence of fit coefficients δ and δ' are summarized in the 3-D Figures 34(a) and 34(b) respectively. As for the coefficients $\alpha(\theta)$ and $\alpha'(\theta)$ these results show coefficients $\delta(\theta)$ and $\delta'(\theta)$ either nearly constant or decreasing with increasing incidence angle. It should be noted that the values of δ do not have as great an influence as values of α at low frequencies. These results are consistent with the expected decrease of the effective impedance (and hence the fit coefficients) of a rough hard surface with increasing grazing angle for a given mean roughness height.

B. Roughness-height dependence of fit coefficients at constant incidence angle

Figures 33(a) and (b) show that for a constant high grazing incidence angle (θ=0.17-0.23rad) the coefficients α and α' generally decrease with increasing average roughness height while for the low grazing incidence angles studied (θ=0.02-0.06rad), the maximum values are found for roughness heights <H>=0.4m. As α (or α') governs the effective impedance at low frequency, it is expected that its values should be greater for small roughness heights as the wave-length is much greater than the roughness size, and therefore the effect of the surface is nearer that for a smooth hard surface. When the roughness size increases and becomes comparable to the larger acoustic wave-lengths (at low frequency) it is expected that the effect of the rough surface will be larger and depart most from that of a smooth hard surface. This is in general consistent with Figure 33(a) and (b) where the coefficients α and α' are found to decrease with increasing roughness sizes except for the smallest roughness at the smallest grazing angles. It is difficult to explain why the rough surface appears harder at low frequency and at grazing angle 0.02rad for 0.4m roughness than for 0.25m roughness (α[0.4m]>α[0.25m]).

The fit coefficients δ and δ' summarized in Figures 34(a) and (b) respectively show a tendency to decrease with increasing average roughness height at constant incidence angle. In other words, the high frequency effective impedance decreases with increasing roughness heights. This is expected for small wave-lengths impinging on even smaller roughness, the surface effect being similar to that of a hard surface. When the roughness size increases and becomes on the order of the wave-length, scattering effects come into play and the effective impedance decreases. The coefficients δ and δ' do not vary as monotonically as the α and α' at constant incidence angle due to the increased effective impedance fit uncertainty created by the apparent high frequency resonance peaks. Since the impedance is dominated by the α (or α'), the small departures from monotonic trend in the δ (or δ') are not particularly important except for very high frequencies

Overall, the effective impedance fit coefficients show clear monotonic variations with incidence angle and average roughness heights. The local non-monotonic variations result from uncertaintes in the fit coefficient values due to the method followed to estimate the effective impedance. The local non-monotonic coefficient variations with angle dependence at constant average roughness height have been removed by the use of the Gaussian best fits. However, local non-monotonic variations with average roughness heights at constant incidence angle remain. Inaccuracies in the effective impedance coefficient values result from (a) the frequency range given emphasis for the fits and (b) the dependence on the five rough surface realizations used in the BEM simulations. A brief analysis of these two factors is given in the next section.

C. Inaccuracies in estimating effective impedance fit coefficients

1. Effect of the fitted frequency range

Figure 35 shows the effect of a variation in the frequency range fitted on the values of fit coefficients α and δ (real part of impedance only) for the case $\langle H \rangle$=0.4m, h=0.65m, θ=0.065rad. In principle, there would not need to be any freedom in the choice of frequency range if the effective impedance roots varied monotonically with frequency and displayed the expected decrease with increasing frequency. Unfortunately, the apparent high frequency resonance-like peaks and the unphysical low frequency behaviour of the effective impedance spectra mean that this is not always the case. Therefore, a relevant frequency range where the effective impedance roots are physically meaningful has to be chosen. This choice introduces some uncertainty in the values of the fit coefficients. Figure 35 shows two viable effective impedance fits for the same roughness profile and geometry. The corresponding fit coefficient values are summarized in Table 16. This example shows the difficulty in choosing the lower frequency bound of the range of interest as it is difficult to estimate the point at which the effective impedance departs from the expected increase with decreasing frequency due to numerical artefacts. A choice of 300Hz as the lower frequency bound produces an effective impedance that increases faster with decreasing frequency than if 200Hz is chosen as the lower frequency bound. In this case the net effect is an uncertainty of the order of 25% in the value of α and 17% in the value of δ. It should be noted however that not all effective impedance curves display such inaccuracies. For example, the effective impedance corresponding to the lowest incidence angle for the roughness height $\langle H \rangle$=0.25m (see Figure 8.b) shows a monotonic variation in the range 200-3000Hz, and the fit appears to be close to the effective impedance for the whole frequency range. The 200Hz lower bound is likely to be the lower limit of validity of the BEM simulations for wave-lengths much larger than the 0.25m roughness scale, and the Z_{eff} oscillations with frequencies below 200Hz are probably due to numerical artefacts. The coefficients obtained in cases of such reduced inaccuracy may be used as a guide to the choice of frequency range for effective impedance in cases of incidence angles where the deduced forms of effective impedance cause the inaccuracy to be higher.

2. Effect of the choice of roughness profiles.

Figure 36 shows the real part of the effective impedance obtained for the two different roughness profiles sets 1-5 and 6-11 (dotted blue and cyan lines respectively). The

two sets are based on random roughness heights in the range 0.3m-0.9m and on identical geometries. A comparison of the two curves shows that they do not overlap and that the effective impedance results depend on the roughness profiles used even though the impedance roots are determined from EA averages over five profiles. The black-dashed and black-continuous lines are fits of the real part of the effective impedance from sets 1-5 and 6-11 respectively for frequencies in the range 100Hz-2000Hz. The fit coefficients summarized in Table 17 show clear variations between the two sets of roughness profiles, therefore, some inaccuracy in the fitting coefficients is introduced by the choice of the five roughness profiles involved in the EA average. In this case the net effect is an inaccuracy of the order of 25% in the value of α and 50% in the value of δ. Combining the effects described in sections VIII.C.1 and VIII.C.2 the inaccuracies on the fit-coefficients α and δ are estimated to be 50% and 70% respectively. These values are reflected as error bars in figures (31 and 32 for example) presenting the fit-coefficients angle dependence. The error bars are centered on the data point assuming thereby that the total uncertainty estimated corresponds to variations between extreme values. As example, Figure 32 shows as squares and circles the incidence angle dependence of δ and δ'. The error bars are all computed by the expression 0.7δ (or δ') that explains the small error bar sizes for small δ (or δ') values at high incidence angle. In Figure 27(a), the fit coefficients α for $Re(Z_{eff})$ and for roughness height <H>=1.5m are seen to increase unexpectedly with increasing grazing angle for the three lowest incidence angles 0.02, 0.04 and 0.065 rad. The next section investigates a possible shadowing effect to account for this result.

3. Shadowing of the source/receiver by roughness peaks in the case <H>=1.5m

The roughness profile No1 of a series of five used for the average complex EA in the case<H>=1.5m is presented in Figure 37. It is the only roughness profile among the five studied that exhibits total shadowing of the source receiver by a roughness cusp for the lowest incidence angle θ=0.02rad (h=1.68m). However, this profile has a particularly strong effect on the average EA (black line in Figure 22(a)) since it produces a shallow and wide ground effect dip (around -4dB from 400Hz to 1000Hz) typical of shadowing effect and similar to that obtained from profile 1 (dark blue line in Figure 22(a)). The EA results showed in Figure 23(a) for a greater incidence angle θ=0.04rad (h=1.85m) exhibit similar features but to a lesser extent because of the higher source/receiver height. As a consequence, the effective impedance and fit coefficients deduced from the average EA are affected by this shadowing effect in the case of the low incidence angles of the average roughness height <H>=1.5m and this effect may cause the counter-intuitive results of low fit coefficient values. It should be noted however that this shadowing effect cannot be invoked to explain the other less pronounced cases of unexpected fit coefficient increase with increasing low grazing angle. Figures 27(a), 28, 29(b) and 30 are examples where only the lowest angle data points are off the general decreasing trend, and it is unclear if some systematic physical phenomenon is involved or if the increase is the result of the method's inaccuracies.

IX EFFECTIVE IMPEDANCE PLANE HEIGHT AND EA FLUCTUATIONS

A. Variation of effective impedance plane height with average roughness

height

In this work, the smooth plane equivalent to the rough surface has been set to a height h_p measured from the lowest cusp. This plane is chosen to give the smoothest low frequency asymptotic effective impedance spectra. The effective impedance plane heights for all parabolic average roughness and incidence angles are reported in Figure 38. The ratio of the assumed effective impedance plane height to the average roughness height is plotted against the average roughness size for all incidence angles. The results show that the ratio h_p /<H> depends on the incidence angle and on the roughness scale. It should be noted that the effective impedance plane height is rarely greater than the average roughness height, only the case <H>=3.5m and θ=0.04rad shows h_p /<H>=1.1. Note also that the average roughness scales 1.5m and 7.5m show narrow ratio ranges 0.5-0.6 and 0.6-0.8 respectively for all incidence angles and the average roughness scales 0.4m and 0.6m show constant values of the ratio h_p /<H>=1. In summary, it is found for BEM simulations with semi-cylindrical and parabolically shaped roughness that the effective impedance plane has to be raised between 0.2× and 1× the average roughness height depending on the average roughness height and the incident angle.

B. Effective impedance sensitivity to complex Excess Attenuation perturbations

The objective of this section is to investigate the sensitivity of the effective impedance to complex EA fluctuations. The red curve in Figure 39 is the magnitude of the complex EA obtained with a source/receiver height h=0.93m, a separation distance d=8m and using the smooth impedance presented as the red and blue lines in Figure 40. The blue curve in Figure 39 is obtained from a sinusoidal perturbation of the complex EA whose magnitude is shown in red. The cyan and magenta curves in Figure 40 are the impedance roots obtained from the sinusoidally-perturbed complex EA. The original impedance is represented by the blue and red curves. The sensitivity of the impedance roots to fluctuations in complex EA is found to be very high. Re(Z) is seen to go negative at low frequencies due to the EA fluctuations, and similarly, −Im(Z) crosses periodically into positive territory. Therefore, it seems that low frequency complex EA fluctuations due either to BEM numerical errors or surface wave induced enhancement, can explain the unexpected negative values Re(Z) and Im(Z) in the effective impedance roots.

C. Theory for surface wave amplitude and comparison with BEM results

The peak of the relative boundary wave amplitude P_B/P_D is determined by two attenuation effects and can be expressed by[28]

$$P_B/P_D = (P_B/P_D)_0 \exp(-\delta r - \beta r^2) \tag{14}$$

where

$$\delta = \alpha k^6 \tag{15}$$

k is the wave-number, α depends on the scattering element and its spacing and $\beta=A^2\varepsilon^4k^6/2$. ε is the scattering parameter, r is the propagation distance, P_B is the amplitude of the cylindrically diverging boundary wave and P_D is the amplitude of the spherically diverging wave. The linear attenuation rate δ, which dominates at shorter ranges and high frequency, has been derived for incoherent scattering in the Rayleigh scattering regime. Assuming that the scattering attenuation mechanism is dominant ($\delta r >> \beta r^2$) one can differentiate (14) with respect to frequency and find that the maximum boundary wave amplitude is given for short range and high frequency as

$$(P_B/P_D)_m=\varepsilon\,(\alpha e)^{-1/4}\,\pi^{1/2}\,(r)^{1/4} \qquad (16)$$

For a 3-D randomly rough surfaces, Medwin gives an expression deduced from a statistical interpretation of Tolstoy's factor[29] for attenuation by scattering from periodic deterministic roughness element

$$\delta = \langle H\rangle^3\{[(1+K)/v]-1\}[1+(1+K)^2/3]\,k^6/(4\pi N) \qquad (17)$$

where v is the dipole interaction factor, K is the virtual mass coefficient of the scatterer. Tolstoy[29] has shown that v=1 for widely separated 3-D scatterers. That is the value used in these calculations although, in general, for 2-D elements

$$v=1+(\pi/6)(V/h^2)(1+K) \qquad (18)$$

where V is the area of the elements and h is the separation distance between elements. The value $\varepsilon=NV_0[(1+K)/v-1]$ used here is also obtained from Tolstoy's work. The area of the average parabolic roughness studied here is evaluated by $V_0=20\langle H\rangle^2/3$ taking into account that the height of the parabolic roughness is $1/10^{th}$ its' length. In this work, K is evaluated by Medwin's empirical relation for wedges,

$$K=1.05(a/b)+0.14(a/b)^2 \qquad (19)$$

where a/b is the wedge slope. A wedge of slope 1/10 is modelled here as this is the average slope of the parabolic roughness. An improvement to the calculations would result from evaluating a more accurate K for parabolic roughness and establish a 2-D version of (17). Using (17) and (19) into (16) and defining $x = [N\langle H\rangle]^{5/4}$ gives a functional $(P_B/P_D)_m(x)$ that is plotted in Figure 41 and compared with the BEM predictions. Figure 41 compares the BEM EA maxima for several of the parabolic roughness cases with surface wave amplitudes deduced from Medwin's theory. The EA maxima are plotted versus $(N\langle H\rangle)^{5/4}$ where N is the number of roughness per unit length and $\langle H\rangle$ is the average roughness height. The enhanced BEM-predicted EA maxima for parabolic roughness profiles show a dependence on the statistical parameter that are in agreement with a surface wave theory from Tolstoy and Medwin. The comparison between theory and predictions for the semi-cylindrical roughness profiles is not as favourable, possibly due to the shape of the scatterers quite different from wedged shapes, and the results are not presented here. The existence of acoustic surface waves have been debated in the early eighties, but experimental measurements of surface waves over small rough surfaces have been published in the past[30,31,32], and more recent measurements of outdoor blast noise[33] propagation over rough sea surface show enhanced sound pressure levels indicating surface wave propagation at long range. These very preliminary results show that the

propagation of surface waves might have to be considered when studying grazing sound propagation over a sea surface.

X. CONCLUSIONS

Satisfactory agreement is found between measured data and BEM predictions of Excess Attenuation using averaged data sets, particularly in the case of wedge-shaped roughness. The effective impedance spectra of randomly rough surfaces have been deduced from complex excess attenuation obtained from either BEM predictions or measurements by finding the impedance roots of the classical expression for the total sound pressure due to a point source above an impedance plane. These effective impedance spectra can be used in the classical expression to reproduce the measured or BEM predicted excess attenuation. The impedance spectra are found to be very sensitive to the roughness profiles in the specular reflection area used in the BEM, and show great effective impedance fluctuations for relatively small (< 1 dB) EA fluctuations. The winding number integral method has been used to conclude that for some roughness profiles there are frequency ranges with only negative real effective impedance roots. As a consequence the complex excess attenuation has been calculated for several random distributions and averaged. Moreover it is found for BEM simulations with semi-cylindrical and parabolically shaped roughness that the effective impedance plane has to be raised between 0.2× and 1× the average roughness height depending on the average roughness height and the incident angle.
An analytical technique based on Twersky's boss theory, where the contributions from randomly spaced semi-cylindrical or elliptical rough scatterers are summed to obtained the total scattered field, has been used also to fit the effective impedance deduced from measurements and BEM predictions above semi-cylindrical roughness. The agreement between effective impedance from averaged measurements, from averaged BEM predictions and from Twersky's fit is better for the smaller cylinders. This is consistent with the small *ka* approximation implicit in Twersky's theory. However, the asymptotic low frequency dependence of Twersky's theory impedance for hard surfaces does not allow the large real values expected from physical considerations. It has been found that an additional attenuation has to be introduced in the theory to account for the correct low frequency dependence, therefore, an improved version of Twersky's theory that models roughness of finite impedance will be investigated in further work.
As a result, empirical frequency dependent polynomial fits of BEM-deduced spectra have been derived for the effective impedance evaluations corresponding to roughness profiles formed by intersecting parabolas and intended to model sea-waves. These are defined by $\alpha f^{1}+\delta$ and $\alpha' f^{-1/2}+\delta'$ for the real and imaginary parts respectively where f is the frequency. Four 6x5 matrices of coefficients α, α', δ and δ' are reported to model the effective impedance of six rough sea states in five cases of acoustic wave incident angle. There are inaccuracies in effective impedance fit coefficients estimates due to the particular choices of roughness profiles used for the BEM EA simulations and the particular choice of frequency ranges for the polynomial fits. In addition, some shadowing of the source and receiver by the roughness cusps prejudices the evaluation of fit coefficients at very low grazing angles. The angle dependent coefficients at constant roughness height and their error bars are fitted successfully with Gaussian curves and these allow extrapolation to lower angle values. It may be concluded that the general trends for the effective impedance fit

coefficients of hard rough surfaces are consistent with the expected decrease in effective impedance with increasing grazing incidence angles (at constant roughness scale) and with decreasing roughness scale (at constant incidence angle). The effective impedance polynomial fits are easy to implement into sonic boom propagation codes, and preliminary predictions indicate that the effect of the sea surface roughness on sonic boom profiles and rise time is comparable to that due to turbulence and molecular relaxation effects.

The BEM-predicted EA enhancement maxima are found to agree with Medwin and Tolstoy's theoretical expressions for surface wave amplitudes that show a five fourth power dependence of the product between the average roughness height and the number of roughness per unit length. This agreement suggests that surface waves are the cause of the BEM-predicted enhanced EA (>6dB). More work is planned to evaluate the likelihood of surface wave propagation when sound impinges at grazing angle over a hard rough surface.

LIST OF TABLES

Table 1: Relation between wind speed and water wave heights

Sea State	Sea Type	Wind Speed (m/s)	Wind Type	Wave rms Height (m)
0	Calm	0-1.5	Light Air	0
1	Rippled	1.5-3	Light Breeze	0-0.1
2	Wavelets	3-5	Gentle Breeze	0.1-0.5
3	Slight	5-8	Modest Breeze	0.5-1.25
4	Moderate	8-10.5	Fresh Breeze	1.25-2.5
5	Rough	10.5-16.5	Strong Breeze	2.5-4
6	Very Rough	16.5-23.5	Gale	4-6
7	High	23.5-27.5	Storm	6-9
8	Very High	27.5-31.5	Violent Breeze	9-14
9	Phenomenal	>31.5	Hurricane	>14

Table 2: Wave characteristics of fully developed seas as a function of wind speed

Wind speed (Km/h)	Average Height (m)	Average Length (m)	Highest 10% wave (m)
20	0.33	10.6	0.75
30	0.88	22.2	2.1
40	1.8	39.7	3.9
50	3.2	61.8	6.8
60	5.1	89.2	10.5
70	7.4	121.4	15.3
80	10.3	158.6	21.4
90	13.9	201.6	28.4

Table 3– Twersky's effective impedance least square fit parameters for small semi-cylindrical roughness

	n (1/m)	Ka (m)	a (m)	b^* (m)	h_s (m)
BEM	5	0.071	0.005	0.202	0.1
Measurements	3	0.137	0.005	0.336	0.1

Table 4– Coefficients of the effective impedance polynomial fit for small semi-cylindrical roughness

	$Re(Z_m)$	$Im(Z_m)$	$Re(Z_{BE})$	$Im(Z_{BE})$
α	4620	291	9471	38276
δ	0	4.2	0	0

Table 5 – Least square fit parameters for Twersky's effective impedance for large semi-cylindrical roughness

	n (1/m)	Ka (m)	a (m)	b^* (m)	h_s (m)
BEM	1	0.071	0.1	0.142	0.1
Measurements	1	0.137	0.1	0.274	0.1

Table 6– Coefficients of the effective impedance polynomial fit for large semi-cylindrical roughness

	$Re(Z_m)$	$Im(Z_m)$	$Re(Z_{BE})$	$Im(Z_{BE})$
α	6672	435	5468	380
δ	0	0	1.85	0

Table 7– Twersky's effective impedance least square fit parameters for wedge roughness

	n (1/m)	Ka (m)	a (m)	b^* (m)	h_s (m)
BEM	1	0.104	0.024	0.208	0.1
Measurements	3	0.137	0.005	0.336	0.1

Table 8– Coefficients of the effective impedance polynomial fit for wedge-roughness profiles

	$Re(Z_m)$	$Im(Z_m)$	$Re(Z_{BE})$	$Im(Z_{BE})$
α	2970	360	9610	467
δ	0	0	0	0

Table 9 –Polynomial fit coefficients α (Hz^{-1}) for $Re(Z_{eff})$ for six average roughness heights and five grazing angles

		Incidence Angle (rad)					
		0.01	**0.02**	**0.04**	**0.065**	**0.17**	**0.23**
<H> (m)	**0.25**	2621	-	2477	2513	2628	2560
	0.4	-	3695	2767	2459	2337	2272
	0.6	-	4023	3660	3285	1265	434
	1.5	-	626	733	758	663	335
	3.5	-	374	297	235	58	54
	7.5	-	187	145	122	46	35

Table 10 –Polynomial fit coefficient α' ($Hz^{-1/2}$) for $Im(Z_{eff})$ for six average roughness heights and five grazing angles

		Incidence Angle (rad)					
		0.01	**0.02**	**0.04**	**0.065**	**0.17**	**0.23**
<H> (m)	**0.25**	164	-	193	189	175	178
	0.4	-	276	357	302	141	129
	0.6	-	180	169	205	147	172
	1.5	-	113	114	109	148	98
	3.5	-	84	123	78	61	47
	7.5	-	80	77	71	43	40

Table 11 –Polynomial fit coefficient δ for $Re(Z_{eff})$ for six average roughness heights and five grazing angles

		Incidence Angle (rad)					
		0.01	**0.02**	**0.04**	**0.065**	**0.17**	**0.23**
<H> (m)	**0.25**	9.3	-	12.7	10	3.1	4.6
	0.4	-	7.2	5.7	5.3	2.8	0
	0.6	-	8.45	4.9	2.1	0	1.2
	1.5	-	7.3	7	5.8	0	0
	3.5	-	4.6	7.5	6	4	2.5
	7.5	-	3.1	3.8	2.9	1.5	0.83

Table 12 –Polynomial fit coefficient δ' for $Im(Z_{eff})$ for six average roughness heights and five grazing angle

		Incidence Angle (rad)					
		0.01	**0.02**	**0.04**	**0.065**	**0.17**	**0.23**
<H> (m)	**0.25**	6.7	-	5.2	2.5	2.8	4.6
	0.4	-	-1.8	-1.7	-1.8	2.5	1.7
	0.6	-	5.3	4.3	0.8	-1.7	-5.3
	1.5	-	-6.2	1	1.9	0	0
	3.5	-	-0.13	0	0	-3.4	-2.5
	7.5	-	-1.5	-1.4	-3	-1.5	-3.5

Table 13 –Best parameter γ in Gaussian fit of angle dependent impedance-fit-coefficients for six average roughness heights

		γ			
		γ_α (Hz^{-1})	$\gamma_{\alpha'}$ ($Hz^{-1/2}$)	γ_δ	$\gamma_{\delta'}$
<H> (m)	0.25	0	0	3.4	3.1
	0.4	2300	125	-1	0
	0.6	0	0	0.5	-3
	1.5	0	0	0	0
	3.5	50	50	2.2	-3.8
	7.5	40	40	0.9	0

Table 14 – Best parameter γ_m in Gaussian fit of angle dependent impedance-fit-coefficients for six average roughness heights

		γ_m			
		$\gamma_{m\,\alpha}$ (Hz^{-1})	$\gamma_{m\,\alpha'}$ ($Hz^{-1/2}$)	$\gamma_{m\,\delta}$	$\gamma_{m\,\delta'}$
<H>(m)	0.25	2550	175	8	5
	0.4	2300	200	8	0
	0.6	4100	172	9	10
	1.5	750	115	8.5	1.5
	3.5	350	53	3.6	4
	7.5	160	42	2.7	-2

Table 15 – Best parameter σ in Gaussian fit of angle dependent impedance-fit-coefficients for six average roughness heights

		σ (rad^2)			
		σ_α	$\sigma_{\alpha'}$	σ_δ	$\sigma_{\delta'}$
<H> (m)	0.25	∞	∞	0.093	0.03
	0.4	0.035	0.1	0.17	∞
	0.6	0.15	∞	0.05	0.06
	1.5	0.29	∞	0.08	0.12
	3.5	0.07	0.12	0.18	0.16
	7.5	0.07	0.11	0.12	∞

Table 16 –Polynomial fit coefficients for two frequency ranges and the same average roughness height and grazing angle

	α	δ
300-2100 Hz	2460	5
200-2000 Hz	1820	6

Table 17 –Polynomial fit coefficients for two sets of roughness profiles and identical frequency ranges, average roughness height and grazing angles

	α	δ
Roughness Profiles 1-5	1002	7.7
Roughness Profiles 6-11	1370	3.8

FIGURES

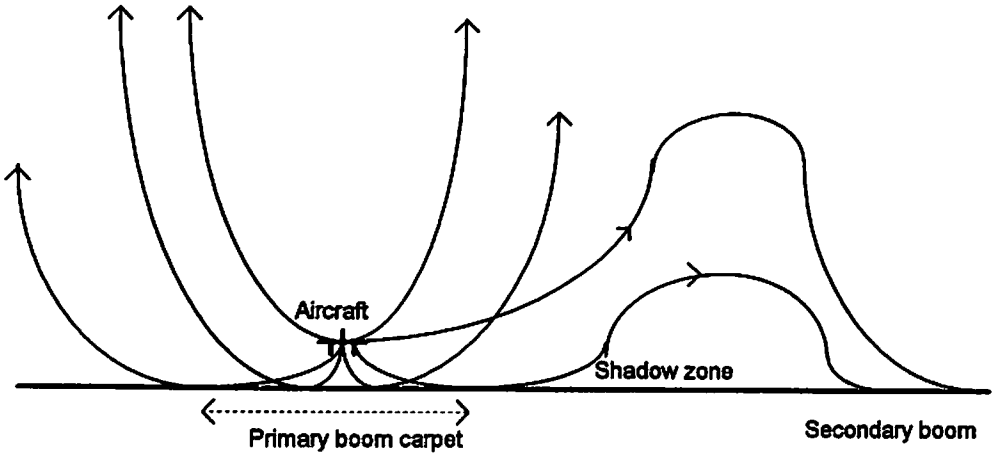

Figure 1- Sonic boom rays in a refracting atmosphere

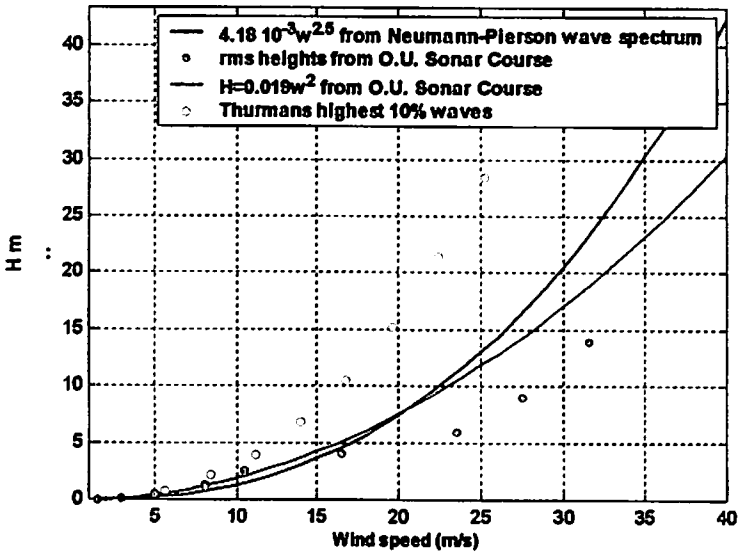

Figure 2- Sea wave height H m as a function of wind speed (ms^{-1})

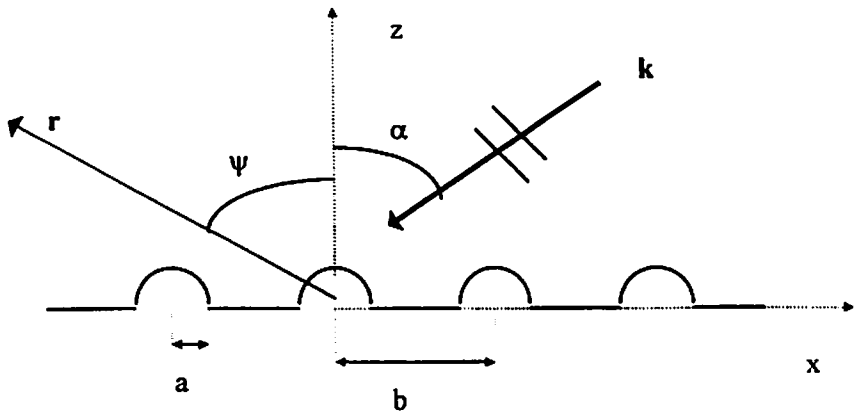

Figure 3 - 2-D representation of a plane wave incident on a surface containing a regularly-spaced grating of semi-cylinders

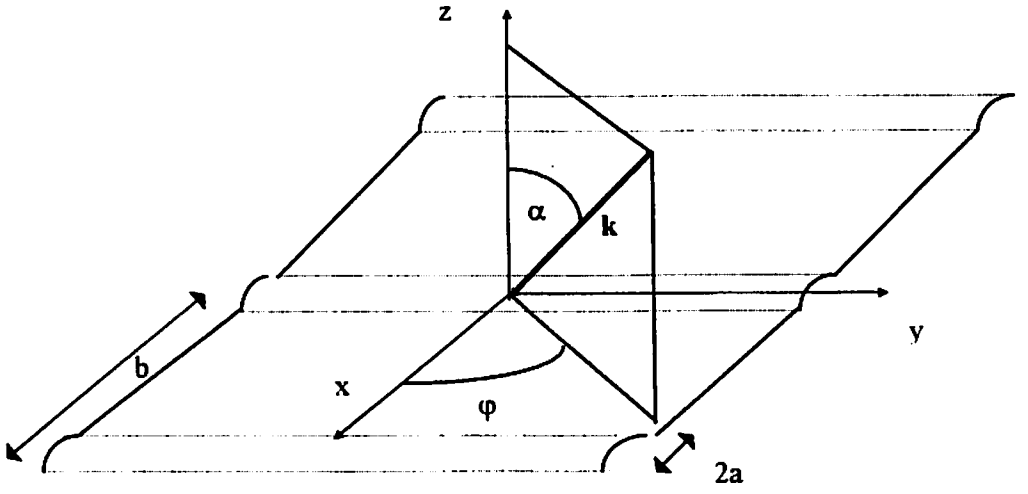

Figure 4- 3-D representation of a plane wave incident on a surface containing a regularly-spaced grating of semi-cylinders

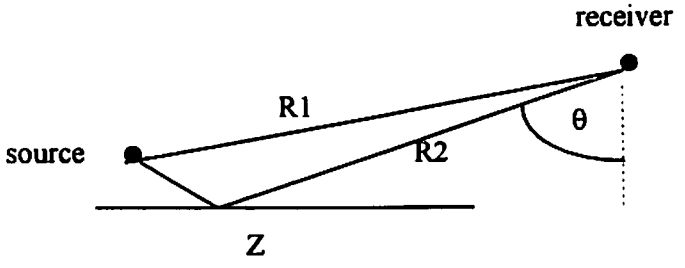

Figure 5 - Geometry used in the classical point source formulation

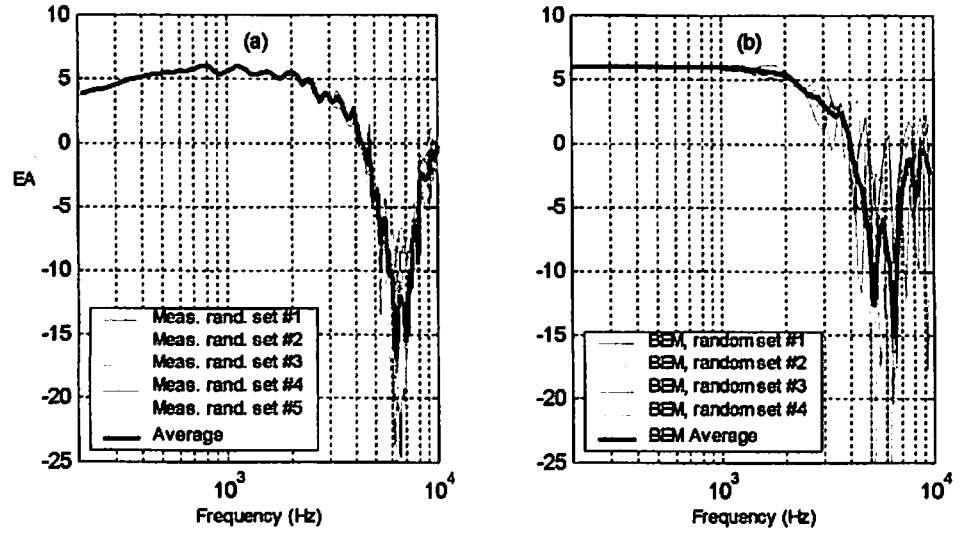

Figure 6- Measured (a) and BEM-predicted (b) excess attenuation spectra above a small semi-cylindrical roughness profile

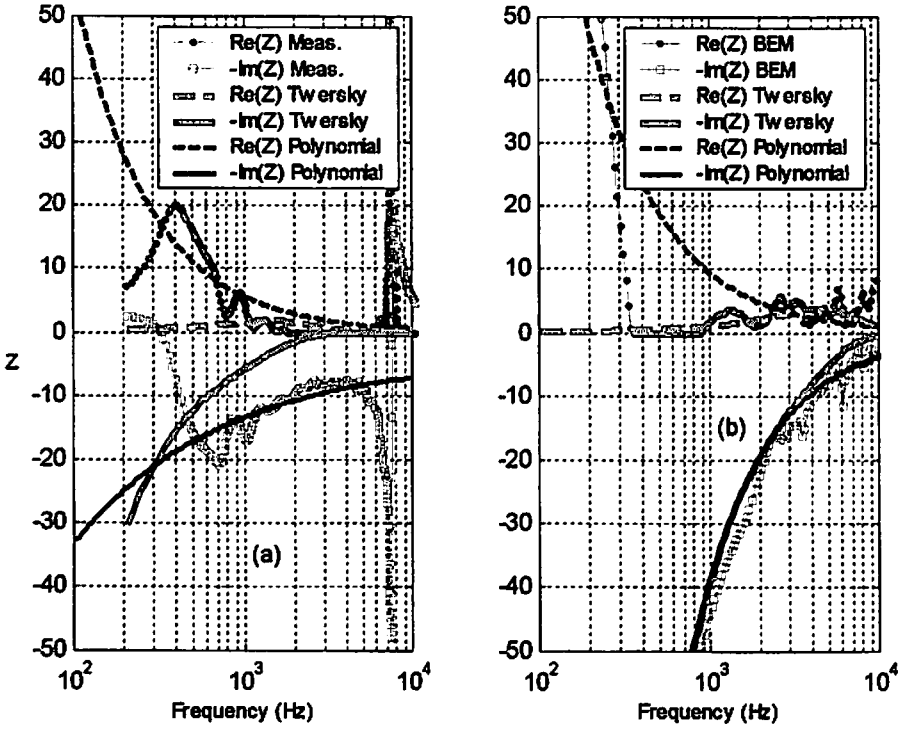

Figure 7- Effective impedance from measured (a) and BEM-predicted (b) excess attenuation above a small semi-cylindrical roughness profile

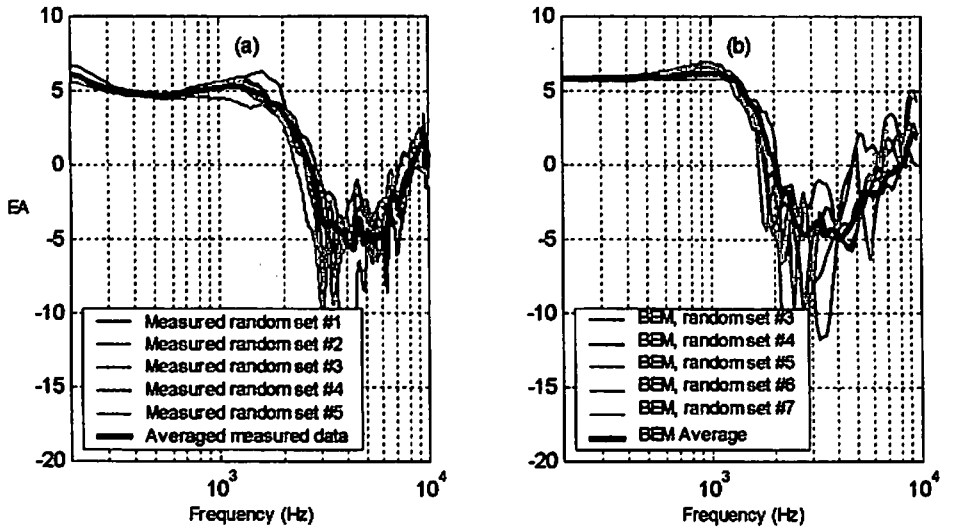

Figure 8- Measured (a) and BEM-predicted (b) excess attenuation spectra above a large semi-cylindrical roughness profile

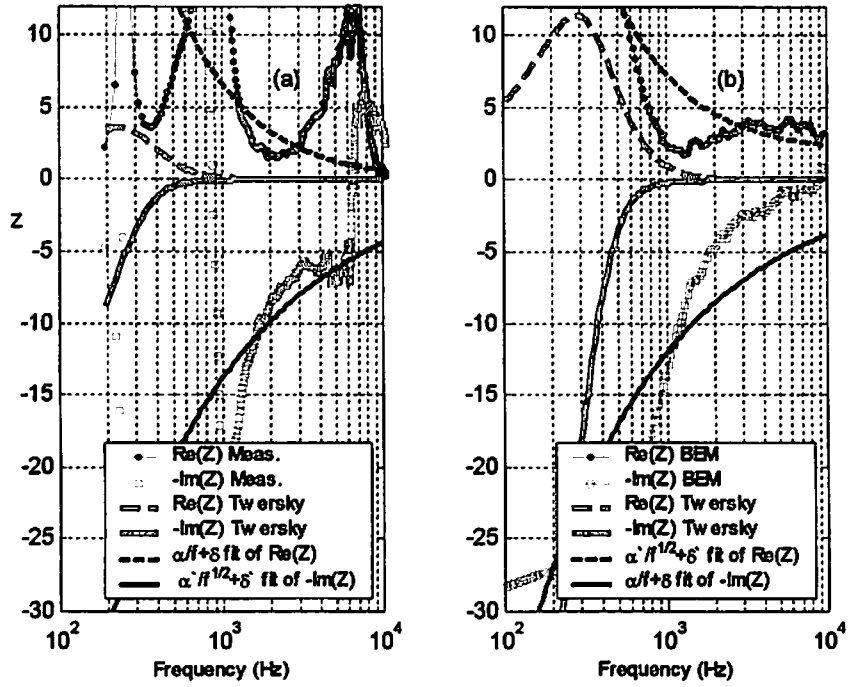

Figure 9- Effective impedance from measured (a) and BEM-predicted (b) excess attenuation above a large semi-cylindrical roughness profile

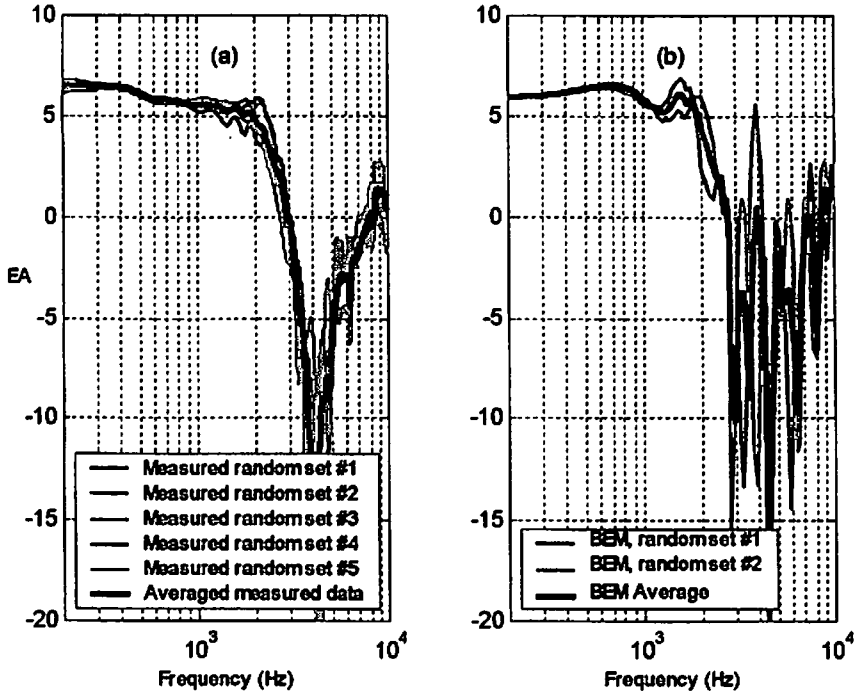

Figure 10- Measured (a) and BEM-predicted (b) excess attenuation spectra above a wedge-roughness profile

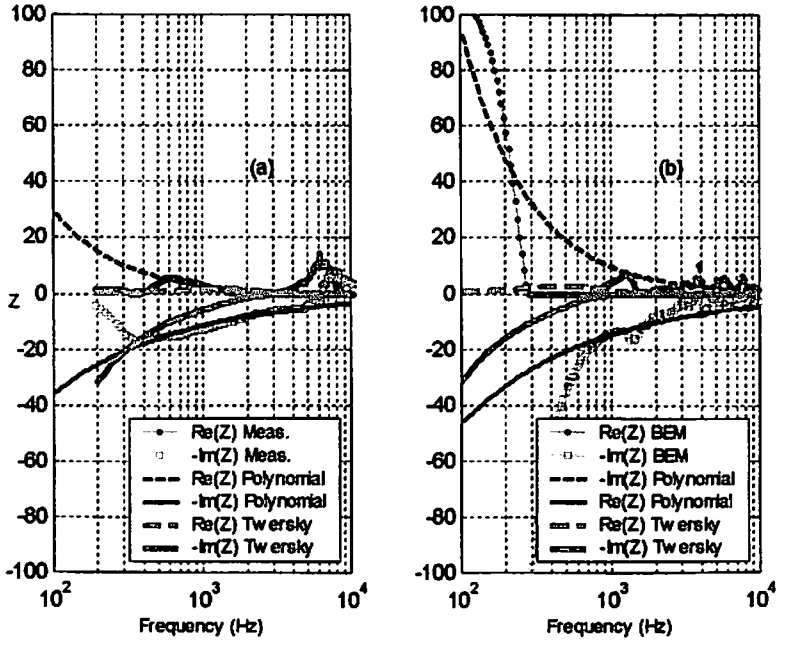

Figure 11- Effective impedance from measured (a) and BEM-predicted (b) excess attenuation above a wedge-roughness profile

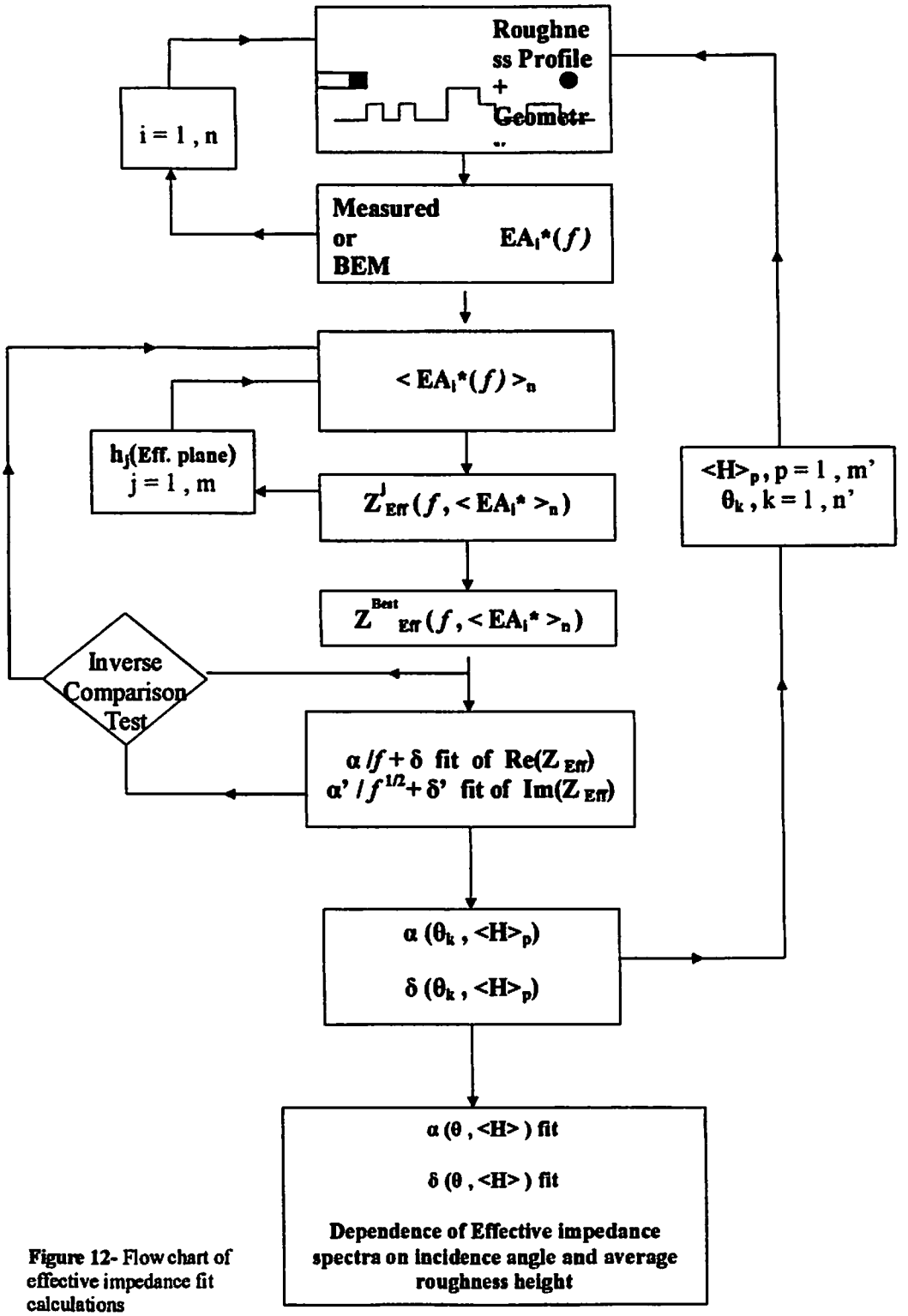

Figure 12- Flow chart of effective impedance fit calculations

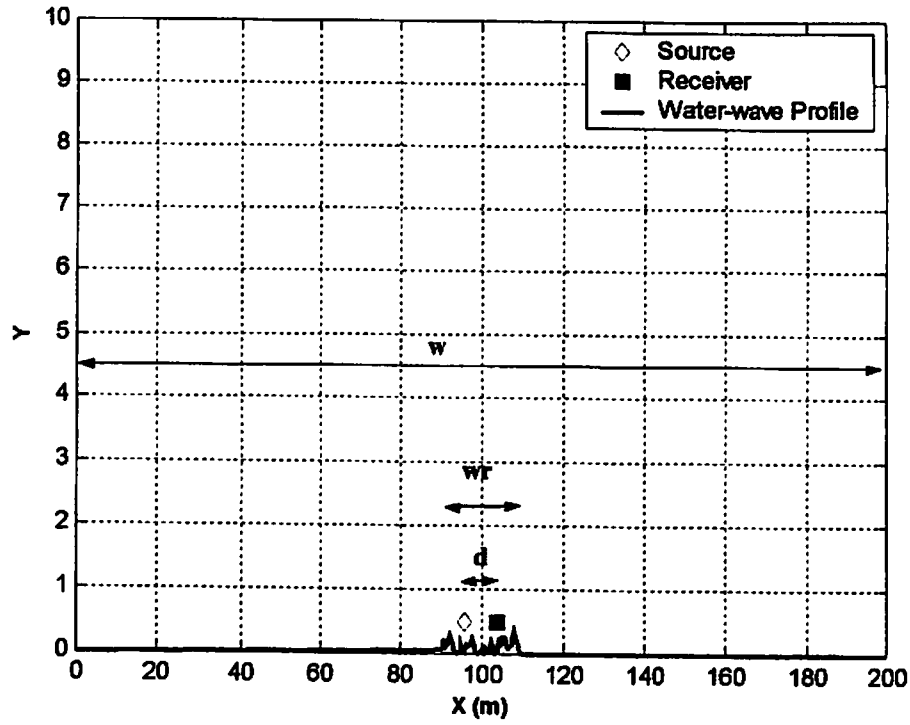

Figure 13- Example of randomly rough parabolic surface modelled with the BEM for cusp heights 0.1m<H<0.4m

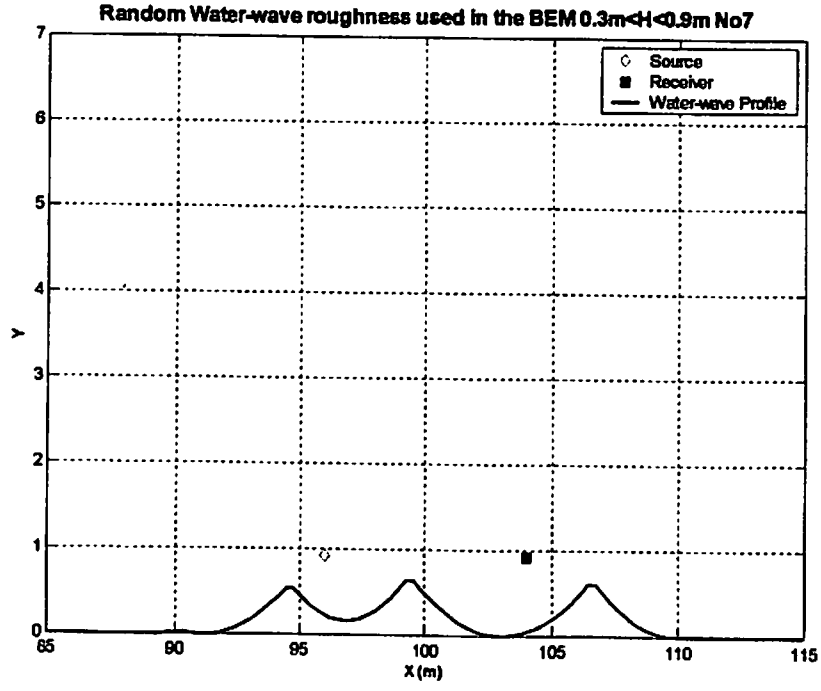

Figure 14- An example parabolic roughness profile with cusp heights 0.3m<H<0.9m

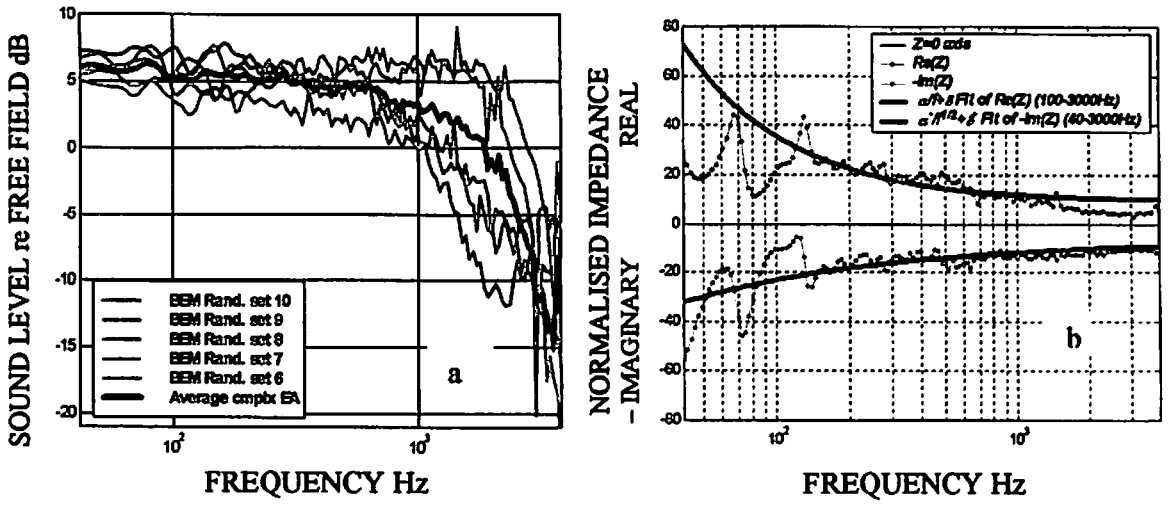

Figure 15 (a) BEM-predicted Excess attenuation Spectra for a point source 0.3 m above the lowest points in five realisations of a 2D surface formed by intersecting parabolas with mean height 0.25m and cusp heights between 0.1m and 0.4m. This corresponds to a grazing angle of 0.012 rad with respect to the horizontal mean height plane. (b) Real and Imaginary parts of the effective impedance spectrum deduced from the mean excess attenuation spectrum and corresponding polynomial fits.

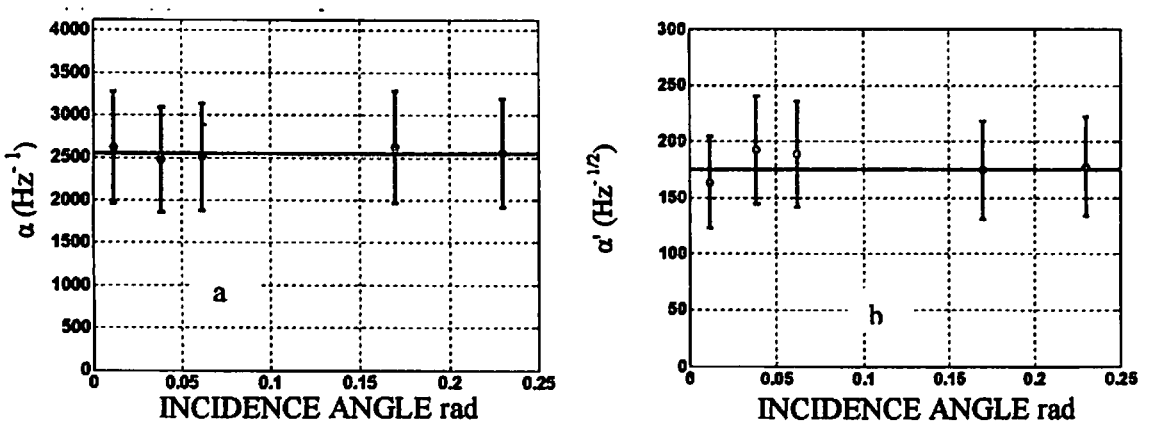

Figure 16 Incidence angle dependence of the fit coefficients α (a) and α' (b) for roughness mean height 0.25m and cusp heights between 0.1m and 0.4m. Continuous lines represent Gaussian curve fits to the respective angle dependence.

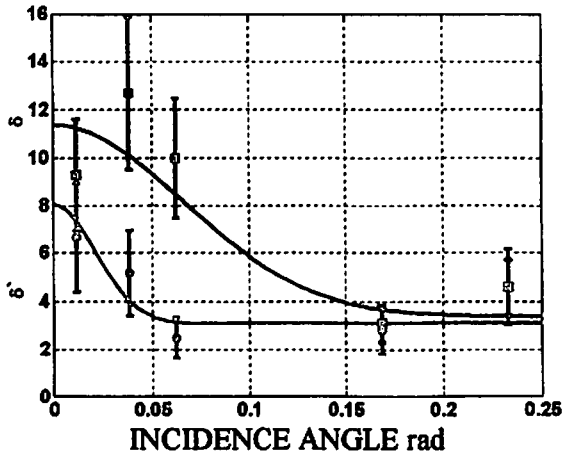

Figure 17 Incidence angle dependence of the fit coefficients δ (blue line) and δ' (red line) for roughness mean height 0.25m. Continuous lines represent Gaussian curve fits to the respective angle dependence.

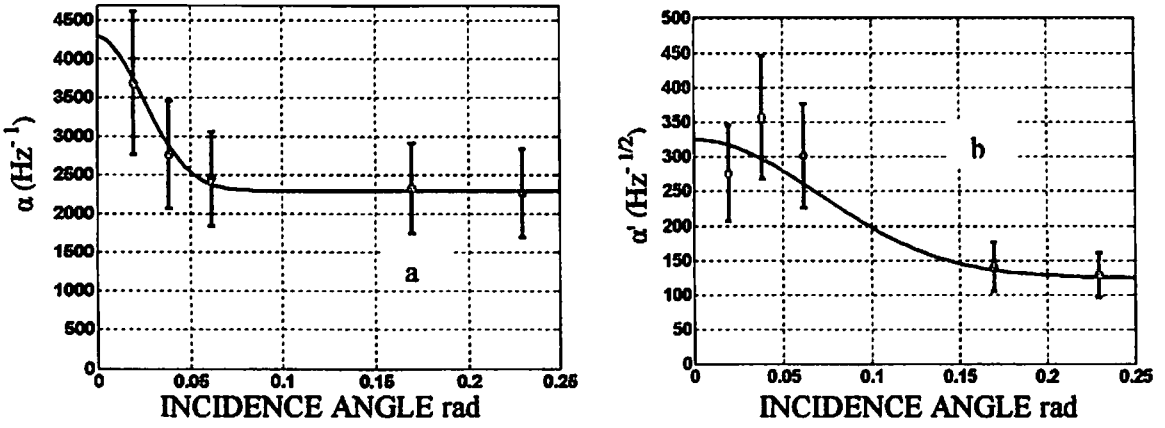

Figure 18 Incidence angle dependence of the fit coefficient α (a) and α' (b) for roughness mean height 0.4m and cusp heights between 0.2m and 0.6m. Continuous lines represent Gaussian curve fits to the respective angle dependence.

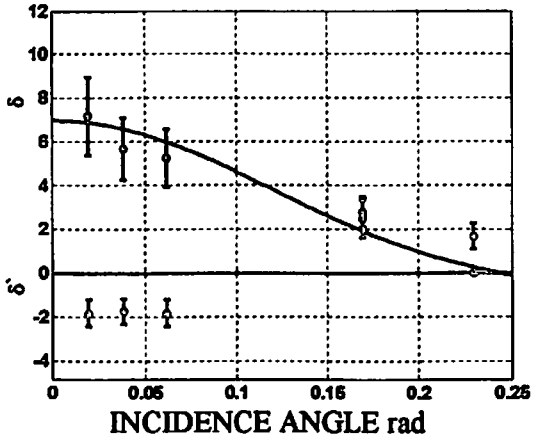

Figure 19 Incidence angle dependence of the fit coefficients δ (blue line) and δ' (red line) for roughness mean height 0.4m. Continuous lines represent Gaussian curve fits to the respective angle dependence.

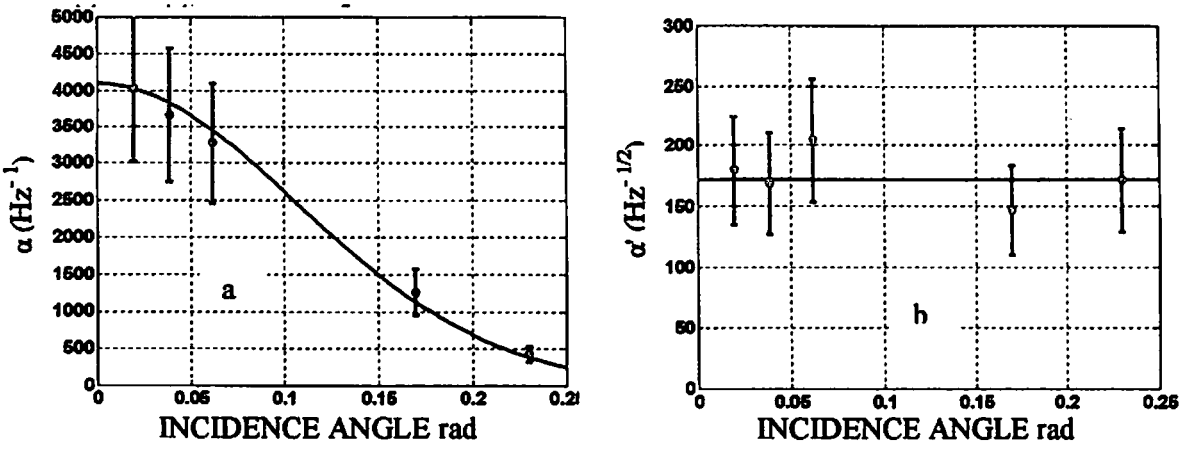

Figure 20 Incidence angle dependence of the fit coefficient α (a) and α' (b) for roughness mean height 0.6m and cusp heights between 0.3m and 0.9m. Continuous lines represent Gaussian curve fits to the respective angle dependence.

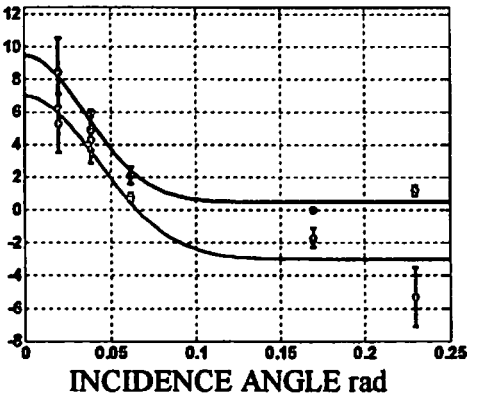

Figure 21 Incidence angle dependence of the fit coefficients δ (blue line) and δ' (red line) for roughness mean height 0.6m. Continuous lines represent Gaussian curve fits to the respective angle dependence.

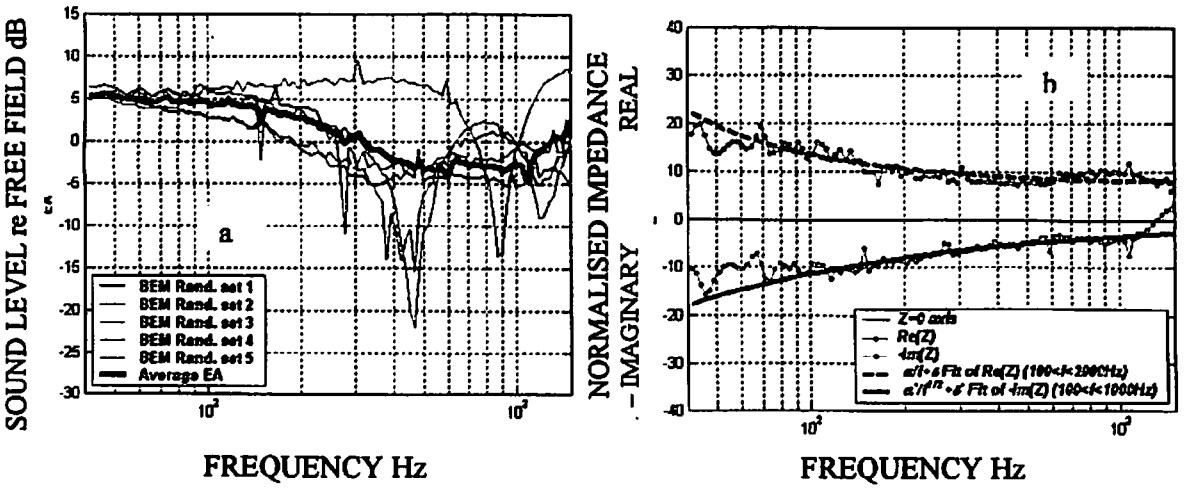

Figure 22 (a) BEM-predicted Excess attenuation Spectra for a point source 1.68 m above the lowest points in five realisations of a 2D surface formed by intersecting parabolas with mean height 1.5m and cusp heights between 1m and 2m. This corresponds to a grazing angle of 0.02 rad with respect to the horizontal mean height plane. (b) Effective impedance spectrum deduced from the mean excess attenuation spectrum and polynomial fits

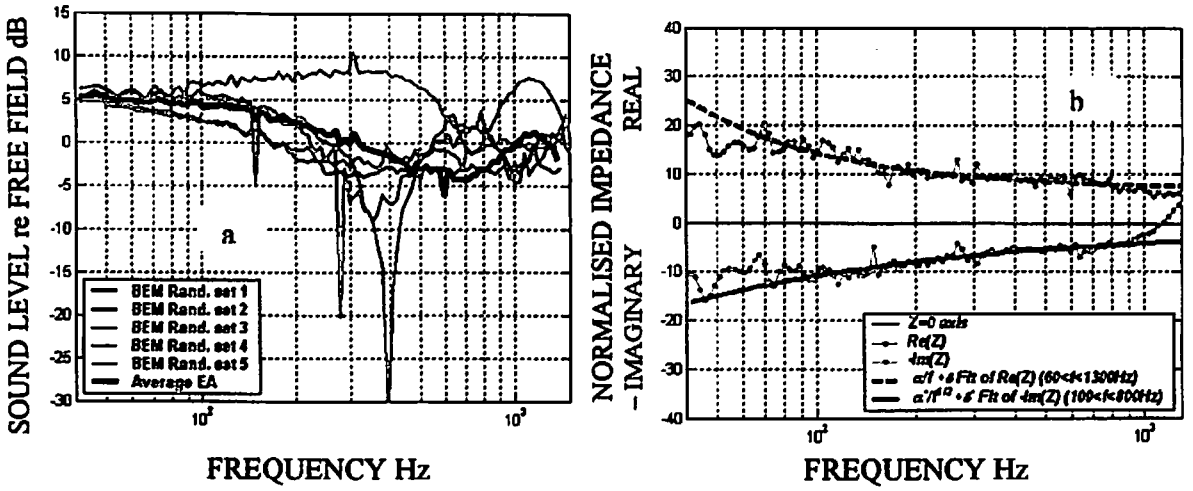

Figure 23 (a) BEM-predicted Excess attenuation Spectra for a point source 1.85 m above the lowest points in five realisations of a 2D surface formed by intersecting parabolas with mean height 1.5m and cusp heights between 1 m and 2 m. This corresponds to a grazing angle of 0.04 rad with respect to the horizontal mean height plane. (b) Real and Imaginary parts of the effective impedance spectrum deduced from the mean excess attenuation spectrum and corresponding polynomial fits.

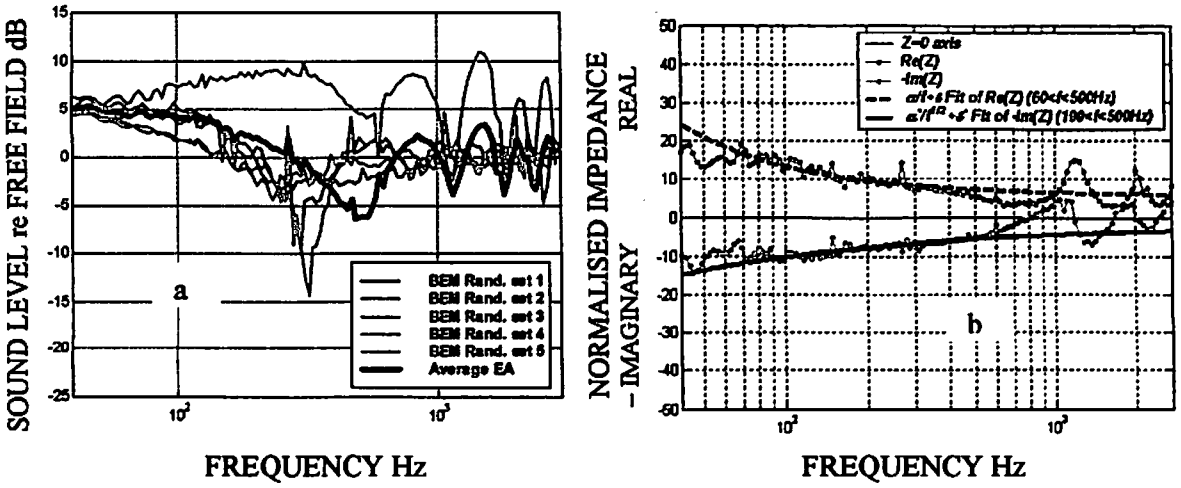

Figure 24 (a) BEM-predicted Excess attenuation Spectra for a point source 2.1 m above the lowest points in five realisations of a 2D surface formed by intersecting parabolas with mean height 1.5m and cusp heights between 1 m and 2 m. This corresponds to a grazing angle of 0.065 rad with respect to the horizontal mean height plane. (b) Real and Imaginary parts of the effective impedance spectrum deduced from the mean excess attenuation spectrum and corresponding polynomial fits.

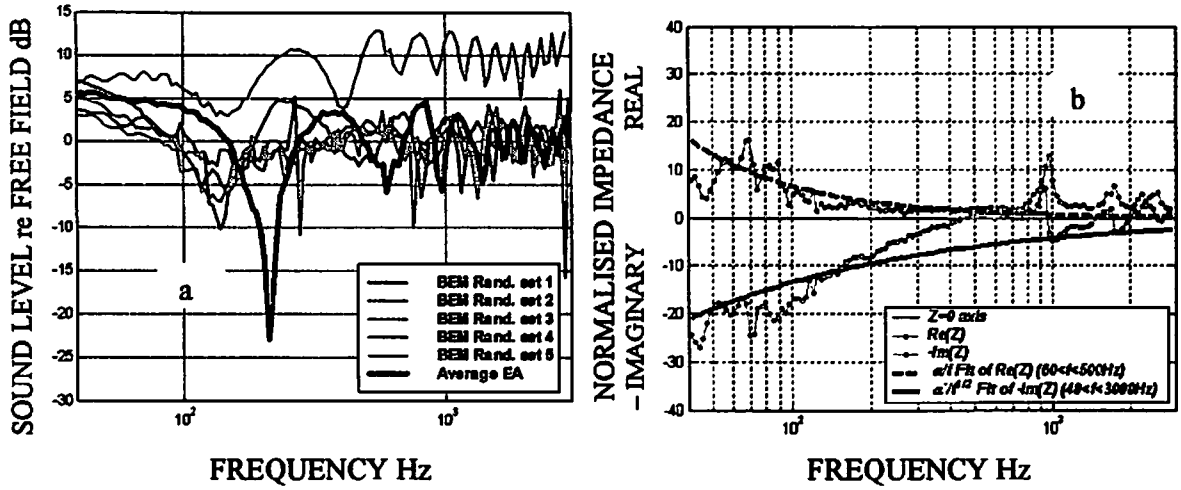

Figure 25 (a) BEM-predicted Excess attenuation Spectra for a point source 3 m above the lowest points in five realisations of a 2D surface formed by intersecting parabolas with mean height 1.5m and cusp heights between 1 m and 2 m. This corresponds to a grazing angle of 0.17 rad with respect to the horizontal mean height plane. (b) Real and Imaginary parts of the effective impedance spectrum deduced from the mean excess attenuation spectrum and corresponding polynomial fits.

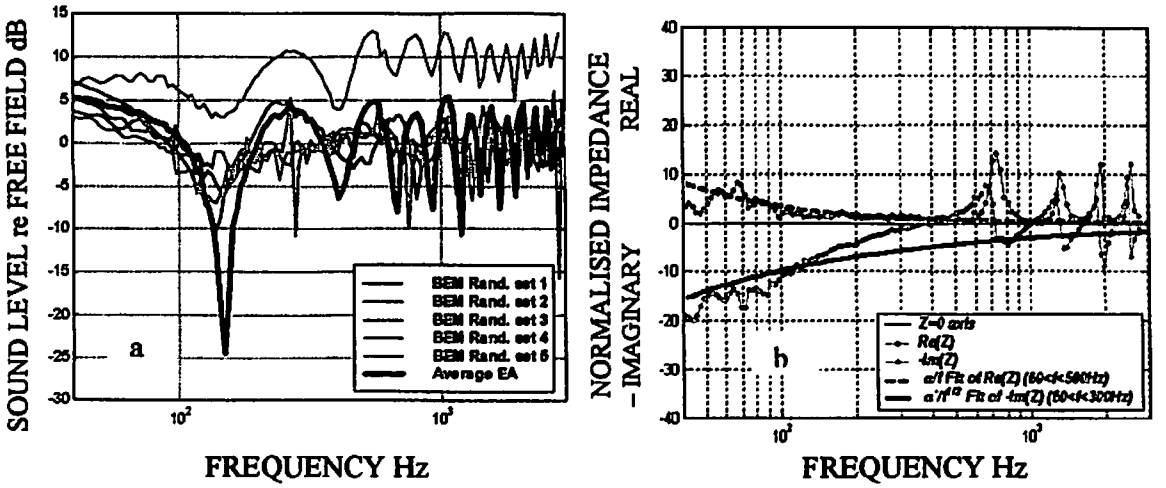

Figure 26 (a) BEM-predicted Excess attenuation Spectra for a point source 3.6 m above the lowest points in five realisations of a 2D surface formed by intersecting parabolas with mean height 1.5m and cusp heights between 1 m and 2 m. This corresponds to a grazing angle of 0.23 rad with respect to the horizontal mean height plane. (b) Real and Imaginary parts of the effective impedance spectrum deduced from the mean excess attenuation spectrum and corresponding polynomial fits.

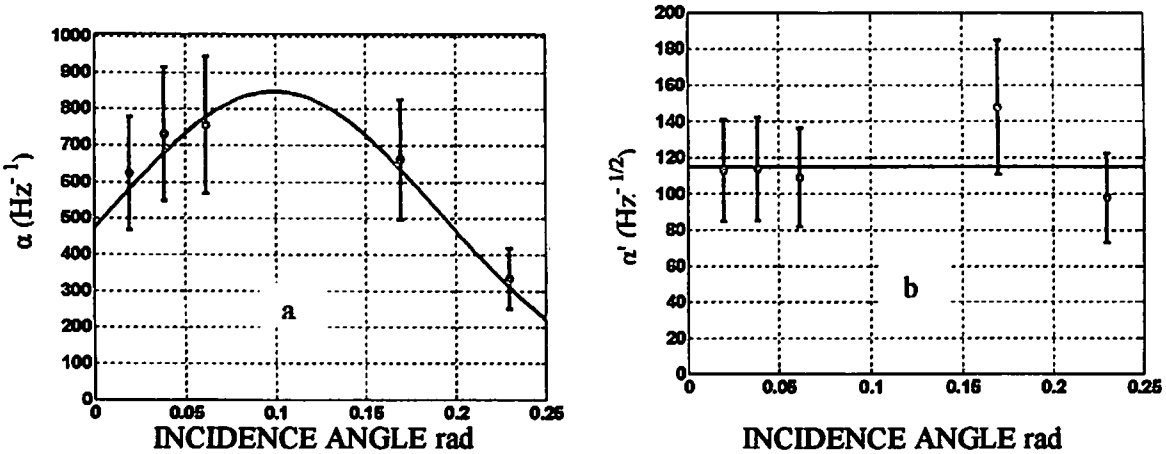

Figure 27 Incidence angle dependence of the fit coefficient α (a) and α' (b) for roughness mean height 1.5 m and cusp heights between 1 m and 2 m. Continuous lines represent Gaussian curve fits to the respective angle dependence.

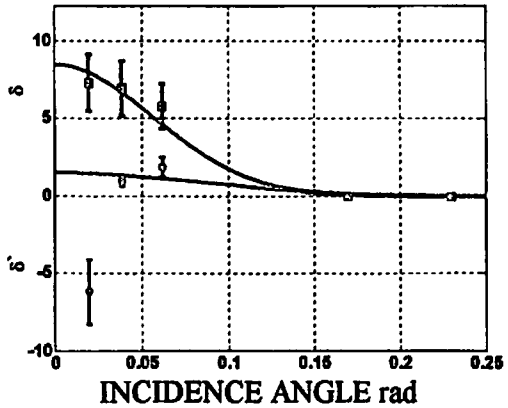

Figure 28 Incidence angle dependence of the fit coefficients δ and δ' for roughness mean height 1.5m. Continuous lines represent Gaussian curve fits to the respective angle dependence

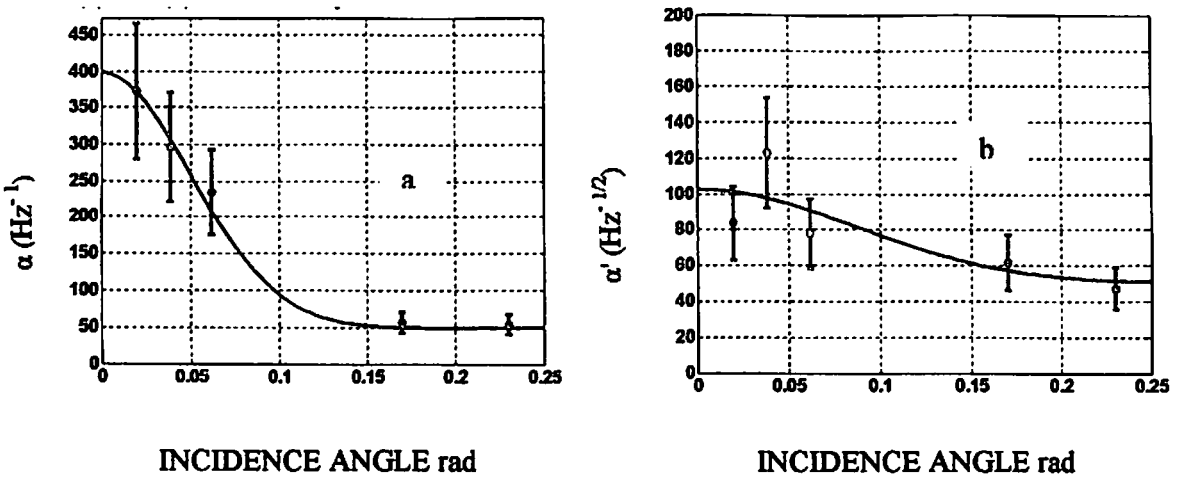

Figure 29 Incidence angle dependence of the fit coefficient α (a) and α' (b) for roughness mean height 3.5 m and cusp heights between 3m and 4 m. Continuous lines represent Gaussian curve fits to the respective angle dependence.

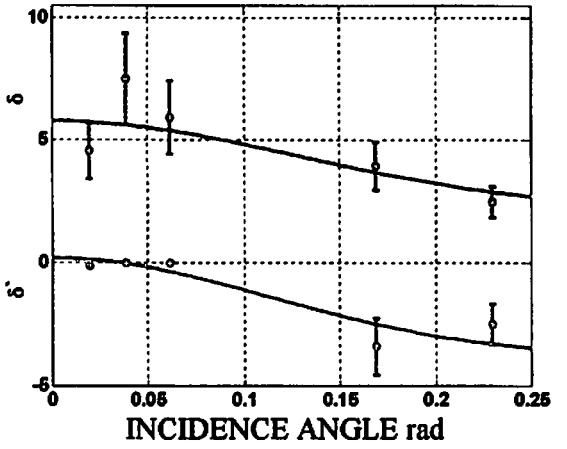

Figure 30 Incidence angle dependence of the fit coefficients δ (blue line) and δ' (red line) for roughness mean height 3.5m. Continuous lines represent Gaussian curve fits to the respective angle dependence.

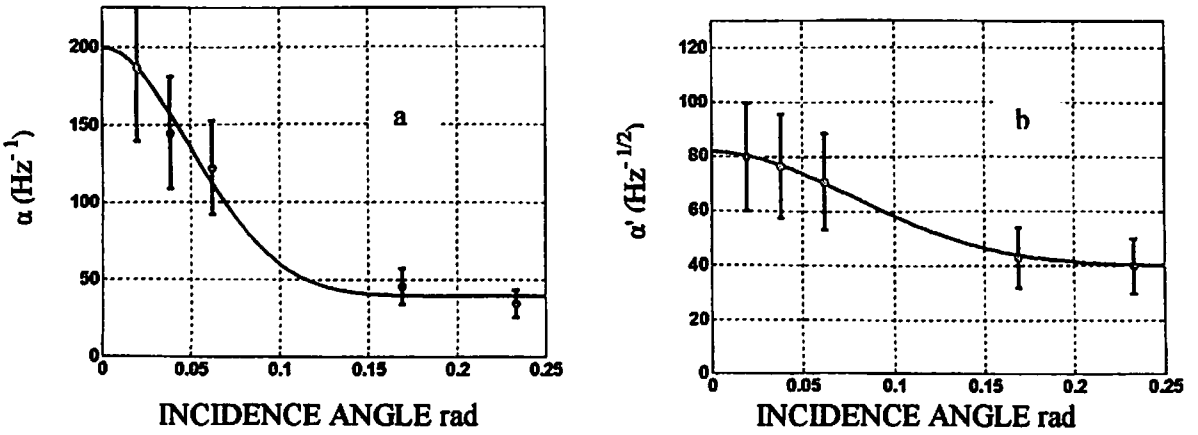

Figure 31 Incidence angle dependence of the fit coefficient α (a) and α' (b) for roughness mean height 7.5 m and cusp heights between 7 m and 8 m. Continuous lines represent Gaussian curve fits to the respective angle dependence.

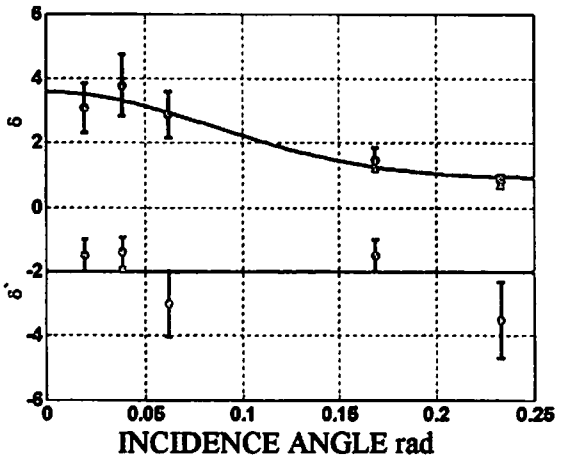

Figure 32 Incidence angle dependence of the fit coefficients δ (blue line) and δ' (red line) for roughness mean height 7.5m. Continuous lines represent Gaussian curve fits to the respective angle dependence.

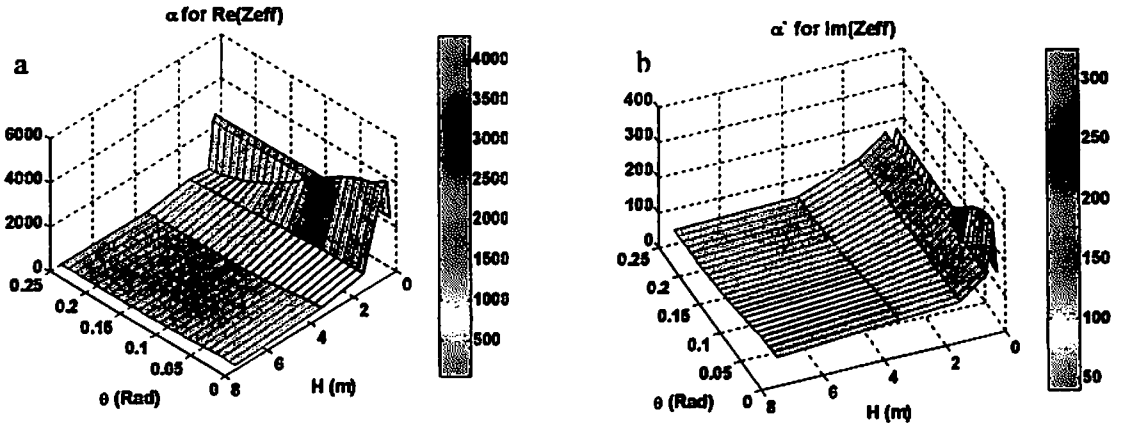

Figure 33 Incidence angle and roughness size dependence of the fit coefficient α for $Re(Z_{eff})$ (a) and α' for $Im(Z_{eff})$ (b)

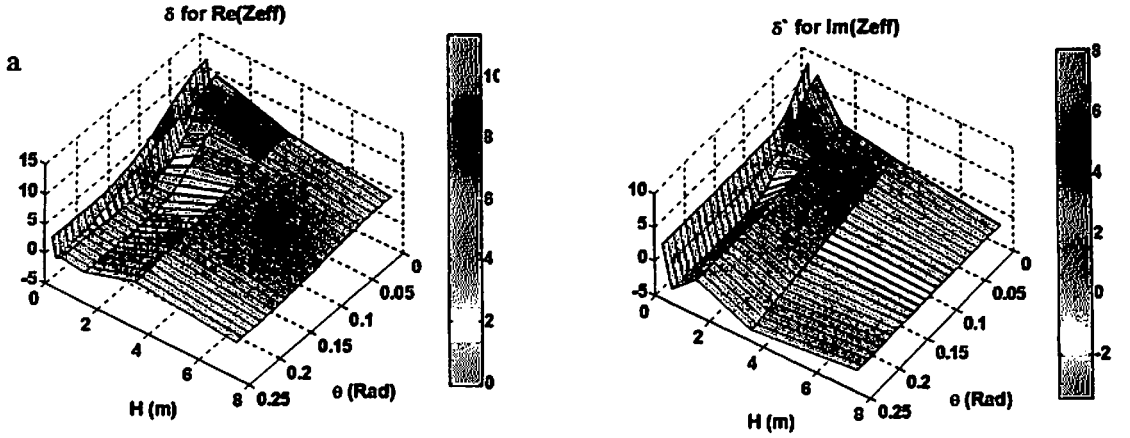

Figure 34 Incidence angle and roughness size dependence of the fit coefficient δ for $Re(Z_{eff})$ (a) and δ' for $Im(Z_{eff})$ (b)

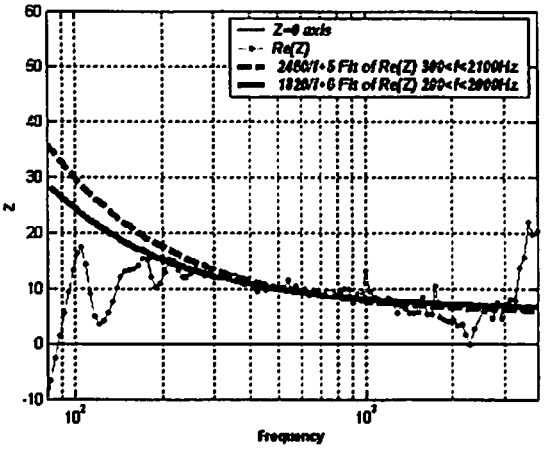

Figure 35 Real part of effective impedance spectrum and variations of fit due to two choices of fitted frequency ranges.

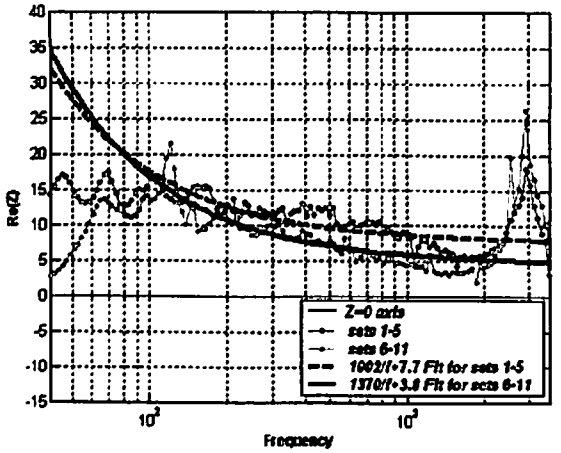

Figure 36 Variations in Real part of effective impedance spectra and fits due to two choices of roughness profiles for identical fitted frequency ranges.

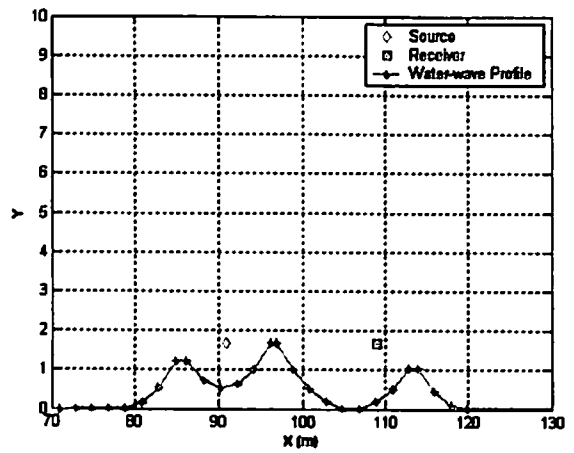

Figure 37 Shadowing in Roughness profile No1 used in the BEM computation of sound attenuation over 1.5m average roughness heights

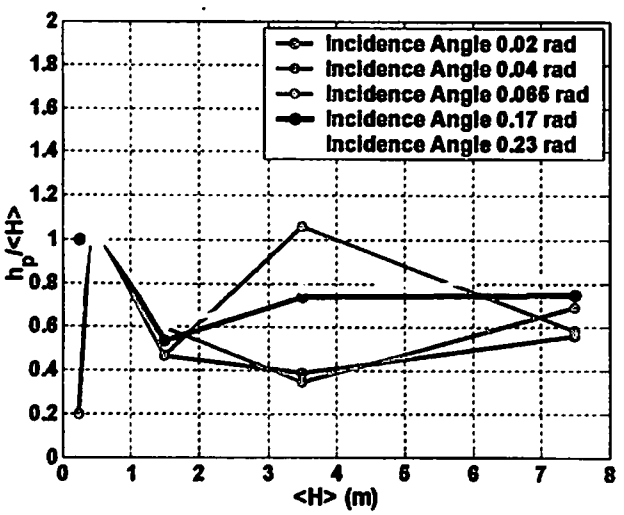

Figure 38- Dependence of the ratio of effective impedance plane height to average roughness height on average roughness height for five incidence angles.

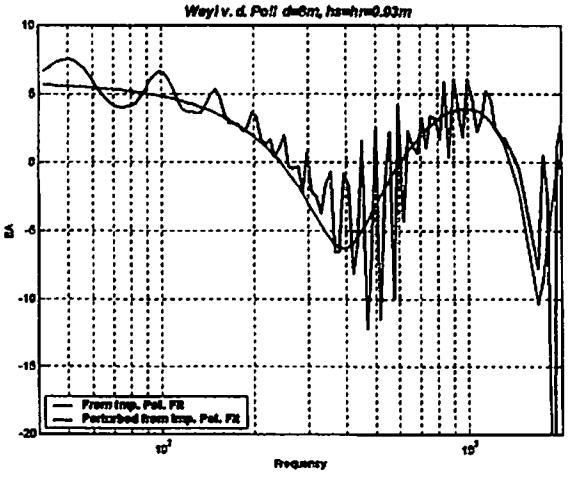

Figure 39- Excess attenuation before and after sinusoidal perturbation

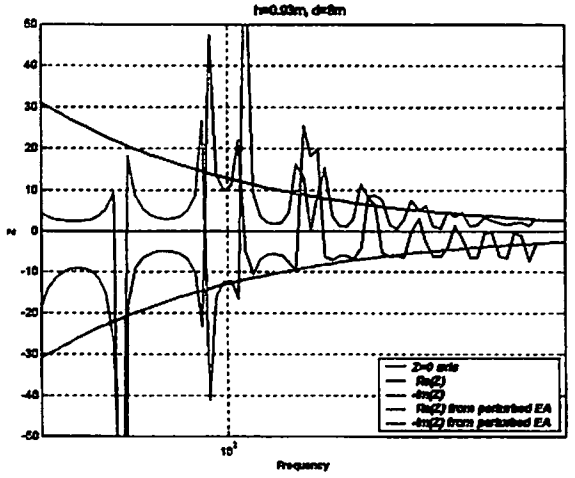

Figure 40- Comparison between the effective impedance from the perturbed and unperturbed excess attenuation

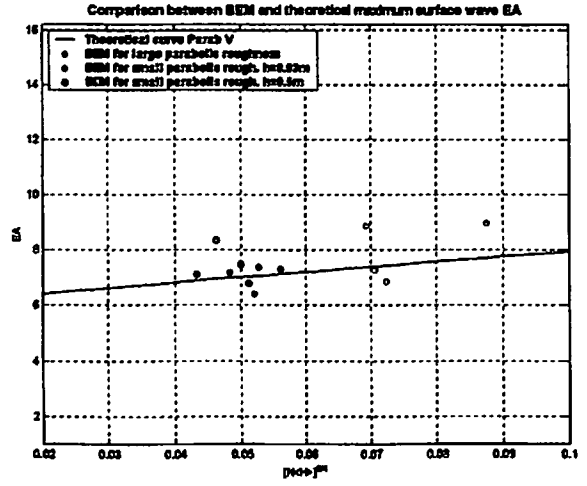

Figure 41- Comparison between BEM excess attenuation maxima and prediction from Medwin's theory of surface waves

References

[1] F. Coulouvrat "Sonic boom in the shadow zone: a geometrical theory of diffraction" ", submitted to J. Acoust. Soc. Am. , (2001).

[2] K. Attenborough and S. Taherzadeh, "Propagation from a point source over a rough finite impedance boundary", J. Acoust. Soc. Am., **98**(3) 1717-22 (1995)

[3] R. J. Lucas and V. Twersky, "Coherent response to a point source irradiating a rough plane" J. Acoust. Soc. Am. **76**, 1847-1863 (1984).

[4] P. Boulanger, K. Attenborough, S. Taherzadeh, T. Waters-Fuller, and Li K. M., "Ground Effect Over Hard Rough Surfaces". J. Acoust. Soc. Am. **104**, 1474-1482 (1998).

[5] K. Attenborough and T. Waters-Fuller, "Effective impedance of rough porous ground surfaces", J. Acoust. Soc. Am., **108**(3) 949-956 (2000)

[6] S. Taherzadeh, and K. Attenborough, "Deduction of ground impedance from measurements of excess attenuation spectra" ". J. Acoust. Soc. Am. **105**, 2039-2042 (1999).

[7] P. R. Brazier –Smith and J. F. M. Scott, "On the determination of the roots of dispersion equations by use of winding number integrals", J. Sound Vib. **145**, 503-510 (1991).

[8] P. Boulanger, K. Attenborough, T. Waters-Fuller, and K. M. Li "Models and Measurements of Sound Propagation from a Point Source over Mixed Impedance Ground". J. Acoust. Soc. Am. **102**, 1432-1442 (1997).

[9] A. Pierce "Atmospheric propagation at larger lateral distances from the flight track" High-Speed Research: 1994 Sonic Boom Workshop, NASA Conference Publication 3279.

[10] "The Sea, Physical Oceanography", Vol. 1, Interscience Publisher, Wiley Editions.

[11] K. Attenborough "Underwater acoustics, Sonar performance modelling" Open University course.

[12] L. Fortuin, "Survey of Literature on Reflection and scattering of Sound Waves at the sea Surface", JASA, **47**, (5) 1969.

[13] H. U. Thurman "Introductory Oceanography", 8th Edition , Prentice Hall.

[14] Revault D'Allonnes, M. "L'océanographie Physique", Que sais-je 92.

[15] M. Rousseau, F. Coulouvrat "Scattering of a High Frequency Acoustic Wave by a Sinusoidal Swell: Asymptotic Formulation, Numerical Simulation and Fluid Motion Influence", Acustica, **86** (2000).

[16] N. Wells "The Atmosphere and Ocean, A physical Introduction", Wiley Editions.

[17] J. L. Rochat and V. W. Sparrow, "A computational analysis of sonic booms penetrating a Realistic ocean surface", J. Acoust. Soc. Am. **109** , 899-908 (2001).

[18] S. N. Chandler-Wilde and D. C. Hothersall "Efficient calculation of the green function for acoustic propagation above a homogeneous impedance plane ", J. Sound and Vib., **180**, 705-724 (1995).

[19] S. N. Chandler-Wilde and D. C. Hothersall, "A uniformly valid far field asymptotic expansion of the green function for two-dimensional propagation above a homogeneous impedance plane" ", J. Sound and Vib., **182**, 665-675 (1995)

[20] H. Bass, "Encyclopedia of Applied Physics", 157

[21] J. P. Chambers, J. M. Sabatier and R. Raspet, "Grazing Incidence propagation over a soft rough surface", J. Acoust. Soc. Am. **102**, 55-59 (1997).

[22] J.F. Allard, L. Kelders and W. Lauriks, "Ultrasonic surface waves above a doubly periodic grating", J. Acoust. Soc. Am. **105**, 2528-2531 (1999).

[23] K. Attenborough, "Acoustical impedance models for outdoor ground surfaces", J. Sound Vib. **99** (4), 521–544 (1985)

[24] K. Attenborough, "Ground parameter information for propagation modeling", J. Acoust. Soc. Am. **92** 418–427 (1992): see also R. Raspet and K. Attenborough, 'Erratum:'Ground parameter information for propagation modeling', J.Acoust. Soc. Am. **92** 3007 (1992)

[25] R. Raspet and J. M. Sabatier, 'The surface impedance of grounds with exponential porosity profiles', J.Acoust.Soc. Am., **99**(1) 147 - 152 (1996)

[26] P. Boulanger, K. Attenborough, "Effective Impedance of Rough Sea Surfaces", D8 SOBER Report, Project n° GRD1-2000-25189 University of Hull, (2002)

[27] P. Boulanger, K. Attenborough, "Effective impedance of rough sea surfaces for varying incidence angle and roughness cale", Task3.4 SOBER Report, Project n° GRD1-2000-25189 University of Hull, (2002)

[28] H. Medwin and G. D'Spain, "Near-grazing, low-frequency propagation over randomly rough, rigid surfaces", J. Acoust. Soc. Am. **79** (3) 657-665 (1986)

[29] I. Tolstoy, "Rough surface boundary wave attenuation due to incoherent scatter", J. Acoust. Soc. Am. **77** (2) 482-488 (1985)

[30] H. Medwin, G. L. D'Spain E. Childs and S. J. Hollis, "Low frequency grazing propagation over periodic steep-sloped rigid roughness elements", J. Acoust. Soc. Am. **76** (6) 1774-1790 (1984)

[31] H. Medwin., J.Baillie, J.Bremhorst, B. J.Savage and I.Tolstoy, "The scattered acoustic boundary wave generated by grazing incidence at a slightly rough rigid surface", J. Acoust. Soc. Am. **66** (4) 1131-1134 (1979)

[32] H. Medwin and G. L.D'Spain,"Near-grazing, low-frequency propagation over randomly rough, rigid surfaces ", J. Acoust. Soc. Am. **79** (6) 657-665 (1986)

[33] D.J. James and G. Kerry, "The Propagation of Blast Noise Across Acoustically Hard Surfaces", Proceeding of Internoise 2000.

Sound Propagation Measurements and Modeling Results from the CASES-99 Experiment

D. Keith Wilson[1] and John M. Noble
U.S. Army Research Laboratory
Computational and Information Sciences Directorate
Adelphi, MD 20783-1197, USA

Abstract

An experimental study of sound propagation in stable, nighttime conditions was performed in conjunction with CASES-99. Low-frequency sound transmissions were continuously recorded at microphones out to a distance of 1.3 km from a loudspeaker over the course of two entire nights. Fading episodes in the received signal energy of 10 to 20 dB, lasting several minutes to an hour, were frequently observed. Strong atmospheric events, such as a density current and solitary wave, were found to have significant effects on acoustical signals, although substantial variability in received sound energy often occurred outside such events. Propagation predictions from a parabolic equation code demonstrate that wind and temperature data from a tall tower, such as the CASES-99 60-m tower, can be used predict the momentary variations in a 50-Hz sound signal with good success. Higher frequencies, however, appear to be very sensitive to fine-scale atmospheric structure along the propagation path that is not available from a single tower. Tethersonde and rawinsonde data are generally too infrequent to model many of the strong variations present in signal.

I Introduction

Fair weather, nighttime conditions are normally viewed as highly favorable to sound propagation. This is because temperature inversions, which are prevalent in such conditions, tend to trap sound energy in a ground-based duct, allowing the sound to propagate efficiently over long distances (Delany, 1977; Embleton, 1996). Beyond this simple fact, however, truly little is known regarding sound propagation at night. The nighttime atmosphere differs fundamentally from the daytime atmosphere, in that radiative cooling of the ground produces stable stratification in the air column. This stable stratification damps turbulence, but supports other types of phenomena such as internal gravity (buoyancy) waves. Therefore it is unclear how well our understanding of propagation in turbulent, daytime conditions carries over to night. Among the pertinent questions are: Which atmospheric phenomena play a primary role in driving acoustic signal variability at night? What data are needed to accurately predict nighttime sound propagation? How high in the atmosphere do horizontally transmitted signals travel before returning to the ground? How stable are the propagating modes in the ground-based duct created by a temperature inversion?

In this paper, we provide results from a sound propagation experiment designed to address these issues. The experiment was undertaken in conjunction with CASES-99, the Cooperative Atmospheric Surface Exchange Study. Poulos et al. (2002) provide a summary of the instrumentation deployed during CASES-99 and highlights of results from the study. Preliminary results from our participation in CASES-99 were presented in a previous paper at this Symposium (Noble et al., 2000). The comprehensive atmospheric boundary-layer measurements recorded during CASES-99 provide a unique opportunity to relate the acoustic signal behavior to the underlying atmosphere. Our experimental set-up for sound propagation is described in Section II. Results over the course of the CASES-99 Intensive Observation Periods (IOP's) 6 and 7 are provided, with an in-depth examination of two strong atmospheric events occuring during IOP 7, in Section III. Sound propagation modeling for the experiment is discussed in Section IV. The propagation modeling leads to some surprising conclusions on the predictability low-frequency sound transmissions.

[1]Present address: U.S. Army Cold Regions Research Laboratory, CEERD-RC, 72 Lyme Rd., Hanover, NH 03755-1290, USA

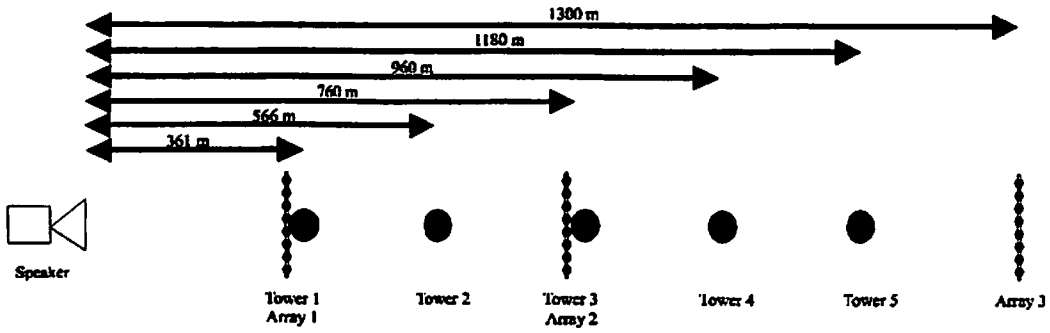

Figure 1: Layout of the sound-propagation path.

II Experiment

CASES-99 was conducted outside of Wichita, Kansas, on a flat, grassy plain. The purpose of the experiment was to improve understanding of atmospheric processes in stable, nighttime conditions and during the morning/evening transitions. Dozens of institutions from the U.S. and Europe particpated. The U.S. Army Research Laboratory participated by setting up a sound transmission experiment with a single sound source positioned roughly 1.8 km southwest of the main 60-m tower. A series of five 6-m towers were placed at distances between 361 and 1180 m on a transmission path running due north from the source, as shown in Figure 1. Each tower had microphones at heights of 0.5, 1, 2, and 3 m. There were also 3 transverse linear arrays placed on the ground at various distances out to 1300 m from the speaker.

Propagation trials were conducted during the CASES-99 IOP's 3 through 7. These IOP's took place on the nights of 9 Oct, 10 Oct, 11 Oct, 13 Oct, and 17 Oct 1999, respectively. These nights were selected for intensive observation because they had generally fair, clear, weather, leading to the development of very stable atmospheric stratification.

The sound source for IOP 3 consisted of a propane cannon, which generates a repeatable, impulsive signal. During the remaining IOP's, a continuous, 50-Hz square wave was broadcast from a loudspeaker at 1-m height. The square wave includes higher odd harmonics of the 50-Hz fundamental (150 Hz, 250 Hz, ...).

The microphone signals were sampled at 12 kHz and recorded onto digital audio tape. Due to the huge amount of data being stored, the tapes had to be changed roughly every 2 hours. A pair of 2-hour sessions were conducted for IOP's 3, 4, and 5. For IOP's 6 and 7, the tapes were exchanged regularly througout the night, providing a nearly continous record of the sound level from dusk until sunrise. In this paper, we focus on these latter two IOP's.

Signal levels were determined by FFT processing of 5-s (60,000-sample) segments with an 80% overlap. The sound energy (or, more precisely, the squared sound pressure, which is proportional to the sound energy) at each frequency of interest f was then determined by adding the squared magnitudes of all bins within ± 2.5 Hz of f. This interval was large enough to capture all spreading of the sound energy in frequency due to Doppler shifts from random scattering, which was found to be well less than 1 Hz.

III Results for IOPs 6 and 7

A Effective Sound Speed

For nearly horizontal propagation paths such as in the present experiment, the behavior of the acoustic signal is determined primarily by the "effective" sound speed field c_{eff}, which is the sum of the actual sound speed

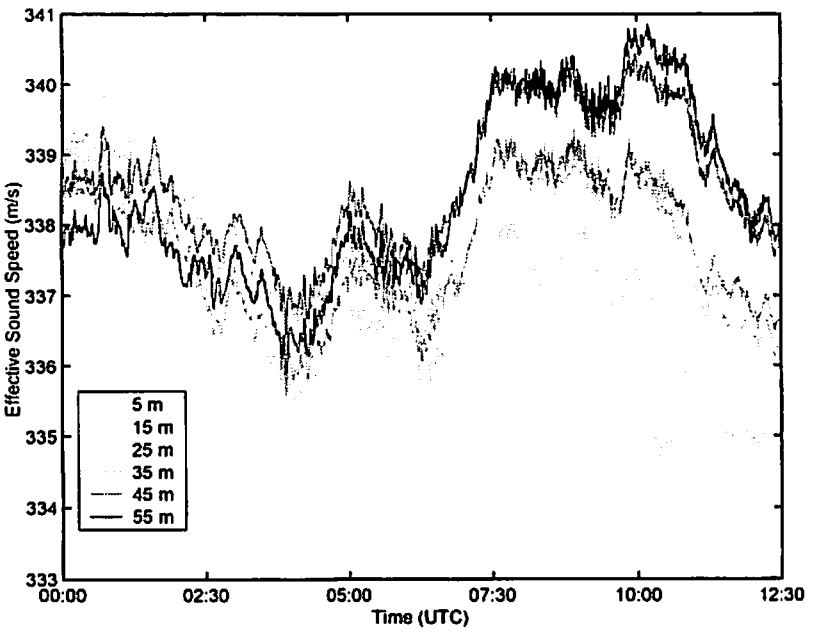

Figure 2: Effective sound speed at several heights on the main tower during IOP 6.

c and the component of the wind velocity in the nominal propagation direction (Ostashev, 1997). Since our propagation path is due north, $c_{\text{eff}} = c + v$, where v is the northward wind component. The sound speed is given by $c = \sqrt{\gamma_d R_d T\,(1 + 0.511r)}$, where γ_d is the specific heat ratio for dry air, R_d is the gas constant for dry air, T is temperature, and r is the water vapor mixing ratio (Ostashev, 1997).

Figures 2 and 3 show the effective sound speed during IOP's 6 and 7 at several heights on the main 60-m tower (Poulos et al., 2002). (The heights shown are from 5 to 55 m, in 10-m intervals. Standard slow-response sensors were used in all cases, except for the winds at 5 and 55 m, where sonic anemometer data were used.) An increase in c_{eff} with height causes downward refraction and ducting of sound near the ground, whereas a decrease causes upward refraction and acoustic "shadow" formation. Roughly similar patterns to the evolution of the c_{eff} profile are evident during both IOP's. The evening starts with a weak decrease in c_{eff} with height and finish with strong, increasing c_{eff}. For IOP 7, however, a very strong event occurs between 0130 and 0200 UTC. Sun et al. (2000) describe this as a density current. A second event of very short duration occurs around 0645 UTC. Immediately before the record ends at 1230 UTC, a third strong event occurs. Although there is much variation in the c_{eff} profile during IOP 6, there appear to be no counterparts to the three events in IOP 7.

Figures 4 and 5 show a bulk approximation to the effective sound-speed gradient. The bulk approximation involves taking the difference between the 55-m and 5-m levels on the main tower (i.e., $\partial c_{\text{eff}} / \partial z \simeq [c_{\text{eff}}(z_2) - c_{\text{eff}}(z_1)] / (z_2 - z_1)$, where $z_1 = 5$ m and $z_1 = 55$ m). The contributions to the bulk gradient from wind, temperature, and humidity are also shown. We see that the trend toward an increasingly positive gradient is due primarily to a shifting of the wind direction on both nights. Propagation was upwind until about 0630 UTC (0130 LST) on both nights, at which time it shifted to downwind. Between roughly 0200 and 0500 UTC, a transition occurs to very strong, positive gradients in c_{eff}. This transition is due to primarily to shifting wind direction combined with the temperature inversion.

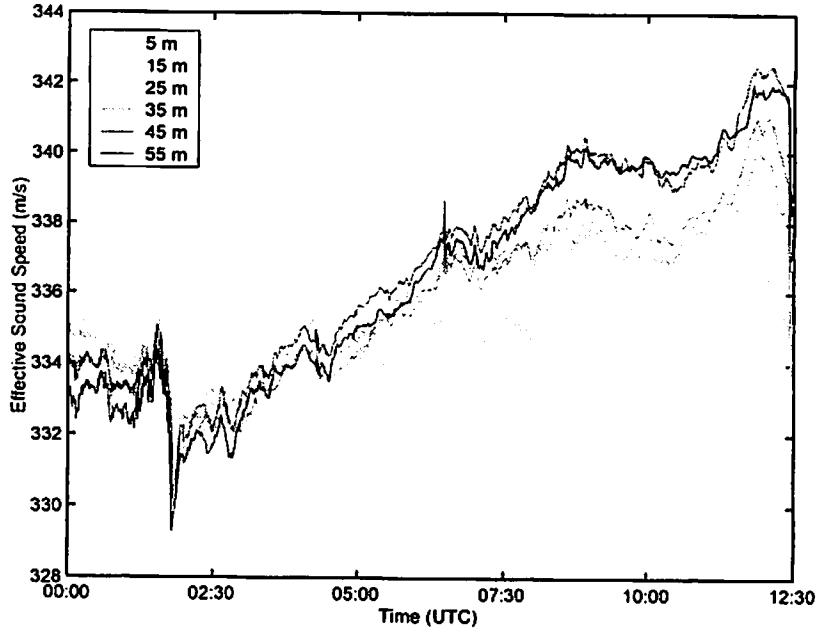

Figure 3: Effective sound speed at several heights on the main tower during IOP 7.

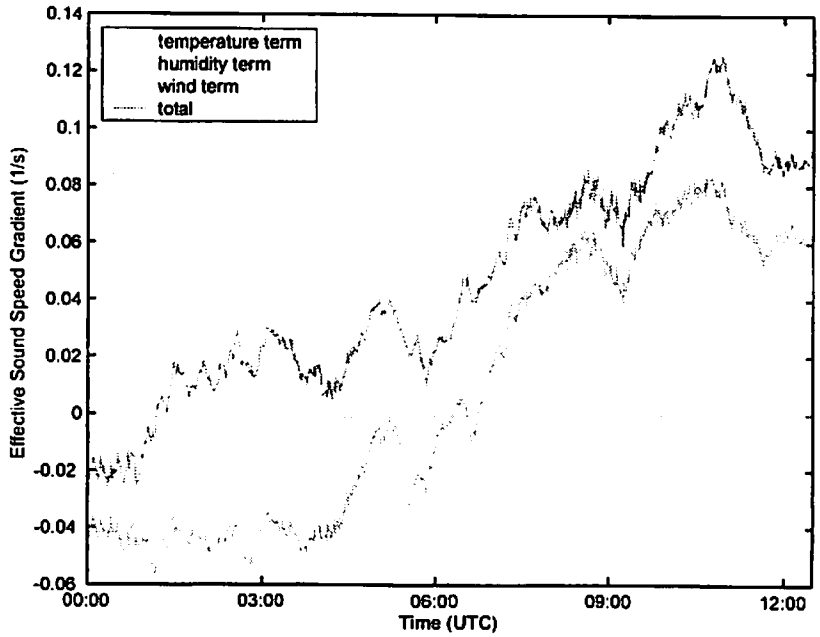

Figure 4: Bulk effective sound-speed gradient and contributions from temperature, humidity and wind during IOP

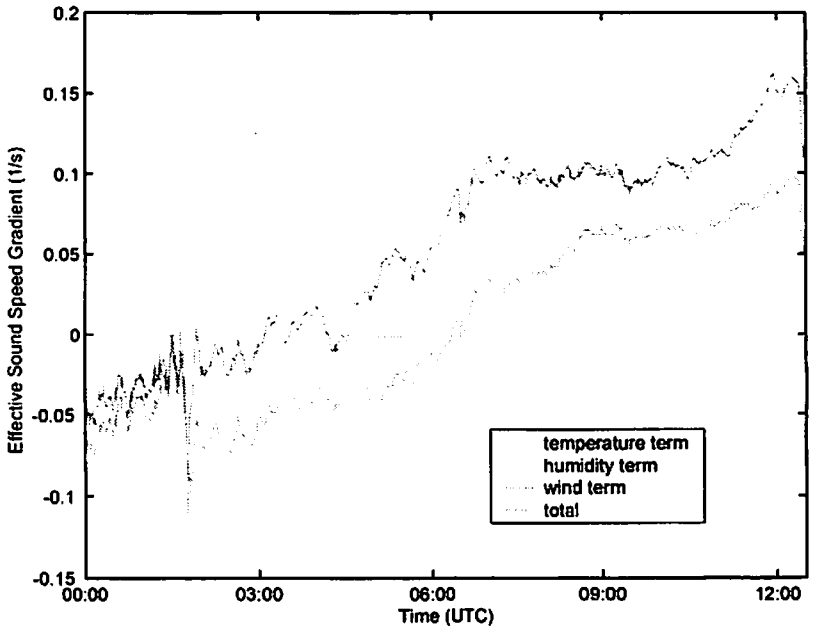

Figure 5: Bulk effective sound-speed gradient and contributions from temperature, humidity and wind during IOP 7.

B Sound Levels

Complete, processed sound levels for 50, 150, 250, and 350 Hz at the 0.5-m microphone on tower 2 (566 m) are shown in Figs. 6 and 7. These figures combine all the recordings for IOP 6 and IOP 7, respectively. The curves have been arbitrarily offset along the vertical axis for better visibility.

During IOP 6, there is a weak tendency for the sound levels to increase from about 0000 UTC to 0230 UTC, decrease from 0230 to 0500 UTC, and then increase once again until sunrise. Superimposed on this general behavior are many strong fading episodes where the sound levels decrease as much as 15 dB over periods ranging from a few minutes to an hour. These variations in sound level are most pronounced at higher frequency. The signal behavior during IOP 7 is similar to IOP 6, although there is a trend for gradually increasing sound levels at all frequencies throughout the night.

The behavior of the sound levels very roughly follows the c_{eff} gradient. In IOP 6 (Fig. 6), the weakening of the negative gradient prior to 0230 UTC allows sound levels to increase. They increase again after roughly 0630 UTC, corresponding to the shifting wind direction. The reason for decreasing sound levels after 0230 UTC is not evident from the c_{eff} profile (Fig. 2), however. In IOP 7 (Fig. 7), the gradual increase in sound levels throughout the night corresponds to a steadily increasing gradient, with a notable disturbance between 0130 and 0200 UTC.

Figure 8 shows a scatter plot of the sound pressure level at 50 Hz vs. the bulk approximation to the effective sound-speed gradient from Figs. 4 and 5. The acoustic data in the figure are again from the 0.5-m microphone on tower 2. A trend for elevated sound levels with increasing gradient is clearly evident, although there is significant scatter to the data. The scatter can be attributed to factors such as the bulk approximation, the lack of measurements above 55 m, and the differing locations of the main tower and propagation path. A similar plot, but for 150 Hz, is given in Figure 8. This plot has a much less regular appearance than the one for 50 Hz. The more complicated relationship between the sound level and gradient at this frequency is probably due to an interference between multiple, propagating modes. This will be discussed further in Section IV.

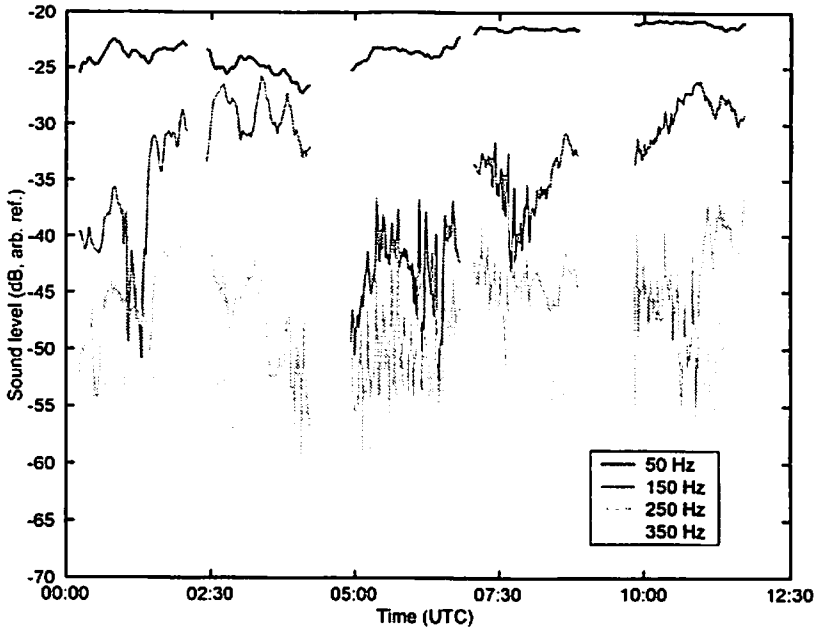

Figure 6: Sound levels at the 0.5-m microphone on tower 2 during IOP 6.

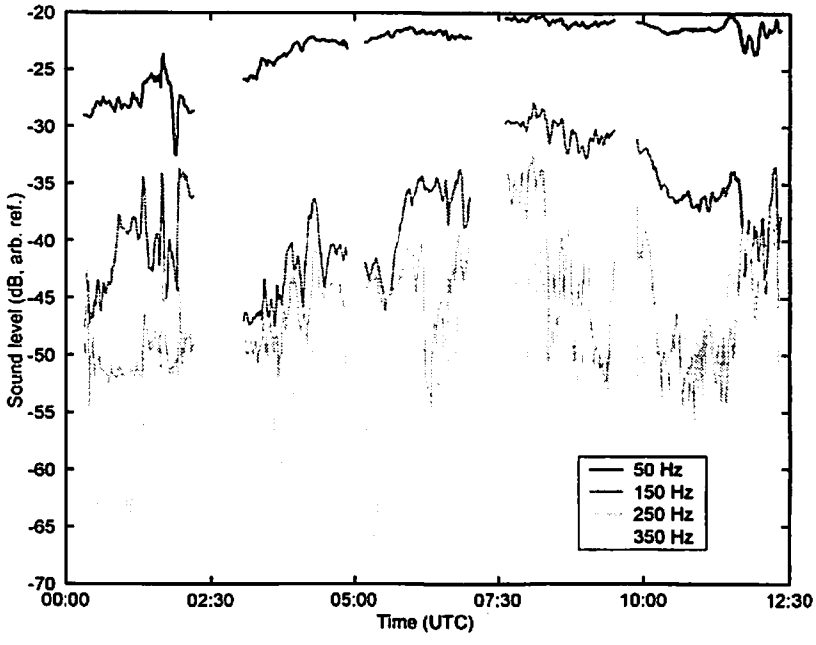

Figure 7: Sound levels at the 0.5-m microphone on tower 2 during IOP 7.

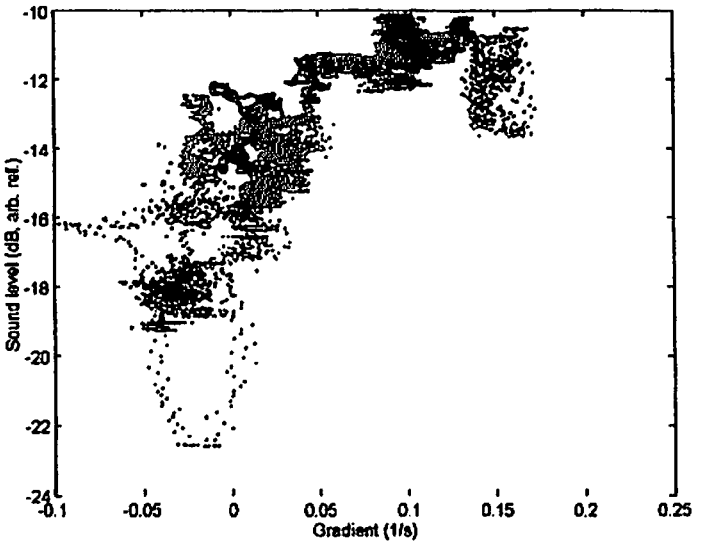

Figure 8: Scatter plot of the sound level at 50 Hz vs. a bulk approximation to the effective sound-speed gradient. Light points are IOP 6; dark are IOP 7.

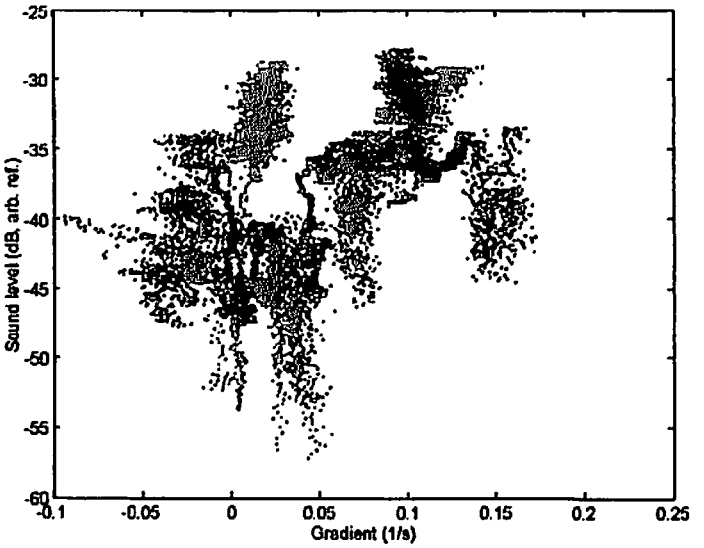

Figure 9: Scatter plot of the sound level at 150 Hz vs. a bulk approximation to the effective sound-speed gradient. Light points are IOP 6; dark are IOP 7.

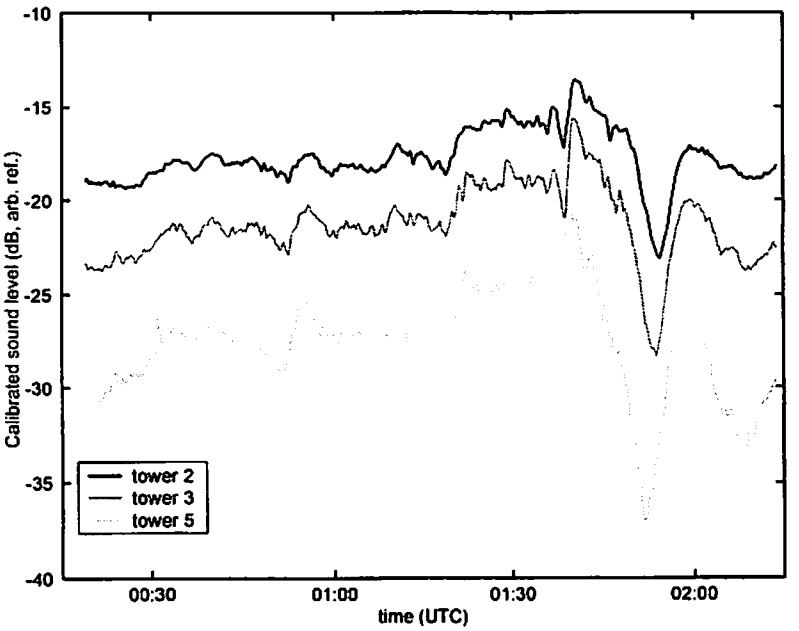

Figure 10: Sound levels at towers 2, 3, and 5 over a two-hour period including Event 1.

C Discrete Events during IOP 7

In this subsection, we consider the behavior of the acoustical signal during the strong events of IOP 7. The two-hour recording including event 1 is shown in Fig. 10; event 3 is shown in Fig. 11. The 50-Hz signal at the 2-m microphones on towers 2, 3, and 5 (570, 760, and 1170 m, respectively) is shown. Event 1 is associated with the passage of a density current and event 3 with gravity waves. We found that event 2, which was associated with a solitary wave and the weakest of the three, had little impact on the acoustic signals.

In Fig. 10, the sound levels peak at 0140 UTC and then start to oscillate with a period of about 15 min. This behavior is remarkably consistent among all microphones and clearly coincides with observations of event 1.

Event 3 and the period leading up to it (Fig. 11) produce more complex behavior in the sound levels. We observe a deep fading in the sound level at 1130 UTC at the more distant microphones. At the same time, the sound level at the near microphone attains a local maximimum. Comparing with Fig. 3, we see that this behavior corresponds to an increase in the effective sound speed above 15 m. Shortly after 1215 UTC, near the onset of event 3, very rapid fluctuations in the sound level are observed at all microphones. These fluctuations are particularly strong at the two more distant microphones.

IV Propagation Modeling

In this section, we use numerical sound propagation calculations to better understand the acoustic signal behavior during the CASES-99 experiment. Atmospheric data from the experiment are used as input for a parabolic equation (PE) propagation code of the type described by West et al. (1992).

Strictly speaking, one would have to measure the atmospheric fields at a spatial resolution finer than an acoustic wavelength (where λ, the acoustic wavelength is about 6.6 m at 50 Hz and 2.2 m at 150 Hz) and a temporal resolution shorter than the acoustic period, to predict all details of the sound propagation. But no currently available measurement system comes close to providing such fine resolution over the entire sound-propagation path. Therefore it is only practical to address the issue of whether the instrumentation available during CASES-

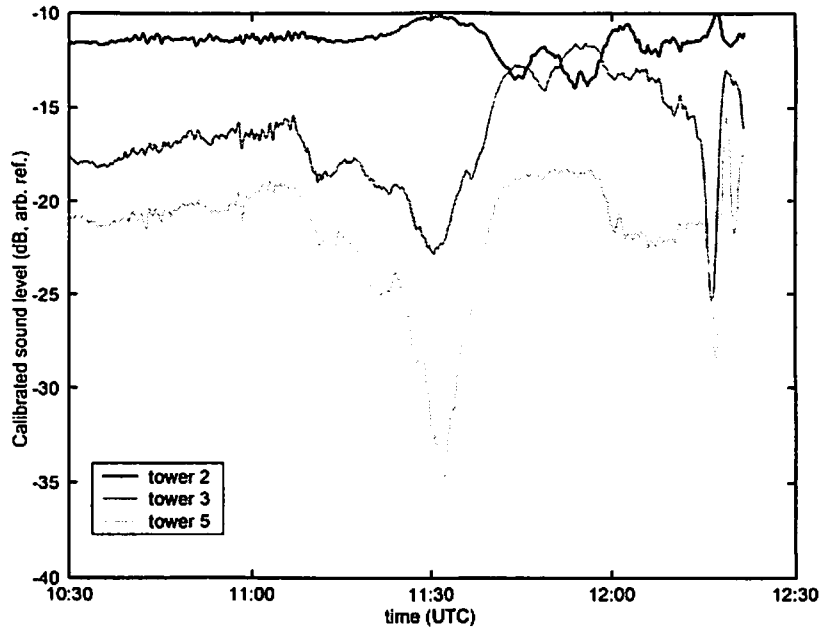

Figure 11: Sound levels at towers 2, 3, and 5 over a two-hour period including Event 3.

99, which generally represented the current state of the art, can adequately predict certain important features of the propagation, such as the average received signal energy and variability caused by changing atmospheric conditions. Since simultaneous data on the wind, temperature, and humidity fields are required, the three main CASES-99 systems of potential interest are (1) the various surface-based towers, particularly the 60-m main tower, (2) the Argonne National Laboratory tethersonde system, and (3) the National Center for Atmospheric Research CLASS rawinsondes. The main advantages of the 60-m tower are the high sampling rate (usually 1 s) and the consistent availability of data. The nearby, shorter towers can provide information on the propagation speed and direction of the discrete events such as those discussed earlier for IOP 7. The tethersonde provides profiles up to roughly 300 m, with an ascent/descent cycle of about 1 hr. The rawinsondes were typically launched at 1-hr intervals. From the standpoint of sound-propagation predictions, one difficulty with the rawinsonde data is that the wind profiles below several hundred m AGL are often unavailable due to the operational characteristics of the GPS system.

It is unclear *a priori* whether the 60-m tower and tethersonde provide profiles high enough into the atmosphere to model the sound propagation well. A rule-of-thumb that is often applied in the acoustics community is that the vertical profiles must be known up to a height equal to 1/10 to 1/5 of the horizontal propagation distance. But this rule-of-thumb cannot be proven in general; in reality the limiting height depends on factors such as the sound frequency, propagation distance, and steepness of the profile gradients.

To address the limiting height issue for this particular experiment, we consider here a test based on truncating the rawinsonde data at various heights and using the truncated profiles as input to the PE. Two test cases were selected on the basis of their distinctive effective sound-speed profile characteristics: (1) 2300 UTC on 17 Oct., an evening case with a shallow, ground-based temperature inversion and no significant low-level jet, and (2) 1100 UTC on 18 Oct., an early morning case with a deep temperature inversion and well developed jet. The effective sound-speed profiles for these cases are shown in Fig. 12. Note that the early morning case results in a deep, strong duct, which will tend to trap sound energy below the jet maximum at 150 m.

In the test applied here, the rawindsonde profiles are replaced with constant values of temperature, humidity, and wind velocity, above the prescribed truncation height. These constant values are chose to match the respective

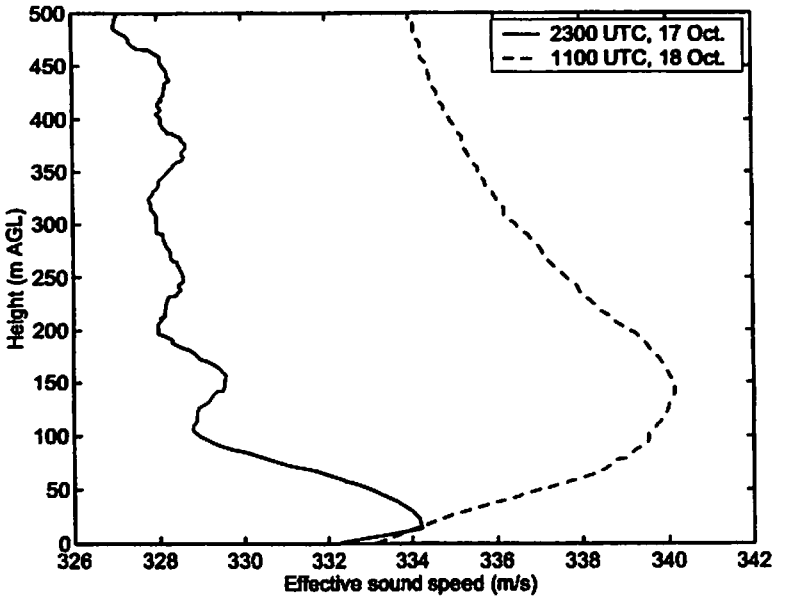

Figure 12: Effective sound-speed profiles for the two cases used in a sensitivity test of the sound-propagation predictions to the height of profile truncation.

profiles at the truncation height. Within the constant layer, an absorbing condition is added to minimize artificial reflections occuring at the top of the numerical grid (Salomons, 1998). The truncation height is moved from 0 m AGL (the case of a homogeneous, non-refracting atmosphere) up to 500 m in 25 m increments. Results are shown in Figs. 13 and 14. The figures show, for receiver distances out to 1.5 km, that the solution becomes nearly constant when the truncation height reaches 75 m to 100 m. Therefore the rule-of-thumb alluded to earlier holds, and is even conservative, for this experiment. We conclude that the tethersonde flights sufficiently covered the altitudes of the atmosphere important in our experiment. The 60-m tower is marginally tall enough to be useful.

In order to predict the sound propagation characteristics from the 60-m tower data during events 1 and 3 of IOP 7, we must make some assumptions about the spatial structure of these events. For lack of a better alternative, we assume that these events have a fixed structure as they move across the CASES-99 site and have a width (spatial extent perpendicular to their direction of translation) that is much larger than the sound transmission path. These assumptions allow the atmospheric fields at any given time and observation point to be mapped back to the main tower according to the equation

$$Q_O(t) = Q_T\left[t - d\cos(\alpha - \theta)/v\right], \tag{1}$$

where $Q(t)$ is the time-varying atmospheric field of interest (temperature, humidity, or wind), the subscripts "O" and "T" indicate the observation and tower positions, respectively, d is the distance from the tower to the observation point, α is the polar angle of the observation point relative to the tower, θ is the direction of translation of the event, and v is the speed of the event. The observation points in this case are locations along the sound-propagation path. According to Sun's analysis of the tower data (2001, personal communication), event 1 propagated at 2.3 m/s from a compass bearing of 47°, whereas event 3 propagated at 1.72 m/s from 267°. To generate profiles for input to the sound-propagation code, we spaced 100 points evenly between the loudspeaker and the 1300 m microphone array. PE predictions were run at 1-min intervals.

The PE code requires two additional inputs that are not readily available from the experiment: the absolute source level and the porous ground parameters. We infer the source level by calculating the mean measured

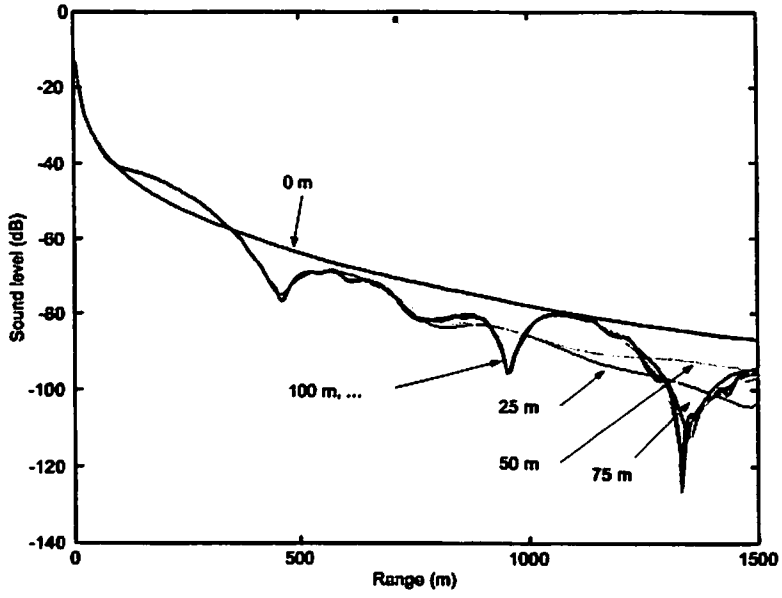

Figure 13: Sound level predictions at 150 Hz for the rawinsonde launch at 2300 UTC on 17 Oct. The effect of truncating the atmospheric profiles above the height indicated on the figure is shown.

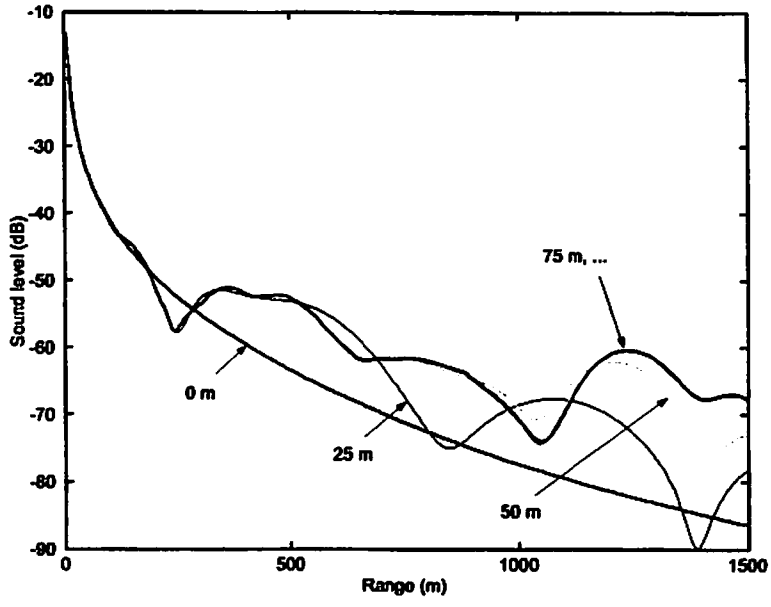

Figure 14: Sound level predictions at 150 Hz for the rawinsonde launch at 1100 UTC on 18 Oct. The effect of truncating the atmospheric pro files above the height indicated on the figure is shown.

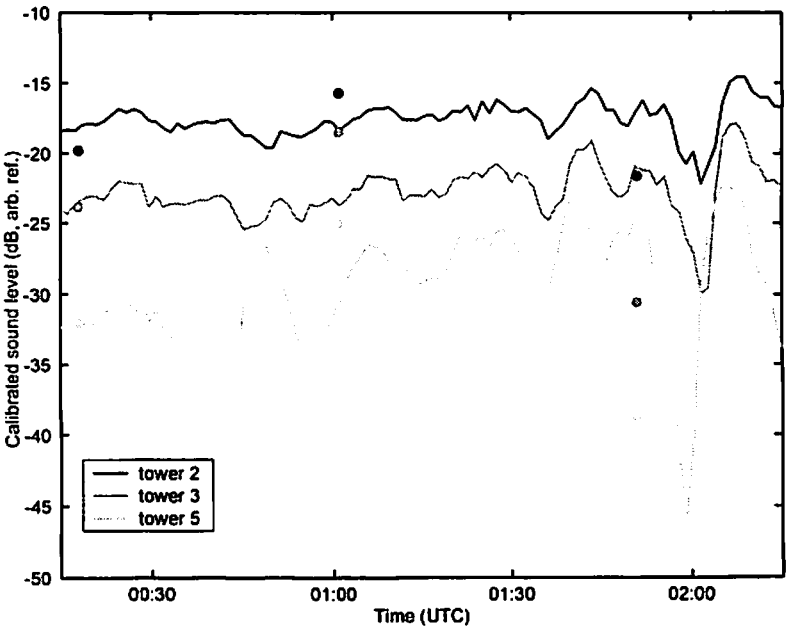

Figure 15: Modeled sound level at 50 Hz for the 2-hr period of IOP 7 including event 1. Lines represent predictions from the main-tower data and circles from the tethersonde data.

sound-pressure level at tower 2 for each frequency and IOP. After running PE predictions for a 0 dB source level (unit strength source), the actual source level then follows by subtracting the predicted sound-pressure level from the measured one (in dB). For the ground parameters, we have used values representative of those previously determined for uncultivated, dry, grassy sites (Martens et al., 1985; Attenborough, 1985)): a static flow resistivity σ =200 kPa s m^{-2}, porosity (volume void fraction) $\Omega = 0.50$, squared tortuosity $q^2 = 1.4$, and pore shape factor $s_B = 1$. These values were used in the Biot-Allard relaxation model for the acoustical properties of a porous medium as described in Wilson (1997).

Model predictions of 50-Hz propagation for events 1 and 3 during IOP 7 are shown in Figs. 15 to 16. The model predictions from the main-tower data have many close similarities to the actual measurements. While the timing and magnitude of the various fluctuations in sound level are not exactly predicted, there are few substantial features in the observations that are not present in the predictions. The predictions could almost certainly be improved if the tower were somewhat higher and/or multiple towers were available closer to the sound propagation path. The predictions from tethersonde data in the figures are plotted at the time of the beginning of the ascent/descent. Profiles are available for only three predictions during the 2-hr period shown in Fig. 15 and once during the 2-hr period of Fig. 16. This infrequency does not allow the evolution of the acoustic signal to be usefully modeled. Predictions at 150 Hz (not shown) are not nearly as successful as the 50-Hz predictions.

V Conclusion

The acoustical measurements during CASES-99 have provided valuable insight into the characteristics of near-ground propagation at night. Fading episodes in the received signal energy of 10 to 20 dB, lasting several minutes to an hour, were frequently observed. The variations in signal energy become more irregular and less clearly related to the effective sound-speed gradient as the acoustic frequency increases. Out to receiver distances of about 1 km from the source, sound levels are determined primarily by the wind and temperature profiles in the lowermost 100 m or so of the atmosphere. Strong discrete events, such as density currents and solitary waves, do

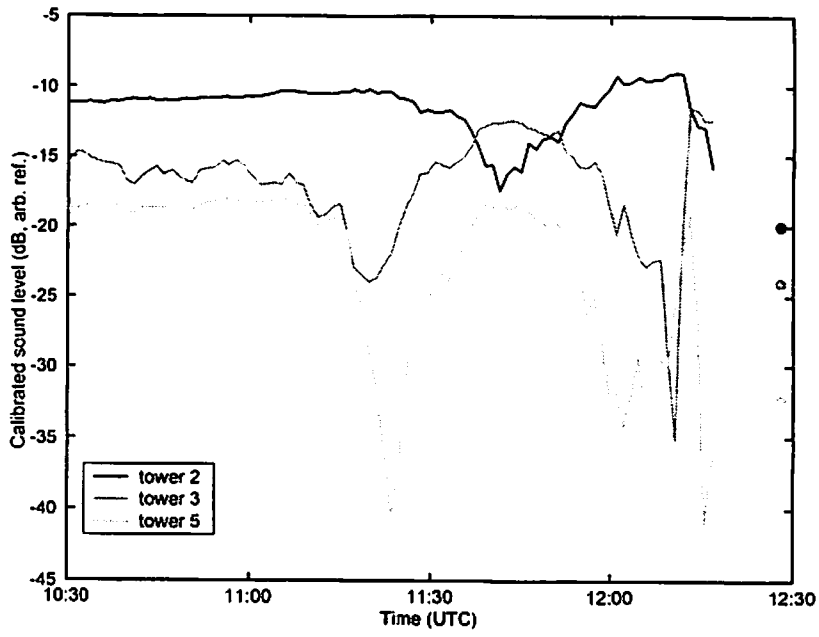

Figure 16: Modeled sound level at 50 Hz for the 2-hr period of IOP 7 including event 3. Lines represent predictions from the main-tower data and circles from the tethersonde data.

have observable effects on acoustical signals, although substantial variability in sound levels occurs outside such events.

Sound propagation model results demonstrated that data from a tall tower, such as the CASES-99 60-m tower, can be used to predict variations in sound levels at 50 Hz with good success. At frequencies 150 Hz and higher, it appears that even the 60-m tower data become ineffective for predicting instantaneous sound levels. The propagation appears to depend too strongly on small-scale structure along the transmission path that cannot be observed at a single tower positioned roughly 1 km from the transmission path.

Tethersonde and rawinsonde data are generally too infrequent to model many of the strong, momentary variations that are present in data. Therefore it must be understood that predictions from sonde data or from numerical weather models provide only snapshots of the actual data; they cannot account for the intermittent episodes of depressed and elevated sound levels, which can be extremely important in determining acoustic detectability of a target.

Of course, we would not normally expect to have a 60-m tower or some similar, in-situ, high-resolution meteorological observation system for predicting sound propagation. Even with promising remote sensing technologies that have undergone rapid development in recent years, such as lidar and acoustic tomography, we are still far from possessing a capability for remotely determining the along-path atmospheric wind and temperature fields at the fidelity necessary to predict moment-by-moment variations in sound levels. Improved understanding is therefore much needed regarding how sound propagation predictions, when based on coarse spatial/temporal data or weather predictions, relate to the actual properties of observed sound levels.

Acknowledgments

We thank S. Burns (NCAR) for his help in accessing the CASES-99 tower data and J. Sun (NCAR) for discussing preliminary results on the three events during IOP 7. We are also grateful to many other CASES-99 participants for the insights they have shared on various occassions, including the workshops sponsored by W. Bach (Army Research Office).

References

Attenborough, K., 1985: Acoustical impedance models for outdoor ground surfaces. *J. Sound Vib.*, **99**, 521–544.

Delany, M. E., 1977: Sound propagation in the atmosphere: a historical review. *Acustica*, **38**, 201–223.

Embleton, T. F. W., 1996: Tutorial on sound propagation outdoors. *J. Acoust. Soc. Am.*, **100**, 31–48.

Martens, M. J. M., L. A. M. van der Heijden, H. H. J. Walthaus, and W. J. J. M. van Rens, 1985: Classification of soils based on acoustic impedance, air flow resistivity, and other physical soil parameters. *J. Acoust. Soc. Am.*, **78**, 970–980.

Noble, J. M., D. K. Wilson, and M. A. Coleman, 2000: CASES-99 field study and preliminary results. In *Ninth International Symposium on Long-Range Sound Propagation*, Delft, Netherlands.

Ostashev, V. E., 1997: *Acoustics in Moving Inhomogeneous Media.* E & FN Spon, London.

Poulos, G. S., W. Blumen, D. C. Fritts, J. K. Lundquist, J. Sun, S. P. Burns, C. Nappo, R. Banta, R. Newsom, J. Cuxart, E. Terradellas, B. Balsley, and M. Jensen, 2002: CASES-99: A comprehensive investigation of the stable nocturnal boundary layer. *Bull. Amer. Meteor. Soc.*, **83**, 555–581.

Salomons, E. M., 1998: Improved Green's function parabolic equation method for atmospheric sound propagation. *J. Acoust. Soc. Am.*, **104**, 100–111.

Sun, J., S. Burns, D. Lenschow, and Q. Oosterhuis, 2000: Turbulence intermittency in the stable boundary layer. In *14th Symposium on Boundary Layer and Turbulence*, American Meteorological Society, Boston, 329–331.

West, M., K. Gilbert, and R. A. Sack, 1992: A tutorial on the parabolic equation (PE) model used for long range sound propagation in the atmosphere. *Appl. Acoust.*, **37**, 31–49.

Wilson, D. K., 1997: Simple, relaxational models for the acoustical properties of porous media. *Appl. Acoust.*, **50**, 171–188.

Wide angle parabolic equation for sound waves in a refractive, turbulent atmosphere

Vladimir E. Ostashev

NOAA/Environmental Technology Laboratory, 325 Broadway, Boulder, CO 80305 and

Physics Department, New Mexico State University, Las Cruces, NM

Philippe Blanc-Benon, Daniel Juvé, and Laurent Dallois

Ecole Centrale de Lyon, 36 Avenue Guy de Collongue, 69131 Ecully, France

Abstract. Wide angle parabolic equations should be used for solutions of many problems of sound propagation in a moving atmosphere. Such equations have recently been derived and used for numerical studies of outdoor sound propagation for two limiting cases: a non-refractive, turbulent atmosphere and refractive, non-turbulent atmosphere. In the present paper, we derive a new wide angle parabolic equation and its Padé (1,1) approximation for a more general case of sound propagation in a refractive, turbulent atmosphere. The derived equations coincide with those obtained earlier for the two limiting cases mentioned above.

1 Introduction

The use of a parabolic equation in analytical and numerical studies of outdoor sound propagation has resulted in much better understanding of this complicated phenomenon, e.g. [4, 6, 8]. Nevertheless, for many geometries of sound propagation in the atmosphere, one needs to use a wide angle parabolic equation rather than a parabolic equation (e.g. see [7]).

Wide angle parabolic equations for sound waves propagating in a moving atmosphere were derived in references [7, 2]. In these references, the equations were obtained for two limiting cases: a non-refractive, turbulent atmosphere and refractive, non-turbulent atmosphere. These equations were subsequently used for numerical studies of sound propagation outdoor [1, 2, 3]. Note that a wide angle parabolic equation in a moving atmosphere was also considered elsewhere [5].

The main goal of the present paper is to derive a new wide angle parabolic equation for sound waves propagating in a refractive, turbulent atmosphere. This new equation can be considered as a combination of those obtained in [7, 2] for the limiting cases of a non-refractive, turbulent atmosphere and refractive, non-turbulent atmosphere.

The paper is organized as follows. A starting equation of our analysis is presented in section 2. In section 3, a new wide angle parabolic equation and its Padé (1,1) approximation are derived. And in Conclusions, the results obtained are presented.

2 Starting equation

In this section, we consider a Helmholtz-type equation for sound waves propagating in a refractive, turbulent atmosphere.

The sound speed $c(\mathbf{R})$ can always be expressed in the following form: $c(\mathbf{R}) = \overline{c}(\mathbf{R}) + \tilde{c}(\mathbf{R})$. Here, $\mathbf{R} = (x_1, x_2, x_3) = (x, y, z)$ are the Cartesian coordinates, $\overline{c}$ and $\tilde{c}$ are the mean value and fluctuations of the sound speed, and $\langle \tilde{c} \rangle = 0$. (The brackets $\langle\ \rangle$ denote ensemble average.) Analogously, the atmospheric density can be expressed as: $\varrho(\mathbf{R}) = \overline{\varrho}(\mathbf{R}) + \tilde{\varrho}(\mathbf{R})$, where $\overline{\varrho}$ and $\tilde{\varrho}$ are the mean value and fluctuations in the density, and $\langle \tilde{\varrho} \rangle = 0$. Finally, the medium velocity

vector is written as: $\mathbf{u}(\mathbf{R}) = \mathbf{V}(\mathbf{R}) + \mathbf{v}(\mathbf{R})$, where $\mathbf{V}$ and $\mathbf{v}$ are the mean value and fluctuations of the medium velocity, and $\langle \mathbf{v} \rangle = 0$.

In [7], a wide angle parabolic equation was derived for the case of a non-refractive, turbulent atmosphere. For this case, $\overline{c} = c_0$, $\overline{\varrho} = \varrho_0$, $\mathbf{V} = 0$, where c_0 and ϱ_0 are constant, and $\tilde{c}$, $\tilde{\varrho}$, $\mathbf{v}$ are not zero. A starting equation for that derivation was a Helmholtz-type equation for the sound pressure p in a non-refractive, turbulent atmosphere (see Eq.(6.1) from [6]):

$$\left[\nabla^2 + k^2(1+\tilde{\varepsilon}) - (\nabla\tilde{\varrho}/\varrho_0)\cdot\nabla - \frac{2i}{\omega}\frac{\partial v_i}{\partial x_j}\frac{\partial^2}{\partial x_i \partial x_j} + \frac{2ik}{c_0}\mathbf{v}\cdot\nabla\right] p(\mathbf{R}) = 0\,. \tag{1}$$

Here, ω is the frequency of a monochromatic sound wave; $k = \omega/c_0$ is the wave number; $\tilde{\varepsilon} = -2\tilde{c}/c_0$; repeated subscripts are summed from 1 to 3, and $\nabla = (\partial/\partial x, \partial/\partial y, \partial/\partial z)$. The range of applicability of Eq. (1) is considered in detail in [6]. In particular, Eq. (1) correctly accounts for terms of order v/c_0, while terms of order v^2/c_0^2 are omitted. Furthermore, in Eq. (1), the sound wavelength λ can be greater or smaller than the scale of the random fields $\tilde{c}$, $\tilde{\varrho}$, and $\mathbf{v}$. When considering atmospheric turbulence, we will use a small parameter $\mu_1 = \max(|\tilde{\varepsilon}|, |\tilde{\varrho}/\varrho_0|, v/c_0) \ll 1$.

On the other hand, in reference [2], a wide angle parabolic equation was derived for the case of a refractive, non-turbulent atmosphere, when $\overline{c}(\mathbf{R})$ is not constant and $\mathbf{V} \neq 0$, while $\tilde{c} = 0$, $\tilde{\rho} = 0$, $\mathbf{v} = 0$. A starting equation for that derivation was the following equation:

$$\left[\nabla^2 + \frac{\omega^2}{\overline{c}^2} + \frac{2i\omega}{\overline{c}^2}\mathbf{V}\cdot\nabla - \frac{(\mathbf{V}\cdot\nabla)^2}{\overline{c}^2}\right] p(\mathbf{R}) = 0\,. \tag{2}$$

Note that the mean density $\overline{\varrho}$ does not appear in this equation. For a monochromatic sound wave, Eq. (2) is essentially the same as Eq. (2.79) from [6]. The range of applicability of Eq. (2) is studied in [6]. This equation can be employed if the characteristic scale of variations of $\overline{c}(\mathbf{R})$ and $\mathbf{V}(\mathbf{R})$ is greater than λ. In this case, Eq. (2) describes the phase of a sound wave to any

order in $V/\bar{c}$ and describes its amplitude to order $V/\bar{c}$. Note that for accurate predictions of the sound field one needs to calculate the phase increments along different sound propagation paths to any order in $V/\bar{c}$, while calculations of sound pressure amplitudes along these paths can be done approximately (to order $V/\bar{c}$).

It is shown in [6, 2] that, in Eq. (2), the operator $(\mathbf{V}\cdot\nabla)^2$ can be replaced by $V_iV_j\frac{\partial^2}{\partial x_i\partial x_j}$. Furthermore, setting $\omega = kc_0$, Eq. (2) takes the form

$$\left[\nabla^2 + k^2(1+\bar{\varepsilon}) + \frac{2ikc_0}{\bar{c}^2}\mathbf{V}\cdot\nabla - \frac{V_iV_j}{\bar{c}^2}\frac{\partial^2}{\partial x_i\partial x_j}\right] p(\mathbf{R}) = 0\,, \tag{3}$$

where $\bar{\varepsilon} = c_0^2/\bar{c}^2 - 1$. In Eq. (3), refraction of sound waves is described by the terms $\bar{\varepsilon}$, $\bar{c}$, and $\mathbf{V}$. When considering a refractive atmosphere, we will use a small parameter $\mu_0 = \max(|\bar{\varepsilon}|, V/c_0) \ll 1$.

Let us now consider an equation for sound waves in a refractive, turbulent atmosphere. Apparently, this equation should contain terms which describe sound scattering, i.e. the terms in Eq. (1) proportional to $\tilde{c}$, $\tilde{\rho}$, and $\mathbf{v}$. Furthermore, this equation should contain terms describing sound refraction, i.e. the terms in Eq. (4) containing $\bar{c}$ and $\mathbf{V}$. Finally, this equation should contain the term $(\nabla^2 + k^2)p$ which describes sound propagation in a free space. Combining all these terms, we obtain the following Helmholtz-type equation for sound waves in a refractive, turbulent atmosphere:

$$\left[\nabla^2 + k^2(1+\bar{\varepsilon}) + \frac{2ikc_0}{\bar{c}^2}\mathbf{V}\cdot\nabla - \right.$$
$$\left. + k^2\tilde{\varepsilon} - (\nabla\tilde{\varrho}/\varrho_0)\cdot\nabla - \frac{2i}{\omega}\frac{\partial v_i}{\partial x_j}\frac{\partial^2}{\partial x_i\partial x_j} + \frac{2ik}{c_0}\mathbf{v}\cdot\nabla\right] p(\mathbf{R}) = 0\,. \tag{4}$$

This equation allows one to calculate the phase increments of sound waves along different sound propagation paths to any order in μ_0. Furthermore, Eq. (4) contains terms of order $v/c_0 \sim \mu_1$.

However, this equation does not contain terms which are proportional to a product of small parameters $\mu_0\mu_1$, and also terms of order $v^2/c_0^2 \sim \mu_1^2$.

In two limiting cases, Eq. (4) coincides with Eqs. (1) and (3). Indeed, if $\bar{\varepsilon} = 0$ and $\mathbf{V} = 0$, Eq. (4) becomes Eq. (1). Furthermore, if $\tilde{\varepsilon} = 0$, $\tilde{\varrho} = 0$, and $\mathbf{v} = 0$, Eq. (4) coincides with Eq. (3).

Note that Eq. (1) can, in principle, be used to approximately account for sound refraction. However, this should be done cautiously. Indeed, in Eq. (1) the vector $\mathbf{v}$ can be replaced by a sum $\mathbf{V} + \mathbf{v}$ to account for sound refraction due to the mean wind velocity $\mathbf{V}$. Comparing the resulting equation with Eq. (4), we reveal that the former equation does not contain terms proportional to V^2 and contains terms proportional to $\partial V_i/\partial x_j$ which are not present in Eq. (4).

3 Wide angle parabolic equation

In this section, starting from Eq. (4), we derive a wide angle parabolic equation in a refractive, turbulent atmosphere and its Padé (1,1) approximation. According to ranges of applicability of Eq. (4), in this derivation we keep terms of order μ_1 and terms of any order in μ_0. On the other hand, terms of order $\mu_0\mu_1$, μ_1^2, $\mu_0^2\mu_1$, $\mu_0\mu_1^2$, μ_1^3, etc., are omitted.

3.1 Derivation of a wide angle parabolic equation

Equation (4) has three terms containing $\partial^2 p/\partial x^2$ which can be written as:

$$\left(1 - \frac{V_x^2}{\bar{c}^2}\right)\frac{\partial^2 p}{\partial x^2} - \frac{2i}{\omega}\frac{\partial v_x}{\partial x}\frac{\partial^2 p}{\partial x^2}\,. \tag{5}$$

We need to modify Eq. (4) so that it would not contain any factors in front of $\partial^2 p/\partial x^2$. In order to do that, we first divide both sides of Eq. (4) by the factor $1 - V_x^2/\bar{c}^2$ and neglect terms of order

$\mu_0\mu_1$. Secondly, to analyze the last term in expression (5), we rewrite Eq. (4) in the form

$$\frac{\partial^2 p}{\partial x^2} = -(\nabla_\perp^2 + k^2)p + O[(\mu_0 + \mu_1)]\,p\,, \tag{6}$$

where $\nabla_\perp = (\partial/\partial y, \partial/\partial z)$. We now replace $\partial^2 p/\partial x^2$ in the last term in expression (5) by the right-hand side of Eq. (6) and omit terms proportional to $\mu_0\mu_1$ and μ_1^2. Then, Eq.(4) can be written as

$$\frac{\partial^2 p}{\partial x^2} = -k^2 Q^2 p\,. \tag{7}$$

Here, the operator Q^2 is given by

$$Q^2 = 1 + F + M\frac{\partial}{\partial x}\,, \tag{8}$$

where $F = F_0 + F_1$, and $M = M_0 + M_1$. The operators F_0 and M_0 contain mean profiles $\bar{c}$ and $\mathbf{V}$, which describe sound refraction:

$$F_0 = \frac{c_0^2}{\bar{c}^2 - V_x^2} - 1 + \frac{V_x^2\nabla_\perp^2}{(\bar{c}^2 - V_x^2)k^2} + \frac{2ic_0}{\bar{c}^2 - V_x^2}\frac{\mathbf{V}_\perp\cdot\nabla_\perp}{k} - \sum_{i,j=2}^{3}\frac{V_iV_j}{\bar{c}^2 - V_x^2}\frac{\partial^2}{k^2\partial x_j\partial x_j}\,, \tag{9}$$

$$M_0 = \frac{2V_x}{(\bar{c}^2 - V_x^2)k^2}\left(ic_0 - \frac{\mathbf{V}_\perp\cdot\nabla_\perp}{k}\right)\,. \tag{10}$$

On the other hand, the operators F_1 and M_1 contain the random fields $\tilde{c}$, $\tilde{\rho}$, and $\mathbf{v}$, which describe sound scattering:

$$\begin{aligned} F_1 \;&=\; \tilde{\varepsilon} + \frac{2i}{\omega}\frac{\partial v_x}{\partial x} + \left(\frac{2i}{\omega}\mathbf{v}_\perp - k^{-2}\nabla_\perp(\tilde{\varrho}/\varrho_0)\right)\cdot\nabla_\perp \\ &+\; k^{-2}\left(1 + \frac{2i}{\omega}\frac{\partial v_x}{\partial x}\right)\nabla_\perp^2 - \frac{2i}{\omega k^2}\sum_{j=2}^{3}(\nabla_\perp v_j)\cdot\nabla_\perp\frac{\partial}{\partial x_j}\,, \end{aligned} \tag{11}$$

$$M_1 = \frac{2i}{\omega}v_x - k^{-2}\frac{\partial(\tilde{\varrho}/\varrho_0)}{\partial x} - \frac{2i}{\omega k^2}\left(\nabla_\perp v_x + \frac{\partial \mathbf{v}_\perp}{\partial x}\right)\cdot\nabla_\perp\,. \tag{12}$$

Starting from Eq. (7) and using a standard approach for deriving a wide angle parabolic equation (e.g. see [7]), we obtain

$$\frac{\partial p}{\partial x} = ik\sqrt{1 + F + M\frac{\partial}{\partial x}}\,p\,. \tag{13}$$

This is a wide angle parabolic equation for sound waves in a moving medium which takes into account both refraction and scattering of sound waves. The right-hand side of this equation contains a pseudo-differential operator $\sqrt{1+F+M\partial/\partial x}$. This operator can be written as a Taylor series:

$$\sqrt{1+F+M\frac{\partial}{\partial x}} = 1+\frac{1}{2}\left(F+M\frac{\partial}{\partial x}\right)-\frac{1}{8}\left(F+M\frac{\partial}{\partial x}\right)^2+\ldots .$$

In this series, the differential operators $\partial^2 p/\partial x^2$, $\partial^3 p/\partial x^3$, ... can be expressed in a form which contains the partial derivative of x of order no higher than one (see section 3.2).

3.2 Padé (1,1) approximation

It is difficult to use Eq. (13) for numerical calculations. Usually a Padé approximation of a wide angle parabolic equation is employed for such calculations. A Padé (1,1) approximation of Eq.(13) can be obtained by the same approach as that in [7]. The result is

$$[q_1+q_2F-ip_2kM]\frac{\partial p}{\partial x} = ik\left[p_1+p_2F+\frac{iq_2M_0}{k}\frac{\partial^2}{\partial x^2}+\frac{iq_2M_1}{k}\frac{\partial^2}{\partial x^2}\right]p\,. \tag{14}$$

Here, q_1, q_2, p_1, and p_2 are numerical coefficients. There is some freedom in choosing numerical values of these parameters, e.g. see [7].

Equation (14) contains terms $M_0\partial^2 p/\partial x^2$ and $M_1\partial^2 p/\partial x^2$ which should be expressed in a form which contains a partial derivative of x of order no higher than one. To do that, we use Eqs. (7) and (8) to write

$$\frac{\partial^2 p}{\partial x^2} = -k^2\left(1+F_0+F_1+M_0\frac{\partial}{\partial x}+M_1\frac{\partial}{\partial x}\right)p\,. \tag{15}$$

Multiplying both sides of this equation by M_0 and neglecting terms of order $\mu_0\mu_1$ and μ_1^2, we have

$$M_0\frac{\partial^2 p}{\partial x^2} = -M_0k^2\left(1+F_0+M_0\frac{\partial}{\partial x}+\frac{\nabla_\perp^2}{k^2}\right)p\,. \tag{16}$$

Analogously, multiplying both sides of Eq. (15) by M_1, we obtain:

$$M_1 \frac{\partial^2 p}{\partial x^2} = -M_1 k^2 \left(1 + \frac{\nabla_\perp^2}{k^2}\right) p \,. \tag{17}$$

Substituting Eqs. (16) and (17) into Eq. (14), we eliminate $\partial^2 p/\partial x^2$ from the latter equation. In the resulting equation, it is convenient to introduce the complex amplitude ψ of a sound field:

$$p(\mathbf{R}) = \exp(ikx)\psi(\mathbf{R}) \,. \tag{18}$$

As a result, Eq. (14) takes the form

$$\begin{aligned} &\left(q_1 + q_2 F - ip_2 kM - q_2 k^2 M_0^2\right) \frac{\partial \psi}{\partial x} \\ &= ik \left[p_1 - q_1 + (p_2 - q_2)(F + ikM) + q_2 k M_0 (kM_0 - iF_0) - \frac{iq_2 M}{k} \nabla_\perp^2\right] \psi \,. \end{aligned} \tag{19}$$

This is a desired Padé (1,1) approximation of the wide angle parabolic equation (13) for sound waves in a refractive, turbulent atmosphere. In the limiting case of a non-refractive, turbulent atmosphere when $\bar{c}$ is constant and $\mathbf{V} = 0$, in Eq. (19) $F_0 = M_0 = 0$ and it coincides with Eq. (20) from [7]. In the other limiting case of a refractive, non-turbulent atmosphere when $\tilde{\varepsilon} = 0$, $\tilde{\varrho} = 0$ and $\mathbf{v} = 0$, in Eq. (19) $M_1 = 0$ and $F_1 = \nabla_\perp^2/k^2$ so that it is essentially the same as Eq. (10) from [2].

Substituting the values of F_0, F_1, M_0 and M_1 into Eq.(19), this equation can be written in a form convenient for numerical computations:

$$A \frac{\partial \psi}{\partial x} = ikB\psi \,, \tag{20}$$

where $A = A_0 + A_1$ and $B = B_0 + B_1$. The operators A_0 and B_0 contain the mean profiles $\bar{c}$ and $\mathbf{V}$:

$$A_0 \;=\; \frac{1}{\bar{c}^2 - V_x^2} \left\{ q_2 \left[c_0^2 - \bar{c}^2 + V_x^2 + \frac{4V_x^2 c_0^2}{\bar{c}^2 - V_x^2} \right] + 2p_2 V_x c_0 \right.$$

$$+\frac{2i}{k}\left[q_2 c_0\left(1+\frac{4V_x^2}{\bar{c}^2-V_x^2}\right)+p_2 V_x\right]\mathbf{V}_\perp\cdot\nabla_\perp$$
$$+\frac{q_2}{k^2}\left[V_x^2\nabla_\perp^2-\left(1+\frac{4V_x^2}{\bar{c}^2-V_x^2}\right)\sum_{i,j=2}^{3}V_iV_j\frac{\partial^2}{\partial x_j\partial x_j}\right]\Bigg\}\,, \tag{21}$$

and

$$\begin{aligned}
B_0 &= \frac{1}{\bar{c}^2-V_x^2}\left\{\left[p_2-q_2+\frac{2q_2V_xc_0}{\bar{c}^2-V_x^2}\right]\left[(c_0-V_x)^2-\bar{c}^2\right]\right.\\
&+\frac{2i}{k}\left[(p_2-q_2)(c_0-V_x)+\frac{q_2V_x}{\bar{c}^2-V_x^2}\left((2c_0-V_x)^2-c_0^2-\bar{c}^2\right)\right]\mathbf{V}_\perp\cdot\nabla_\perp\\
&+\frac{V_x}{k^2}\left[(p_2-q_2)V_x+\frac{2q_2c_0\bar{c}^2}{\bar{c}^2-V_x^2}\right]\nabla_\perp^2\\
&+\frac{1}{k^2}\left[q_2-p_2+\frac{2q_2V_x}{\bar{c}^2-V_x^2}(2V_x-3c_0)\right]\sum_{i,j=2}^{3}V_iV_j\frac{\partial^2}{\partial x_j\partial x_j}\\
&\left.+\frac{2iq_2V_x\bar{c}^2}{k^3(\bar{c}^2-V_x^2)}(\mathbf{V}_\perp\cdot\nabla_\perp)\nabla_\perp^2-\frac{2iq_2V_x}{k^3(\bar{c}^2-V_x^2)}\sum_{i,j,e=2}^{3}V_iV_jV_e\frac{\partial^3}{\partial x_j\partial x_j\partial x_e}\right\}\,,
\end{aligned} \tag{22}$$

Furthermore, the operators A_1 and B_1 contain the random fields $\tilde{c}$, $\tilde{\rho}$, and $\mathbf{v}$:

$$\begin{aligned}
A_1 &= q_1+q_2\tilde{\varepsilon}+\frac{2iq_2}{\omega}\frac{\partial v_x}{\partial x}+\frac{ip_2}{k}\frac{\partial(\tilde{\varrho}/\varrho_0)}{\partial x}+\frac{2p_2v_x}{c_0}\\
&+ k^{-1}\left[\frac{2iq_2\mathbf{v}_\perp}{c_0}-\frac{2p_2}{\omega}\left(\nabla_\perp v_x+\frac{\partial\mathbf{v}_\perp}{\partial x}\right)-\frac{q_2}{k}\nabla_\perp(\tilde{\varrho}/\varrho_0)\right]\cdot\nabla_\perp\\
&+ \frac{q_2}{k^2}\left[\left(1+\frac{2i}{\omega}\frac{\partial v_x}{\partial x}\right)\nabla_\perp^2-\frac{2i}{\omega}\sum_{j=2}^{3}(\nabla_\perp v_j)\cdot\nabla_\perp\frac{\partial}{\partial x_j}\right]\,,
\end{aligned} \tag{23}$$

and

$$\begin{aligned}
B_1 &= p_1-q_1+(p_2-q_2)\left[\tilde{\varepsilon}+\frac{2i}{\omega}\frac{\partial v_x}{\partial x}-\frac{i}{k}\frac{\partial(\tilde{\varrho}/\varrho_0)}{\partial x}-\frac{2v_x}{c_0}\right]\\
&+ \frac{p_2-q_2}{k}\left[\frac{2i\mathbf{v}_\perp}{c_0}-k^{-1}\nabla_\perp(\tilde{\varrho}/\varrho_0)+\frac{2}{\omega}\left(\nabla_\perp v_x+\frac{\partial\mathbf{v}_\perp}{\partial x}\right)\right]\cdot\nabla_\perp\\
&+ k^{-2}\left[(p_2-q_2)\left(1+\frac{2i}{\omega}\frac{\partial v_x}{\partial x}\right)+q_2\left(\frac{i}{k}\frac{\partial(\tilde{\varrho}/\varrho_0)}{\partial x}+\frac{2v_x}{c_0}\right)\right]\nabla_\perp^2\\
&- \frac{2i(p_2-q_2)}{\omega k^2}\sum_{j=2}^{3}(\nabla_\perp v_j)\cdot\nabla_\perp\frac{\partial}{\partial x_j}-\frac{2q_2}{\omega k^3}\left(\nabla_\perp v_x+\frac{\partial\mathbf{v}_\perp}{\partial x}\right)\cdot\nabla_\perp\nabla_\perp^2\,.
\end{aligned} \tag{24}$$

Equation (20) with the operators A_0, B_0, A_1, and B_1 given by Eqs. (21)-(24) seems rather involved. However, in references [1, 2, 3] numerical codes were developed for solving Eq. (20)

for two limiting cases: a non-refractive, turbulent atmosphere and refractive, non-turbulent atmosphere. Combining these codes, one obtains a numerical code for solution of Eq. (20). Thus, numerical solution of Eq. (20) can easily be achieved. Also note that, for these two limiting cases, references [1, 2, 3] present many numerical examples of sound propagation outdoor obtained on the basis of the wide angle parabolic equation (20).

4 Conclusions

We obtained a Helmholtz-type equation for sound waves propagating in a refractive, turbulent atmosphere. Starting from this equation, a wide angle parabolic equation and its Padé (1,1) approximation were derived. The derived equations coincide with those obtained previously for two limiting cases: a non-refractive, turbulent atmosphere and refractive, non-turbulent atmosphere. For these limiting cases, numerical codes have already been developed in references [1, 2, 3] for solving the wide angle parabolic equation (20). Combining these codes, we will obtain a numerical code for solution of Eq. (20) in a general case of a refractive, turbulent atmosphere.

Acknowledgments. This material is partly based upon work supported by the U.S. Army Research Office under contract number DAAG19-01-1-0640.

References

[1] Ph. Blanc-Benon, L. Dallois, and D. Juvé, "Long range sound propagation in a turbulent atmosphere within the parabolic approximation", *Acustica-acta acustica*, 87, 659-669 (2001).

[2] L. Dallois, Ph. Blanc-Benon, D. Juvé, and V.E. Ostashev, "A wide angle parabolic equation for sound waves in moving media", *Proc. 8th Intern. Symp. on Long Range Sound Propagation*, Penn State University, 194-208 (1998).

[3] L. Dallois, "Propagation des ondes acoustiques dans les milieux en mouvement: extension grand angle de l'approximation parabolique". Ph.D. Thesis, Ecole Centrale de Lyon, ECL,n^o 2000-37 (2000).

[4] K.E. Gilbert, R. Raspet, and X. Di, "Calculation of turbulence effects in an upward-refracting atmosphere", *J. Acoust. Soc. Am.*, **87**, 2428-2437 (1990).

[5] J.F. Lingevitch, M.D. Collins, D.K. Dacol, D.P. Drob, J.C.W. Rogers, and W.L. Siegmann, "A wide angle and high Mach number parabolic equation", *J. Acoust. Soc. Am.*, **111**, 729-734 (2002).

[6] V.E. Ostashev, *Acoustics in Moving Inhomogeneous Media* E & FN SPON, London, 1997.

[7] V.E. Ostashev, D. Juvé, and Ph. Blanc-Benon, "Derivation of a wide angle parabolic equation for sound waves in inhomogeneous moving media", *Acustica-acta acustica*, **83**, 455-460 (1997).

[8] E. Salomons, *Computational atmospheric acoustics*, Kluwer Academic Publishers, Dordrecht, 2001.

STARTING EQUATIONS FOR DIRECT NUMERICAL SIMULATION OF SOUND PROPAGATION IN THE ATMOSPHERE

Vladimir E. Ostashev,
NOAA/Environmental Technology Laboratory, Boulder, CO 80305
and Physics Department, New Mexico State University, Las Cruces, NM 88003
Lanbo Liu,
Department of Geology and Geophysics, University of Connecticut, Storrs, CT 06269
and U.S. Army Cold Regions Research and Engineering Laboratory, Hanover, NH 03755
D. Keith Wilson, Mark L. Moran,
U.S. Army Cold Regions Research and Engineering Laboratory, Hanover, NH 03755
David F. Aldridge,
Sandia National Laboratories, Albuquerque, NM 87185
David Marlin,
U.S. Army Research Laboratory, White Sands Missile Range, NM

Abstract. Direct numerical simulation of sound propagation outdoors has recently been proposed to provide detailed calculations of complex propagation phenomenon. In the present paper, we derive two closed sets of equations which can be used as starting equations for the direct numerical simulation. The first set contains three coupled equations (one of which is vectorial) for the sound pressure, acoustic velocity, and acoustic density. This set exactly describes sound propagation in a moving atmosphere. The second set contains two coupled equations (one of which is vectorial) for the sound pressure and acoustic velocity. Though the second set is approximate, it has the same or a wider range of applicability than equations for the sound pressure which have been used previously for analytical and numerical studies of sound propagation in a moving atmosphere. In a companion paper published in this Proceedings, the second set of equations is used for direct numerical simulation of sound propagation in the atmosphere. Note that both sets of equations obtained in the present paper can also be used for analytical studies of sound propagation in the atmosphere.

I Introduction

Sound waves propagating in the atmosphere are affected by many factors: stratification of temperature and wind velocity, atmospheric turbulence, impedance ground, terrain, and different obstacles (buildings, trees, etc.). In the past several decades, this complicated phenomenon has been intensively studied analytically and numerically. (See Refs. [7, 11] and the references therein.) Numerical studies have been mainly based on a solution of a parabolic or wide-angle parabolic equation for the sound pressure. The latter studies have allowed prediction of the sound pressure with a good accuracy. However, the results obtained are limited to one-way (forward) sound propagation. This limitation can be overcome with recently proposed direct numerical simulation (DNS) of sound propagation outdoors [3, 6, 10].

DNS is based on a solution of first-order (with respect to time) differential equations using finite-difference approximations. We use the term DNS in this paper to draw an association with DNS of turbulence [12] and other simulation techniques that are closely related. Elsewhere, the general technique is referred to as finite-difference, time-domain (FDTD) modeling [5, 6] or an Eulerian sound propagation model [3, 10]. The main goal of the present paper is to derive starting equations for DNS and to study the range of applicability of these equations. Note that these equations can also be used in analytical studies of sound propagation and scattering in a moving atmosphere.

A rigorous description of sound propagation in a moving atmosphere must be based on the linearized equations of fluid dynamics. In the present paper, starting from these linearized equations, we derive two sets of equations which can be used for DNS of sound propagation in a moving atmosphere. The first set is an exact consequence of linearized equations of fluid dynamics. The second set, which is simpler than the first, describes sound propagation only approximately. The range of applicability of the second set is studied by comparing it to equations for the sound pressure already known in the literature.

II Equations of fluid dynamics and their linearization

A complete set of fluid dynamic equations is given by:

$$\left(\frac{\partial}{\partial t}+\bar{\mathbf{v}}\cdot\nabla\right)\bar{\mathbf{v}}+\frac{\nabla\tilde{P}}{\tilde{\varrho}}-\mathbf{g}=\mathbf{F}/\tilde{\varrho}\,, \tag{1}$$

$$\left(\frac{\partial}{\partial t}+\bar{\mathbf{v}}\cdot\nabla\right)\tilde{\varrho}+\tilde{\varrho}\nabla\cdot\bar{\mathbf{v}}=\tilde{\varrho}Q\,, \tag{2}$$

$$\left(\frac{\partial}{\partial t}+\bar{\mathbf{v}}\cdot\nabla\right)\tilde{S}=0\,, \tag{3}$$

$$\tilde{P}=\tilde{P}(\tilde{\varrho},\tilde{S})\,. \tag{4}$$

Here, $\bar{\mathbf{v}}$ is the velocity, $\tilde{P}$ is the pressure, $\tilde{\varrho}$ is the density, and $\tilde{S}$ is the entropy in a medium. All these functions depend both on the Cartesian coordinates $\mathbf{R}=(x,y,z)$ and the time t. Furthermore in Eqs. (1)–(4), $\mathbf{g}=(0,0,g)$ is the acceleration due to gravity; $\mathbf{F}$ and Q characterize a force acting on the medium and a mass source, respectively; and $\nabla=(\partial/\partial x,\partial/\partial y,\partial/\partial z)$.

Equations (1)–(4) describe the ambient state of the medium and a sound wave propagating in the medium. To obtain equations only for a sound wave, we write: $\tilde{P}=P+p$, $\tilde{\varrho}=\varrho+\eta$, $\bar{\mathbf{v}}=\mathbf{v}+\mathbf{w}$, and $\tilde{S}=S+s$. Here, P, ϱ, $\mathbf{v}$, and S are the ambient values of the pressure, density, medium velocity, and entropy, and p, η, $\mathbf{w}$, and s are their fluctuations due to a propagating sound wave. This sound wave is generated by the mass source Q and/or the force $\mathbf{F}$. In linear acoustics, it is assumed that a sound wave disturbs the ambient state of a medium only slightly. In this approximation, Eqs. (1)–(4) are linearized with respect to p, η, $\mathbf{w}$, and s:

$$\frac{d\mathbf{w}}{dt}+(\mathbf{w}\cdot\nabla)\mathbf{v}+\frac{\nabla p}{\varrho}-\frac{\eta\nabla P}{\varrho^2}=\mathbf{F}/\varrho\,, \tag{5}$$

$$\frac{d\eta}{dt} + (\mathbf{w}\cdot\nabla)\varrho + \varrho\nabla\cdot\mathbf{w} + \eta\nabla\cdot\mathbf{v} = \varrho Q\,, \tag{6}$$

$$\frac{ds}{dt} + (\mathbf{w}\cdot\nabla)S = 0\,, \tag{7}$$

$$p = c^2\eta + hs\,. \tag{8}$$

Here, $c = \sqrt{\partial P(\varrho,S)/\partial\varrho}$ is the adiabatic sound speed, $h = \partial P(\varrho,S)/\partial S$ is a parameter, and $d/dt = \partial/\partial t + \mathbf{v}\cdot\nabla$.

Equations (5)–(8) comprise a complete set of linearized equations of fluid dynamics for p, η, $\mathbf{w}$, and s. In order to solve these equations, one needs to know the ambient quantities c, ϱ, $\mathbf{v}$, P, S, and h. The ambient quantities ϱ, $\mathbf{v}$, P, and S satisfy Eqs. (1)–(4) with $\mathbf{F} = 0$ and $Q = 0$; c and h can be found if P is known. (Strictly speaking, Eq. (1) for the ambient quantities should be added by a term which allows to account for viscosity of a medium. This term is usually omitted in derivation of equations for sound waves.)

Equations (5)–(8) were derived by D. Blokhintzev in 1946 [2] and since then have been widely used in the literature, e.g. Refs. [1, 4, 7, 9]. Generally speaking, Eqs. (5)–(8) cannot be exactly reduced to one equation for the sound pressure p. Therefore, in previous work, Eqs. (5)–(8) have been reduced to equations for p by making use of different approximations or assumptions about the ambient medium. These equations for p (which are presented in section V) were subsequently used for analytical and numerical studies of sound propagation. All these equations contain second or higher order derivatives of the sound pressure p with respect to time t and cannot be used as starting equations for DNS of sound propagation.

III Set of equations for p, $\mathbf{w}$, and η

In this section, we derive a closed set of equations for p, $\mathbf{w}$, and η and compare it with starting equations for DNS employed in references [3, 10].

A Arbitrary equation of state

Applying the operator d/dt to both sides of Eq. (8) and after some algebra, one can derive the following equation:

$$\frac{dp}{dt} + \mathbf{w}\cdot\nabla P = c^2\frac{d\eta}{dt} + c^2\mathbf{w}\cdot\nabla\varrho + \left(c^2\right)'\frac{d\varrho}{dt}. \tag{9}$$

This equation coincides with Eq. (2.66) from [7]. In Eq. (9), $(c^2)'$ are fluctuations in the squared adiabatic sound speed due to a propagating sound wave, given by:

$$\left(c^2\right)' = \beta\eta + \alpha s, \tag{10}$$

where $\beta = \partial^2 P(\varrho,S)/\partial\varrho^2$ and $\alpha = \partial^2 P(\varrho,S)/\partial\varrho\partial S$.

Let us multiply Eq. (6) by c^2 and then add to Eq. (9). In the resulting equation, $d\varrho/dt$ is replaced with $-\varrho\nabla\cdot\mathbf{v}$ according to the continuity equation for the ambient medium. As a result, we obtain

$$\frac{dp}{dt} + \mathbf{w}\cdot\nabla P + \varrho c^2 \nabla\cdot\mathbf{w} + \left(c^2\eta + \varrho(c^2)'\right)\nabla\cdot\mathbf{v} = \varrho c^2 Q. \tag{11}$$

In Eq. (10), we replace s by its value from Eq. (8). The resulting formula for $(c^2)'$ is substituted into Eq. (11). Then, we arrive at a desired equation for dp/dt:

$$\frac{dp}{dt} + \mathbf{w}\cdot\nabla P + \varrho c^2 \nabla\cdot\mathbf{w} + \left\{\left[\varrho\beta + c^2(1-\alpha\varrho/h)\right]\eta + (\alpha\varrho/h)\,p\right\}\nabla\cdot\mathbf{v} = \varrho c^2 Q. \tag{12}$$

Equations (5), (6), and (12) make a closed set of equations for p, $\mathbf{w}$, and η. This set is an exact consequence of Eqs. (5)–(8). In order to solve this set, we need to know the following ambient quantities: c, ϱ, $\mathbf{v}$, P, α, β, and h. Equations (5), (6), and (12) can be used as starting equations for DNS of sound propagation in a moving atmosphere.

Note that Eq. (12) can be derived by a different approach. Applying the operator $(\partial/\partial t + \bar{\mathbf{v}}\cdot\nabla)$ to both sides of Eq. (4) and using Eq. (3), we have

$$\left(\frac{\partial}{\partial t} + \bar{\mathbf{v}}\cdot\nabla\right)\tilde{P} = \tilde{c}^2\left(\frac{\partial}{\partial t} + \bar{\mathbf{v}}\cdot\nabla\right)\tilde{\varrho}. \tag{13}$$

Here, $\tilde{c} = \sqrt{\partial\tilde{P}(\tilde{\varrho},\tilde{S})/\partial\tilde{\varrho}}$. Linearizing Eq. (13) with respect to acoustic quantities, taking into account that $\tilde{c}^2 = c^2 + (c^2)'$, and after some algebra, we obtain Eq. (12).

B Ideal gas

To a good approximation, the atmosphere can be considered as an ideal gas with the following equation of state:

$$P = P_0(\varrho/\varrho_0)^\gamma \exp\left[(\gamma-1)(S-S_0)/R_a\right]. \tag{14}$$

Here, the subscript 0 indicates reference values of P, ϱ, and S; $\gamma = 1.4$ is the ratio of specific heats at constant pressure and constant volume; and R_a is the gas constant for the air. Equation (14) allows us to calculate the values of coefficients α, β, and h in Eq. (12). Furthermore, taking into account that $c^2 = \gamma P/\varrho$ for an ideal gas, Eq. (12) takes the form

$$\frac{dp}{dt} + \mathbf{w}\cdot\nabla P + \varrho c^2 \nabla\cdot\mathbf{w} + \gamma p\nabla\cdot\mathbf{v} = \varrho c^2 Q. \tag{15}$$

Equations (5), (6), and (15) make a closed set of equations for p, $\mathbf{w}$, and η for the considered case of sound propagation in an ideal gas. These equations contain the following ambient quantities: c, ϱ, $\mathbf{v}$, and P.

In references [3, 10], a closed set of equations for p and $\mathbf{w}$ was used for DNS of sound propagation in and ideal gas, see Eqs. (12) and (13) from [3]. The latter of these equations coincides with Eq. (15) if $Q = 0$. The former is an approximation of Eq. (5). Indeed, let us replace η in Eq. (5) by its value from Eq. (8) and neglect the term proportional to s. The resulting equation coincides with Eq. (12) from [3] if $\mathbf{F} = 0$. (In Eq. (12) from [3], there is a term describing sound

attenuation; this term is not present in Eq. (5).) Thus, for an ideal gas and $\mathbf{F} = 0$ and $Q = 0$, Eqs. (12) and (13) from [3] are equivalent to Eqs. (5) and (15) of the present paper if s can be set to 0. This approximation has often been used in the literature. For a stratified medium, it implies that the spatial scale of the variations in the ambient density is much larger than the sound wavelength and that a proportionality of p to $\sqrt{\varrho}$ is ignored. More detailed discussion of this topic can be found in section 2.2.4 in [7].

IV Set of equations for p and w

To a very good approximation, the atmosphere can be modeled as an incompressible gas, i.e. $\nabla \cdot \mathbf{v} = 0$. Furthermore, in all previous studies with which we are familiar, the effects of the ambient pressure and its fluctuations on outdoor sound propagation have been ignored. Therefore, one can assume that, in Eqs. (5) and (12), terms proportional to ∇P can be approximately omitted. As a result of these approximations, Eqs. (12) and (5) become

$$\frac{dp}{dt} + \varrho c^2 \nabla \cdot \mathbf{w} = \varrho c^2 Q, \tag{16}$$

$$\frac{d\mathbf{w}}{dt} + (\mathbf{w} \cdot \nabla)\mathbf{v} + \frac{\nabla p}{\varrho} = \mathbf{F}/\varrho. \tag{17}$$

Equations (16) and (17) were derived in Ref. [8] (see also Eqs. (2.68) and (2.69) from Ref. [7]). A set of Eqs. (16) and (17) can also be used as starting equations for DNS of sound propagation in a moving atmosphere. This set is simpler than the set of Eqs. (5), (6) and (12). Furthermore, Eqs. (16) and (17) contain fewer number of the ambient quantities: c, ϱ, and $\mathbf{v}$. Note that equations for p which have been used so far for analytical and numerical studies of sound propagation in a moving atmosphere also contain only these ambient quantities. These equations are presented in section V.

Estimates in section 2.3.1 of Ref. [7] show that, in Eqs. (5) and (12), terms proportional to ∇P can be ignored to order v/c. These estimates provide sufficient conditions for applicability of Eqs. (16) and (17). Actually, a range of applicability of these equations can be much wider. In the next section, we will show that, in most of important particular cases, Eqs. (16) and (17) describe sound propagation to any order in v/c. Furthermore, they have the same or wider range of applicability as equations for p which have been used so far for analytical and numerical studies of sound propagation in moving media.

V Comparison of the set of equations for p and w with equations for p known in the literature

In this section we compare the set of Eqs. (16) and (17) with equations for p known in the literature. This will allow us to better understand a range of applicability of this set. Note that all equations for p presented below contain the following ambient quantities: c, $\mathbf{v}$, and ϱ. For simplicity in this section, we set $\mathbf{F} = 0$ and $Q = 0$.

A Non-moving medium

Let $\mathbf{v} = 0$. Starting from Eqs. (16) and (17), the following equation for p can be derived

$$\frac{\partial}{\partial t}\left(\frac{1}{\varrho c^2}\frac{\partial p}{\partial t}\right) - \nabla\cdot\left(\frac{\nabla p}{\varrho}\right) = 0\,. \tag{18}$$

This equation is an exact equation for sound pressure in a non-moving medium, e.g. see Eq. (4.1.17) from Ref. [4]. Thus, for the case of a non-moving medium, Eqs. (16) and (17) exactly describe sound propagation.

B Homogeneous, uniformly moving medium

If the ambient quantities do not depend on $\mathbf{R}$ and t, the medium is homogeneous and uniformly moving. In this case, the following equation can be derived starting from Eqs. (16) and (17):

$$\left(\frac{\partial}{\partial t} + \mathbf{v}\cdot\nabla\right)^2 p - c^2\nabla^2 p = 0\,. \tag{19}$$

This equation is an exact equation for sound waves in a homogeneous, uniformly moving medium, see section 2.3.6 from Ref. [7] and references therein. Thus, Eqs. (16) and (17) exactly describe sound propagation in a homogeneous, uniformly moving medium. In particular, they correctly account for terms of any order in v/c.

C Stratified moving medium

A stratified moving medium is the medium where the ambient quantities (e.g. c, ϱ, $\mathbf{v}$, etc.) depend only on the vertical coordinate z. Furthermore, the vertical component of $\mathbf{v}$ is assumed to be zero: $\mathbf{v} = (\mathbf{v}_\perp, 0)$. Here, $\mathbf{v}_\perp$ is a horizontal component of the medium velocity.

For a stratified moving medium, it is convenient to express p and $\mathbf{w}$ in Eqs. (16) and (17) as Fourier integrals. For example,

$$p(\mathbf{r}, z, t) = \int\int d\mathbf{a}\int d\omega \exp(i\mathbf{a}\cdot\mathbf{r} - i\omega t)\hat{p}(\mathbf{a}, z, \omega). \tag{20}$$

Here, $\mathbf{r} = (x, y)$ are the horizontal coordinates, $\mathbf{a}$ is the horizontal component of the wave vector, ω is the frequency of a sound wave, and $\hat{p}$ is the spectral density of p. After some algebra, Eqs. (16) and (17) can be reduced to a single equation for $\hat{p}$:

$$\frac{\partial^2\hat{p}}{\partial z^2} + \left(\frac{2\mathbf{a}\cdot\mathbf{v}'_\perp}{\omega - \mathbf{a}\cdot\mathbf{v}_\perp} - \frac{\varrho'}{\varrho}\right)\frac{\partial\hat{p}}{\partial z} + \left(\frac{(\omega - \mathbf{a}\cdot\mathbf{v}_\perp)^2}{c^2} - a^2\right)\hat{p} = 0. \tag{21}$$

Here, $\varrho' = d\varrho/dz$, and $\mathbf{v}'_\perp = d\mathbf{v}_\perp/dz$.

Equation (21) coincides with Eq. (2.61) from Ref. [7] if in the latter equation $g = 0$. (Terms proportional to g are important only for describing internal gravity waves in the atmosphere and, therefore, are ignored in our analysis.) For the considered case of a stratified moving medium, Eq. (2.61) from Ref. [7] is an exact consequence of linearized equations of fluid dynamics, Eqs. (5)-(8). Thus, Eqs. (16) and (17) exactly describe sound propagation in a stratified moving medium and, hence, correctly account for terms of any order in v/c.

D Geometric acoustics

Now solve Eqs. (16) and (17) by using the geometric acoustics method. Let

$$p(\mathbf{R},t) = \left[p_1 + \frac{p_2}{ik_0} + \frac{p_3}{(ik_0)^2} + ...\right] e^{ik_0\Theta}, \tag{22}$$

$$\mathbf{w}(\mathbf{R},t) = \left[\mathbf{w}_1 + \frac{\mathbf{w}_2}{ik_0} + \frac{\mathbf{w}_3}{(ik_0)^2} + ...\right] e^{ik_0\Theta}. \tag{23}$$

Here, k_0 is the reference wavenumber, $\Theta(\mathbf{R},t)$ is the phase function, and $p_n(\mathbf{R},t)$ and $\mathbf{w}_n(\mathbf{R},t)$ are the amplitude factors. Substituting Eqs. (22) and (23) into Eqs. (16) and (17) and using the method of geometric acoustics, one can derive the eikonal equation for Θ and the transport equation for p_1. The eikonal equation reads:

$$\frac{d\Theta}{dt} = -c|\nabla\Theta|. \tag{24}$$

This equation coincides with the eikonal equation for sound waves in moving media (e.g. see Eq. (3.15) from [7]). Thus, in the geometric acoustics approximation, Eqs. (16) and (17) exactly describe the phase of a sound wave and account for terms of any order in v/c in the phase.

The transport equation for p_1 reads:

$$\frac{\varrho\mathbf{n}}{c}\cdot\frac{d}{dt}\left(\frac{\mathbf{n}p_1}{\varrho c}\right) + \frac{d}{dt}\left(\frac{p_1}{c^2}\right) + \frac{\mathbf{n}\cdot\nabla p_1}{c} + \varrho\nabla\cdot\left(\frac{\mathbf{n}p_1}{\varrho c}\right) + \frac{p_1\mathbf{n}\cdot(\mathbf{n}\cdot\nabla)\mathbf{v}}{c^2} = 0. \tag{25}$$

This equation coincides with Eq. (3.18) from Ref. [7] if in the latter equation $\nabla\cdot\mathbf{v} = 0$. Equation (3.18) from Ref. [7] is an exact transport equation for p_1 in the geometric acoustics. Thus, for the incompressible medium, Eqs. (16) and (17) exactly describe the amplitude of a sound wave in the geometric acoustics approximation and account for terms of any order in v/c in the amplitude.

E Turbulent medium

Starting from Eqs. (16) and (17) and making certain additional assumptions about the ambient medium, the following equation for the sound pressure of a monochromatic sound wave can be derived (see Eq. (6.1) from Ref. [7]):

$$\left[\Delta + k_0^2(1+\varepsilon) - \left(\nabla\ln\frac{\varrho}{\varrho_0}\right)\cdot\nabla - \frac{2i}{\omega}\frac{\partial v_i}{\partial x_j}\frac{\partial^2}{\partial x_i\partial x_j} + \frac{2ik_0}{c_0}\mathbf{v}\cdot\nabla\right] p(\mathbf{R}) = 0\,. \tag{26}$$

Here, $\Delta = \partial^2/\partial x^2 + \partial^2/\partial y^2 + \partial^2/\partial z^2$; $\varepsilon = c_0^2/c^2 - 1$; k_0, c_0 and ϱ_0 are the reference values of the wavenumber, adiabatic sound speed, and density (the first two of these quantities are related by $\omega = k_0c_0$); x_1, x_2, x_3 stand for x, y, z and similar for v_i; and the dependence of p on the time factor $\exp(-i\omega t)$ is omitted.

Equation (26) has been used for calculations of the sound scattering cross section in a turbulent medium and for developing the diagram technique, see Ref. [7] and references therein. Also starting from Eq. (26), the parabolic and wide-angle parabolic equations were derived and widely

used for numerical studies of outdoor sound propagation. The parabolic equation for p is given by

$$2ik_0\frac{\partial p}{\partial x}+\left(\frac{\partial^2}{\partial y^2}+\frac{\partial^2}{\partial z^2}\right)p+2k_0^2\left(1+\varepsilon/2-v_x/c_0\right)p=0\,, \tag{27}$$

where the predominant direction of sound propagation coincides with the x-axis.

Thus, a set of Eqs. (16) and (17) has a wider range of applicability than Eqs. (26) and (27), which have been used for studies of sound propagation and scattering in turbulent media.

F Other equations for sound waves in moving media

There are other equations for sound waves in moving media known in the literature (see Refs. [4, 7]). Among these are equations for the velocity quasi-potential, Pierce's equations, and the Andreev-Rusakov-Blokhintzev equation. Most of these equations have narrower ranges of applicability than equations for p presented above. Furthermore, they have been used for calculations of sound propagation in moving media very seldom.

VI Conclusions

In this paper, the linearized equations of fluid dynamics were exactly reduced to a closed set of equations [(5), (6) and (12)] for p, $\mathbf{w}$, and η. This set can be used as starting equations for DNS of sound propagation in a moving atmosphere. It contains the following ambient quantities: c, ϱ, $\mathbf{v}$, P, α, β, and h.

To good accuracy, the atmosphere can be modeled as an ideal gas. In this case, Eq. (12) simplifies and can be written as Eq. (15). Thus, for an ideal gas, a closed set of equations for p, $\mathbf{w}$, and η is given by Eqs. (5), (6) and (15). This set contains the following ambient quantities: c, ϱ, $\mathbf{v}$, and P. The set reduces to starting equations for DNS, which were used in references [3, 10], if the fluctuations in entropy s due to a sound wave are ignored.

Assuming that a moving medium is incompressible and ignoring terms proportional to ∇P, Eqs. (5), (6) and (12) were reduced to a closed set of Eqs. (16) and (17) for p and $\mathbf{w}$. This set is simpler than that for p, $\mathbf{w}$, and ϱ. Furthermore, it contains a fewer number of the ambient quantities: c, ϱ, and $\mathbf{v}$. Note that all equations for the sound pressure p, which have been used so far for analytical and numerical studies of sound propagation in a moving atmosphere, contain only these ambient quantities. Moreover, it was shown that Eqs. (16) and (17) have the same or wider range of applicability than these equations for p. Thus, a relatively simple set of Eqs. (16) and (17), which is however rather general, seems very attractive as starting equations for DNS. This set is used in a companion paper [5] for DNS of sound propagation in a moving atmosphere.

Finally, note that the closed sets of equations obtained in the present paper can also be used for analytical studies of sound propagation and scattering in a moving atmosphere. The related studies are underway.

Acknowledgments. This work was partially supported by the DoD High-Performance Computing Modernization Office grant "High-Resolution Modeling of Acoustic Wave Propagation in Atmospheric Environments" and the U.S. Army Research Office grant DAAG19-01-1-0640.

References

[1] D. F. Aldridge, "Acoustic wave equations for a linear viscous fluid and an ideal fluid," SAND Report SAND2002-2060, Sandia National Laboratories, Albuquerque, NM (2002). (Available from the U.S. Dept. of Commerce National Technical Information Service, http://www.ntis.gov/ordering.htm.)

[2] D. I. Blokhintzev, *Acoustics of an Inhomogeneous Moving Medium* [in Russian], Nauka, Moscow, 1946 [English translation, Physics Dept. Brown Univ., Providence, RI (1956)].

[3] R. Blumrich and D. Heinman, "A linearized Eulerian sound propagation model for studies of complex meteorological effects," *J. Acoust. Soc. Am.* **112**, 446–455 (2002).

[4] L. M. Brekhovskikh and O. A. Godin, *Acoustics of Layered Media*, Springer-Verlag, Berlin, 1992.

[5] L. Liu, D. K. Wilson, M. L. Moran, V. E. Ostashev, and D. F. Aldridge, "Simulation of sound wave propagation in moving media with two-dimensional finite-difference time-domain method," Proc. 10th Intern. Symp. on Long Range Sound Propagation, Grenoble, France (2002).

[6] M. L. Moran, D. K. Wilson, L. Liu, D. F. Aldridge, and V. E. Ostashev, "FDTD acoustic wave propagation in complex atmospheric environments: Initial results," 2002 MSS Specialty meeting on Battlefield Acoustic and Seismic Sensing, Johns Hopkins APL, Laurel, MD (2002).

[7] V. E. Ostashev, *Acoustics in Moving Inhomogeneous Media*, E&FN SPON, London, 1997.

[8] V. E. Ostashev, "On sound wave propagation in a three-dimensional inhomogeneous moving medium, " *Diffraction and Wave Propagation in Inhomogeneous Media*, 42–49, MPTI Press, Moscow, 1987.

[9] A. D. Pierce, *Acoustics — An introduction to its physical principles and applications*, McGraw-Hill, 1989.

[10] E. M. Salomons, R. Blumrich, and D. Heinman, "Eulerian time-domain model for sound propagation over a finite-impedance ground surface. Comparison with frequency-domain models," *Acustica-acta acustica* **88**, 483–492 (2002).

[11] E. M. Salomons, *Computational atmospheric acoustics*, Kluwer Academic Publishers, Dordrecht, 2001.

[12] P. R. Spalart, "Strategies for turbulence modeling and simulations," *Intern. J. Heat and Fluid Flow* **21**, 252–262 (2000).

The Gaussian Beam Method Revisited

M West and RA Sack
Acoustical Software Limited, Bury, UK, email: acoustical@cwcom.net

Abstract

Computational procedures for broadband multi-frequency predictions of long range sound propagation are still not sufficiently fast for many practical applications. The Gaussian Beam method makes use of ray paths to "home in" on a small region where it obtains solutions using a *local* Parabolic Equation(PE) and consequently it is extremely fast. This paper describes a feasibility study of the method for flat ground predictions and explores a number of implementation problems not addressed in the literature.

1. Purpose

In many recent applications the user requires :

- Predictions for ranges up to 2km and most typically up to 1km at very high speeds typically two orders of magnitude faster than standard current FFP or PE .
- Predictions with the same accuracy as that from an FFP or PE.
- Predictions over a very limited receiver zone typically a few 10's of metres square.
- Predictions over a wide audio bandwidth for atmospheric propagation, typically 20Hz to 1-4 kHz . The upper frequency limit is necessarily set both by the maximum range and the meteorology.
- Predictions which take full account of the meteorology.

This is a subset of the general requirements for LRSP predictors (the so called LSRP-Lou Sutherland Requirements for Predictors[1]) which Dr Sutherland believes will soon be realised.

Gabillet et al[2] have shown that the Gaussian Beam method has considerable potential for atmospheric predictions in view of its remarkable computational efficiency and its use of a local field solution both consequences of the Gaussian Beam construction. It is the purpose of this paper to re-examine the underlying mathematics of the method and its algorithmic implementation to discover to what extent this potential can be realised for atmospheric applications and for meeting the above requirements.

At the outset two important constraints must be flagged up. The first is the need for beams in the vicinity of the receiver position. Gabillet et al[2] showed that in conditions of strong upward refraction this may not be possible and the method is then flawed. The second constraint , also identified by Gabillet et al[2], is that the beam width must always be less than the zone over which atmospheric parameter changes can be considered to be small (ie to have negligible effects on the field). In practice this means that the method has a low frequency limit (approximately 200Hz). This paper will assume that these constraints apply and also that the atmosphere can be

considered to be horizontally stratified with a linear sound speed variation occurring over each stratum. The description of the method and the discussion presented may be considered to be the first part of a feasibility study for this method.

2. Previous Work

This study was inspired by Gabillet et al's[2] seminal work, which was the first to adapt the earlier extensive literature on Gaussian Beam methods for seismological propagation to the atmospheric problem. Gabillet et al's[2] results are reviewed in sections 10 and 11 .

Figure 1 shows the key publications shown in a time line format. Cereveny et al(1982)[3] were the first to develop the Gaussian Beam concept which permitted a true field solution close to a ray. They extracted this solution by solving a time dependent PE set up local to the ray. This solution gives the beam significant and crucial advantages over conventional ray solution methods (see below).Cerveny et al[3] used a complex constant, ε, known as the "beam parameter" which allows some limited control of the beam width and curvature. The choice of this parameter has a critical effect on the solution. Muller(1984) [4] reviewed the six available procedures for finding ε and showed that not only could rays be traced through triangular zones with linear sound speed variation but that within such regions optimum beam width estimates could be obtained which could in turn be used for finding ε. Muller also gives a derivation of the asymptotic expansions for a cylindrical wave into Gaussian beams in a form more amenable to computation than that of Cerveny et al[3]. Weber (1988)[5] reviewed the eight available procedures for determination of ε, the eighth being Cerveny's (1985)[6] recent addition which used curvature and beam width values determined at the beam endpoint nearest to the receiver. Weber made a small modification to Option 8 ,his new Option 9, which used a beam width evaluated along the whole length of the beam. Gabillet et al[2] used this option for ε. We have implementeded Options 7,8 and 9 in this study.

Most of the previous work in this area had been for seismological applications however there are two noteworthy contributions in other fields viz Porter and Bucker's (1986)[7] paper on an underwater implementation and Felsen's(1990)[8] paper on em wave propagation. Porter and Bucker used beam windows to make the computation more efficient by omitting solutions where beam end points were too far from the receiver to give a significant contribution. They also provided the first correction for errors produced when beams overlap. Unfortunately this was obtained by empirical means and may not easily be generalised and in particular may not be easily adapted to the atmospheric case. Porter and Bucker[7] provide the only detailed derivation of the Gaussian beam equations which is reworked here in a form that excludes their confusing use of a transformation incorporating the radial distance from the source. Felsen[8] and Weber[5] examined the effect of first order discontinuities on the Gaussian Beam which we have adapted to allow inclusion of ground reflection effects making use of the complex ground impedance.

Gabillet et al[2] in their paper gave an excellent and succinct overview of the literature and of the method but did not give detail of the mathematics or of its implementation. They did not for example include any detail of how they included ground reflection effects. Their paper very usefully concentrated on comparison of predictions in specific cases with the FFP and with model measurements. Most of these tests used a linear sound speed gradient and a small number of strata. These comparisons showed that in all cases where the criteria in section 1 are satisfied their Gaussian Beam model was able to produce very accurate results.

3. The Gaussian Beam Concept

We consider the two dimensional problem with a cylindrical source. (It is possible to set up Gaussian Beams in three dimensions[5] however if we are working to the requirements in section 1 this has no advantages over a two dimensional solution which can easily be adapted for a point source.) The source is broken down into a large set of beams each based on a central ray. One beam's path through the atmosphere is easily traced by applying the well known ray trace equations[9] for the central ray (see below). The usual high frequency ray approximation must apply to the rays, which means that variations in the medium must be negligible over a wavelength. We infer from this that a stratum must have a thickness greater than a wavelength.

Cerveny et al[3] showed that in the vicinity of the nearest point on a ray to the receiver R, referred to as the "ray end point", a parabolic wave equation can be set up which has a solution, u, which can be obtained in terms of the distance from the ray, two parameters p and q, known as the "dynamic ray trace parameters" and of course the beam parameter, ε. In the derivation of the solution u we also obtain two ordinary differential equations, referred to as the "Auxilliary Beam Equations" for parameters p and q which can be solved by integrating along the ray as it is traced through each stratum. The individual ray solution ,u, is obtained at a receiver point R with normal distance from the beam, n (see Figure 2). Since we are using a local solution we have approximately free field conditions when the solution, u, is a Gaussian function of n. This means that most of the beam energy is concentrated close to the central ray and that the beam strength falls off rapidly with n. A separate partial solution is obtained for each beam launched at the source. The total field at R is obtained by integrating Φu over all beam launch angles where Φ is a weighting function determined at the source.

Ray tube methods, and indeed all prediction methods based on rays, have fallen into disrepute because of their significant limitations in dealing with all the practical cases where rays cross. Many such ray methods have resorted to drastic empirical "fixes" in order to obtain approximate predictions in regions where ray crossings occur[10]. Ray crossings commonly occur when

- the sound speed profile is upward refracting and the source is elevated. A caustic is formed as a result of the upward bound rays crossing those which graze the ground first,

- the sound speed profile has a turning point changing from upward to downward refraction (this often gives rise to a caustic with strong focussing or enhancement on the ground), and when
- ground reflections are significant such that reflected rays cross direct rays giving rise to multiple caustics.

Gaussian Beams can provide solutions irrespective of the presence of ray crossings. Since the beams are based on a central ray this appears at first sight quite surprising. It is ,however, the combination of the central ray with the solutions of the auxiliary equations, which give the beam its ability to cope with ray crossing zones. The solutions of the auxiliary equations are computed along the central ray which only functions as a transformed coordinate system. These solutions are then used in a local PE field solution to give the elemental (single ray) solution. Provided the beam always retains a sufficient width there will be an implicit averaging of the field over the volume of the beam which will take proper account of the complex field within it. This is a remarkable property of the Gaussian Beam which makes it greatly superior to all ray methods which rely on the rays themselves to provide an approximate field solution. The use of Blokhintzev's ray invariant property, which is fundamental to all ray tube methods, is completely flawed if the ray tube passes through any region with ray crossings since each of the rays making up the tube must cross so destroying the tube .[9] The Gaussian Beam on the other hand has its width (and curvature) set up with a sufficient degree of independence of the path of rays adjacent to the central ray to guarantee that it never suffers from any of these ray crossing problems.

4. Central Ray Path Calculation

In the literature surveyed above very little information on ray tracing is provided. This is often the case as there is such an enormous literature on ray tracing pre 1980. The Gaussian Beams may be constructed in two or three dimensions , however for the ranges of interest here a two dimensional model will be sufficient for all but the most extreme meteorological cases. The ray trace procedure summarised below is a general one which is three dimensional and applicable to propagation through any inhomogeneous medium. It is particularised here for the two dimensional stratified atmosphere case.

We use Walkden and West's[9] ray tracing equations which are a development of Thompson's original ray tracing equations in three dimensions. These equations are given in terms of the Cartesian coordinates x,y and z

$$\frac{dx}{dz} = \frac{\alpha U + c^2 k_1}{c^2 \Phi_z} \quad ; \quad \frac{dy}{dz} = \frac{\alpha V + c^2 k_2}{c^2 \Phi_z} \qquad (1)$$

where U and V are the x and y components of the wind vector at point x,y,z and $\underline{k}$ is the ray launch vector at the source point and its components can be expessed in terms of the ray launch angles (see reference 9) . c is the sound speed at point x,y,z. The other terms in (1) are given by

$$\Phi_z = \sqrt{\alpha^2 - c^2(k_1^2 + k_2^2)}/c \quad , \quad \alpha^2 = \left|\underline{k}^2\right| c^2 \quad , \quad \underline{k} = (k_1, k_2, \Phi_z) \qquad (2)$$

The x direction is usually aligned with the wind vector at the source height. These equations and their use are described in detail in reference 9. In the two dimensional case with a stratified medium with the above x alignment, when we only have a resolved wind speed component U (no V) and only a k_1 component (no k_2), the above ray tracing equations are drastically simplified. The stratified assumption allows us to take a linear variation of U and c in each stratum which gives a circular ray path through that stratum.

The above ray trace is used principally as a coordinate system for constructing the Gaussian Beam. Although the ray is notionally along the centre of the beam the ray is not itself part of the field solution described below.

5. Derivation of the Local Field Solution

Cerveny et al[3] have given a derivation of the field solution for the cylindrical source case which has been reworked and modified by Porter and Bucker[7] to accommodate a point source. Cerveny et al[3] extract their local PE by solving asymptotically for $\omega \to \infty$ whereas Porter and Bucker[7] give the solution initially with higher order terms before taking the asymptotic case. Porter and Bucker's treatment is followed here for the cylindrical source with their confusing extension for a point source (and their typographical errors) removed. The resulting derivation throws light on the approximations involved and may be helpful in obtaining a higher order solution.

We start with the Helmholtz equation in u which is the required field variable (complex acoustic pressure) as a function of (x,y,z)

$$\nabla^2 u + \frac{\omega^2}{c^2} u = 0 \qquad (3)$$

We now introduce the ray centred coordinate system (s,n,θ) based on the arc length along the ray from the source ,s, the normal distance from the ray n, and the angle θ from the plane of the ray arc (see Figure2). We wish to apply the general orthogonal transformation to (3) into the new coordinate system (s,n, θ) . We apply transformation scale factors (h_s,h_n,h_θ) .The factor h_s is easily found by considering a small ray arc length ds (Figure 3). This arc will increase in size to ds' = (1+nc_n/c)ds at a distance n from the ray since the radius of curvature of the ray is c/c_n ,which means that h= 1+nc_n/c and the scale factors are then (h,1,n). Considering the 2D case the lhs of the transformed coordinates Helmholtz equation becomes

$$\nabla^2 u + \frac{\omega^2}{c^2} u = \frac{1}{h}\left\{\frac{u_{ss}}{h} + \left(\frac{1}{h}\right)_s u_s + h u_{nn} + u_n h_n + h\frac{\omega^2}{c^2} u\right\} = 0 \qquad (4)$$

which is identical to Cerveny et al's[3] equation (4).

We now make the parabolic substitution for u as a product of a modulator U(s,n) and a carrier $\Psi(\tau(s))$.

$$u(s,n) = U(s,n)\Psi(\tau(s)) \tag{5}$$

This is not the usual parabolic substitution where the carrier is a function of the range variable only. In this case the carrier is a function of the travel time τ along the ray from the source to the point at arc length s. The carrier is

$$\Psi(\tau(s)) = e^{-i\omega\tau(s)} \quad and \quad \tau(s) = \int_{s=0}^{s} \frac{1}{c(s)} ds \tag{6}$$

This carrier is permissible provided there is a local linear relationship between τ and s. Equation (4) now becomes

$$\frac{1}{h}\left\{\left[-\frac{\omega^2}{c^2} - i\omega\left(\frac{1}{c}\right)_s\right]U - 2i\frac{\omega}{c}U_s + U_{ss}\right\} + hU_{nn} + h\frac{\omega^2}{C^2}U$$
$$+\left(U_s - \frac{i\omega}{c}U\right)\left(\frac{1}{h}\right)_s + h_n U_n = 0 \tag{7}$$

where c refers to the value of sound speed at point s on the ray and C is the sound speed value at point (s,n) distant n from the ray. Note $(1/c)_s = -c_s/c^2$. We now follow Cerveny et al[3] and introduce a frequency stretching

$$v = \omega^{1/2} n \tag{8}$$

The distance along the normal to the ray, n , is being stretched here so that an artificial reduction of its value occurs as frequency increases. This ensures that the effective beam width, ie the width containing most of the energy, reduces with increase of frequency. This is essential to avoid the ratio beam width/wavelength getting too large and the beam not correctly sampling the field. Cerveny et al[3] note that the 1/2 power was arrived at by tests on "sample problems". From (8) $U_n = \omega^{1/2} U_v$ and $U_{nn} = \omega U_{vv}$ so that (7) can now be written

$$\omega^2 h\left(\frac{1}{C^2} - \frac{1}{h^2 c^2}\right)U +$$
$$\omega\left[\frac{ic_s}{hc^2}U - \frac{i}{c}\left(\frac{1}{h}\right)_s U - \frac{2i}{hc}U_s + hU_{vv}\right] +$$
$$\omega^{1/2}(U_v h_n) + \frac{1}{h}U_{ss} + U_s\left(\frac{1}{h}\right)_s = 0 \tag{9}$$

Equation (9) is fully accurate as no approximations have been made up to this point. Equation (9) is a Modulator Wave Equation (MWE). Cerveny et al[3] give the asymptotic ($\omega \to \infty$) form of (9) without proof. We therefore now follow Porter and Bucker[7] who more usefully propose a solution of (9) in the form of a power series in $\omega^{-1/2}$

$$U(s,\nu,\omega) = U^{(0)} + \frac{U^{(1)}}{\omega^{1/2}} + \frac{U^{(2)}}{\omega} + \ldots. \tag{10}$$

Porter and Bucker give expansions for $1/C^2$ and $1/h^2$ as power series in n with coefficients respectively in terms of n derivatives of c and h so that the bracketed term on the first line of (9) is

$$\frac{1}{C^2} - \frac{1}{h^2 c^2} = a_1 n + a_2 n^2 + \ldots\ldots = a_1 \nu \omega^{-1/2} + a_2 \nu^2 \omega^{-1} + \ldots\ldots \tag{11}$$

$$where \quad a_1 \; ; \; -\frac{2c_n}{c^3} \quad , \quad a_2 \; ; \; -\frac{c_{nn}}{c^3}$$

We now collect terms in (9) in $\omega^{3/2}$, ω and $\omega^{1/2}$

$$\omega^{3/2}\{a_1 h\nu U\} + \omega\left\{\frac{-c_{nn}}{c^3} h\nu^2 U + \frac{ic_s}{hc^2} U - \frac{2i}{hc} U_s + hU_{vv}\right\} + \omega^{1/2}\{U_v h_n\} + \frac{1}{h} U_{ss} = 0 \tag{12}$$

We are now ready to substitute the expansion of U given in (10) .We introduce the notation

$$B^{(n)} = \left[-h\frac{c_{nn}}{c^3}\nu^2 + \frac{ic_s}{hc^2}\right] U^{(n)} - \frac{2i}{hc} U_s^{(n)} + hU_{vv}^{(n)} \tag{13}$$

and expand (12) to include terms of second order accuracy . We collect terms in powers of $\omega^{1/2}$

$$\omega^{3/2}\left\{a_1 h\nu U^{(0)}\right\} + \omega\left\{B^{(0)} + a_1 h\nu U^{(1)}\right\} + \omega^{1/2}\left\{U_v^{(0)} h_n + B^{(1)} + a_1 h\nu U^{(2)}\right\} +$$
$$\left\{\frac{1}{h} U_{ss}^{(0)} + U_v^{(1)} h_n + B^{(2)}\right\} + \omega^{-1/2}\left\{\frac{1}{h} U_{ss}^{(1)} + U_v^{(2)} h_n\right\} + \omega^{-1}\left\{\frac{1}{h} U_{ss}^{(2)}\right\} = 0 \tag{14}$$

We have gone to some trouble to obtain this expansion which is not given in the literature ,the interest there being only in the $O(\omega)$ term. The explanation for the restriction to $O(\omega)$ can be seen by neglecting the first term in (14) and dividing through by ω so that when $\omega \to \infty$ all the terms except the second disappear. The solution so obtained would then only be applicable for high frequencies. We wish to use the additional terms in (14) to allow us to extract solutions for $U^{(1)}$ and $U^{(2)}$ as

well as $U^{(0)}$ to give a second order accurate U applicable over a wider frequency range. Initial attempts have provided prototype numerical procedures which to some extent compromise the speed of the zeroth order solution below. This work is ongoing and will be reported at a later date. We will now follow Cerveny et al[3] in taking only the O(ω) terms in (14). With the additional approximations of $h \approx 1$ and $U^{(1)}=0$ we have

$$\left[-\frac{c_{nn}}{c^3}\nu^2+\frac{ic_s}{c^2}\right]U^{(0)}-\frac{2i}{c}U_s^{(0)}+U_{\nu\nu}^{(0)}=0 \qquad (15)$$

We make the simplifying substitution

$$U(s,\nu)=\sqrt{c(s)}\,W(s,\nu) \qquad (16)$$

which gives the local Parabolic Wave Equation

$$\frac{2i}{c}W_s+W_{\nu\nu}-\frac{\nu^2 c_{nn}}{c^3}W=0 \qquad (17)$$

We follow Cerveny et al[3] by seeking a solution

$$W(s,\nu)=A(s)\exp[-i\nu^2\Gamma(s)/2] \qquad (18)$$

where we want to solve (17) for A(s) and Γ(s). We substitute (18) into (17) which leads to two differential equations

$$\begin{aligned} &2A_s/c+A\Gamma=0 \\ &\Gamma_s/c+\Gamma^2+c_{nn}/c^3=0 \end{aligned} \qquad (19)$$

The second equation is a Riccati Equation which is solved by replacing it with two first order equations in new Dynamic Beam Variables p and q

$$\frac{dp}{ds}=\frac{-c_{nn}q}{c^2} \quad and \quad \frac{dq}{ds}=cp \qquad (20)$$

The Γ in (19) is simply p/q. Solving the first equation in (19) gives $A(s)=A_0/\sqrt{q}$ .From (20) ,(18) and (16) we can now write the partial single beam solution in (5) as

$$u(s,n)=A_0\sqrt{\frac{c(s)}{q(s)}}\exp(-i\omega\left\{\tau(s)+\frac{p(s)}{q(s)}n^2\right\}) \qquad (21)$$

We note that this solution u is taken at a small distance n from the ray where the receiver is located and that the presence of the n^2 term ensures a Gaussian variation of the beam amplitude with n. The values of s and n taken at the point on the ray closest to the receiver, the ray endpoint, are easily determined from the ray geometry. The dynamic beam parameters p and q vary along the ray and must be obtained by solving equations (20) numerically along the central ray. For the stratified case this is straightforward. Porter and Bucker[7] have shown that if n is greater than 5 beam widths the contribution of that beam becomes negligible. They recommend this "beam windowing" as a means of increasing computational efficiency.

Muller[4] has drawn attention to the need for care in dealing with the square root in (21). He notes that the 1/q has zeros where it crosses the real axis corresponding to the zeros of the real function $q_2(s)$. Each crossing corresponds to an increase in phase of A(s) of $\pi/2$. The number of crossings, σ, is found simply by counting the sign changes of $q_2(s)$ during the stepwise solution of the auxiliary equations along the central ray. The extra phase to be added is then

$$Phase = \eta\frac{\pi}{2}\ ,\ for\ even\ \sigma:\eta=\sigma,\quad for\ odd\ \sigma:\eta=\sigma+1$$

6. Numerical Solution of the Auxilliary Equations for the Dynamic Beam Parameters

The complex quantities p and q must satisfy equations (20) -the two differential equations derived from the Riccati equation. These solutions can each be given as a linear combinations of two of two real quantities. Without loss of generality we can write

$$\begin{aligned} p(s) &= \varepsilon p_1(s) + p_2(s) \\ q(s) &= \varepsilon q_1(s) + q_2(s) \\ \varepsilon &= \varepsilon_1 + i\varepsilon_2 \end{aligned} \qquad (22)$$

where ε is the unknown Gaussian Beam Parameter which is discussed below. We now wish to solve the equations

$$\frac{dp_i}{ds} = \frac{-c_m q_i}{c^2}\ \ and\ \ \frac{dq_i}{ds} = cp_i\ \ ,\ i=1,2 \qquad (23)$$

We set up a numerical solution with starting values given by Gabillet et al[2]

$$\begin{aligned} p_1(0) &= 0, \quad p_2(0) = 1; \quad p(0) = 1 \\ q_1(0) &= 1, \quad q_2(0) = 0; \quad q(0) = \varepsilon \end{aligned} \qquad (24)$$

For a stratified atmosphere made up from layers each of which has a linear sound speed variation within each layer $c_{nn}=0$ so from the first pair of equations in (23)

$$p_1(s) = 0, \quad p_2(s) = 1; \quad p(s) = 1 \tag{25}$$

Since p_1 is always zero, in this case q_1 must retain its starting value

$$q_1(s) = 1 \tag{26}$$

We can obtain $q_2(s)$ with the "trivial" integration of the equation $dq_2/ds=c(s)$ done over each stratum. We note that q_2 accumulates along the ray, each increment in its value being acquired at the top of each layer when the ray is upbound. A similar integration of $1/c(s)$ (see equation (6)) is performed for each stratum so that we can also accumulate $\tau(s)$.

7. Determination of the Gaussian Beam Parameter

The choice of ε is the most difficult aspect of setting up a Gaussian Beam predictor. There is an extensive literature on how to set up the parameter which has been reviewed by Weber[5]. Weber presents the various methods of choosing the parameter as options which he subcategorises as

- ε is contant –Options 1,2,3
- ε chosen at the endpoint -Options 4,5,6
- ε determined along the beam -Option 7
- ε determined by "mixed" criteria –Options 8,9

Weber concluded that the last category was the only one capable of exercising control over both beam width and curvature along its whole length. Weber's modification of Cerveny et al's[3] method (Option 8), which he refers to as Option 9, he claims as the preferred method. Option 9 was adopted by Gabillet et al[2] who claimed it gave satisfactory results. We have found that Options 7 and 9 gave very similar results and both could fail giving erroneous predictions when they allow beam widths to become too small or too large. We only describe these two methods here as none of the other options offer sufficient control of the beam width and curvature along the beam length in the atmospheric case.

The derivation of the Gaussian Beam method above relies on the partial solutions, u, being valid within the width of the beam at a distance n from the central ray. If n lies outside of the zone around the ray, where the medium properties are substantially different from those close to the ray, the solutions will be erroneous. This means that the overall beam width must not be allowed to get too big at any point along the central ray. Another way of looking at the effect of beam width is to note that the beam effectively averages the field across its width and this averaging is

accumulative along the full beam length. If the beam width is too large (more than a few wavelengths in practice) the field is over smoothed, conversely if the beam gets too narrow we revert to a ray solution with all its associated difficulties when crossings are encountered. In addition to getting the width correct it is vital to ensure that the curvature is never too large as this creates unwanted oscillations in the solutions. Curvature of the beams is assumed to be small at the points where they are reflected from the ground. The beam parameter is the only means of exerting control over beam width and curvature and it therefore has a crucial effect on the reliability of the predictor.

The beam width, L, is taken as the distance from the central ray at which the beam amplitude is 1/e of that at its centre and the phase front curvature, K, is taken as rate of change of phase along the normal to the ray. L and K were shown by Cerveny, et al[3] to have the following relations to p/q

$$L^2 = -\frac{2}{\omega}\frac{1}{\mathrm{Im}[p(s)/q(s)]} \quad ; \quad K = -c(s)\mathrm{Re}[p(s)/q(s)] \tag{27}$$

Note that L depends on the inverse of the square root of the frequency which comes from the frequency stretching used in the derivation of the beam solution. This means that beams get narrower as frequency increases. L and K are only controlled through the values of p and q principally at the ray endpoint. In the stratified atmosphere it is only q which has an effect, p being 1 and $q(s) = \varepsilon + q_2(s)$. In addition in the stratified case L and K have the values

$$L^2 = \frac{2d}{\omega \varepsilon_2} \quad ; \quad K = -c(s)\frac{(\varepsilon_1 + q_2)}{d} \quad ; \quad d = (\varepsilon_1 + q_2)^2 + \varepsilon_2^{\,2} \tag{28}$$

and q_2 increases as we move along the ray from a value of zero at the source. Equations (28) show that ε_1 and ε_2 set both L and K along the whole beam length. In order to constrain L and K to acceptable values ideally we would need to alter ε_1 and ε_2 along the whole length of the beam which is of course not permissible. The choice of these parameters must therefore be a compromise which will ensure that L and K have values as near as possible to the ideal ones over most of the beam length.

7.1 Klimes's[11] Method for Beam Parameter

Klimes attempts to control the beam width along its complete length by minimizing the beam volume defined as

$$Volume = \int_0^{s_{END}} L(s)^2 ds \tag{29}$$

Weber[5] has summarized Klimes method in his Option 7 and gives the real and imaginary parts of the beam parameter as

$$\varepsilon_1 = \frac{-B_{12}}{B_{11}} \quad , \quad \varepsilon_2 = \frac{(B_{22}B_{11} - B_{12}{}^2)^{1/2}}{B_{11}}$$
$$B_{ij} = \int_0^{s_{END}} q_i(s)\, q_j(s) ds \qquad i, j = 1, 2 \tag{30}$$

In the stratified case $q_1=0$ so that the B's become

$$B_{11} = s_{END} \quad , \quad B_{12} = \int_0^{s_{END}} q_2(s) ds \, , \quad B_{22} = \int_0^{s_{END}} q_2(s)^2 ds \tag{31}$$

Provided that the sound speed varies linearly over each stratum the above B's may be obtained analytically, the integrations becoming trivial. Klimes has noted that this method may only be satisfactorily used in this or similar cases where B can be found analytically since otherwise numerical instabilities arise. Klimes also notes that the solution can become unstable if the B's get too big. Referring to (28) this would be when beam width is allowed to get too big. The minimization of the beam volume does not, of course, guarantee that the beam width cannot become too large in some regions (or too small in others) .

7.2 Weber's[5] Modification of Cerveny's[6] Mixed Criteria Method for Beam Parameter

Weber summarises Cerveny's(1985)[6] mixed criteria method in his Option 8. He gives the real and imaginary parts of the beam parameter in terms of parameters M^R, M^I, $M_1{}^R$, and $M_2{}^R$ which are defined as follows

$$M = \frac{p}{q} \quad , \quad M^R = \mathrm{Re}[M] \quad , \quad M^I = \mathrm{Im}[M]$$
$$M_1{}^R = \frac{p_1}{q_1} \quad , \quad M_2{}^R = \frac{p_2}{q_2} \tag{32}$$

For the stratified case

$$M = \frac{1}{q} \quad , \quad M^R = \mathrm{Re}\left[\frac{1}{q}\right], \quad M^I = \mathrm{Im}\left[\frac{1}{q}\right]$$
$$M_1{}^R = 0 \quad , \quad M_2{}^R = \frac{1}{q_2} \tag{33}$$

These parameters are applicable at any point on the beam and are evaluated in Cerveny's method at the ray end point. Taking the definitions of p and q given in equation (22) we obtain the following relationships also applicable anywhere on the beam

$$\varepsilon_1 = \frac{(M^R - M_2^R)(M_1^R - M_2^R) - (M^I)^2}{den}\begin{Bmatrix} q_2 \\ q_1 \end{Bmatrix}, \quad \varepsilon_2 = \frac{-M^I}{den}\begin{Bmatrix} 1 \\ q_1^2 \end{Bmatrix} \tag{34}$$

$$den = (M_1^R - M^R)^2 + (M^I)^2$$

The unknown is M (or M^R and M^I).

Cerveny[6] now imposes two conditions allowing M to be found. The first condition is "at the ray endpoint there should be a plane phase front" (phase front curvature, K, is zero) which from (27) means that $M^R = 0$ if we assume that the medium is approximately homogeneous between the ray endpoint and the receiver. If this is not the case M^R can be found using the procedure given in Weber's[5] paper under Option 8. The second condition is that L^2 is a minimum at the source. Weber shows this is achieved by applying the condition in (35) at the endpoint

$$M^I = -\left|M^R - M_2^R\right| \tag{35}$$

Referring to equation (34) we now have all the M's evaluated at the ray endpoint. In the stratified case with $M^R=0$ equation (34) becomes

$$\varepsilon_1 = 0 \ , \ \varepsilon_2 = -\frac{1}{q_2(s_{END})} \tag{36}$$

Referring to equation (28) for curvature of the wavefront at the source, K(0), we can indeed see that it is zero if $\varepsilon_1=0$.

Weber[5] in his Option 9 ,which constitutes his new contribution, returns to equation (34) and uses Cerveny's[6] first condition of zero K at the receiver with the M^R obtained exactly as described above. ($M^R = 0$ in our case). Instead of Cerveny's second condition of minimum beam width at the source Weber proposes a new beam width setting based on the sound speed properties of the medium through which the beam has traveled along its whole length from the source to its endpoint. Once this beam width, L, is known (27) allows us to find M^I which can be used in (34).

Weber[5] gives the following equations for calculating the beam width

$$l^2 = \frac{1}{N}\sum_{i=1}^{N} D_i^2 \quad , \quad L(\omega)^2 = l^2 \frac{\omega_{MAIN}}{\omega} \tag{37}$$

where ω_{MAIN} is the actual angular frequency close to the frequency used for setting up the Gaussian Beam. As we are working only with single frequencies here L=*l*. The atmosphere is broken up into many concatenated triangular zones in each of which which the sound speed is either constant or varies linearly. The distance D_i is the "minimum distance from the point of intersection of the central ray with a point on a side of one triangle to the nearest corner". (see Figure 4a) . Muller[4] has used triangular zones for his solution of the auxiliary equations. In the stratified atmosphere there is a little arbitrariness in how we define the triangles- one possible scheme is shown in Figure 4b. This scheme is easily implemented since the D_i^2 will be the square of the ray chord in each layer. Weber[5] claims that this option takes proper account of the structure of the atmosphere along the beam's path and consequently the above calculation sets up a representative beam width. It must be emphasized that the beam width calculated in this manner is by no means an optimum value and that we do not have a guarantee that local widths cannot get too small or too large. In the stratified case however we can maintain a roughly constant beam width by ensuring that all arc chord lengths are similar. This would require fatter strata on the steep ray portions and thinner strata on shallow ray portions. It is not usually possible to alter strata thickness in this way. Our tests with this method have shown that it sets beam widths on the large side and the preferred width should be between 1/3rd and 1/10th of the calculated value. It is very important to ensure that the beam has most of its energy concentrated close to the central ray and that there is no possibility of any of this energy within one stratum seeping across the nearest stratum interface. This means that the beam width should be much less than the stratum width when the ray is traveling near to the horizontal.

8. Beam Reflection at the Ground

Weber[5] gives a detailed treatment of reflection and transmission of Gaussian Beams at a first order discontinuity ie at an interface between two regions with a difference in sound speed gradients. We can treat the air ground interface as a first order discontinuity, at least as far as the ground reflected wave is concerned, provided that the beam is not incident at angles close to grazing. In this case p and q are not altered by the reflection process and can be found at the ray endpoint by continuing the stepwise solution of the auxiliary equations immediately after a reflection. The solution ,u, in equation (21) will now require an additional factor given by

$$RTOT(\theta_{source}) = R(\theta_{INC})^{NREFL}$$

$$R(\theta_{INC}) = \frac{Z_{GND}\cos(\theta_{INC}) - 1}{Z_{GND}\cos(\theta_{INC}) + 1} \quad , \; Z_{GND} \; in \; \rho c \; units. \tag{38}$$

where N_{REFL} is the number of ground reflections and θ_{INC} is the angle of incidence of the beam central ray on the ground (measured from the normal to the ground). The ground impedance is easily calculated from known ground parameters with one of the many available models.[12]

Since p and q are unchanged by the ground reflection, beam width and curvature must also remain unchanged. This is perfectly permissible for a beam and demonstrates another advantage of using beams rather than ray tubes. (Ray tubes suffer large changes in section on reflection which generate incorrect drops in tube amplitude which have to be empirically offset.)

The ground reflection factor in (38) is satisfactory provided the incident beam curvature is small and provided the beam is not close to grazing incidence. It is interesting to note that the total solution at the receiver, obtained when all the partial solutions, u, are summed, will still take into account the cylindrical wave effects which would occur when we have a cylindrical source above a flat ground surface in a homogeneous atmosphere. (This is analogous to the "sphericity effect" of a point source near a flat ground.)

9. Expansion of the Cylindrical Source into Gaussian Beams

Cerveny et al[3] consider a homogeneous medium and propose a total field solution at the receiver point as a weighted integration of the partial field solutions u(α)

$$u_{TOT}(\alpha) = \int_0^{2\pi} \Phi(\alpha) u_\alpha(s,n) d\alpha \qquad (39)$$

where α is the central ray launch angle and Φ is an unknown weighting function which is found by equating u_{TOT} with the asymptotic cylindrical field. This leads to a weighting function

$$\Phi(\alpha) = -\frac{i}{4\pi}\left(\frac{\varepsilon(\alpha)}{c_0}\right)^{1/2} \qquad (40)$$

The weighting function will be different for each launch angle α. Muller[4] has given a detailed derivation of the weighting function when the source has directional characteristics and when the frequency used for the Gaussian beam differs from that of the spectral component considered. We evaluate (39) with a weighted summation of the partial solutions for each central ray. This is satisfactory provided the launch angle interval, Δα, is sufficiently small (0.1-0.2 degrees) and there are sufficient rays to populate the receiver region.

Porter and Bucker[7] carry out a similar matching of the asymptotic point source field with the Gaussian Beam solution and show that the above weighting function must then include the expected constant$\sqrt{[}$ cos(α)/r] factor, r being the horizontal distance between source and receiver.

10. Initial Results

Only downwind profiles were used in this first round of tests. We followed Gabillet et al[2] and used a linear sound speed gradient. (Gradients were in the range 0.02 to 0.1 taken over a total depth of 50m divided equally into 10 layers, the source height was 5m, receiver height 2.5m and the frequency was 500Hz.) Comparisons were made with predictions from a wide angle PE model for a total range of 1000m. Like Gabillet et al[2] we found the Gaussian Beam program preformed well giving excellent agreement provided the beam width was correctly "tuned" (typical beam widths were $1/20^{th}$ of the value calculated with equation (37)). With a receiver height of 1m there was a deterioration in the Gaussian Beam solution accuracy with a maximum error of 3dB occurring about 200m from the source. A similar deterioration occurred when the frequency was reduced to 250 Hz for the 2.5m receiver height. These findings are similar to those of Gabillet et al[2].

Tests were also performed with more realistic downward refracting logarithmic sound speed profiles, based on a sound speed function of height ,z , of 340+aln (z/0.1) with a in the range 0.02 to 0.1. Stratum thicknesses of 0.2, 1, 2, 4, 8, 16, 32, 64m were used with the above sound speed values set at the top of each stratum and with linear variation of sound speed within each stratum. The source and receiver heights were the same as for the linear tests above. Poor results were obtained at the larger ranges (700-1000m) even at 500Hz. The test data used here is similar to that used by Gabillet et al[2] but our results were much worse than theirs.

11 Concluding Remarks

We believe that the problems of overlapping beams and of beams straddling two strata ,which can occur for beams travelling close to horizontal ,are responsible for the poor results with the logarithmic sound speed profile. Gabillet et al[2] discussed these sources of error at length. They noted the importance of ensuring beam width is kept sufficiently small to minimise occurrences of these near horizontal beams overlapping or straddling two strata yet large enough for them to give a representative field solution without suffering ray crossing errors. Gabillet et al[2] also noted the importance of keeping the receiver height greater than a few wavelengths to prevent beams overlapping the ground. We cannot explain at this stage why our results were inferior to the comparable cases in Gabillet et al's[2] paper but it is clear that a great deal of fine tuning of the Gaussian Beam method is required to guarantee predictions which are as good as those from PE or FFP models. It is also clear that if the method is to be applicable to realistic sound speed profiles it will require major improvements to the basic algorithm. Others have also encountered problems in setting up Gaussian Beam methods which use realistic meteorological profile data .Gilbert[13] has noted in relation to his "Gaussbeam" program, that satisfactory results could only be obtained when multiple reflections of the beams from the ground could be eliminated. This was possible in a specific application[14] where small buildings broke up the ground reflections sufficiently to permit their omission. Referring to one of our central ray

plots in Figure 5 it is clear that ground reflections are indeed the main source of the grazing beams in the vicinity of the receiver.

Porter and Bucker[7] have proposed an interesting empirical correction for grazing beam error near the sea- air boundary (acting as a second order discontinuity) which involves the addition of a term to the ratio p/q. We are investigating the feasibility of making a similar empirical modification for the atmospheric case and will report the results of this study at a later date.

11. References

1. **L Sutherland** On Requirements for Long Range Sound Predictors. *Private Communication September(2000).*
2. **Y Gabillet, H Schroeder, G A Daigle and A L'Esperance** Application of the Gaussian Beam Approach to Sound Propagation in the Atmosphere: Theory and Experiments. *J. Acoust. Soc. Amer. 93(6), 3105-3116 (1993).*
3. **V Cerveny, M M Popov and I Psencik** Computation of Wave Fields in Inhomogeneous Media-Gaussian Beam Approach. *Geophys. J.R.Astron.Soc. 70,109-128(1982).*
4. **G Muller** Efficient Calculation of Gaussian-Beam Seismograms for Two-Dimensional Inhomogeneous Media. *J.R.Astro.Soc.79,153-166(1984).*
5. **M Weber** Computation of Body-Wave Seismograms in Absorbing 2-D Media Using the Gaussian Beam Method:Comparison with Exact Methods. *Geophys. J.92,9-24(1988).*
6. **V Cerveny** Gaussian Beam Synthetic Seismograms. *J.Geophys. 58,44-72 (1985).*
7. **M B Porter and H P Bucker** Gaussian Beam Tracing for Computing Ocean Acoustic Fields. *J.Acoust.Soc.Amer.82,1349-1359(1987).*
8. **L P Felsen** Gaussian Beam Analysis of Propagation from an Extended Plane Aperture Distribution Through Dielectric Layers. I: Plane Layer and II: Circular Cylindrical Layer. *IEEE Trans. Antennas Propag.38,1607-1624(1990).*
9. **F Walkden and M West** Prediction of Enhancement Factor for Small Explosive Sources in a Stratified Moving Atmosphere. *J. Acoust. Soc. Amer. 84(1),321-326(1988).*
10. **M West** The Larkhill Ray Invariant (LARRI) Model. *Computer Software for the Ministry of Defence, Copyright M West and the University of Salford (1993).*
11. **L Klimes** Preliminary Information on the Program Package SW83 for Computation of Seismic Wavefields in 3-D Media (in Czech). *Research Report No. 67 for Geofyzika Brno, Institute of Geophysics, Charles University, Prague (1983).*
12. **K Attenborough** Acoustical Impedance Models for Outdoor Sound Surfaces. *J. Sound Vib.99(4),521-544(1985).*
13. **K Gilbert** The Gaussbeam Program and its Application to Sites with Small Buildings. *Private Communication September (2002).*
14. **R L Bronsdon** A Propagation Model Based on Gaussian Beams that Accounts for Wind and Temperature Inversions. *Proc. 8th International symposium on Long Range Sound Propagation, The Pennsylvania State University, USA (1998).*

Figure 1 Time Line for GB Method

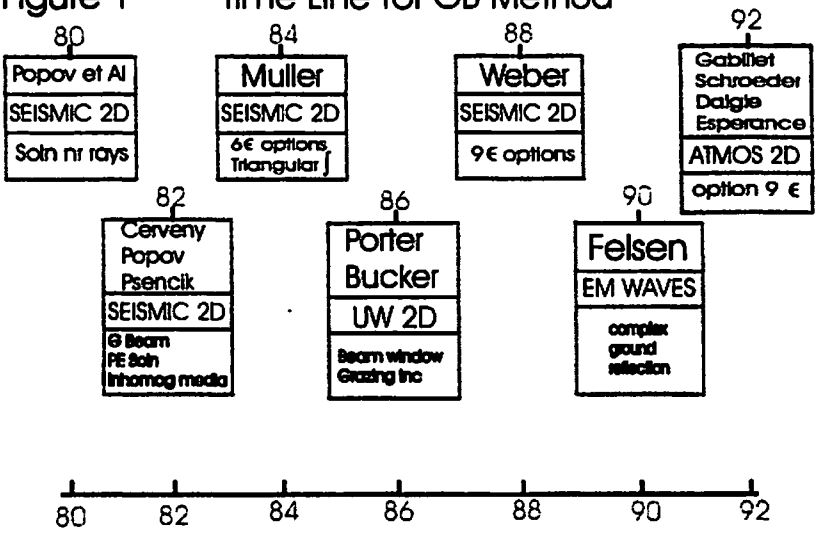

Figure 2 **Gaussian Beam Concept**

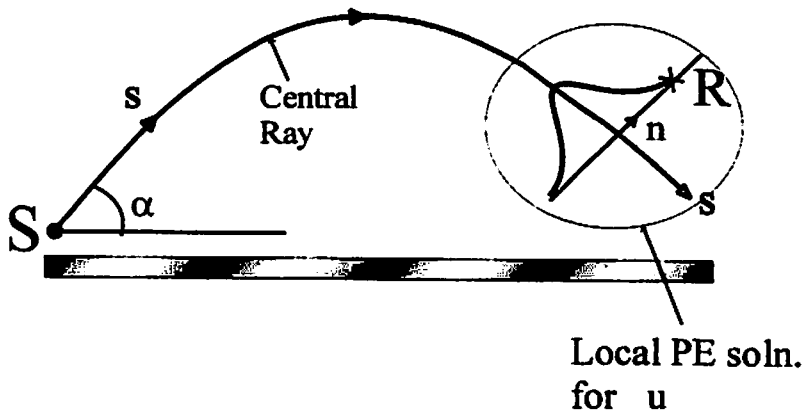

Figure 3 **Geometry for Ray Centred Coordinate System Scale Factors**

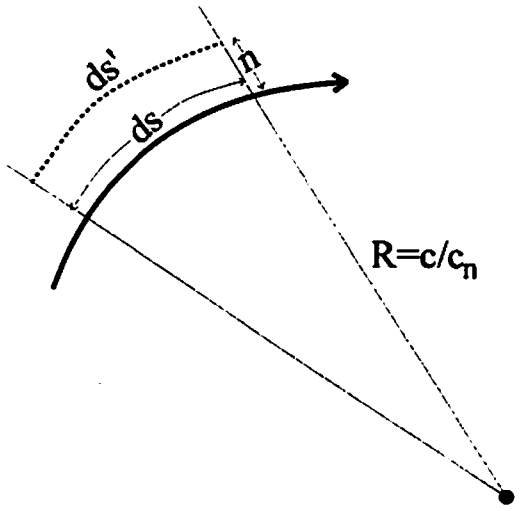

Figure 4 Determination of Beam Width

$$l^2 = \left(\frac{1}{N} \sum_{i=1}^{N} D_i^2 \right) \quad , \quad l \simeq l$$

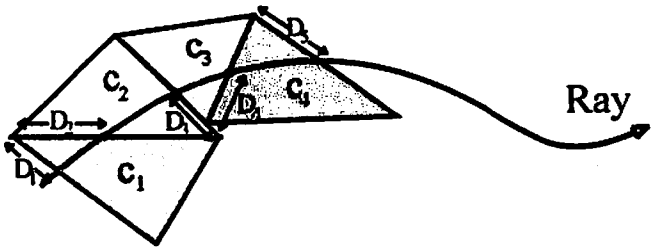

Figure 4a Concatenated Triangular Zones

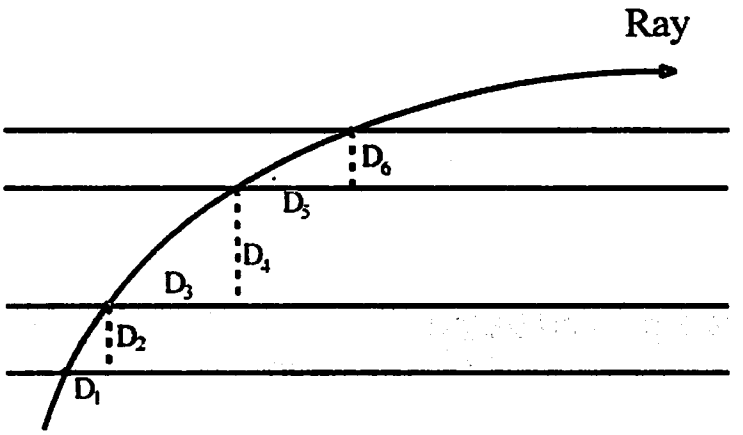

Figure 4b Triangular Zones for Stratified Atmosphere

Figure 5 Gaussian Beam Central Rays

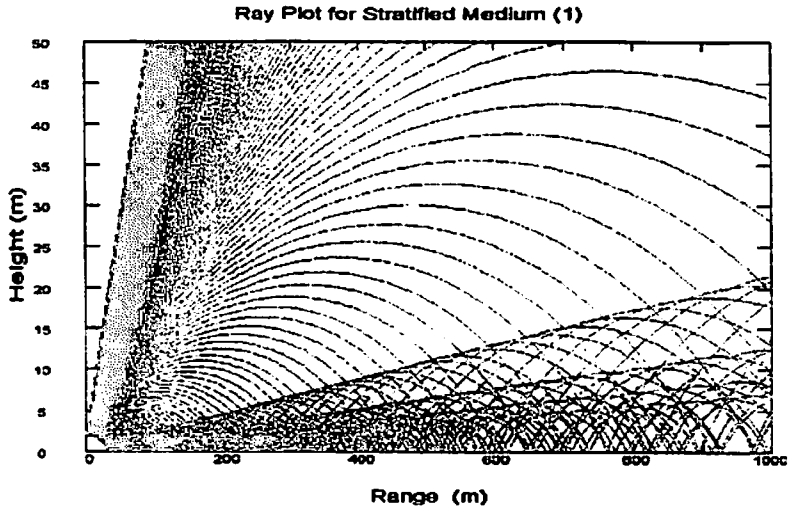

Log/0.5 Strata
Approx log sound speed
Ray Increment angle 0.2 degrees
Range 1000m, depth 50m

Coupling of PE with BEM or with a ray model for the calculation of the effect of complex noise barriers in a refracting atmosphere

Ingrid M. Noordhoek and Erik M. Salomons

TNO TPD, Sound and Vibration Division, P.O. Box 155, 2600 AD Delft, The Netherlands
noordhoek@tpd.tno.nl

The effect of complex noise barriers in a refracting atmosphere can be calculated using a hybrid model in which the Parabolic Equation (PE) model is coupled to the Boundary Element Method or to a ray model. BEM or the ray model is used in the region near the source and noise barrier(s) and PE is used elsewhere. The coupling of the models is tested by comparing results of the hybrid models with results of the ray model and PE for a simple straight noise screen. Results show that the hybrid models are accurate. Furthermore, calculations with the hybrid models are performed for a barrier with a T-top and for a configuration with (tilted) barriers at both sides of the road.

Introduction

The Parabolic Equation (PE) model gives accurate results for the sound field of a harmonic monopole source in a refracting atmosphere above a ground surface. A barrier may be included in the PE method by setting the sound pressure equal to zero at the grid points covered by the barrier (Kirchhoff approximation). This approximation gives accurate results in the region behind a simple straight barrier that is not too close to source or receiver. For complex noise barriers, however, this approximation is less accurate.

For the calculation of the effect of complex noise barriers in a refracting atmosphere, PE can be used in combination with the two-dimensional Boundary Element Method (BEM) or "TOMAS", a three-dimensional ray model developed at TNO TPD based on diffraction theory and geometrical acoustics. BEM or TOMAS is used in the region near the source and noise barrier(s) and PE is used elsewhere. TOMAS is faster than BEM, but is limited to obstacles that consist of flat surfaces that are large compared to wavelength. The two-dimensional BEM can handle arbitrary barrier shapes provided that they are infinitely long and perpendicular to the vertical plane through the source and receiver.

The coupling of the models will be tested by comparing results of the hybrid models BEM+PE and TOMAS+PE with results of the basic models TOMAS and PE for a simple straight noise screen in a neutral or refracting atmosphere. Furthermore, as a demonstration of calculations with these hybrid models, BEM+PE results for a barrier with a T-top will be considered, as well as TOMAS+PE results for a situation with tilted barriers at both sides of a road.

Method

The coupling of the models is performed by means of a starting vector for PE (see Fig. 1) that contains the spectrum of the complex sound pressure as a function of height. The starting vector for PE is located behind the noise barrier. BEM or TOMAS is used to calculate the sound propagation from the source to the starting vector for PE. Next, PE is used to calculate the sound propagation from the starting vector to the receiver.

In the BEM or TOMAS calculations of sound propagation from the source to the starting vector for PE, the refracting atmosphere is approximated by a neutral atmosphere. PE can handle a realistic refracting atmosphere. Therefore, the location of the starting vector is chosen as close as possible behind the noise screen. The location of the starting vector could even be chosen at the same horizontal position as the noise screen, but in that case the discontinuity in the sound pressure in the starting vector leads to small numerical oscillations in the PE results. These oscillations are avoided by choosing the starting vector at a distance of 1 m behind the noise screen.

With PE and TOMAS, propagation of spherical sound waves is calculated. With the two-dimensional BEM model, however, propagation of cylindrical sound waves is calculated. Therefore, when BEM is coupled to PE, the complex pressure in the starting vector for PE is multiplied by a spherical correction factor equal to the free field of a spherical wave divided by the spherical field of a cylindrical wave.

In order to reduce computation time, the height of the starting vector for PE is not chosen equal to the PE grid height, but limited to a height of 50 m. For heights above 50 m, the amplitude of the complex sound pressure is interpolated linearly to zero at the top of the grid. The phase of the complex sound pressure is extrapolated to the top of the grid.

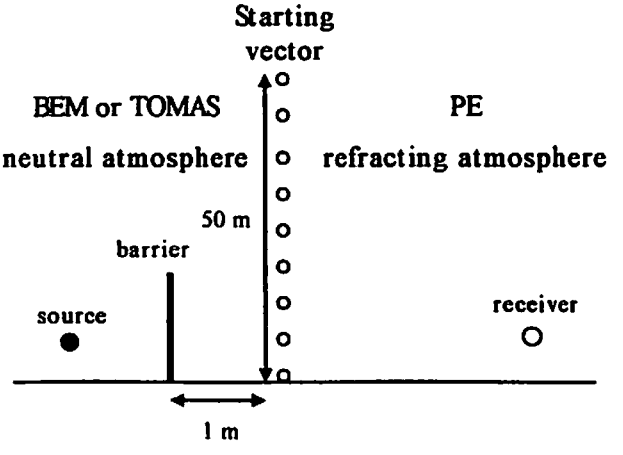

Fig. 1. Coupling of the models by means of a starting vector for PE.

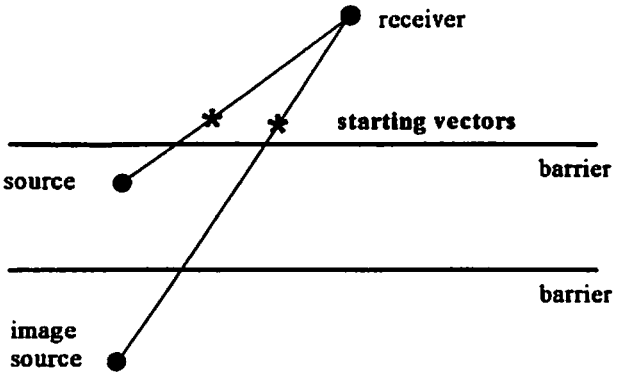

Fig. 2. Top view of a situation with a sound source between two parallel noise screens.

Figure 2 shows the method that is used to model a situation with a sound source between two parallel noise screens. In this situation, two calculations with the hybrid TOMAS+PE method are performed for each point source: one calculation in the vertical plane through the original source and the receiver, and one calculation in the vertical plane through the image source and the receiver. The results from these two calculations are summed to obtain the resulting sound pressure at the receiver. In the TOMAS calculations, only first order sound rays (i.e. sound rays with at most one reflection at a noise screen) are considered. This results in a total of 27 potential sound rays for each sound source.

Situations

Single noise screen
Figures 3 and 4 show configurations with a single straight noise screen. These configurations are representative for situations with a noise screen along a road. The sound source is located at a height of 0.5 m above porous asphalt. The porous asphalt is modelled using the impedance model of Hamet *et al.* [1][2] with a flow resistivity of 5 kPa s m^{-2}, a porosity of 0.2, a structure constant of 5, and a layer thickness of 0.04 m. The model of Hamet *et al.* is a theoretical model for porous materials with a rigid frame. The barrier is located at 10 m from the source. The receiver is located at a height of 1.5 m above grassland. The grassland is modelled using the empirical impedance model of Delany and Bazley [3] with an effective flow resistivity of 200 kPa s m^{-2}.

In Fig. 3, the barrier height is 1 m and the receiver is located at a distance of 20, 200, or 2000 m from the source. In Fig. 4, the barrier height is 4 m and the receiver is located at a distance of 200 m from the source.

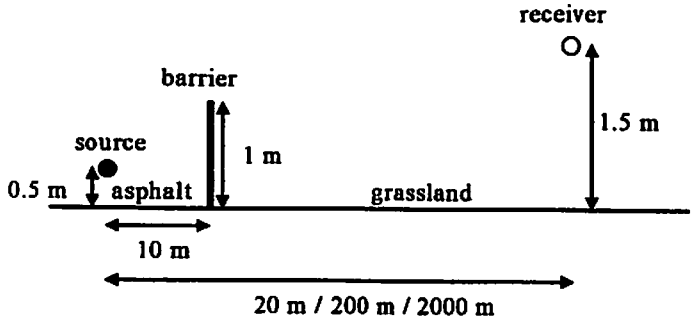

Fig. 3. Configuration with a single straight noise screen for which calculations with the hybrid TOMAS+PE model are performed.

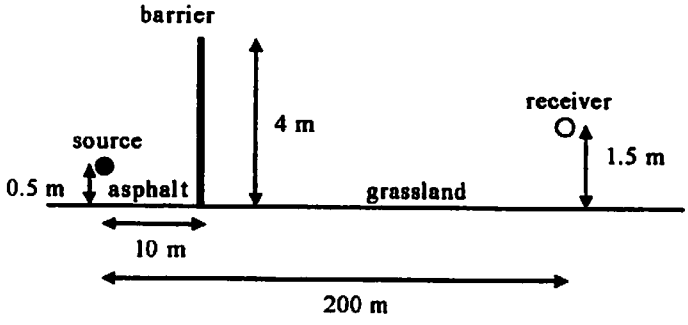

Fig. 4. Configuration with a single straight noise screen for which calculations with both hybrid models TOMAS+PE and BEM+PE are performed.

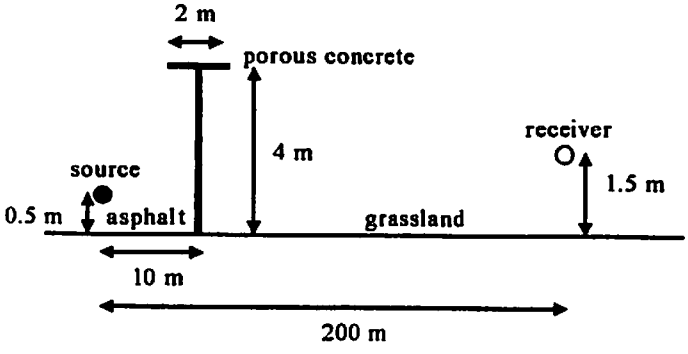

Fig. 5. Configuration for a barrier with a T-top for which calculations with the hybrid BEM+PE model are performed.

Figure 5 shows the configuration for a barrier with a T-top. The barrier has a height of 4 m and a flat horizontal top with a width of 2 m. The top consists of porous concrete and is modelled using the impedance model of Hamet *et al.* with a flow resistivity of 10 kPa s m^{-2}, a porosity of 0.25, a structure constant of 4, and a layer thickness of 0.1 m. The receiver is located at a distance of 200 m from the source.

Calculations for the situations in Figs. 3, 4, and 5 are performed for a non-refracting atmosphere and for a refracting atmosphere. For the refracting atmosphere, a downward-refracting logarithmic sound speed profile was assumed, with a ground roughness length of 0.1 m. For a thermally neutral atmosphere this profile corresponds to wind blowing from the source to the receiver, with a wind speed of 4.6 m/s at a height of 10 m. The wind speed profile is range-independent, so screen-induced wind speed gradients are ignored.

Barriers at both sides of the road
The height of the barriers is 6 m. Calculations are performed for straight noise screens and for noise screens with an outward tilt of 20 degrees. The distance between the barrier tops is 40 m. The ground surface consists of porous asphalt between the barriers and grassland elsewhere. There are two driving lines, each represented by four incoherent point sources at a height of 0.75 m. For the source spectrum, a representative traffic noise emission spectrum is used. The receiver distance ranges from 25 m to 2 km from the centre of the road and the receiver height ranges from 0 to 50 m. Calculations are performed for a realistic refracting atmosphere in which the disturbance of the prevailing wind speed profile by the presence of the noise barrier between the source and the receiver is taken into account. The prevailing wind speed profile is logarithmic, with a ground roughness length of 0.1 m. The wind blows in the direction of the receiver, perpendicular to the noise barriers and the wind speed is 4 m/s at a height of 10 m.

Results

Single noise screen
For the situation in Fig. 3, calculations with the basic models TOMAS and PE and with the hybrid model TOMAS+PE are performed. Figures 6, 7 and 8 show 1/3-octave band spectra of the sound pressure relative to free field, for source-receiver distances of 20, 200, and 2000 m, respectively. For the non-refracting atmosphere (solid lines), results of the hybrid TOMAS+PE model agree with results of the basic models TOMAS and PE (although TOMAS results are slightly lower in the first dip of the spectrum). For the refracting atmosphere (dashed lines), results of the hybrid TOMAS+PE model agree with results of PE. This indicates that the hybrid model TOMAS+PE is accurate.

Figure 6 shows that for the source-receiver distance of 20 m, results for the refracting atmosphere are almost equal to results for the non-refracting atmosphere. This indicates that for the combination of this refracting atmosphere and the source-receiver distance of 20 m, atmospheric refraction may be neglected. To model sound propagation over a complex noise barrier in this situation, TOMAS (or BEM) could be used directly instead of coupling it to PE.

For the source-receiver distance of 200 m and especially for 2000 m, however, results for the refracting atmosphere deviate considerably from results for the non-refracting atmosphere (see Figs. 7 and 8). For the largest part of the spectrum, the sound pressure level is considerably higher for the refracting atmosphere than for the non-refracting atmosphere. This

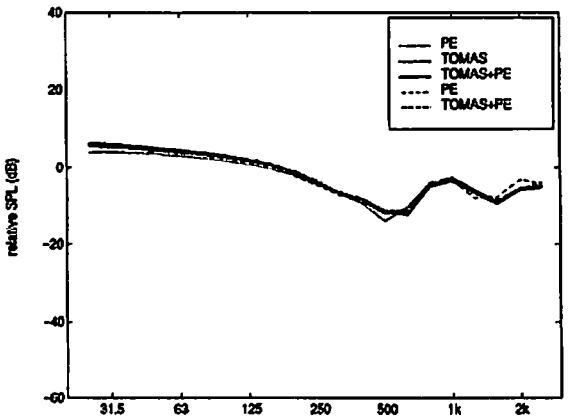

Fig. 6. Results for the situation in Fig. 3 and a source-receiver distance of 20 m. Solid lines are for a non-refracting atmosphere; dashed lines are for the refracting atmosphere.

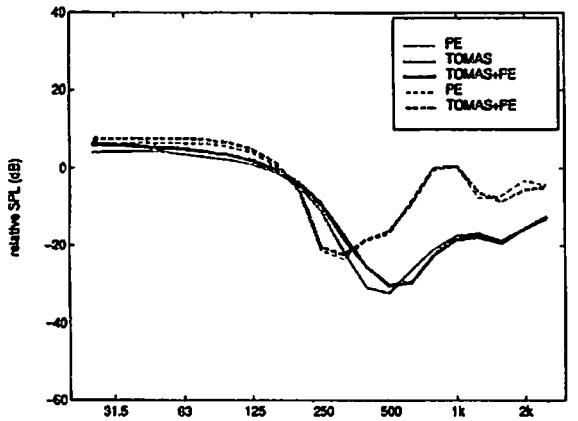

Fig. 7. Same as Fig. 6 but for a source-receiver distance of 200 m.

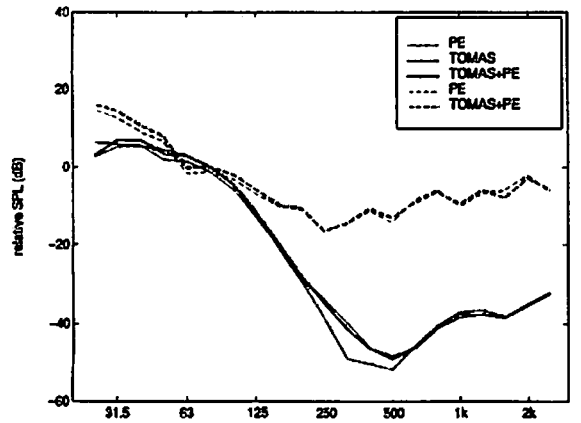

Fig. 8. Same as Fig. 6 but for a source-receiver distance of 2000 m.

indicates that for the combination of this refracting atmosphere and the source-receiver distances of 200 and 2000 m, atmospheric refraction may not be neglected. To model sound propagation over a complex noise barrier in these situations, the coupling of TOMAS (or BEM) to PE is essential to obtain accurate results.

For the situation in Fig. 4, calculations with PE, TOMAS, and the hybrid models TOMAS+PE and BEM+PE are performed. Figure 9 shows that the results of the hybrid models TOMAS+PE and BEM+PE agree with results of the basic models TOMAS and PE. This indicates that the hybrid models TOMAS+PE and BEM+PE are accurate.

For the situation in Fig. 5, calculations with the hybrid model BEM+PE model are performed. To evaluate the effect of the T-top barrier, the results are compared with results for a simple straight barrier with equal height (situation in Fig. 4). Figure 10 shows that for the non-refracting atmosphere as well as for the refracting atmosphere, the sound pressure level is slightly higher for the straight barrier than for the T-top barrier for the largest part of the spectrum.

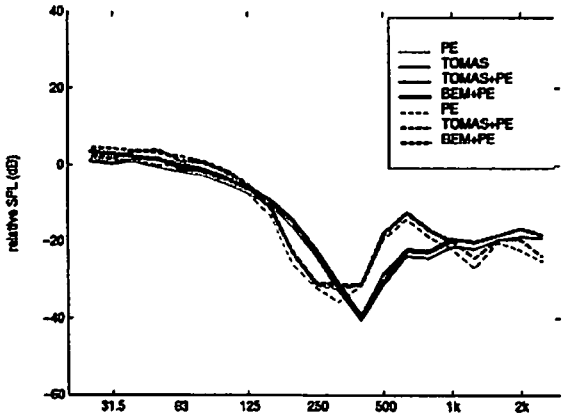

Fig. 9. Results for the situation in Fig. 4. Solid lines are for a non-refracting atmosphere, dashed lines are for the refracting atmosphere.

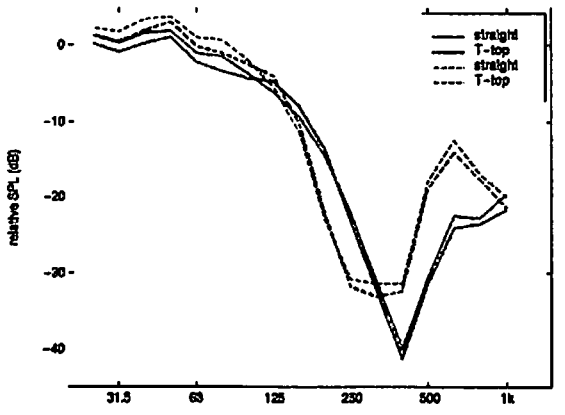

Fig. 10. BEM+PE results for the situation in Fig. 5 for a barrier with a T-top (blue lines) and for the situation in Fig. 4 for a simple straight barrier with equal height (red lines). Solid lines are for a non-refracting atmosphere; dashed lines are for the refracting atmosphere.

Barriers at both sides of the road

Figure 11 presents TOMAS+PE results for a situation with straight reflecting barriers at both sides of the road (bottom graph) compared with a reference situation with a single straight barrier between the road and the receiver (top graph). Shown are iso-dB(A) contours of the A-weighted equivalent sound pressure level as a function of receiver position. The difference between two contours is 5 dB(A). A comparison of the top and bottom graphs in Fig. 11 shows that the presence of the noise screen at the opposite side of the road increases the sound pressure level by approximately 5 dB(A) over the whole range of receiver positions.

The increase of the sound pressure level due to reflections at the noise barrier at the opposite side of the road may be diminished by using tilted instead of straight sound barriers. Figure 12 shows TOMAS+PE results for a situation with tilted reflecting barriers at both sides of the road (middle graph) compared to the same reference situation as in Fig. 11 (top graph). A comparison of the top and middle graphs in Fig. 12 shows that now the presence of the noise screen at the opposite side of the road hardly increases the sound pressure level over the whole range of receiver positions. For distances up to 600 m, the sound pressure level does not increase due to the tilted barrier at the opposite side of the road; for larger distances, the increase in sound pressure level is 1 dB(A).

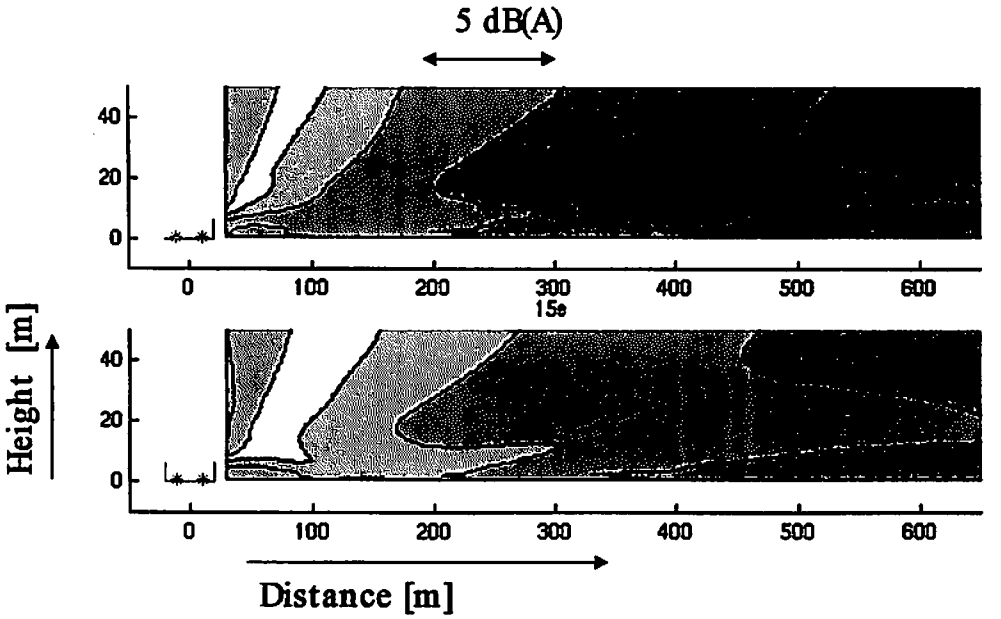

Fig. 11. Iso-dB(A) contours of the A-weighted equivalent sound pressure level as a function of receiver position for a reference situation with a single straight barrier between the road and the receiver (top graph) and a situation with straight reflecting barriers at both sides of the road (bottom graph).

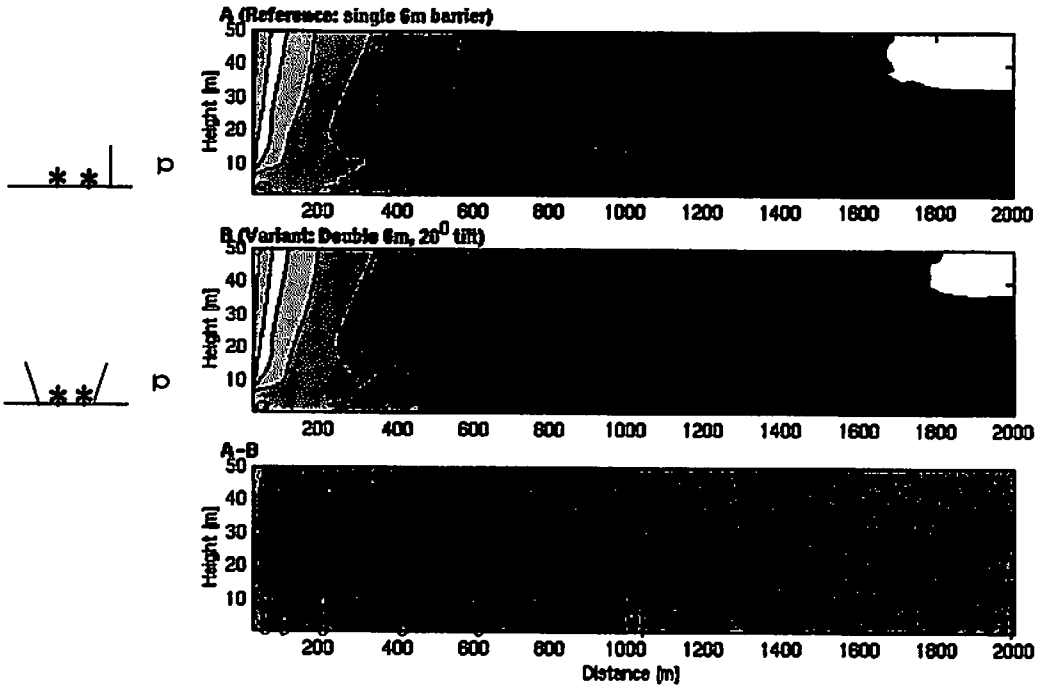

Fig. 12. Iso-dB(A) contours of the A-weighted equivalent sound pressure level as a function of receiver position for a reference situation with a single straight barrier between the road and the receiver (top graph) and a situation with tilted reflecting barriers at both sides of the road (middle graph). The bottom graph shows the difference between the top graph and the middle graph.

Conclusions

For the calculation of the effect of complex noise barriers in a refracting atmosphere, the hybrid models TOMAS+PE or BEM+PE may be used. The results of these hybrid models agree with the results of the basic models TOMAS and PE for a simple straight barrier in a neutral or a refracting atmosphere. This indicates that the hybrid models are accurate. A condition for using the hybrid models is that refraction can be neglected in the region between the source and the noise barrier.

An example of a situation for which the hybrid BEM+PE model is useful is a barrier with a T-top in a refracting atmosphere. The hybrid TOMAS+PE model may be used, for example, to calculate the efficiency of tilted barriers at both sides of a road.

References

[1] J.F. Hamet and M.C. Bérengier, "Acoustical characteristics of porous pavements: a new phenomenological model," Proc. Internoise 93 (Leuven, Belgium) 641-646 (1993).

[2] M.C. Bérengier, M.R. Stinson, G.A. Daigle, and J.F. Hamet, "Porous road pavements: Acoustical charaterization and propagation effects,"J. Acoust. Soc. Am. **101**, 155-162 (1997).

[3] M.E. Delany and E.N. Bazley, "Acoustical properties of fibrous absorbent materials," Appl. Acoust. 3, 105-116 (1970).

Acknowledgements

This work has been carried out by TNO TPD, partly as a part of the Harmonoise project, co-financed by the EC, and partly under contract of the Road and Hydraulic Engineering Division (RWS-DWW), Ministry of Transport, Public Works and Water Management of The Netherlands.

Outdoor sound propagation in complex environments : experimental validation of a PE approach

N. BLAIRON (1), PH. BLANC-BENON (1), M. BÉRENGIER (2) AND D. JUVÉ(1)
(1) Centre Acoustique, LMFA UMR CNRS 5509,
Ecole Centrale de Lyon, 69134 Ecully Cedex, France
(2) Laboratoire Central des Ponts et Chaussées, Centre de Nantes
Route de Bouaye, BP 4129, 44341 Bouguenais Cedex, France

During the last decade, the propagation of sound above plane and heterogeneous grounds has been extensively studied analytically, numerically and/or experimentally. However in complex environments, the modelling of outdoor noise pollution implies to take into account the mixed influence of the terrain topography and the atmospheric conditions. An outdoor site near Saint-Berthevin (France) has been selected to study the influence of meteorological conditions on traffic noise. Acoustical and meteorological measurements are performed simultaneously. This survey provides a database for seasonal noise level variations in complex situations (non-flat terrains, mixed grounds). In this paper we present a method which evaluates the propagation of an acoustic wave above non flat terrain using a PE method and which includes realistic meteoroligical parameters. In our approach the effects of the topography are modelled using appropriate rotated coordinates systems in order to treat the non-flat ground as a succession of flat domains. The PE algorithm is based on a wide-angle parabolic equation in which the influence of the wind velocity and temperature are incorporated. Our model of outdoor sound propagation is validated both with classical numerical benchmark cases (propagation above curved surfaces) and recent experiments done in St-Berthevin.

1 Description of the model

1.1 Wide-Angle Parabolic Equation

The Helmholtz equation in two dimensions is classicaly used to solved outdoor propagation problems. For an acoustical wave $\hat{p}(\mathbf{r},\omega)$ at the pulsation ω, this equation is in the frequency domain:

$$\left[\Delta + k_0^2(1+\epsilon)\right]\hat{p}(\mathbf{r},\omega) = 0 \tag{1.1}$$

where $k_0 = \omega/c_0$, c_0 is a reference celerity, $\epsilon = (c_0/c(\mathbf{r}))^2 - 1$ is the variation of the standard refraction indice and $c(\mathbf{r})$ is the celerity at the point $\mathbf{r}$(x,z). $\mathbf{x}$ and $\mathbf{z}$ are respectively the horizontal and the vertical directions. Equation (1.1) is exact for a homogeneous and motionless medium. It still remains exact when only the celerity $c(\mathbf{r})$ varies. For numerical simulations of outdoor sound propagation, parabolic equations have been derived using the approximation of the effective sound speed. In this conventional approach the real moving atmosphere is replaced by a hypothetical motionless medium with the effective sound speed $c_{eff} = c + v_x$, where v_x is the wind velocity component along the direction of propagation between the source and the receiver. When the source and the receiver are closed to the ground, the preferred direction of sound propagation is nearly horizontal, and standard parabolic equation can be used to predict sound pressure levels.

The previous wave equation (Eq.1.1) was reduced to a wide-angle parabolic equation by Thomson et Chapman [1]. The first step is to write the equation for forward propagation:

$$\left[\frac{\partial}{\partial x} - ik_0\sqrt{Q}\right]\hat{p}(\mathbf{r},\omega) = 0 \tag{1.2}$$

where $Q = 1 + \epsilon + \frac{1}{k_0^2}\frac{\partial^2}{\partial z^2}$. From here, the square of the propagation operator Q is simplified using a Padé approximation to yield (Collins [2]):

$$\sqrt{Q} = \frac{1 + p\mathcal{L}}{1 + q\mathcal{L}}$$

where $\mathcal{L} = Q - 1$, $p = 3/4$ and $q = 1/4$. This procedure leads to the following scheme:

$$[1 + q\mathcal{L}]\frac{\partial\phi(\mathbf{r})}{\partial x} = ik_0[(p-q)\mathcal{L}]\phi(\mathbf{r}) \tag{1.3}$$

where ϕ is the envelope of the pressure field $\hat{p}(\mathbf{r})$: $\phi(\mathbf{r}) = \hat{p}(\mathbf{r})\exp(-ik_0x)$. To get the numerical scheme, we use a second-order finite difference method. This finite difference method allows to use a impedance boundary condition. We use a gaussian starting field.

1.2 Non flat ground

We are interested in modelling the acoustic propagation above a non flat ground. Range-dependant problems have first been solved with the PE by approximating the environment as a sequence of range-independant regions (see Jensen and Kuperman [3]). In the case of underwater acoustics, a sloping ocean bottom becomes a sequence of stair steps. For weakly range-dependent problems, this approach gives rise to solutions that are accurate in many cases. For problems involving sloping ocean bottom, however, it gives rise to an error of 2 dB in a benchmark test in which the angle of the slope is inferior to 3 degrees (benchmark test 3 in Jensen and Ferla [4]).

The stair steps approximation at the ocean bottom can be avoided by rotating the coordinates (Collins [5]). The rotated PE solution is as accurate as the two-way coupled mode solution (Yevick et Thomson [6]).

We want to use the rotated PE in the case of a variable slope. So the ground has to be discretized as a succession of flat domains. In the case of two domains (see figure 1), the PE is computed until the line l1.

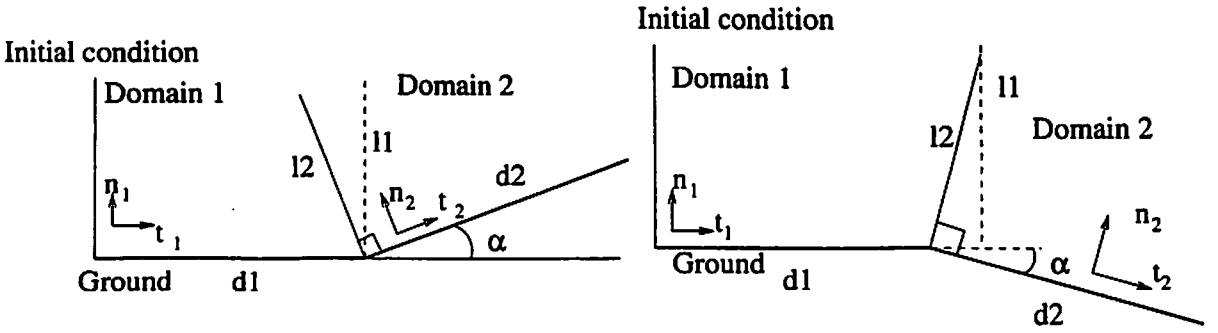

Figure 1: Schematic representation of the rotation of the coordinates systems in the upslope case (left) and the downslope case (right).

The values of the pressure in the first domain are then used to calculate an initial solution for the second domain along the line l2 (figure 1). If we call $p_1(t_1, n_1) = \phi_1(t_1, n_1)e^{ik_0 t_1}$ and $p_2(t_2, n_2) = \phi_2(t_2, n_2)e^{ik_0 t_2}$ the pressure in the domains 1 and 2, the continuity of the pressure along l2 is written as :

$$\phi_2(0, n_2) = \phi_1(t_1|_{l2}, n_1|_{l2})e^{ik_0 t_1|_{l2}} \qquad (1.4)$$

where $t_1|_{l2} = d1 - n_2 \sin\alpha$ and $n_1|_{l2} = n_2 \cos\alpha$. In the case of downslope propagation, we notice that the calculation in the first domain must be done slightly beyond the slope discontinuity so that the rotated PE for the second domain can be initialized.

1.3 Validation of the model for non flat ground

The wide-angle parabolic equation (WAPE Eq. 1.3) is included in the rotated PE method. In order to validate the method, we consider the propagation above a wedge. A reference solution can be established analytically as the sum of a geometrical field and a diffracted field (Pierce [7]). The first benchmark case is the propagation above the wedge drawned on the left in figure 1, with $d1 = 60$ meters and $\alpha = 20$ degrees. In figure 2, we draw on the left the pressure amplitude calculated analytically and on the right the pressure amplitude calculated by the rotated PE method. The pressure amplitude is relative to a Dirac source located at 2 meters above the ground. The acoustic frequency is 340 Hz. The qualitative agreement between the solution is good. The patterns of interferencies above the slope are well predicted by the rotated PE.

In order to have a more quantitative validation of the rotated PE method, we evaluate the pressure amplitude on the same benchmark case on a line perpendicular to the slope at 40 meters of the bottom discontinuity. We consider the case of a positive slope and of a negative slope (see figure 1). We chose d1=60 metres, d2=40 meters and $\alpha = 20$ degrees. The unit point source is located at 2 meters above the ground. The acoustic frequency is 340 Hz. On figure 3, we compare two analytical solutions and the PE solution. The first analytical solution is the geometrical

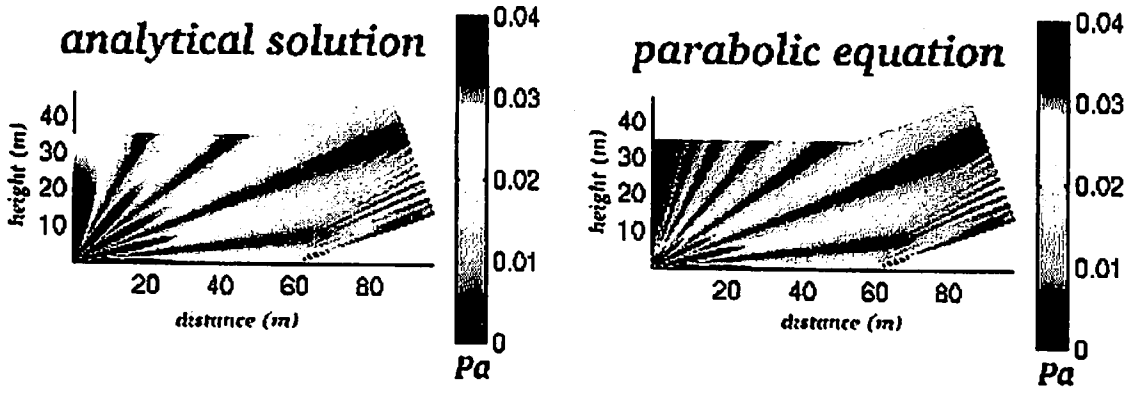

Figure 2: Comparison of the non flat ground model (right) with a analytical solution (left). Parameters: $h_s = 2$ meters; $d1 = 60$ meters; $d2 = 40$ meters.

part of the pressure ; the second is the total analytical pressure field (geometrical plus diffracted). The agreement between the PE solution and the second analytical solution (geometrical plus diffracted field) is excellent in both cases (upslope and downslope). The difference between the two analytical solutions is due to diffracted part of the pressure field. We conclude that the rotated PE method calculates accurately the diffracted part of the field above the wedge.

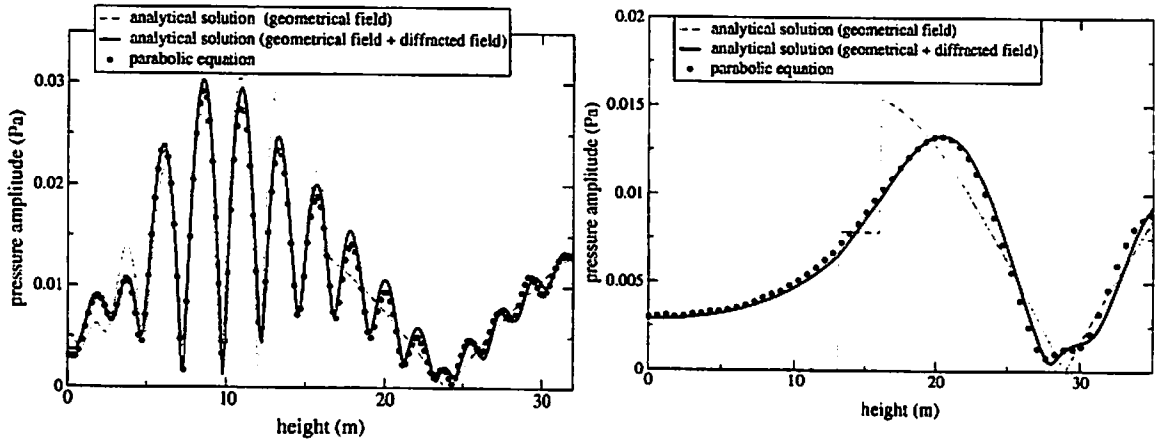

Figure 3: Analytical validation of the model for non flat ground in the cases of a flat ground followed by upslope (left) and downslope (right). Parameters: $h_s = 2$ meters; $d1 = 60$ meters; $d2 = 40$ meters.

Others numerical comparisons in the cases of the wedge and curved surfaces have been done (Blairon [8]) : the rotated PE method gives accurate results until a angle of 40 degrees and for frequencies between 100 and 3200 Hz.

2 Outdoor measurements

Outdoor meteorological and acoustical measurements were carried out in Saint-Berthevin (France) in october 2001 (Blairon [8]). The site has complex features: it is

non flat and the ground impedance is heterogeneous. Meteorological measurements of wind and temperature at several heights during the acoustical measurements allow us to model the mean profiles of wind and temperature above the ground.

On the figure 4 we can see a photo of the terrain above which were carried out the experiments. For the calculations, the ground is modelled as a succession of 3 flat domains (see figure 4) : the first is 25 meters long and has a slope of 10.21 degrees, the second is 75 meters long and has a slope of 17.42 degrees and the third is 25 meters long and has a slope of 8.61 degrees. The relative angle between the first and the second domain is then of 7.21 degrees and of 8.81 degrees between the second and the third domain. Five microphones were used to give measures between 25 and 100 meters of the source (they are called M1, M2, M3, M4 and M5 on the figure 4). The reference microphone was located at a distance of 10 meters from the source (M_{ref}).

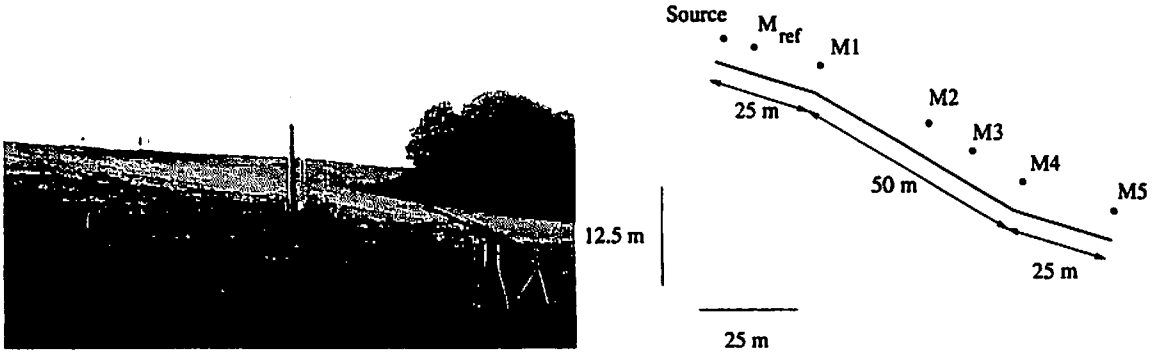

Figure 4: Photography of the site with the source, the microphones and the meteorological tower (left) and representation of the ground as 3 flat domains for the calculations (right).

2.1 Impedance measurements

The numerical scheme can include an impedance boundary condition. The value of the impedance Z ($Nm^{-3}s$) is defined by a measurable quantity, the flow resistivity σ ($Nm^{-4}s$), through an impedance model. Models using more than one parameters have been proposed by Attenborough [9]. We use the classical Delany and Bazley model [10] because the parameter σ can be determined experimentally. This models gives Z as a function of the frequency f:

$$Z = \rho_0 c_0 \left[1 + 0.0571 \left(\frac{\rho_0 f}{\sigma} \right)^{-0.754} + i0.087 \left(\frac{\rho_0 f}{\sigma} \right)^{-0.732} \right] \tag{2.1}$$

where c_0 is a reference celerity speed ($m.s^{-1}$) and ρ_0 is the air density ($kg.m^{-3}$).

We measured the ground impedance between the source and the microphone M5. The method of ground characterization uses short range attenuation measurements.

These measurements are used to fit the result of a propagation model including the one-parameter described by (Eq. 2.1). The results of the measurements are :

- around the source: $\sigma = 600.10^3 N.m^{-4}s$
- around M1: $\sigma = 90.10^3 N.m^{-4}s$
- around M2: $\sigma = 160.10^3 N.m^{-4}s$
- around M4: $\sigma = 200.10^3 N.m^{-4}s$

2.2 Meteorological measurements

The first hundreds meters above the ground are characterized by the presence of an atmospheric boundary layer where mean gradients of wind and temperature and turbulent fluctuations exist. When the topography is smooth enough, the leading wind component is the horizontal component. It can be modelled with a logarithmical profile :

$$u(z) = a \ln(z/z_0) \; for \; z > z_0 \tag{2.2}$$

where z_0 is the rugosity of the ground (0.1 meter for a field).

With the bidimensional model, only the wind component in the direction of propagation is taken into account. If we call θ the angle between the horizontal wind direction and the sound propagation direction, the quantity $U(z)\cos\theta$ must be introduced in the effective celerity c_{eff}. The effective celerity used in the propagation equation (1.2) is defined with the velocity and the temperature field as:

$$c_{eff}(z) = c(0)\sqrt{\frac{T(z)+273.15}{273.15}} + u(z)\cos(\theta)$$

We use a meteorological tower to evaluate the meteorological paramaters used in the calculation of acoustical propagation. The tower is located on the slope, far from the measurement line for the acoustical propagation not to be perturbed. The tower is equiped with thermometers and anemometers to measure the temperature, the direction and intensity of wind. These thermometers and anemometers are located at 1, 3 and 10 meters high. The data are recorded every minutes. We give the fluctuations of the wind velocity (see figure 5), of the wind direction (see figure 6) and of the temperature (see figure 7) recorded during the acoustic measurements.

The meteorological measurements allow us to know the meteorological paramaters for the sound propagation model. During the acoustic measures 5, 6 and 7, the wind was moderate (see figure 5). The wind parameter a (see Eq. 2.2) was equal to 0.5 for measure 5 and 0.65 for measures 6 and 7. During the measure 10, the wind is very low ($1\ m.s^{-1}$). The reference for the wind direction is the orientation of the line of propagation. This one was measured and is equal to 210 degrees. The measures 5, 6 and 7 were done with downwind condition (0-20 degrees). The measure 10 was done with crosswind condition (110 degrees). The temperature measurements show very low temperature gradients ; we use then in the model only the mean value. The whole meteorological parameters are summarized in the following table 1.

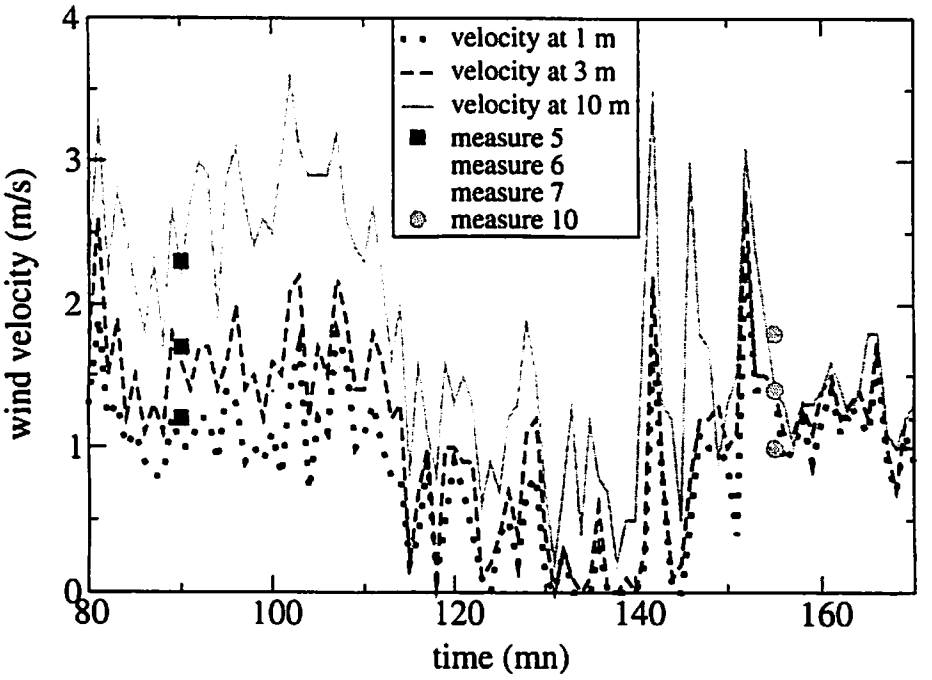

Figure 5: Measurement of the fluctuations of the velocity field at 3 heights (1, 3 and 10 meters)

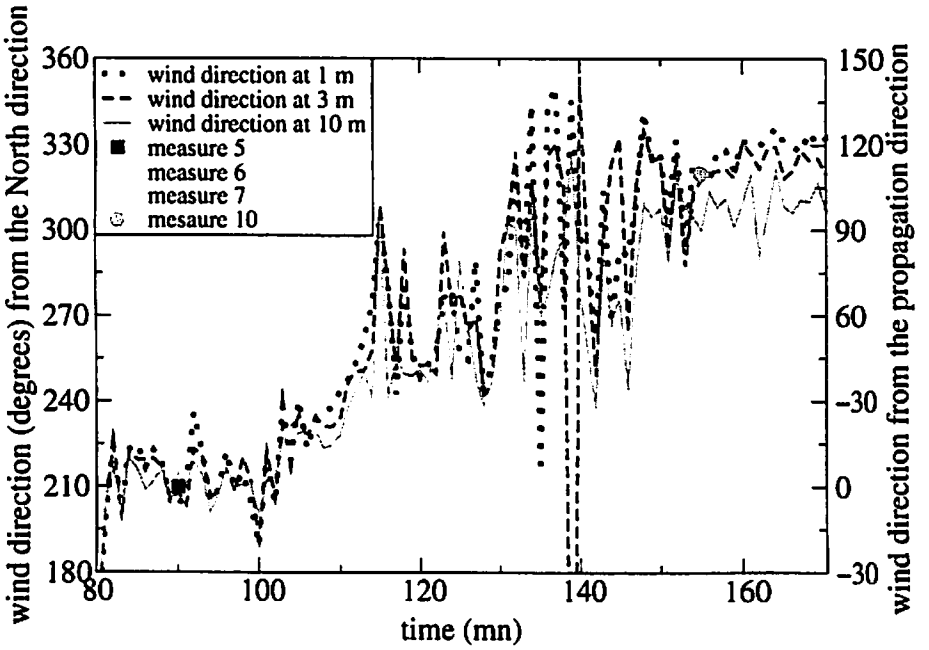

Figure 6: Measurement of the fluctuations of the velocity field direction at 3 heights (1, 3 and 10 meters)

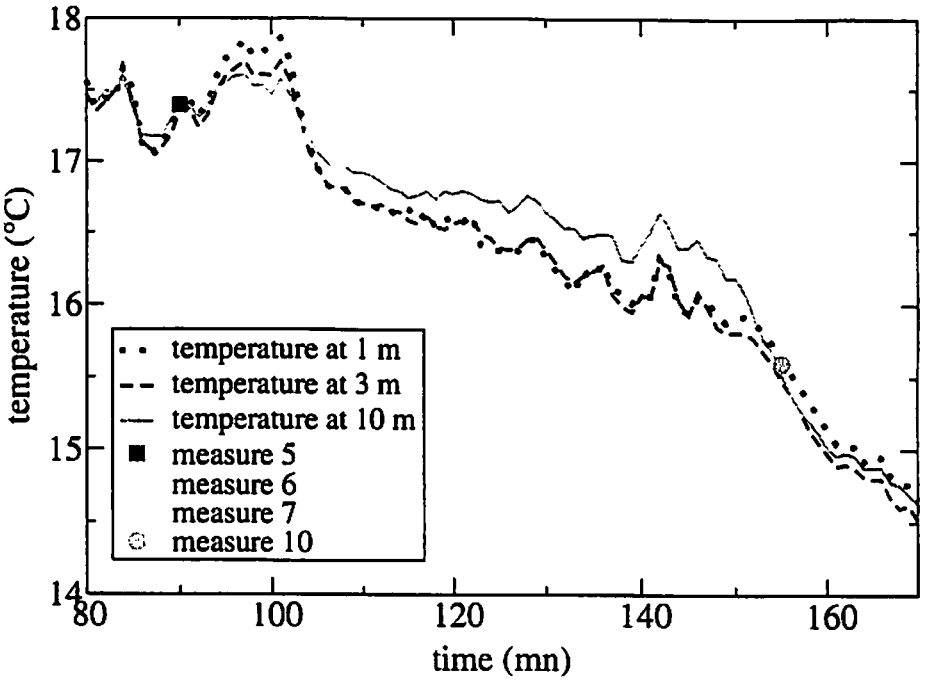

Figure 7: Measurement of the fluctuations of the temperature field at 3 heights (1, 3 and 10 meters)

measure	wind parameter a	wind direction θ	temp. T	propagation condition
5	0.5	0 degree	290.5 K	downwind/moderate wind
6 and 7	0.65	20 degrees	290 K	downwind/moderate wind
10	0.4	110 degrees	288.5 K	crosswind/low wind

Table 1: Meteorological parameters for the model of sound propagation.

2.3 Acoustic measurements

Acoustic measurements are done at the positions defined on the figure 4. We use a data recorder with four channels. The source is impulsive and omnidirectional. For a single measure, the signal is averaged over 10 snapshots. The relative sound pressure level is the difference of the spectrum at the microphone M1, M2, M3, M4 or M5 and the spectrum at the reference microphone M_{ref}.

We draw on figure 8 the relative pressure levels for measures 6, 7 and 10. The meteorological conditions are very closed for the measures 6 and 7. The wind is moderate and blows in the direction of the propagation. The relative pressure levels are very closed for measures 6 and 7. This shows the good reproducibility of the experimental procedure. The meteorological conditions for the measure 10 are different : the wind is very low and perpendicular to the direction of propagation. The acoustic spectra is different from the spectra of measure 6 and 7. This shows the influence of the meteorological parameters on the acoustic propagation.

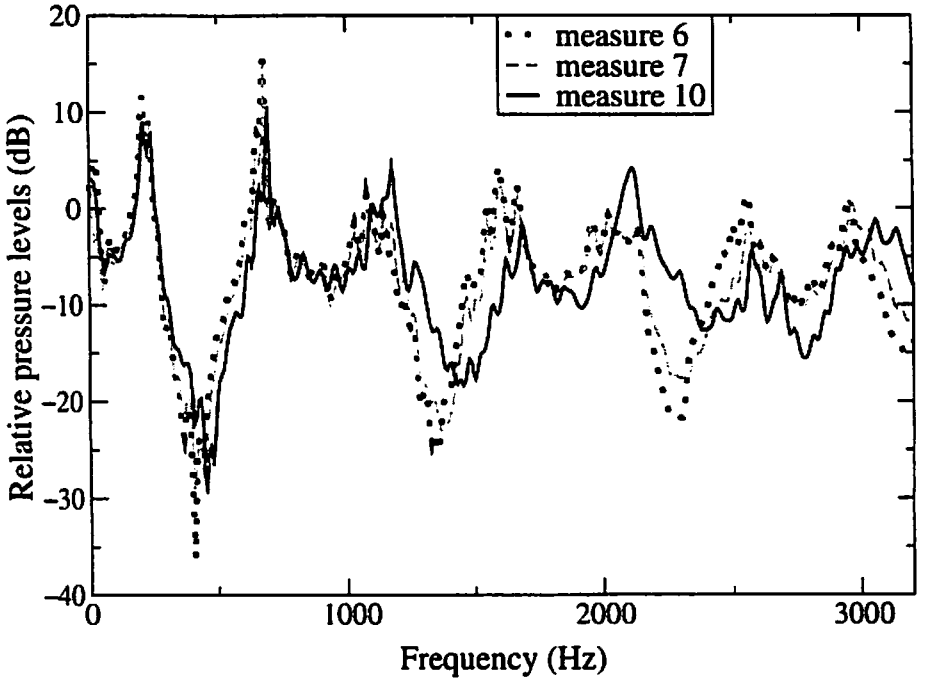

Figure 8: Three measures of the relative sound pressure level. The distance between the source and the receiver is 25 meters and h_s=h_m=2 m.

2.4 Comparison measure-model

We want now to compare the results of the measurements and those of the model. We present four series of measurements : they are called measures 5, 6 and 7 and 10. We note that the measures 6 and 7 were done for the same geometrical and meteorological conditions.

The measure 5 was done with microphones M1 (25 m), M2 (50 m) and M4 (75 m) (see figure 4). The geometrical parameters are h_s = 0.6 and h_m = 2 meters.

The wind was moderate and the propagation was downwind ; the meteorological parameters are summarized in table 1. In the following figures (9, 10 and 11), we give the results of the measurements and those of the model. We use the model with a wind profile defined by the measured parameter a and without wind profile.

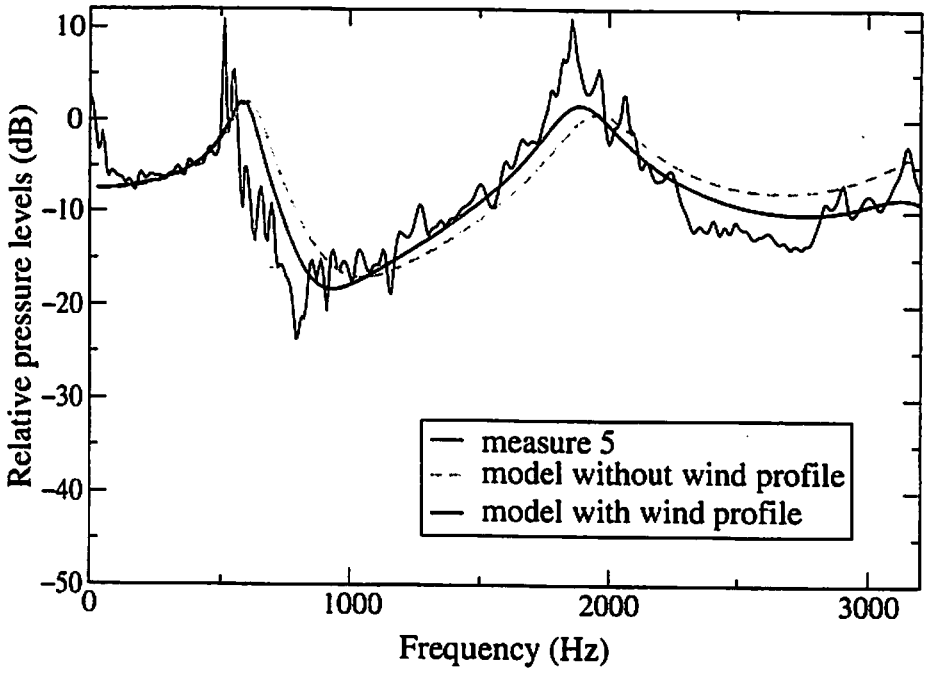

Figure 9: Experimental validation of the model for a non flat ground. Parameters: $h_s = 0.6$ meters; $h_m = 2$ meters; Microphone 1; $D = 25$ meters. Measure 5.

The comparison of the experimental results and those of the model on figures 9, 10 and 11 shows that the model gives accurate relative pressure levels. Besides, the comparison of the model with and without wind profile show the influence of the meteorological parameters. For a distance of 75 meters and above 2000 Hz (figure 11), the relative sound pressure level is 15 dB higher with the wind profile.

We present now the results of the measures 6 and 7 and those of the model (figures 12, 13 and 14). The sound pressure level was recorded at microphones M1 (25 m), M2 (50 m) and M4 (75 m) (see figure 4). The wind was moderate and the propagation was downwind; the meteorological parameters are summarized in table 1.

The meteorological parameters for the measures 6 and 7 and the measure 5 were very closed. The difference between the measures 6 and 7 and the measure 5 is the height of the source; the mesures and the model show that there are more interferencies with a source higher above the the ground. The comparison between the results of the measures 6 and 7 and those of the model (figures 12, 13 and 14) shows that the model is accurate. The results of the model with and without wind profile show the influence of the meteorological parameters on the sound level: at 75 meters, the sound level is 10 dB higher with the wind profile.

The meteorological parameters of the measure 10 are different from those of the

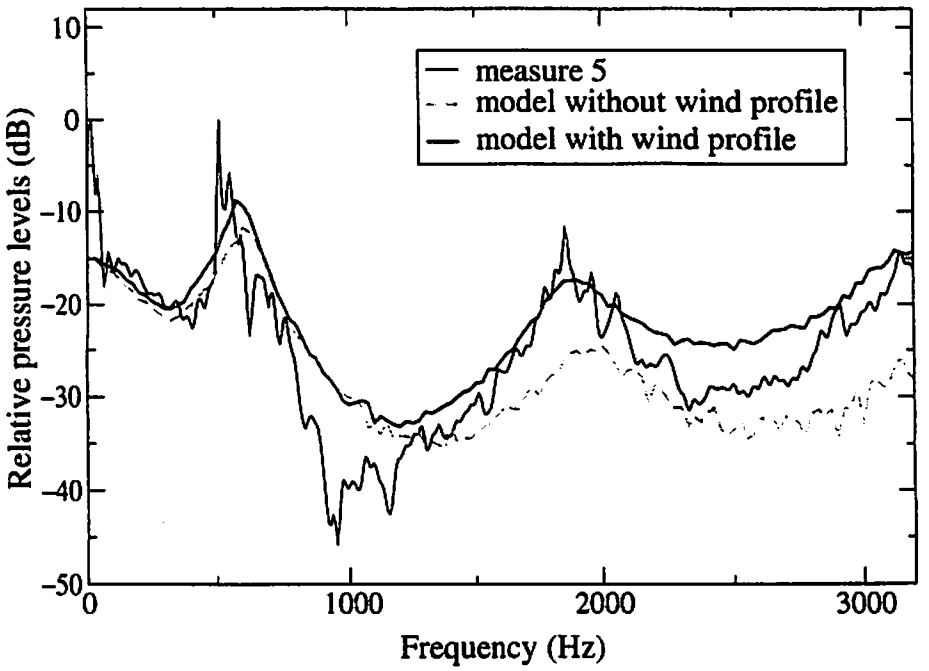

Figure 10: Experimental validation of the model for a non flat ground. Parameters: $h_s = 0.6$ meters; $h_m = 2$ meters; Microphone 2; $D = 50$ meters. Measure 5.

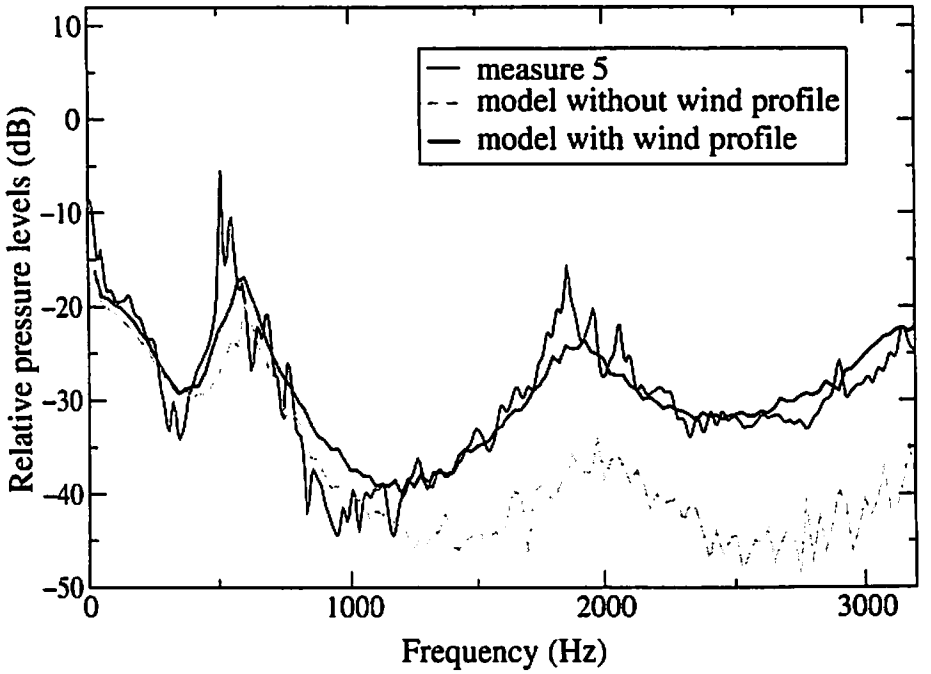

Figure 11: Experimental validation of the model for a non flat ground. Parameters: $h_s = 0.6$ meters; $h_m = 2$ meters; Microphone 4; $D = 75$ meters. Measure 5.

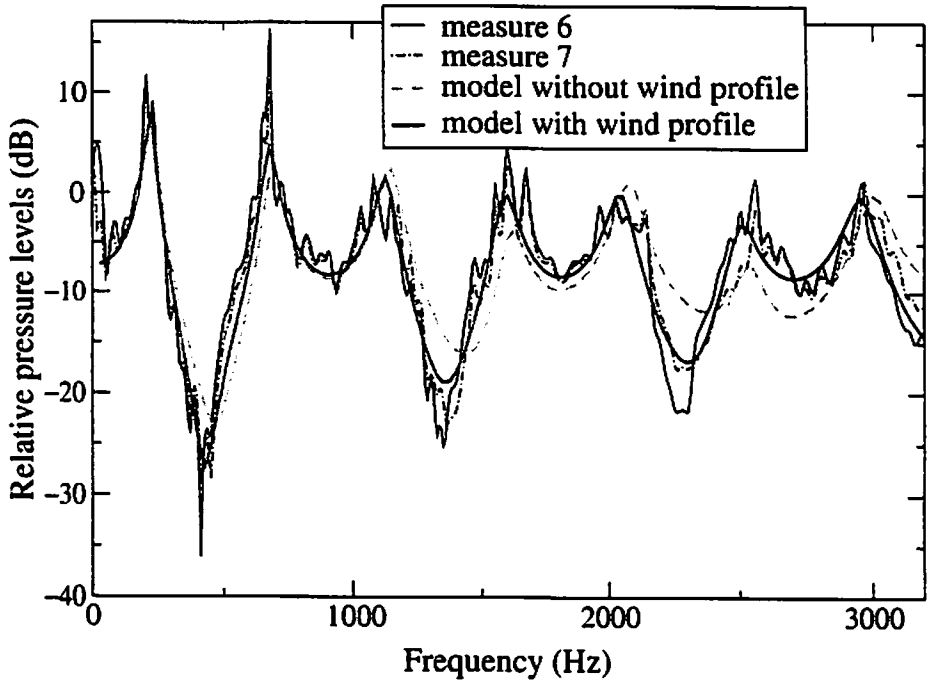

Figure 12: Experimental validation of the model for a non flat ground. Parameters: $h_s = 2$ meters; $h_m = 2$ meters; Microphone 1; $D = 25$ meters. Measures 6 and 7.

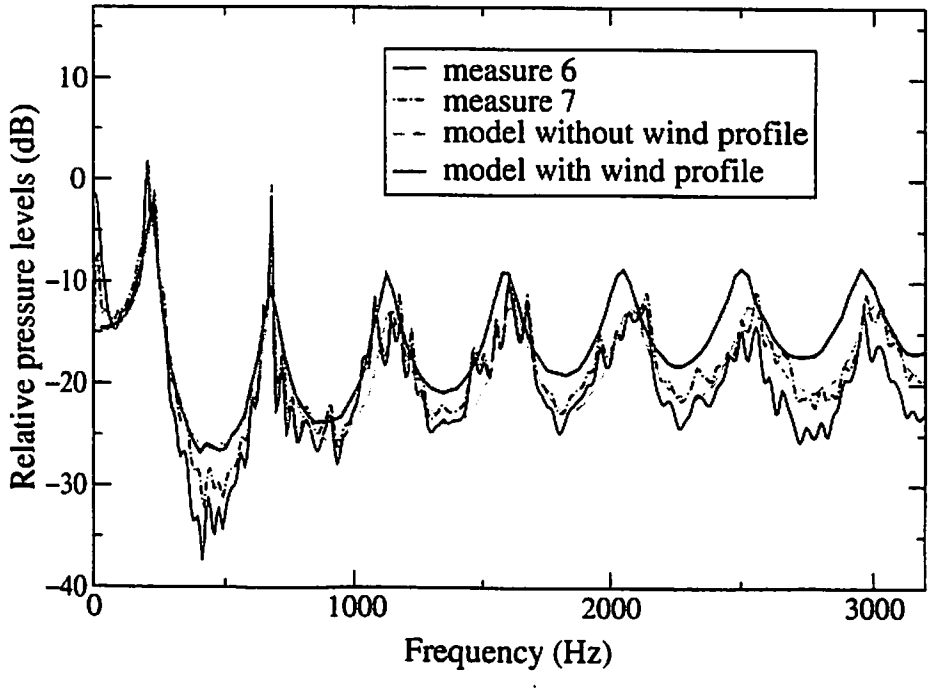

Figure 13: Experimental validation of the model for a non flat ground. Parameters: $h_s = 2$ meters; $h_m = 2$ meters; Microphone 2; $D = 50$ meters. Measures 6 and 7.

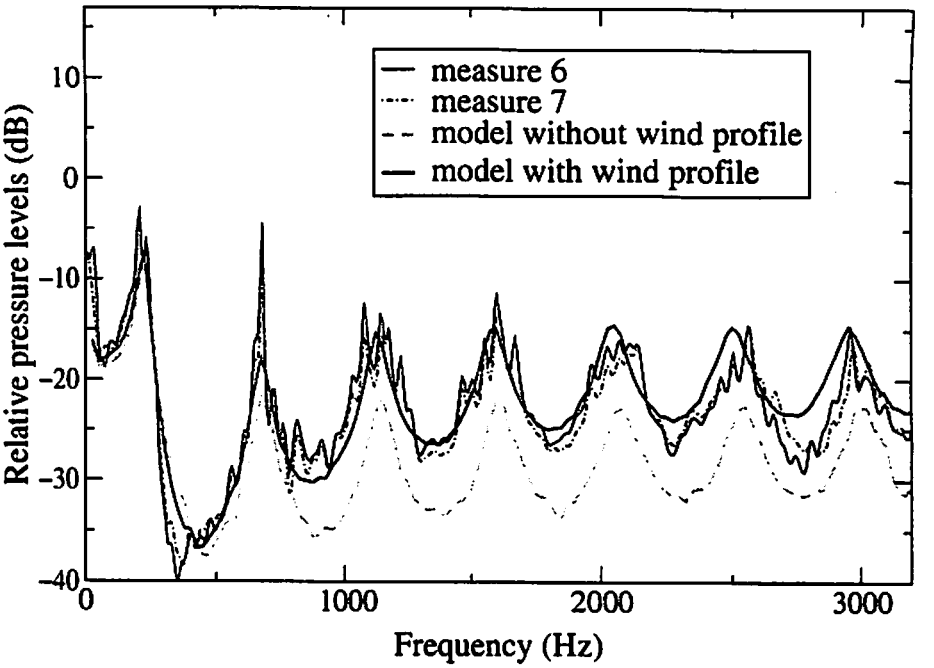

Figure 14: Experimental validation of the model for a non flat ground. Parameters: $h_s = 2$ meters; $h_m = 2$ meters; Microphone 4; $D = 75$ meters. Measures 6 and 7.

measures 6 and 7. The wind is very low (1 $m.s^{-1}$) and blows perpendicularly to the direction of propagation. The wind in the direction of propagation is then closed to zero and the model is used without wind profile. The geometrical parameters are $h_s = h_m = 2$ meters and the sound pressure level was recorded at the microphone M1 (25 m). For comparison, we give the sound pressure level at the same distance for the measure 6. And we give the results of the model for the parameters of the measure 6 (downwind).

We have already described the differences of the results of the measures 6 and 10 (figure 8). The cause of these differences is the different wind profile. We use the model for the conditions of the measure 10 (no wind profile in the direction of propagation). The result must be compare to the results of measure 10 : we see that the model is accurate. We use the model with the conditions of the measure 6 (downwind) : the comparison with the results of the measure 6 is good. So we can say that the model reacts satisfactorily with the meteorological parameters.

3 Conclusion

We have developped a model for outdoor sound propagation. The model is based on a wide-angle parabolic equation which can include the profiles of wind and temperature through the definition of an effective sound celerity. The ground impedance can be include in the model as a boundary condition. The model was developped to handle sound propagation over a non flat ground. This specification was fulfilled by using a rotated PE method. The model has been validated with analytical results for the wedge case. Outdoor measurements of acoustic attenuation and meteorological

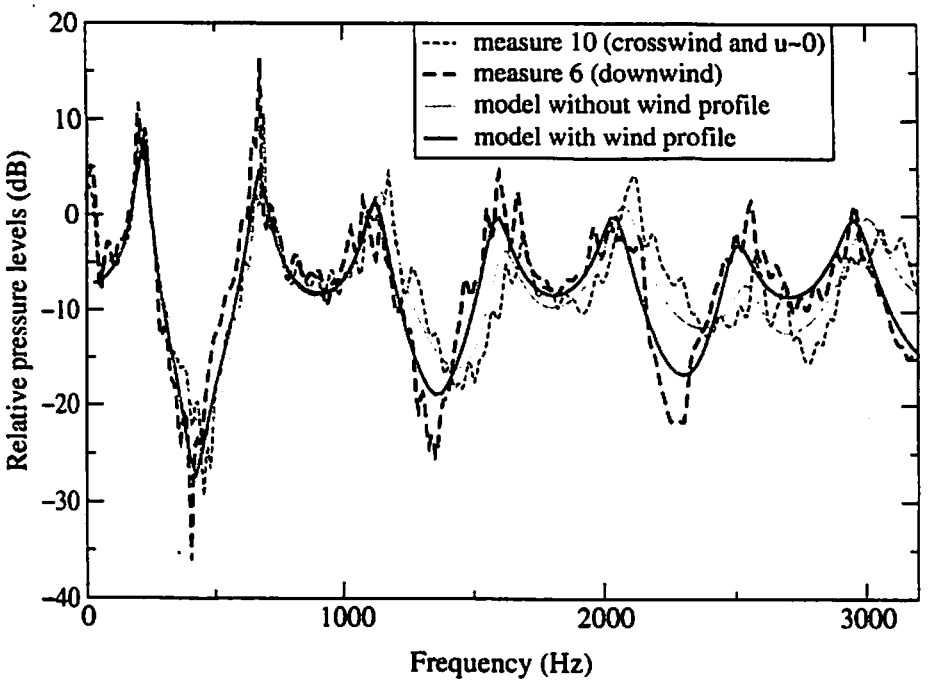

Figure 15: Experimental validation of the model for a non flat ground. Parameters: $h_s = 2$ meters; $h_m = 2$ meters; Microphone 1; $D = 25$ meters. Measure 10 (cross and lateral wind) and measure 6 (downwind).

parameters were performed simulnaneously on a complex site (mixed terrain, non flat ground). The reproducibility of the measurements was verified and measurements under different meteorological conditions have been done. Comparisons between the measurements and the model with and without a moving atmosphere are very good.

References

[1] D. J. Thomson and N. R. Chapman. A wide-angle split-step algorithm for the parabolic equation. *J. Acoust. Soc. Am.*, 74(6):1848–1854, 1983.

[2] M. D. Collins. A split-step padé solution for the parabolic equation method. *J. Acoust. Soc. Am.*, 93:1736–1742, 1993.

[3] F. B. Jensen and W. A. Kuperman. Sound propagation in a wedge shaped-ocean with a penetrable bottom. *J. Acoust. Soc. Am.*, 67:1564–1566, 1980.

[4] F. B. Jensen and C. M. Ferla. Numerical solutions of range-dependant benchmark problems in ocean acoustics. *J. Acoust. Soc. Am.*, 87(4):1499–1510, 1990.

[5] M. D. Collins. The rotated parabolic equation and the sloping ocean bottoms. *J. Acoust. Soc. Am.*, 87(3):1035–1037, 1990.

[6] D. Yevick and D. J. Thomson. Nonlocal boundary conditions for finite-difference parabolic equation solvers. *J. Acoust. Soc. Am.*, 106(1):143–150, 1999.

[7] A. D. Pierce. *Acoustics : An Introduction to Its Physical Principles and Applications.* Acoustical Society of America, 1981.

[8] N. Blairon. *Effets de la topographie sur la propagation des ondes acoustiques dans l'atmosphère : modélisation avec l'équation parabolique et validation sur un site extérieur.* PhD thesis, Ecole Centrale de Lyon, France, 2002.

[9] H. M. Hess, K. Attenborough, and N. W. Heap. Ground characterization by short-range propagation measurements. *J. Acoust. Soc. Am.*, 87(5):1975–1986, 1990.

[10] M. E. Delany and E. N. Bazley. Acoustical properties of fibral materials. *Applied Acoustics*, 3:105–116, 1970.

10th Symposium on Long Range Sound Propagation
Grenoble, 12-13 September 2002

A HYBRID GFPE-BEM APPROACH FOR COMPLEX OUTDOOR SOUND PROPAGATION

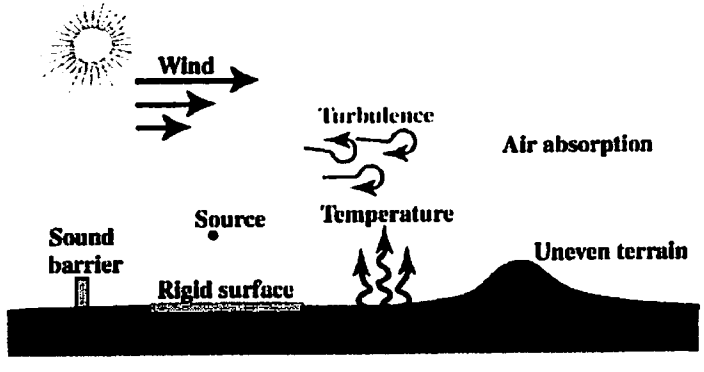

Eric PREMAT, Jérôme DEFRANCE
Maud PRIOUR, François ABALLEA

CSTB

Content

- Introduction
- Theoretical approach
- Some results
- Scale model measurements
- Conclusion

Introduction

Environmental Noise

- **Traffic noise regulations** **==> sound prediction at long ranges**
  ==> meteorological effects
- **France : NMPB**
- **EC : European Directive** **==> Harmonoise european project**

Introduction

Environmental Noise

Objectives of the European Directive

(Harmonoise project)

a) Determination of noise exposure to environmental noise

b) Inform the public on noise exposure and its effects

c) Adoption of action plans

- **to reduce noise where necessary (health issue)**
- **to preserve environmental noise quality where it is good**

Introduction

Complex outdoor sound propagation

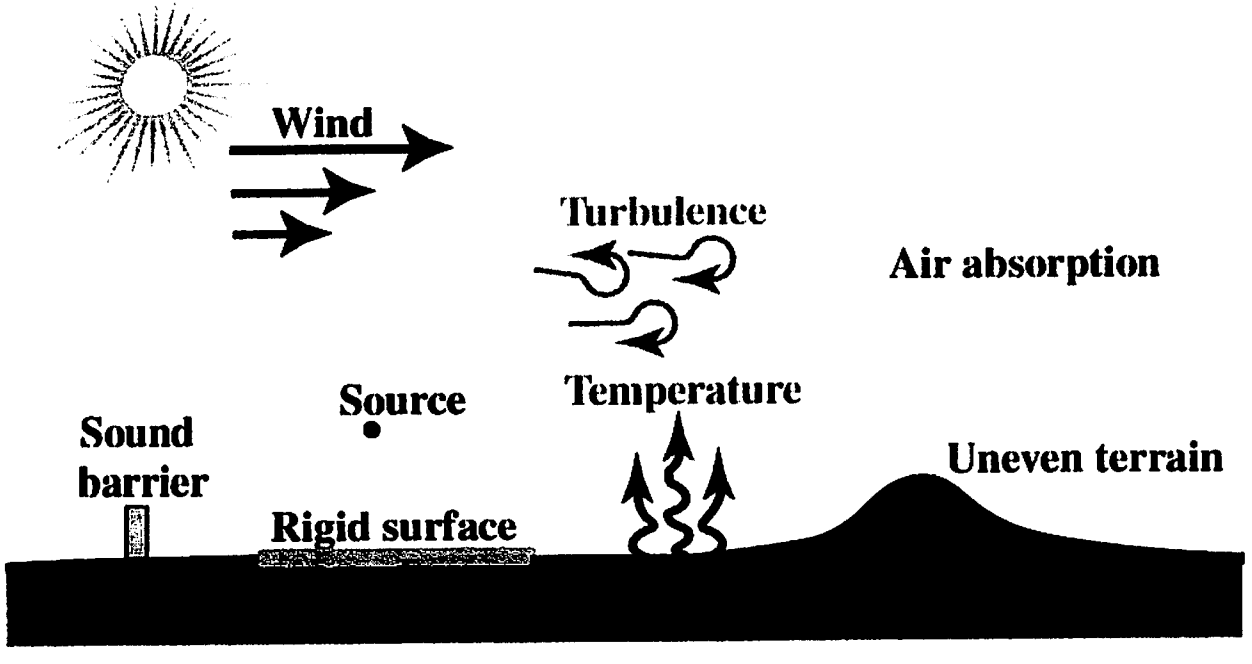

Need for models for sound propagation above complex boundaries with meteo

Introduction

Complex outdoor sound propagation

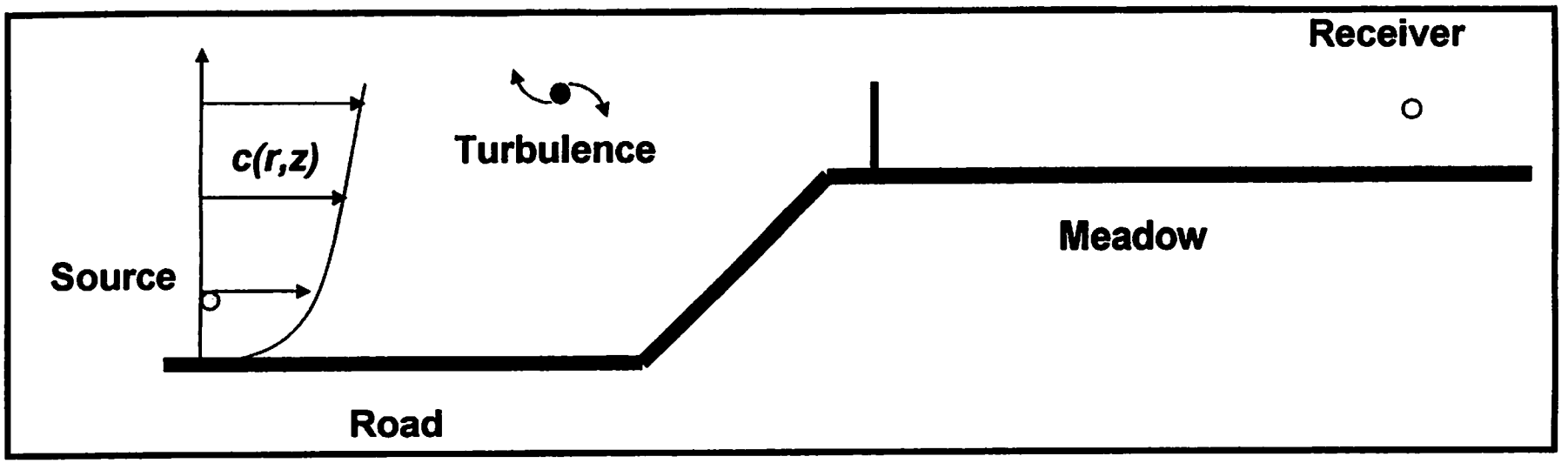

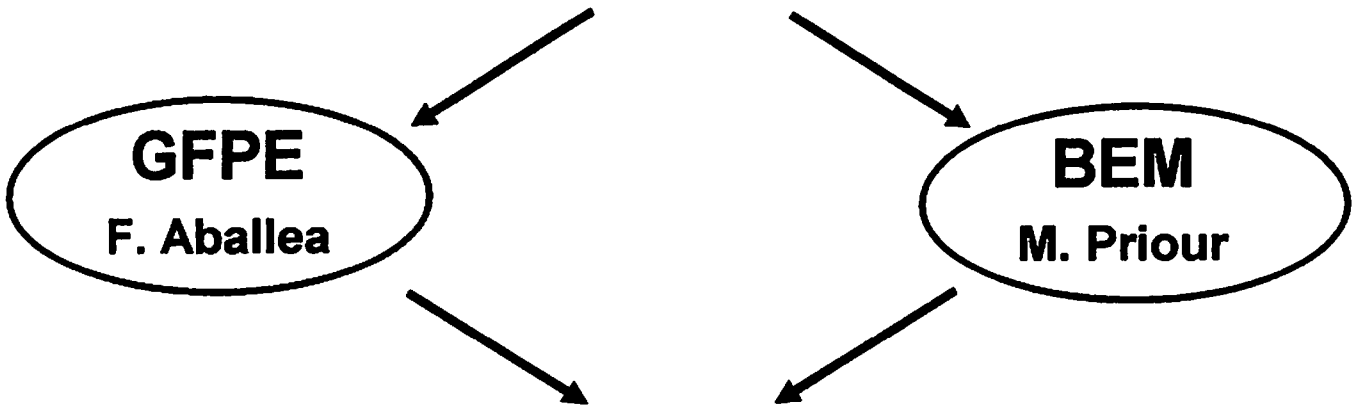

Hybrid GFPE - BEM approach

Theoretical approach

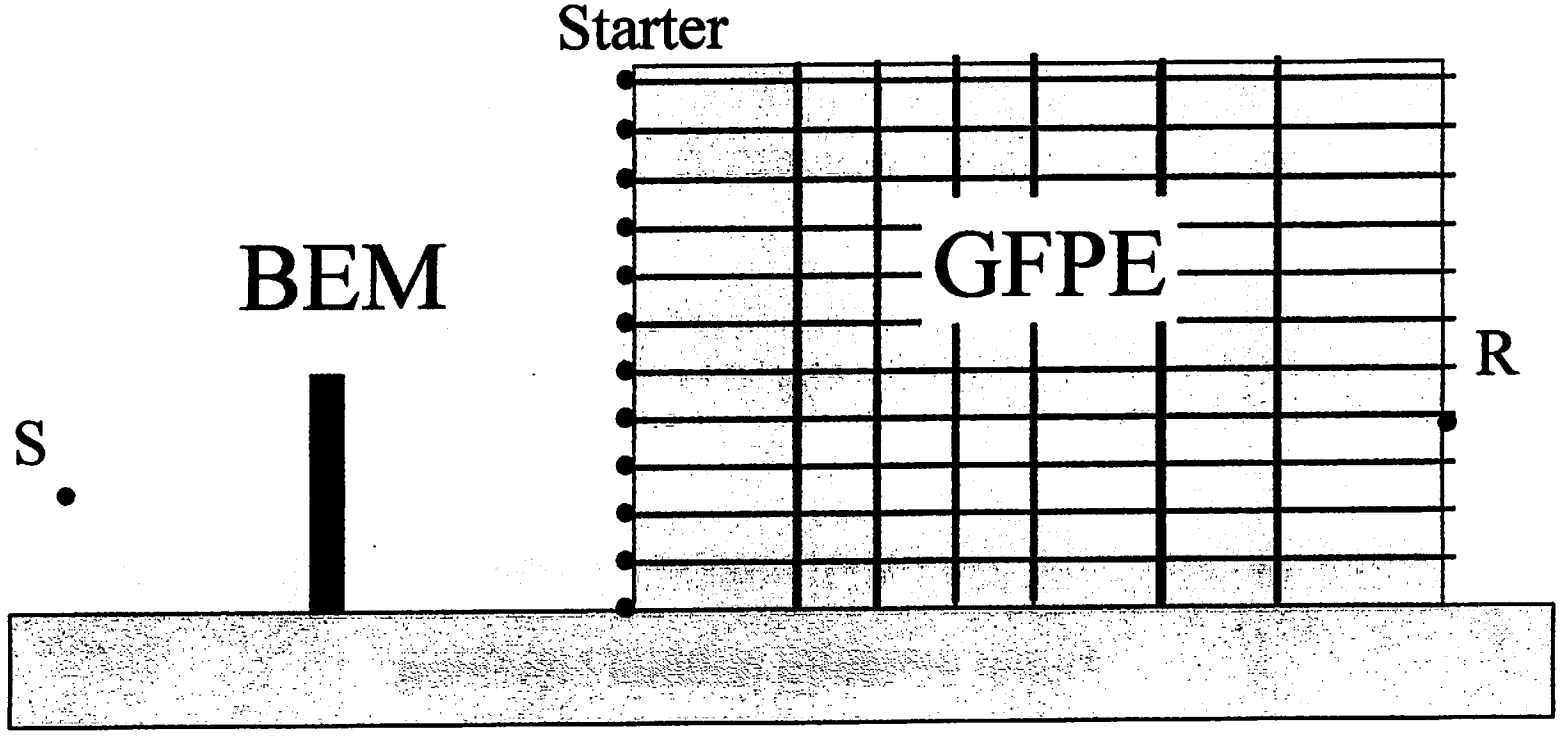

Sketch of the coupling BEM/GFPE

Theoretical approach

The BEM calculation for the starter

Boundary Integral Equation theory

Direct formulation : Helmholtz integral equation (unknown functions : pressure and velocity)

$$p(M) = p_0(M) + \int_S \left[p(M) \frac{\partial G}{\partial n_S}(S,M) - G(S,M) \frac{\partial p}{\partial n_S}(M) \right] dS, M \in \Omega$$

Use of a variational approach for solving the BIE

⇩

MICADO-BEM code

Theoretical approach

The GFPE propagation code

incident wave

$$\Psi(r+\Delta r,z)=\left\{\frac{1}{2\pi}\left[\int_{-\infty}^{+\infty}\left(\tilde{\Psi}(r,k_z)+R(k_z)\tilde{\Psi}(r,-k_z)\right)\times e^{i\Delta r\left(\sqrt{k_0^2-k_z^2}-k_0\right)}e^{ik_z z}dk_z\right]\right\}$$

reflected wave

$$+\left\{2i\beta\times\tilde{\Psi}(r,\beta)\times e^{i\Delta r\left(\sqrt{k_0^2-\beta^2}-k_0\right)}e^{-i\beta z}\right\}e^{i\frac{\Delta r\delta k^2(z)}{2k_r}}$$

surface wave

$$\beta=\frac{k_0}{Z_g}\qquad \tilde{\Psi}(r,k_z)=\int_0^{\infty}exp(-ik_z z')\Psi(r,z')dz'$$

PARABOLE-GFPE code

Some results

rigid ground
homogeneous atmosphere

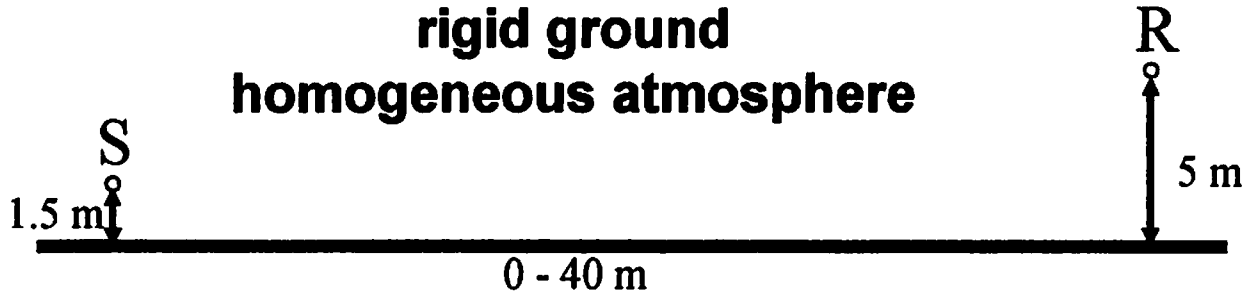

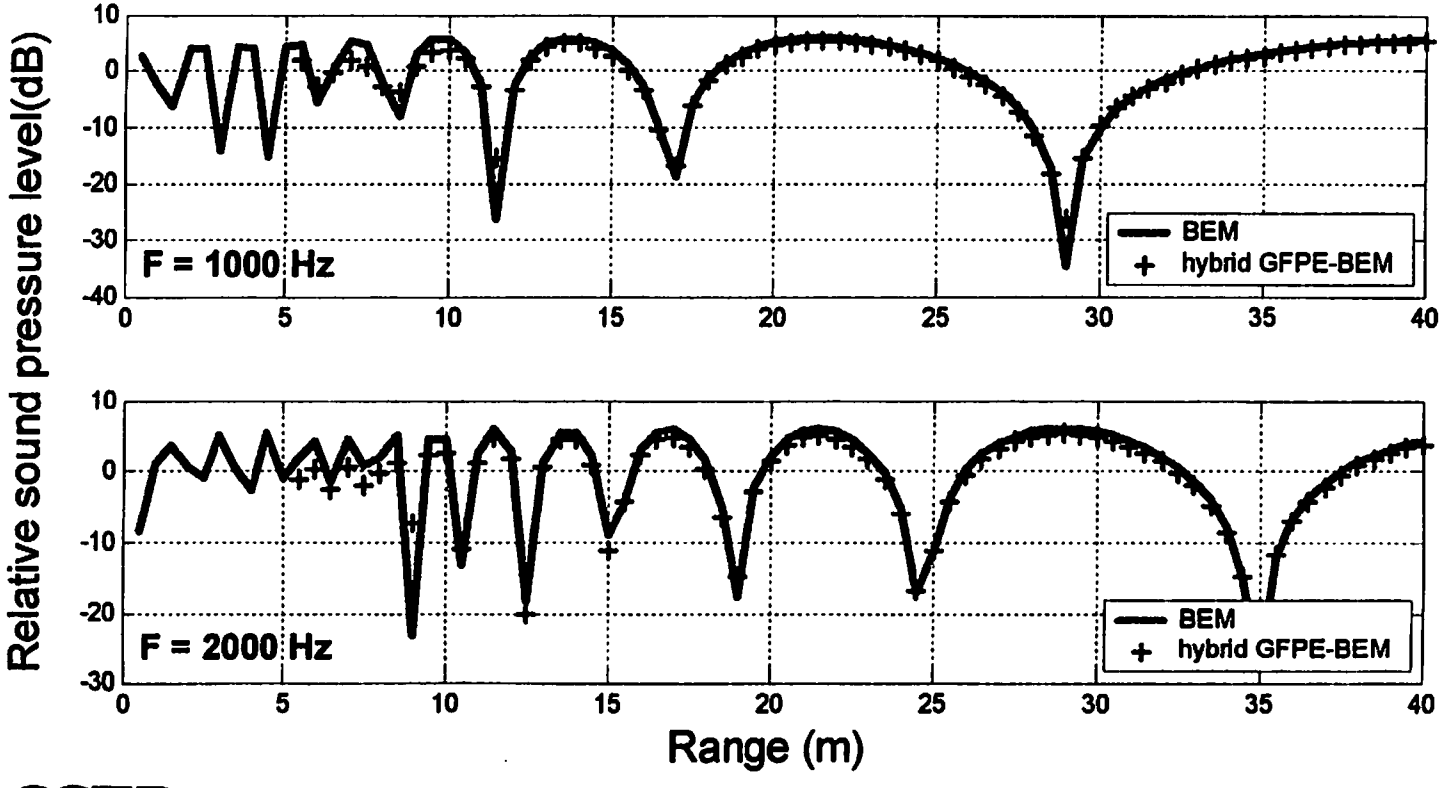

rigid ground
downward refraction

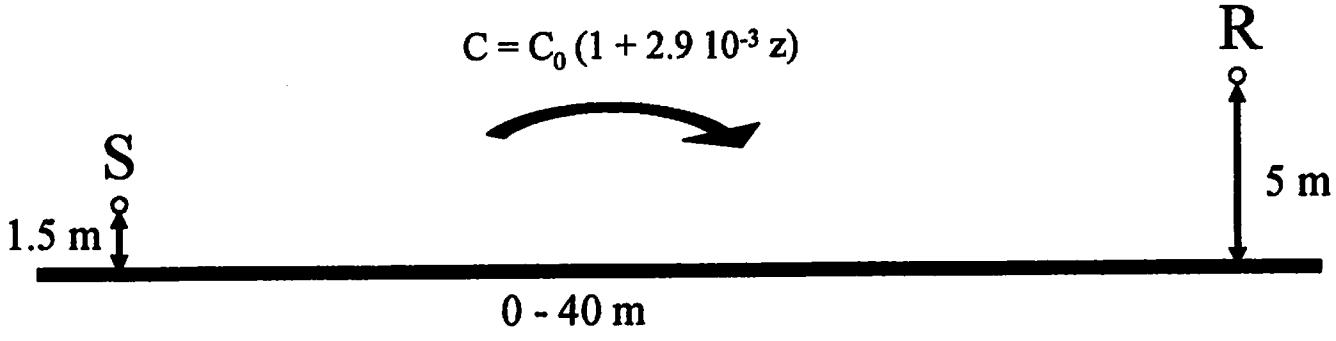

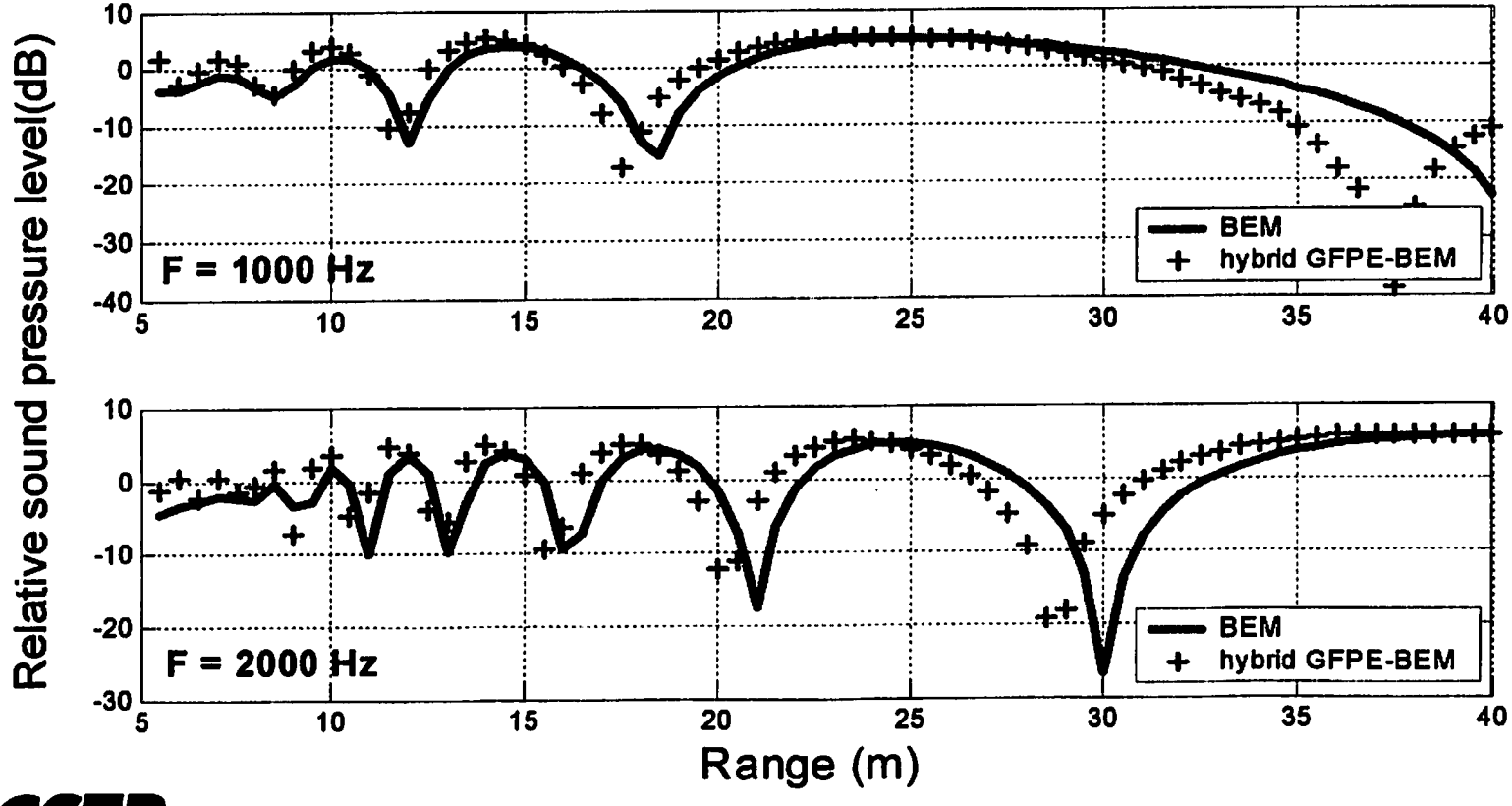

rigid ground + noise barrier
homogeneous atmosphere

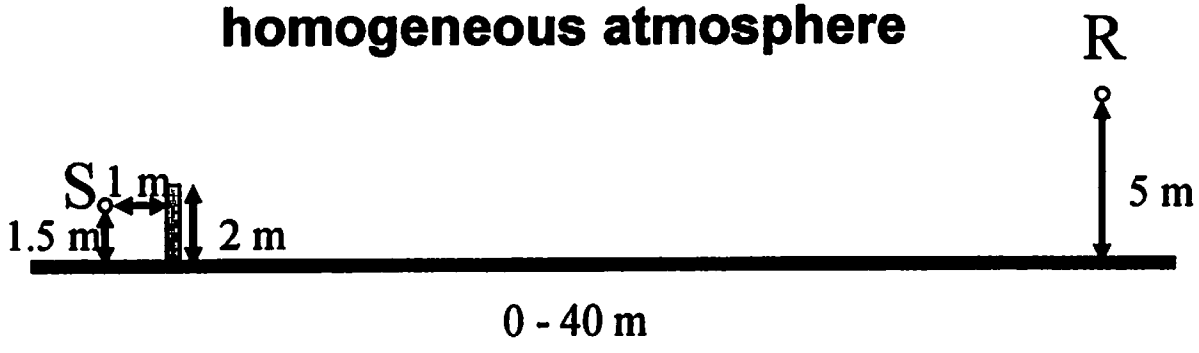

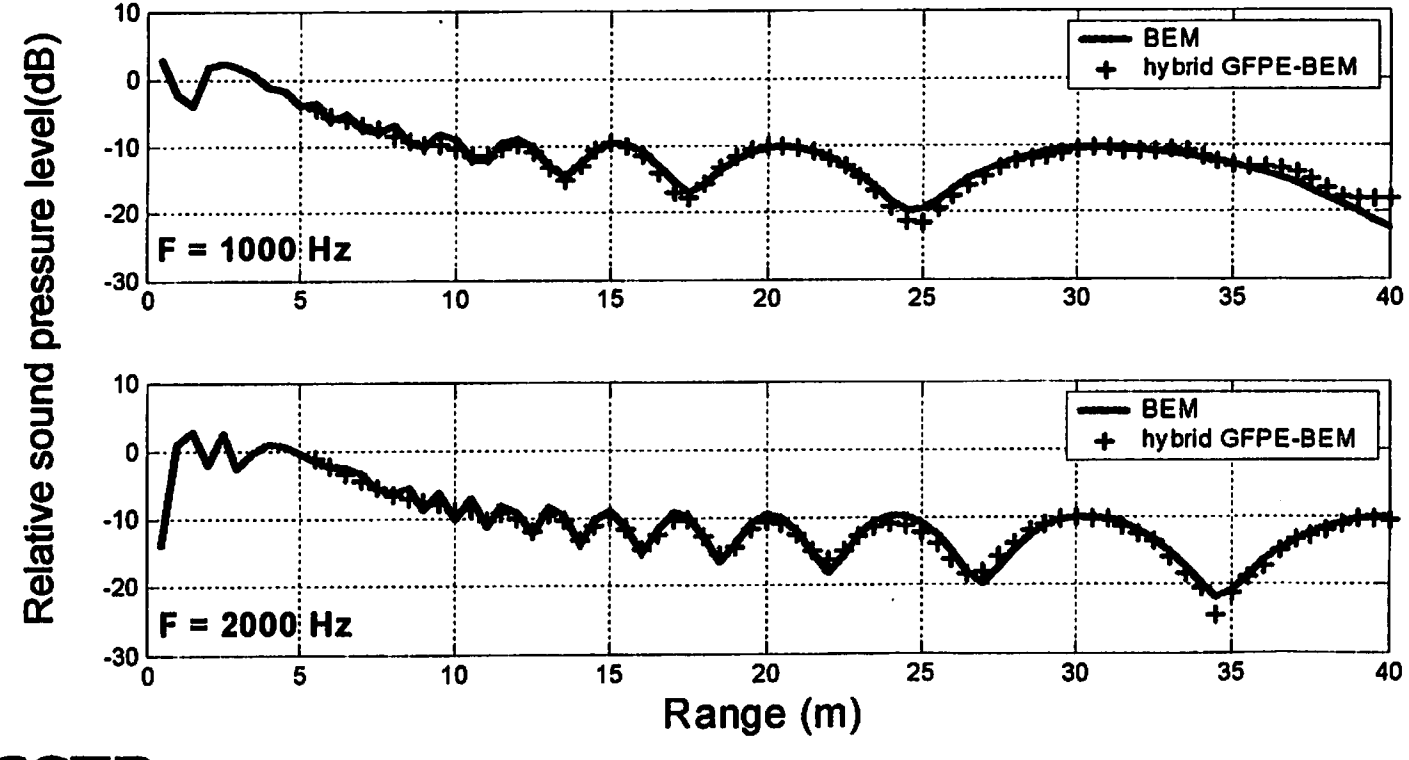

rigid ground + noise barrier
downward refraction

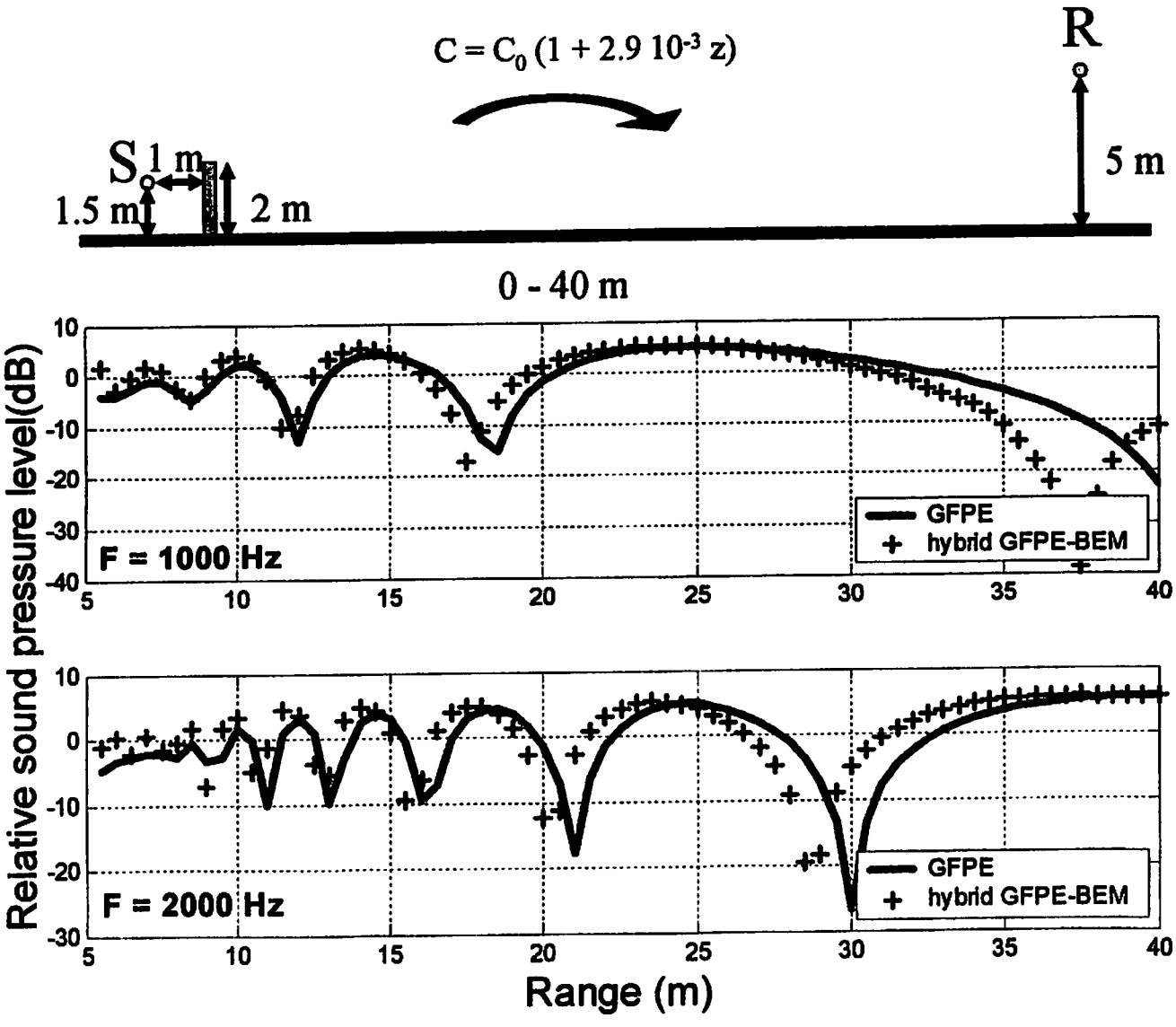

Scale model measurements

scale model measurements 1/20 - Time Delay Spectrometry
Frequency range [1000 Hz, 20000 Hz]
3 surfaces: flat, convex (Rc = 5 m), concave (Rc = 10.2 m)
rigid and felt-covered surfaces ($\sigma_1 = \infty$ cgs, σ_2 = 3600 cgs)

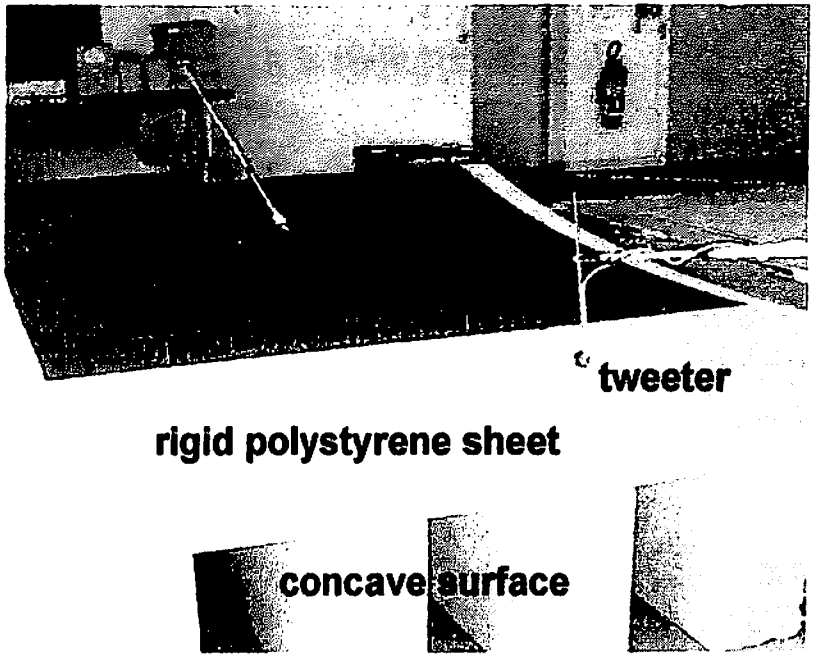

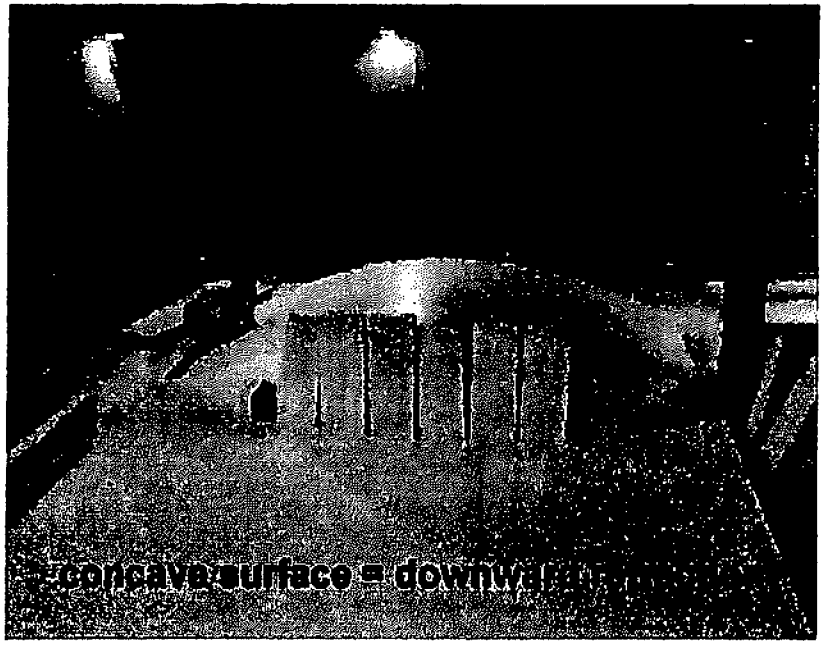

CSTB

Scale model configurations
complex impedance jumps

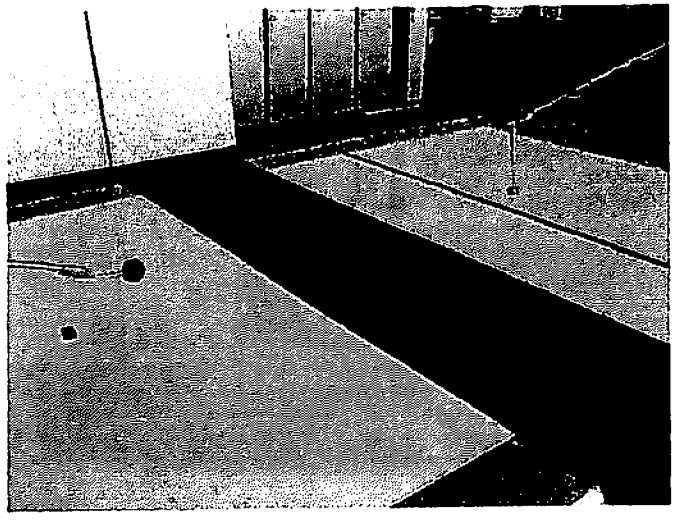

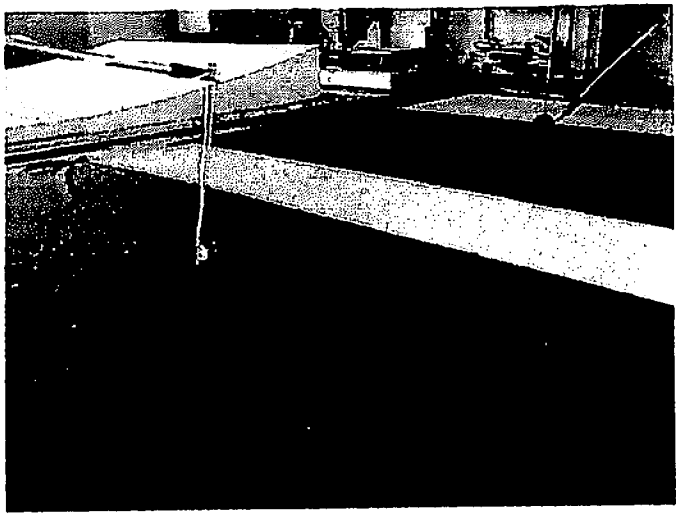

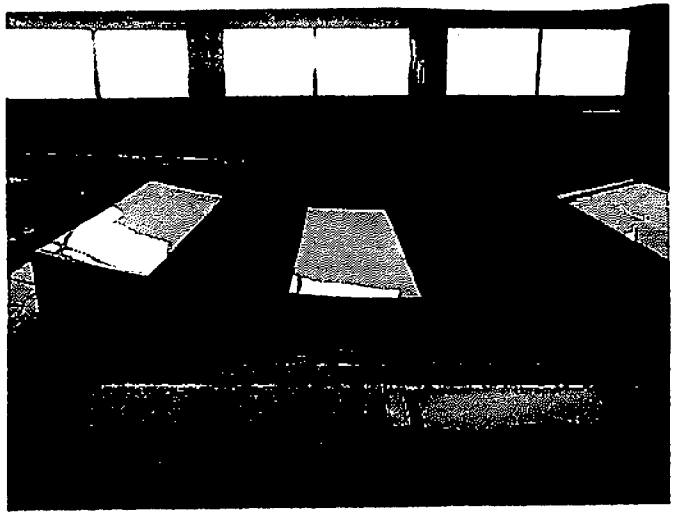

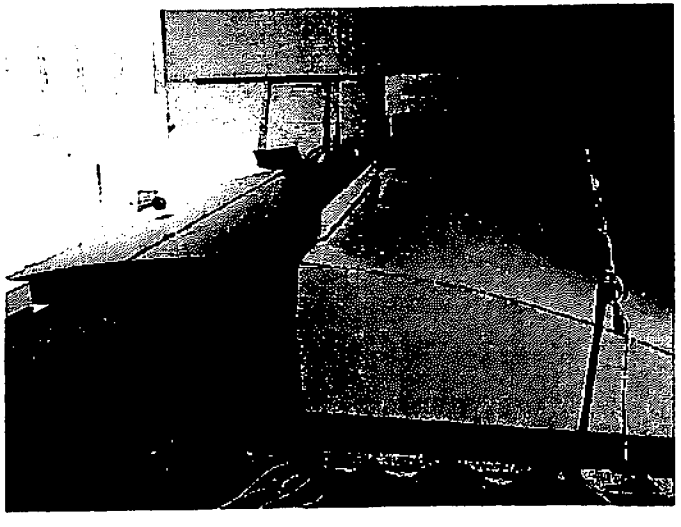

CSTB

Scale model configurations
complex noise barriers & crownings

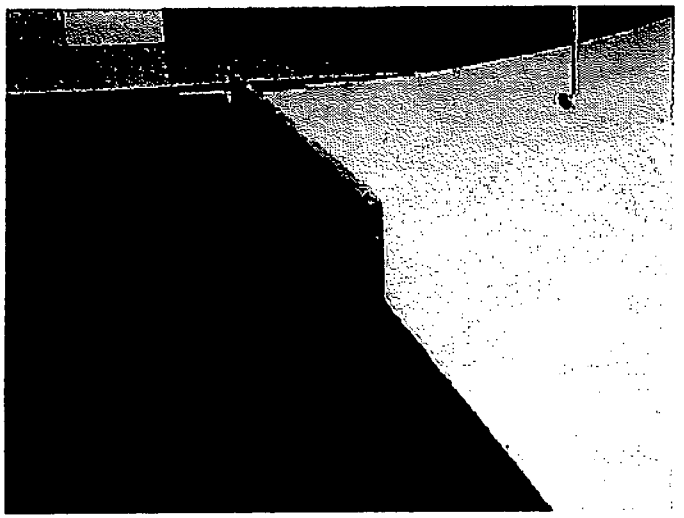

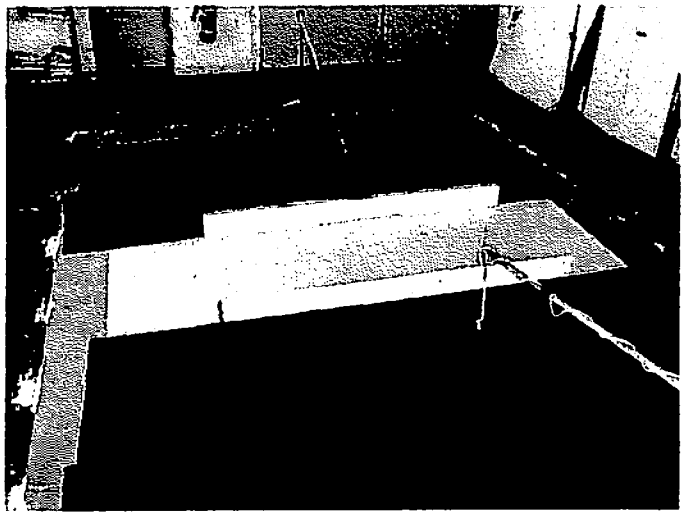

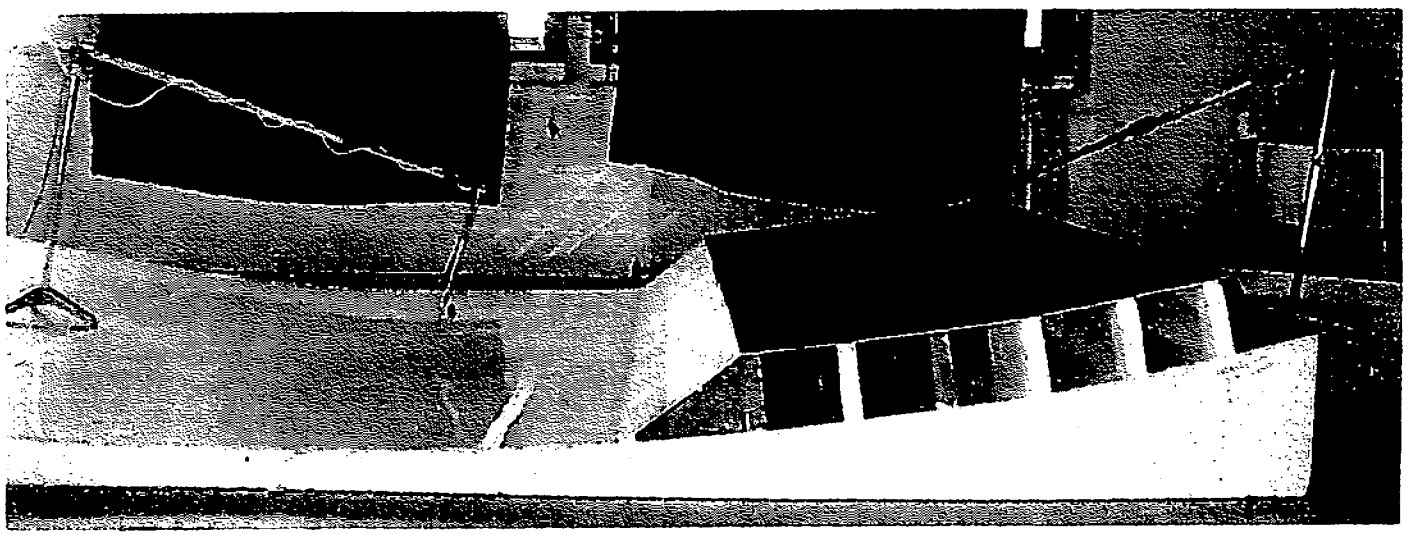

CSTB

Scale model measurements

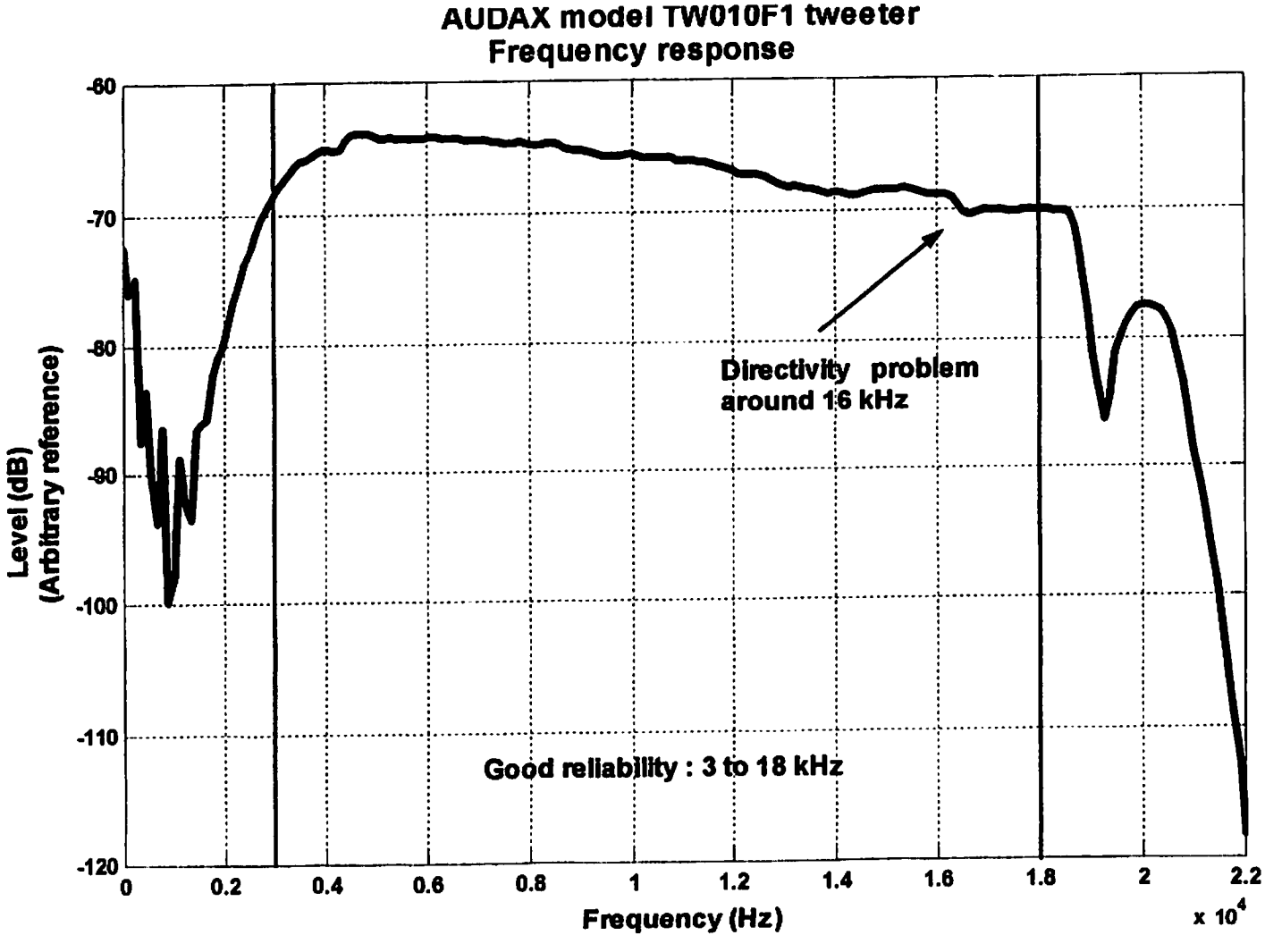

Scale model measurements

rigid ground + T-shaped noise barrier
homogeneous atmosphere

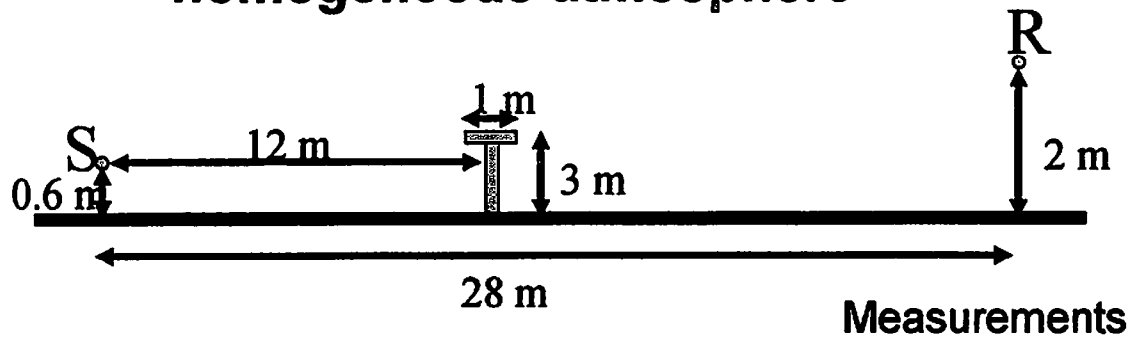

Measurements at scale 1/20

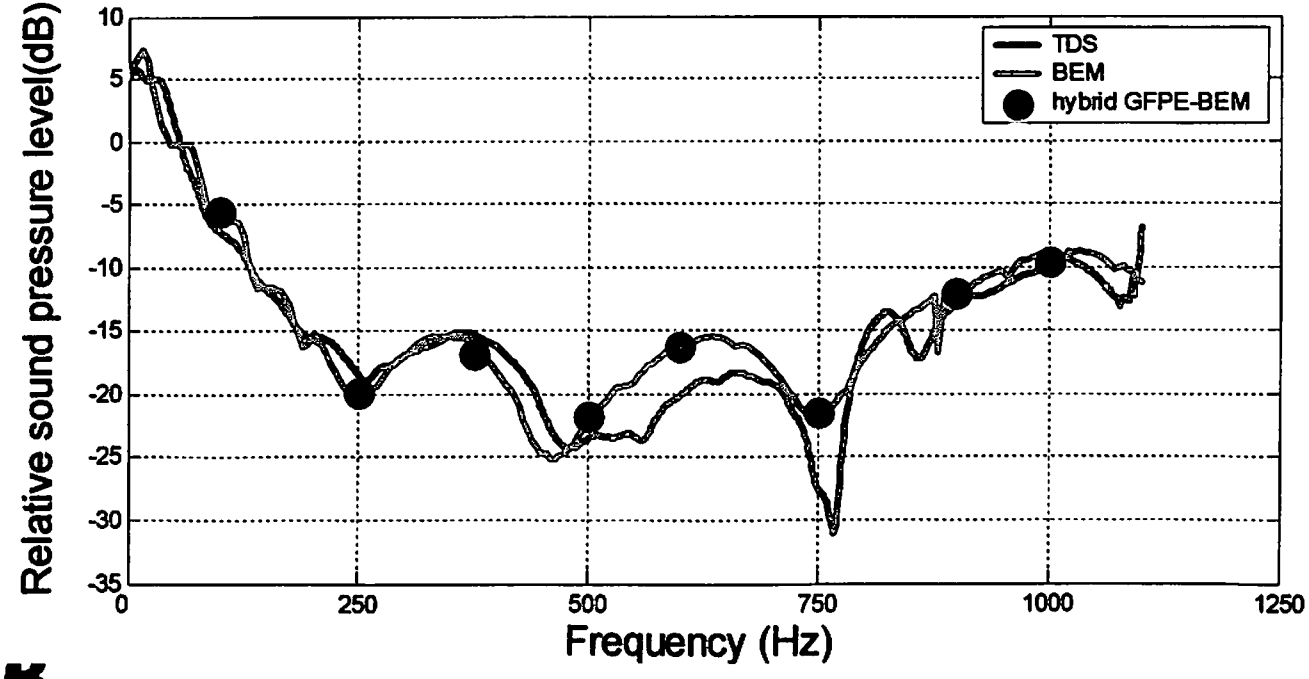

CSTB
le futur en construction

Scale model measurements

road embankment
homogeneous atmosphere

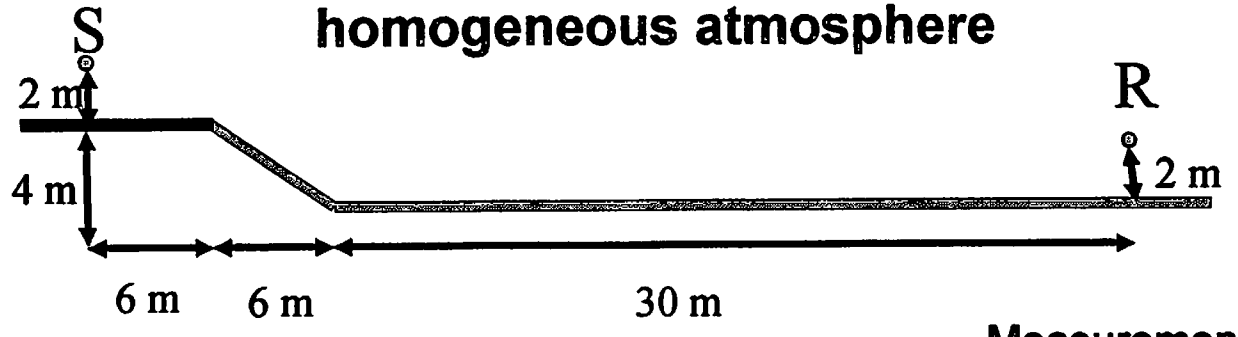

Measurements at scale 1/20

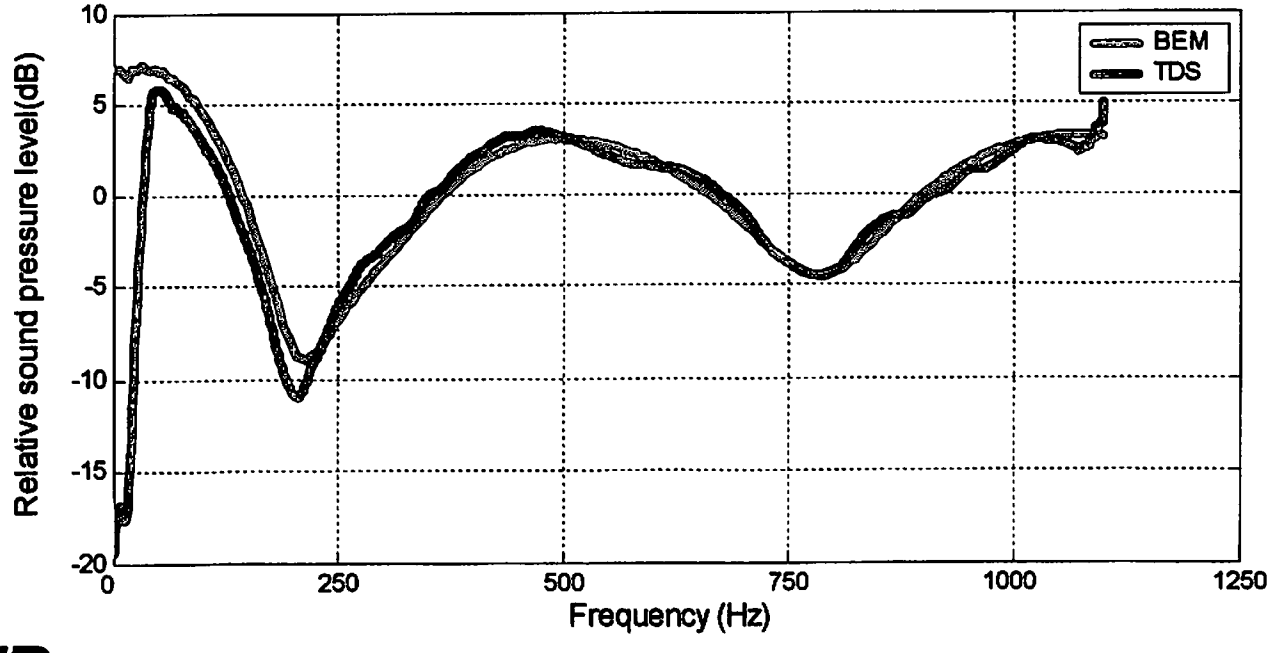

CSTB
le futur en construction

Conclusions

- **First results: good agreement model / measurements**

  to be continued

- **Improvements for meteorological effects**
- **Validity of the approximation**

  BEM in homogeneous conditions + GFPE with meteo

- **Investigations in progress :** ***topo-GFPE and Meteo-BEM***
- **Applications :**

  impedance strips, uneven impedance grounds

  road embankments, various diffracting shapes

Parameterization of the near-ground sound-speed gradient based on turbulence similarity theory

D. Keith Wilson
U.S. Army Cold Regions Research and Engineering Laboratory, ATTN: CEERD-RC, 72 Lyme Rd., Hanover, NH 03755-1290, USA

Abstract

The gradient of the effective sound speed (actual sound speed plus the component of the wind vector in the propagation direction) in the atmospheric surface layer is systematically analyzed with turbulence similarity theory. An equation is developed that parameterizes the gradient with just three nondimensional quantities dependent upon the atmospheric state and propagation conditions. The first of these is a ratio of turbulence scales representing the relative strength of sound-speed and wind-speed fluctuations. The second is a ratio of the actual height to a transitional height where the near-ground wind-speed gradients and the adiabatic lapse rate are roughly balanced. The third is simply the cosine of the angle between the propagation direction and mean wind. When the magnitude of the sound-speed/wind-speed scale ratio is large, refraction is unconditionally upward or downward, depending on sign of the ratio. A small value for this ratio indicates nearly neutral atmospheric stratification, for which refraction is determined by the wind direction for small values of the nondimensional height ratio and is upward for larger values. The relative contributions of temperature and humidity to the sound-speed gradient are also studied.

I Introduction

The air/ground interface creates sharp vertical gradients in the near-ground wind, temperature, and humidity profiles. These gradients refract sound energy, creating substantial diminishment or enhancement of sound levels relative to what would be observed in a homogeneous medium. Therefore, techniques for systematically modeling the near-ground gradients and the resulting refraction are potentially very valuable in outdoor sound propagation. The Monin-Obukhov (MO) similarity theory (Monin and Obukhov, 1954) is an appropriate candidate for developing such a systematic model, as it is now widely used to model turbulence statistics in thermally stratified flows such as the atmospheric surface layer (roughly the lowermost 50 to 100 m of the atmosphere) (Stull, 1988; Garratt, 1992). Although several previous authors (Johnson et al., 1987; Klug, 1991; L'Espérance et al., 1993) have previously applied MO similarity to sound refraction calculations in the atmosphere, the application has been on a case-by-case basis. That is, particular values of the MO scaling parameters were determined for cases of interest and then used to calculate the wind and temperature profiles. In this paper, the general, fundamental characteristics of near-ground sound refraction as implied by MO similarity are considered. In particular, it is shown that a set of distinctive refraction regimes emerges whose boundaries have a quantifiable dependence on a set of three simple, dimensionless parameters.

II Monin-Obukhov Equation for the Effective Gradient

For nominally horizontal propagation of sound near the ground, an effective sound speed can be defined as[1]

$$c_{\text{eff}}(z,\alpha) = \langle c(z)\rangle + \langle U(z)\rangle \cos\alpha \tag{1}$$

[1]The reader is referred to Ostashev (1997) for more detailed discussions of the effective sound speed concept and its limitations.

where z is the height above the ground, U is the horizontal wind speed, and α is the angle between the source-receiver path and the wind vector. The angle brackets indicate ensemble means, which are assumed in this paper to depend only on height. Refraction of sound is determined primarily by the vertical gradient of the effective sound speed; gradients such that $\partial c_{\text{eff}}/\partial z < 0$ result in upward refraction of sound waves, whereas $\partial c_{\text{eff}}/\partial z > 0$ results in downward refraction. Therefore, the behavior of this gradient controls the basic nature of the sound propagation. The sound speed in air is given by (Ostashev, 1997)

$$c = \sqrt{\gamma_a R_a T\,(1+\eta q)}, \tag{2}$$

where $\gamma = C_p/C_v$ is the ratio in air of the specific heats for constant pressure and constant volume, R is the gas constant, the subscript a indicates dry air, $\eta = 0.511$, T is temperature, and q is the water vapor mixing ratio (mass of vapor divided by mass of dry air in a sample).

Let us write $T = T_0 + \Delta T$ and $q = q_0 + \Delta q$, where T_0 and q_0 are constant reference values for the temperature and humidity (for example, the mean values at the standard atmospheric observation height of 2 m), and ΔT and Δq are small perturbations whose mean values generally depend on height. Substituting these expansions into Eq. (2) and keeping only the first-order contributions in ΔT, Δq, and q_0, one has

$$c = c_0\left[1 + \frac{1}{2}\left(\frac{\Delta T}{T_0} + \eta \Delta q\right)\right], \tag{3}$$

where $c_0 = \sqrt{\gamma_a R_a T_0\,(1+\eta q_0)}$. The result of substituting Eq. (3) into Eq. (1) and differentiating with respect to height is

$$\frac{\partial c_{\text{eff}}}{\partial z} = \frac{c_0}{2T_0}\frac{\partial \langle \Delta T\rangle}{\partial z} + \frac{c_0 \eta}{2}\frac{\partial \langle \Delta q\rangle}{\partial z} + \cos\alpha \frac{\partial \langle U\rangle}{\partial z}. \tag{4}$$

The quantities $\partial\langle \Delta T\rangle/\partial z$ and $\partial\langle \Delta q\rangle/\partial z$ in Eq. 4 can be replaced by $\partial\langle T\rangle/\partial z$ and $\partial\langle q\rangle/\partial z$, since T_0 and q_0 are height-independent.

For simplicity, initially consider only the contributions from the temperature and wind gradients to $\partial c_{\text{eff}}/\partial z$. According to the Monin-Obukhov similarity theory, the gradients of temperature and wind can be written in the following forms (Monin and Obukhov, 1954; Stull, 1988; Garratt, 1992):

$$\frac{kz}{P_t T_*}\left(\frac{\partial \langle T\rangle}{\partial z} + \Gamma_d\right) = \phi_h(\zeta), \tag{5}$$

and

$$\frac{kz}{u_*}\frac{\partial \langle U\rangle}{\partial z} = \phi_m(\zeta), \tag{6}$$

where $k = 0.40$ is von Kármán's constant, $P_t = 0.95$ is the turbulent Prandtl number in neutral stratification, $\Gamma_d = g/C_p = 0.0098$ °K/m is the dry adiabatic lapse rate (accounting for the decrease of temperature with height due to compression in the air column), g is gravitational acceleration, u_* is the friction velocity, $T_* = -\langle w'T'\rangle_s / u_*$ is a temperature scale, and $\langle w'T'\rangle_s$ is the covariance of vertical velocity (w) and temperature at the surface. (The primes indicate the fluctuation of a quantity about the mean value at that height, e.g., $T' = T - \langle T\rangle$.) The ϕ's are heat and mass transfer functions, dependent on the dimensionless height ratio $\zeta = z/L_o$, where $L_o = -u_*^3 T_0/kg\langle w'T'\rangle_s$ is the Obukhov length. These functions are expected to have a universal dependence on ζ for any well mixed turbulent layer over a reasonably homogeneous fetch (flat ground with uniform roughness elements). The following forms for ϕ_h and ϕ_m are recommended based on Högström (1996) and Wilson (2001):

$$\phi_{h,m}(\zeta) = \begin{cases} (1 + a_{h,m}|\zeta|^{2/3})^{-1/2}, & \zeta < 0 \\ 1 + b_{h,m}\zeta, & \zeta \geq 0 \end{cases}, \tag{7}$$

where the a's and b's are constants with the values $a_h = 7.9$, $a_m = 3.6$, $b_h = 8.4$, and $b_m = 5.3$. The case $\zeta < 0$ corresponds to buoyantly unstable conditions, which typically occur when the sun heats the ground. Buoyantly

stable conditions ($\zeta > 0$) typically occur when the ground cools at night. In the limit $|\zeta| \to 0$, the gradient functions equal 1 and the wind and temperature profiles take on their familiar logarithmic forms (Garratt, 1992). Of course, the gradient functions can be integrated to determine the actual height dependence of the wind speed and temperature. The interested reader may refer to Stull (1988) or Wilson (2001) for the customary procedure. The result is

$$\langle T(z)\rangle = \langle T(z_r)\rangle - \Gamma_d (z - z_r) + \frac{P_t T_*}{k}\left[\ln\frac{z}{z_r} - \Psi_h\left(\frac{z}{L_o}\right) + \Psi_h\left(\frac{z_r}{L_o}\right)\right]. \tag{8}$$

and

$$\langle U(z)\rangle = \frac{u_*}{k}\left[\ln\frac{z}{z_0} - \Psi_m\left(\frac{z}{L_o}\right) + \Psi_m\left(\frac{z_0}{L_o}\right)\right], \tag{9}$$

where z_r is a reference height at which the temperature is known, z_0 is the surface roughness length, and

$$\Psi_{h,m}(\zeta) = \begin{cases} 2\ln\left[\left(1+\phi_{h,m}^{-1}\right)/2\right], & \zeta < 0 \\ -b_{h,m}\zeta, & \zeta \geq 0 \end{cases}. \tag{10}$$

Substituting Eqs. (5) and (6) into Eq. (4) and still neglecting humdity, we can write the vertical dependence of the effective sound-speed gradient in the following dimensionless form:

$$\frac{kz}{u_*}\frac{\partial c_{\text{eff}}}{\partial z} = \frac{c_0 P_t T_*}{2T_0 u_*}\phi_h(\zeta) - \frac{\Gamma_d c_0 kz}{2T_0 u_*} + \cos(\alpha)\,\phi_m(\zeta). \tag{11}$$

Using the thermodynamic relation $C_p = C_v + R$ and sound-speed equation for an ideal gas, $c_0^2 = \gamma R T_0$, we find $\Gamma_d = gT_0(\gamma - 1)/c_0^2$. This relationship allows the previous equation to be rewritten as

$$\frac{kz}{u_*}\frac{\partial c_{\text{eff}}}{\partial z} = P_t A\phi_h(\zeta) - \frac{\gamma - 1}{4A}\zeta + \cos(\alpha)\,\phi_m(\zeta), \tag{12}$$

where

$$A = \frac{c_0 T_*}{2T_0 u_*}. \tag{13}$$

Eq. (12) is the basic expression of the effective sound-speed gradient based on MO similarity. Given values for the atmospheric scaling variables u_* and T_* (and applying the relationship $\zeta = zkgT_*/u_*^2 T_0$), it provides a formula for the gradient as a function of $\cos\alpha$ and z. The first term in Eq. (12) represents the contribution from the potential temperature gradient. It is positive in stable conditions ($\zeta, T_* > 0$) and negative in unstable conditions ($\zeta, T_* < 0$). The second term, originating from the adiabatic temperature lapse, is always negative since A and ζ have the same sign. The third term, from the wind gradient, is positive for downwind propagation and negative for upwind propagation.

The validity of Eq. (12) is of course limited to situations when the MO similarity theory is valid. The theory requires that the near-ground atmosphere can be modeled as a constant vertical-flux layer; that is, the covariances of vertical velocity with quantities such as temperature and horizontal velocity must all be nearly equal to their surface values throughout the layer. As a result, the predictions are typically restricted to heights $z < 0.1 z_i$, where z_i is the thickness of the overall atmospheric boundary layer (about 500 to 2000 m) (Stull, 1988; Garratt, 1992). Generally, for ground-based sources and receivers separated by horizontal distances less than about 0.5 to 1 km, the sound energy will propagate mostly through this constant vertical-flux layer. Application of the MO similarity theory is furthermore tenuous when $\zeta \gtrsim 1$, due to weak turbulent mixing and stratification in the surface layer during buoyantly stable conditions (Garratt, 1992, p. 50). Unfortunately, there is no known surface-layer similarity theory for this situation.

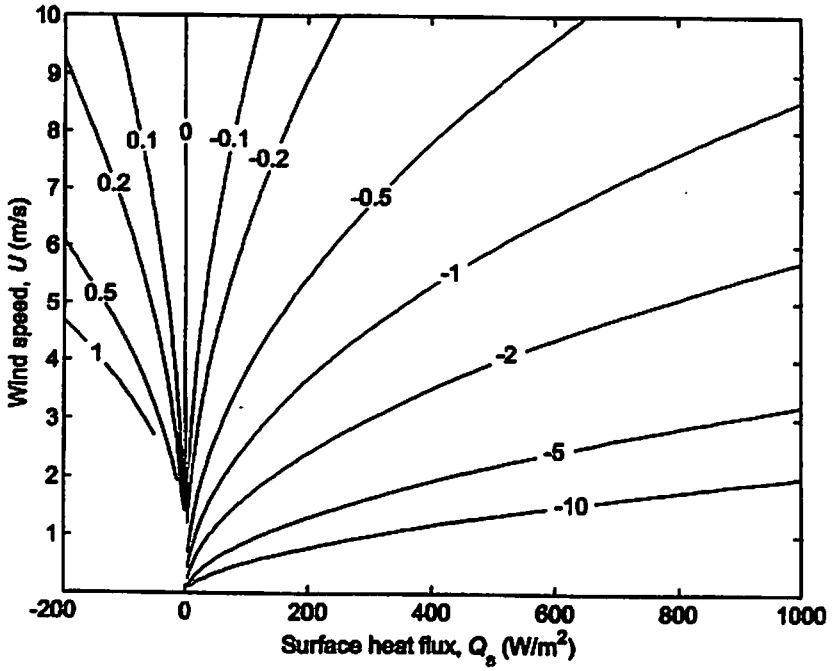

Figure 1: Dependence of the parameter A (ratio of the sound-speed scale c_* to the friction velocity u_*) on the surface heat flux and wind speed at 2-m height. The calculation is for a surface roughness length $z_0 = 0.01$ m.

III Alternative Similarity Formulation

Many alternative parameterizations to Eq. (12) are possible. Although Eq. (12) is the natural parameterization from the standpoint of the Monin-Obukhov theory, it is somewhat cumbersome to apply this equation systematically to sound refraction because the normalizing factor, kz/u_*, depends on height. One might ask whether there are alternatives that would provide a more convenient, insightful propagation framework. In this section, one such alternative is developed.

I begin by defining a sound-speed scale as $c_* = -\langle w'c' \rangle_s / u_*$. From Eq. (3) (without the humidity term) we have $c' = (c_0/2T_0)\, T'$, leading to $c_* = (c_0/2T_0)\, T_*$. Therefore, equivalently to Eq. 13, one has

$$A = \frac{c_*}{u_*}. \tag{14}$$

Hence A is simply the ratio of the sound-speed scale to the friction velocity. Physically, this ratio represents the strength of the fluctuations in the actual sound speed divided by the strength of the fluctuations in the wind speed. The dependence of A on the underlying atmospheric forcings of wind speed and sensible heat flux, $Q_s = \rho_0 C_p \langle w'T' \rangle_s = -\rho_0 C_p u_* T_*$, is illustrated in Fig. 1 by contours of constant values of A for a range of these forcing parameters. These calculations were performed by first solving for u_* from $\langle U(z) \rangle$ in Eq. (9). Although the equation is nonlinear in u_* (recall that L_o depends on u_*), it can be solved by a simple iterative method (L'Espérance et al., 1993). A wind-speed observation height $z = 2$ m and surface roughness $z_0 = 0.01$ m [characteristic of fairly level grass plains (Stull, 1988)] were used. Once u_* is determined, the ratio A follows from Q_s. In fair, summer weather at mid-latitudes, the heat flux varies roughly over the range -50 W/m^2 $< Q_s <$ 600 W/m^2 during a diurnal cycle (Stull, 1988).

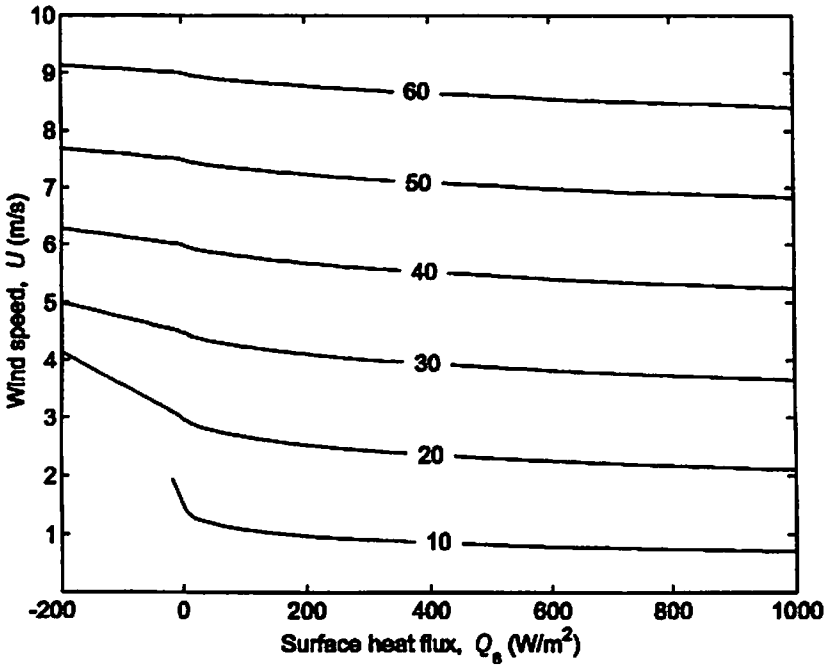

Figure 2: Dependence of the length scale L_g on the surface heat flux and wind speed at 2-m height. This scale indicates the height at which contributions to the effective sound-speed gradient from wind gradients and the adiabatic lapse rate are approximately in balance. The calculation is for a surface roughness length $z_0 = 0.01$ m.

Next, let us define a new nondimensional height

$$\overline{z} = \frac{z}{L_g}, L_g = \frac{c_0 u_*}{kg}. \tag{15}$$

The quantity $\overline{z}$ indicates the relative importance of wind gradients and the adiabatic temperature lapse rate for sound refraction. For $\overline{z} \ll 1$, wind gradients are dominant. As $\overline{z}$ increases, the wind gradients weaken and eventually, when $\overline{z} \gg 1$, the adiabatic temperature lapse rate controls refraction. The length scale L_g can be thought of as a transition height where the contributions to $\partial c_{\text{eff}}/\partial z$ from wind gradients and the adiabatic temperature lapse are roughly in balance. Contours of constant values of L_g, as a function of the wind speed and sensible heat flux, are plotted in Fig. 2.

It can be shown from Eqs. (13) and (15) that $\zeta = 2A\overline{z}$. Using this relationship and dividing Eq. (12) through by $\overline{z}$, an equation is produced in which the gradient is normalized by the constant factor c_0/g:

$$\frac{c_0}{g}\frac{\partial c_{\text{eff}}}{\partial z} = \frac{P_t A}{\overline{z}}\phi_h(2A\overline{z}) - \frac{\gamma - 1}{2} + \frac{\cos\alpha}{\overline{z}}\phi_m(2A\overline{z}). \tag{16}$$

Eq. (16) is the main result of this paper. It shows that the effective sound-speed gradient can be determined from just three nondimensional parameters, A, $\overline{z}$, and $\cos\alpha$, that depend on the conditions of the near-ground atmosphere. Near the ground (small values of $\overline{z}$), either the first or third term in Eq. (16) dominates, depending on the values of $|A|$ and $\cos\alpha$. Higher in the atmosphere (large values of $\overline{z}$), the second term, attributable to the adiabatic lapse rate, dominates. In this region, the gradient is $\partial c_{\text{eff}}/\partial z \simeq -(\gamma - 1)g/2c_0 = -0.0058\ \text{s}^{-1}$.

IV Water Vapor Effects

Let us now consider how the presence of water vapor modifies the preceeding analysis. The MO form of the humidity gradient is $\partial q/\partial z = (P_q q_* / kz)\,\phi_w(\zeta)$, where $q_* = -\langle w'q' \rangle_s / u_*$. The constant P_q and the function ϕ_w are usually assumed to be the same as P_t and ϕ_h (Garratt, 1992). The temperature gradient is still given by Eq. (5) in humid air, although the actual temperature should strictly be replaced by the virtual temperature $T_v = T(1 + \mu q)$ (including replacing $\langle w'T' \rangle_s$ with $\langle w'T_v' \rangle_s$ in the definition of the Obukhov length), where $\mu = 0.607$. [See, for example, Eqs. (2.24), (2.32), (3.25) in Garratt (1992). The purpose of the virtual temperature is to account for the effect of water vapor (which is less dense than dry air) on buoyancy.] However, if we assume $\phi_w = \phi_h$, Eq. (5) can be applied to either the virtual or actual temperature. The net result is that Eq. (16) applies to humid as well as dry air, although A must be defined from Eq. (14) with

$$c_* = \frac{c_0}{2}\left(\frac{T_*}{T_0} + \eta q_*\right). \tag{17}$$

Furthermore, ζ is no longer exactly $2A\bar{z}$, but rather

$$\zeta = 2A\bar{z}\frac{1 + \mu q_* T_0/T_*}{1 + \eta q_* T_0/T_*}. \tag{18}$$

The quantity q_*/T_* is proportional to the Bowen ratio β, which is defined as the ratio of the sensible to the latent heat flux at the surface. [The role of the Bowen ratio in determining the relative contributions of temperature and humidity to the acoustic index-of-refraction was previously pointed out by Wesely (1976).] Specifically,

$$\beta = \frac{\rho_s C_p \langle w'T' \rangle_s}{\rho_s L_v \langle w'q' \rangle_s} = \frac{C_p T_*}{L_v q_*}, \tag{19}$$

where ρ_s is the density of air at the surface and L_v is the latent heat of vaporization for water (Stull, 1988). Substituting for q_*/T_* and replacing the constants with numerical values, Eqs. (17) and (18) become

$$c_* = \frac{c_0 T_*}{2T_0}\left(1 + \frac{0.061}{\beta}\right), \tag{20}$$

and

$$\zeta = 2A\bar{z}\frac{0.073 + \beta}{0.061 + \beta}. \tag{21}$$

Figure 3 shows typical values of the Bowen ratio over various ground types. Note that small values of β, which are characteristic of moist ground surfaces, produce the largest changes in c_* and ζ in comparison to dry air. One finds that when $\beta = 0.5$, a typical value for grassland, c_* exceeds its dry value of $(c_0/2T_0)\,T_*$ by 12% whereas ζ exceeds its dry value of $2A\bar{z}$ by only 2%. For a more extreme value, $\beta = 0.2$ (characteristic of saturated ground), the corrections amount to 30% and 5%, respectively. Therefore the correction to c_* from humidity (and therefore the contribution from the humidity gradient to the sound-speed gradient) can be significant, particularly over a wet surface, although the contribution from the temperature gradient is still almost always larger. The humidity correction to ζ can usually be neglected.

If the air is saturated (as it would be in fog or in a cloud), the dry adiabatic lapse rate in Eq. (5) should no longer be used. The adiabatic lapse rate in saturated air varies between roughly 0.004 °K/m and 0.007 °K/m, depending on the air temperature (Wallace and Hobbs, 1977).

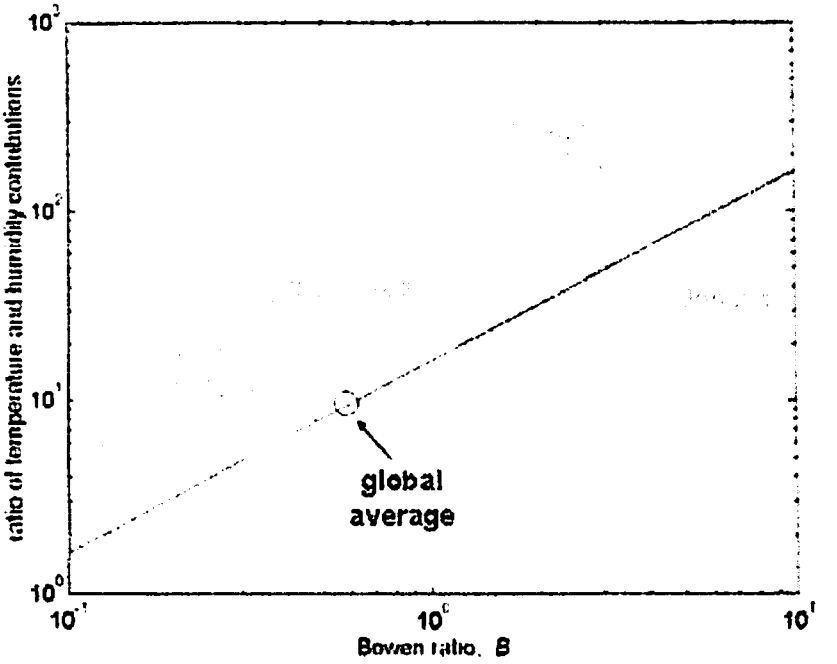

Figure 3: Ratio of the contribution of temperature gradients and humidity gradients to the overall sound-speed gradient as a function of the Bowen ratio.

V Results and Discussion

Figures 4 through 12 are polar plots of the gradient calculated from Eq. (16) for nine different values of A between -2 and 2. Each plot shows a polar representation of the gradient versus α at seven different values of $\bar{z}$. The reference temperature T_0 was set to 293 °K for the calculations in these figures, although the particular value of T_0 has very little effect on the results. The calculations also assume the relationship $\zeta = 2A\bar{z}$; as discussed in the previous section, this relationship is exact for dry air but is still is a good approximation in humid air.

On the basis of Figs. 4 through 12, the behavior of the gradient can be categorized into three distinct regimes depending on the value of A:

1. $A \lesssim -1$: Refraction of sound is upward for all propagation directions relative to the wind. This regime is dominated by a strong negative sound-speed (temperature and/or humidity) gradient, typically resulting from intense solar heating of the ground during the daytime or possibly from a very moist ground.

2. $-0.1 \lesssim A \lesssim 0.1$: Refraction by wind gradients dominates near the ground ($\bar{z} \lesssim 0.1$). The effective sound-speed gradient is positive for downwind propagation and negative for upwind propagation (to within about $\pm 10°$). However, when $\bar{z} \gtrsim 1$, upward refraction prevails for all propagation directions, as a result of the adiabatic lapse in temperature.

3. $A \gtrsim 1$: Refraction of sound is downward for all propagation directions relative to the wind. This regime is dominated by a strong positive sound-speed (temperature) gradient, which frequently occurs on clear nights with light winds.

Values such that $0.1 \lesssim |A| \lesssim 1$ represent transitions between these regimes.

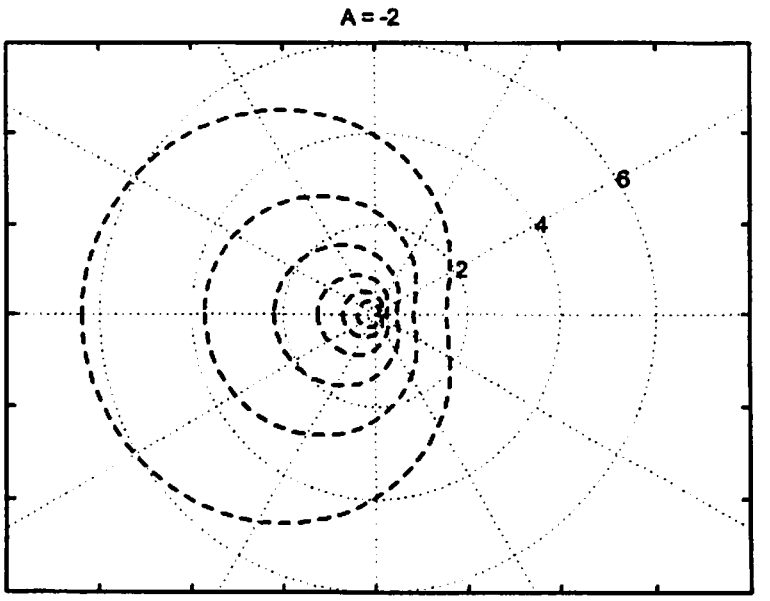

Figure 4: Polar plot of the magnitude of the effective sound-speed gradient (s^{-1}) versus the propagation angle relative to the wind. Upwind is to the left of the plot and downwind is to the right. The case $A = -2$ is shown at seven different values of $\bar{z}$: 0.01, 0.016, 0.025, 0.04, 0.063, and 0.1. (Gradients diminish with increasing $\bar{z}$.) Dashed contours represent negative values of the gradient and solid contours represent positive values.

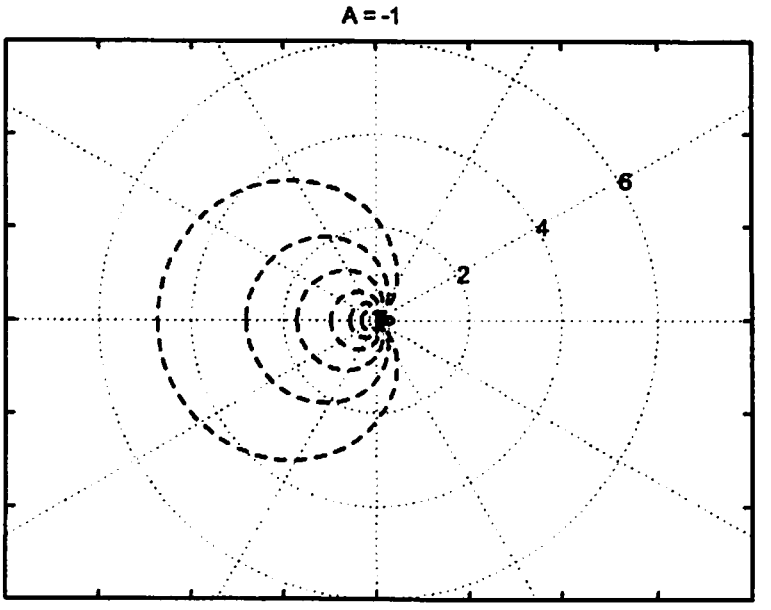

Figure 5: Same as Fig. 4, except for $A = -1$.

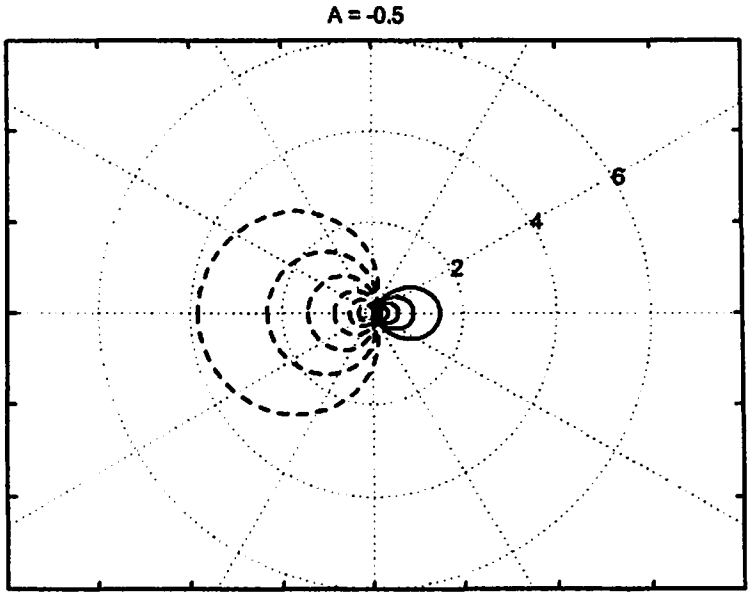

Figure 6: Same as Fig. 4, except for $A = -0.5$.

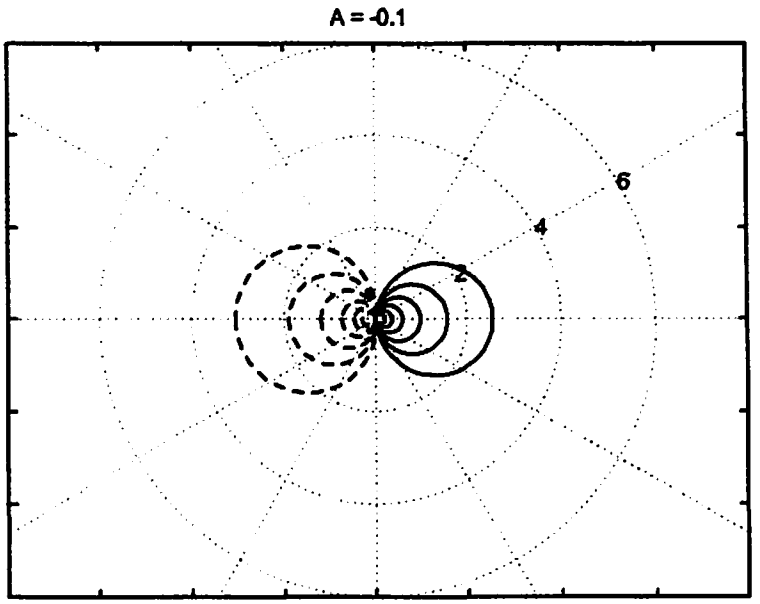

Figure 7: Same as Fig. 4, except for $A = -0.1$.

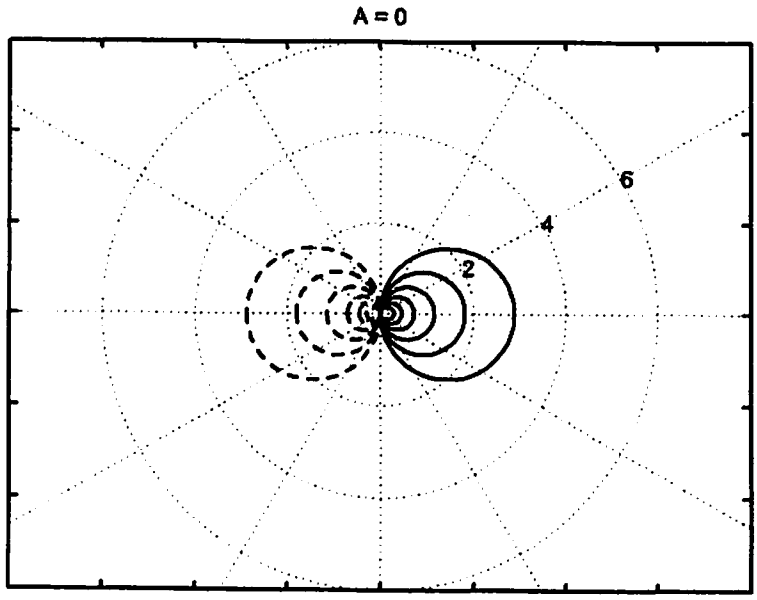

Figure 8: Same as Fig. 4, except for $A = 0$.

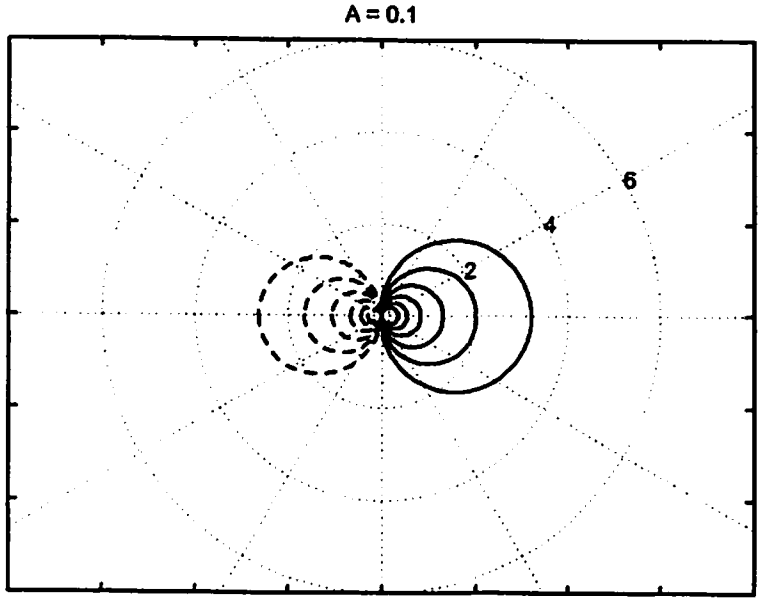

Figure 9: Same as Fig. 4, except for $A = 0.1$.

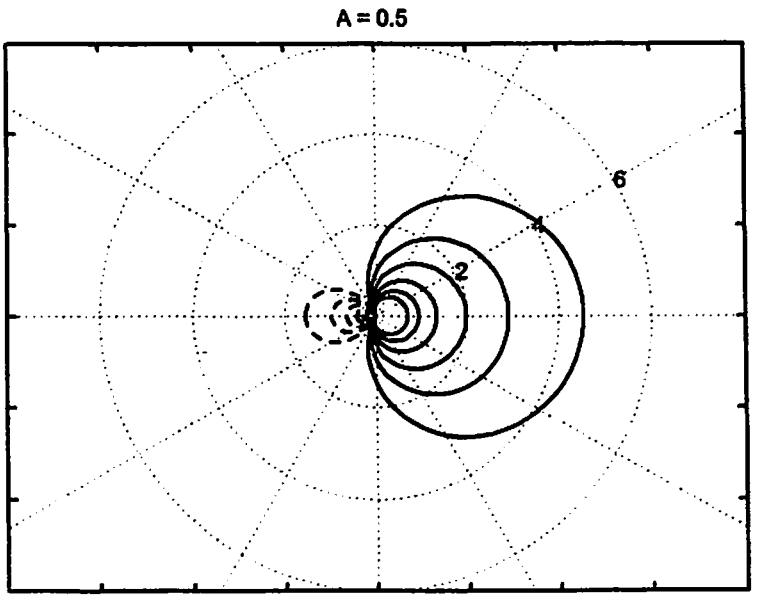

Figure 10: Same as Fig. 4, except for $A = 0.5$.

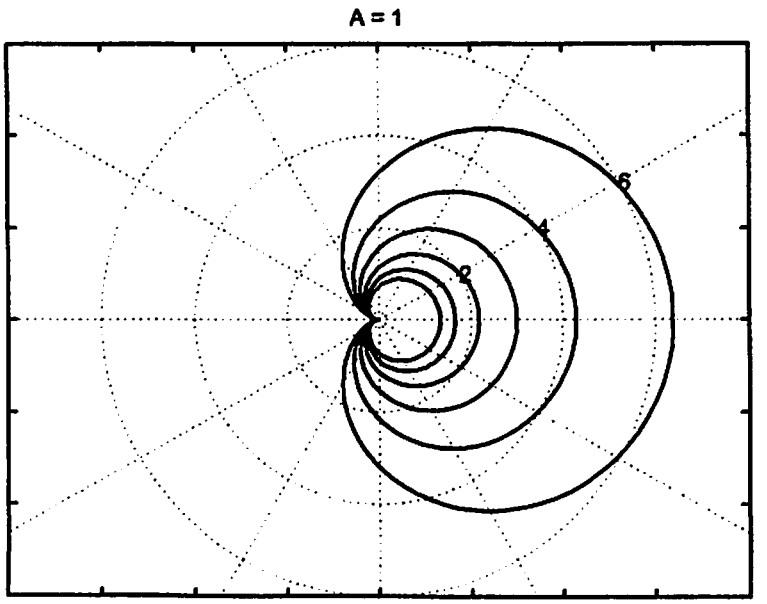

Figure 11: Same as Fig. 4, except for $A = 1$.

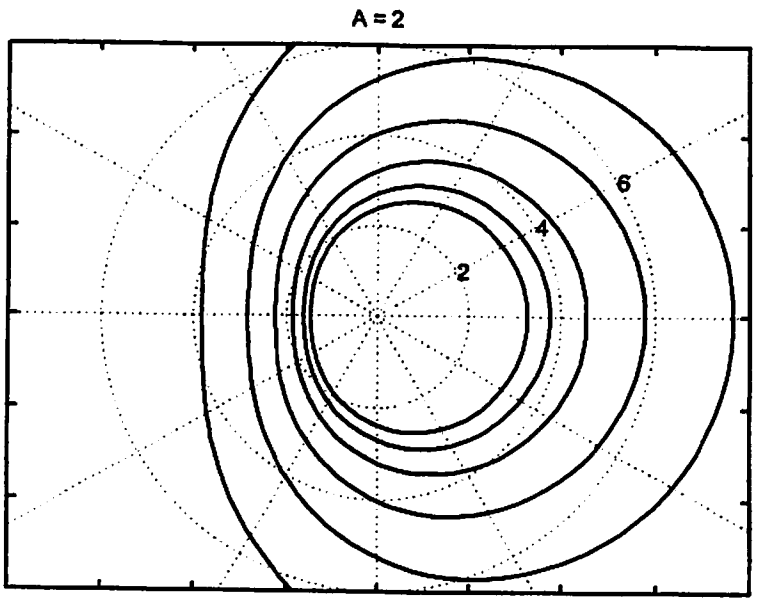

Figure 12: Same as Fig. 4, except for $A = 2$.

With regard to Figs. 4 through 12, it is particularly notable that strong gradients ($|\partial c_{\text{eff}}/\partial z| \gtrsim 1\ \text{s}^{-1}$) are almost always present near the ground. Only in particular propagation directions, for which the wind and sound-speed gradients nearly cancel each other, are small gradients in c_{eff} observed. Such cancellation of the gradient appears only when $|A| \lesssim 1$. It is evident in the downwind direction for $A \simeq -1$ (Fig. 5) and gradually shifts toward crosswind as A is increased. For $A = 0$, the cancellation direction is exactly crosswind. By the time A is increased to 1 (Fig. 11), the cancellation direction is exactly upwind. We find, very importantly, that *in no atmospheric condition are refractive effects simultaneously small for all propagation directions.* Thus, while the assumption of a constant sound-speed atmosphere may serve a useful role in deriving analytical solutions of propagation phenomena, it apparently never approximates realistic conditions in the surface layer.

VI Conclusion

In this paper, Monin-Obukhov similarity theory was used to develop a parameterization of the effective sound-speed gradient. The final result involves just three nondimensional quantities dependent upon the atmospheric conditions and propagation geometry. It is a "universal" parameterization in the sense that it should apply to propagation over reasonably flat ground with uniform roughness elements.

The first of the nondimensional parameters (designated A) is the ratio of the sound-speed scale (c_*) to the friction velocity (u_*) and represents the relative strengths of the turbulent fluctuations in sound speed and wind speed. The second ($\overline{z}$) is the ratio of the actual height above the ground to a transitional height where wind gradients and the adiabatic lapse rate contribute roughly equally to the effective sound speed gradient. The third parameter is the cosine of the angle between the propagation direction and the wind direction. Using these parameters, three distinct propagation regimes can be identified: one ($A \lesssim -1$) where refraction is upward at all propagation angles relative to the mean wind, a second ($A \gtrsim 1$) where it is downward for all propagation angles, and a third ($|A| \lesssim 0.1$) where refraction is determined by the wind direction when $\overline{z} \lesssim 0.1$ and is upward for $\overline{z} \gtrsim 1$.

The results in this paper demonstrate that atmospheric conditions supporting a small value of the near-ground effective sound-speed gradient are very rare, and in no situation does a small gradient occur in all propagation directions simultaneously. The contribution of temperature fluctuations to the sound-speed scale c_* (and therefore to the effective sound-speed gradient) is generally more important than that from humidity fluctuations, although the humidity contribution appears to be significant (around 30%) over wet surfaces.

Acknowledgments

I thank G. A. Daigle (National Research Council Canada), V. E. Ostashev (NOAA Environmental Technologies Laboratory), D. W. Thomson (Pennsylvania State University), and L. C. Sutherland for their helpful comments that have led to improvement of this paper.

References

Garratt, J. R. (1992): *The Atmospheric Boundary Layer.* Cambridge University Press, Cambridge, England.

Högström, U. (1996): Review of some basic characteristics of the atmospheric surface layer. *Boundary-Layer Meteorol.*, **78**, 215–246.

Johnson, M. A., R. Raspet, and M. T. Bobak (1987): A turbulence model for sound propagation from an elevated source above ground level. *J. Acoust. Soc. Am.*, **81**, 638–646.

Klug, H. (1991): Sound speed profiles determined from outdoor sound propagation measurements. *J. Acoust. Soc. Am.*, **90**, 475–481.

L'Espérance, A., J. Nicolas, D. K. Wilson, D. W. Thomson, Y. Gabillet, and G. Daigle (1993): Sound propagation in the atmospheric surface layer: Comparison of experiment with FFP predictions. *Appl. Acoust.*, **40**, 325–346.

Monin, A. S. and A. M. Obukhov (1954): Basic laws of turbulent mixing in the atmosphere near the ground. *Tr. Akad. Nauk SSR Geofiz. Inst.*, **24**, 163–187.

Ostashev, V. E. (1997): *Acoustics in Moving Inhomogeneous Media.* E & FN Spon, London.

Stull, R. B. (1988): *An Introduction to Boundary Layer Meteorology.* Kluwer, Dordrecht, Germany.

Wallace, J. M. and P. V. Hobbs (1977): *Atmospheric Science: An Introductory Survey.* Academic Press, New York.

Wesely, M. L. (1976): The combined effect of temperature and humidity fluctuations on the refractive index. *J. Appl. Meteor.*, **15**, 43–49.

Wilson, D. K. (2001): An alternative function for the wind and temperature gradients in unstable surface layers. *Boundary-Layer Meteorol.*, **99**, 151–158.

Simulation of sound propagation through a turbulent atmosphere using the Linearized Euler Model

Dietrich Heimann, Reinhard Blumrich

Institut für Physik der Atmosphäre,
DLR, Oberpfaffenhofen,
82234 Weßling, F.R.Germany.

Abstract

The paper shows how turbulence effects can be considered in coupled numerical simulations using an atmospheric model for the mean wind, a diagnostic generator for turbulent fluctuations, and a Linearized Euler (LE) time-domain model for the propagation of acoustical waves. After the turbulence generator is described, two different ways how turbulence can be considered in LE simulations are discussed. In opposite to frequency-domain (e.g. PE model) simulations, the time integration of the LE model enables the consideration of transient turbulence states during one model simulation. It is shown that a single model run with transient turbulence yields similar results at far less costs than averaging the results of multiple runs with frozen turbulence.

1 Introduction

The propagation of linear acoustical waves in an inhomogeneous atmosphere can be described by the linearized Euler (LE) equations of fluid dynamics. These equations can be numerically integrated in the time [1],[2],[3]. However, the high computational effort needed to run an LE model prevented it from being used in outdoor acoustics for a long time. Only nowadays the performance of computers reached a level that made the LE model more and more feasible in outdoor acoustics [4],[5]. Besides its still high computational demands the linearized Euler (LE) time-domain model is a universal tool to simulate the influence of 3D wind and temperature distributions on the 3D propagation of sound over irregular terrain without major approximations and limitations. It is therefore well suited to simulate the influence of turbulence on the propagation of acoustical waves.

Up to now, the relative contribution of turbulent scattering of sound energy to the total acoustical excess attenuation due to refraction, atmospheric absorption and ground effects has been investigated in various computational studies. In many cases frequency-domain models were used that are based on the parabolic approximation of the Helmholtz equation, e.g. [6], [7], [8]. In these studies a greater number of acoustical simulations are performed, each one based on a specific random realisation of turbulence. The state of turbulence is assumed to be stationary (frozen) during the travel time of the sound through the computational domain. The resulting ensemble of sound pressure amplitudes is subsequently averaged in order to imitate a temporal mean of sound level over the characteristic time scale of turbulence.

Because of the high computational demand of the LE model, the concept of multiple model runs with frozen turbulence is presently not feasible. At least a sufficiently high number of realisations

cannot be archived with reasonable effort. Therefore, it is investigated whether or not it is possible to use the concept of transient turbulence realisations within a single model run as a less expensive alternative. In principle, this concept is adequate to a time-domain model. It cannot be used by a frequency-domain model.

In the following we propose a procedure how simulations of an inhomogeneous turbulent atmosphere can be consistently coupled with an LE model of sound propagation. A numerical turbulence generator is introduced that provides non-divergent turbulent wind fields. Test simulations show that the concept of transient turbulence is feasible. Comparisons with results of multiple frequency-domain simulations published by other authors suggest that the transient turbulence concept brings about plausible results.

2 The Linearized Euler (LE) model

In the following we assume that any three-dimensional motion $\mathbf{U}$ in the atmosphere is composed of a mean wind $\overline{\mathbf{U}}$, a turbulent deviation from the mean wind $\mathbf{U}'$, and a superimposed particle velocity according to acoustical waves $\mathbf{U}''$:

$$\mathbf{U} = \overline{\mathbf{U}} + \mathbf{U}' + \mathbf{U}'' \tag{1}$$

The mean wind and the turbulent motion can be combined to the meteorological air motion $\mathbf{U}_{met} = \overline{\mathbf{U}} + \mathbf{U}'$ which forms the environment of the sound waves.

Analogously, we can define other variables such as the pressure

$$p = \overline{p} + p' + p'' = p_{met} + p'' \tag{2}$$

with the mean air pressure $\overline{p}$, the turbulent pressure fluctuation p', and the sound pressure p''.

The LE model is based on the Euler equations for adiabatic processes in a friction-less, non-rotating, non-buoyant atmosphere. These equations are linearised with respect to a meteorological background given by the wind $\mathbf{U}_{met}$, the air pressure p_{met} and the air density ρ_{met}. Finally, the model consists of a set of two linear differential equations:

$$\frac{\partial \mathbf{U}''}{\partial t} = -(\mathbf{U}_{met} \cdot \nabla)\,\mathbf{U}'' - (\mathbf{U}'' \cdot \nabla)\,\mathbf{U}_{met} - \alpha_{met} \nabla p'' - \alpha'' \nabla p_{met} \tag{3}$$

$$\frac{\partial p''}{\partial t} = -\mathbf{U}_{met} \nabla p'' - \mathbf{U}'' \cdot \nabla p_{met} - \kappa\, p_{met}\, \nabla \cdot \mathbf{U}'' - \kappa\, p'' \nabla \cdot \mathbf{U}_{met} \tag{4}$$

with the specific volume $\alpha_{met} = \dfrac{1}{\rho_{met}}$ and $\alpha'' = -\dfrac{1}{\kappa}\dfrac{p''}{p_{met}}\dfrac{1}{\rho_{met}}$ and $\kappa = \dfrac{c_p}{c_v}$.

The complete derivation of the model equations are given by [4]. Since the terms containing ∇p_{met} are relatively small and in case the meteorological wind is non-divergent ($\nabla \cdot \mathbf{U}_{met} = 0$), Eqs. (3) and (4) can be simplified to

$$\frac{\partial \mathbf{U}''}{\partial t} = -(\mathbf{U}_{met} \cdot \nabla)\mathbf{U}'' - (\mathbf{U}'' \cdot \nabla)\mathbf{U}_{met} - \alpha_{met} \nabla p'' \tag{5}$$

$$\frac{\partial p''}{\partial t} = -\mathbf{U}_{met} \nabla p'' - \kappa\, p_{met}\, \nabla \cdot \mathbf{U}'' \tag{6}$$

The equations (5) and (6) are numerically integrated in time on an orthogonal staggered grid using forward-in-time, centred-in-space finite differences. The source of sound can be a pulse or a steadily emitting source by specifying the sound pressure in the source region at the initial state or during the time integration, respectively.

The LE model is a universal tool for the simulation of sound in a complex environment. Acoustically soft ground can be treated as proposed by [5]. Reflecting obstacles can be considered by setting the perpendicular components of the particle velocity to zero at the side walls of the obstacle grid cells. Any three-dimensional meteorological wind field ($\mathbf{U}_{met}(x,y,z)$), pressure field ($p_{met}(x,y,z)$), and density field ($\rho_{met}(x,y,z)$) can be used as background. There are no restrictions as with the effective sound speed approach (sound propagation parallel to the wind) or the parabolic equation (PE) approximation (quasi-horizontal sound propagation).

The universality with respect to the meteorological background makes the LE model particularly suitable to the simulation of sound in a turbulent atmosphere and above complex terrain. Figure 1 shows simulated sound waves that are reflected by and diffracted at a wall.

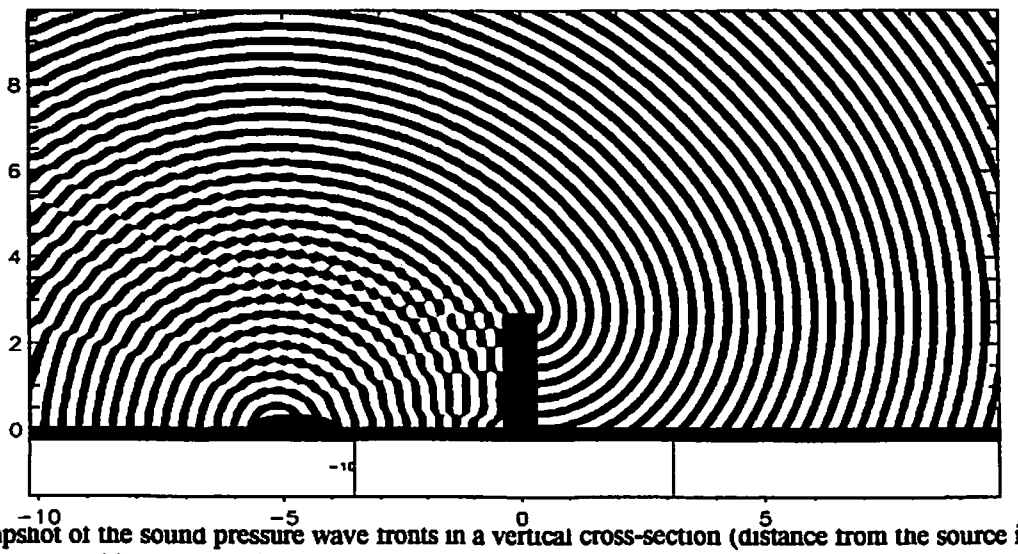

Figure 1: Snapshot of the sound pressure wave fronts in a vertical cross-section (distance from the source in meters vs. height above ground in meters). The 1000 Hz sound emerges from a source at ground. In this example the ground is non reflecting while the 3 m high wall is totally reflecting.

3 Main flow and turbulence

If air flows over a rough and plane ground, turbulence is generated by shear forces and buoyancy forces. Shear forces result from the no-slip kinematic boundary condition at the ground surface. Buoyancy forces play a role as soon as the stratification of the atmosphere is different from neu-

tral and irregular vertical motions of air parcels are either enhanced (unstable or convective boundary layer) or damped (stable boundary layer). Turbulence acts as a friction to the mean flow. It extracts momentum from the atmosphere and transports it downward to the surface. In the state of equilibrium a range-independent logarithmic (neutral stratification) or mixed logarithmic-linear (non-neutral stratification) vertical wind speed establishes in the atmospheric surface layer.

Above irregular topography (i.e. in the presence of obstacles or hills and valleys) the situation is much more complicated. In this case the mean flow is disturbed and diverted above or around the irregularities. Moreover, the increased wind gradients above and beside the irregularities give rise to the generation of additional turbulence. As a consequence, both mean flow and turbulence are highly range-dependent.

For the simulation of the propagation of sound in such an environment the detailed knowledge of the turbulent atmosphere in three dimensions is required. Measurements are difficult, if not even impossible, though numerical simulation is a possible way to gain these information.

Large-eddy simulations (LES) or direct numerical simulations (DNS) of turbulent flow are state-of-the-art tools (e.g. [9]) in atmospheric physics, but it is rather expensive to gain a sufficiently long time-series of different states of turbulence for subsequent acoustical simulations with these models. A less expensive way is the use of a mean flow model, i.e. a model that is based on equations that are averaged over the time-scale of turbulence. In this case the effect of turbulence on the mean wind has to be fully parameterised. It is convenient to use a turbulence parameterisation scheme that involves a prognostic equation of the turbulent kinetic energy $\overline{E}$ which provides the local strength of turbulence. The turbulent kinetic energy is defined as the specific kinetic energy of the turbulent wind fluctuations, i.e. it is a function of the variance of the turbulent wind fluctuations:

$$\overline{E} = 0.5\left(\overline{\mathbf{U}'\cdot\mathbf{U}'}\right) = 0.5\left(\overline{u'^2+v'^2+w'^2}\right) = 0.5\,\sigma_{U'}^2 \tag{7}$$

The spatial distribution of the turbulent kinetic energy can be used in a numerical turbulence synthesiser in order to generate a greater number of turbulence realisations that are consistent with the mean wind field above a given topography.

4 Numerical turbulence generator

Once the mean wind field $\overline{\mathbf{U}}$ and the distribution of the turbulent kinetic energy $\overline{E}$ is determined, a numerical turbulence generator is used to produce non-divergent random fields of u', v', w' that

- locally match the predicted turbulent kinetic energy,
- fulfil a given turbulent energy density spectrum,
- reproduce the turbulent momentum flux.

The turbulence generator is based on the superposition of circular or elliptic eddies of different size (diameter) and amplitude. The size is varied between the quadruple extension of a grid cell and the double height of the computational domain. The eddies are described by 3D stream functions $\mathbf{\Phi}_{l,n}$, where the index l indicates the size class and n counts the eddies within the size class. The position of the eddy centres are randomly distributed inside the model domain. A specific amplitude S_l of the stream function is appointed to each size class according to an appropriate energy spectrum (e.g. Kolmogorov or Prandtl spectrum). This amplitude is further weighted by the local value of the square-root of the turbulent kinetic energy.

The turbulent velocity components are given by the curl of the sum of the weighted eddy stream functions

$$\mathbf{U}' = \nabla \times \left(\sum_l \sum_n S_l \sqrt{\overline{E}} \mathbf{\Phi}_{l,n} \right) \tag{8}$$

The turbulent fluctuations can be superimposed to the mean flow $\overline{\mathbf{U}}$ according to Equation (1).

The numerical turbulence generator is implemented in the sound propagation model. It is very efficient in producing a greater number of turbulence realisations.

Figure 2 illustrates a simulated mean wind field $\overline{\mathbf{U}}$ of an air flow across a noise barrier and the respective distribution of turbulent kinetic energy $\overline{E}$. It also shows the snapshot of a turbulent wind field $\mathbf{U}_{met} = \overline{\mathbf{U}} + \mathbf{U}'$ for the same situation.

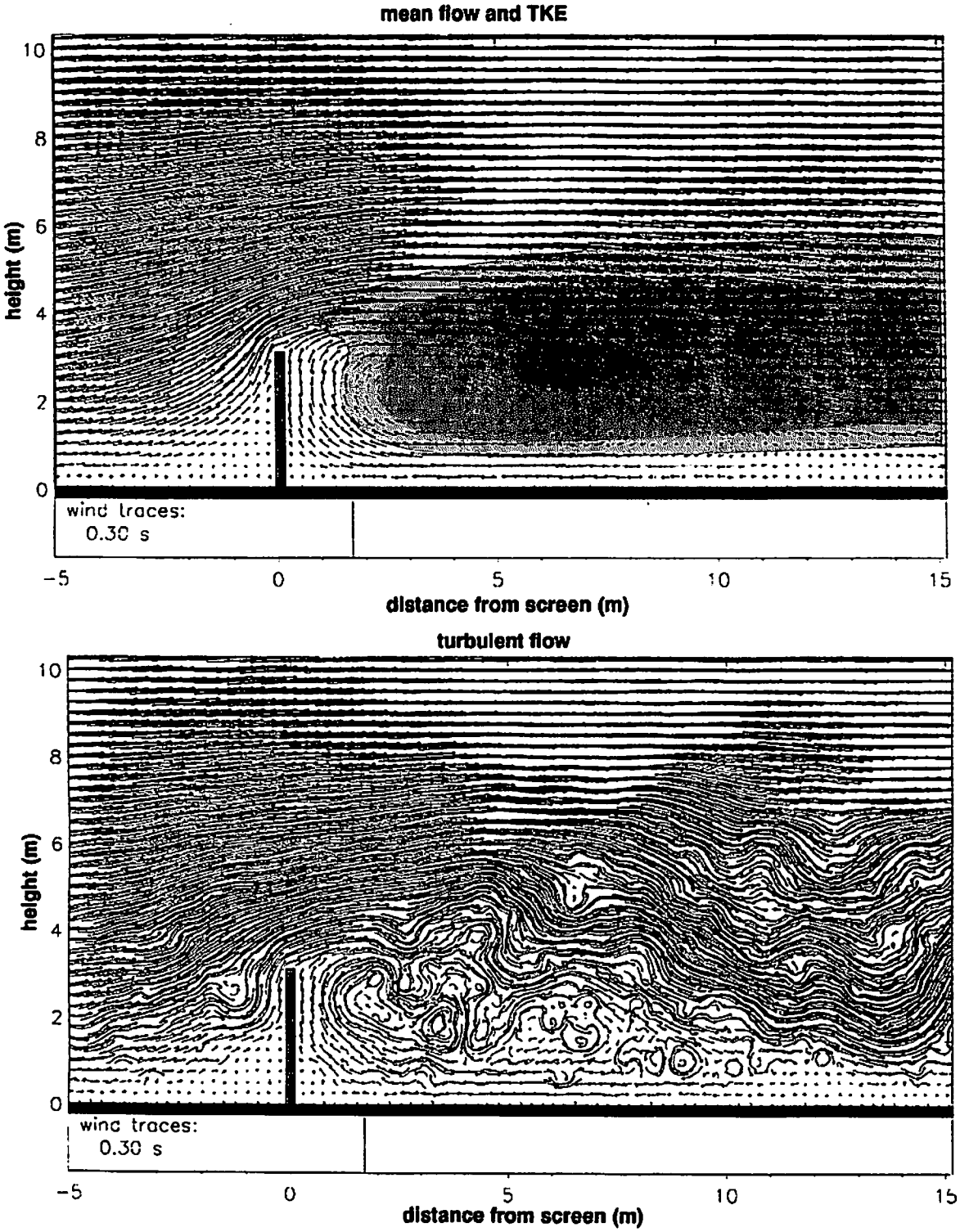

Figure 2: Top: Simulated flow field across a noise screen. The color shade shows the qualitative distribution of turbulent kinetic energy that is produced by the barrier. Bottom: a particular realisation of the turbulent flow field for the same situation.

5 Consideration of turbulence in the LE model

In principle, the LE code is able to handle both frozen and transient turbulence. In the first case a momentary field of turbulent fluctuations is added to the mean flow field and is kept as a constant meteorological background throughout the full time-dependent acoustical simulation, i.e. until the sound has propagated from the source to all boundaries of the model domain. The results of several simulations are subsequently averaged. Many simulations are needed in order to achieve a statistically significant result. In the second case many different realisations of turbulence replace each other during a single simulation either by a smooth transition or an abrupt change. The transient turbulence approach has the advantage that a rather high number of turbulence realisations are encountered during only one simulation. However, in the transient case the turbulence would change within unrealistically short time intervals.

In the following both methods are tested. For this purpose 2D acoustical simulations were performed over flat and perfectly reflecting ground. Vertical profiles of the mean wind speed and turbulent kinetic energy were simulated in advance with the 1D version of the FITNAH meteorological mesoscale model [10]. A statically neutral stratification (vertical temperature gradient $\partial T/\partial z = -9.9\,\mathrm{K/km}$) under the condition of a geostrophic wind speed of $U_g = 10\,\mathrm{m/s}$ and a roughness length of $z_o = 0.1\,\mathrm{m}$ was assumed. The resulting mean wind speed $\overline{U}$ and turbulent kinetic energy $\overline{E}$ at 10 m above ground amount to 4 m/s and 0.4 m^2/s^2, respectively. A sound source was placed directly on the ground. It emits a constant tone of 500 Hz. The sound propagates in upwind direction such that an acoustical shadow can form. The numerical grid spacing was set to 5 cm in order to resolve one wave length by approximately 12 grid cells. Figure 3 shows the acoustical result under the influence of the mean wind without turbulence.

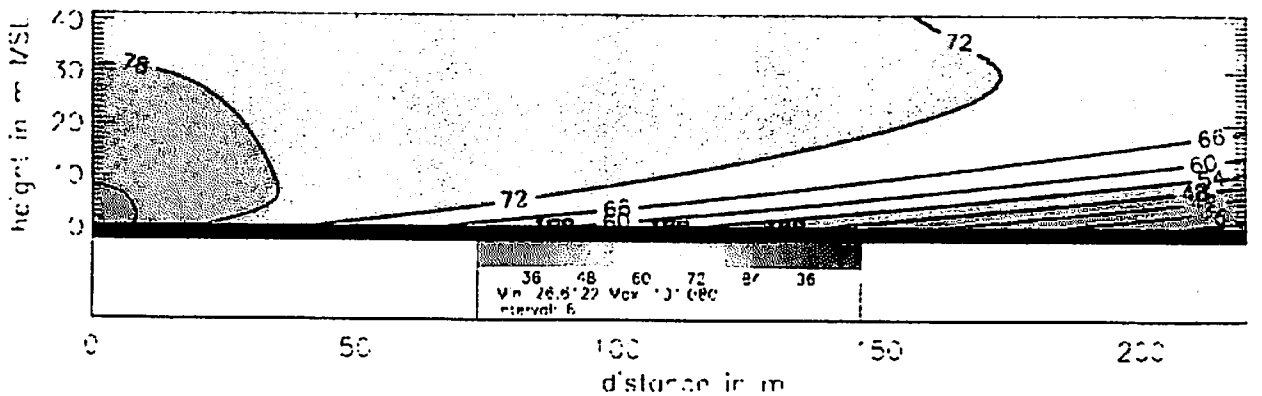

Figure 3: Vertical cross-section of sound level (dB) for upwind propagation in a non-turbulent atmosphere.

In a first set of simulations the effect of frozen turbulence was investigated. The numerical turbulence generator was invoked at the beginning of the simulation. An ensemble of ten simulations were performed with different realisations of turbulence. Some results are displayed in Figure 4. It shows the simulated distribution of sound level for two of the ten turbulence realisations (panels b and c). They are apparently distorted as compared with the non-turbulent case (panel a). The energy-equivalent mean sound level (panel d) that was averaged over the ten results still shows irregularities. The sound level difference between the average turbulent case and the non-turbulent case (panel e) is generally below 1 dB. Only in the shadow zone the turbulence causes an increase of the sound level by up to 3 dB.

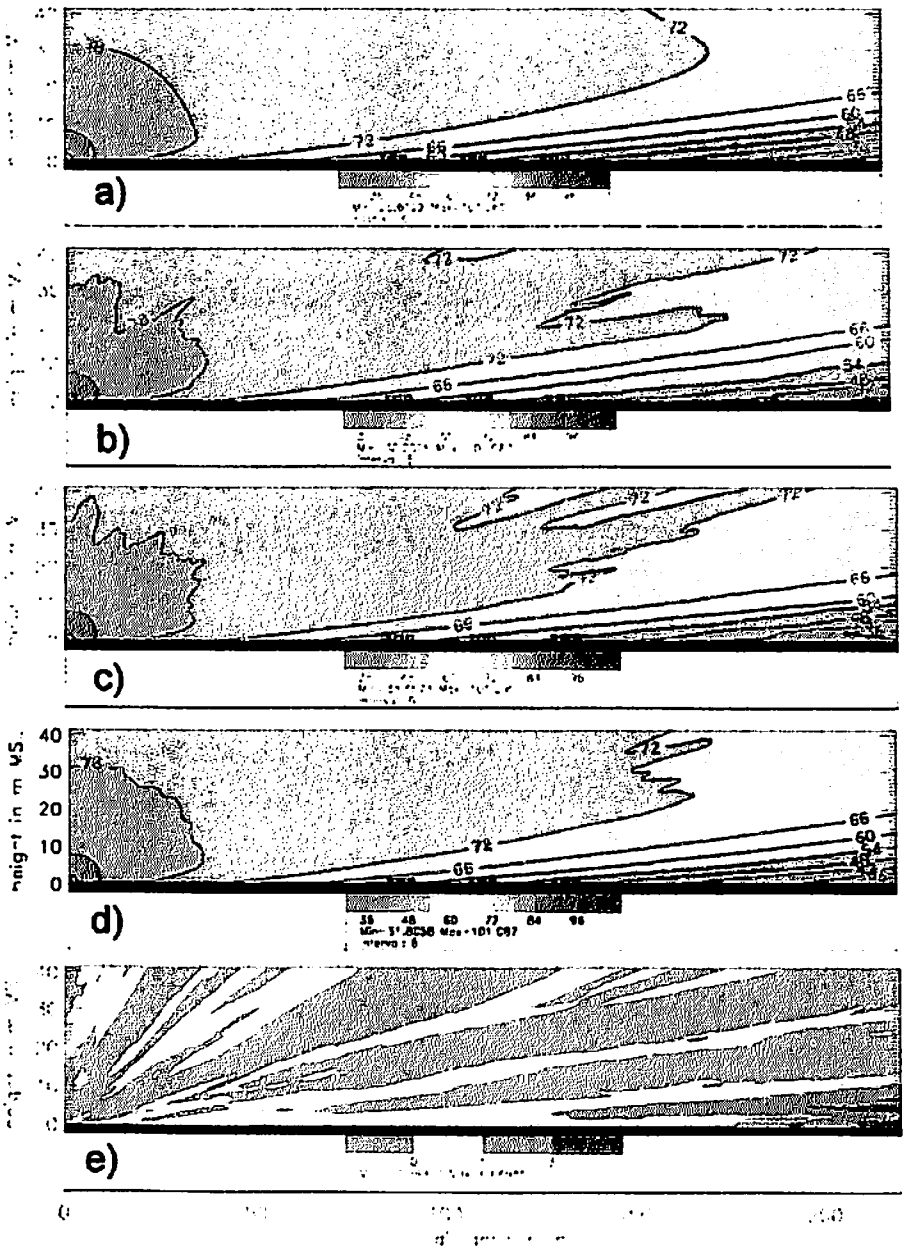

Figure 4: Vertical cross-sections of the sound level (dB) resulting from frozen turbulence LE model simulations. (a) non-turbulent reference, (b) and (c) two different turbulence realisations, (d) mean sound level over 10 turbulence realisations, (e) effect of the turbulence (sound level difference (d) minus (a)).

In a second set of simulations the concept of transient turbulence was applied. Variations were accomplished with respect to the simulation time and the time interval for the exchange of turbulence realisations. Both parameters determine the number of different turbulence simulations.

The duration τ of a sound propagation simulation is given by

$$\tau = m \cdot \tau_{\min} = m\frac{L}{c} \quad ; \quad m > 1$$

where L is the length of the computational domain and c is the speed of sound. $\tau_{\min}$ is the travel time of the sound from the source to the domain boundary and defines the minimum simulation time. Simulations were performed for m=1, m=2, and m=3.

The exchange interval $\Delta\tau$ of turbulence realisations was set to

$$\Delta\tau = n \cdot \frac{1}{f}$$

where f is the frequency. Simulations were accomplished for n=1 and n=3.

Eventually, the number of turbulence realisations during one simulation is given by

$$N = \frac{\tau f}{n}$$

For the performed simulations with transient turbulence N varies between 116 and 636.

As compared with the frozen turbulence runs (m = 1; $n = \tau f$, N = 1) a far greater number of turbulence realisations can be considered with the transient turbulence concept at the computational cost of just one (m=1) or two (m=2) frozen turbulence runs.

The results seem to justify the application of the transient turbulence concept as Figure 5 shows. Again we find an increase of the sound level in the shadow zone by more than 3 dB. However, the resulting difference field (Fig. 5e) is much smoother than the corresponding field for 10 frozen realisations (Fig. 4e).

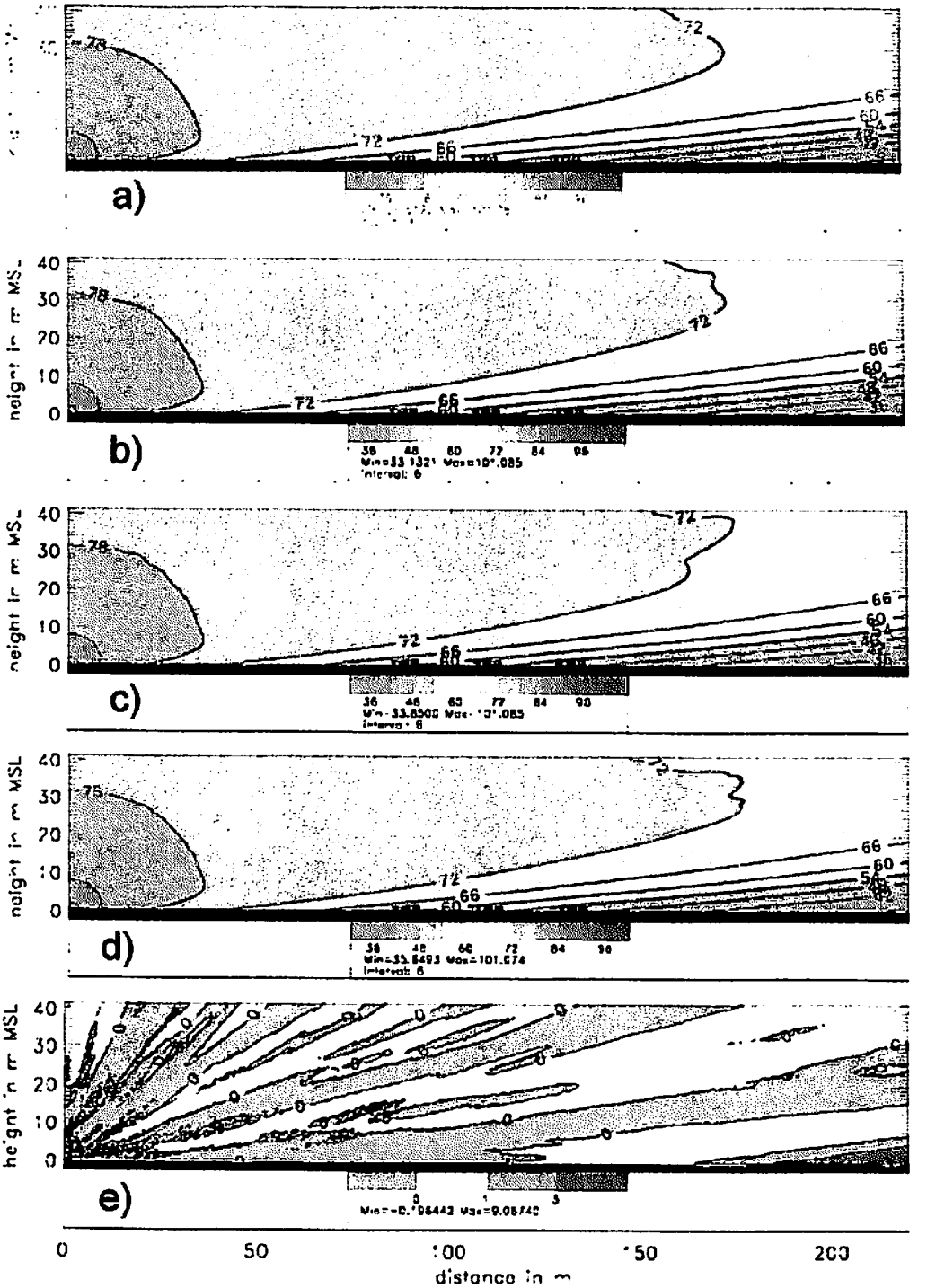

Figure 5: Vertical cross-sections of the sound level (dB) resulting from transient turbulence LE model simulations. (a) non-turbulent reference, (b),(c) and (d) two different turbulence realisations, (e) effect of the turbulence (sound level difference (d) minus (a)).

6 Comparison with other results

A further transient turbulence simulation was performed in order to compare the results of the LE model with results of a parabolic equation (PE) model that were attained by Blanc-Benon et al. [8]. In this simulation a tone with a frequency of $f = 424$ Hz was emitted at 3.7 m above ground. The pertinent sound level was evaluated as a function of range again at 3.7 m above ground. A constant temperature and a logarithmic wind profile

$$u(z) = -2\frac{\mathrm{m}}{\mathrm{s}}\ln\left(\frac{z}{0.006\mathrm{m}}\right) \quad \text{for} \quad z \geq z_o = 0.01\,\mathrm{m}$$

were assumed (upwind sound propagation). The turbulent kinetic energy was set to $\overline{E} = 0.5\,\sigma_{U'}^2 = 0.5\,\mathrm{m^2 s^{-2}}$ and thus agrees with the prescribed standard deviation of the turbulent wind speed fluctuations of $\sigma_{U'} = 1\,\mathrm{m\,s^{-1}}$ in [8]. Turbulent density fluctuations were neglected in both simulations. In other aspects the generation of turbulence does not completely agree. The random Fourier mode (RFM) technique used in [8] is different from the turbulence generator that was applied here. For the LE simulation 50 size classes of turbulent eddies with diameters between $L = 0.28$ m and $L = 245$ m were defined. This corresponds to turbulence wave numbers between $k = 22.4\,\mathrm{m^{-1}}$ and $k = 0.025\,\mathrm{m^{-1}}$. In [8] 400 spectral modes between $k = 10^3\,\mathrm{m^{-1}}$ and $k = 10^{-3}\,\mathrm{m^{-1}}$ were used. Sensitivity tests in [8] show that a shift in the cut-off wave number from $10^3\,\mathrm{m^{-1}}$ to $10\,\mathrm{m^{-1}}$ does not influence the scattering of 424 Hz sound waves. As a further difference, a van Karman spectrum was applied in [8] while the spectrum was based on the pure $k^{-5/3}$ law in this paper. However, within the range of resolved turbulence wave numbers the van Karman spectrum does not differ much from the $k^{-5/3}$ law. The LE model was run in the transient turbulence mode with $N = 636$ turbulence realisations. A total number of 20 PE simulations were performed for different frozen states of turbulence.

Figure 6 shows remarkable similarities between LE and PE results. In both simulations the sound level relative to free field propagation levels off inside the shadow zone approx. 170 m away from the source. From there it remains at a value of about -40 dB. The figure also shows that the average of the 20 frozen turbulence PE simulations is less smooth than the LE result which is based on 636 transient turbulence situations.

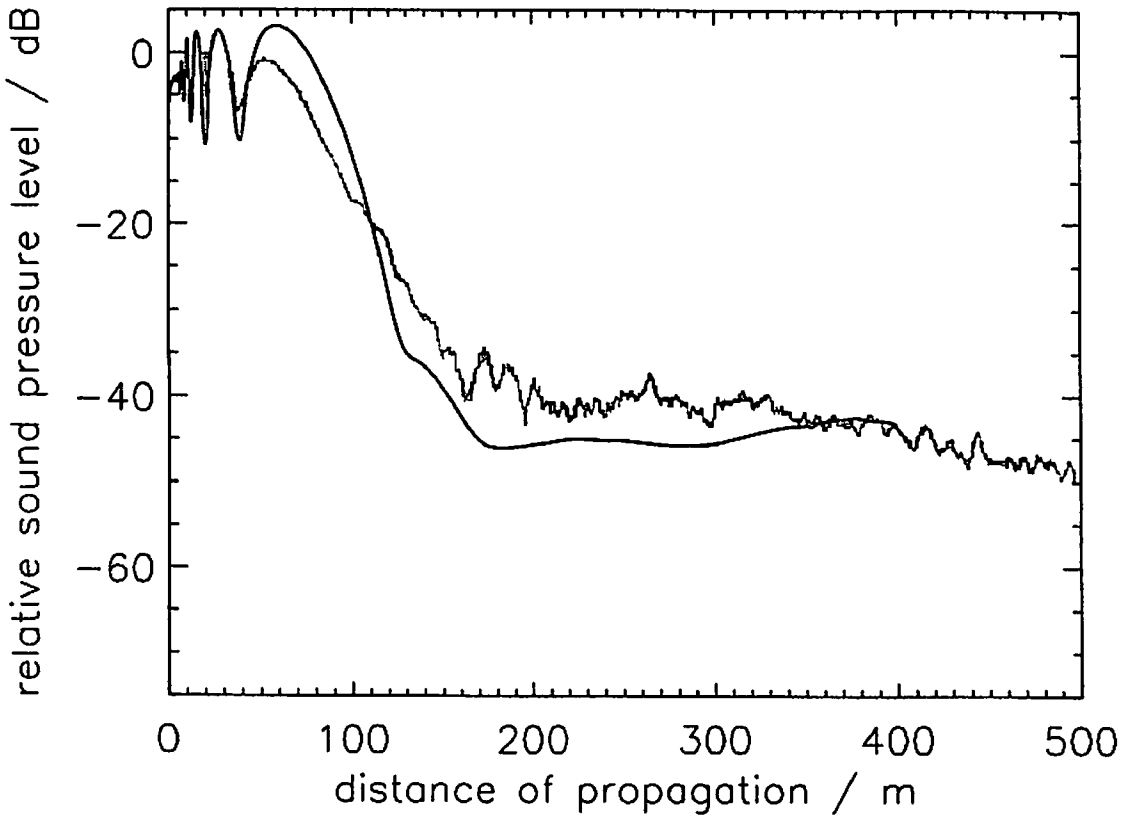

Figure 6: Comparison of the transient turbulence LE model result (black curve) with the average of 20 frozen turbulence PE model results (red curve) for nearly the same meteorological condition. The PE result was adapted from Figure 8a in [8].

7 Conclusions

In this paper an efficient method is introduced to consider non-divergent transient turbulence patterns in a linearised Euler (LE) time-domain model. The time integration of the LE model makes it possible to allow for a greater number of transient turbulence states during only one single simulation. The transient turbulence concept therefore requires significantly less computer time than the traditional frozen turbulence concept which is based on a high number of simulations. Numerical experiments show that the concept of transient turbulence produce results that are in agreement with those attained by applying the frozen turbulence concept but at much less computational expenses.

References

[1] Pierce A.D., 1981: Acoustics - An introduction to its physical principles and applications. McGraw-Hill, New York, Section 1.5.

[2] Ostashev V.E., 1997: Acoustics in moving inhomogeneous media, E & FN Spon, London, Section 2.1.

[3] Caine P., Walkden F., West M., 1988: On a non-linear phenomenon in two and three dimensional sound propagation. 3rd Symp. Long-Range Sound Propagation, Jackson, Mississippi USA, March 1988.

[4] Blumrich R., Heimann D., 2002: A linearized Eulerian sound propagation model for studies of complex meteorological effects. J.Acoust.Soc.Am., 112, 446-455.

[5] Salomons E.M., Blumrich R., Heimann D., 2002: Eulerian time-domain model for sound propagation over a finite-impedance ground surface. Comparison with frequency-domain models. Acta Acustica, 88, 483-492.

[6] Wilson D.K., 2000: A turbulence spectral model for sound propagation in the atmosphere that incorporates shear and buoyancy forcings. J.Acoust.Soc.Am., 108, 2021-2038.

[7] Salomons E.M., Ostashev V.E., Clifford S.F., Lataitis R.J., 2001: Sound propagation in a turbulent atmosphere near the ground: an approach based on the spectral representation of refractive-index fluctuations. J.Acoust.Soc.Am., 109, 1881-1893.

[8] Blanc-Benon Ph., Dallois L., Juvé D., 2001: Long range sound propagation in a turbulent atmosphere within the parabolic approximation. Acta acustica, 87, 659-669.

[9] Metais O., Ferziger Joel (Eds.), 1997: New Tools in Turbulence Modelling: Les Houches School, May 21-31, 1996 (Centre De Physique Des Houches, 5), Discussion of large-eddy simulation and direct numerical simulation in turbulence modeling. Springer Verlag, Berlin.

[10] Heimann D., Groß G., 1999: Coupled simulation of meteorological parameters and sound level in a narrow valley. Applied Acoustics, 56, 73-100.

The modelling of long range sound propagation: recent developments in the PE method.

Laurent Dallois Philippe Blanc-Benon Daniel Juvé

Centre Acoustique, LMFA UMR 5509
École Centrale de Lyon, 69134 Écully Cedex, France.

Abstract

Acoustic waves propagating in the atmosphere are strongly influenced by the environment. Acoustic signals vary in both space and time, and the dominant source of this variability is the turbulence of the atmospheric boundary layer. Even if the turbulence does not play a significant role for line-of-sight propagation, its effects are of main importance for sound scattering in the acoustic shadow zones and for long range propagation. Nevertheless not all the turbulent fields are of equal importance in the turbulent scattering process, and the turbulence spectrum used in our numerical simulation could be cut below a "cut-off" limit depending of the turbulence model and of the PE method.

In this paper, we examine the influence of scale resolution on numerical simulation of long range sound propagation through the atmosphere. Specifically, we answer the questions: How does the inclusion/exclusion of statistical inhomogeneities of the turbulent field affect our results, what portion of the velocity and temperature spectra must be adequately resolved. The "cut-off" scale introduced by the turbulence modelling, give us a minimum step of advancement for a numerical simulation based on a wide-angle PE algorithm. However, especially for a three-dimensional resolution, this marching step would be still to small to have an efficient algorithm with acceptable CPU times. By using the phase screen method, this step can be increased without loosing significant details in the numerical simulation. When it comes to the case of acoustic propagation in the presence of wind, the phase screen method should be modified in order to incorporate the influence of the wind velocity and wind velocity gradients. Numerical simulations will be presented to illustrate the efficiency of the new numerical scheme, and to demonstrate how the prediction of sound pressure levels over long propagation distances are affected by these additional terms which incorporate the influence of both the mean and the fluctuating wind components.

1 Introduction

Parabolic equations (PE methods) are well suited to model the sound propagation over large distances into inhomogeneous medium. However, they are restricted to problems where all the acoustic paths between the source and the receiver remain close to a straight line, the line-of-sight. During the last decades, wide-angle parabolic equations (WAPEs) have been investigated in order to extend the methods to more complex medium where acoustic paths between the source and the receiver are more distinct [1]. Using a better approximation for the propagation operator, the validity angle of the PEs can be increased. For example, Taylor series of higher orders can be used. Unfortunately, it appears this is not sufficient when it comes to moving medium as the atmosphere. To get consistent WAPEs, the propagation operator has also to be modified in order to model velocity effects at larger propagation angles. Whereas small-angle PEs need only one component of the velocity field, the projection on the direction of propagation, WAPEs have to keep the whole components

of the velocity field. Recent WAPEs have been proposed to take care of such cases, and the first section of this paper is devoted to them.

The wide-angle improvements of the PE methods should not degrade its efficiency considering swiftness, stability or versatility. These qualities are of the most importance in the perspective of three dimensional computations as an increase factor of 100 to 1000 is expected for the number of mesh points. Even if the memory on current computers is sufficient for such 3D cases, any slowdown in the numerical methods would be a real trouble. One other advantage of WAPEs when compare to classical PEs is that Δx, the advancement step of the numerical resolution, can be increased if a large validity angle is not of concern. Thus, WAPE resolutions need less computational steps than equivalent PE resolutions. So, depending on the duration of one iteration of the numerical resolution, the total CPU time can be reduced. This is moreover true when the program is intend to run on a parallel computer. The second section of this paper deals with the well known split-step Padé algorithm and how it can be extend to higher order keeping in mind the improvements on the velocity inclusion proposed in the first section.

If a larger Δx reduces the running time of the code, it also diminishes the sensitivity to the smaller inhomogeneity scales of the medium. The larger is the advancement step, the smoother appears the medium to the PE solver. A solution to incorporate small scale effects of a motionless medium is to use the phase screen method. For each step, the mean effects of the smaller scales are included through a multiplicative phase term. However, such a method is no more valid for a moving medium. In the third section of this paper, the phase screen method is extended to take care of the smaller inhomogeneities of the turbulent field. The drawback is the phase term becomes an operator which involves more calculations.

2 The wide angle parabolic equation in a moving medium

The best way to get a PE including velocity terms is to depart from a wave equation for sound propagation in an inhomogeneous moving media. As no exact wave equation can be derived from the Euler's equations in presence of a velocity field, some more assumptions on velocity are needed. Depending on the choice of these assumptions, different wave equations are derived, leading to different PEs. In this part, two WAPEs are presented using two different wave equations. One of the WAPEs has been presented by Dallois *et al.* [2] and the other one by Ostashev *et al.* [3]. A WAPE for moving media has been also derived by Godin (see [4] and [5]). This equation is very similar to the second WAPE described in this section and it is the reason why this equation is not discussed in this paper.

The first wave equation is adequate for medium whose length scale, L, are much greater than the acoustical length scale, $\lambda \ll L$. Actually, this wave equation is exact for uniform moving medium; it is known in the literature as the convected wave equation. For an harmonic source of frequency $\omega = kc$, c being the speed of sound, the wave equation becomes:

$$\left[\Delta + k^2 - \frac{2ik}{c}\, \boldsymbol{v}\cdot\boldsymbol{\nabla} + \frac{v_i v_j}{c^2}\frac{\partial^2}{\partial x_i \partial x_j}\right] p'(r) = 0, \tag{1}$$

where p' denotes the acoustic pressure, and $\boldsymbol{v}$ stands for the velocity in the medium. The density of the medium is assumed to be uniform in the whole paper.

As a one way equation is needed, the forward and backward acoustical waves are split to keep only the forward direction. Thus, a "general" parabolic equation is obtained:

$$\frac{\partial p'}{\partial x} = ik\sqrt{1+\mathcal{L}}\, p'. \tag{2}$$

The operator $\mathcal{L}$ depends on the wave equation previously chosen. In order to calculate the square root of an operator, it has to be approximated using a finite development like a

truncated Taylor series for example. To get a wide angle parabolic equation, the square root is approximated by a Padé approximation at the order (1,1):

$$ik\sqrt{1+\mathcal{L}} = ik\frac{1+p\mathcal{L}}{1+q\mathcal{L}}.$$

This method has first been employed by Claerbout [6] using the Helmholtz equation as wave equation. An assumption on the velocity of the medium is needed in the process; the Mach number $M = v/c$ has to be less than one, *i.e.* $v \lesssim c$. The maximum order of the parabolic equation is $\mathcal{O}(\mu M, M^2)$ where $\mu = c/c_0 - 1$ and c_0 is a reference sound speed. During the derivation appears occurrences of the derivative $\partial p'/\partial x$ associated to terms of order M and M^2. To keep only the $\partial p'/\partial x$ located at the left side of the equation, they are replaced recursively using the equation itself. Only the terms of the relevant order for the derivation are kept.

When this process is applied to the wave equation (equation (1)) for large scale velocity inhomogeneities, a wide angle parabolic equation is obtained which for two dimensional problem is written as:

$$\left[1 + q\mathcal{F}_1 - ipk\mathcal{M}_1 - qk^2\mathcal{M}_1^2\right]\frac{\partial\psi}{\partial x} = ik\left[(p-q)\mathcal{F}_1 + ik(p-q)\mathcal{M}_1 - iqk\mathcal{M}_1\mathcal{F}_1 + qk^2\mathcal{M}_1^2\right]\psi, \quad (3)$$

where:

$$\mathcal{F}_1 = \frac{1}{c^2 - v_x^2}\left[c_0^2 + 2i\,c_0\frac{v_x}{k}\frac{\partial}{\partial z} + \frac{c^2 - v_x^2}{k^2}\frac{\partial^2}{\partial z^2}\right] - 1,$$

$$\mathcal{M}_1 = \frac{2v_x}{k(c^2 - v_x^2)}\left(i\,c_0 - \frac{v_x}{k}\frac{\partial}{\partial z}\right).$$

ψ stands for the complex amplitude of the acoustical field and is related to p' by the relation $p' = \exp(ikx)\,\psi$. This equation is named MW-WAPE for Mean Wind Wide Angle Parabolic Equation. An extended derivation of this equation can be found into [2] and [7].

The second wave equation is intended to be used for sound propagation into weakly turbulent medium. This time, the assumption $\lambda \ll L$ is reduced to the weaker one $\lambda \lesssim L$ but an assumption on the Mach number is added. The Mach number has to be much less than one, $v \ll c$ (as oppose to the $v \lesssim c$ of the MW-WAPE). The monochromatic version of this wave equation is:

$$\left[\Delta + k^2 - \frac{2ik}{c}\,\boldsymbol{v}\cdot\boldsymbol{\nabla} - \frac{2i}{kc}\frac{\partial v_i}{\partial x_j}\frac{\partial^2 p'}{\partial x_i\,\partial x_j}\right]p'(r) = 0. \quad (4)$$

The order of this equation is $\mathcal{O}(\mu\lambda/L, M\lambda/L)$. As expected, this equation is very similar to the equation 1 except for the last term which involve the gradient of the velocity field in place of a term depending on M^2. Starting from the wave equation derived by Godin [8], the same WAPE would be obtained as Godin's wave equation differs from the equation (4) by weaker order terms than the ones kept into the development of the PE (equation (4)).

If the same procedure is applied to the multi scales wave equation (4), an other wide-angle parabolic equation is obtained. In two dimensions, this equation is:

$$\left[1 + q\mathcal{F}_2 - ipk\mathcal{M}_2\right]\frac{\partial\psi}{\partial x} = ik\left[(p-q)\mathcal{F}_2 + ik(p-q)\mathcal{M}_2 - \frac{iq}{k}\mathcal{M}_2\frac{\partial^2}{\partial z^2}\right]\psi, \quad (5)$$

where:

$$\mathcal{F}_2 = \epsilon + \frac{2i}{k}\left(\frac{\partial M_x}{\partial x} + M_z\frac{\partial}{\partial z}\right) + \frac{1}{k^2}\left[1 + \frac{2i}{k}\left(\frac{\partial M_x}{\partial x} - \frac{\partial M_z}{\partial z}\right)\right]\frac{\partial^2}{\partial z^2},$$

$$\mathcal{M}_2 = \frac{2i}{k} M_x - \frac{2i}{k^3} \left(\frac{\partial M_x}{\partial z} + \frac{\partial M_z}{\partial x} \right) \frac{\partial}{\partial z}.$$

This equation is denoted in this paper as TW-WAPE for Turbulent Wind Wide Angle Parabolic Equation. An extended derivation this equation can be found into [3], [9] and [7]. It can be noticed that if all the velocities in (3) and (5) are zero, these equations reduce to the classical Padé(1,1) PE derived from the Helmholtz equation. Finally, Ostashev *et al.* [10] presented recently an other WAPE combining both of the two WAPE described in this paper. The idea is to divide the medium fields into two parts depending on the length scales and to process each of these parts using the more appropriate WAPE.

The diffraction of a plane wave by an infinite core vortex was used as a test case for the two WAPEs presented here(see [11]). This problem has already been studied in [12], [13] and [14] using analytical and computational works. Candel [15] already tries to apply the PE method to this problem using a small-angle parabolic equation. On the figure 1 is plotted the configuration which is used and on the figures 2(a) and 2(b) are plotted some of the results. The curves correspond to the amplitude of the scattered sound wave (scattering cross section) along a circle of radius 2.5λ centered on the core of the vortex. The circulation Γ is such that the Mach number of the problem is 0.5. The maximum of the velocity field is reached at a distance $D = \lambda/4$ from the center of the vortex. The curves are plotted only for the forward angles where the PEs are valid. The plain curve is a reference solution obtained using a code (SPRINT-2D from Bailly [16]) solving the linearized Euler's equations. The result given by a WAPE which not fully integrated the velocity components is plotted on the left graph (figure 2(a)) and is quite different from the reference solution. The result given by a MW-WAPE is plotted on the right graph (figure 2(b)). The reference result is now well reproduce. Actually, even the M^2 variation of the amplitude along the forward direction ($\theta = 0$) is obtained (see [11]).

3 Higher-Order split-step Padé

The two WAPEs presented in the section 2 (equations (3) and (5)) are derived using a Padé (1,1) approximation. However, higher Padé approximants could have been used in order to increase the validity domain of the method. Lets say a word on the split-step Padé methods has proposed by Collins (see [17] and [18]).

The split-step Padé method goes one step further into the exact resolution of the equation (2). A general solution of this equation for a single advancement step Δx is:

$$\psi(x + \Delta x) = \exp\left\{ ik \int_x^{x+\Delta x} \left(\sqrt{1 + \mathcal{L}} - 1 \right) \mathrm{d}x' \right\} \psi(x). \tag{6}$$

as long as $\mathcal{L}$ is not including some $\partial/\partial x$ operator. If ever, the x-derivatives have to be replace using the chosen wave equation for the even derivative or an appropriate expansion of the equation (2) for the odd derivative. As previously, only terms of the relevant orders has to be kept. If the medium is mostly invariant over the advancement step Δx, the square root can be removed from the integral. This means that the length scales of the medium are greater than Δx. Thus, a simpler equation of propagation is obtained:

$$\psi(x + \Delta x) = \exp\left\{ ik\Delta x \left(\sqrt{1 + \mathcal{L}} - 1 \right) \right\} \psi(x). \tag{7}$$

The operator $\mathcal{L}$ is enclosed into an exponential and it is this exponential, lets denote it by $\mathcal{Q}$, which has to be expanded using Padé approximants. An important improvement is that the coefficients of the expansion are now depending on the wave number k. A second important advantage is that increasing the order of the expansion is simpler and the resulting numerical

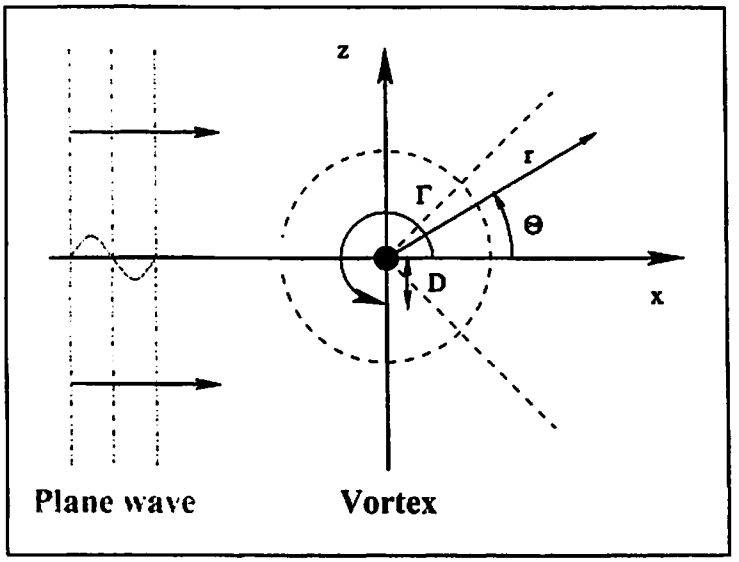

Figure 1: Sound scattering by a vortex : scheme

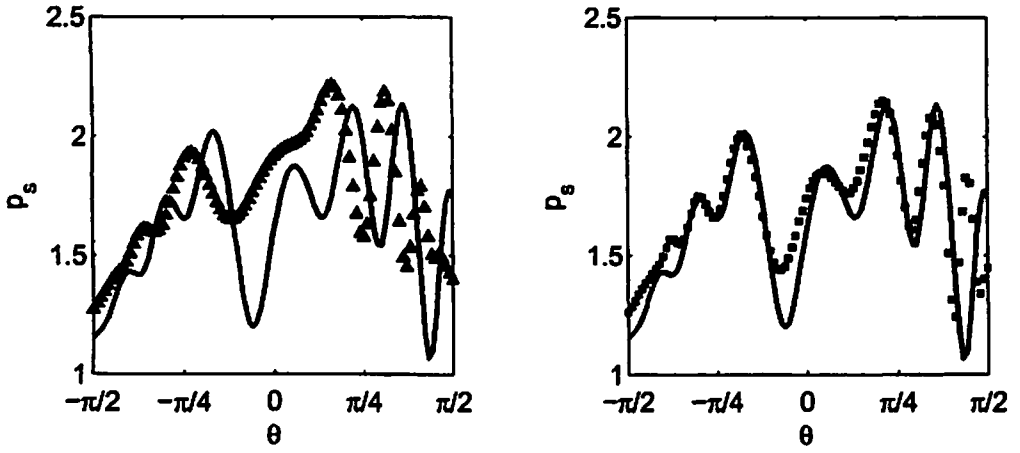

(a) WAPE resolution

(b) MW-WAPE resolution

Figure 2: Sound scattering by a vortex : $M = 0.5$
(——) reference solution, (▲) standard WAPE, (■) MW-WAPE.

scheme is more accurate. However, the Padé approximation as a rational fraction of two polynomials of degree n:

$$\mathcal{Q}_{n,n} = \frac{1 + p_1\mathcal{L} + \cdots + p_n\mathcal{L}^n}{1 + q_1\mathcal{L} + \cdots + q_n\mathcal{L}^n} \tag{8}$$

is not of much use. Actually, it is better to write the expansion as a sum or a product of fractions including only first degree polynomial:

$$\mathcal{Q}_{n,n} = 1 + \sum_{i=1}^{n} \frac{\alpha_i\mathcal{L}}{1 + \beta_i\mathcal{L}} \tag{9}$$

or

$$\mathcal{Q}_{n,n} = \prod_{i=1}^{n} \frac{1 + \mu_i\mathcal{L}}{1 + \nu_i\mathcal{L}} \tag{10}$$

This could be done by finding the roots of the denominator of the equation (8). These roots correspond to the inverse of the β_i and ν_i. The α_i and the μ_i in (9) and (10) are found by solving a system involving the p_i and the q_i. Details can be found into [7].

Each of the previous series has its interest. The sum is especially useful if the code is intended to be parallelize. Each fraction can be solved by a different process on a different CPU. Doing this, a higher order for the approximation does not change much the resolution time if the process number is also increase. In that case, it is worthwhile using a longer advancement step Δx. The product approximation is less devoted to the acceleration of the problem resolution than to the increasing of the validity angle of the PE. The rational fractions of the product has to be solved sequentially. As the CPU time to solved each fraction is similar to the one to solve the Padé (1,1) approximation, Δx has to be n-times greater than the classical advancement step to have a time improvement. Actually, this is not true and time of resolution is greater using this decomposition when compare to the Padé (1,1) development:

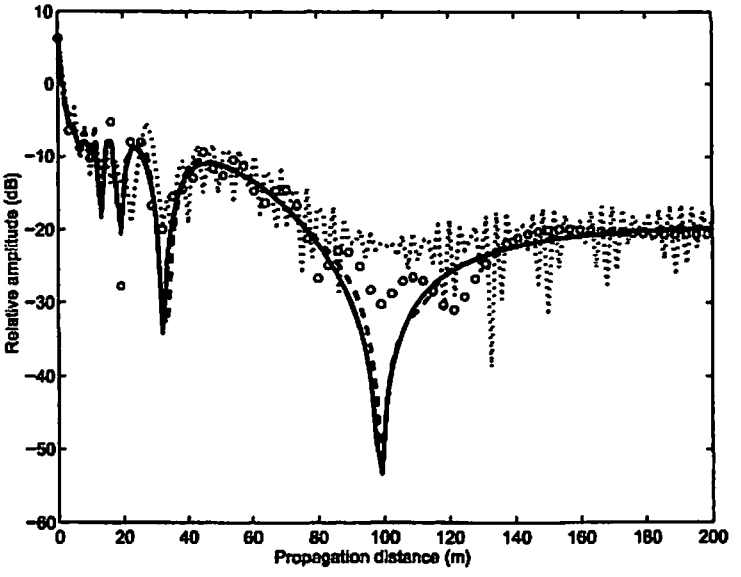

Figure 3: Propagation over the ground for a fixed $\Delta x = 1.6\lambda$
(——) Padé (8,8), (- - -) Padé (4,4), (o) Padé (2,2), (· · ·) Padé (1,1).

On the figure 3, transmission losses for a point source above the ground are plotted for different orders of the Padé development. A model of rigid ground is used there but

impedance model could also been applied (see [7]). The product expansion of the Padé approximant is used here (equation (10)). The advancement step is fixed to the value $\Delta x = 1.6\lambda$ where λ is the wavelength of the acoustic wave. The Padé (1,1) development is unable to calculate the acoustic field for such a long Δx. Actually, it would work for an advancement step eight times smaller, $\Delta x = 0.2\lambda$. The development of the operator should be at least a Padé (4,4) approximation to get somewhat like the actual acoustic field. Finally, a good result is obtained for the Padé (8,8) as it could have been expected.

One problem of increasing the order of the approximation is the stability of our numerical scheme. One advantage of the product approximation on the sum one is that the stability is assumed if the associated ν_i and μ_i are complex conjugate. Actually, using a numerical code to find the roots of the polynomials, this has to be forced into the program to avoid instability due to rounding errors. However, Padé (8,8) approximants are the highest order which has been achieved with success. At higher orders, the norm of ν_i and μ_i are becoming larger and larger, bringing an other kind of instability into the code. At least, the Padé (8,8) approximants correspond to a Taylor development of order 16 (a polynomial of degree 16).

Them the validity angle is of concern, one other problem is that at the higher order the gain on the angle is weak and it is difficult to increase it beyond 60 degrees on both side of the propagation direction. The initial condition is also a limiting factor. The initial condition has also a validity angle which has to be respected. The validity angles of both the WAPE and the initial condition should remain mostly the same. Actually, the Gaussian source is derived using the exact solution of the simpler small-angle PE. This means its validity angle is the same than the one of a standard PE, more or less 15 degrees. This is not enough when using WAPEs with a larger validity angle and other initial conditions have to be used as numerical starters.

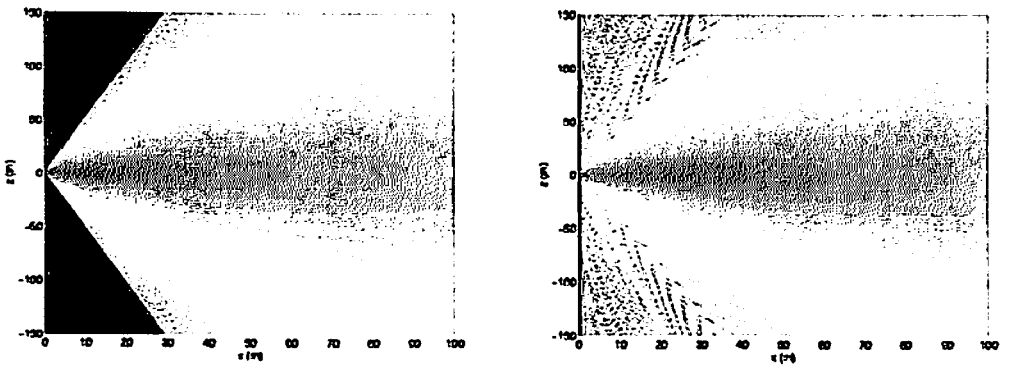

(a) Split-step Padé (1,1)

(b) Split-step Padé (4,4)

Figure 4: Transmission loss in a uniform medium : $\nu = 340$ Hz.

To illustrate the increasing of the angle of validity, the acoustic field obtained for two different Padé development for propagation in a uniform medium are compared on figure 4. The initial condition is the one proposed by Greene [19] for the WAPEs. On the left figure (figure 4(a)) a Padé (1,1) is used. The limitation on the resolution angle is clearly seen there. As expected, on the right figure (figure 4(b)) where a Padé (4,4) is used, the acoustic field is more expanded around the forward direction. However, even if the solution is no more contained by PE limitation, it looks like a sound beam and not like the acoustic field generated by a point source. This is due to the limiting angle of the initial condition which is actually an initial condition for a sound beam.

4 The phase screen method

In the previous section (3), it has been showed that it is sometimes of interest to use a large advancement step Δx. However, a large numerical step filters the smaller inhomogeneities of the medium. Actually it affects all the inhomogeneities smaller than the length Δx itself. To counteract this, the simulation have to take account of the field values between x and $x+\Delta x$. These smaller scales are of importance when turbulent medium are considered. The phase screen method (see Gilbert *et al.* [20]) is based on the assumption that the medium fields can be written as the sum of a mean part, which includes the larger scales, and a spatially fluctuating part including the smaller ones. On the figure 5 is plotted a schematic energy spectrum of the underlying medium. In one hand, the larger scales denoted by L include not only the large scale of the turbulent field but also the mean field of the problem such as the atmospheric profile. On the other hand, the small scales denoted by l contains mainly the tail of the turbulent spectrum. The separation between the two contributions (large scales, small scales) is chosen as being the length Δx. So, the spectrum is cut at the wave number $k_c = 2\pi/\Delta x$ which is close to the acoustical wave number of the source k. This separation length can be seen as a "cut-off" limit of the inhomogeneities of the media. Below this limit, only the mean effect of the inhomogeneities are retained. In the paper, the choice to link this length to the advancement step Δx has been done. Even if it seems a reasonable one, a smaller limit could have been chosen.

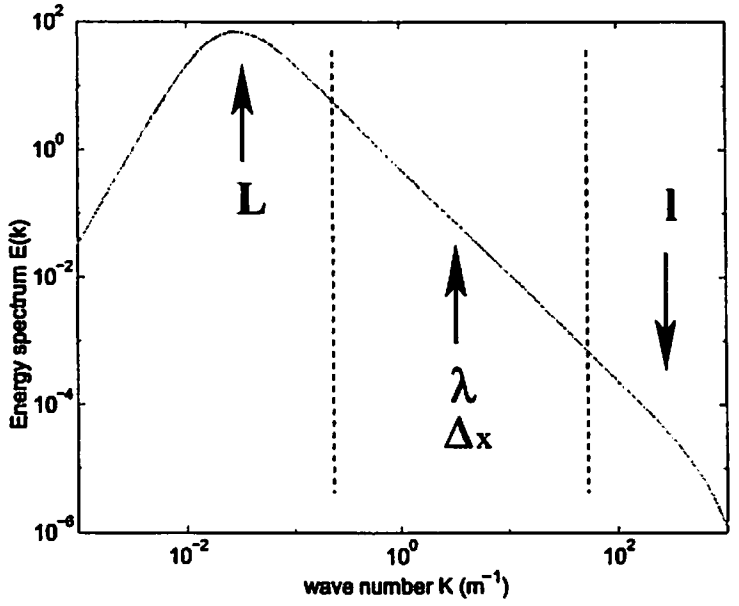

Figure 5: Splitting between the large and the small length scales.

Doing the separation, all fields are split as:

$$n = 1 + \mu_0(X, Z) + \epsilon\mu_1(x, z)$$

and

$$v = v_0(X, Z) + \epsilon v_1(x, z)$$

where the 0 index denotes the mean part of the medium variables, the refractive index n and the velocity v, and the index 1 denotes the fluctuating part these variables. The ϵ coefficient indicates the smallness of the terms into the fluctuating part compare to the ones into the

mean part. The difference which is assume between the variables (X, Z) and (x, z) is that (X, Z) are of order $\mathcal{O}(1)$ when they are similar to L ($L \gg \Delta x$) and (x, z) are of order $\mathcal{O}(1)$ when they are similar to l ($l \ll \Delta x$).

The operator $\mathcal{L}$ depends on the medium variables n and v and can be also split into a mean part, $\mathcal{L}_0$, and a fluctuating part $\mathcal{L}'$. Due to the small coefficient ϵ, $\mathcal{L}'$ can be moved out from the square root using first order approximation and assuming that $\mathcal{L}_0$ and $\mathcal{L}'$ can commute, the equation (6) is transformed as:

$$\psi(x+\Delta x) = \exp\left\{\frac{ik}{2}\int_x^{x+\Delta x} \mathcal{L}'\,\mathrm{d}x'\right\} \exp\left\{ik\int_x^{x+\Delta x}\left(\sqrt{1+\mathcal{L}_0}-1\right)\,\mathrm{d}x'\right\}\psi(x). \quad (11)$$

Now, two operators are applied to $\psi(x)$; the first one is related to the fluctuating part of the medium and the second one to the mean part. By construction, the length scales of the mean part are greater than the advancement step Δx. This satisfies the assumption used to pass from the equation (6) to the equation (7) (see section 3). Thus, the square root can be removed from the integral. However, this assumption is no more true when it comes to the fluctuating part of the medium and $\mathcal{L}'$ has to be kept inside the integral. As the $\mathcal{L}$ operator is a linear combination of derivatives along directions perpendicular to x, the integral affects only the coefficients of the derivatives. So μ', v' or combinations of them as just to be replaced by their mean values on the interval from x to $x+\Delta x$. For example:

$$\tilde{\mu} = \frac{1}{\Delta x}\int_x^{x+\Delta x} \mu'\,\mathrm{d}x' \quad \text{and} \quad \tilde{v}_i = \frac{1}{\Delta x}\int_x^{x+\Delta x} v_i'\,\mathrm{d}x'.$$

Using the resulting operator which is denoted by $\tilde{\mathcal{L}}$, the equation (11) becomes:

$$\psi(x+\Delta x) = \exp\left\{\frac{ik\,\Delta x}{2}\tilde{\mathcal{L}}\right\} \exp\left\{ik\,\Delta x\left(\sqrt{1+\mathcal{L}_0}-1\right)\right\}\psi(x). \quad (12)$$

which has to be solved using numerical methods.

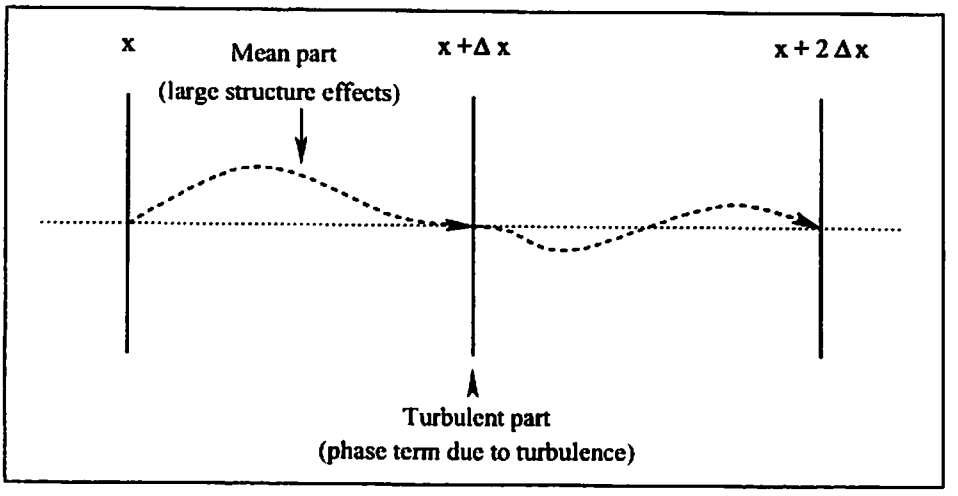

Figure 6: Phase screen method.

The idea behind the phase screen method is illustrated on figure 6. A very accurate solving method is used on the larger scales of the medium to get an appropriate frame for the acoustic field along the propagation. The smaller scale contributions are concentrated on small variations of the phase of this acoustic field which are applied at each step of the resolution. Whatever small are these variations, their cumulating effects strongly modified

the acoustic field. It is expected that, as long as the method uses a statistically good description of the smaller scales, it does not need to be as accurate as the one use for the mean field.

In a motionless medium, $\bar{\mathcal{L}}$ is reduced to $\tilde{\mu}$, a single scalar, and does not involved any derivative. Thus, this operator is just a multiplicative term, actually a phase term. This is no more true when velocity is involved. The coefficient into the exponential is a complex number including a real and an imaginary part. This means that the amplitude of the solution is also modified by the fluctuating components of the medium. An explanation is that velocity components perpendicular to the direction of an acoustic wave are effective on the amplitude of the wave and not on the phase. An other explanation is that the larger scale are related to the refraction of the wave and the smaller scales are more related to the diffraction of the sound wave. As parabolic equation are unable to include backscattering wave, they are partly absorbed by the model and this explains the non-conservative form of equation (12).

A more important difference with the motionless case is that $\bar{\mathcal{L}}$ is involving derivative operator, and the exponential has to be expanded in some way to use it. The two operators have to be treated sequentially. The second exponential operator (the larger scale operator) is identical to the one previously encounters into the section 3 and can be solved using split-step Padé methods. Actually, the operator including the fluctuating part is solved using the same method at the same order. However to reduce solving time, simpler method such as split-step Padé (1,1) or even Taylor expansions could have been used. The phase screen method is particularly useful when the integral of the smaller scales is easily obtained, for example when using a stochastic field generated by summation of Fourier modes.

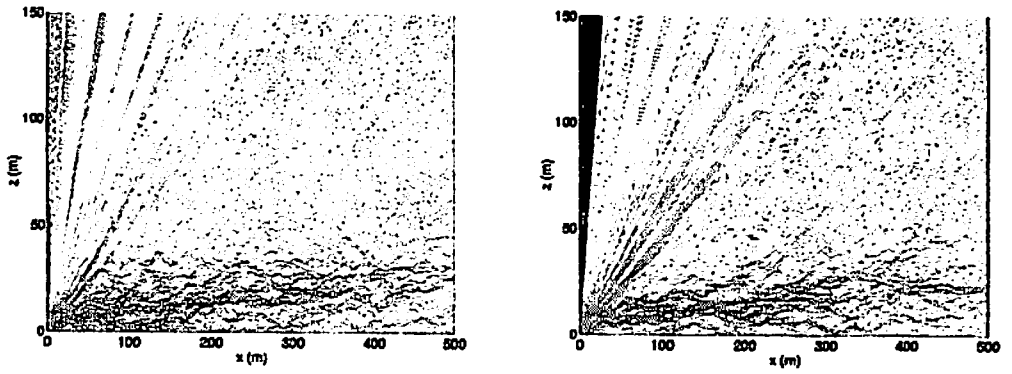

(a) $\Delta x = 0.1\lambda$ (b) $\Delta x = 0.8\lambda$

Figure 7: Transmission loss in a turbulent medium: split-step Padé (8,8), $\nu = 340$ Hz.

On the figure 7 is compared the acoustic field generated using phase screen method in moving medium with two different advancement steps Δx. On the left figure (fig. 7(a)), the step is 0.1λ long. That means the smaller scales are accurately resolved. On the right figure (fig. 7(b)), the step is eight times larger, $\Delta x = 0.8\lambda$. As the interest of this method is in the small scales, the sound diffraction into a shadow zone has been chosen as test case. The shadow zone is created by imposing a logarithmic profile of temperature. A stochastic velocity field generated by summation of Fourier modes is added as a model of an atmospheric turbulence; a von Kărmăn spectrum has been used. The same split-step Padé (8,8) numerical scheme is used for both of them. The two calculating fields are far from being the same but their global behaviour are mostly identical. Actually, if the results are averaging on several realisations of the turbulent field, the mean values are equal. Thus,

it is definitely less time consuming to use a split-step Padé (8,8) with $\Delta x = 0.8\lambda$ in order to approximate the mean acoustical field. However, higher statistical moments should also be investigated and it is expected the higher is the statistical moment, the worse are the results.

5 Conclusion

Parabolic equation methods for long range sound propagation into the atmosphere are now well known and widely used. The next steps is to increase the details of the atmospheric model. Up to now, the more general principles has been investigated using basic models for the propagating medium. A possible improvements could be to model propagating medium where velocity is related to temperature and density fields or to have a turbulent field resulting from DNS or LES simulations. Usual meteorological models are still unable to give such details, but ultimately they should be used as underlying medium to atmospheric long range sound propagation studies. However, the propagation models must also be improved to be able to integrate these new details. This is the purpose of the improvements of the WAPE methods presented in this paper. A realistic inclusion of the velocity field is an important step, and the equations of the section 2 seems to be a good starting point on this subject. Moreover, velocity effects are of main importance when acoustic wave propagation is used like a tomographic tool as velocity breaks the reversal principle. The split-step Padé method is a very general scheme as it can be used in a wide variety of ways. The order of the scheme can be easily modified to fit given requirements concerning the validity angle or the computation time. Finally, small scales effects are still an open question which can be investigated using the phase screen method. As it has been presented in this paper, phase screen method can be applied to other cases than the motionless medium. It is definitely a useful method when only averaged results are needing. It should be investigated further in order to obtain the "cut-off" frequency below which inhomogeneities does not affect sound propagation. This frequency would be related to the smaller scales to be resolved in atmospheric modelling.

References

[1] E.M. Salomons. *Computational atmospheric acoustics.* Kluwer Academic Publishers, 2001.

[2] L. Dallois, Ph. Blanc-Benon, and D. Juvé. A wide angle parabolic equation for sound waves in inhomogeneous moving media: Applications to atmospheric sound propagation in moving media. *J. Comput. Acoust.*, 9(2):477–494, 2001.

[3] V.E. Ostashev, D. Juvé, and Ph. Blanc-Benon. Derivation of a wide-angle parabolic equation for sound waves in inhomogeneous moving media. *Acta Acustica united with Acustica*, pages 455–460, 1997.

[4] O.A. Godin and A.V. Mokhov. Parabolic equation modeling of ocean current influence on acoustic field. In M. Weydert, editor, *European conference on underwater acoustic*, pages 280–283, Elsevier, 1992.

[5] O.A. Godin. A wide-angle, energy-conserving parabolic equation for sound in moving medium. In *Theoretical and Computational Acoustics'97*, pages 329–340. World Scientific Publishing, 1999.

[6] J.F. Claerbout. *Fundamentals of Geophysical Date Processing with Applications to Petroleum Prospect.* McGraw-Hill, New York, 1976.

[7] L. Dallois. *Propagation des ondes acoustiques dans les milieux en mouvement: extension grand angle de l'approximation parabolique.* PhD thesis ECL 2000-37, École Centrale de Lyon, 2000.

[8] L.M. Brekhovskikh and O.A. Godin. *Acoustics of Layered Media II*, volume 10 of *Wave Phenomena*. Spinger-Verlag, second edition, 1999.

[9] L. Dallois, Ph. Blanc-Benon, D. Juvé, and V. Ostashev. A wide angle parabolic equation for sound waves in moving media. In *Proc. Eight International Symposium on Long Range Sound Propagation*, pages 194–208, Applied Research Lab, The Pennsylvania State University, 1998.

[10] Ostashev V.E., Blanc-Benon Ph., Juvé D., and Dallois L. Wide angle parabolic equation for sound waves in a refractive, turbulent atmosphere. In *Proc. Tenth International Symposium on Long Range Sound Propagation*, Grenoble, France, 2002.

[11] L. Dallois and Ph. Blanc-Benon. Wide-angle parabolic equarions for moving media: soud diffraction by a core vortex. In *7th AIAA/CEAS Aeroacoustic Conference*, 2001. AIAA Paper 2001-2256.

[12] T. Colonius, S.K. Lele, and P. Moin. The scattering of sound waves by a vortex: Numerical simulations and analytical solutions. *J. Fluid Mech.*, 260:271–298, 1994.

[13] R. Ford and S.G. Llewellyn Smith. Scattering of acoustic waves by a vortex. *J. Fluid Mech.*, 386:305–328, 1999.

[14] M.S. Howe. On the scattering of sound by a rectilinear vortex. *J. Sound Vib.*, 227(5):1003–1017, 1999.

[15] S. Candel. Numerical solution of wave scattering problems in the parabolic approximation. *J. Fluid Mech.*, 90:465–507, 1979.

[16] C. Bailly and D. Juvé. Numerical solution of acoustic propagation problems using linearized Euler equations. *AIAA Journal*, 38(1):22–29, 2000.

[17] M.D. Collins. A split-step Padé solution for the parabolic equation method. *J. Acoust. Soc. Am.*, 93:1736–1742, 1993.

[18] M.D. Collins. Generalization of the split-step Padé solution. *J. Acoust. Soc. Am.*, 96:382–385, 1994.

[19] R.R. Greene. A high-angle one-way wave equation for seismic wave propagation along rough and sloping interfaces. *J. Acoust. Soc. Am.*, 77(6):1991–1998, 1985.

[20] K.E. Gilbert, Xiao Di, S. Khanna, M.J. Otte, and J.C. Wyngaard. Electromagnetic wave propagation through simulated atmospheric refractivity fields. *Radio Science*, 34(6):1413–1435, 1999.

Sound Propagation in a Turbulent Atmosphere: An Approach Using Substitute Sources

Jens Forssén
Centre Acoustique, Ecole Centrale de Lyon, France
(On leave from Chalmers University of Technology, Göteborg, Sweden)

Abstract

The substitute-sources method (SSM) was previously implemented for a single noise barrier in a turbulent atmosphere by applying a substitute surface between the barrier and the receiver [1, 2]. Here, the method is extended, aiming to more general applicability to traffic noise propagation in urban environments. In the method, multiple substitute surfaces are used along the propagation path. The atmospheric turbulence causes a transfer of the initially coherent field into a residual, random field along the propagation path. The mean sound level at the receiver position is found from uncorrelated addition of the substitute surfaces' contributions. The calculation of each contribution is based on a mutual coherence function (MCF) for a turbulent atmosphere. The strength of the substitute sources and the Green functions to the received pressure are calculated for a non-turbulent atmosphere, here by using a fast field program (FFP). A special MCF for the residual field is derived. Examples are calculated for a turbulent atmosphere with upward refraction or without refraction. The results are compared with those from a parabolic equation method (PE) for the refractive cases and with an analytical solution otherwise. The results show good agreement, which indicates that the SSM could be useful for predictions of outdoor sound propagation.

1 Introduction

A substitute-sources method (SSM) was previously developed to predict the increased noise level behind a single barrier due to a turbulent atmosphere [1, 2]. The approach presented here aims to be applicable to more variations along the propagation path, e.g. multiple barriers and range dependent ground and medium properties. Of main interest is the prediction of noise propagation in urban environments, for instance for city planning purposes. In urban situations the propagation is expected to be influenced by many things: atmospheric turbulence, sound speed profiles that may vary with range, multiply reflecting and diffracting

buildings and barriers, and range varying ground properties. Parabolic equation methods (PE) are largely applicable to such situations [3, 4, 5]. Potentially applicable methods are those based on finite elements (FEM) or finite differences, boundary element methods (BEM) [6, 7] and fast field programs [8].

The approach with substitute sources presented here enables calculations for steep geometries, for instance when a high barrier is located close to the source or to the receiver [2]. PE methods are in general limited to not too steep geometries, but a high barrier can be modelled if the diffraction is calculated by other means and inserted into the PE solution. The SSM models the propagation outward from the source, as also the PE does. This means that backscattering is neglected, unless calculated separately and added (as can be done in the PE [5]).

In the SSM, the sound field due to an original source is represented by a distribution of sources on a plane surface. The surface is called a substitute surface and the sources are called substitute sources, which can be seen as Huygens' secondary sources. Here, many substitute surfaces are put between the source and the receiver, with separation distances large compared with the wavelength. (See Figure 1.) The propagation is calculated in steps from one surface to the next for a non-turbulent atmosphere. The effect of turbulence is that it causes a loss in coherence of the sound field. Within each step the unperturbed, coherent field loses power into a residual, random field. The coherent field is further propagated toward the receiver and at each substitute surface the residual, random part is taken out. The contributions from different surfaces are assumed to be uncorrelated, and the total power at the receiver is found by adding the power from the coherent field to the powers from the residual fields. The strengths of the substitute sources are calculated as for a non-turbulent atmosphere and scaled in amplitude to fulfill the power of the residual field. The Green function for the sound pressure at the receiver due to each substitute source is also found for a non-turbulent atmosphere. From one substitute surface, each of the sources' contributions is decomposed into a direct and a ground reflected part. All the contributions are summed up to give the estimated power by taking into account their mutual coherence due to the turbulence. A mutual coherence function for the residual field is derived.

Since the calculation of the source strengths and the Green functions do not involve turbulence, many methods could be used. For instance ray-methods would be efficient for a homogeneous atmosphere or a linear sound speed profile. Here, a fast field program (FFP) is used throughout. The following section describes the theory and thereafter a few examples are calculated. The examples are for a hard and a finite impedance ground surface, with or without an upward refracting atmosphere. All calculations are for two-dimensional situations.

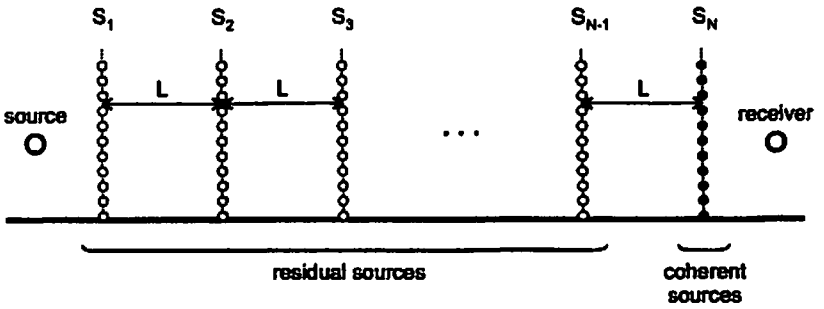

Figure 1. Substitute surfaces S_i, with separation distance L.

2 Theory

The description of the theory is divided into five subsections. The use of the Rayleigh integral for representing the sound field is described in the first subsection. Thereafter the mutual coherence function (MCF) or transverse coherence function, Γ, and the extinction coefficient, γ, for a turbulent atmosphere are shown. In the third subsection the MCF for the residual field is derived, and thereafter the calculation scheme is described. The fifth subsection is about the Gaussian turbulence model that is used here.

2.1 The Rayleigh integral

The Rayleigh integral can be used to calculate the sound pressure level in a medium provided that the particle velocity in normal direction to a plane surface and the Green function for the medium are known. The propagation through either a snapshot of a turbulent atmosphere or through a non-turbulent atmosphere, with for instance refraction, could be described by a Green function. The plane surface is here one of the substitute surfaces S_i, $i = 1 \ldots N$, and the normal component of the velocity, v_i, of the sound field at the surface S_i is the strength of the substitute sources. In the two-dimensional (2-D) implementation used here, the surface is transformed into a line, but still referred to as a substitute surface. The resulting pressure amplitude at a receiver position, $p(x, y)$, from the velocity on surface S_i can be written

$$p(x,y) = \frac{j\omega\rho_0}{2\pi} \int_l v_i(y_S) G(x_S, y_S, x, y) \mathrm{d}y_S, \tag{1}$$

where l is the line of integration, ω is the angular frequency of a time-oscillation, $e^{j\omega t}$, with time t, and ρ_0 the medium density. In equation (1) G is the Green function which in general depends on the position (x_S, y_S) on the surface and on the receiver position. The velocity, v_i, and the Green functions are here found from FFP calculations.

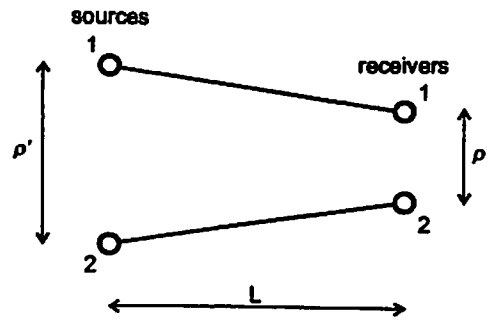

Figure 2. A pair of sound rays with transverse separation ρ' at the start and ρ at range L.

2.2 Coherence in a turbulent atmosphere

The subject of line-of-sight propagation in a random medium has been studied extensively (e.g. [9, 10, 11, 12, 13]), and the theoretical results most useful here relate to the correlation between acoustic pressure signals that have travelled from monopole sources through different parts of the medium. In Figure (2) a geometry with two sources and two receivers are shown; ρ' and ρ are transverse separations and L is the longitudinal distance or range. For the case where the pressure p_1 is only due to source 1 and pressure p_2 is only due to source 2, the mutual coherence function for p_1 and p_2 can be written as

$$\Gamma_{12} = \frac{\langle p_1 p_2^* \rangle + \langle p_1^* p_2 \rangle}{\langle \hat{p}_1 \hat{p}_2^* \rangle + \langle \hat{p}_1^* \hat{p}_2 \rangle}, \tag{2}$$

where the complex conjugate is denoted by an asterisk (*), p_1 and p_2 are the fluctuating pressure amplitudes in the turbulent atmosphere and $\hat{p}_1$ and $\hat{p}_2$ are the amplitudes without turbulence (e.g. [14]). In the usual definition of the MCF there is only one source (i.e. coinciding source positions in Figure 2). This MCF is here referred to as $\Gamma^0(\rho, L)$, where ρ is the distance between the receivers and L is the range. The reciprocal problem has the same MCF, i.e. when there are two sources and one receiver.

The extinction coefficient, γ, is related to the decay over distance of the mean field in a turbulent atmosphere. If the pressure amplitude due to a point source in free field is $\hat{p}$ without turbulence, then the mean amplitude in turbulence will be

$$p_c = \langle p \rangle = \hat{p} e^{-\gamma L}, \tag{3}$$

where L is the distance of propagation [13]. The mean pressure amplitude, p_c, is also called the coherent field. The total field is the sum of the mean field and the residual, fluctuating field, $p = \langle p \rangle + p_r$, with $\langle p_r \rangle = 0$.

In the case the two paths are largely separated, the fluctuations in p_1 and p_2 will be independent. The mutual coherence will then not depend on the separation, ρ, and can be written as a function of the extinction coefficient γ [13]:

$$\Gamma_{12} = \mathrm{e}^{-2\gamma L}. \tag{4}$$

If the situation of propagation involves a ground surface, the effect of turbulence is that it makes the interference less strong. The received pressure amplitude is the sum of the direct and the ground reflected contributions. Without turbulence the amplitude is constant, $\hat{p} = \hat{p}_1 + \hat{p}_2$, whereas with turbulence the amplitude will fluctuate, $p = p_1 + p_2$. The long-term average of the square of the pressure amplitude is then computed as [15, 16, 17]

$$\langle |p|^2 \rangle = |\hat{p}_1|^2 + |\hat{p}_2|^2 + 2|\hat{p}_1\hat{p}_2| \cos\left[\arg\left(\frac{\hat{p}_2}{\hat{p}_1}\right)\right] \Gamma_{12}(\rho, L). \tag{5}$$

The case with a ground surface is special since the ground reflected ray changes direction. A good approximation of the MCF in equation (5) is taking $\rho = \rho_{\max}$, where $\rho_{\max}$ is the maximum vertical separation between the direct and the ground reflected rays; $\rho_{\max} = 2h_S h_R/(h_S + h_R)$, where h_S and h_R are the source and receiver heights. Hence Γ_{12} in equation (5) is calculated as for no ground but with the adjusted transverse distance: $\Gamma_{12} = \Gamma^0(\rho_{\max}, L)$ [18].

That Γ_{12} is chosen as $\Gamma^0(\rho_{\max}, L)$ can be schematically explained as follows. It can be shown that the MCF can be generally written as

$$\Gamma^0(\rho, L) = \mathrm{e}^{-LU(\rho)}, \tag{6}$$

where U is a function that depends on the turbulence model and on ρ. (See Appendix for a more detailed description.) For a flat geometry with equal source and receiver heights ($h_S = h_R \ll L$), the distance of propagation is approximately L, and the ground reflection is at range $\frac{L}{2}$. At the range $\frac{L}{2}$ the separation between the two rays is $\rho_{\max}$ and the MCF is $\Gamma^0(\rho_{\max}, \frac{L}{2}) = \exp[-\frac{L}{2}U(\rho)]$ there. The decorrelation has a multiplicative property over range, whereby the total MCF, at the range of the receiver, will be $\Gamma^0(\rho_{\max}, \frac{L}{2})^2 = \Gamma^0(\rho_{\max}, L)$, using equation (6). The argument can be generalised and extended to situations where the source and the receiver are not at the same height (see Appendix). The calculation of other special cases are also shown in the Appendix, for instance the coherence between a direct wave from one source and a ground reflected wave from another source. (The results for these cases are not applied in the implementation of the SSM used here, but can be useful in further implementations.)

For M contributions p_j, $j = 1 \ldots M$, the long-term average of the square of the total pressure amplitude can be computed as [16]

$$\langle |p_{tot}|^2 \rangle = \sum_{j=1}^{M} |\hat{p}_j|^2 + 2 \sum_{j=1}^{M-1} \sum_{k=j+1}^{M} |\hat{p}_j\hat{p}_k| \cos\left[\arg\left(\frac{\hat{p}_k}{\hat{p}_j}\right)\right] \Gamma^0_{jk}. \tag{7}$$

The equation corresponding to equation (7) but for a continuous source distribution can be written as

$$\langle|p_{tot}|^2\rangle = \langle \int\int p(y)p^*(y')dydy'\rangle = \tag{8}$$

$$\int\int |\hat{p}(y)\hat{p}(y')| \cos\left[\arg\left(\frac{\hat{p}(y')}{\hat{p}(y)}\right)\right] \Gamma^0 dydy',$$

where y and y' are positions on the substitute surface. If there would be a homogeneous atmosphere, $\Gamma^0 \equiv 1$, equation (8) could be seen as the same as the square of the Rayleigh integral in equation (1).

The quantity $\langle|p_{tot}|^2\rangle$ is proportional to the power of the signal at the receiver. In the following, the quantity $\frac{1}{2}\langle|p_{tot}|^2\rangle$ is referred to as the power. (The sound pressure level is then found as $L_p = 10\lg\frac{\frac{1}{2}\langle|p_{tot}|^2\rangle}{2\cdot10^{-5}}$ dB re $2\cdot10^{-5}$ Pa.) Hence, when there is a turbulent atmosphere between a substitute surface and the receiver, the received mean power can be calculated as

$$W_{tot} = \frac{1}{2}\langle|p_{tot}|^2\rangle = \frac{1}{2}\left(\frac{\omega\rho_0}{2\pi}\right)^2 \int_l\int_l |vGv'G'| \cos\left[\arg\left(\frac{v'G'}{vG}\right)\right] \Gamma^0 dy\, dy'. \tag{9}$$

2.3 Coherence of the residual field

In Figure (3) a situation is described where only a part, L', of the range of propagation is through turbulence. This case could be formulated as

$$\langle|p_{tot}|^2\rangle = |\hat{p}_1|^2 + |\hat{p}_2|^2 + 2|\hat{p}_1\hat{p}_2| \cos\left[\arg\left(\frac{\hat{p}_2}{\hat{p}_1}\right)\right] \Gamma', \tag{10}$$

where Γ' is the MCF for a turbulent layer with thickness L'. If $\rho' \ll L' + L$, the propagation distance through the turbulence will be approximately L', and then the decrease in power in the coherent field can be approximated by the factor $e^{-2\gamma L'}$, using equation (3). At the receiver, the contribution due to the coherent field can then be written as

$$\langle|p_c|^2\rangle = e^{-2\gamma L'}\left(|\hat{p}_1|^2 + |\hat{p}_2|^2 + 2|\hat{p}_1\hat{p}_2| \cos\left[\arg\left(\frac{\hat{p}_2}{\hat{p}_1}\right)\right]\right). \tag{11}$$

Since the coherent pressure field, p_c, and the residual pressure field, p_r, are uncorrelated, one gets $\langle|p_{tot}|^2\rangle = \langle|p_c|^2\rangle + \langle|p_r|^2\rangle$, and the residual contribution is given by:

$$\langle|p_r|^2\rangle = \langle|p_{tot}|^2\rangle - \langle|p_c|^2\rangle = \tag{12}$$

$$\left(1 - e^{-2\gamma L'}\right)\left(|\hat{p}_1|^2 + |\hat{p}_2|^2 + 2|\hat{p}_1\hat{p}_2| \cos\left[\arg\left(\frac{\hat{p}_2}{\hat{p}_1}\right)\right] \frac{\Gamma' - e^{-2\gamma L'}}{1 - e^{-2\gamma L'}}\right).$$

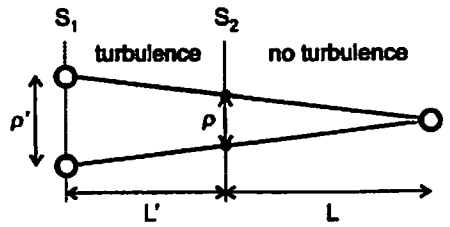

Figure 3. Propagation through a turbulent layer.

From the above equation a MCF for the residual field, $\tilde{\Gamma}$, can be generally defined as

$$\tilde{\Gamma} = \frac{\Gamma^0 - e^{-2\gamma L}}{1 - e^{-2\gamma L}}. \tag{13}$$

It can be noted that, as Γ^0 approaches the value $e^{-2\gamma L}$ for large ρ, $\tilde{\Gamma}$ approaches zero. The equations (12) and (13) constitute the main theoretical result of this paper, and can be seen as describing the transfer of the coherent field into a random field and how the contribution from the random field is calculated.

For the case with a turbulent layer (as in equation 12), Γ' can be found from the multiplicative property as

$$\Gamma' = \frac{\Gamma^0(\rho', L' + L)}{\Gamma^0(\rho, L)}, \tag{14}$$

with $\Gamma^0(\rho', L' + L)$ and $\Gamma^0(\rho, L)$ calculated as for the same turbulence throughout the source-to-receiver range.

If there is turbulence also after the range L', the MCF for the residual field should be multiplied by $\Gamma^0(\rho, L)$. For the coherent field the contribution is then found from multiplying the mixed term in equation (11) (the last term in the parentheses) by the same function, $\Gamma^0(\rho, L)$.

2.4 Numerical method

In the SSM the sound field is represented by a distribution of sources on each substitute surface. The above derived mutual coherence function for the residual field is applied to each pair of source contributions when calculating the powers from all but the last surface. The power $\tilde{W}_i$ from the residual field from surface S_i can be written

$$\tilde{W}_i = \frac{1}{2}\langle |p_i|^2 \rangle = \frac{1}{2}\left(\frac{\omega\rho_0}{2\pi}\right)^2 \int_l \int_l |v_i G_i v_i' G_i'| \cos\left[\arg\left(\frac{v_i' G_i'}{v_i G_i}\right)\right] \tilde{\Gamma}\Gamma^0 \mathrm{d}y \, \mathrm{d}y', \tag{15}$$

where $\tilde{\Gamma}$ is the MCF for the residual field and Γ^0 for the medium after the next surface, S_{i+1}. The contribution, W_N^0, from the last surface, i.e. from the coherent source field, is found from setting $\tilde{\Gamma} = 1$ in the above equation. When the integrals in equation (15) are discretised, the solution takes the form of equation (7).

In equation (15) the distribution of power between different surfaces is ignored. Taking into account the correct loss in power to the residual field within each step, the total power at the receiver can be found as

$$W_{tot} = \left(1 - e^{-2\gamma L}\right)\left(\tilde{W}_1 + e^{-2\gamma L}\tilde{W}_2 + e^{-4\gamma L}\tilde{W}_3 + \ldots + e^{-2(N-2)\gamma L}\tilde{W}_{N-1}\right) \quad (16)$$

$$+e^{-2(N-1)\gamma L}W_N^0 = \left(1 - e^{-2\gamma L}\right)\left(\sum_{i=1}^{N-1} e^{-2(i-1)\gamma L}\tilde{W}_i\right) + e^{-2(N-1)\gamma L}W_N^0,$$

where L is the distance between the substitute surfaces and $e^{-2(N-1)\gamma L}W_N^0$ is the power from the last surface.

In the present formulation of the method the assumption that the contributions from different substitute surfaces are uncorrelated relies on L being large compared with the correlation length of the turbulence. For smaller values of L it might be possible to find corrections to γ and $\tilde{\Gamma}$ if necessary. The study of this can belong to future work.

2.5 Gaussian turbulence model

To describe the turbulence, it is assumed to be homogeneous and isotropic, that is, the fluctuations are assumed to follow the same statistics for all points and the statistics are independent of rotation. In the Gaussian turbulence model the temperature fluctuations of the medium are described by a Gaussian spectrum, and here the velocity fluctuations are omitted. All the above assumptions simplify the turbulence modelling and results in a poor description of realistic situations. The turbulence modelling can however be improved in future implementations of the SSM, but the simplifications used here facilitate a first evaluation of the method. For the Gaussian turbulence model the mutual coherence function can be written as

$$\Gamma^0(\rho, L) = \exp\left[-2\gamma L\left(1 - \frac{\phi(\rho/l)}{\rho/l}\right)\right], \quad (17)$$

where l is usually referred to as the correlation length or the scale of the fluctuations, $\phi(\rho/l) = \int_0^{\rho/l} \exp(-t^2)dt$ and

$$\gamma = \frac{\sqrt{\pi}k^2 l}{2}\mu_0^2, \quad (18)$$

where μ_0^2 is the variance of the index of refraction fluctuations [19, 20, 13]. (It could be noted that $\mu_0^2 = \frac{1}{4}\sigma_T^2$, where σ_T^2 is the variance of the relative temperature

fluctuations.) Following the same references, the MCF for plane wave propagation can be written

$$\Gamma^{\mathrm{pl}}(\rho, L) = \exp\left[-2\gamma L\left(1 - \mathrm{e}^{-\rho^2/l^2}\right)\right]. \tag{19}$$

(In equations (17) and (19) it can be seen that for large separations, $\rho \gg l$, the MCF becomes independent of ρ and reduces to equation (4).) The MCF (17) is deduced for a three-dimensional turbulence. It can however be shown that the MCF for two dimensions is the same for the Gaussian turbulence model [14, 21].

3 Implementation and calculated examples

A few examples are calculated to study the behaviour of the SSM, involving upward refraction and no refraction for a hard or a soft, grass-like ground surface. The calculations without turbulence are made using a fast field program (FFP) implemented according to Salomons [17]. In the FFP the sound field is transformed into a wave number domain and this is used to efficiently calculate the velocity from the pressure derivative which is transformed into a multiplication.

The parts of the non-turbulent sound field that are wanted are the normal velocities at the surfaces, i.e. the strength of the substitute sources, and the Green functions for the received pressure due to these velocities. In a model using the mutual coherence function all contributions are seen as rays, for which the separation, ρ, and the range, L, can be defined. The received pressure due to a source on a surface is therefore decomposed into a direct and a ground reflected contribution. The decomposition is done by making FFP calculations both with and without a ground surface. Subtracting the two results gives the ground reflected contribution and the calculation without the ground gives the direct contribution. The values of the input parameters ρ and L for the coherence $\tilde{\Gamma}$ are here approximated as for straight rays. Taking into account the curvature of a pair of rays due to the refraction would alter the values of ρ and L. Here, however, it is assumed that the corresponding error in $\tilde{\Gamma}$ is negligible, but this could be improved in future implementations.

For upward refraction a shadow region is formed and, in general, the sound field cannot be decomposed into defined rays. In the SSM, however, the approach is different since the field due to the original source is substituted by a surface of sources. The sources at large enough height will be above the limiting ray of the shadow region and will thereby have direct rays to the receiver. Hence, it is assumed that the dominating contribution comes from the substitute sources that are above the limiting ray to the receiver, whereby the error from applying the MCF $\tilde{\Gamma}$ also to the other rays is negligible.

For the results shown here the FFP is used to calculate directly the velocities at all surfaces. Another possible approach is to calculate a matrix of Green

functions relating all velocities on one surface to all the velocities on the following surface, and apply the matrix repeatedly. This approach would be motivated for instance if there is a an impedance jump of the ground surface, or other range varying properties. Concerning computational demands, the SSM and the PE are fairly similar, and in the SSM the computation time is dominated by the FFP calculations.

For the cases with upward refraction, a logarithmic effective sound speed profile is used up to 30 m height. Above that height the sound speed is taken as constant to improve the numerical stability of the FFP. The logarithmic sound speed profile is $c(y) = c_0 - b \cdot \ln(y/y_{\text{rough}} + 1)$, with $b = 0.43$ m/s and the roughness height $y_{\text{rough}} = 0.05$ m [17]. For the turbulence the correlation length $l = 1$ m and the variance of the index of refraction $\mu_0^2 = 2 \cdot 10^{-6}$ or $5 \cdot 10^{-5}$ are used. The larger value for μ_0^2 models a strong turbulence and is chosen for the examples without refraction to give a strong turbulence effect at relatively short propagation range.

In the calculations with the SSM presented here, only the plane wave MCF is used. The motivation is that between one substitute surface and the next, most pairs of rays toward the receiver can be approximated as parallel. The MCF for the residual field is then calculated as $\tilde{\Gamma} = [\Gamma^{\text{pl}} - \exp(-2\gamma L)]/[1 - \exp(-2\gamma L)]$. Moreover, in the examples calculated here, the MCF $\tilde{\Gamma}$ dominates the decorrelation and $\tilde{\Gamma}\Gamma^0$ is approximated as $\tilde{\Gamma}$, i.e. $\Gamma^0 = 1$ is used.

The discretisation in height in the SSM, i.e. the distance between the discrete substitute sources is $\lambda/5$ for the non-refractive cases and $\lambda/10$ for the cases with upward refraction, where λ is the sound wavelength. These values were found from numerical tests without including the turbulence effects. The height used for the substitute surfaces is about half the maximum propagation range, and the top third is windowed to give a smooth decay with height of the source strengths. The windowing is used to reduce spurious oscillations in the solution [1]. The separation in range between the substitute surfaces, L, is 10 m in all examples, and the results are calculated every 5 meters.

The calculations for the soft ground uses a normalised ground impedance of $3.71 - j3.68$ at the frequency 500 Hz and $5.56 - j6.10$ at 1000 Hz. These values are for a grass-like surface and come from the Delany and Bazely model using a flow resistivity of 200 kNs/m^4 (e.g. [16]). (The sign of the imaginary part of the impedance is consistent with the time-dependence used here and with a normal vector pointing into the ground.)

The calculated results are shown in Figures (4–9). Figures (4–7) are for a non-refractive atmosphere, for hard and soft ground, and for the frequencies $f = 500$ Hz and $f = 1000$ Hz. Figures (8–9) are for upward refraction, for hard and soft ground, for $f = 500$ Hz. (Other data are given in the Figure captions.) The results are plotted as sound pressure level relative to free field as a function of propagation range from the source.

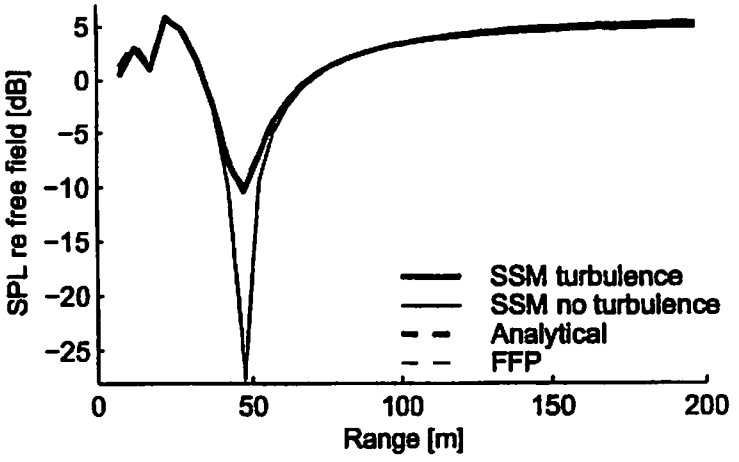

Figure 4. Result for hard ground,
$f = 500$ Hz, $\mu_0^2 = 5 \cdot 10^{-5}$, $h_S = 2$ m, $h_R = 4$ m.

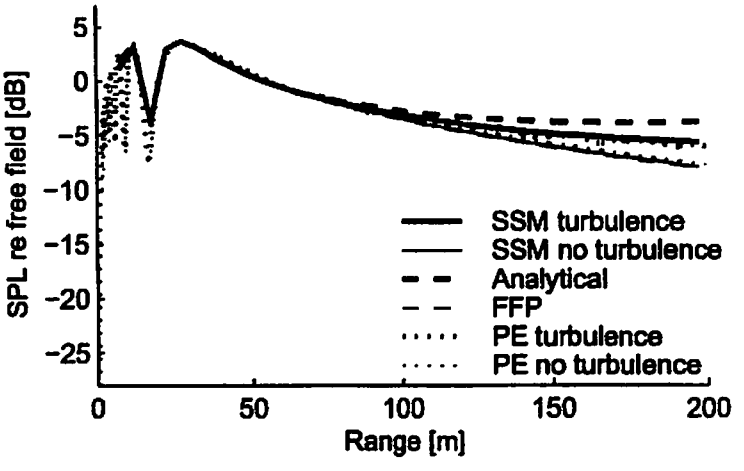

Figure 5. Result for soft ground,
$f = 500$ Hz, $\mu_0^2 = 5 \cdot 10^{-5}$, $h_S = 2$ m, $h_R = 4$ m.

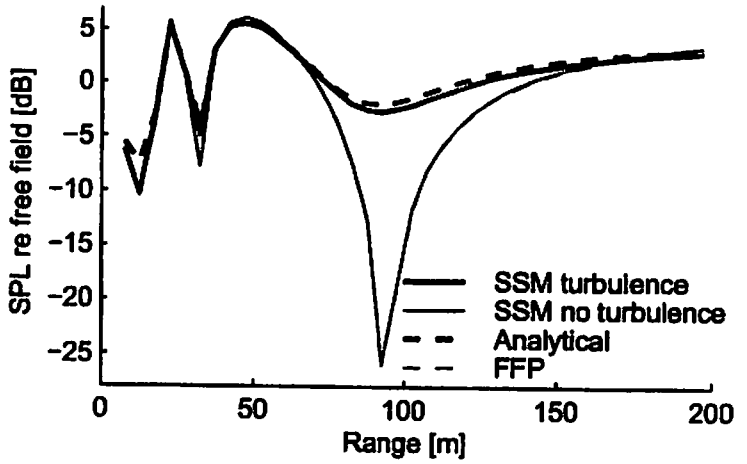

Figure 6. Result for hard ground,
$f = 1000$ Hz, $\mu_0^2 = 5 \cdot 10^{-5}$, $h_S = 2$ m, $h_R = 4$ m.

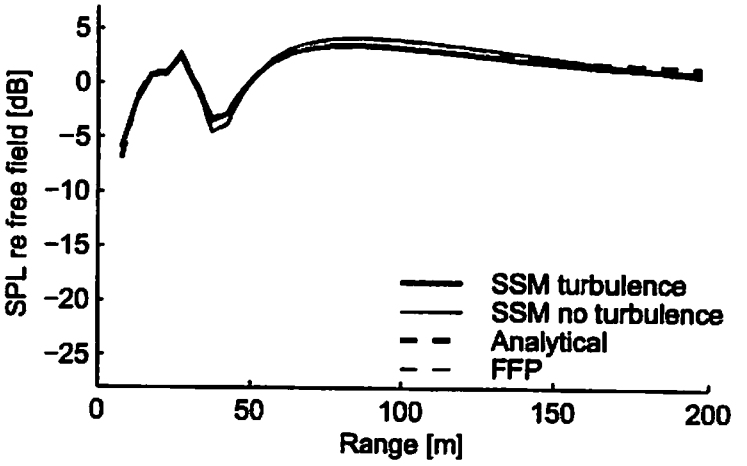

Figure 7. Result for soft ground,
$f = 1000$ Hz, $\mu_0^2 = 5 \cdot 10^{-5}$, $h_S = 2$ m, $h_R = 4$ m.

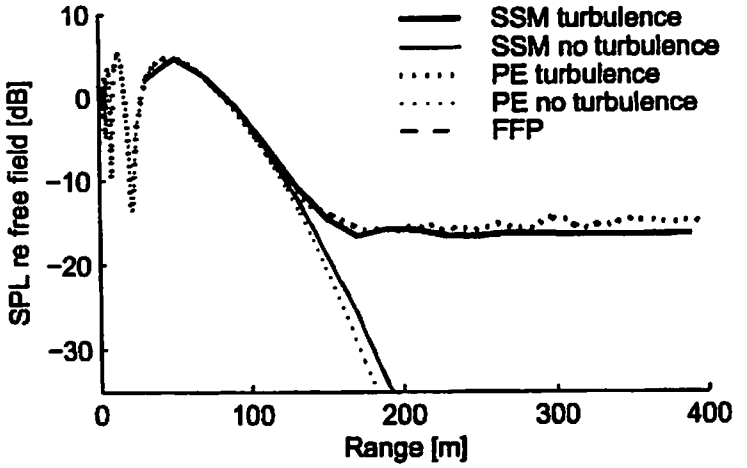

Figure 8. Result for hard ground and upward refraction, $f = 500$ Hz, $\mu_0^2 = 2 \cdot 10^{-6}$, $h_S = 2$ m, $h_R = 2$ m.

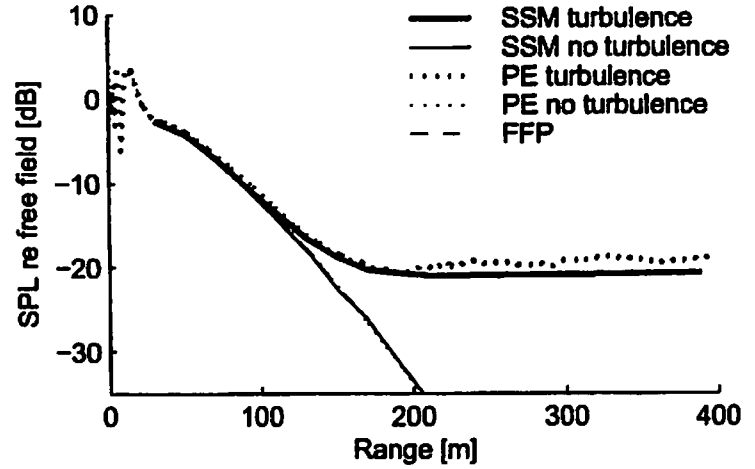

Figure 9. Result for soft ground and upward refraction, $f = 500$ Hz, $\mu_0^2 = 2 \cdot 10^{-6}$, $h_S = 2$ m, $h_R = 2$ m.

For the calculations without refraction (Figures 4–7) the two thicker curves show the results for a turbulent atmosphere. The solid line is for the SSM and the dashed line is the analytical solution using the MCF for the direct and ground reflected rays from the source to the receiver, as described in Subsection 2.2. The two thinner curves are for no turbulence; the dashed line for the FFP directly and the solid line for the SSM without turbulence, i.e. where all power is calculated from the last substitute surface without decorrelation. (These two curves are almost indistinguishable in the Figures.)

In the examples with upward refraction (Figures 8 and 9), a comparison is made with a parabolic equation method (PE). In the PE calculations 50 realisations of the turbulence are used to estimate the power at the receiver. (The PE implementation used here is mainly based on Ref. [3] and is described in detail in Ref. [22].) The dotted curves show the PE results, with and without turbulence.

For an atmosphere without refraction, the effect of turbulence is mainly that it reduces the interference, as can be seen in Figures (4–7). Most of the SSM results show good agreement with the analytical in these examples. However, for the soft ground at $f = 500$ Hz (Figure 5), there is a significant discrepancy. To provide an additional comparison, the PE method is applied also to this case, and the results are shown in the same figure. The PE results are similar to those from the SSM, which indicates that the analytical solution may give a significant error in this case. A possible explanation is that the turbulence scattering results in a larger loss into the ground than what is given by the analytical ray model. For upward refraction the main effect of the turbulence is that is limits the acoustic shadow, as can be seen in Figures (8) and (9). The results from the SSM are shown to agree well with the PE results.

4 Conclusions

The good agreement shown in the comparison with the other methods indicate that the extended substitute-sources method presented here could be a useful tool for predictions of outdoor sound propagation. The approach also enables application to steep geometries, as shown in a previous implementation for a single barrier [2].

In future work, range dependent properties of the atmosphere and the ground could be taken into account. For example, with small changes in the method, a ground impedance that is step-wise constant over range could be modelled.

Acknowledgments

The work presented here was made during a post-doctoral fellowship at the Acoustics Research Centre, University of Salford, UK. The author wishes to thank Professor Y. W. Lam for the invitation and hosting.

The author also wishes to thank Wolfgang Kropp and Mikael Ögren for their help with preparing the manuscript. The fellowship was funded by STINT (The Swedish Foundation for International Cooperation in Research and Higher Education).

Appendix

The mutual coherence function (MCF) $\Gamma^0(\rho, L)$, or transverse coherence function, describes the correlation between the pressure amplitudes at two receiver positions at the range L from a monopole source. The range L is also called the longitudinal distance. The transverse separation between the receivers is ρ. In this paper the MCF is defined as in equation (2).

The main assumption made when finding the analytical solution for the MCF is weak scattering due to the turbulence. At the end of the Appendix the assumptions are briefly summarised. With the notation used here, the MCF for a homogeneous and isotropic turbulence can be written as

$$\Gamma^0(\rho, L) = \exp\left[B_\chi(\rho, L) - B_\chi(0, L) + B_\phi(\rho, L) - B_\phi(0, L)\right], \tag{20}$$

where B_χ and B_ϕ are correlation functions of the log-amplitude fluctuations, χ, and the phase fluctuations, ϕ (e.g. [19]). The relation to the fluctuating pressure amplitude, p, is $p = \hat{p}\exp(\chi + \mathrm{j}\phi)$, where $\hat{p}$ is the amplitude without turbulence. For χ_1 and χ_2 at two receivers with separation ρ at range L from a single source, the correlation function for the log-amplitude fluctuations can be written as $B_\chi(\rho, L) = \langle \chi_1 \chi_2 \rangle$. The correlation function for the phase fluctuations is defined in the same way: $B_\phi(\rho, L) = \langle \phi_1 \phi_2 \rangle$. As a physical explanation of what equation (20) describes, the sum of variances $B_\chi(0, L) + B_\phi(0, L) = \langle \chi^2 \rangle + \langle \phi^2 \rangle$ can be seen as causing a loss of the coherent wave into the residual field. The correlation $B_\chi(\rho, L) + B_\phi(\rho, L)$ results in a compensating factor because some of the fluctuations are the same for both rays.

For a spherical wave the correlation functions can be found as

$$B_{\chi,\phi}(\rho, L) = \tag{21}$$

$$\frac{\pi^2 k^2}{2} \int_0^L \int_0^\infty K \left\{ 1 \mp \cos\left[\frac{K^2 x}{k} \left(1 - \frac{x}{L} \right) \right] \right\} J_0\left(K\rho \frac{x}{L} \right) \Phi_{\text{eff}}(0, K) \mathrm{d}K \mathrm{d}x,$$

where B_χ is for the minus-sign of $\mp$ and B_ϕ for the plus-sign and where J_0 is the Bessel function of zero order [19, 20, 13]. As defined in Refs. [19, 13] $\Phi_{\text{eff}}(K_x, K_y, K_z)$ is a three-dimensional spectral density for a moving random medium, and in equation (21) $K_x = 0$ and $K = \sqrt{K_y^2 + K_z^2}$. (For a detailed description the reader is referred to Chapter 7 in Ref. [13].) For the special case

where Φ_{eff} models Gaussian index of refraction fluctuations in a non-moving atmosphere, the equations (17–19) are arrived at, which can be seen as a model for the temperature fluctuations in turbulence.

After integrating equation (21) over K, the resulting MCF can be written as

$$\Gamma^0(\rho, L) = \exp\left[-\int_0^L u(\rho\frac{x}{L})\mathrm{d}x\right], \tag{22}$$

where the function u depends on only one variable. Making the substitution $t = x/L$ gives

$$\Gamma^0(\rho, L) = \exp\left[-L\int_0^1 u(\rho t)\mathrm{d}t\right], \tag{23}$$

which can be written as $\exp[-LU(\rho)]$. Using equation(22), the properties of the MCF can be studied and the special problems of interest here can be solved.

If the propagation through the turbulence is divided into two ranges, the multiplicative property of the MCF can be shown. (See Figure 10a.) The total MCF can be written

$$\Gamma_{\text{tot}} = \Gamma^0(\rho_2, L_1 + L_2) = \exp\left[-\int_0^{L_1+L_2} u(\rho_2\frac{x}{L_1+L_2})\mathrm{d}x\right] = \tag{24}$$

$$\exp\left[-\int_0^{L_1} u(\rho_2\frac{x}{L_1+L_2})\mathrm{d}x\right]\exp\left[-\int_{L_1}^{L_1+L_2} u(\rho_2\frac{x}{L_1+L_2})\mathrm{d}x\right].$$

Since $\rho_2/(L_1+L_2) = \rho_1/L_1$, the first factor in the last step in equation (24) is equal to $\Gamma^0(\rho_1, L_1)$. If there is turbulence only after range L_1, the MCF is given by only the last factor in equation (24), and the result can be written: $\Gamma_{\text{tot}} = \Gamma^0(\rho_2, L_1+L_2)/\Gamma^0(\rho_1, L_1)$.

The situation of a direct and a ground reflected ray is shown in Figure (10b). For a flat geometry ρ is much smaller than L and the distance of propagation is approximately equal to L for both rays. Using the multiplicative property over range (as in equation 24), the total MCF can be written $\Gamma_{\text{tot}} = \Gamma^0(\rho, L_1)\Gamma^0(\rho, L_2)$, and using equation (23) gives $\Gamma^0(\rho, L_1)\Gamma^0(\rho, L_2) = \Gamma^0(\rho, L_1+L_2)$.

For the case when a direct and a ground reflected ray do not meet (Figure 10c), the total MCF can be found as

$$\Gamma_{\text{tot}} = \frac{\Gamma^0(\rho, L_1+L_1')}{\Gamma^0(\rho_1, L_1')}\frac{\Gamma^0(\rho, L_2+L_2')}{\Gamma^0(\rho_2, L_2')}. \tag{25}$$

The situation with crossing rays (Figure 10d) can be solved as $\Gamma_{\text{tot}} = \Gamma^0(\rho_1, L_1)\Gamma^0(\rho_2, L_2)$. If there are both crossing rays and a ground reflection, the solution can be found after dividing the propagation into three ranges.

If the pair of sources (or receivers) are not at the same range, it can be seen as an additional independent decorrelation (Figure 10e). The solution for that

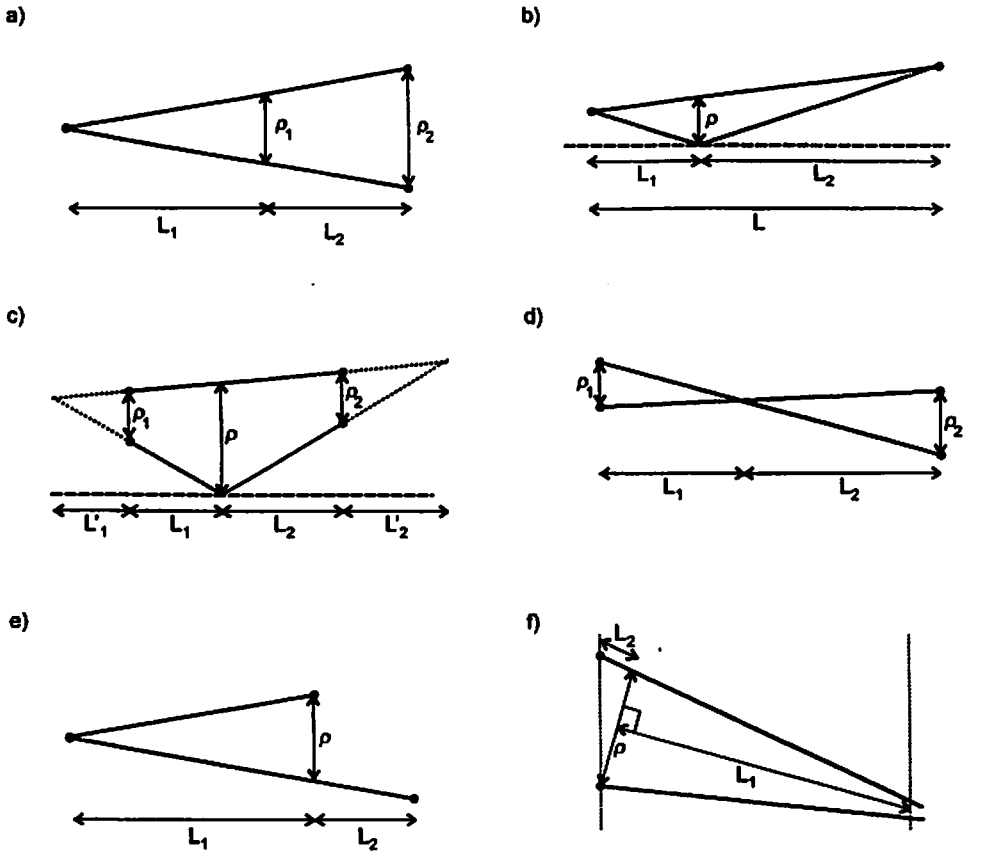

Figure 10. Different cases of ray pairs.

case can be written: $\Gamma_{tot} = \Gamma^0(\rho, L_1)\exp(-\gamma L_2)$. This result could be used in the SSM to model the rays that deviate largely from horizontal direction, as shown in Figure (10f).

The assumptions in the derivation of the mutual coherence in a turbulent atmosphere can be summarised as follows: homogeneous and isotropic turbulence; weak fluctuations of the medium ($\mu_0^2 \ll 1$); sound wavelength much smaller than the large turbulence scales and a rapidly decreasing turbulence strength at smaller scales; weak fluctuations in the sound field due to each inhomogeneity ($\mu_0^2 k^2 l^2 \ll 1$); and a correlation length of the sound field that is large compared with the wavelength [19, 20, 13]. Moreover, at longer ranges of propagation, the amplitude fluctuations stop to increase with range. The saturation gives an upper limit to the log-amplitude fluctuations, $B_\chi(0, L) < 1$ approximately. An approximation for longer ranges is to take $\gamma/2$ instead of γ in the calculation of the MCF [23, 17].

References

[1] Forssén J. Calculation of noise barrier performance in a turbulent atmosphere by using substitute sources above the barrier. Acustica–Acta Acustica, Vol. 86, 2000, pp. 269-75.

[2] Forssén J. Calculation of noise barrier performance in a three-dimensional turbulent atmosphere using the substitute-sources method. Acustica–Acta Acustica, Vol. 88, 2002, pp. 181-189.

[3] Gilbert, K. E., Raspet, R. and Di, X. Calculation of turbulence effects in an upward-refracting atmosphere. J. Acoust. Soc. Am., Vol. 87, 1990, pp. 2428-2437.

[4] Sack, R. A. and West, M. A parabolic equation for sound propagation in two dimensions over any smooth terrain profile: The generalised terrain parabolic equation (GT-PE). Applied Acoustics Vol. 45, 1995, pp. 113-129.

[5] West, M., and Lam, Y. A Two Way Vertical Interface Parabolic Equation (TV-PE) Model for Atmospheric Propagation in the Presence of Severe Terrain Features. Proc. 9th Int. Symp. on Long-Range Sound Propagation, The Hague, Netherlands, 2000, pp. 167-177.

[6] Premat, E. and Gabillet, Y. A new boundary-element method for predicting outdoor sound propagation and application to the case of a sound barrier in the presence of downward refraction. J. Acoust. Soc. Am., Vol. 108, 2000, pp. 2775-2783.

[7] Salomons, E. M., Geerlings, A. C., and Duhamel, D. Comparison of a ray model and a fourier-boundary element method for traffic noise situations with multiple diffractions and reflections. Acustica–Acta Acustica, Vol. 83, 1997, pp. 35-47.

[8] Taherzadeh, S., Li, K. M., and Attenborough, K. A hybrid BIE/FFP scheme for predicting barrier efficiency outdoors. J. Acoust. Soc. Am., Vol. 110, 2001, pp. 918-924.

[9] Tatarskii, V. I. The effects of the turbulent atmosphere on wave propagation, Keter Press. Jerusalem, 1971.

[10] Chernov, L. A. Wave propagation in a random medium. McGRAW-HILL, New York, 1960.

[11] Rytov, S. M. and Kravtsov, Yu. A. and Tatarskii, V. I. Principles of statistical radio physics. Part 4, Wave propagation through random media. Springer, Berlin, 1989.

[12] Ishimaru, A. Wave propagation and scattering in random media IEEE Press (and Oxford University Press, Oxford), New York, 1997.

[13] Ostashev V. E. Acoustics in moving inhomogeneous media. E & FN Spon (an imprint of Thomson Professional), London, 1997.

[14] Salomons, E. M. The fluctuating field of a monopole source in a turbulent atmosphere above a ground surface. Time-averaged sound pressure level and statistical distributions. Proc. 8th Int. Symp. on Long-Range Sound Propagation, The Pennsylvania State University, 1998, pp. 326-351.

[15] Clifford, S. F. and Lataitis, R. J. Turbulence effects on acoustic wave propagation over a smooth surface. J. Acoust. Soc. Am., Vol. 73, 1983, pp. 1545-1550.

[16] L'Espérence, A., Herzog, P., Daigle, G. A. and Nicolas, J. R. Heuristic model for outdoor sound propagation based on an extension of the geometrical ray theory in the case of a linear sound speed profile. Applied Acoustics, Vol. 37, 1992, pp. 111-139.

[17] Salomons, E. M. Computational atmospheric acoustics. Kluwer Academic Publishers, Dordrecht, 2001.

[18] Ostashev V, Clifford S, Lataitis R, Blanc-Benon P, Juve D. The effects of atmospheric turbulence on the interference of the direct and ground reflected waves. Proc. 29th Inter-Noise, Nice, 2000, pp. 217-222.

[19] Ostashev, V. E., Mellert, V., Wandelt, R. and Gerdes, F. Propagation of sound in a turbulent medium. I. Plane waves. J. Acoust. Soc. Am., Vol. 102, 1997, pp. 2561-2570.

[20] Ostashev, V. E., Gerdes, F., Mellert, V., Wandelt, R. Propagation of sound in a turbulent medium. II. Spherical waves. J. Acoust. Soc. Am., Vol. 102, 1997, pp. 2571-2578.

[21] Salomons, E. M. Fluctuations of spherical waves in a turbulent atmosphere: effect of the axisymmetric approximation in computational methods. J. Acoust. Soc. Am., Vol. 108, 2000, pp. 1528-1534.

[22] Forssén, J., Calculation of sound reduction by a screen in a turbulent atmosphere using the parabolic equation method. Acustica–Acta Acustica, Vol. 84, 1998, pp. 599-606.

[23] Daigle, G. A. and Piercy, J. E. and Embleton, T. F. W., Line-of-sight propagation through atmospheric turbulence near the ground. J. Acoust. Soc. Am., Vol. 74, 1983, pp. 1505-1513.

Acoustic Beamforming in Atmospheric Turbulence

S. L. Collier* and D. K. Wilson†

*U.S. Army Research Laboratory, ATTN: AMSRL-CI-EE,
2800 Powder Mill Road, Adelphi, MD 20783-1197
301–394–2641, scollier@arl.army.mil

†Currently with:
Engineering Research and Development Center
U.S. Army Cold Regions Research and Engineering Laboratory
ATTN: CEERD-RC, 72 Lyme Road, Hanover, NH 03755-1290
603–646–4764, D.Keith.Wilson@erdc.usace.army.mil

Tenth International Symposium on Long Range Sound Propagation

Grenoble, France, 12–13 September 2002

Abstract

Acoustic beamforming arrays are becoming increasingly widely used for localization of sound sources in the atmosphere. Atmospheric turbulence often degrades the performance of these arrays by randomly distorting the propagating wavefronts. In this paper, we characterize this degradation by calculating the Cramer-Rao lower bounds (CRLBs) on the accuracy of source bearing estimates for a monochromatic wave propagating along a line-of-sight path through atmospheric turbulence. Both an incident plane wave and a spherical wave are considered. Von Kármán's spectrum is used to model the turbulence. Properties of the solution for different scattering strength and diffraction regimes are discussed. The theoretical CRLBs are then compared to data collected with a 32-element microphone array during several distinct atmospheric conditions [Wilson et al., Acoustics Research Letters Online **106**, L24–L29 (1999)]. Data from local weather sensors are used to determine the parameters in the von Kármán spectrum. The observed experimental standard deviations are typically found to be two to three times larger than the theoretical calculations, a behavior consistent with the nature of the CRLB.

Introduction

Acoustic sensor arrays have long been used in underwater applications such as target detection, identification, and location. Generally, these systems perform direction finding by determining the wavefront angle of arrival (AOA) from the phase differences across the array. Sound waves are strongly affected by the environment, whether it be oceanic or atmospheric. Both media are random in nature and may strongly distort the wavefront. The resulting random variations in the wavefront's orientation and intensity are perceived as fluctuations in the apparent bearing angles and strength of the source. As such, the error in estimating the wavefront's AOA will increase as the propagation distance increases and/or the intensity of the turbulence increases. (These acoustic phenomena are analogous to scintillation and quivering of optical images, as are often observed above a roadway on a sunny afternoon.) The net effects of these distortions can have a substantial impact on direction-finding in both the atmosphere [1, 2] and the ocean [3, 4].

The performance of a sensor array may be quantified by calculating the mean square error (MSE) between the estimated parameter (such as the AOA) and its actual value. The lower bound of the MSE is the Cramer-Rao lower bound (CRLB), which is calculated from the Fisher information (FI) [5, 6]. There already exists much

work in the open literature that characterizes the CRLB of array processors in the presence of noise only, (e.g., see Ottersten *et al.* [7] and the references therein). Recently, Song and Ritcey [8] developed a model that directly incorporates the effects of random media on acoustic waves into the calculation of the CRLBs of AOA estimates. Specifically, they considered propagation in an ocean channel with random inhomogeneities having a Gaussian spatial correlation. Using the general framework of Song and Ritcey, Wilson [9] calculated the performance bounds on AOA estimates using various correlation functions that are representative of atmospheric turbulence.

Song and Ritcey [8] and Wilson [9] modeled the received signal as a complex, zero-mean, Gaussian random variable. These models, in which the real and imaginary components of the received signal are approximated as Gaussian random variables with equal variances, are reasonable for strong or weak scattering in the presence of strong diffraction (the Rytov extension region) [10]. The assumption that the signal of interest has a zero-mean, implicitly treats the case of waves strongly scattered by the turbulence. A strong scattering event occurs when the turbulence is sufficiently strong, and/or the wavefronts propagate a sufficient distance, so that the phase of the received signal at each sensor is completely randomized. However, in many practical problems the variance of the index-of-refraction fluctuations is sufficiently small, or the propagation distance is sufficiently short, that the waves have only been weakly scattered when they arrive at the array. A weakly scattered wave has a mean component significantly larger than the standard deviation of the real and imaginary parts of the signal. In geometric acoustics, both scattering and diffraction are weak, and the phase variance dominates the signal behavior [10]. Therefore, the previous signal models of Refs. [8, 9] are not applicable for geometric acoustics.

This paper provides an analysis of the CRLBs of AOA[1] estimates for a passive sensor array operating in a turbulent medium. For simplicity a single monochromatic source and a line-of-sight propagation path are assumed. Three-dimensional (3D) propagation is considered. In *Sec. I*, background information about the phenomenology of atmospheric turbulence and about the CRLB are reviewed. In *Sec. II*, the case of strong diffraction is addressed. The zero-mean assumption is avoided, so that the model is valid for both strong and weak scattering. To capture scattering by eddies in both the energy-containing and inertial subranges, a von Kármán spectrum is used for the turbulence [11]. Furthermore, the analysis from Ref. [9] is expanded to include the propagation distance, SNR, turbulence parameters, and phase of the source in the unknown parameter set. The extent to which the estimates of the AOAs will degrade when they are simultaneously estimated with other parameters is determined by calculating the coupling between the estimates. In *Sec. III*, a statistical model of the received signal is developed for geometric acoustics. Preliminary results are analyzed assuming a von Kármán turbulence spectrum.

I Background

I A Phenomenology

The atmospheric boundary layer generally refers to the layer of air directly above the earth's surface in which effects, such as heating, cooling, and friction, are felt on a short time scale (less than a day). This layer is usually one-half a kilometer to several kilometers thick. Fluctuations in momentum, heat, or matter may result in turbulent motions that have scales on the order of the depth of the boundary layer or less. Some characteristics of turbulent flows are: they have purely rotational motion; they are three-dimensional; and they are dissipative and thus require energy to be sustained. When a tangential force exists at a boundary, a shear turbulence occurs. Buoyant turbulent motion may result, e.g., from the thermal heating of the ground which induces an upward motion of the air. Turbulent motion may be characterized by an inner scale length and an outer scale length ($\mathcal{L}$). In between the inner and outer scales lies the inertial subrange, characterized by a cascade of energy to progressively smaller scales. (See, e.g., Reference [12].)

As an acoustic wavefront propagates from the source to the sensor array, it is distorted by random fluctuations in the atmosphere. A coherence loss results when the phase and amplitude relationship between the sensors becomes random. Let the separation between the sensors be d, and let $\mathcal{L}$ be the characteristic length of the largest turbulent eddies. For $d \ll \mathcal{L}$ the wavefronts will be smooth and nearly planar when arriving at the sensor

[1]The theoretical treatment in this paper applies to the AOAs, which represent the orientation of the wavefront normal when the sound reaches the array. For propagation in the atmosphere, the average horizontal (azimuthal) AOA is usually very close to the actual angle of bearing (AOB) of the source, thereby making acoustic arrays well suited to determining the horizontal position of a source. However, for the vertical (elevational) AOA, the situation is quite different. Atmospheric refraction may bend the soundwaves upward or downward, thus interfering with the ability to determine the AOB. As such, most existing acoustic ground sensors do not attempt to determine the elevation of a near-ground source.

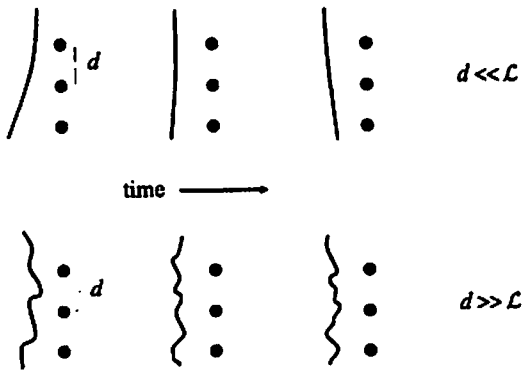

Figure 1: Turbulence-induced distortion of acoustic wavefronts impinging on a sensor array.

array. But if $d \gg \mathcal{L}$, the wavefronts will have a rough and random appearance when observed on the scale of the array. These cases are depicted in Fig. 1. In both cases, there is a coherence loss between the sensor signals.

Knowing $\mathcal{L}$ is essential to designing a sensor array. Typical values of $\mathcal{L}$ during the daytime range between 50 m (for strong winds and little solar heating of ground) and 500 m (for sunny afternoons with light winds). Many sensor arrays have an aperature of about 1 m. Therefore, the case $d \ll \mathcal{L}$ generally applies. It is also generally desirable to space array elements less than one-half a wavelength apart to prevent spurious source images (e.g., spatial aliasing effects).

I B Cramer-Rao Lower Bound

Consider the $N \times 1$ random vector $\mathbf{x}$ (either real or complex) whose probability density function (PDF) is parameterized by the $\mathcal{N} \times 1$ real vector $\boldsymbol{\Theta}$. The minimum MSE of any unbiased[2] estimator $\hat{\boldsymbol{\Theta}}$ about its actual value $\boldsymbol{\Theta}$ may be calculated from the Cramer-Rao theorem [5, 6] which gives

$$\langle\, (\Theta_\nu - \hat{\Theta}_\nu)^2 \,\rangle \geq \left[\mathbf{J}^{-1}(\boldsymbol{\Theta})\right]_{\nu\nu}, \tag{1}$$

where $\mathbf{J}(\boldsymbol{\Theta})$ is the $\mathcal{N} \times \mathcal{N}$ FI matrix. The right-hand side of this equation is the CRLB. The FI is related to the probability likelihood $\wp(\mathbf{x}; \boldsymbol{\Theta})$ (PDF of $\mathbf{x}$ with $\boldsymbol{\Theta}$ as a parameter) by

$$[\mathbf{J}(\boldsymbol{\Theta})]_{\lambda\nu} = -\left\langle \frac{\partial^2 \ln \wp(\mathbf{x}; \boldsymbol{\Theta})}{\partial\Theta_\lambda \partial\Theta_\nu} \right\rangle, \tag{2}$$

where the expectation value is taken with respect to $\wp(\mathbf{x}; \boldsymbol{\Theta})$ and the derivatives are evaluated at the true value of $\boldsymbol{\Theta}$.

If $\mathbf{x}$ is a Gaussian random variable with the $N \times N$ covariance matrix $\mathbf{C}(\boldsymbol{\Theta})$ and $N \times 1$ mean vector $\boldsymbol{\mu}(\boldsymbol{\Theta})$, then its probability likelihood function may be written

$$\wp(\mathbf{x}; \boldsymbol{\Theta}) = \begin{cases} \dfrac{1}{\pi^N \det[\mathbf{C}(\boldsymbol{\Theta})]} \exp\left\{-[\mathbf{x} - \boldsymbol{\mu}(\boldsymbol{\Theta})]^\dagger \mathbf{C}^{-1}(\boldsymbol{\Theta})\,[\mathbf{x} - \boldsymbol{\mu}(\boldsymbol{\Theta})]\right\} & \text{if } \mathbf{x} \text{ is complex} \\ \dfrac{1}{(2\pi)^{N/2} \det^{1/2}[\mathbf{C}(\boldsymbol{\Theta})]} \exp\left\{-\dfrac{1}{2}[\mathbf{x} - \boldsymbol{\mu}(\boldsymbol{\Theta})]^{\mathrm{T}} \mathbf{C}^{-1}(\boldsymbol{\Theta})\,[\mathbf{x} - \boldsymbol{\mu}(\boldsymbol{\Theta})]\right\} & \text{if } \mathbf{x} \text{ is real} \end{cases} \tag{3}$$

The corresponding FI is [5]

$$[\mathbf{J}(\boldsymbol{\Theta})]_{\lambda\nu} = \begin{cases} \mathrm{tr}\left(\mathbf{C}^{-1}\dfrac{\partial \mathbf{C}}{\partial\Theta_\lambda}\mathbf{C}^{-1}\dfrac{\partial \mathbf{C}}{\partial\Theta_\nu}\right) + 2\mathrm{Re}\left(\dfrac{\partial\boldsymbol{\mu}^\dagger}{\partial\Theta_\lambda}\mathbf{C}^{-1}\dfrac{\partial\boldsymbol{\mu}}{\partial\Theta_\nu}\right) & \text{if } \mathbf{x} \text{ is complex} \\ \dfrac{1}{2}\mathrm{tr}\left(\mathbf{C}^{-1}\dfrac{\partial \mathbf{C}}{\partial\Theta_\lambda}\mathbf{C}^{-1}\dfrac{\partial \mathbf{C}}{\partial\Theta_\nu}\right) + \left(\dfrac{\partial\boldsymbol{\mu}^{\mathrm{T}}}{\partial\Theta_\lambda}\mathbf{C}^{-1}\dfrac{\partial\boldsymbol{\mu}}{\partial\Theta_\nu}\right) & \text{if } \mathbf{x} \text{ is real} \end{cases} \tag{4}$$

where the dependence on $\boldsymbol{\Theta}$ is understood. If there are M independent and identically distributed data sets, then the likelihood function will be the product of M identical distribution functions, and hence the FI is M

[2] An estimator is said to be unbiased if and only if $\langle \hat{\boldsymbol{\Theta}} \rangle = \boldsymbol{\Theta}$.

times the quantity given in Eq. (4). We use the convention that the subscripts $\lambda, \nu \in [1, \ldots, \mathcal{N}]$ are the indices on the parameters and that $i, j \in [1, \ldots, N]$ are the indices on the elements of the sensor array.

Let us define $\sigma_\nu \equiv \sqrt{[\mathbf{J}^{-1}]_{\nu\nu}}$. We loosely refer to either σ or σ^2 as the CRLB, as the meaning should be evident from the units involved. The minimum value of σ_ν^2 is $\sigma_{\nu_0}^2 \equiv 1/J_{\nu\nu}$, i.e., the CRLB when Θ_ν is the only unknown. As the number of unknowns increases, σ_ν^2 will increase.

For example, suppose that there are two unknowns. The FI is

$$\mathbf{J} = \begin{bmatrix} J_{11} & J_{12} \\ J_{12} & J_{22} \end{bmatrix}, \tag{5}$$

as it is symmetric for real unknown parameters. For λ and ν cyclic (i.e., if $\lambda = 1$ then $\nu = 2$, etc.)

$$\sigma_\lambda^2 = \left(J_{\lambda\lambda} - J_{\lambda\nu}^2/J_{\nu\nu}\right)^{-1} = \sigma_{\lambda_0}^2 \left(1 - \zeta_{12}\right)^{-1} \tag{6}$$

where

$$\zeta_{12} \equiv \frac{J_{12}^2}{J_{11}J_{22}} = 1 - \frac{\sigma_{1_0}^2}{\sigma_1^2} = 1 - \frac{\sigma_{2_0}^2}{\sigma_2^2}, \qquad 0 \le \zeta_{12} \le 1. \tag{7}$$

Only if $J_{12} = 0$ does $\sigma_\lambda^2 = \sigma_{\lambda_0}^2$, and the estimates of Θ_1 and Θ_2 are said to be uncoupled. As ζ_{12} increases, σ_λ^2 increases from its minimum value of $\sigma_{\lambda_0}^2$, and a degradation of the estimates of Θ_1 and Θ_2 results. The quantity ζ_{12} thus provides a measure of the strength of the coupling between, and hence degradation of, the estimates of Θ_1 and Θ_2: if $\zeta_{12} = 0$, the estimates are uncoupled and the CRLBs retain their minimum values; if $\zeta_{12} \ll 1$, the estimates of θ_1 and θ_2 are weakly coupled and the CRLBs increase only slightly; and if $\zeta_{12} = 1$, the estimates are fully coupled, the CRLBs are infinite, and hence neither Θ_1 nor Θ_2 can be estimated. It is therefore advantageous to determine the conditions underwhich the estimates of Θ_1 and Θ_2 will decouple. If there are more than two coupled parameter estimates, we define the coupling (i.e., partial correlation) between the λth and νth parameter estimates to be

$$\zeta_{\lambda\nu} \equiv \frac{J_{\lambda\nu}^2}{J_{\lambda\lambda}J_{\nu\nu}}. \tag{8}$$

In this way, we have a measure of the coupling strength between any two given parameters.

II Strong Diffraction

II A Theoretical Model

Calculation of the FI requires a priori knowledge of the PDF of the received signal. In this section a theoretical model that incorporates the effects of turbulence on the source signal is developed to describe the PDF of the received signal. Let us define the notation that shall be used throughout this paper: $[\cdot]^*$ denotes the complex conjugate, $[\cdot]^{\mathrm{T}}$ the transpose, $[\cdot]^\dagger$ the Hermitian adjoint (complex conjugate transpose), and $\langle\cdot\rangle$ the ensemble average.

Consider an acoustic array with N sensors. We assume that the signal at each sensor results from: (1) the wave that has propagated from the source of interest with ϕ and θ as the azimuthal and elevational angles of arrival, respectively, and (2) random noise. Let $\mathbf{p}(\phi, \theta, t)$ and $\mathbf{n}(t)$ be the time-varying complex envelops of the two contributions, respectively. These column vectors have N elements, one element corresponding to each sensor. The source contribution is time dependent because of the random turbulent effects. The noise, which is also time dependent, may result from wind noise or other competing sources. The total received signal is

$$\mathbf{s}(\phi, \theta, t) = \mathbf{p}(\phi, \theta, t) + \mathbf{n}(t). \tag{9}$$

Let us assume that the source and the noise signals are uncorrelated and that the noise signals at the sensors are mutually uncorrelated with equal variance. Let us further assume that the noise component has a Gaussian distribution with a zero mean and variance σ_n^2. Although exact solutions for the pressure field of the source and its PDF are unknown, solutions to its first and second moments can be found in the literature. We therefore approximate that $\mathbf{p}$ has a Gaussian distribution with mean μ and covariance matrix $\mathbf{C}_p$, whose elements are

$$\mu_i = \langle p_i \rangle \qquad \text{and} \qquad [\mathbf{C}_p]_{ij} = \langle p_i p_j^* \rangle - \mu_i \mu_j^*. \tag{10}$$

We use the results in the open literature for acoustic wave propagation in a random medium to determine the first moment μ_i and the second moment $\langle p_i p_j^* \rangle$ as discussed in the following section. The total signal s is thus Gaussian distributed with mean μ and covariance

$$\mathbf{C} = \mathbf{C}_p + \sigma_n^2 \mathbf{I}_N. \tag{11}$$

This signal model, in which the real and imaginary parts are modeled as Gaussian random variables with equal variances, is reasonable for strong or weak scattering in the presence of strong diffraction (the Rytov extension region). It is less well suited to situations where both scattering and diffraction are weak (geometric acoustics), in which case the phase variance dominates the signal behavior [10].

II A.1 First and Second Moments: Normal Incidence

The pressure field associated with a sound wave propagating in a moving medium is characterized by a closed set of fluid dynamic equations. The small angle parabolic equation method may be used to reduce this set of equations to a single wave equation. The Markov approximation, which assumes that the turbulence field has vanishing correlation in the direction of propagation, may then be used to obtain the statistical moments of the sound field in closed form. These approximations are valid in far field, for small scattering angles, and for $\mathcal{L} \gg \lambda > \ell$, where λ is the wavelength, and $\mathcal{L}$ and ℓ are, respectively, the outer (integral) and inner (Kolmogorov) length scales of the turbulence. We use the solution for the first and second moments of the pressure field as given by Ostashev [11], who generalized the results of [13] and [14] to include fluctuations in the medium velocity. The solution for the second moment is, however, strictly valid for normal incidence across two sensors. These results are outlined in the following paragraphs.

Consider a wave that is propagating with wave vector $\mathbf{k}$, $k = 2\pi/\lambda$. Let the observation point be $\mathbf{r}_i$. For both a plane wave and a spherical wave, the pressure field in a homogeneous medium may be written in the form

$$p_H(\mathbf{r}_i) = p_0(r_i)\, e^{i\Phi_i} \tag{12}$$

where p_0 is the pressure amplitude and Φ_i is the total phase. If ϵ is the phase of the source, then

$$\text{Plane wave :} \qquad \Phi_i = \epsilon - \mathbf{k}\cdot\mathbf{r}_i \qquad p_0 = \text{constant independent of } r_i \tag{13}$$

$$\text{Spherical wave :} \qquad \Phi_i = \epsilon + kr_i \qquad p_0(r_i) = \frac{Ar_0}{r_i},\ \mathcal{A} = \text{pressure at } r_i = r_0 \tag{14}$$

By using the small angle parabolic and Markov approximations, one finds that the first and second moments of the pressure field in an inhomogeneous medium undergo an exponential attenuation. Let

$$\mathbf{r}_i = [x,\ y_i,\ z_i] \tag{15}$$

such that

$$x \gg R_i\,, \quad R_i = \left(y_i^2 + z_i^2\right)^{1/2}. \tag{16}$$

Consider first a plane wave that is propagating along the x-axis with wave number $\mathbf{k} = -k\hat{\mathbf{e}}_x$, $k = 2\pi/\lambda$. The first moment at $\mathbf{r}_i$ is

$$\mu_i = \langle p(\mathbf{r}_i) \rangle = p_H(\mathbf{r}_i)\, e^{-\gamma x} \tag{17}$$

where γ is the extinction coefficient for the first moment and $p_H(\mathbf{r}_i)$ is the sound pressure field in the absence of random inhomogeneities. Here the propagation is strictly along the x-axis, therefore $p_H(\mathbf{r}_i) = p_0\, e^{i(\epsilon + kx)}$.

Consider now a spherical wave that is propagating with wave number $\mathbf{k} = k\hat{\mathbf{e}}_r$. The solutions to the moments in a random medium are obtained by using the parabolic approximation for a spherical wave propagating in free space. For $x \gg R_i$, the parabolic approximation is the first order approximation in R_i/x,

$$\frac{\exp(ikr_i)}{r_i} \approx \frac{1}{x}\exp(ikx)\exp\left(i\frac{kR_i^2}{2x}\right). \tag{18}$$

For a spherical wave, the first moment is also given by Eq. (17) where $p_H(\mathbf{r}_i)$ is now described by the approximations

$$p_0 \approx \frac{Ar_0}{x} \quad \text{and} \quad \Phi_i \approx \epsilon + kx + \frac{kR_i^2}{2x}. \tag{19}$$

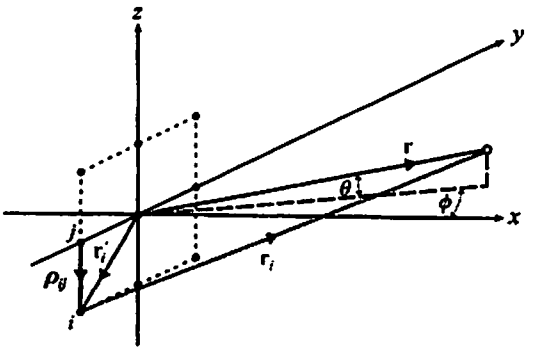

Figure 2: Coordinate system. The closed circles represent the sensors. For a plane wave, the open circle represents the point in the plane of the source at which $\mathbf{r}$ is normal to the wavefront. For a spherical wave, the open circle represents the source. The azimuthal and elevational AOAs, ϕ and θ, are defined with respect to $\hat{\mathbf{r}}$.

The first moment represents the unscattered (deterministic) part of the wavefield. We define the saturation parameter parameter Ω as

$$\Omega = 1 - e^{-2\gamma x}. \tag{20}$$

When $\gamma x \ll 1$, the saturation parameter is close to 0, scattering is small, and the signal at a single sensor exhibits little variability. When $\gamma x \gg 1$, $\Omega \approx 1$, and the scattered part of the field dominates.

Consider now two points near the x-axis, $\mathbf{r}_i = [x, y_i, z_i]$ and $\mathbf{r}_j = [x, y_j, z_j]$, where $x \gg R_i,\ R_j$. The second moment is

$$\langle p(\mathbf{r}_i)\, p^*(\mathbf{r}_j) \rangle = p_H(\mathbf{r}_i)\, p_H^*(\mathbf{r}_j)\ e^{-\alpha(\rho_{ij})x}, \tag{21}$$

where $\rho_{ij} = \mathbf{r}_i - \mathbf{r}_j$ is the sensor separation vector (transverse to the propagation direction), $\alpha(\rho_{ij})$ is the extinction coefficient for the second moment, and $p_H(\mathbf{r}_i)$ is given by Eqs. (12 & 13) for a plane wave and Eqs. (12 & 19) for a spherical wave. For both propagation cases we may write

$$p_H(\mathbf{r}_i)\, p_H^*(\mathbf{r}_j) = p_0^2 e^{i\Phi_{ij}} \tag{22}$$

where Φ_{ij} is the total phase difference between the ith and jth sensors

$$\Phi_{ij} = \Phi_i - \Phi_j. \tag{23}$$

The extinction coefficients for the first and second moments are related by

$$\gamma = \alpha(\infty)/2. \tag{24}$$

II A.2 First and Second Moments: Oblique Incidence

As solutions for the second moment for oblique incidence are not available in the open literature, we must derive approximate expressions for the moments for oblique incidence. Let $[\cdot]^\perp$ and $[\cdot]^\parallel$ denote the components of a vector transverse and parallel to $\hat{\mathbf{k}}$, respectively. [For plane-wave propagation, $\mathbf{k}$ is no longer parallel to the x-axis.] For both a plane wave and a spherical wave, we define r to be the propagation distance of the wavefront to the center of the array. However, the definition of the vector $\mathbf{r}$ depends upon the case considered: for a plane wave, $\mathbf{r}$ is the vector from the center of the array normal to the plane of the source; for a spherical wave, $\mathbf{r}$ is the vector from the center of the array to the source. A list of vectors and their definitions is given in Table 1. For both a plane wave and a spherical wave, the azimuthal and elevational AOAs, ϕ and θ, are measured with respect to the center of the array, so that $\hat{\mathbf{r}} = [\cos\phi\cos\theta,\ \sin\phi\cos\theta,\ \sin\theta]$. An illustration is given in Fig. 2.

For oblique incidence, we must take care in deriving approximations for the moments. A consistent treatment of both the phases and attenuations of the moments is necessary to ensure that the covariance matrix $\mathbf{C}_p$ is nonsingular. For plane-wave propagation, we assume that the attenuation of the moments may be approximated by the values for normal incidence. We are thus assuming that the largest source of variation of the first moment from the center of the array to the ith sensor is due to the phase not the attenuation. Similarly, we assume that the change in the second moment from normal incidence is due primarily to the the change in the phase

	Plane Wave	Spherical Wave
$\mathbf{r} = [x,\ y,\ z]$	Vector from the center of the array normal to the plane of the source	Vector from the center of array to the source
$x = \cos\phi\cos\theta$ $y = \sin\phi\cos\theta$ $z = \sin\theta$	Components of $\mathbf{r}$ in terms of the azimuthal and elevational angles of arrival ϕ and θ	
$r = \lvert\mathbf{r}\rvert$	Propagation distance of the wavefront to the center of the array	
$\hat{\mathbf{r}} = \mathbf{r}/r$	Unit vector in direction of $\mathbf{r}$	
$\hat{\mathbf{e}}_r$	N/A	Radial orthogonal unit vector in spherical coordinates
$\mathbf{k}$	Wave number. $\lvert\mathbf{k}\rvert = k = 2\pi/\lambda$, where λ is the wavelength	
	$\mathbf{k} = -k\hat{\mathbf{r}}$	$\mathbf{k} = k\hat{\mathbf{e}}_r$
$\mathbf{r}'_i = [x'_i,\ y'_i,\ z'_i]$	Vector from the center of the array to the ith sensor	
$\mathbf{r}_i = \mathbf{r} - \mathbf{r}'_i$	As defined	Vector from the source to the ith sensor
$r_i = \lvert\mathbf{r}_i\rvert$	As defined	Propagation distance of the wavefront to the ith sensor
$r_i^{\parallel} = \lvert\mathbf{r}_i \cdot \hat{\mathbf{k}}\rvert$	Propagation distance of the wavefront to the ith sensor	$r_i^{\parallel} = r_i$
$r_i^{\perp} = \lvert\mathbf{r}_i \times \hat{\mathbf{k}}\rvert$	Magnitude of the component of $\mathbf{r}_i$ transverse to wave propagation	$r_i^{\perp} = 0$
$\boldsymbol{\rho}_{ij} = \mathbf{r}'_i - \mathbf{r}'_j$	Vector between the jth and ith sensors, as $\mathbf{r}_i - \mathbf{r}_j = \mathbf{r}'_j - \mathbf{r}'_i$	
$\rho_{ij} = \lvert\boldsymbol{\rho}_{ij}\rvert$	Distance between the ith and jth sensors	
$\rho_{ij}^{\perp} = \lvert\boldsymbol{\rho}_{ij} \times \hat{\mathbf{k}}\rvert$	Magnitude of the component of $\boldsymbol{\rho}_{ij}$ transverse to wave propagation	

Table 1: Definitions of vectors and their magnitudes. Physical descriptions are provided when possible. Refer to Fig. 2.

differences, not the attenuation. For spherical-wave propagation, the second moment for normal incidence was calculated using the parabolic approximation, where $p_H(\mathbf{r}_i)$ was approximated by expanding about $r_i^{\parallel}$ up to first order in $1/r_i^{\parallel}$. For oblique incidence, we expand $p_H(\mathbf{r}_i)$ about r up to first order in $1/r$. In doing so, we assume that the attenuation of the wave across the array is constant and may be approximated by that at the array center. Performing the expansion we find

$$p_0 \approx \frac{\mathcal{A}r_0}{r} \quad \text{and} \quad \Phi_i \approx \epsilon + k\left[r - \hat{\mathbf{r}}\cdot\mathbf{r}'_i + \frac{r_i'^2 - (\hat{\mathbf{r}}\cdot\mathbf{r}'_i)^2}{2r}\right]. \tag{25}$$

Therfore, for both plane-wave and spherical-wave propagation, the moments for oblique incidence are approximated as

$$\text{First Moment}: \qquad \mu_i \approx p_0 e^{-\gamma r} e^{\imath\Phi_i} \tag{26}$$

$$\text{Second Moment}: \qquad \langle p_i p_j^* \rangle \approx p_0^2 e^{-\alpha(\rho_{ij})r} e^{\imath\Phi_{ij}} \tag{27}$$

where

p_0 and Φ_i are given by $\begin{cases} \text{Eq. (13)} & \text{Plane Wave} \\ \text{Eq. (25)} & \text{Spherical Wave} \end{cases}$.

It follows that the saturation parameter, for both a plane wave and a spherical wave, is now

$$\Omega \approx 1 - e^{-2\gamma r}. \tag{28}$$

The approximation for the first moment is valid if for every i and j,

$$\text{Plane Wave:} \qquad e^{-\gamma r_i^{\parallel}} \approx e^{-\gamma r_j^{\parallel}} \approx e^{-\gamma r} \tag{29}$$

$$\text{Spherical Wave:} \qquad \frac{e^{-\gamma r_i}}{r_i} \approx \frac{e^{-\gamma r_j}}{r_j} \approx \frac{e^{-\gamma r}}{r}. \tag{30}$$

And the approximation for the second moment is valid if for every i and j,

$$\alpha\left(\rho_{ij}^{\perp}\right) \approx \alpha\left(\rho_{ij}\right) \tag{31}$$

and

$$\text{Plane Wave:} \qquad e^{-\alpha(\rho_{ij}) r_i^{\parallel}} \approx e^{-\alpha(\rho_{ij}) r_j^{\parallel}} \approx e^{-\alpha(\rho_{ij}) r} \tag{32}$$

$$\text{Spherical Wave:} \qquad \frac{e^{-\alpha(\rho_{ij}) r_i}}{r_i r_j} \approx \frac{e^{-\alpha(\rho_{ij}) r_j}}{r_i r_j} \approx \frac{e^{-\alpha(\rho_{ij}) r}}{r^2}. \tag{33}$$

Because of these approximations, we restrict our investigation to near-normal incidence to a planar array for 3D propagation [a linear array for two-dimensional (2D) propagation].

II A.3 Covariance Matrix and Mean

As we have assumed that the noise has a zero mean, the mean of the total pressure field is μ, which is given by Eq. 26. The covariance matrix of the total pressure field [Eq. (11)] is

$$C_{ij} = p_0^2 \left[e^{-\alpha(\rho_{ij}) r} - e^{-2\gamma r}\right] e^{\mathrm{i}\Phi_{ij}} + \delta_{ij}\sigma_n^2. \tag{34}$$

The mutual coherence function (MCF) between the ith and jth sensors is defined to be the positive square root of

$$\Gamma_{ij}^2 = \frac{\langle p_i p_j^* \rangle \langle p_i^* p_j \rangle}{\langle p_i p_i^* \rangle \langle p_j p_j^* \rangle}. \tag{35}$$

Thus for both the plane-wave and spherical-wave treatments here,

$$\Gamma_{ij} = |\langle p_i p_j^* \rangle| / p_0^2 = e^{-\alpha(\rho_{ij}) r}. \tag{36}$$

The minimum value of the MCF for $\rho_{ij} \to \infty$ is $\Gamma_{\min} = e^{-2\gamma r}$.

An advantage to this formulation of the first and second moments is that the resulting covariance matrix $\mathbf{C}_p$ and mean $\boldsymbol{\mu}$ may be written in terms of the MCF matrix $\boldsymbol{\Gamma}$, a steering vector $\boldsymbol{s}$, and a steering matrix $\boldsymbol{\mathcal{S}}$. The steering vector is defined to be

$$\boldsymbol{s} = \left[e^{\mathrm{i}\Phi_1}, e^{\mathrm{i}\Phi_2}, \cdots, e^{\mathrm{i}\Phi_N}\right]^{\mathrm{T}}. \tag{37}$$

The steering matrix represents the phase delay between the sensors due solely to the difference in propagation path. As $\boldsymbol{\mathcal{S}} = \boldsymbol{s} \otimes \boldsymbol{s}^{\dagger}$, where $\otimes$ is the (right) Kronecker product,

$$\mathcal{S}_{ij} = \exp\left(\mathrm{i}\Phi_{ij}\right). \tag{38}$$

Therefore

$$\boldsymbol{\mu} = p_0 \Gamma_{\min}^{1/2} \boldsymbol{s} \qquad \text{and} \qquad \mathbf{C}_p = p_0^2 \boldsymbol{\Gamma} \odot \boldsymbol{\mathcal{S}} - p_0^2 \Gamma_{\min} \boldsymbol{\mathcal{S}} = p_0^2 \left(\boldsymbol{\Gamma} - \Gamma_{\min} \mathbf{1}_N\right) \odot \boldsymbol{\mathcal{S}}, \tag{39}$$

where $\odot$ is the Hadamard product (element-by-element multiplication) and $\mathbf{1}_N$ is an $N \times N$ matrix of ones.

II A.4 von Kármán Turbulence Model

The extinction coefficients depend on the structure of the random medium. For a plane wave

$$\alpha(\rho) = 2\pi k^2 \left[f(0) - f(\rho)\right], \tag{40}$$

and for a spherical wave

$$\alpha(\rho) = 2\pi k^2 \int_0^1 \left[f(0) - f(\rho u)\right] du, \tag{41}$$

where f is the 2D (or projected) correlation function for the sound-speed fluctuations [11, 15, 16]. For most random media, including a turbulent atmosphere, $\alpha(\rho)$ initially increases monotonically with increasing ρ, but when ρ exceeds $\mathcal{L}$, $\alpha(\rho)$ asymptotically approaches a constant value. Since $f(\rho) \to 0$ in the limit $\rho \to \infty$, this constant value is simply 2γ, given by

$$2\gamma = 2\pi k^2 f(0) = 2\varsigma^2 k^2 \mathcal{L}, \tag{42}$$

where ς^2 is the index-of-refraction variance. Hence the second moment will initially decrease with increasing ρ, but will eventually "saturate" at a fixed minimum value.

Many acoustic sensor arrays have a sensor spacing larger than the height of the array from ground. As such, the performance of these arrays is affected by the large eddies of the energy-containing (or source) subranges of the turbulence spectrum. The isotropic, homogeneous von Kármán turbulence model describes the inertial subrange of the turbulence spectrum more realistically than the commonly used Gaussian models, and it still behaves reasonably in the energy-containing subrange. The von Kármán form for the 2D correlation function is dependent upon the source of the sound speed fluctuations: a scalar field is induced by temperature or humidity fluctuations and a vector field is induced by wind velocity fluctuations. The 2D correlation functions for a scalar field f_s and a vector field f_v, may be written in the form (see Eq. (49) in Ref. [16] and Eq. (7.112) in Ref. [11])

$$f_s(\rho, \varsigma^2, l) = \frac{2\varsigma^2 l}{\sqrt{\pi}\,\Gamma(1/3)} \left(\frac{\rho}{2l}\right)^{5/6} K_{5/6}\left(\frac{\rho}{l}\right) \tag{43}$$

$$f_v(\rho, \varsigma^2, l) = \frac{2\varsigma^2 l}{\sqrt{\pi}\,\Gamma(1/3)} \left(\frac{\rho}{2l}\right)^{5/6} \left[K_{5/6}\left(\frac{\rho}{l}\right) - \frac{\rho}{2l} K_{1/6}\left(\frac{\rho}{l}\right)\right], \tag{44}$$

where $l = \Gamma(1/3)\mathcal{L}/\left[\sqrt{\pi}\Gamma(5/6)\right]$ is a characteristic length scale, $\Gamma(x)$ is the Gamma function, and $K_\nu(x)$ is the modified Bessel function of order ν. The equation for f_s in this paper differs somewhat from that of Ref. [9] due to the manner in which the scalar energy spectrum was defined in that paper. The equation in this paper is consistent with the more standard definition found in Ref. [11].

The MCF for an incident plane wave is plotted in Fig. 3 as a function of the index-of-refraction variance ς^2 and the characterstic length scale normalized by the wavelength l/λ for both a scalar and a vector von Kármán spectrum. In presenting the results, it is natural to use normalized length scales, (e.g., r/λ, d/λ, etc.), as then the coherence has no explicit wavelength dependence. In (a) and (b) the MCFs are calculated for $\rho/\lambda = 0.5$ and $r/\lambda = 500$. The coherence for both spectra decreases significantly in the regions where the index-of-refraction variance is large, $\varsigma^2 \sim 10^{-4}$, and the normalized length scale is small, $10 < l/\lambda < 1$. In (c) and (d) the same is calculated but for $\rho/\lambda = 3/\sqrt{2}$. The larger sensor separation leads to a more rapid decrease in the MCFs as functions of the turbulence parameters. For both sensor separations the MCF for the vector spectrum is more sensitive to the changes in the turbulence parameters, and its minimum with respect to the turbulence parameters (for a fixed finite sensor separation and normalized propagation distance) is smaller than that for the scalar spectrum. [We note that $\alpha(\rho_{ij})r$ is dependent upon the product of $\varsigma^2 r/\lambda$. Therefore, one may view the x-axis in Fig. 3 as a change in the product of $\varsigma^2 r/\lambda$.] In Fig. 4 the same is plotted but for an incident spherical wave. The function $\Gamma_{\min}$ (the minimum value of the MCF as a function of sensor separation ($\rho = \infty$) for fixed propagation distance and fixed turbulence parameters) is the same for both a scalar and a vector spectrum and for both a plane wave and spherical wave. It is plotted in Fig. 5. Even though its value is only dependent upon the product $\varsigma^2 r l/\lambda^2$, it is plotted versus the turbulence parameters at $r/\lambda = 500$ for ease of comparison with Figs. 3 and 4.

II B Formulation

II B.1 Fisher Information of Theoretical Model

The dependence of the FI on all the unknown parameters except the signal-to-noise ratio has clearly been established. The SNR is related to the noise variance by SNR $= p_0^2/\sigma_n^2$. It is often useful to express the SNR

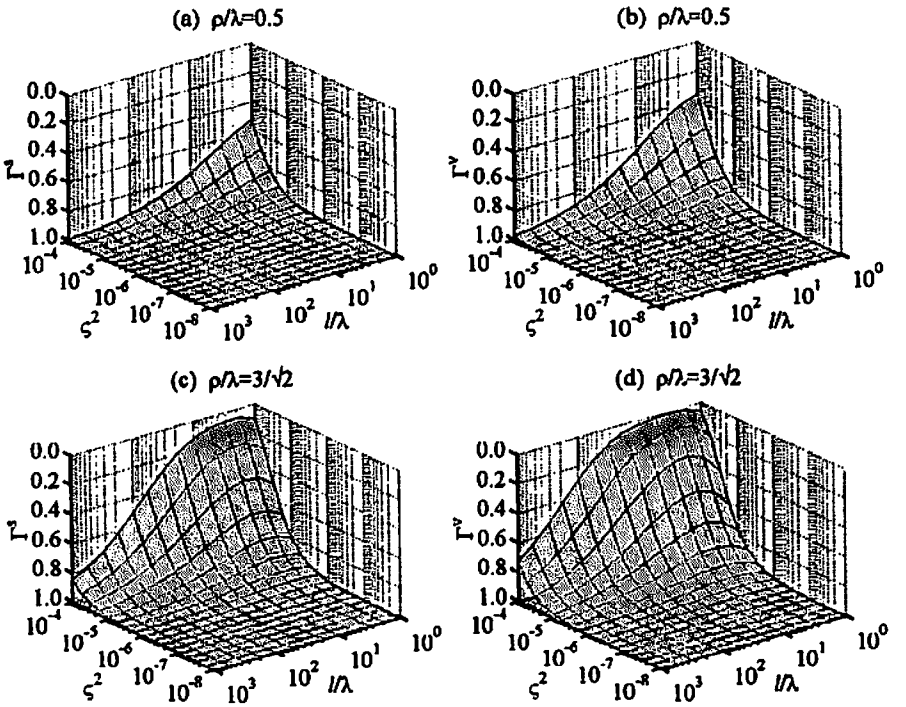

Figure 3: Coherence for an incident plane wave: (a) and (c) are for a scalar von Kármán spectrum; (b) and (d) are for a vector von Kármán spectrum. All calculations are for $r/\lambda = 500$.

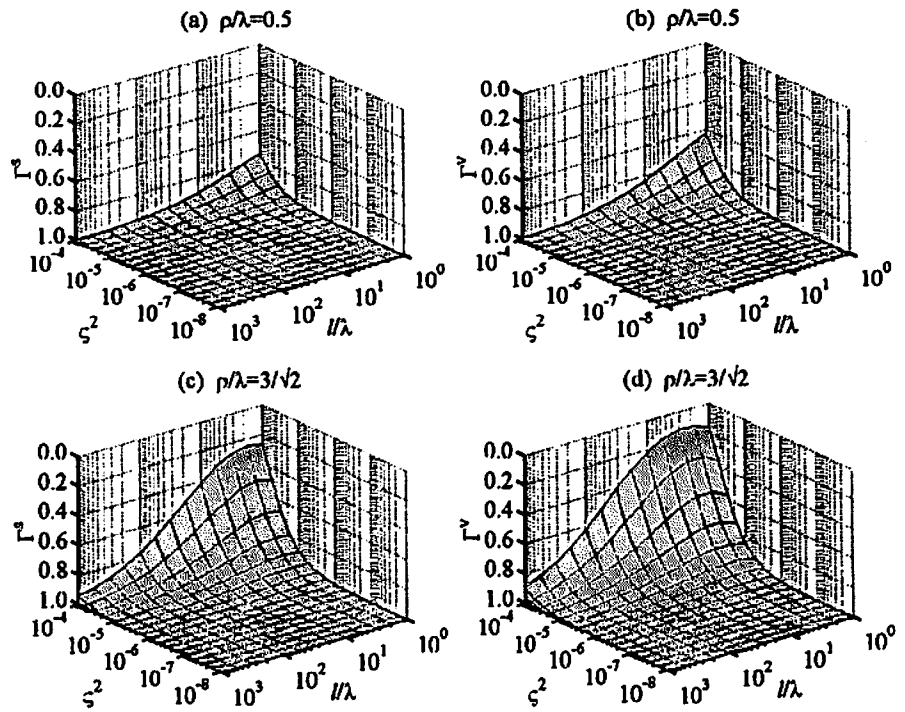

Figure 4: Coherence for an incident spherical wave: (a) and (c) are for a scalar von Kármán spectrum; (b) and (d) are for a vector von Kármán spectrum. All calculations are for $r/\lambda = 500$.

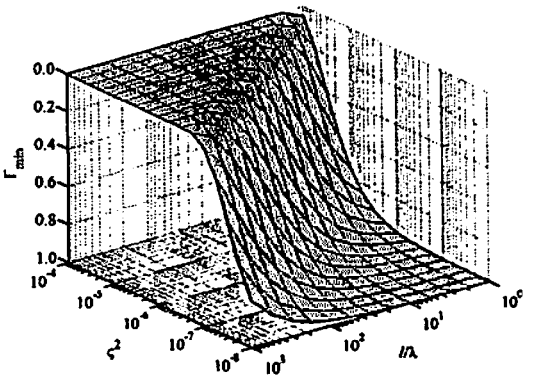

Figure 5: Minimum coherence ($\rho = \infty$) for von Kármán spectra, $\Gamma_{\min} = e^{-2\gamma r}$. Calculation is for $r/\lambda = 500$.

in decibels SNR_{dB}, $\text{SNR} = 10^{\text{SNR}_{\text{dB}}/10}$. For the plane wave case, p_0 is a constant, and we treat the SNR as the unknown. In this way, the exact value of p_0 is not needed for the calculation, as the FI may be renormalized by p_0^2. For a spherical wave p_0 is dependent upon r, therefore we consider SNR_0, the signal-to-noise ratio at a distance $\mathcal{R}_0$, as the unknown. Then $\sigma_n^2 = (\mathcal{A}r_0)^2/(\text{SNR}_0\mathcal{R}_0^2)$. By renormalizing the FI by $(\mathcal{A}r_0)^2$, the explicit value of $\mathcal{A}r_0$ is not needed.

The FI may be calculated from Eq. (4) for those parameters we wish to consider as unknowns: ϕ, θ, ϵ, r, l, ς^2, or SNR. For a nonzero mean, ϵ must be treated as an unknown parameter [21, 22]. While the derivatives of the covariance matrix and mean are straight forward, the derivatives with respect to turbulence parameter l are tedious. For brevity, none of the derivatives are presented here. We may interchangeably refer to the CRLB of the elevation and zenith, for as they are related by a linear transformation, their CRLBs are the same. (Linear transformations preserve the efficiency of an estimator [5].)

II B.2 No Turbulence

Let us begin by examining the case of no turbulence. In the absence of turbulence

$$\mu = \left[p_0(r_1)\, e^{\imath\Phi_1},\ p_0(r_2)\, e^{\imath\Phi_2},\ \ldots,\ p_0(r_N)\, e^{\imath\Phi_N}\right]^{\mathrm{T}} \quad \text{and} \quad \mathbf{C} = \sigma_n^2 \mathbf{I}_N\,. \tag{45}$$

The FI is given by

$$J_{\lambda\nu} = \frac{MN}{\sigma_n^4}\frac{\partial\sigma_n^2}{\partial\Theta_\lambda}\frac{\partial\sigma_n^2}{\partial\Theta_\nu} + \frac{2M}{\sigma_n^2}\sum_{i=1}^{N}\left[p_0^2(r_i)\frac{\partial\Phi_i}{\partial\Theta_\lambda}\frac{\partial\Phi_i}{\partial\Theta_\nu} + \frac{\partial p_0(r_i)}{\partial\Theta_\lambda}\frac{\partial p_0(r_i)}{\partial\Theta_\nu}\right]. \tag{46}$$

For a plane wave, p_0 is independent of r_i [Eq. (13)]. This is also true for a spherical wave in the parabolic approximation [Eq. (19)] and in the approximation of Eq. (25). It follows that for p_0 independent of r_i, the FI is

$$J_{\lambda\nu} = \frac{MN}{\sigma_n^4}\frac{\partial\sigma_n^2}{\partial\Theta_\lambda}\frac{\partial\sigma_n^2}{\partial\Theta_\nu} + \frac{2MN}{\sigma_n^2}\frac{\partial p_0^2}{\partial\Theta_\lambda}\frac{\partial p_0^2}{\partial\Theta_\nu} + 2M\frac{p_0^2}{\sigma_n^2}\sum_{i=1}^{N}\frac{\partial\Phi_i}{\partial\Theta_\lambda}\frac{\partial\Phi_i}{\partial\Theta_\nu}. \tag{47}$$

By setting $J_{\lambda\nu} = 0$, we may determine the conditions underwhich the estimates of Θ_λ and Θ_ν will decouple.

(a) Plane Wave For a plane wave, p_0 and Φ_i are as given in Eq. (13). Let us consider ϕ, θ, ϵ, and r as the unknowns. Recall that

$$\Phi_i = \epsilon - \mathbf{k}\cdot\mathbf{r}_i = \epsilon + k\hat{\mathbf{r}}\cdot(\mathbf{r} - \mathbf{r}_i') = \epsilon + kr - k\hat{\mathbf{r}}\cdot\mathbf{r}_i' \tag{48}$$

where

$$\hat{\mathbf{r}}\cdot\mathbf{r}_i' = x_i'\cos\phi\cos\theta + y_i'\sin\phi\cos\theta + z_i'\sin\theta \tag{49}$$

$$\frac{\partial(\hat{\mathbf{r}}\cdot\mathbf{r}_i')}{\partial\phi} = -x_i'\sin\phi\cos\theta + y_i'\cos\phi\cos\theta \tag{50}$$

$$\frac{\partial(\hat{\mathbf{r}}\cdot\mathbf{r}_i')}{\partial\theta} = -x_i'\cos\phi\sin\theta - y_i'\sin\phi\sin\theta + z_i'\cos\theta\,. \tag{51}$$

From Eq. (47) the elements of the FI matrix are

$$J_{\phi\phi} = 2Mk^2\frac{p_0^2}{\sigma_n^2}\sum_{i=1}^{N}\left[\frac{\partial(\hat{\mathbf{r}}\cdot\mathbf{r}_i')}{\partial\phi}\right]^2 = 2Mk^2\cos^2\theta\frac{p_0^2}{\sigma_n^2}\sum_{i=1}^{N}(x_i'\sin\phi - y_i'\cos\phi)^2 \tag{52}$$

$$J_{\theta\theta} = 2Mk^2\frac{p_0^2}{\sigma_n^2}\sum_{i=1}^{N}\left[\frac{\partial(\hat{\mathbf{r}}\cdot\mathbf{r}_i')}{\partial\theta}\right]^2 = 2Mk^2\frac{p_0^2}{\sigma_n^2}\sum_{i=1}^{N}(x_i'\cos\phi\sin\theta + y_i'\sin\phi\sin\theta - z_i'\cos\theta)^2 \tag{53}$$

$$J_{\epsilon\epsilon} = 2MN\frac{p_0^2}{\sigma_n^2} \tag{54}$$

$$J_{rr} = k^2 J_{\epsilon\epsilon} \tag{55}$$

$$\begin{aligned} J_{\phi\theta} &= 2Mk^2\frac{p_0^2}{\sigma_n^2}\sum_{i=1}^{N}\left[\frac{\partial(\hat{\mathbf{r}}\cdot\mathbf{r}_i')}{\partial\phi}\right]\left[\frac{\partial(\hat{\mathbf{r}}\cdot\mathbf{r}_i')}{\partial\theta}\right] \\ &= 2Mk^2\cos\theta\frac{p_0^2}{\sigma_n^2}\sum_{i=1}^{N}\Big[\left(x_i'^2 - y_i'^2\right)\cos\phi\sin\phi\sin\theta + x_i'y_i'\left(\sin^2\phi - \cos^2\phi\right)\sin\theta \\ &\qquad -x_i'z_i'\sin\phi\cos\theta + y_i'z_i'\cos\phi\cos\theta\Big] \end{aligned} \tag{56}$$

$$J_{\phi\epsilon} = 2Mk\frac{p_0^2}{\sigma_n^2}\sum_{i=1}^{N}\left[-\frac{\partial(\hat{\mathbf{r}}\cdot\mathbf{r}_i')}{\partial\phi}\right] = 2Mk\cos\theta\frac{p_0^2}{\sigma_n^2}\sum_{i=1}^{N}(x_i'\sin\phi - y_i'\cos\phi) \tag{57}$$

$$J_{\phi r} = kJ_{\phi\epsilon} \tag{58}$$

$$J_{\theta\epsilon} = 2Mk\frac{p_0^2}{\sigma_n^2}\sum_{i=1}^{N}\left[-\frac{\partial(\hat{\mathbf{r}}\cdot\mathbf{r}_i')}{\partial\theta}\right] = 2Mk\frac{p_0^2}{\sigma_n^2}\sum_{i=1}^{N}(x_i'\cos\phi\sin\theta + y_i'\sin\phi\sin\theta - z_i'\cos\theta) \tag{59}$$

$$J_{\theta r} = kJ_{\theta\epsilon}\,. \tag{60}$$

Therefore, the estimate of ϵ will decouple from the estimates of ϕ and θ for every value of ϕ and θ if

$$\sum_{i=1}^{N}x_i' = \sum_{i=1}^{N}y_i' = \sum_{i=1}^{N}z_i' = 0\,, \tag{61}$$

i.e., if the center of the array is located at the origin. The estimate of r will also decouple from the estimates of ϕ and θ if Eq. (61) is satisfied. The estimates of ϕ and θ will decouple from one another if

$$\sum_{i=1}^{N}y_i'^2 = \sum_{i=1}^{N}x_i'^2 \qquad \text{and} \qquad \sum_{i=1}^{N}x_i'y_i' = \sum_{i=1}^{N}x_i'z_i' = \sum_{i=1}^{N}y_i'z_i' = 0. \tag{62}$$

Symmetric planar array configurations such as a circular array with sensors placed at equal angular intervals, or a rectangular grid with sensors placed at the lattice points, meet these requirements provided that the array is located in the xy-plane and that the array center is located at the origin. (If both r and ϵ are unknown, then the quantity $\epsilon' = \epsilon + kr$ (the phase of the signal at the array center) may be treated as the unknown, and the same results hold. Nielsen [17] has performed an analysis for a multiple-frequency, far-field, sine wave signal imbedded in Gaussian noise. The conditions he found for the estimates of the elevation, azimuth, and phase at the array center to decouple are the same as for the case presented here. Among the literature which examine array configurations that result in the decoupling of the angle estimates, Refs. [18, 19, 20] may be of interest to the reader.)

Suppose that the center of a sensor array is located at the origin. Then if the sensors are configured so that Eq. (62) is satisfied,

$$\frac{1}{\sigma_\phi^2} = 2Mk^2\cos^2\theta\frac{p_0^2}{\sigma_n^2}\sum_{i=1}^{N}x_i'^2 \qquad \text{and} \qquad \frac{1}{\sigma_\theta^2} = 2Mk^2\frac{p_0^2}{\sigma_n^2}\sum_{i=1}^{N}\left(x_i'^2\sin^2\theta + z_i'^2\cos^2\theta\right). \tag{63}$$

At $\theta = \pi/2$, the CRLB of ϕ is singular. Therefore, such array configurations cannot be used to estimate the azimuthal AOA of a wave that is propagating along the z-axis. Specifically, a planar array must be located in

the xy-plane in order for Eq. (62) to be satisfied. Thus it cannot be used to estimate the azimuth of a normally incident wave. Due to the limitations of the model discussed in *Sec. II A.2*, we want to investigate waves that arrive with near-normal incidence at a planar array [for 2D propagation, near-normal incidence at a linear array]. Therefore in the full simulation, the estimates of the azimuth and elevation will always be coupled as we cannot choose the xy-plane as the array plane.

(b) Spherical Wave Let us now consider a spherical wave in the approximation given in Eq. (25). From Eq. (46) the elements of the FI matrix are

$$J_{\phi\phi} = \frac{2Mp_0^2k^2}{\sigma_n^2}\sum_{i=1}^{N}\left[\left(1+\frac{\hat{\mathbf{r}}\cdot\mathbf{r}_i'}{r}\right)\frac{\partial\left(\hat{\mathbf{r}}\cdot\mathbf{r}_i'\right)}{\partial\phi}\right]^2 \tag{64}$$

$$J_{\theta\theta} = \frac{2Mp_0^2k^2}{\sigma_n^2}\sum_{i=1}^{N}\left[\left(1+\frac{\hat{\mathbf{r}}\cdot\mathbf{r}_i'}{r}\right)\frac{\partial\left(\hat{\mathbf{r}}\cdot\mathbf{r}_i'\right)}{\partial\theta}\right]^2 \tag{65}$$

$$J_{\epsilon\epsilon} = \frac{2MNp_0^2}{\sigma_n^2} \tag{66}$$

$$J_{rr} = \frac{2MNp_0^2}{\sigma_n^2 r^2} + \frac{2Mp_0^2k^2}{\sigma_n^2}\sum_{i=1}^{N}\left[1-\frac{r_i'^2-\left(\hat{\mathbf{r}}\cdot\mathbf{r}_i'\right)^2}{2r^2}\right]^2 \tag{67}$$

$$J_{\phi\theta} = \frac{2Mp_0^2k^2}{\sigma_n^2}\sum_{i=1}^{N}\left[\left(1+\frac{\hat{\mathbf{r}}\cdot\mathbf{r}_i'}{r}\right)\frac{\partial\left(\hat{\mathbf{r}}\cdot\mathbf{r}_i'\right)}{\partial\phi}\right]\left[\left(1+\frac{\hat{\mathbf{r}}\cdot\mathbf{r}_i'}{r}\right)\frac{\partial\left(\hat{\mathbf{r}}\cdot\mathbf{r}_i'\right)}{\partial\theta}\right] \tag{68}$$

$$J_{\phi\epsilon} = -\frac{2Mp_0^2k}{\sigma_n^2}\sum_{i=1}^{N}\left[\left(1+\frac{\hat{\mathbf{r}}\cdot\mathbf{r}_i'}{r}\right)\frac{\partial\left(\hat{\mathbf{r}}\cdot\mathbf{r}_i'\right)}{\partial\phi}\right] \tag{69}$$

$$J_{\phi r} = -\frac{2Mp_0^2k^2}{\sigma_n^2}\sum_{i=1}^{N}\left[\left(1+\frac{\hat{\mathbf{r}}\cdot\mathbf{r}_i'}{r}\right)\frac{\partial\left(\hat{\mathbf{r}}\cdot\mathbf{r}_i'\right)}{\partial\phi}\right]\left[1-\frac{r_i'^2-\left(\hat{\mathbf{r}}\cdot\mathbf{r}_i'\right)^2}{2r^2}\right] \tag{70}$$

$$J_{\theta\epsilon} = -\frac{2Mp_0^2k}{\sigma_n^2}\sum_{i=1}^{N}\left[\left(1+\frac{\hat{\mathbf{r}}\cdot\mathbf{r}_i'}{r}\right)\frac{\partial\left(\hat{\mathbf{r}}\cdot\mathbf{r}_i'\right)}{\partial\theta}\right] \tag{71}$$

$$J_{\theta r} = -\frac{2Mp_0^2k^2}{\sigma_n^2}\sum_{i=1}^{N}\left[\left(1+\frac{\hat{\mathbf{r}}\cdot\mathbf{r}_i'}{r}\right)\frac{\partial\left(\hat{\mathbf{r}}\cdot\mathbf{r}_i'\right)}{\partial\theta}\right]\left[1-\frac{r_i'^2-\left(\hat{\mathbf{r}}\cdot\mathbf{r}_i'\right)^2}{2r^2}\right] \tag{72}$$

$$J_{r\epsilon} = \frac{2Mp_0^2k}{\sigma_n^2}\sum_{i=1}^{N}\left[1-\frac{r_i'^2-\left(\hat{\mathbf{r}}\cdot\mathbf{r}_i'\right)^2}{2r^2}\right]. \tag{73}$$

Again the estimates of ϕ, θ, ϵ, and r will always be coupled. However, notice that the summations on the lowest order terms are the same as those for the plane-wave case. Therefore, we can use the results from the plane-wave case to minimize the couplings.

II B.3 Turbulence

Let us now consider the full problem with turbulence. Recall for both a plane wave and a spherical wave, the the mean and covariance matrix may be written in the forms given in Eq. (39). Let us rewrite these expressions as

$$\boldsymbol{\mu} = \mathbf{m}\odot\boldsymbol{s} \quad \text{and} \quad \mathbf{C} = \mathbf{X}\odot\boldsymbol{S}, \tag{74}$$

where $\boldsymbol{s}$ and $\boldsymbol{S}$ are the steering array and steering vector previously defined, $\mathbf{X}$ is the real symmetric matrix given by $X_{ij} = C_{ij}/e^{\imath\Phi_{ij}}$, and $\mathbf{m}$ is the real column vector given by $m_i = \mu_i/e^{\imath\Phi_i}$. Matrices and vectors that may be decomposed into these forms may also be written as

$$\boldsymbol{\mu} = \mathbf{Sm} \quad \text{and} \quad \mathbf{C} = \mathbf{SXS}^\dagger, \tag{75}$$

where $\mathbf{S}$ is a diagonal matrix of the phases, $\mathbf{S} = \mathbf{diag}\left[e^{\imath\Phi_1}, e^{\imath\Phi_2}, \ldots, e^{\imath\Phi_N}\right]$. Note that $\mathbf{S}^{-1} = \mathbf{S}^\dagger$ and that

$$\frac{\partial\mathbf{S}}{\partial\Theta_\lambda} = \imath\mathbf{S}\mathbf{D}_\lambda \quad \text{where} \quad \mathbf{D}_\lambda = \mathbf{diag}\left[\frac{\partial\Phi_1}{\partial\Theta_\lambda}, \frac{\partial\Phi_2}{\partial\Theta_\lambda}, \ldots, \frac{\partial\Phi_N}{\partial\Theta_\lambda}\right]. \tag{76}$$

Using these properties, the commutation of diagonal matrices, and the properties of the trace, it can be shown that

$$J_{\lambda\nu} = 2M\mathrm{tr}\left(\mathbf{D}_\lambda\mathbf{X}\mathbf{D}_\nu\mathbf{X}^{-1}\right) - 2M\mathrm{tr}\left(\mathbf{D}_\lambda\mathbf{D}_\nu\right) + M\mathrm{tr}\left(\mathbf{X}^{-1}\frac{\partial\mathbf{X}}{\partial\Theta_\lambda}\mathbf{X}^{-1}\frac{\partial\mathbf{X}}{\partial\Theta_\nu}\right)$$
$$+ 2M\frac{\partial\mathbf{m}^{\mathrm{T}}}{\partial\Theta_\lambda}\mathbf{X}^{-1}\frac{\partial\mathbf{m}}{\partial\Theta_\nu} + 2M\mathbf{m}^{\mathrm{T}}\mathbf{D}_\lambda\mathbf{X}^{-1}\mathbf{D}_\nu\mathbf{m}. \tag{77}$$

For the problem at hand, only the phase term Φ_i is dependent upon the AOAs. Therefore, as expected, the estimates of the AOAs can only couple to the estimates of other parameters that appear in the phase terms: ϕ, θ, ϵ, and r. Also notice that there is no explicit dependence on Φ_i in Eq. (77), only on its derivatives. Therefore, for $\Theta_\nu = \epsilon$, $\mathbf{D}_\nu = \mathbf{I}_N$, and hence $\mathbf{J}$ has no dependence on ϵ. This is an expected result, as the actual value of the phase of the source should not affect our ability to estimate the other parameters. Now, $\mathbf{m}$ is dependent upon r, ℓ, and ς^2; and $\mathbf{X}$ is also dependent upon these parameters as well as SNR (SNR_0) for a plane wave (spherical wave). Hence the estimates of r, ℓ, ς^2, and SNR (SNR_0) can be coupled.

Equation (77) is valid for any complex Gaussian process in which the equations in (75) hold. Therefore, Equation (77) may also be applied to the study by Song and Ritcey [8] when considering a single source: In their analysis the only dependence on the AOA is in the phase terms; therefore for a single source, the estimate of the AOA is uncoupled from the estimate of the noise variance.

(a) Plane Wave Let us consider a plane wave propagating through turbulence. We assume that the wave is propagating near the x-axis and thus take the yz-plane to be the array plane. The origin is taken to be at the center of the array. As noted earlier, the estimates of θ and ϕ are coupled for this choice. Numerically, we find that the estimates of θ and ϕ are uncoupled from the estimates of l, ς^2, and SNR, as expected from the discussion above. However, unlike the no turbulence case, placing the center of the array at the origin is not a sufficient condition for the estimates of ϕ and θ to decouple from the estimates of r and ϵ: a symmetric array configuration such as a rectangular grid with mirror symmetry in y about the origin and mirror symmetry in z about the origin must be used, though the stronger condition of uniform spacing is not necessary. The estimates of r, l, ς^2, and SNR are all coupled.

(b) Spherical Wave For the spherical-wave analysis, we again assume that the wave is propagating near the x-axis, take the array plane to be yz-plane, and take the origin to be at the array center. Numerically we observe that: the estimates of ϕ, θ, r and ϵ are all coupled; the estimates of ϕ and θ are uncoupled from the estimates of l, ς^2, and SNR_0; and the estimates of r, l, ς^2, and SNR_0 are all coupled.

II C Results

For both the plane-wave and spherical-wave analyses, the array geometry considered is a 4×4 square grid with spacing of d. In all figures, $d/\lambda = 0.5$. As the CRLB (σ) for M independent and identically distributed datasets is $1/\sqrt{M}$ times the CRLB (σ) for one dataset, all results are presented for $M = 1$.

II C.1 Plane Wave

The values of σ_ϕ, σ_θ, σ_{ϕ_0}, and σ_{θ_0} are the same for normal incidence due to symmetry. In Fig. 6(a), σ_ϕ for normal incidence is plotted as a function of ς^2 and l/λ for $r/\lambda = 500$ and $\mathrm{SNR} = 10$ dB. A vector von Kármán turbulence spectrum is used. A peak is evident in σ_ϕ at large ς^2 and small l/λ. In this region both Γ_{ij} and $\Gamma_{\min}$ are approaching their mimimum values as functions of the turbulence parameters. In fact, in the limit that Γ_{ij} and $\Gamma_{\min}$ simultaneously approach zero, $\sigma_\phi^2 \to \infty$ as $\mathbf{C} \to \sigma_n^2\mathbf{I}_N$ and $\mu \to 0$. For small values of ς^2 and l/λ, both Γ_{ij} and $\Gamma_{\min}$ are approaching the maximum value of 1.0, and hence σ_ϕ^2 is approaching the limit for no turbulence. The behavior for other values of the SNR (providing that the SNR does not dominate the signal) is similar, with σ_ϕ increasing with decreasing SNR. The corresponding percent difference between σ_ϕ calculated with a zero mean and with a nonzero mean is plotted in Fig. 6(b). Using a nonzero mean reduces the CRLB. The largest percent difference occurs for large ς^2 and small l/λ. In this region, however, the CRLB is large and the AOAs cannot be estimated accurately. In the regions where $\Gamma_{\min} \approx 1$, the percent difference is small, though nonzero. In the regions where $\Gamma_{\min} \approx 0$, the percent difference is zero, as it should be.

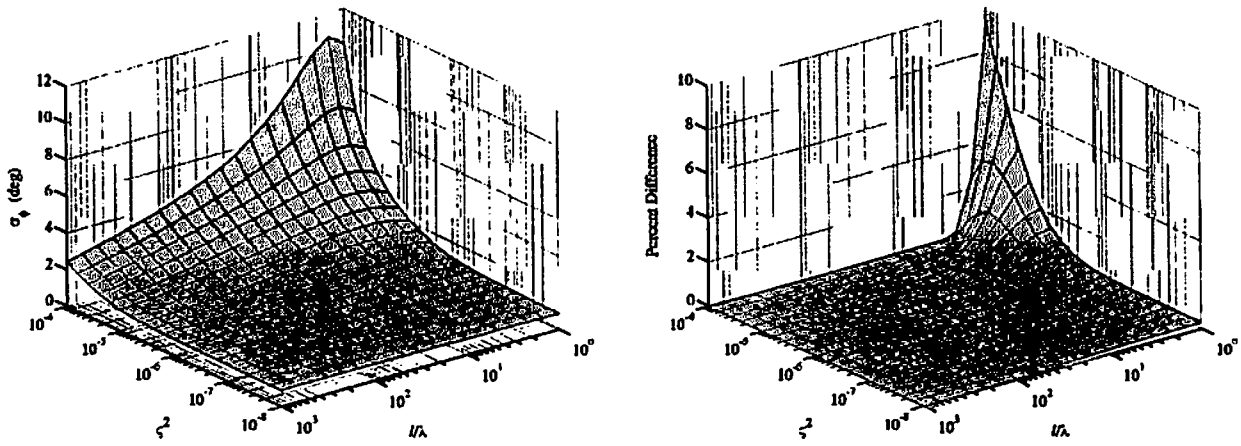

(a) (b)

Figure 6: (a) CRLB of ϕ for a plane wave as a function of turbulence parameters. Calculation is for normal incidence, $r/\lambda = 500$, SNR = 10 dB, and a vector von Kármán spectrum. (b) Corresponding percent difference of σ_ϕ for a plane wave calculated with a zero mean and with a nonzero mean.

In Fig. 7(a), σ_ϕ for normal incidence is examined as a function of the normalized propagation distance r/λ for a couple of values of the SNR, ς^2, and l/λ. A vector von Kármán spectrum is used. The points (lines) correspond to a SNR of 5 dB (10 dB) for every value of r/λ. Though the graph extends to smaller values of r/λ than are valid for the turbulence model, it is useful to see the limiting behavior of our model. [Recall the limits given in *Secs. II A.1–II A.2.* In particular, the approximations in Eqs. (29–33) must hold.] For $\varsigma^2 = 10^{-6}$ and $r/\lambda \lesssim 400$, σ_ϕ is limited by the SNR. As r/λ increases, σ_ϕ is driven primarily by the values of the turbulence parameters, in particular, the index-of-refraction variance. The corresponding percent difference of σ_ϕ calculated with a zero mean and with a nonzero mean is shown in Fig. 7(b).

All plots presented have been for normal incidence. The results for other values of ϕ and θ are similar. As ϕ

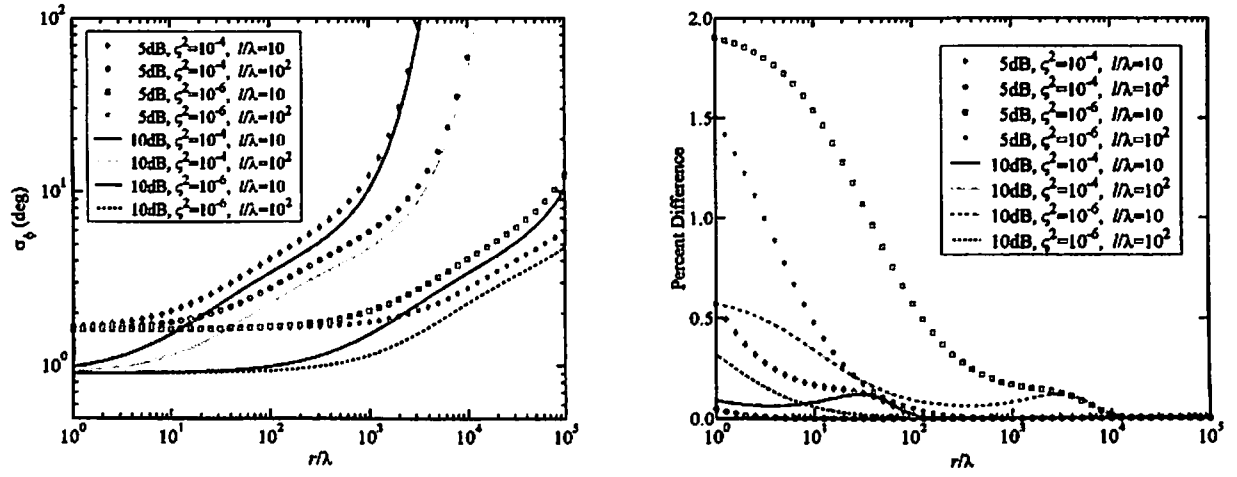

(a) (b)

Figure 7: (a) CRLB of ϕ for a plane wave as a function of normalized propagation distance. All curves are for normal incidence and a vector von Kármán spectrum. (b) Correpsonding percent difference of σ_ϕ calculated with a zero mean and with a nonzero mean

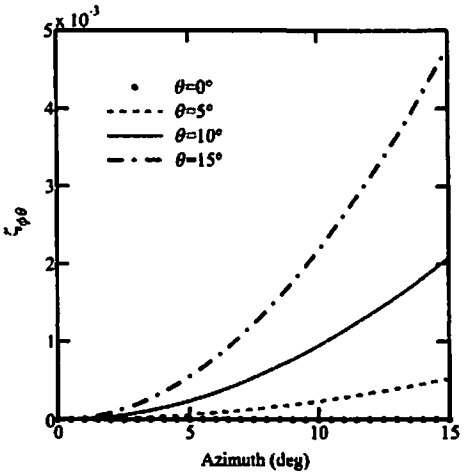

Figure 8: Coupling between the estimates of ϕ and θ for a square array configuration.

and θ increase, σ_ϕ and σ_θ increase. The angular dependence of σ_ϕ and σ_θ is discussed in Ref. [21] for the same array geometry that is considered here. Of particular interest is the coupling $\zeta_{\phi\theta}$. In Ref. [21], for this array geometry, $\zeta_{\phi\theta}$ is found to be the same as for the no turbulence case:

$$\zeta_{\phi\theta} = \frac{\sin^2\phi\sin^2\theta}{\cos^2\theta + \sin^2\phi\sin^2\theta} \approx \phi^2\theta^2 - \frac{1}{3}\phi^4\theta^2 + \frac{2}{3}\phi^2\theta^4, \tag{78}$$

regardless of the the value of r/λ, d/λ, SNR, l/λ, or ς^2, and regardless of the von Kármán spectrum used. It is shown in Fig. 8. The coupling is weak: for ϕ, $\theta \leq 15°$, $\zeta_{\phi\theta} \lesssim 5 \times 10^{-3}$.

A vector von Kármán spectrum was considered in Fig. 6. The analogous results using a scalar von Kármán spectrum are similar. As a function of turbulence parameters, the shape of the curves are nearly identical, but the value of σ_ϕ is for the most part smaller. The largest difference occurs in the regions where the MCF for the scalar spectrum is appreciably larger than the MCF for a vector spectrum (refer back to Fig. 3). More details of the results for a scalar spectrum are given in Ref. [21]. The percent difference of σ_ϕ using a zero mean and a nonzero mean is also smaller; in particular, the peak at large ς^2 and small l/λ is reduced. Again, the use of a nonzero mean reduces the CRLB.

II C.2 Spherical Wave

As we are assuming spherical propagation of the wave, the signal-to-noise ratio is now dependent upon r. Recall that the signal-to-noise ratio evaluated at $r = \mathcal{R}_0$ is denoted SNR_0.

Again, the values of σ_ϕ, σ_θ, σ_{ϕ_0}, and $\sigma_{\theta 0}$ are the same at for normal incidence due symmetry. In Fig. 9(a), σ_ϕ for normal incidence is plotted versus l/λ and ς^2 for $r/\lambda = 500$ and $\text{SNR}_0 = 10$ dB at $\mathcal{R}_0/\lambda = 500$. A vector von Kármán spectrum is used. The overall values of σ_ϕ are smaller than for the plane-wave case. This is expected as the values of the MCF for a plane wave are smaller than for a spherical (refer back to Figs. 3–4). The corresponding percent difference of σ_ϕ calculated with a zero mean and with a nonzero mean is given in Fig. 9(b). As with the plane wave case, the use of a nonzero mean reduces the CRLBs of the AOAs. The results are similar for other values of the SNR.

In Fig. 10(a), σ_ϕ for normal incidence is plotted versus the normalized propagation distance. Two values of ς^2, l/λ, and SNR_0 evaluated at $\mathcal{R}_0/\lambda = 500$ are considered. A vector von Kármán spectrum is used. Again, the graph is extended to include smaller values of r/λ than are valid for the turbulence model. At small values of r/λ, we see that σ_ϕ is dependent upon the values of the turbulence parameters (particularly ς^2) and is independent of the value of SNR_0. Note the difference between the outward spherical propagation and the plane wave propagation depicted in Fig. 7(a). The corresponding percent difference of σ_ϕ calculated with a zero mean and with a nonzero mean is given in Fig. 10(b).

Again, only the results for normal incidence have been shown. For other values of ϕ and θ, the results are similiar and σ_ϕ and σ_θ increase with increasing ϕ and θ. At $\phi = \theta = 0$, the coupling between the estimates of ϕ

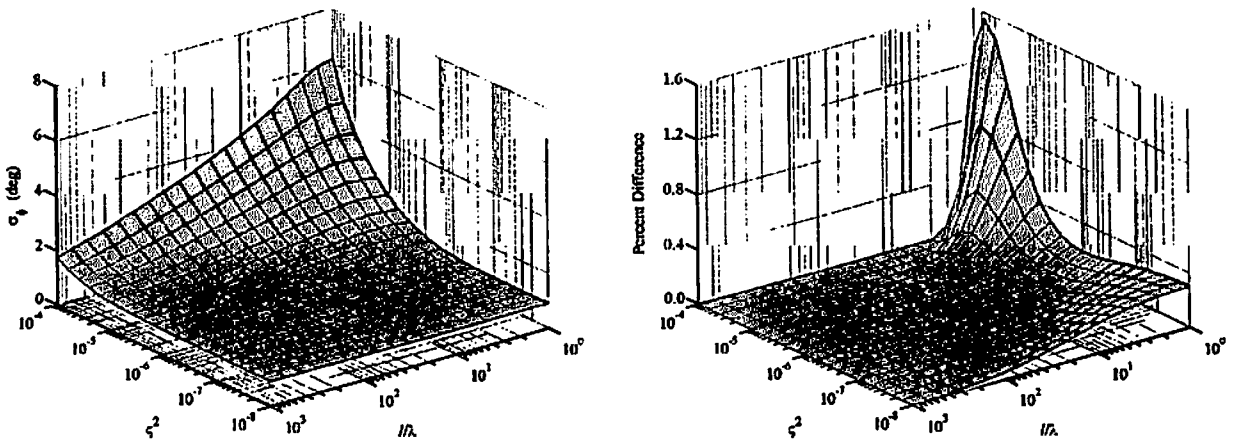

(a) (b)

Figure 9: (a) CRLB of ϕ for a spherical wave as a function of turbulence parameters. Calculation is for normal incidence, $r/\lambda = 500$, $\mathrm{SNR}_0 = 10\,\mathrm{dB}$ at $\mathcal{R}_0/\lambda = 500$, and a vector von Kármán spectrum. (b) Corresponding percent difference of σ_ϕ calculated with zero mean and with a nonzero mean.

and θ and the estimates of r and ϵ is zero. At $r/\lambda = 500$ and $l/\lambda = 10$, we find that for $\phi = \theta = 15°$: $\zeta_{\phi\, r/\lambda}$ and $\zeta_{\theta\, r/\lambda}$ are on the order of 10^{-9} for $\varsigma^2 = 10^{-6}$, and on the order of 10^{-11} for $\varsigma^2 = 10^{-4}$; $\zeta_{\phi\epsilon}$ and $\zeta_{\theta\epsilon}$ are on the order of 10^{-9} for $\varsigma^2 = 10^{-6}$, and on the order of 10^{-20} for $\varsigma^2 = 10^{-4}$; and $\zeta_{\phi\theta}$ is on the order of 10^{-3}, moreover, $\zeta_{\phi\theta}$ for this array geometry is the same as for the plane-wave case. Therefore, the coupling between the estimates of ϕ and θ and estimates of ϵ and r/λ are negigible for these cases. Moreover, as r/λ increases, these couplings rapidly approach zero. Reference [22] addresses the angular dependence and couplings in more detail.

As with the plane wave case, the results for a scalar von Kármán spectrum are very similar to those for a vector spectrum. The CRLBs of the AOAs are smaller for a scalar spectrum. The use of a nonzero mean reduces the CRLBs of the AOAs, though the percent difference is not as pronounced as for the vector spectrum.

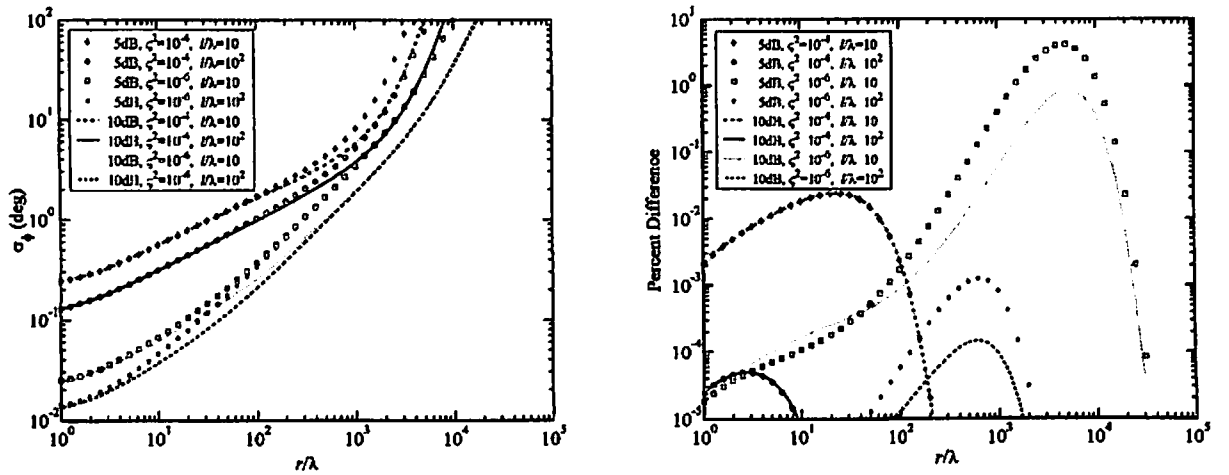

(a) (b)

Figure 10: (a) CRLB of ϕ for a spherical wave as a function of normalized propagation distance. Calculation is for normal incidence, SNR_0 evaluated at $\mathcal{R}_0/\lambda = 500$, and a vector von Kármán spectrum. (b) Corresponding percent difference of σ_ϕ for a spherical wave calculated with a zero mean and with a nonzero mean.

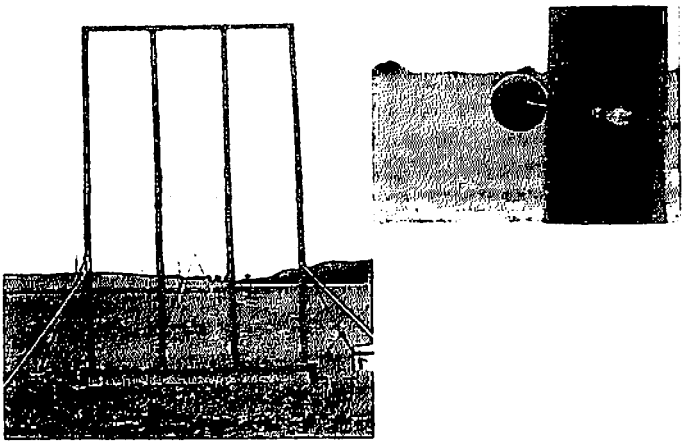

Figure 11: Left: Fiberglass beams and anchors used to support the microphone array. Right: Close up view of a microphone and mounting bracket.

II D Comparison to Experiment

II D.1 Array Design and Data Collection

For the purpose of accurately monitoring changes in apparent source bearing angles and intensity resulting from propagation through the atmosphere, researchers from the Army Research Laboratory and Penn State's Applied Research Laboratory collaborated in the design and construction of an "imaging" microphone array [1]. Completed in June 1998, the array was a vertical planar configuration with 32 microphones. The microphones were arranged in eight horizontal rows and four vertical columns. The rows were spaced 0.75 m apart and the columns 0.98 m. The array was supported with four vertical fiberglass beams anchored in cement, as shown in Fig. 11. It was constructed on mostly flat, agricultural land.

The large size of the array created a relatively narrow beam pattern at the low frequencies. The on-axis beam pattern of the array at 250 Hz is shown in Fig. 12. The initial nulls occur at $\theta \simeq \pm 13°$ and $\phi \simeq \pm 20°$, where θ is the elevation angle and ϕ the azimuthal angle. The initial sidelobes (aliased regions) are at $\theta \simeq \pm 19°$ and $\phi \simeq \pm 31°$, with the corresponding levels being -13 and -12 dB.

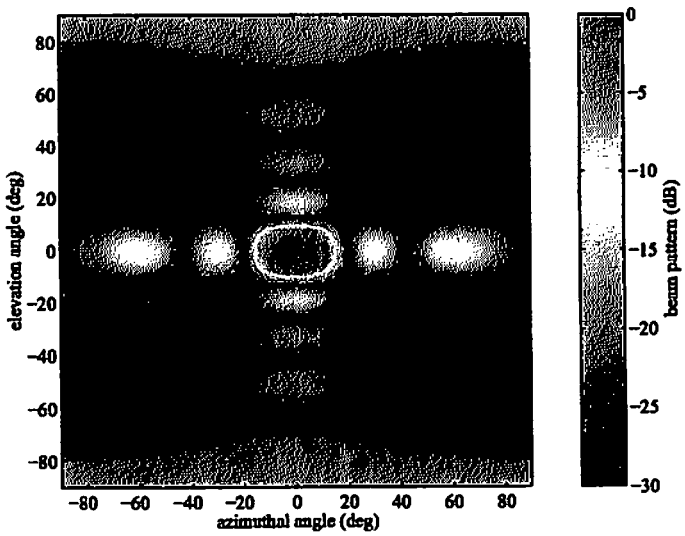

Figure 12: Beam pattern of the array at $f = 250$ Hz, as a function of the azimuthal and elevation angles (both defined relative to normal incidence).

Date	Time of day	Wind speed (m/s)	Wind direction (deg off array axis)	Temperature difference (°C)
18 June 1998	1738–1758	2.3	61	0.05
18 June 1998	2220–2240	0.1	169	1.17
19 June 1998	1033–1053	0.4 (2.4)	160 (73)	−0.10 (−0.19)

Table 2: Summary of the three experimental trials analyzed in this paper. Time of day is in local daylight savings time. Direction is the angle between the propagation path and the wind vector (0° is downwind propagation, 180° is upwind). Temperature difference is the temperature at 10 m height minus the temperature at 2 m. Data are one-hour averages incorporating the 20-min measurement period. (Shown in parentheses for 19 June 1033–1053 is the following hour.)

The acoustic source in the experiment consisted of a pair of 18-in. woofers, each driven by a 200-W amplifier. Tones at 50, 100, 150, 200, and 250 Hz were broadcast. The source was located 1.2 m above the ground at a distance of 770 m from the array.

The microphone signals were digitally sampled and written to hard disk for later analysis. Each trial generated about 0.5 Mbyte of data per second. The data was analyzed by applying fast Fourier transforms (FFTs) to 1-s data segments and then averaging over 10-s intervals. A two-dimensional spatial FFT beamformer was then applied over the array aperture to determine the arrival angles. More details on the signal processing are provided in [1].

A total of six 20-min trials were run, encompassing several distinct meteorological conditions. Three of these trials were selected for analysis here: 1738 and 2220 on 18 June, and 1033 on 19 June. They are summarized in Tab. 2. The first of these trials took place on a moderately windy evening. Propagation was marginally downwind. The second trial was on a clear, still night, with a strong temperature inversion. The third was on a cloudy morning with light winds, shortly after a rain shower. The temperature gradient was very small for this final trial; in meteorological terminology such conditions are called nearly neutral.

II D.2 Experimental Results

Figure 13 show the wavefront arrival angles monitored at the imaging array. These angles were determined by tracking the maximum of the FFT-beamformer output. Results for both the azimuth and elevation angles are shown at the source frequencies of 150 and 250 Hz.

For all three atmospheric cases, at both 150 and 250 Hz, the azimuthal angle varies around a mean of about 2°. (See Fig. 13(a–b).) Because this bias was consistent from trial to trial, it is probably due to imperfect alignment between the array axis and source bearing. These results illustrate that determination of azimuthal bearings with acoustic arrays is nearly unaffected by atmospheric conditions, so long as a sufficiently long record is available for averaging.

The average elevation angles (Fig. 13(c–d)) show much less consistency from trial to trial. Because the ground was fairly flat, the actual source elevation is very close to 0°. Discrepancies are attributable to atmospheric refraction, which focuses the sound energy upward or downward, depending on the direction of propagation and the wind and temperature gradients.

Refraction appears strongest for the nighttime trial (2220 on 18 June), due to the temperature inversion (positive temperature gradient) that had developed on this night. (The existence of the temperature inversion is evidenced by the large positive temperature difference in Table 1.) At 150 Hz, the mean elevation for this trial was 10°, which corresponds to an apparent source height of 130 m! At 250 Hz, the mean elevation was 6.1°, corresponding to 83 m. These results demonstrate that, for ground-to-ground transmission paths, refraction effects can greatly interfere with determination of the true elevation angle of a source.

Another interesting behavior seen in Fig. 13(c–d) is that the refraction is weakest for the cloudy, light wind condition (1033 on 19 June). Because of the clouds and light wind, there were no strong temperature or wind gradients to refract the sound. As a result, the source elevation is very near to the horizon (0°).

The variance in the arrival angles also exhibits a distinct dependence on atmospheric conditions, being highest for the moderately windy afternoon (1738 on 18 June). For this trial, at 250 Hz, the standard deviations of the elevation and azimuth were 1.2° and 1.4°, respectively. These values correspond to displacements of 17 m in the apparent vertical position and 18 m in the apparent horizontal position of the source.

At night, the variations are observed to occur more slowly, although they are substantial nonetheless. Because

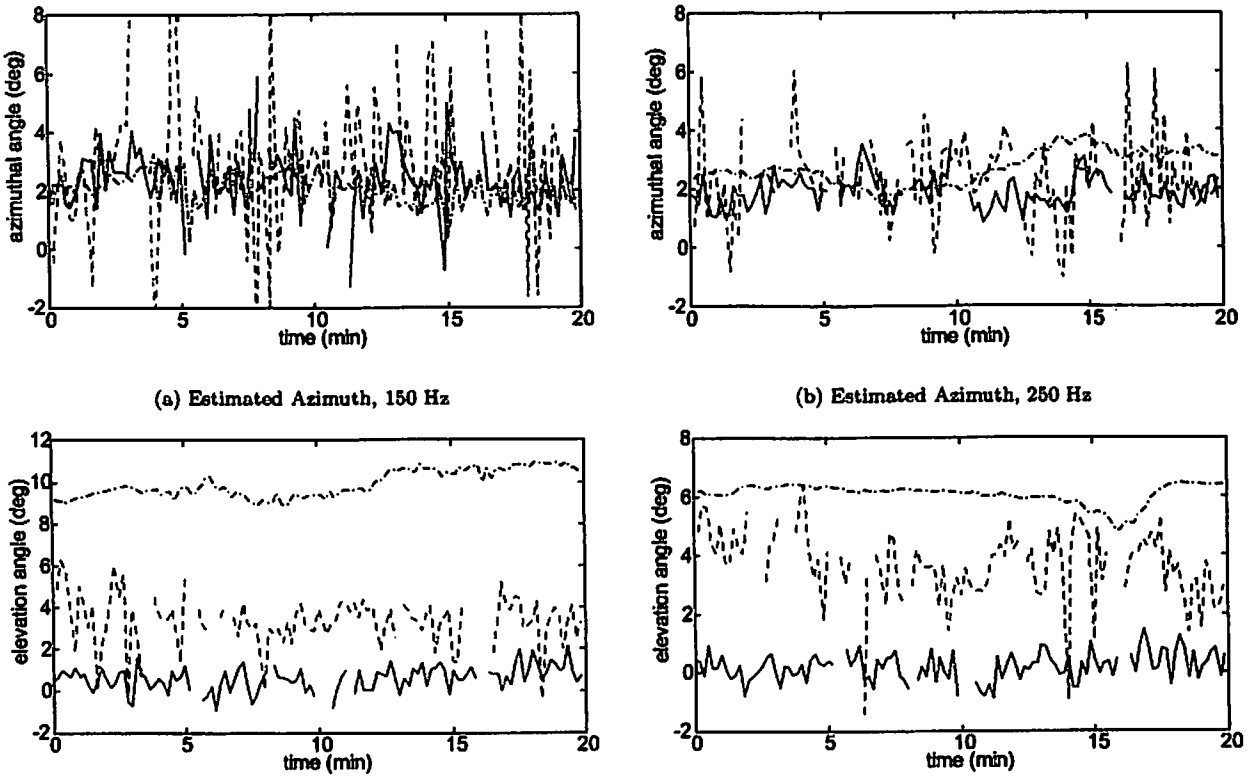

(a) Estimated Azimuth, 150 Hz

(b) Estimated Azimuth, 250 Hz

(c) Estimated Elevation, 150 Hz

(d) Estimated Elevation, 250 Hz

Figure 13: Estimated AOAs (using FFT beamformer) for source frequency of 150 and 250 Hz. Three 20-min trials are shown, starting at 1738 on 18 June 1998 (red dashed line), 2220 on 18 June (blue dash-dotted line), and 1033 on 19 June (green solid line).

the wind speed is so low for this trial (0.1 m/s) and a strong temperature gradient existed, atmospheric turbulence was very weak during this trial and probably is not the primary cause of the arrival-angle variations. We are uncertain of the actual physical mechanism driving the variations. Some likely candidates are gravity (buoyancy) waves, known to form in stable fluid layers, or evolution of a low-level jet (elevated region of high wind speed) [23].

The data presented in Fig. 13 vividly demonstrate how the atmosphere disrupts attempts to acoustically track targets. In principle, these effects could be mitigated by averaging the estimated arrival angles over a long duration of time; but in actuality, such averaging is tactically impractical because the target can move significantly during the averaging period.

II D.3 Comparison to CRLB

In order to compare the results of the theoretical model for the CRLB to experimental findings, it is necessary to generalize the treatment of the 2D correlation function to include contributions to the sound speed fluctuations from both vector and scalar von Kármán spectra. Models based on von Kármán's spectrum have been developed to calculate the 2D correlation function that include contributions to the sound speed variations from wind and temperature fluctuations, produced by both shear and buoyancy instabilities [15]. The 2D correlation function $b(\rho)$ is given by [11]

$$b(\rho) = f_s(\rho,\, \varsigma^2_{T,S+B}\,,\, l_{T,S+B}) + f_v(\rho,\, \varsigma^2_{V,S}\,,\, l_{V,S}) + f_v(\rho,\, \varsigma^2_{V,B}\,,\, l_{V,B})\,, \tag{79}$$

where the subscripts s and v denote scalar or vector spectrum, 'T' and V denote temperature or wind velocity fluctuations, and s and b denote shear or buoyancy instabilities. (The standard notation is to use b for the total 2D correlation function, and f_s and f_v for the contributions from the vector and scalar components.) We use the

Trial	Freq (Hz)	Estimated AOAs (deg)		Standard Deviation (deg)			
				Azimuth		Elevation	
		Azimuth	Elevation	Exp	CRLB	Exp	CRLB
1738 18 June	150	2.26	3.27	2.76	0.79	1.20	0.54
	200	1.82	4.15	1.76	0.62	1.34	0.43
	250	2.57	4.53	1.40	0.52	1.24	0.38
1033 19 June	150	2.31	0.65	1.06	0.75 (0.83)	0.58	0.48 (0.59)
	200	1.11	0.56	0.83	0.57 (0.67)	0.50	0.37 (0.49)
	250	1.93	0.23	0.54	0.46 (0.58)	0.48	0.30 (0.44)

Table 3: AOAs estimated from FFT beamforming, their observed experimental standard deviations, and the comparable CRLBs. CRLBs are calculated with the meteorological data from the hour incorporating the trial, and the quantity in parentheses from the following hour following the trial.

turbulence models of Wilson [16] and Ostashev and Wilson [15] to calculate the values of the ς^2's and l's based on the array height and atmospheric conditions. The extinction coefficient for the second moment may then be calculated using $b(\rho)$ in Eq. (40) for an incident plane wave and in Eq. (41) for a spherical wave.

These turbulence models are not valid at night. Therefore, let us consider two of the previously analyzed trials: 1738 on 18 June and 1033 on 19 June. Using the meteoroligical data from the hour incorporating the run, the CRLB of the azimuth and elevation are calculated assuming spherical propagation of the wavefront. Table 3 compares the experimental standard deviations of the azimuth and elevation to the CRLB for three different frequencies. (For the CRLB calculations, the unknown parameter vector is $\boldsymbol{\Theta} = [\phi, \theta, r/\lambda, \epsilon]^{\mathrm{T}}$. The couplings between the estimates of the AOAs and the estimates of r/λ and ϵ are negligible for the cases considered here.)

The CRLB is the theoretical lower bound of the MSE of an unbiased estimator about its actual value. Generally speaking, the trends in the data are well predicted by the theoretical model: the standard deviation for the azimuth is larger than for the elevation, and it decreases with increasing frequency. (The agreement for the trial starting at 1033 can be improved if we use the meteorological data from the hour beginning at 1100. This discrepancy may be due to changing wind direction during the actual hour of the trial, which resulted in a measured mean wind speed (determined by vector averaging) that is unrepresentative of the trial period.) Both of these trends are expected, as the size of the array baseline relative to the wavelength is an important factor determining the AOA accuracy. However, the observed standard deviations tend to be several times larger than the theoretical CRLB. This is characteristic of the CRLB, as it is not usually an attainable lower bound. There are several other factors that may also contribute: (1) The theoretical model does not incoroporate physical factors such as the interaction of the sound with the ground, or the gusting of the wind, which may be significant. (2) The FFT beamformer is not optimal, and another estimation method, such a MLE which incorporates the effects of a random medium, should be used. We note that Song and Ritcey [8] found that the beamforming method using a Bartlett processor which *did not* include random media effects performed considerably worse than the MLE which *did* incoroporate random media effects.

II E Conclusions

The performance bounds of acoustic arrays operating in atmospheric turbulence with fluctuations described by a von Kármán spectrum have been examined. This analysis features four main improvements upon earlier work: (1) The performance bounds have been generalized to weak as well as strong scattering. (2) Multiple unknowns such as the propagation distance of the wavefront, turbulence parameters, phase of the source, and signal-to-noise ratio have been incorporated. (3) AOA estimates for three-dimensional problems (i.e., two bearing angles) have been considered. (4) A multivariate analysis for an incident spherical wave has been developed in addition to that for an incident plane wave.

Our primary interest here was to analyze the Cramer-Rao lower bounds of the angles of arrival for the case of strong diffraction. For an incident plane wave, we have found that an appropriate choice of coordinate system and array geometry leads to the decoupling of the estimates of the AOAs from the estimates of the other parameters: the normalized propagation distance (r/λ), SNR, turbulence parameters (l/λ and ς^2), and phase angle of the source (ϵ). In order to remain consistent with the small-angle approximation, we had to choose a coordinate

system that resulted in the coupling of the estimates of the azimuth and zenith; the coupling, however, was small. For large values of the index-of-refraction variance and moderate to small values of the normalized length scale, we have found that the CRLBs of the AOAs increase significantly at large propagation distances. However, for smaller values of the index-of-refraction variance and normalized propagation distance, the SNR is the limiting factor.

For an incident spherical wave, we have found that the estimates of the AOAs are coupled to the estimates of the normalized propagation distance, the phase angle of the source, and to one another. The estimates of the AOAs are uncoupled from the estimates of the turbulence parameters and SNR_0. For the array geometry considered, the couplings between the estimates of the AOAs and the estimates of source phase and normalized propagation distance are negigible, and the coupling of the estimates of the azimuth and elevation is weak. For small values of the normalized propagation distance, the CRLBs of the AOAs are dependent upon turbulence parameters and independent of SNR_0.

We have found that for both a plane wave and a spherical wave, the use of a nonzero mean reduces the CRLBs of the AOAs from that calculated with a zero mean. The effect is more prevelant for a vector von Kármán spectrum than for a scalar. However, the largest percent difference occurs in the regions where the CRLBs are large, and hence the AOAs cannot be well estimated. Therefore, for this analysis the inclusion of a nonzero mean is not very significant. However, for other models of the MCF, the percent difference may be more significant, and thus a nonzero mean should be considered.

The results demonstrate that scattering by atmospheric turbulence significantly affects the performance of acoustic sensor arrays. While only a single array with a simple geometry was considered in this analysis, the results indicate that the effects of atmospheric turbulence should be included in performance bounds calculations for other more complicated systems as well.

This analysis would benefit from an improved model of the second moment for oblique incidence. Future efforts should attempt to incorporate the additional phenomena of ground reflections and refraction by atmospheric wind and temperature gradients. These phenomena will likely have a considerable impact on the ability to estimate the elevation. Numerical techniques will be required to model these effects.

III Geometric Acoustics

III A Motivation

In geometric acoustics, the real and imaginary components of the signal no longer have equal covariances, as the phase amplitude fluctuations dominate the signal behavior. Therefore, it is necessary to develop a statistical model for the received signal in the geometric acoustics limit.

In this section, a tilde $\tilde{}$ is used to denote all complex quantities and the absence of a tilde denotes a real quantity. Furthermore, we use the standard notation that $\mathbf{x} \sim \mathcal{N}_N(\mathbf{C}_\mathbf{x}, \boldsymbol{\mu}_\mathbf{x})$ means that the real $N \times 1$ random vector $\mathbf{x}$ has a Gaussian PDF with real $N \times N$ covariance matrix $\mathbf{C}_\mathbf{x}$ and real $N \times 1$ mean vector $\boldsymbol{\mu}_\mathbf{x}$. Similarly, $\tilde{\mathbf{x}} \sim \mathcal{CN}_N(\tilde{\mathbf{C}}_{\tilde{\mathbf{x}}}, \tilde{\boldsymbol{\mu}}_{\tilde{\mathbf{x}}})$ means that the complex $N \times 1$ random vector $\tilde{\mathbf{x}}$ has a complex Gaussian PDF with complex $N \times N$ covariance matrix $\tilde{\mathbf{C}}_{\tilde{\mathbf{x}}}$ and complex $N \times 1$ mean vector $\tilde{\boldsymbol{\mu}}_{\tilde{\mathbf{x}}}$. If we write

$$\tilde{\mathbf{x}} = \mathbf{x}^{(u)} + \mathrm{i}\mathbf{x}^{(v)}, \tag{80}$$

where the superscripts (u) and (v) respectively refer to the real and imaginary components, then by definition the covariance and mean of a complex Gaussian satisfy

$$\tilde{\boldsymbol{\mu}}_{\tilde{\mathbf{x}}} = \boldsymbol{\mu}_{\mathbf{x}^{(u)}} + \mathrm{i}\boldsymbol{\mu}_{\mathbf{x}^{(v)}} \quad \text{and} \quad \tilde{\mathbf{C}}_{\tilde{\mathbf{x}}} = 2\left[\mathbf{C}_{\mathbf{x}^{(u)}\mathbf{x}^{(u)}} + \mathbf{C}_{\mathbf{x}^{(v)}\mathbf{x}^{(u)}}\right] \tag{81}$$

where

$$\mathbf{C}_{\mathbf{x}^{(u)}\mathbf{x}^{(u)}} = \mathbf{C}_{\mathbf{x}^{(v)}\mathbf{x}^{(v)}} \qquad \mathbf{C}_{\mathbf{x}^{(u)}\mathbf{x}^{(u)}} = \left[\left\langle x_i^{(u)} x_j^{(u)} \right\rangle\right] \qquad \mathbf{C}_{\mathbf{x}^{(v)}\mathbf{x}^{(v)}} = \left[\left\langle x_i^{(v)} x_j^{(v)} \right\rangle\right] \tag{82}$$

$$\mathbf{C}_{\mathbf{x}^{(u)}\mathbf{x}^{(v)}} = -\mathbf{C}_{\mathbf{x}^{(v)}\mathbf{x}^{(u)}} \qquad \mathbf{C}_{\mathbf{x}^{(u)}\mathbf{x}^{(v)}} = \left[\left\langle x_i^{(u)} x_j^{(v)} \right\rangle\right] \qquad \mathbf{C}_{\mathbf{x}^{(v)}\mathbf{x}^{(u)}} = \left[\left\langle x_i^{(v)} x_j^{(u)} \right\rangle\right]. \tag{83}$$

III A.1 Signal Model

Suppose a source emits a complex signal that is received at an N-element array as $\tilde{\mathbf{p}} = [\tilde{p}_1, \tilde{p}_2, \ldots, \tilde{p}_N]^\mathrm{T}$. Let $\tilde{\mathbf{p}} = \mathbf{p}^{(u)} + \mathrm{i}\mathbf{p}^{(v)}$, where $\mathbf{p}^{(u)}$ and $\mathbf{p}^{(v)}$ are the real and imaginary components, respectively. The reduced

waveform, or phasor, at the ith sensor is defined to be

$$\tilde{\psi}_i = \tilde{p}_i / \tilde{p}_i^H \,, \tag{84}$$

where $\tilde{p}_i^H$ is the wavefunction in the absence of random inhomogeneities. If the corresponding real $2N \times 1$ partitioned vectors are

$$\mathbf{p} = \left[\mathbf{p}^{(u)}, \mathbf{p}^{(v)}\right]^{\mathrm{T}} \qquad \boldsymbol{\psi} = \left[\boldsymbol{\psi}^{(u)}, \boldsymbol{\psi}^{(v)}\right]^{\mathrm{T}} , \tag{85}$$

then we may write

$$\mathbf{p} = \mathbf{A}\boldsymbol{\psi} \,, \tag{86}$$

where $\mathbf{A}$ is the $2N \times 2N$ transformation matrix

$$\mathbf{A} = \begin{bmatrix} \boldsymbol{\zeta} & -\boldsymbol{\xi} \\ \boldsymbol{\xi} & \boldsymbol{\zeta} \end{bmatrix} \tag{87}$$

and

$$\boldsymbol{\zeta} = \mathbf{diag}\left[\zeta_1, \zeta_2, \ldots, \zeta_N\right] \qquad \zeta_i = A_i \cos \Phi_i \tag{88}$$

$$\boldsymbol{\xi} = \mathbf{diag}\left[\xi_1, \xi_2, \ldots, \xi_N\right] \qquad \xi_i = A_i \sin \Phi_i \,. \tag{89}$$

If $\tilde{\mathbf{p}}$ is a plane wave, then

$$\tilde{p}_i^H = p_0 e^{i\Phi_i} \qquad A_i = p_0 \;\forall\, i \qquad \Phi_i = \mathbf{k} \cdot \mathbf{r}_i + \epsilon \tag{90}$$

where p_0 is the initial amplitude, $\mathbf{k}$ is the wave number, $\mathbf{r}_i$ is the vector from the source to the ith sensor, and ϵ is the phase of the source. Whereas, if $\tilde{\mathbf{p}}$ is a spherical wave, then

$$A_i = \mathcal{A} r_0 / r_i \quad \text{and} \quad \Phi_i = k r_i + \epsilon \,, \tag{91}$$

where $\mathcal{A}_i$ is the amplitude at $r_i = r_0$. The total received complex signal at the array, $\tilde{\mathbf{s}}$, is the sum of the source signal, $\tilde{\mathbf{p}}$, and the noise, $\tilde{\mathbf{n}}$.

III A.2 Properties of Transformation Matrix

If $A_i = A \;\forall\, i$, we may write

$$\mathbf{M} = \mathbf{A}/A = \begin{bmatrix} \alpha & -\beta \\ \beta & \alpha \end{bmatrix} \qquad \alpha = \zeta/A \qquad \beta = \xi/A \,. \tag{92}$$

Note that $\mathbf{M}^{\mathrm{T}} = \mathbf{M}^{-1}$ and that $\mathbf{M}$ commutes with partitioned matrices of the form

$$\begin{bmatrix} \mathbf{D}_1 & -\mathbf{D}_2 \\ \mathbf{D}_2 & \mathbf{D}_1 \end{bmatrix} , \tag{93}$$

where $\mathbf{D}_1$ and $\mathbf{D}_2$ are $N \times N$ diagonal matrices. [For example, as previously noted, $A_i = A = p_0 \;\forall\, i$ for a plane wave. This also holds for spherical waves whose attenuation may be approximated as constant across the array.]

Now suppose that Φ_i is dependent on Θ_λ, but that A is not. Then

$$\frac{\partial \mathbf{M}}{\partial \Theta_\lambda} = \begin{bmatrix} \dfrac{\partial \alpha}{\partial \Theta_\lambda} & -\dfrac{\partial \beta}{\partial \Theta_\lambda} \\ \dfrac{\partial \beta}{\partial \Theta_\lambda} & \dfrac{\partial \alpha}{\partial \Theta_\lambda} \end{bmatrix} , \tag{94}$$

where

$$\frac{\partial \alpha_i}{\partial \Theta_\lambda} = -\sin \Phi_i \frac{\partial \Phi_i}{\partial \Theta_\lambda} \quad \text{and} \quad \frac{\partial \beta}{\partial \Theta_\lambda} = \cos \Phi_i \frac{\partial \Phi_i}{\partial \Theta_\lambda} \,. \tag{95}$$

Thus

$$\frac{\partial \boldsymbol{\alpha}}{\partial \Theta_\lambda} = -\boldsymbol{\beta}\mathbf{D}_\lambda = -\mathbf{D}_\lambda \boldsymbol{\beta} \quad \text{and} \quad \frac{\partial \boldsymbol{\beta}}{\partial \Theta_\lambda} = \boldsymbol{\alpha}\mathbf{D}_\lambda = \mathbf{D}_\lambda \boldsymbol{\alpha} \,, \tag{96}$$

where

$$\mathbf{D}_\lambda = \mathbf{diag}\left[\frac{\partial \Phi_1}{\partial \Theta_\lambda}, \frac{\partial \Phi_2}{\partial \Theta_\lambda}, \ldots, \frac{\partial \Phi_N}{\partial \Theta_\lambda}\right]. \tag{97}$$

Letting

$$\mathbf{T}_\lambda = \begin{bmatrix} \mathbf{0} & -\mathbf{D}_\lambda \\ \mathbf{D}_\lambda & \mathbf{0} \end{bmatrix}, \tag{98}$$

we write

$$\frac{\partial \mathbf{M}}{\partial \Theta_\lambda} = \mathbf{T}_\lambda \mathbf{M} = \mathbf{M}\mathbf{T}_\lambda. \tag{99}$$

[For example, in many models the only dependence on the wavefront AOAs is in the phase terms Φ_i.]

III B Formulation

Consider the complex random vector $\tilde{\boldsymbol{\psi}} = \boldsymbol{\psi}^{(u)} + \mathrm{i}\boldsymbol{\psi}^{(v)}$, where $\boldsymbol{\psi}^{(u)}$ and $\boldsymbol{\psi}^{(v)}$ are the real and imaginary components, respectively. Suppose that $\boldsymbol{\psi}^{(u)}$ and $\boldsymbol{\psi}^{(v)}$ are uncorrelated, $\boldsymbol{\psi}^{(u)} \sim \mathcal{N}_N(\boldsymbol{\mu}_{\boldsymbol{\psi}^{(u)}}, \mathbf{C}_{\boldsymbol{\psi}^{(u)}})$, and $\boldsymbol{\psi}^{(v)} \sim \mathcal{N}_N(\boldsymbol{\mu}_{\boldsymbol{\psi}^{(v)}}, \mathbf{C}_{\boldsymbol{\psi}^{(v)}})$. Let $\boldsymbol{\psi}$ be the corresponding $2N \times 1$ real partitioned vector

$$\boldsymbol{\psi} = \begin{bmatrix} \boldsymbol{\psi}^{(u)} \\ \boldsymbol{\psi}^{(v)} \end{bmatrix}, \tag{100}$$

$\boldsymbol{\psi} \sim \mathcal{N}_{2N}(\boldsymbol{\mu}_{\boldsymbol{\psi}}, \mathbf{C}_{\boldsymbol{\psi}})$, where

$$\boldsymbol{\mu}_{\boldsymbol{\psi}} = \begin{bmatrix} \boldsymbol{\mu}_{\boldsymbol{\psi}^{(u)}} \\ \boldsymbol{\mu}_{\boldsymbol{\psi}^{(v)}} \end{bmatrix} \quad \text{and} \quad \mathbf{C}_{\boldsymbol{\psi}} = \begin{bmatrix} \mathbf{C}_{\boldsymbol{\psi}^{(u)}} & \mathbf{0} \\ \mathbf{0} & \mathbf{C}_{\boldsymbol{\psi}^{(v)}} \end{bmatrix}. \tag{101}$$

And suppose that $\tilde{\boldsymbol{\eta}} = \boldsymbol{\eta}^{(u)} + \mathrm{i}\boldsymbol{\eta}^{(v)}$, $\boldsymbol{\eta}^{(u)} \sim \mathcal{N}_N(\boldsymbol{\mu}_{\boldsymbol{\eta}^{(u)}}, \mathbf{C}_{\boldsymbol{\eta}^{(u)}})$, $\boldsymbol{\eta}^{(v)} \sim \mathcal{N}_N(\boldsymbol{\mu}_{\boldsymbol{\eta}^{(v)}}, \mathbf{C}_{\boldsymbol{\eta}^{(v)}})$, and $\boldsymbol{\eta}^{(u)}$ and $\boldsymbol{\eta}^{(v)}$ are uncorrelated. Analogously, we define $\boldsymbol{\eta} \sim \mathcal{N}_{2N}(\boldsymbol{\mu}_{\boldsymbol{\eta}}, \mathbf{C}_{\boldsymbol{\eta}})$.

Let $\boldsymbol{\zeta} = \boldsymbol{\psi} + \boldsymbol{\eta}$ and $\mathbf{s} = \mathbf{A}\boldsymbol{\zeta}$, where $\mathbf{A} = A\mathbf{M}$ is as previously defined. If $\boldsymbol{\psi}$ and $\boldsymbol{\eta}$ are uncorrelated, then [24]

$$\boldsymbol{\zeta} \sim \mathcal{N}_{2N}(\boldsymbol{\mu}_{\boldsymbol{\zeta}}, \mathbf{C}_{\boldsymbol{\zeta}}) \qquad \boldsymbol{\mu}_{\boldsymbol{\zeta}} = \boldsymbol{\mu}_{\boldsymbol{\psi}} + \boldsymbol{\mu}_{\boldsymbol{\eta}} \qquad \mathbf{C}_{\boldsymbol{\zeta}} = \mathbf{C}_{\boldsymbol{\psi}} + \mathbf{C}_{\boldsymbol{\eta}} \tag{102}$$

$$\mathbf{s} \sim \mathcal{N}_{2N}(\boldsymbol{\mu}_{\mathbf{s}}, \mathbf{C}_{\mathbf{s}}) \qquad \boldsymbol{\mu}_{\mathbf{s}} = \mathbf{A}\boldsymbol{\mu}_{\boldsymbol{\zeta}} = A\mathbf{M}\boldsymbol{\mu}_{\boldsymbol{\zeta}} \qquad \mathbf{C}_{\mathbf{s}} = \mathbf{A}\mathbf{C}_{\boldsymbol{\zeta}}\mathbf{A}^{\mathrm{T}} = A^2\mathbf{M}\mathbf{C}_{\boldsymbol{\zeta}}\mathbf{M}^{\mathrm{T}}. \tag{103}$$

[For the special case when $\boldsymbol{\mu}_{\boldsymbol{\eta}} = \mathbf{0}$, $\mathbf{C}_{\boldsymbol{\eta}}$ is a diagional matrix, and $\mathbf{C}_{\boldsymbol{\eta}^{(u)}} = \mathbf{C}_{\boldsymbol{\eta}^{(v)}}$,

$$\boldsymbol{\mu}_{\mathbf{s}} = A\mathbf{M}\boldsymbol{\mu}_{\boldsymbol{\psi}} \quad \text{and} \quad \mathbf{C}_{\mathbf{s}} = A^2\mathbf{M}\mathbf{C}_{\boldsymbol{\psi}}\mathbf{M}^{\mathrm{T}} + A^2\mathbf{C}_{\boldsymbol{\eta}}, \tag{104}$$

as $\mathbf{M}$ and $\mathbf{C}_{\boldsymbol{\eta}}$ commute.]

Suppose that the pdf of $\mathbf{s}$ is parameterized by the real vector $\boldsymbol{\Theta}$. The Fisher information (FI) matrix for the real multivariate Gaussian random vector $\mathbf{s}$ is given by the second equality in Eq. (4). Consider the first term of the FI. As $\mathbf{M}$ is a orthogonal matrix,

$$\mathbf{C}_{\mathbf{s}}^{-1} = p_0^{-2}\mathbf{M}\mathbf{C}_{\boldsymbol{\zeta}}^{-1}\mathbf{M}^{\mathrm{T}}. \tag{105}$$

If $\mathbf{C}_{\boldsymbol{\zeta}}$ and p_0 are independent of $\boldsymbol{\Theta}$, then

$$\frac{\partial \mathbf{C}_{\mathbf{s}}}{\partial \Theta_\lambda} = p_0^2\frac{\partial \mathbf{M}}{\partial \Theta_\lambda}\mathbf{C}_{\boldsymbol{\zeta}}\mathbf{M}^{\mathrm{T}} + p_0^2\mathbf{M}\mathbf{C}_{\boldsymbol{\zeta}}\frac{\partial \mathbf{M}^{\mathrm{T}}}{\partial \Theta_\lambda} = p_0^2\mathbf{M}\mathbf{T}_\lambda\mathbf{C}_{\boldsymbol{\zeta}}\mathbf{M}^{\mathrm{T}} + p_0^2\mathbf{M}\mathbf{C}_{\boldsymbol{\zeta}}\mathbf{M}^{\mathrm{T}}\mathbf{T}_\lambda^{\mathrm{T}}. \tag{106}$$

Therefore,

$$\begin{aligned}
\mathrm{tr}\left(\mathbf{C}_{\mathbf{s}}^{-1}\frac{\partial \mathbf{C}_{\mathbf{s}}}{\partial \Theta_\lambda}\mathbf{C}_{\mathbf{s}}^{-1}\frac{\partial \mathbf{C}_{\mathbf{s}}}{\partial \Theta_\nu}\right) =& \mathrm{tr}\left(\mathbf{M}\mathbf{C}_{\boldsymbol{\zeta}}^{-1}\mathbf{T}_\lambda\mathbf{C}_{\boldsymbol{\zeta}}\mathbf{M}^{\mathrm{T}}\mathbf{M}\mathbf{C}_{\boldsymbol{\zeta}}^{-1}\mathbf{T}_\nu\mathbf{C}_{\boldsymbol{\zeta}}\mathbf{M}^{\mathrm{T}}\right) + \mathrm{tr}\left(\mathbf{M}\mathbf{C}_{\boldsymbol{\zeta}}^{-1}\mathbf{T}_\lambda\mathbf{C}_{\boldsymbol{\zeta}}\mathbf{M}^{\mathrm{T}}\mathbf{T}_\nu^{\mathrm{T}}\right) \\
&+ \mathrm{tr}\left(\mathbf{T}_\lambda^{\mathrm{T}}\mathbf{M}\mathbf{C}_{\boldsymbol{\zeta}}^{-1}\mathbf{T}_\nu\mathbf{C}_{\boldsymbol{\zeta}}\mathbf{M}^{\mathrm{T}}\right) + \mathrm{tr}\left(\mathbf{T}_\lambda^{\mathrm{T}}\mathbf{T}_\nu^{\mathrm{T}}\right) \\
=& \mathrm{tr}\left(\mathbf{C}_{\boldsymbol{\zeta}}^{-1}\mathbf{T}_\lambda\mathbf{C}_{\boldsymbol{\zeta}}\mathbf{T}_\nu^{\mathrm{T}}\right) + \mathrm{tr}\left(\mathbf{C}_{\boldsymbol{\zeta}}^{-1}\mathbf{T}_\nu\mathbf{C}_{\boldsymbol{\zeta}}\mathbf{T}_\lambda^{\mathrm{T}}\right) + 2\mathrm{tr}\left(\mathbf{T}_\lambda\mathbf{T}_\nu\right) \\
=& \mathrm{tr}\left(\mathbf{C}_{\boldsymbol{\zeta}^{(u)}}^{-1}\mathbf{D}_\lambda\mathbf{C}_{\boldsymbol{\zeta}^{(v)}}\mathbf{D}_\nu\right) + \mathrm{tr}\left(\mathbf{C}_{\boldsymbol{\zeta}^{(v)}}^{-1}\mathbf{D}_\lambda\mathbf{C}_{\boldsymbol{\zeta}^{(u)}}\mathbf{D}_\nu\right) \\
&+ \mathrm{tr}\left(\mathbf{C}_{\boldsymbol{\zeta}^{(u)}}^{-1}\mathbf{D}_\nu\mathbf{C}_{\boldsymbol{\zeta}^{(v)}}\mathbf{D}_\lambda\right) + \mathrm{tr}\left(\mathbf{C}_{\boldsymbol{\zeta}^{(v)}}^{-1}\mathbf{D}_\nu\mathbf{C}_{\boldsymbol{\zeta}^{(u)}}\mathbf{D}_\lambda\right) - 4\mathrm{tr}\left(\mathbf{D}_\lambda\mathbf{D}_\nu\right) \\
=& 2\mathrm{tr}\left(\mathbf{C}_{\boldsymbol{\zeta}^{(u)}}^{-1}\mathbf{D}_\lambda\mathbf{C}_{\boldsymbol{\zeta}^{(v)}}\mathbf{D}_\nu\right) + 2\mathrm{tr}\left(\mathbf{C}_{\boldsymbol{\zeta}^{(v)}}^{-1}\mathbf{D}_\lambda\mathbf{C}_{\boldsymbol{\zeta}^{(u)}}\mathbf{D}_\nu\right) - 4\mathrm{tr}\left(\mathbf{D}_\lambda\mathbf{D}_\nu\right).
\end{aligned} \tag{107}$$

The first and third equalities result from simple matrix multiplication. The second equality results from the fact that $\mathbf{M}$ is orthogonal, $\mathbf{M}$ and $\mathbf{T}$ commute, and from the properties of the trace. And the last equality results from the properties of the trace and the fact that $\mathbf{C}_{\zeta^{(u)}}$ and $\mathbf{C}_{\zeta^{(v)}}$ are symmetric matrices.

Consider now the second term of the FI. If $\boldsymbol{\mu}_\zeta$ is independent of $\boldsymbol{\Theta}$, then

$$\frac{\partial \boldsymbol{\mu}_s}{\partial \Theta_\nu} = p_0 \frac{\partial \mathbf{M}}{\partial \Theta_\nu} \boldsymbol{\mu}_\zeta = p_0 \mathbf{M} \mathbf{T}_\nu \boldsymbol{\mu}_\zeta \,. \tag{108}$$

Therefore,

$$\begin{aligned} \frac{\partial \boldsymbol{\mu}_s^{\mathrm{T}}}{\partial \Theta_\lambda} \mathbf{C}_s^{-1} \frac{\partial \boldsymbol{\mu}_s}{\partial \Theta_\nu} &= \boldsymbol{\mu}_\zeta^{\mathrm{T}} \mathbf{T}_\lambda^{\mathrm{T}} \mathbf{M}^{\mathrm{T}} \mathbf{M} \mathbf{C}_\zeta^{-1} \mathbf{M}^{\mathrm{T}} \mathbf{M} \mathbf{T}_\nu \boldsymbol{\mu}_\zeta = \boldsymbol{\mu}_\zeta^{\mathrm{T}} \mathbf{T}_\lambda^{\mathrm{T}} \mathbf{C}_\zeta^{-1} \mathbf{T}_\nu \boldsymbol{\mu}_\zeta \\ &= \boldsymbol{\mu}_{\zeta^{(v)}}^{\mathrm{T}} \mathbf{D}_\lambda \mathbf{C}_{\zeta^{(u)}}^{-1} \mathbf{D}_\nu \boldsymbol{\mu}_{\zeta^{(v)}} + \boldsymbol{\mu}_{\zeta^{(u)}}^{\mathrm{T}} \mathbf{D}_\lambda \mathbf{C}_{\zeta^{(v)}}^{-1} \mathbf{D}_\nu \boldsymbol{\mu}_{\zeta^{(u)}} \,. \end{aligned} \tag{109}$$

Hence, when the only dependence on $\boldsymbol{\Theta}$ is in the transformation matrix $\mathbf{M}$, the FI is

$$\begin{aligned} J_{\lambda\nu} =& \mathrm{tr}\left(\mathbf{C}_{\zeta^{(u)}}^{-1} \mathbf{D}_\lambda \mathbf{C}_{\zeta^{(v)}} \mathbf{D}_\nu\right) + \mathrm{tr}\left(\mathbf{C}_{\zeta^{(v)}}^{-1} \mathbf{D}_\lambda \mathbf{C}_{\zeta^{(u)}} \mathbf{D}_\nu\right) - 2\mathrm{tr}\left(\mathbf{D}_\lambda \mathbf{D}_\nu\right) \\ &+ \boldsymbol{\mu}_{\zeta^{(v)}}^{\mathrm{T}} \mathbf{D}_\lambda \mathbf{C}_{\zeta^{(u)}}^{-1} \mathbf{D}_\nu \boldsymbol{\mu}_{\zeta^{(v)}} + \boldsymbol{\mu}_{\zeta^{(u)}}^{\mathrm{T}} \mathbf{D}_\lambda \mathbf{C}_{\zeta^{(v)}}^{-1} \mathbf{D}_\nu \boldsymbol{\mu}_{\zeta^{(u)}} \,. \end{aligned} \tag{110}$$

III C Two-Element Array

Consider a 2-element array. Let

$$\mathbf{C}_{\zeta^{(u)}} = \begin{bmatrix} u_{11} & u_{12} \\ u_{12} & u_{22} \end{bmatrix} \quad \mathbf{C}_{\zeta^{(v)}} = \begin{bmatrix} v_{11} & v_{12} \\ v_{12} & v_{22} \end{bmatrix} \quad \mathbf{D}_\lambda = \begin{bmatrix} d_1^\lambda & 0 \\ 0 & d_2^\lambda \end{bmatrix}. \tag{111}$$

Then

$$\mathrm{tr}\left(\mathbf{C}_{\zeta^{(v)}}^{-1} \mathbf{D}_\lambda \mathbf{C}_{\zeta^{(u)}} \mathbf{D}_\nu\right) = \frac{u_{11} v_{22} d_1^\lambda d_1^\nu - u_{12} v_{12} \left(d_1^\lambda d_2^\nu + d_2^\lambda d_1^\nu\right) + u_{22} v_{11} d_2^\lambda d_2^\nu}{v_{11} v_{22} - v_{12}^2} \,. \tag{112}$$

Now let

$$\boldsymbol{\mu}_{\zeta^{(u)}} = \begin{bmatrix} u_1 \\ u_2 \end{bmatrix} \quad \text{and} \quad \boldsymbol{\mu}_{\zeta^{(v)}} = \begin{bmatrix} v_1 \\ v_2 \end{bmatrix} . \tag{113}$$

Then

$$\boldsymbol{\mu}_{\zeta^{(v)}}^{\mathrm{T}} \mathbf{D}_\lambda \mathbf{C}_{\zeta^{(u)}}^{-1} \mathbf{D}_\nu \boldsymbol{\mu}_{\zeta^{(v)}} = \frac{u_{22} v_1^2 d_1^\lambda d_1^\nu - u_{12} v_1 v_2 \left(d_1^\lambda d_2^\nu + d_2^\lambda d_1^\nu\right) + u_{11} v_2^2 d_2^\lambda d_2^\nu}{u_{11} u_{22} - u_{12}^2} \,. \tag{114}$$

After assembling all the contributions to the FI, we find

$$\begin{aligned} J_{\lambda\nu} =& d_1^\lambda d_1^\nu \left(\frac{u_{22} v_{11}}{u_{11} u_{22} - u_{12}^2} + \frac{u_{11} v_{22}}{v_{11} v_{22} - v_{12}^2} - 2 + \frac{u_{22} v_1^2}{u_{11} u_{22} - u_{12}^2} + \frac{v_{22} u_1^2}{v_{11} v_{22} - v_{12}^2}\right) + \\ & d_2^\lambda d_2^\nu \left(\frac{u_{11} v_{22}}{u_{11} u_{22} - u_{12}^2} + \frac{u_{22} v_{11}}{v_{11} v_{22} - v_{12}^2} - 2 + \frac{u_{11} v_2^2}{u_{11} u_{22} - u_{12}^2} + \frac{v_{11} u_2^2}{v_{11} v_{22} - v_{12}^2}\right) - \\ & \left(d_1^\lambda d_2^\nu + d_2^\lambda d_1^\nu\right) \left[u_{12} v_{12} \left(\frac{1}{u_{11} u_{22} - u_{12}^2} + \frac{1}{v_{11} v_{22} - v_{12}^2}\right) + \frac{u_{12} v_1 v_2}{u_{11} u_{22} - u_{12}^2} + \frac{v_{12} u_1 u_2}{v_{11} v_{22} - v_{12}^2}\right] . \end{aligned} \tag{115}$$

Sometimes of particular interest is when $u_{11} = u_{22}$, $u_1 = u_2$, $v_{11} = v_{22}$, and $v_1 = v_2$. In this case

$$\begin{aligned} J_{\lambda\nu} =& \left(d_1^\lambda d_1^\nu + d_2^\lambda d_2^\nu\right) \left[u_{11} v_{11} \left(\frac{1}{u_{11}^2 - u_{12}^2} + \frac{1}{v_{11}^2 - v_{12}^2}\right) - 2 + \frac{u_{11} v_1^2}{u_{11}^2 - u_{12}^2} + \frac{v_{11} u_1^2}{v_{11}^2 - v_{12}^2}\right] - \\ & \left(d_1^\lambda d_2^\nu + d_2^\lambda d_1^\nu\right) \left[u_{12} v_{12} \left(\frac{1}{u_{11}^2 - u_{12}^2} + \frac{1}{v_{11}^2 - v_{12}^2}\right) + \frac{u_{12} v_1^2}{u_{11}^2 - u_{12}^2} + \frac{v_{12} u_1^2}{v_{11}^2 - v_{12}^2}\right] . \end{aligned} \tag{116}$$

Notice that when

$$d_1^\lambda d_1^\nu + d_2^\lambda d_2^\nu = 0 \quad \text{and} \quad d_1^\lambda d_2^\nu + d_2^\lambda d_1^\nu = 0 \,, \tag{117}$$

$J_{\lambda\nu} = 0$ for any value of u_{11}, u_{12}, u_1, v_{11}, v_{12}, and v_1.

III C.1 Plane Wave

Consider the transformation for a plane wave. For this simplyfied problem, we consider $\boldsymbol{\Theta} = [\phi, \epsilon]^{\mathrm{T}}$, where ϕ is the AOA and ϵ is the phase of the source. Let $\mathbf{r}_i = \mathbf{r} - \mathbf{r}'_i$, where $\mathbf{r}$ is the normal vector from the array center to the source plane and $\mathbf{r}'_i = [x'_i, y'_i]$ is the vector from the array center to the ith sensor. Refer back to Fig. 2. As $\hat{\mathbf{r}} = [\cos\phi, \sin\phi]$,

$$\Phi_i = kr - k\hat{\mathbf{r}} \cdot \mathbf{r}'_i + \epsilon = kr - k\left(x'_i \cos\phi + y'_i \sin\phi\right) + \epsilon, \tag{118}$$

and thus

$$\mathbf{D}_\epsilon = \mathbf{I}_2 \quad \text{and} \quad \mathbf{D}_\phi = k \begin{bmatrix} x'_1 \sin\phi - y'_1 \cos\phi & 0 \\ 0 & x'_2 \sin\phi - y'_2 \cos\phi \end{bmatrix}. \tag{119}$$

From the previous section, if $u_{11} = u_{22}$, $u_1 = u_2$, $v_{11} = v_{22}$, and $v_1 = v_2$, then $J_{\epsilon\phi} = 0$ when

$$\begin{aligned} & d_1^\epsilon d_1^\phi + d_2^\epsilon d_2^\phi = 0 \quad \text{and} \quad d_1^\epsilon d_2^\phi + d_2^\epsilon d_1^\phi = 0 \\ \Rightarrow \quad & (x'_1 + x'_2)\sin\phi - (y'_1 + y'_2)\cos\phi = 0 \quad \Rightarrow \quad \text{true } \forall\ \phi \text{ when } x'_1 = -x'_2 \text{ and } y'_1 = -y'_2. \end{aligned} \tag{120}$$

Let $x'_1 = -x'_2 = 0$ and $y'_1 = -y'_2 = d/2$. The CRLB of ϕ is then simply $1/J_{\phi\phi}$. As

$$d_1^\phi = -d_2^\phi = -\frac{kd}{2}\cos\phi, \tag{121}$$

it follows that

$$J_{\phi\phi} = \frac{k^2 d^2 \cos^2\phi}{2}\left[(u_{11}v_{11} + u_{12}v_{12})\left(\frac{1}{u_{11}^2 - u_{12}^2} + \frac{1}{v_{11}^2 - v_{12}^2}\right) - 2 + \frac{(u_{11} + u_{12})v_1^2}{u_{11}^2 - u_{12}^2} + \frac{(v_{11} + v_{12})u_1^2}{v_{11}^2 - v_{12}^2}\right]. \tag{122}$$

The only assumptions made thus far about the covariances and means is that they are independent of $\boldsymbol{\Theta}$ *and that* $u_{11} = u_{22}$, $u_1 = u_2$, $v_{11} = v_{22}$, *and* $v_1 = v_2$. Recall that

$$u_{11} = \left[\mathbf{C}_{\zeta^{(u)}}\right]_{11} = \left[\mathbf{C}_{\psi^{(u)}} + \mathbf{C}_{\eta^{(u)}}\right]_{11} \quad \text{and} \quad u_1 = \left[\mu_{\zeta^{(u)}}\right]_1 = \left[\mu_{\psi^{(u)}} + \mu_{\eta^{(u)}}\right]_1, \tag{123}$$

etc.

For a sound wave propagating through turbulence, we are interested in the total signal given by $\mathbf{s} = \mathbf{p} + \mathbf{n}$, where $\mathbf{p}$ is the signal of interest and $\mathbf{n}$ is the noise. Now $\mathbf{s}$ is the transformation $\mathbf{M}\boldsymbol{\zeta}$. If we assume that the noise at each sensor is uncorrelated and equal, and that the real and imaginary components are the same, each with a variance of $\sigma_n^2/2$, then $\mathbf{C}_\eta = (\sigma_n^2/2A^2)\mathbf{I}_{2N} = (\sigma_n^2/2p_0^2)\mathbf{I}_{2N}$, where $N = 2$ for the present consideration. [I.e., we recover the standard complex Gaussian distribution with $\mathbf{C}_{\tilde{\eta}} = \left(\sigma_n^2/p_0^2\right)\mathbf{I}_{2N}$.] We thus have that

$$u_{11} = \left[\mathbf{C}_{\psi^{(u)}}\right]_{11} + \left[\mathbf{C}_{\eta^{(u)}}\right]_{11} = \left[\mathbf{C}_{\psi^{(u)}}\right]_{11} + \frac{1}{2}\frac{\sigma_n^2}{p_0^2} = u_{22} = \left[\mathbf{C}_{\psi^{(u)}}\right]_{22} + \frac{1}{2}\frac{\sigma_n^2}{p_0^2} \tag{124}$$

$$u_{12} = \left[\mathbf{C}_{\psi^{(u)}}\right]_{12} + \left[\mathbf{C}_{\eta^{(u)}}\right]_{12} = \left[\mathbf{C}_{\psi^{(u)}}\right]_{12} \tag{125}$$

$$v_{11} = \left[\mathbf{C}_{\psi^{(v)}}\right]_{11} + \left[\mathbf{C}_{\eta^{(v)}}\right]_{11} = \left[\mathbf{C}_{\psi^{(v)}}\right]_{11} + \frac{1}{2}\frac{\sigma_n^2}{p_0^2} = v_{22} = \left[\mathbf{C}_{\psi^{(v)}}\right]_{22} + \frac{1}{2}\frac{\sigma_n^2}{p_0^2} \tag{126}$$

$$v_{12} = \left[\mathbf{C}_{\psi^{(v)}}\right]_{12} + \left[\mathbf{C}_{\eta^{(v)}}\right]_{12} = \left[\mathbf{C}_{\psi^{(v)}}\right]_{12} \tag{127}$$

$$u_1 = \left[\mu_{\psi^{(u)}}\right]_1 = u_2 = \left[\mu_{\psi^{(u)}}\right]_2 \tag{128}$$

$$v_1 = \left[\mu_{\psi^{(v)}}\right]_1 = v_2 = \left[\mu_{\psi^{(v)}}\right]_2. \tag{129}$$

III C.2 Plane Wave: Real and Imaginary Covariances Equal

Let us now assume that the real and imaginary covariances are equal, i.e., $u_{11} = v_{11} = u_{22} = v_{22}$ and $u_{12} = v_{12}$. Then assuming $x'_1 = -x'_2 = 0$ and $y'_1 = -y'_2 = d/2$,

$$J_{\phi\phi} = \frac{k^2 d^2 \cos^2\phi}{2}\left[2\frac{u_{11}^2 + u_{12}^2}{u_{11}^2 - u_{12}^2} - 2 + \frac{(u_{11} + u_{12})\left(u_1^2 + v_1^2\right)}{u_{11}^2 - u_{12}^2}\right] = \frac{k^2 d^2 \cos^2\phi}{2}\frac{4u_{12}^2 + (u_{11} + u_{12})\left(u_1^2 + v_1^2\right)}{u_{11}^2 - u_{12}^2}. \tag{130}$$

For the strong diffraction limit, we have

$$\left[\mathbf{C}_{\tilde{\psi}}\right]_{11} = \left[\mathbf{C}_{\tilde{\psi}}\right]_{22} = 1 - \Gamma_{\min} = \left[\mathbf{C}_{\psi^{(u)}}\right]_{11} + \left[\mathbf{C}_{\psi^{(v)}}\right]_{11} = 2\left[\mathbf{C}_{\psi^{(u)}}\right]_{11} \quad \Rightarrow u_{11} = \frac{1}{2}\left(1 - \Gamma_{\min} + \frac{\sigma_n^2}{p_0^2}\right) \tag{131}$$

$$\left[\mathbf{C}_{\tilde{\psi}}\right]_{12} = \Gamma - \Gamma_{\min} = \left[\mathbf{C}_{\psi^{(u)}}\right]_{12} + \left[\mathbf{C}_{\psi^{(v)}}\right]_{12} = 2\left[\mathbf{C}_{\psi^{(u)}}\right]_{12} \quad \Rightarrow u_{12} = \frac{1}{2}\left(\Gamma - \Gamma_{\min}\right) \tag{132}$$

$$\left[\mu_{\tilde{\psi}}\right]_1 = \left[\mu_{\tilde{\psi}}\right]_2 = \Gamma_{\min}^{1/2} = \left[\mu_{\psi^{(u)}}\right]_1 + \mathrm{i}\left[\mu_{\psi^{(v)}}\right]_1 \quad \Rightarrow u_1 = \Gamma_{\min}^{1/2} \quad \text{and} \quad v_1 = 0 \tag{133}$$

Thus

$$J_{\phi\phi} = k^2 d^2 \cos^2\phi \frac{2\Gamma^2 + \Gamma_{\min}\left(1 - 3\Gamma + \frac{\sigma_n^2}{p_0^2}\right)}{1 - \Gamma^2 - 2\Gamma_{\min}\left(1 - \Gamma\right) + \frac{\sigma_n^2}{p_0^2}\left[2\left(1 - \Gamma_{\min}\right) + \frac{\sigma_n^2}{p_0^2}\right]} \tag{134}$$

which agrees with previous findings for a two-element array [21].

III D Geometric Acoustics Model

In geometric acoustics, the covariances of the real and imaginary components are not equal, and the complex phasor at the ith sensor may be approximated by

$$\tilde{\psi}_i \approx (1 + \chi_i) + \mathrm{i}\varphi_i\,, \tag{135}$$

where χ_i is the log-amplitude fluctuation and φ_i is the phase fluctuation. From Ref. [10], χ and φ are Gaussian random variables. Therefore, the real part of $\tilde{\psi}$, $\psi^{(u)} = 1 + \chi$, is Gaussian, as is the imaginary part, $\psi^{(v)} = \varphi$. However, the variance of the phase fluctuations is much larger than the variance of the log-amplitude fluctuations. We assume plane-wave propagation and that φ_i and χ_j are uncorrelated for every i and j. Therefore, we may use the statistical model for a plane wave that was formulated in *Sec. III B* for the $2N \times 1$ partitioned real vector $\boldsymbol{\psi}$. Moreover, we assume that that noise contribution is uncorrelated across the sensors, $\tilde{\eta} \sim \mathcal{CN}_N\left(0, \left(\sigma_n^2/p_0^2\right)\mathbf{I}_N\right)$, so that $\eta \sim \mathcal{N}_{2N}\left(0, \left(\sigma_n^2/2p_0^2\right)\mathbf{I}_{2N}\right)$. Hence the $2N \times 1$ vector $\boldsymbol{\zeta} = \boldsymbol{\psi} + \boldsymbol{\eta}$ is also fully described by the statistical model that was developed in *Sec. III B*.

We assume that

$$\begin{aligned}
&\langle\chi_i\rangle = -\sigma_\chi^2 \quad \forall\, i && \left\langle\chi_i^2\right\rangle = \sigma_\chi^2 \quad \forall\, i && \langle\chi_i\chi_j\rangle = b_{ij}^{\chi}\,,\ i \neq j && \langle\chi_i\varphi_j\rangle = 0 \quad \forall\, i, j \\
&\langle\varphi_i\rangle = 0 \quad \forall\, i && \left\langle\varphi_i^2\right\rangle = \sigma_\varphi^2 \quad \forall\, i && \langle\varphi_i\varphi_j\rangle = b_{ij}^{\varphi}\,,\ i \neq j &&
\end{aligned} \tag{136}$$

where $\sigma_\chi^2 < 1$ and $\sigma_\chi^2/\sigma_\varphi^2 < 1$. And the noise contribution is described by

$$\begin{aligned}
&\left\langle\eta_i^{(u)}\right\rangle = 0 \quad \forall\, i && \left\langle\eta_i^{(u)2}\right\rangle = \sigma_n^2/2 \quad \forall\, i && \left\langle\eta_i^{(u)}\eta_j^{(u)}\right\rangle = 0 \quad \forall\, i, j\,,\ i \neq j && \left\langle\eta_i^{(u)}\eta_j^{(v)}\right\rangle = 0 \quad \forall\, i, j \\
&\left\langle\eta_i^{(v)}\right\rangle = 0 \quad \forall\, i && \left\langle\eta_i^{(v)2}\right\rangle = \sigma_n^2/2 \quad \forall\, i && \left\langle\eta_i^{(v)}\eta_j^{(v)}\right\rangle = 0 \quad \forall\, i, j\,,\ i \neq j &&
\end{aligned} \tag{137}$$

Now let us specifically consider a two-element array and ϕ and ϵ as the unknowns. We choose $x_1' = x_2' = 0$ and $y_1' = -y_2' = d/2$, so that the estimates of ϕ and ϵ decouple as discussed in *Sec. III C.1*. The elements of covariance matrix and mean of $\boldsymbol{\zeta}$ are

$$\begin{aligned}
&u_1 = u_2 = 1 - \sigma_\chi^2 && u_{11} = u_{22} = \sigma_\chi^2 - \sigma_\chi^4 + \frac{1}{2}\frac{\sigma_n^2}{p_0^2} && u_{12} = b_{ij}^{\chi} - \sigma_\chi^4 \\
&v_1 = v_2 = 0 && v_{11} = v_{22} = \sigma_\varphi^2 + \frac{1}{2}\frac{\sigma_n^2}{p_0^2} && v_{12} = b_{12}^{\varphi}
\end{aligned} \tag{138}$$

Therefore, the CRLB of the AOA is $1/J_{\phi\phi}$ where, from Eq. (122),

$$J_{\phi\phi} = \frac{k^2 d^2 \cos^2\phi}{2}\left[\left(u_{11}v_{11} + u_{12}v_{12}\right)\left(\frac{1}{u_{11}^2 - u_{12}^2} + \frac{1}{v_{11}^2 - v_{12}^2}\right) - 2 + \frac{\left(v_{11} + v_{12}\right)u_1^2}{v_{11}^2 - v_{12}^2}\right]. \tag{139}$$

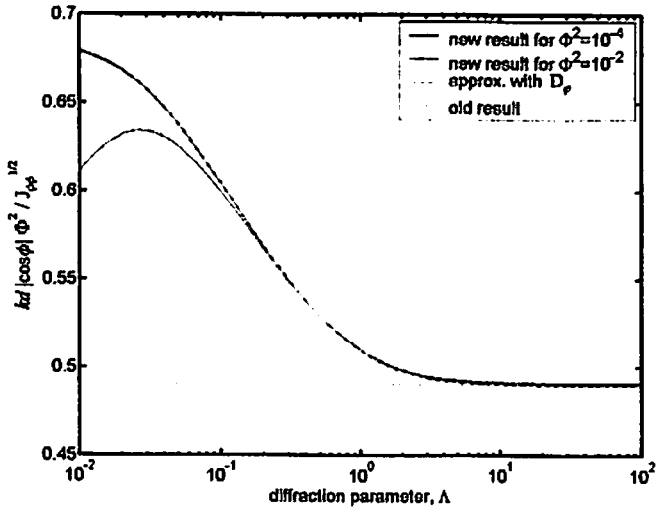

Figure 14: Comparison of the new expression derived in this section for a two-element array with the one in the previous section, which was valid only for strong diffraction. Calculations are for a von Kármán spectrum with $d/\lambda = 0.5$. Here Φ^2 is the strength parameter. For geometric acoustics, $\sigma_\varphi^2 = \Phi^2$ and $\sigma_\chi^2 \sim \Lambda^{p/2}\Phi^2$ where p is power spectrum exponent [10, 25].

III D.1 Turbulence Model

From the theory of waves propagating in a random medium [11], we have that the transverse correlation functions of χ and φ, assuming that the propagation is along the x-axis, are

$$B_\chi(x, r^\perp) = \left\langle \chi(x, r'^\perp),\ \chi(x, r'^\perp + r^\perp) \right\rangle = \frac{\pi^2 k^2 x}{2} \int_0^\infty d\kappa\, \kappa \left[1 - \frac{\kappa_F^2}{\kappa^2} \sin \frac{\kappa^2}{\kappa_F^2}\right] J_0(\kappa r^\perp)\, \Phi_{\text{eff}}(0, \kappa) \tag{140}$$

$$B_\varphi(x, r^\perp) = \left\langle \varphi(x, r'^\perp),\ \varphi(x, r'^\perp + r^\perp) \right\rangle = \frac{\pi^2 k^2 x}{2} \int_0^\infty d\kappa\, \kappa \left[1 + \frac{\kappa_F^2}{\kappa^2} \sin \frac{\kappa^2}{\kappa_F^2}\right] J_0(\kappa r^\perp)\, \Phi_{\text{eff}}(0, \kappa) \tag{141}$$

where $\mathbf{r}_1 = \left[x, \mathbf{r}'^\perp\right]$ and $\mathbf{r}_2 = \left[x, \mathbf{r}'^\perp + \mathbf{r}^\perp\right]$ are the observation points, $k = 2\pi/\lambda$ is the wavenumber, $\Phi_{\text{eff}}(0, \kappa)$ is the effective spectral density, and $\kappa_F^2 = k/x$ is the square of the Fresnel wave number.

As the transverse correlation functions are only dependent upon the magnitude of the sensor separation, the second moments [b_{ij}^φ and b_{ij}^χ] for normal incidence may be determined from the transverse correlation functions.

For geomtric acoustics $(x/\lambda)/(l/\lambda)^2 \ll 1$ and $\langle \chi^2 \rangle = B_\chi(x, 0) \ll 1$, where l is the length scale of the largest inhomogeneity. Using these and Φ_{eff} for a von Kármán spectrum, we obtain approximate solutions for $B_\chi(x, r^\perp)$ and $B_\varphi(x, r^\perp)$.

III D.2 Preliminary Results

Let us return to the result for a two-element array given in Eq. (139). In the very weak scattering limit, the phase-fluctuations dominate, and the leading term is

$$J_{\phi\phi} \sim \frac{(kd\cos\phi)^2}{D_\varphi(x, d)} \tag{142}$$

where D_φ is the structure function

$$D_\varphi(x, d) = 2\left[B_\varphi(x, 0) - B_\varphi(x, d)\right]. \tag{143}$$

This result is what one would expect based on simple geometric arguments involving the variance of the phase difference between the sensors. An example is given in Fig. 14.

The premilinary results of the full 3D calculation for the CRLB as a function of range is shown in Fig. 15. Calculation is for a plane wave normally incident on a 4×4 square array with adjacent sensor spacing of $d/\lambda = 0.5$. Zero noise variance and a von Kármán turbulence spectrum in the geometric acoustics limit is considered.

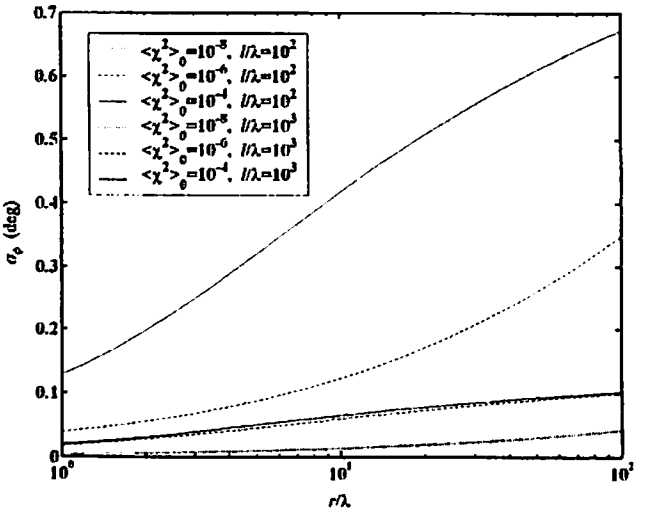

Figure 15: Normalized range dependence of the CRLB of the AOA in the geometric acoustics regime. No noise is considered. Here $\langle \chi^2 \rangle_0$ is the initial value of σ_χ^2 at $r/\lambda = 1$.

III E Conclusions

We have developed a statistical model to descripe the PDF for propagation in the geometric acoustics regime. This model is shown to decay to known limits. The preliminary results show the need to correctly model the signal.

Acknowledgments

S. L. Collier was supported by an American Society for Engineering Education postdoctoral fellowship. The authors are grateful to B. M. Sadler and A. Swami of ARL, V. E. Ostashev of NOAA/Environmental Technology Laboratory, and R. J. Kozick of Bucknell University for many helpful discussions.

References

[1] D. K. Wilson, C. R. Tate, D. C. Swanson, and D. M. Reichard, "Acoustic scintillations and angle-of-arrival fluctuations observed outdoors with a large planar vertical michrophone array," Acoustics Research Letters Online, **106**, L24-L29 (1999).

[2] B. G. Ferguson, "Variability in the passive ranging of acoustic sources in air using a wavefront curvature technique," J. Acoust. Soc. Am. **108**, 1535–1544 (2000).

[3] B. J. Uscinski and D. E. Reeve, "The effect of ocean inhomogeneities on array output," J. Acoust. Soc. Am. **87**, 2527–2534 (1990).

[4] E. Y. Gorodetskaya, A. I. Malekhanov, A. G. Sazontov, and N. K. Vdovicheva, "Deep-water acoustic coherence at long ranges: Theoretical prediction and effects on large-array signal processing," IEEE J. Ocean. Eng. **24**, 156–171 (1999).

[5] Steven M. Kay, *Fundamentals of Statistical Signal Processing: Estimation Theory* (PTR Prentice Hall, Englewood Cliffs, NJ, 1993).

[6] Louis L. Scharf, *Statistical Signal Process: Detection, Estimation, and Time Series Analysis* (Addison-Wesley, Reading, MA, 1991).

[7] B. Ottersten, M. Viberg, P. Stoica, and A. Nehorai, "Exact and large sample maximum likelihood techniques for parameter estimation and detection in array processing," J. Acoust. Soc. Am. **99**, 1370-1379 (1996).

[8] Bong-Gee Song and James A. Ritcey, "Angle of arrival estimation of plane waves propagating in random media," J. Acoust. Soc. Am. **99**, 1370-1379 (1996).

[9] D. Keith Wilson, "Performance bounds for acoustic direction-of-arrival arrays operating in atmospheric turbulence," J. Acoust. Soc. Am. **103**, 1306-1319 (1998).

[10] Stanley M. Flatte, *Sound Transmission through the Fluctuating Ocean* (Cambridge University Press, New York, 1979).

[11] Vladimir E. Ostashev, *Acoustics in Moving Inhomogeneous Media* (E & FN Spon, London, 1997).

[12] J. R. Garratt, *The Atmospheric Boundary Layer* (Cambridge University Press, New York, 1992).

[13] Akira Ishimaru, *Wave Propagation and Scattering in Random Media* (IEEE Press, Piscataway, NJ, 1997).

[14] S. M. Rytov, Yu. A. Kravtsov, and V. I. Tatarskii, *Principles of Statistical Radiophysics 4: Wave Propagation Through Random Media* (Springer-Verlag, New York, 1989).

[15] V. E. Ostashev and D. K. Wilson, "Relative Contributions from Temperature and Wind Velocity Fluctuations to the Statistical Moments of a Sound Field in a Turbulent Atmosphere," Acustica **86**, 260-268 (2000).

[16] D. Keith Wilson, "A turbulence spectral model for sound propagation in the atmosphere that incorporates shear and buoyancy forcings," J. Acoust. Soc. Am. **108**, 2021-2038 (2000).

[17] Richard O. Nielsen, "Estimation of Azimuth and Elevation Angles for a Plane Wave Sine Wave with a 3-D Array," IEEE Trans. Sig. Proc. **42**, 3274-3276 (1994).

[18] Richard O. Nielsen, "Azimuth and Elevation Angle Estimation with a Three-Dimensional Array," IEEE J. Ocean Engineering **19**, 84-86 (1994).

[19] Adam N. Mirkin and Leon H. Sibul, "Cramer-Rao Bounds on Angle Estimation with a Two-Dimensional Array," IEEE Trans. Sig. Proc. **39**, 515-517 (1991).

[20] Yingbo Hua and Tapan K. Sarkar, "A Note on the Cramer-Rao Bound for 2-D Direction Finding Based on 2-D Array," IEEE Trans. on Sig. Proc. **39**, 1215-1218 (1991).

[21] S. L. Collier and D. K. Wilson, "Performance Bounds for Passive Sensor Arrays Operating in a Turbulent Medium: Plane-Wave Analysis," submitted to J. Acoust. Soc. Am.

[22] S. L. Collier and D. K. Wilson, "Performance Bounds for Passive Sensor Arrays Operating in a Turbulent Medium: II. Spherical-Wave Analysis," submitted to J. Acoust. Soc. Am.

[23] Mahrt, L., "Stratified atmospheric boundary layers," Boundary-Layer Meteorol. **90**, 375–396 (1999).

[24] Y. L. Tong, *The Multivariate Normal Distribution* (Springer-Verlag, New York, 1990).

[25] D. Keith Wilson, "Weak Scattering of Sound Waves in Random Media That Have Arbitrary Power-Law Spectra," Army Research Laboratory Technical Report, ARL-TR-1866 (1999).

Sound propagation through inhomogeneous, anisotropic, and intermittent atmospheric turbulence

Vladimir E. Ostashev
NOAA/Environmental Technology Laboratory, 325 Broadway, Boulder, CO 80305
and Physics Department, New Mexico State University, Las Cruces, NM 88003

D. Keith Wilson
U.S. Army Cold Regions Research and Engineering Laboratory, 72 Lyme Rd., Hanover, NH 03755

Abstract. Atmospheric turbulence is intrinsically inhomogeneous, anisotropic, and intermittent. The paper is devoted to studies of the effects of turbulence inhomogeneity, anisotropy, and intermittency on the statistical moments of plane and spherical waves for the case of line-of-sight sound propagation. Formulas for the coherence functions of plane and spherical waves and the mean sound field propagating through inhomogeneous, anisotropic turbulence are derived. Furthermore, these statistical moments and the structure functions of phase and log-amplitude fluctuations of plane and spherical waves are calculated for the case of sound propagation through intermittent turbulence. Finally, numerical results show that the turbulence inhomogeneity, anisotropy, and intermittency can significantly affect the statistical moments of a sound field.

I Introduction

In this paper, we study line-of-sight sound propagation through random flow fields having several properties intrinsic to actual atmospheric turbulence: inhomogeneity, anisotropy, and intermittency. The statistical moments we consider (for both plane and spherical sound waves) are the coherence function, the mean field, and the structure functions of phase and log-amplitude fluctuations. Note that formulas for the correlation functions and variances of phase and log-amplitude fluctuations are readily obtainable from those for the corresponding structure functions. Taken together, these statistical moments of a sound field are important for many practical concerns of atmospheric acoustics, such as source detection and recognition, noise pollution near highways and airports, and remote sensing.

In reference [10], formulas for the above-mentioned statistical moments of a sound field were presented for the case of homogeneous, isotropic turbulence. However, statistics of turbulence in the atmospheric boundary layer (ABL), during both the daytime or nighttime, often cannot be adequately modeled as homogeneous and isotropic. An important example of inhomogeneity is the dependence of the integral length scale (outer scale) and of the structure parameters of temperature and velocity fluctuations on the height h above ground level. During high-wind conditions, the length scales typically are proportional to h whereas the structure parameters are proportional to $h^{-2/3}$ [3, 11]. Previous studies, both experimental [16] and theoretical [12, 13, 19], demonstrated that turbulence anisotropy caused by stretching of the eddies in wind shear can significantly affect the scattered sound field for line-of-sight sound propagation. Furthermore, intermittency of atmospheric turbulence (the tendency of turbulence to occur in bursts of activity) significantly affects the observed statistical properties of the scattered intensity [17, 4, 8].

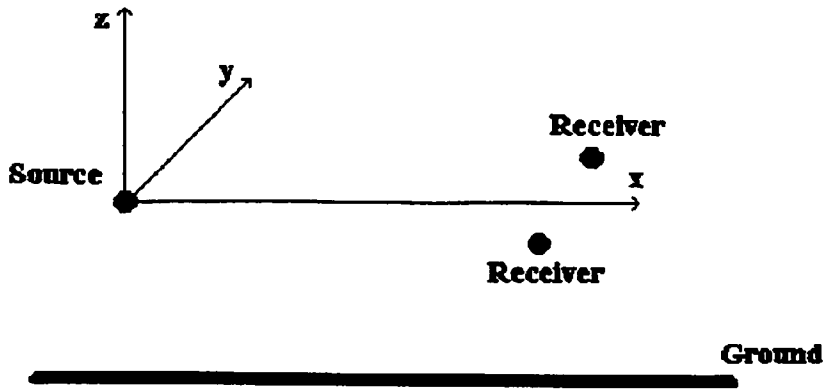

Figure 1: Geometry of line-of-sight sound propagation.

The geometry of line-of-sight sound propagation problem we consider in this paper is shown in Fig. 1. In this figure, the x-axis of the Cartesian coordinate system x, y, z is in the direction of predominant sound propagation, and $\mathbf{r} = (y, z)$ are the coordinates perpendicular to this axis. We will consider that either a point source is located in the center of the coordinate system or a plane sound wave is incident from the left on a random medium filling the space domain $x > 0$ and $z > 0$. Two receivers are located at the points $(x, \mathbf{r}_1)$ and $(x, \mathbf{r}_2)$; their geometrical center is close to the x-axis. A sound wave reflected from the ground (if there is any) is ignored.

This paper is organized as follows. In section II, we derive formulas for the coherence function and mean sound field of plane and spherical sound waves propagating through inhomogeneous, anisotropic turbulence. In section III, we numerically study the effects of turbulence inhomogeneity and anisotropy on the coherence function for the case of shear-driven turbulence. In section IV, we derive formulas for the coherence function, mean field, and the structure functions of phase and log-amplitude fluctuations of plane and spherical waves propagating through intermittent atmospheric turbulence. Furthermore, we numerically study the effects of turbulence intermittency on the coherence function and mean sound field.

II Coherence function and mean field in inhomogeneous, anisotropic turbulence

In this section, we derive formulas for the coherence function and mean field using a simple approach similar to that in Ref. [14]. A more rigorous derivation of these formulas, starting from closed equations for these statistical moments in inhomogeneous, anisotropic turbulence [20], will be given elsewhere.

The transverse coherence function Γ measured with the use of two receivers located at the

points $(x, \mathbf{r}_1)$ and $(x, \mathbf{r}_2)$ is defined as:

$$\Gamma(x; \mathbf{r}_1, \mathbf{r}_2) = \langle p(x, \mathbf{r}_1) p^*(x, \mathbf{r}_2) \rangle. \tag{1}$$

Here, p is the sound field, and $\langle\ \rangle$ denotes ensemble average. In order to calculate Γ, we need to know the sound field p.

A Spherical wave

For a point source located at the origin of the coordinate system (x, y, z), the sound field p can be written in the geometric acoustics approximation as:

$$p_s(x, \mathbf{r}) = \frac{A_s}{x} \exp\left(ikx + \frac{ikr^2}{2x} + i\phi(x, \mathbf{r}) \right). \tag{2}$$

Here, A_s is the amplitude factor, k is the sound wave number, the function ϕ describes phase fluctuations due to temperature and velocity inhomogeneities in the atmosphere, and the subscript (or superscript) "s" stands for "spherical". In Eq. (2), it is assumed that $x \gg r$. Furthermore, the amplitude fluctuations are ignored since, in geometric acoustics, their variance is much less than that of phase fluctuations (e.g. [14]).

Substituting Eq. (2) into Eq. (1), we have

$$\Gamma_s(x; \mathbf{r}_1, \mathbf{r}_2) = \frac{|A_s|^2}{x^2} \exp\left(\frac{ik(r_1^2 - r_2^2)}{2x} \right) \langle \exp\left[i(\phi(x, \mathbf{r}_1) - \phi(x, \mathbf{r}_2)) \right] \rangle. \tag{3}$$

Let ξ be a random field with normal distribution and $\langle \xi \rangle = 0$. Then, $\langle \exp(i\xi) \rangle = \exp(-\langle \xi^2 \rangle / 2)$. Using this formula in Eq. (3) and taking into account that the difference $\phi(x, \mathbf{r}_1) - \phi(x, \mathbf{r}_2)$ is such a random field, we obtain

$$\Gamma_s(x; \mathbf{r}_1, \mathbf{r}_2) = \frac{|A_s|^2}{x^2} \exp\left[\frac{ik(r_1^2 - r_2^2)}{2x} - \frac{1}{2} D_\phi^s(x, \mathbf{r}_1, \mathbf{r}_2) \right]. \tag{4}$$

Here,

$$D_\phi^s(x; \mathbf{r}_1, \mathbf{r}_2) = \langle [\phi(x, \mathbf{r}_1) - \phi(x, \mathbf{r}_2)]^2 \rangle \tag{5}$$

is the transverse structure function of phase fluctuations.

It is convenient to introduce the transverse coordinates

$$\mathbf{r}_- = \mathbf{r}_1 - \mathbf{r}_2, \text{ and } \mathbf{r}_+ = (\mathbf{r}_1 + \mathbf{r}_2)/2. \tag{6}$$

We furthermore denote the coherence function as $\Gamma_s(x; \mathbf{r}_+, \mathbf{r}_-)$ and the structure function of the phase fluctuations as $D_\phi^s(x; \mathbf{r}_+, \mathbf{r}_-)$. A formula for $D_\phi^s(x; \mathbf{r}_+, \mathbf{r}_-)$ was derived in [13] using the Rytov method and Markov approximation:

$$D_\phi^s(x; \mathbf{r}_+, \mathbf{r}_-) = \pi k^2 x \int_0^1 d\eta \int d\mathbf{K}_\perp \left[1 - e^{i\eta \mathbf{K}_\perp \cdot \mathbf{r}_-} \right] \cos^2\left(\frac{\eta(1-\eta) K_\perp^2}{2K_F^2} \right) \Phi_{\text{eff}}(\eta x, \eta \mathbf{r}_+; 0, \mathbf{K}_\perp). \tag{7}$$

Here, $K_F = \sqrt{k/x}$ is inversely proportional to the size of the first Fresnel zone, and the effective three-dimensional spectral density $\Phi_{\text{eff}}(x, \mathrm{r}_+; 0, \mathbf{K}_\perp)$ is a linear combination of the three-dimensional spectral densities of temperature and velocity fluctuations:

$$\Phi_{\text{eff}}(x, \mathrm{r}_+; K_x, \mathbf{K}_\perp) = \frac{\Phi_T(x, \mathrm{r}_+; K_x, \mathbf{K}_\perp)}{T_0^2} + \frac{4\Phi_{xx}(x, \mathrm{r}_+; K_x, \mathbf{K}_\perp)}{c_0^2}. \tag{8}$$

Here, T_0 and c_0 are the mean values of the temperature and adiabatic sound speed, and K_x and $\mathbf{K}_\perp$ are the components of the turbulence wave vector. The presence of x and r_+ among the dependent variables of Φ_{eff} is due to anisotropy and inhomogeneity of the turbulence.

In geometric acoustics approximation, $K_F \gg K_\perp$ (e.g. see [14]). Therefore, in this approximation, in Eq. (7) $\cos^2(\eta(1-\eta)K_\perp^2/2K_F^2)$ can be replaced by 1. Substituting the resulting formula into Eq. (4), we obtain a desired formula for the coherence function of a spherical sound wave propagating through inhomogeneous, anisotropic turbulence:

$$\Gamma_s(x; \mathrm{r}_+, \mathrm{r}_-) = \frac{|A_s|^2}{x^2} \exp\left[\frac{ik\mathrm{r}_+ \cdot \mathrm{r}_-}{x} - \frac{\pi k^2 x}{2} \int_0^1 d\eta \int d\mathbf{K}_\perp \left(1 - e^{i\eta \mathbf{K}_\perp \cdot \mathrm{r}_-}\right) \right.$$
$$\left. \times \Phi_{\text{eff}}(\eta x, \eta \mathrm{r}_+; 0, \mathbf{K}_\perp)\right]. \tag{9}$$

This equation was obtained using a geometric acoustic approximation. However, the range of applicability of Eq. (9) is wider: it can be derived starting from a parabolic equation and using the Markov approximation.

In many cases, it is convenient to choose the coordinate system (x, y, z) in such a way that the x-axis passes through the geometrical center of two receivers located at (x, r_1) and (x, r_2). In this case, $\mathrm{r}_+ = 0$ and Eq. (9) simplifies

$$\Gamma_s(x; 0, \mathrm{r}_-) = \frac{|A_s|^2}{x^2} \exp\left[-\frac{\pi k^2 x}{2} \int_0^1 d\eta \int d\mathbf{K}_\perp \left(1 - e^{i\eta \mathbf{K}_\perp \cdot \mathrm{r}_-}\right) \Phi_{\text{eff}}(\eta x, 0; 0, \mathbf{K}_\perp)\right]. \tag{10}$$

Equations (9) and (10) for the coherence function generalize those known in the literature. Equation (10) coincides with Eq. (7.71) from [10] for the limiting case of homogeneous, isotropic turbulence with temperature and velocity fluctuations. Furthermore, Eq. (10) can be obtained from Eq. (3.28) in [6] for the distinct limiting case of inhomogeneous, anisotropic turbulence with temperature fluctuations only.

B Plane wave

The coherence function of a plane sound wave Γ_p propagating through inhomogeneous, anisotropic turbulence can be expressed in terms of the structure function of phase fluctuations D_ϕ^p by approach similar to that in the previous subsection:

$$\Gamma_p(x; \mathrm{r}_+, \mathrm{r}_-) = I_0 \exp\left[-\frac{1}{2} D_\phi^p(x; \mathrm{r}_+, \mathrm{r}_-)\right]. \tag{11}$$

Here, I_0 is the intensity of a plane wave in absence of turbulence and the sub- or superscript "p" stands for "plane".

The structure function D_ϕ^p is related to the correlation function of phase fluctuations B_ϕ^p by the following formula:

$$D_\phi^p(x; \mathrm{r}_+, \mathrm{r}_-) = 2\left[B_\phi^p(x; \mathrm{r}_+, 0) - B_\phi^p(x; \mathrm{r}_+, \mathrm{r}_-)\right]. \tag{12}$$

This formula generalizes Eq. (7.57) from [10] to the case of inhomogeneous, anisotropic turbulence. Equation (30) from [12] gave a formula for B_ϕ^p that is applicable here. Substituting this formula into Eq. (12), we have

$$D_\phi^p(x;\mathbf{r}_+,\mathbf{r}_-) = \pi k^2 x \int_0^1 d\eta \int d\mathbf{K}_\perp \left[1 - e^{i\mathbf{K}_\perp\cdot\mathbf{r}_-}\right] \cos^2\left(\frac{(1-\eta)K_\perp^2}{2K_F^2}\right) \Phi_{\text{eff}}(\eta x, \mathbf{r}_+; 0, \mathbf{K}_\perp). \quad (13)$$

Substituting Eq. (13) into Eq. (11), we obtain a desired formula for the coherence function of a plane sound wave propagating through inhomogeneous, anisotropic turbulence with temperature and velocity fluctuations

$$\Gamma_p(x;\mathbf{r}_+,\mathbf{r}_-) = I_0 \exp\left[-\frac{\pi k^2 x}{2} \int_0^1 d\eta \int d\mathbf{K}_\perp \left(1 - e^{i\mathbf{K}_\perp\cdot\mathbf{r}_-}\right) \Phi_{\text{eff}}(\eta x, \mathbf{r}_+; 0, \mathbf{K}_\perp)\right]. \quad (14)$$

For $\mathbf{r}_+ = 0$, Eq. (13) simplifies

$$\Gamma_p(x;0,\mathbf{r}_-) = I_0 \exp\left[-\frac{\pi k^2 x}{2} \int_0^1 d\eta \int d\mathbf{K}_\perp \left(1 - e^{i\mathbf{K}_\perp\cdot\mathbf{r}_-}\right) \Phi_{\text{eff}}(\eta x, 0; 0, \mathbf{K}_\perp)\right]. \quad (15)$$

Equations (14) and (15) also generalize those known in the literature. Equation (15) is essentially the same as Eq. (15) from [19] for homogeneous, anisotropic turbulence and coincides with Eq. (7.63) from [10] for homogeneous, isotropic turbulence. Also, Eq. (15) is the same as Eq. (3.21) from [6] for inhomogeneous, anisotropic turbulence with temperature fluctuations only.

C Mean sound field

When the distance $\mathbf{r}_-$ between two receivers tends to infinity, the sound fields p at these receivers are uncorelated. In this case, the left-hand side of Eq. (15) can be written as $\Gamma_p = \langle p\rangle\langle p^*\rangle$. On the right-hand side of Eq. (15), the term $\exp(i\mathbf{K}_\perp\cdot\mathbf{r}_-)$ oscillates rapidly and does not contribute to the integral over $\mathbf{K}_\perp$. As a result, we have:

$$\langle p\rangle\langle p^*\rangle = I_0 \exp\left[-\frac{\pi k^2 x}{2} \int_0^1 d\eta \int d\mathbf{K}_\perp \Phi_{\text{eff}}(\eta x, 0; 0, \mathbf{K}_\perp)\right]. \quad (16)$$

Using this equation, we obtain a desired formula for the mean sound field propagating through inhomogeneous, anisotropic turbulence with temperature and velocity fluctuations:

$$\langle p(x,\mathbf{r})\rangle = p_0(x,\mathbf{r}) \exp\left[-\frac{\pi k^2 x}{4} \int_0^1 d\eta \int d\mathbf{K}_\perp \Phi_{\text{eff}}(\eta x, 0; 0, \mathbf{K}_\perp)\right], \quad (17)$$

where $p_0(x,\mathbf{r})$ is the sound field in a medium without turbulence. Note that Eq. (17) is also valid for a spherical sound wave and can be obtained from Eq. (10) by setting $\mathbf{r}_- \to \infty$.

Equation (17) is the same as Eq. (14) in [19] for homogeneous, anisotropic turbulence. It also coincides with Eq. (7.60) from [10] for homogeneous, isotropic turbulence.

III Coherence in shear-driven turbulence

In this section, we study the effects of inhomogeneity and anisotropy of atmospheric turbulence on the coherence function of a plane sound wave Γ_p given by Eq. (15). In the integrand of this equation, we need to specify the effective spectral density $\Phi_{\text{eff}}(x, 0; 0, \mathrm{K}_\perp)$.

We will assume that the turbulence is generated by ground-based wind shear, as often is the case in windy conditions during the day or night. Buoyancy forces in the flow and temperature fluctuations will be neglected here. An anisotropic spectrum of shear driven turbulence was developed by Mann [7]. This spectrum was generalized by Wilson [19] to account for vertical inhomogeneity in the ABL. The resulting inhomogeneous, anisotropic spectrum was employed in references [12, 13] to derive a formula for the effective three-dimensional spectral density $\Phi_{\text{eff}}(x, 0; 0, \mathrm{K}_\perp)$ for the case when the sound propagation path, i.e., the x-axis, is parallel to the ground. In this case, $\Phi_{\text{eff}}(x, 0; 0, \mathrm{K}_\perp)$ does not depend on x; however, it does parametrically depend on the height h of the sound path above the ground. A formula for $\Phi_{\text{eff}}(h; 0, \mathrm{K}_\perp)$ is given by Eq. (42) from [12]. This formula can be written in the following form:

$$\Phi_{\text{eff}}(h; 0, \mathrm{K}_\perp) = \mathcal{F}\left[\mathrm{K}_\perp, \theta, \Gamma_M, \sigma_M^2, L_M\right]. \tag{18}$$

Here, $\mathcal{F}$ is an involved function, θ is the azimuthal angle between the x-axis and the direction of the mean horizontal wind, and Γ_M, σ_M^2, and L_M are the parameters in Mann's spectrum. We will use the following values of these parameters [19]:

$$\sigma_M^2 = 1.52\, u_*^2, \qquad L_M = 0.587\, h, \qquad \Gamma_M = 3.58\,, \tag{19}$$

where u_* is the friction velocity.

The behavior of the Mann model with regard to sound propagation is illustrated in Fig. 2. The four curves in this figure show the plane-wave coherence function [Γ_p, Eq. (15)] for sound propagation in the along-wind and crosswind directions as a function of the normalized receiver separation r_-/h. Separations in both the vertical and horizontal directions, perpendicular to the propagation path, are shown. Eqs. (18) and (19) were used to calculate the turbulence spectrum. Furthermore, when plotting Fig. 2 we assumed that $I_0 = 1$, $u_*/c_0 = 8.8 \times 10^{-4}$, $kx = 2 \times 10^5$, and $kh = 20$. (Note that the vertical separations greater than h in Fig. 2 are physically impossible; however, the extension of the separation axis beyond $r_-/h > 1$ serves to illustrate the general behavior of the solution.)

The effects of turbulence anisotropy on the coherence function Γ_p are clearly seen from the figure: along-wind, the coherence is significantly less than crosswind. Furthermore, the coherence functions differ for vertical and horizontal separation of receivers. Finally, it follows from Fig. 2 that the coherence function depends on h. This is a manifestation of the effect of turbulence inhomogeneity on the coherence function.

IV Statistical moments in intermittent atmospheric turbulence

Intermittency refers here to the tendency of turbulence to occur in bursts of activity. This phenomenon has been well documented since being first recognized by Kolmogorov [5] and Obukhov

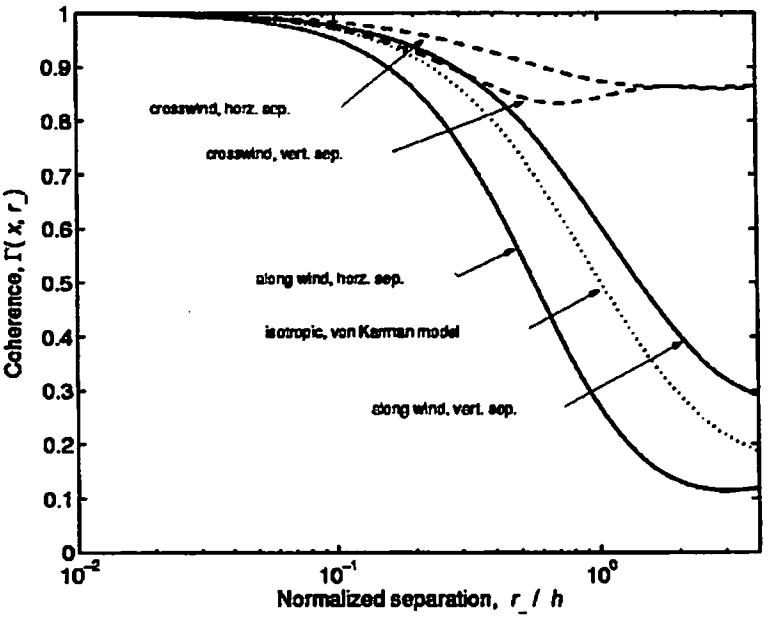

Figure 2: Coherence function of a sound field propagating through the anisotropic turbulence. The calculations are based on the Mann model for a constant shear layer. Dependence of the coherence on the propagation direction relative to the wind, as well as the direction of the sensor separation, is shown.

[9]. In sections II and III, we assumed that the turbulence is not intermittent. The main goal of the present section is to generalize formulas for the statistical moments of a sound field presented above to the case of sound propagation through intermittent turbulence. The analysis is similar to that in [15, 18]. Note that theoretical and experimental studies of laser beam propagation through intermittent turbulence were reported elsewhere [1, 2].

The formulas for the coherence function, mean field, and the structure function of phase fluctuations presented in section II contain the effective spectral density Φ_{eff}, which is a linear combination of temperature and velocity fluctuations. For simplicity, in what follows we assume that the temperature fluctuations may be ignored. Then, we may write Φ_{eff} as

$$\Phi_{\text{eff}}(x, \mathbf{r}_+; 0, \mathbf{K}_\perp) = C_v^2(x)\Phi(x, \mathbf{r}_+; 0, \mathbf{K}_\perp). \tag{20}$$

Here, C_v^2 is the structure parameter of velocity fluctuations which characterizes the intensity of turbulence, and the function Φ is defined as:

$$\Phi(x, \mathbf{r}_+; 0, \mathbf{K}_\perp) = \frac{4\Phi_{xx}(x, \mathbf{r}_+; 0, \mathbf{K}_\perp)}{c_0^2 C_v^2(x)}. \tag{21}$$

Equations (20) and (21) allow us to factor out C_v^2 in an expression for Φ_{eff}. This is an important step in our analysis: in theories of waves in random media (e.g. [15, 18]), the turbulence intermittency is modeled by assuming that $C_v^2(x)$ is a random function along the sound propagation path. ($C_v^2(x)$ should be interpreted in this context as a weighted, average value over the plane positioned at x that is perpendicular to the propagation direction. The weighting is in proportion to the relative importance of scattering of sound at each point in the plane.)

A Phase and log-amplitude fluctuations

We substitute the value of Φ_{eff} given by Eq. (20) into Eqs. (13) and (7) for the structure functions of phase fluctuations of plane and spherical waves. Then, both sides of the resulting equations are averaged over an ensemble of realizations of C_v^2. As a result, we obtain formulas for the mean values of the structure functions of phase fluctuations of plane and spherical sound waves propagating through intermittent turbulence

$$\langle D_\phi^p(x; \mathbf{r}_+, \mathbf{r}_-)\rangle = \pi k^2 x \int_0^1 d\eta\, \overline{C_v^2}(\eta x) \int \mathbf{K}_\perp \left[1 - e^{i\mathbf{K}_\perp \cdot \mathbf{r}_-}\right] \cos^2\left(\frac{(1-\eta)K_\perp^2}{2K_F^2}\right) \times \Phi(\eta x, \mathbf{r}_+; 0, \mathbf{K}_\perp), \tag{22}$$

and

$$\langle D_\phi^s(x; \mathbf{r}_+, \mathbf{r}_-)\rangle = \pi k^2 x \int_0^1 d\eta\, \overline{C_v^2}(\eta x) \left[1 - e^{i\eta\mathbf{K}_\perp \cdot \mathbf{r}_-}\right] \cos^2\left(\frac{\eta(1-\eta)K_\perp^2}{2K_F^2}\right) \times \Phi(\eta x, \eta\mathbf{r}_+; 0, \mathbf{K}_\perp). \tag{23}$$

Here, $\overline{C_v^2}$ is the mean value of C_v^2. It follows from Eqs. (22) and (23) that $\langle D_\phi^p\rangle$ and $\langle D_\phi^s\rangle$ do not depend on the variance of C_v^2 which characterizes the intensity of turbulence intermittency. Furthermore, formulas for $\langle D_\phi^p\rangle$ and $\langle D_\phi^s\rangle$ coincide with those for D_ϕ^p and D_ϕ^s if in the latter formulas Φ_{eff} is replaced by its mean value.

Other statistical moments of phase and log-amplitude fluctuations of plane and spherical waves propagating through intermittent turbulence can be obtained from Eqs. (22) and (23). Indeed, replacing $\cos^2$ in Eqs. (22) and (23) by $\sin^2$, we obtain formulas for the structure functions $\langle D_\chi^p \rangle$ and $\langle D_\chi^s \rangle$ of log-amplitude fluctuations of plane and spherical sound waves propagating through intermittent turbulence. Furthermore, if in the formulas for $\langle D_{\phi,\chi}^p \rangle$ and $\langle D_{\phi,\chi}^s \rangle$ the square brackets in the integrand are replaced by $(1/2)e^{i\mathbf{K}_\perp \cdot \mathbf{r}_-}$ and $(1/2)e^{i\eta \mathbf{K}_\perp \cdot \mathbf{r}_-}$, respectively, we obtain formulas for the correlation functions of phase and log-amplitude fluctuations of plane and spherical waves propagating through intermittent turbulence, $\langle B_{\phi,\chi}^p \rangle$ and $\langle B_{\phi,\chi}^s \rangle$. Due to similarity of all these formulas, we conclude that the statistical moments of phase and log-amplitude fluctuations mentioned above do not depend on the variance of C_v^2 and are basically the same as for non-intermittent turbulence.

B Mean field and coherence function

The value of Φ_{eff} given by Eq. (20) is substituted into Eqs. (10), (15) and (17) for the coherence functions and mean field. Then, the resulting equations can be written as one formula:

$$G = A \exp\left\{ -\int_0^x dx' C_n^2(x') D(x') \right\} . \tag{24}$$

Here, G stands for Γ_p, Γ_s or $\langle p \rangle$, and the functions A and D are different for the coherence functions of plane and spherical waves, and the mean sound field. For the case of the coherence function of a plane wave, A and D are given by:

$$A = I_0, \quad D(x') = \frac{\pi k^2}{2} \int d\mathbf{K}_\perp \left[1 - e^{i\mathbf{K}_\perp \cdot \mathbf{r}_-} \right] \Phi(x', 0; 0, \mathbf{K}_\perp) . \tag{25}$$

For the case of the coherence function of a spherical wave:

$$A = \frac{|A_s|^2}{x^2}, \quad D(x') = \frac{\pi k^2}{2} \int d\mathbf{K}_\perp \left[1 - e^{ix'\mathbf{K}_\perp \cdot \mathbf{r}_-/x} \right] \Phi(x', 0; 0, \mathbf{K}_\perp). \tag{26}$$

Finally, for the mean sound field,

$$A = p_0(x, \mathbf{r}), \quad D(x') = \frac{\pi k^2}{4} \int d\mathbf{K}_\perp \Phi(x', 0; 0, \mathbf{K}_\perp) . \tag{27}$$

The mean value of the function G, which will be denoted as $\langle G \rangle$, gives us the mean values of Γ_p, Γ_s, and $\langle p \rangle$. The function $\langle G \rangle$ can be obtained by averaging both sides of Eq. (24):

$$\langle G \rangle = A \left\langle \exp\left\{ -\int_0^x dx' C_n^2(x') D(x') \right\} \right\rangle . \tag{28}$$

References [15, 18] consider the coherence function of a plane wave and the mean field propagating through intermittent but otherwise homogeneous turbulence. In this case, in Eq. (28) the function D does not depend on x and can be factored out from the integral. A probability density function (pdf) of the remaining integral normalized to x can be approximated by a log-normal pdf given by Eq. (34) from [18]. Therefore, the mean value of the exponent on the right-hand side of Eq. (28) can be evaluated.

However, for the considered case of inhomogeneous turbulence (and also for Γ_s in homogeneous turbulence), the function D does depend on x. In this case, in order to calculate $\langle G \rangle$, one needs

to make some assumptions or approximations. We will assume that the distance x of sound propagation is less than the characteristic scale L of $C_v^2(x)$. In this case, C_v^2 can be factored out from the integral in Eq. (28):

$$\langle G \rangle = A \left\langle \exp(-C_v^2 \tilde{D}) \right\rangle, \tag{29}$$

where $\tilde{D}(x) = \int_0^x dx' D(x')$. Furthermore, we will assume that, in Eq. (29), a pdf of C_v^2 can be approximated by Eq. (34) from [18]:

$$P\left(C_v^2\right) = \frac{\exp\left\{-\left[\ln\left(C_v^2/\overline{C_v^2}\right) + \sigma^2/2\right]^2 / (2\sigma^2)\right\}}{\sqrt{2\pi}\sigma C_v^2}. \tag{30}$$

Here, σ^2 is the variance of $\ln C_v^2$. Using Eq. (35) from [18], this variance can be estimated as:

$$\sigma^2 = \mu \ln(L/x), \tag{31}$$

where μ is a numerical parameter. Following [18], we will assume that $\mu = 0.25$.

Using the pdf of C_v^2 given by Eq. (30), we can calculate $\langle \exp(-C_v^2 \tilde{D}) \rangle$ on the right-hand side of Eq. (29). After some algebra, we obtain a desired formula for $\langle G \rangle$ in intermittent turbulence (i.e. a formula for the mean values of Γ_p, Γ_s, and $\langle p \rangle$):

$$\langle G(d) \rangle = \frac{A}{\sqrt{2\pi}\sigma} \int_{-\infty}^{\infty} d\xi \exp\left[-d\exp(-\xi - \sigma^2/2) - \xi^2/(2\sigma^2)\right]. \tag{32}$$

Here, the parameter $d = \overline{C_v^2}\tilde{D}$.

To better understand the physical meaning of the parameter d, let us consider the case of nonintermittent turbulence when $\sigma^2 = 0$ and $C_v^2 = \overline{C_v^2}$. In this case, the integral over ξ in Eq. (32) can be evaluated analytically:

$$G = A\exp(-d). \tag{33}$$

Comparing this formula with Eqs. (10), (15) and (17), we conclude that d equals the expressions in the exponents of the formulas for the coherence functions and mean field. Therefore, parameter d describes the loss of coherence of plane and spherical sound waves due to increases in receiver separation $\mathbf{r}_-$, propagation distance x, and the sound wave number k.

In Fig. 3, the solid curve corresponding to $\sigma^2 = 0$ is the dependence of G on d given by Eq. (33). The other curves in Fig. 3 correspond to the dependence of $\langle G \rangle$ on d calculated with the use of Eq. (32) for different values of σ^2: 0.16, 0.36, and 0.64. (According to Eq. (31), these values correspond to the following ratios of x/L: 0.53, 0.24, 0.08.) It follows from the figure that an increase in σ (i.e., an increase in intermittency of turbulence), results in an increase of $\langle G \rangle$. Thus, increasing turbulence intermittency results in improved coherence of plane and spherical sound waves propagating in a turbulent atmosphere. This result is consistent with conclusions made in [15, 18].

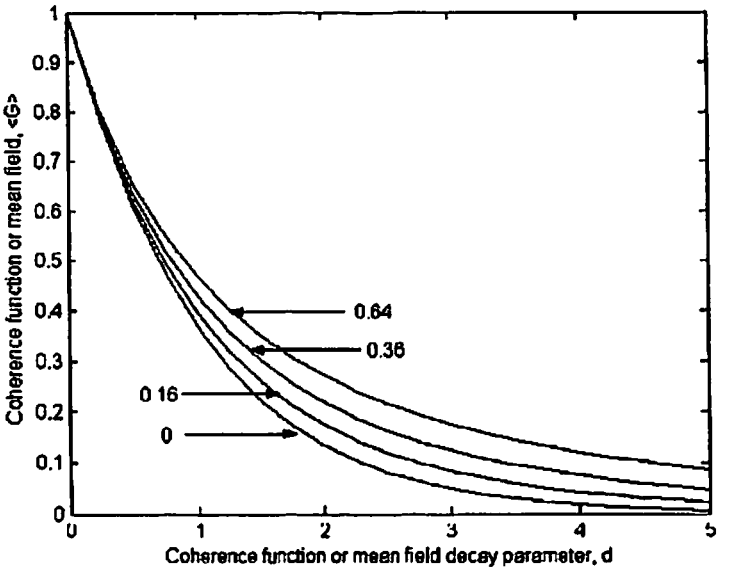

Figure 3: The coherence function or mean field propagating through intermittent turbulence virsus the parameter d for different values of the variance σ.

V Conclusions

We have derived formulas for the coherence functions of plane and spherical sound waves and the mean sound field propagating through inhomogeneous, anisotropic turbulence with temperature and velocity fluctuations. These formulas generalize those known in the literature in limiting cases, such as homogeneous, isotropic turbulence. Numerical studies have shown that inhomogeneity and anisotropy of shear-driven turbulence significantly affect the coherence function of a plane sound wave. Note that turbulence in both the daytime and nighttime ABL's is often created by near-ground wind shear.

We have also shown that the structure and correlation functions of phase and log-amplitude fluctuations of plane and spherical sound wave propagating through intermittent turbulence do not depend on the degree of the intermittency, as characterized by the variance σ^2 of fluctuations in $\ln C_v^2$. Finally, we derived analytical formulas for the coherence functions of plane and spherical sound waves and the mean field propagating in intermittent turbulence. Numerical results showed that these statistical moments of a sound field significantly depend on intensity of intermittency: The higher the value of σ^2 the more coherent is the sound field propagating in the atmosphere.

Acknowledgments. This material is partly based upon work supported by the U.S. Army Research Office under contract number DAAG19-01-1-0640 (administered by W. Bach).

References

[1] R. Frehlich, "Laser scintillation measurements of the temperature spectrum in the atmospheric surface layer," *J. Atmos. Sci.* **49**, 1494–1509 (1992).

[2] J. Gozani, "Effect of the intermittent atmosphere on laser scintillations," *Optics Letters* **24**, 436–438 (1999).

[3] J. C. Kaimal and J. J. Finnigan, *Atmospheric Boundary Layer Flows: Their Structure and Measurement*, (Oxford U.P., New York, 1994).

[4] M. Kelly, R. Raspet, and H. E. Bass, "Scattering of sonic booms by anisotropic turbulence in the atmosphere," *J. Acoust. Soc. Am.* **107**, 3059–3064 (2000).

[5] A. N. Kolmogorov, "A refinement of previous hypotheses concerning the local structure of turbulence in a viscous incompressible fluid at high Reynolds number," *J. Fluid Mech.* **13**, 82–85 (1962).

[6] A. S. Gurvich, A. I. Kon, V. L. Mironov, and S. S. Khmelevtsov, *Laser Radiation in the Turbulent Atmosphere* (in Russian, Nauka, Moscow, 1976).

[7] J. Mann, "The spatial structure of neutral atmospheric surface layer turbulence," *J. Fluid Mech.* **273**, 141–168 (1994).

[8] D. E. Norris, D. K. Wilson, and D. W. Thomson, "Atmospheric scattering for varying degrees of saturation and turbulent intermittency," *J. Acoust. Soc. Am.* **109**, 1871–1880 (2001).

[9] A. M. Obukhov, "Some specific features of atmospheric turbulence," *J. Fluid Mech.* **13**, 77–81 (1962).

[10] V. E. Ostashev, *Acoustics in Moving Inhomogeneous Media* (E& FN SPON, London, 1997).

[11] V. E. Ostashev and D. K. Wilson, "Relative contributions from temperature and wind velocity fluctuations to the statistical moments of a sound field in a turbulent atmosphere," *Acustica* **86**, 260–268 (2000).

[12] V. E. Ostashev, and D. K. Wilson, "Log-amplitude and phase fluctuations of a plane wave propagating through anisotropic, inhomogeneous turbulence," *Acustica — acta acustica* **87**, 685–694 (2001).

[13] V. E. Ostashev, and D. K. Wilson, "Spherical wave propagation through inhomogeneous, anisotropic turbulence: log-amplitude and phase correlations," *J. Acoust. Soc. Am.*, submitted for publication (2002).

[14] S. M. Rytov, Yu. A. Kravtsov, and V. I. Tatarskii, *Principles of Statistical Radio Physics. Part 4, Wave Propagation through Random Media* (Springer, Berlin, 1989).

[15] V. I. Tatarskii and V. U. Zavorotny, "Wave propagation in random media with fluctuating turbulent parameters," *J. Opt. Soc. Am.* **2**, 2069–2076 (1985)

[16] D. K. Wilson and D. W. Thomson, "Acoustic propagation through anisotropic, surface-layer turbulence," *J. Acoust. Soc. Am.* **96**, 1080–1095 (1994).

[17] D. K. Wilson, J. C. Wyngard, and D. I. Havelock, "The effect of turbulent intermittency on scattering into an acoustic shadow zone," *J. Acoust. Soc. Am.* **99**, 3393–3400 (1996).

[18] D. K. Wilson, "Performance bounds for acoustic angle-of-arrival arrays operating in atmospheric turbulence," *J. Acoust. Soc. Am.* **103**, 1306–1319 (1998).

[19] D. K. Wilson, "Calculated coherence and extinction of sound waves propagating through anisotropic, shear-induced turbulent velocity fluctuations," *J. Acoust. Soc. Am.* **105**, 658–671 (1999).

[20] D. K. Wilson and V. E. Ostashev, "Statistical moments of the sound field propagating in a random, refractive medium near an impedance boundary", *J. Acoust. Soc. Am.* **109**, 1909–1922 (2001).

On the knowledge gained from continuously observing infrasound in the Netherlands

Läslo Evers and Hein Haak

evers@knmi.nl
http://www.knmi.nl/~evers

KNMI

How can infrasound be measured?

- Low frequent microphone
- High frequent barometer

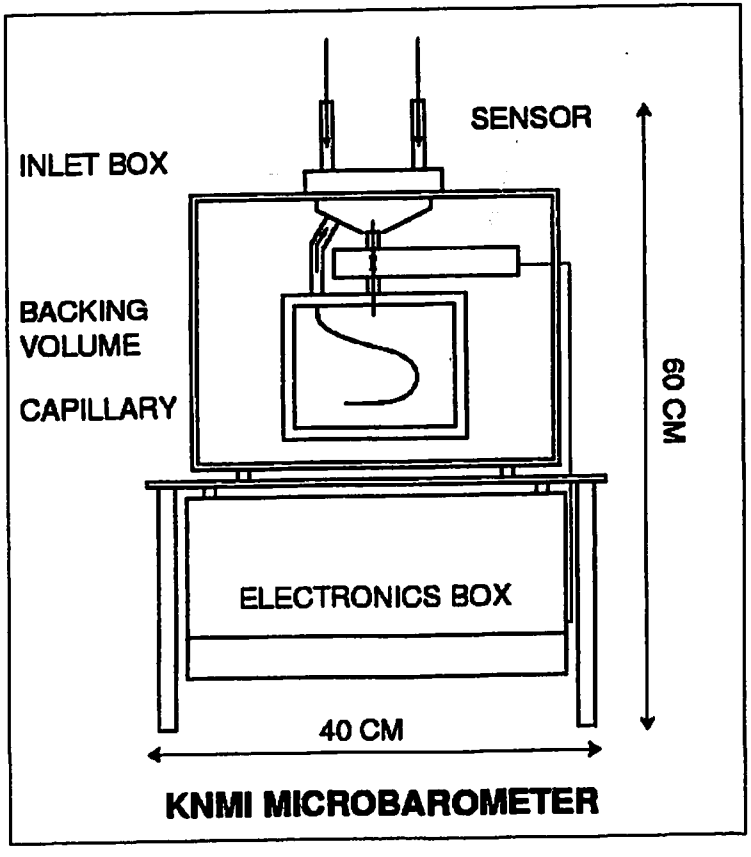

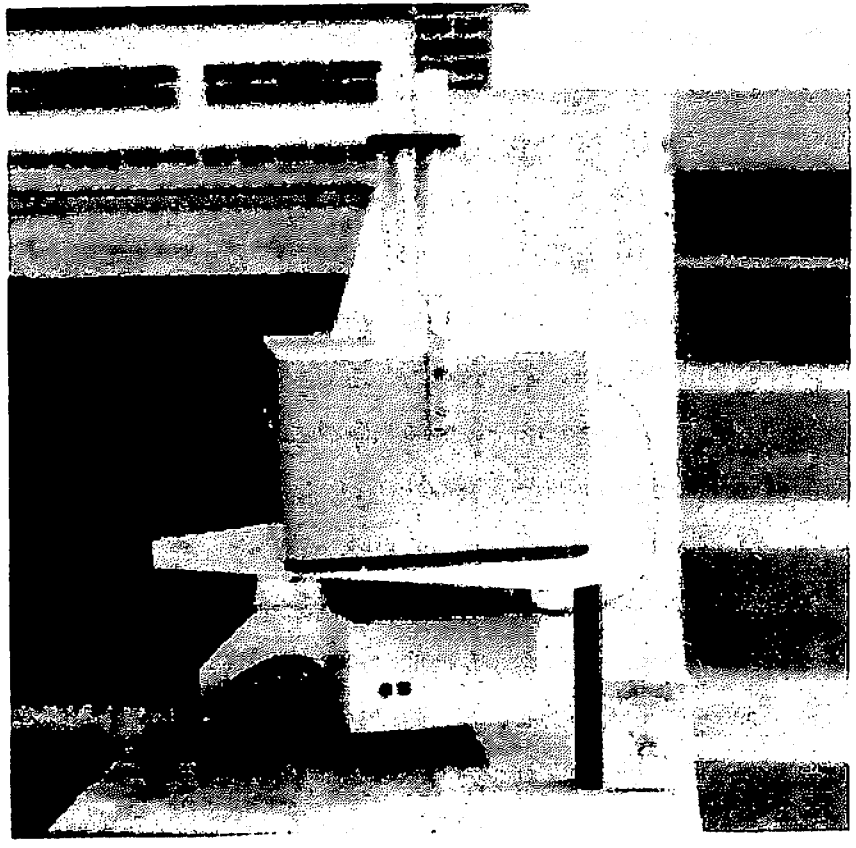

KNMI

Arrays for infrasound measurement

- Infrasound has low signal-to-noise ratios (snr)
  → signal stacking to enhance snr
- Array processing for source characterization
  → arrival time, apparent sound speed and back azimuth
- Spatial and temporal sampling
  → waveform coherency, 3D information, ...

KNMI

Array response

- Elementary wave

$$f(\mathbf{r}, t) = e^{i(\omega t - \mathbf{k}\cdot\mathbf{r})} = e^{i\omega(t - \mathbf{p}\cdot\mathbf{r})}$$

with: frequency ω, travel-time t, wavenumber $\mathbf{k}$, position vector $\mathbf{r}$ and slowness $\mathbf{p}$

- Normalized array response

$$R(\omega, \mathbf{p}) = \left| \frac{1}{N} \sum_{j=1}^{N} e^{-i\omega(\mathbf{p}\cdot\mathbf{r}_j)} \right|^2$$

KNMI

Array design criteria

- Isotropic or omni-directional response
  → circular shaped main lob
- High resolution, minimal energy spreading.
  → delta-like main lob
- Avoid spatial aliasing
  → side lobs low amplitude and far from main lob

Monochromatic response to 0.2 Hz plane wave

Infrasound from a meteor

KNMI

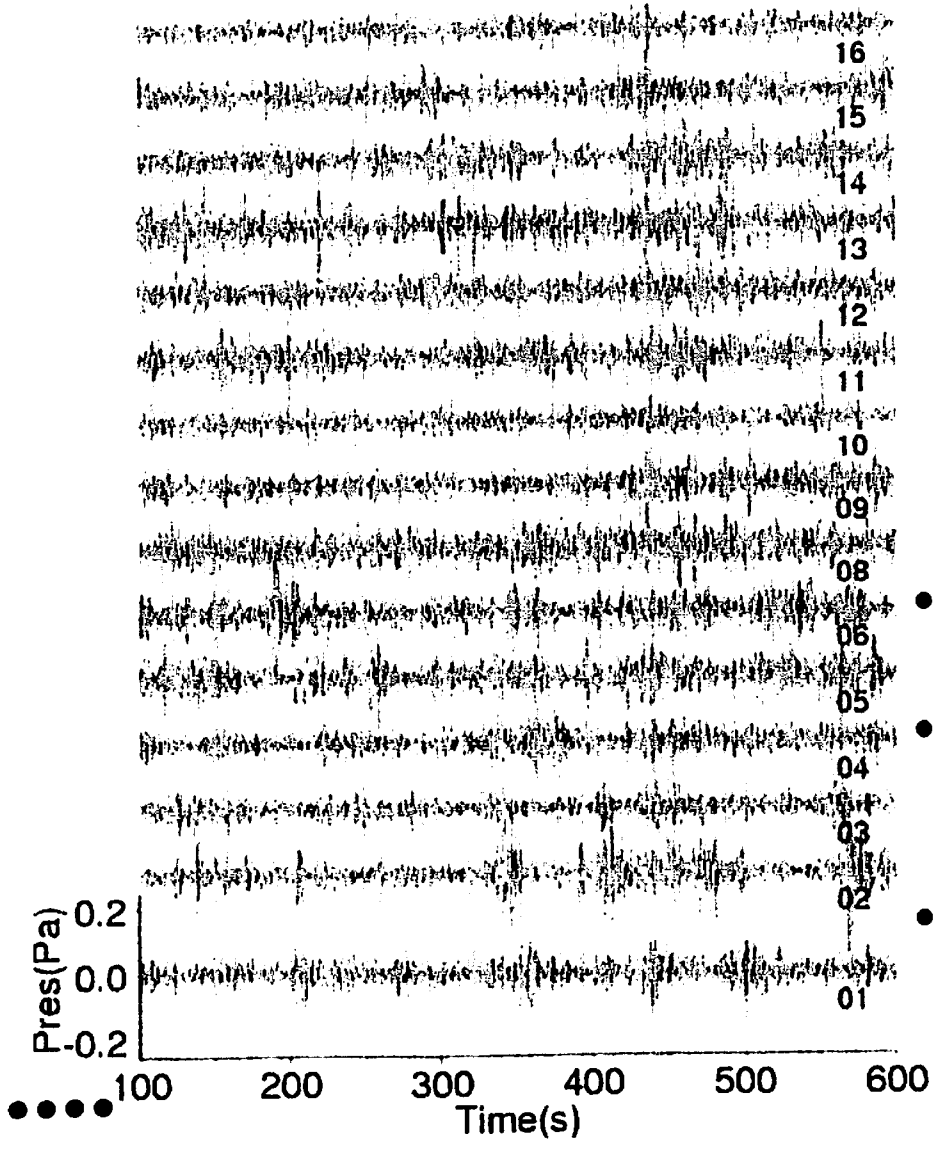

- Time since 2001.10.27 19u28m47.4s GMT
- From 400 to 500 slight increase in amplitude and frequency
- Band pass filter 0.5 to 1.5 Hz

Time domain processing

KNMI

Koninklijk Nederlands Meteorologisch Instituut

•••• Frequency domain Fisher analysis

KNMI

- Frequency–slowness power spectrum

$$P(\omega, \mathbf{p}) = \left| \sum_{n=1}^{N} A_n(\omega) \cdot e^{-i\omega \mathbf{p} \cdot \mathbf{r}_n} \right|^2$$

with: $A_n(\omega)$ being the Fourier transforms of recordings at N number of instruments located by $\mathbf{r}_n$ position vectors.

- Fisher coherency

$$S_F(\omega, \mathbf{p}) = \frac{E(\omega,\mathbf{p})}{E(\omega) - E(\omega,\mathbf{p})} \cdot (N-1)$$

$$E(\omega, \mathbf{p}) = \left| \frac{1}{N} \sum_{j=1}^{N} A_j(\omega) \cdot e^{-i\omega \mathbf{p} \cdot \mathbf{r}_j} \right|^2$$

$$E(\omega) = \frac{1}{N} \sum_{j=1}^{N} |A_j(\omega)|^2$$

••••

Frequency-slowness analysis

KNMI

Koninklijk Nederlands Meteorologisch Instituut

Koninklijk Nederlands Meteorologisch Instituut

KNMI

Localization through cross bearing

24 hours of infrasound data

KNMI

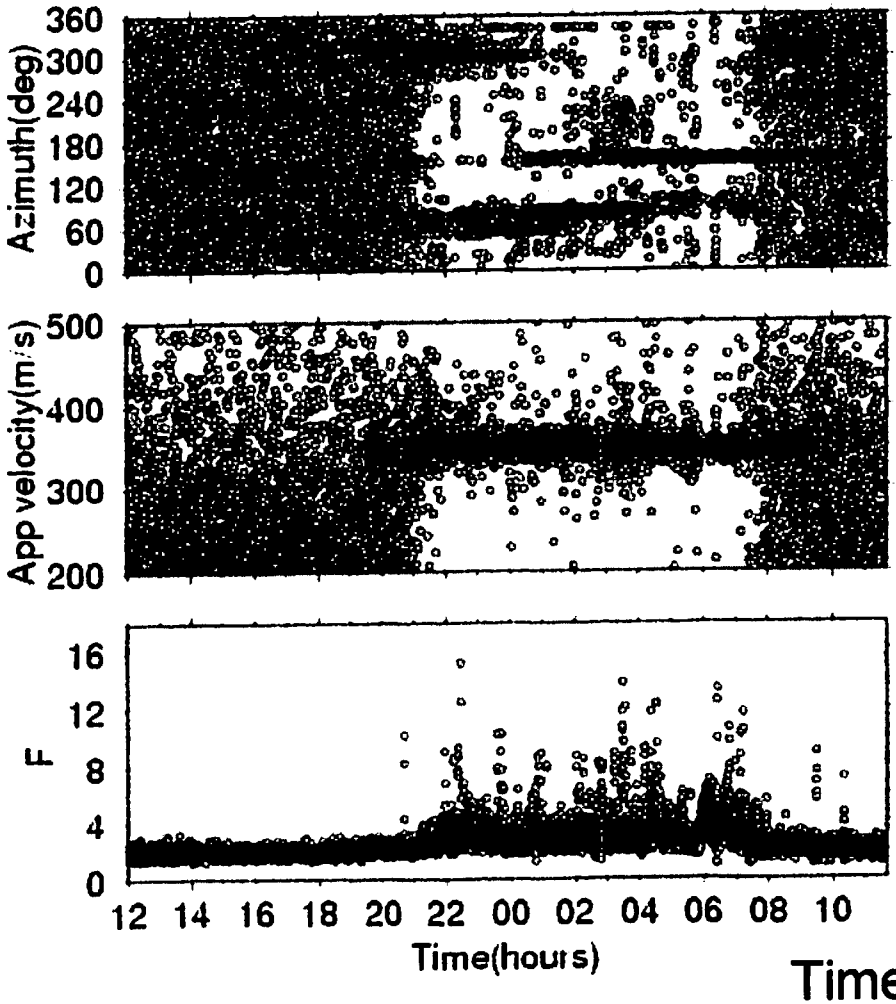

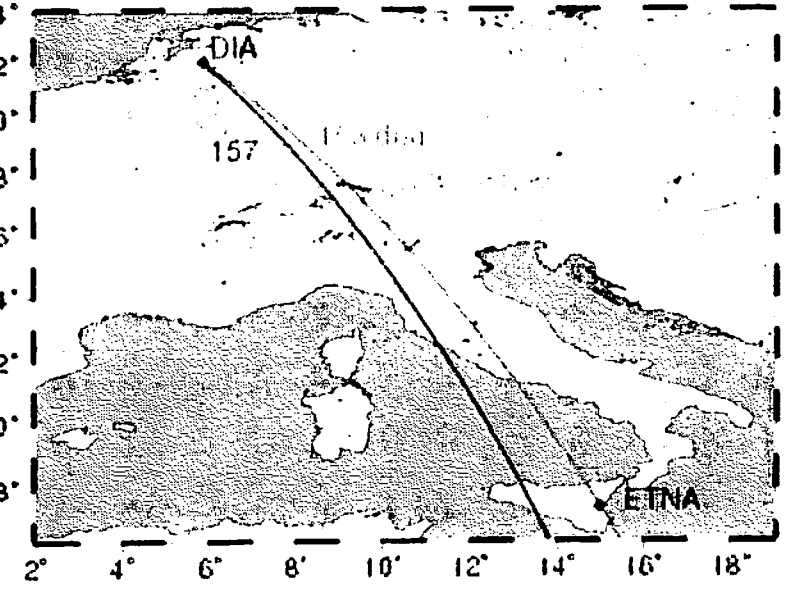

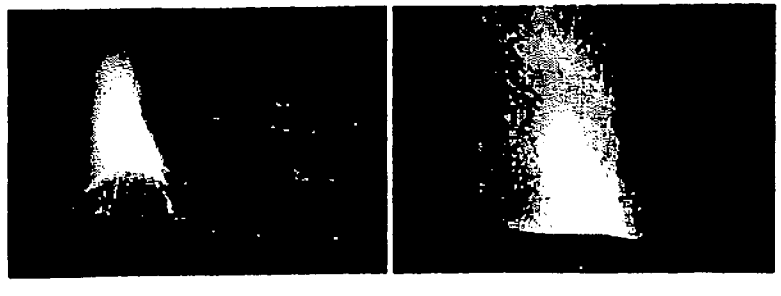

Time axis starts on 2001, July 28

Example of Etna's infrasound

Theory on raytracing

KNMI

- Temperature dependent sound speed

$$c = \sqrt{\gamma_g r \Theta}$$

with: ratio of specific heats γ_g, gas constant r ($\gamma_g r = 402.8$ m^{2}s^{-2}K^{-1}) and absolute temperature Θ

- Effective sound speed

$$v_{eff} = c + \hat{\mathbf{n}} \cdot \mathbf{u}$$

with: unit normal to wavefront $\hat{\mathbf{n}}$, wind speed $\mathbf{u}$

- Snell's law for a moving medium

$$\frac{v_{eff_1}}{cos\theta_1} = \frac{v_{eff_2}}{cos\theta_2} = \ldots.$$

Atmospheric models

Atmospheric trajectories

Koninklijk Nederlands Meteorologisch Instituut

Summary and outlook

KNMI

- Huge amount of infrasound
- Infrasonic activity monitored at long ranges
- Knowledge of atmospheric properties derived from infrasound
- Gain insight in weather dependent sound propagation
- Information on sources in atmosphere through passive measurements

A THEORETICAL ANALYSIS OF THE AWSUM(K) FLUCTUATION-BASED PROCESSORS.

Kenneth E. Gilbert and Carrick L. Talmadge
National Center for Physical Acoustics,
University of Mississippi,
Coliseum Drive, University, MS 38677.

ABSTRACT

Non-linear signal processing algorithms, developed originally for ocean acoustics and named "AWSUM(K)," have been applied in this laboratory to atmospheric acoustic signals measured in the presence of severe wind noise. The name of the processors stems from the first-order (K=1) processor called "WISPR ," which stands for Wagstaff's Integration Silencing Processor after its originator, R. A. Wagstaff. The AWSUM (Advanced WISPR SUMmation) processors are higher-order extensions (K>1) of the first-order WISPR processor. It has been found that the AWSUM(K) processors, which filter out strong signals and pass weak signals, can provide dramatic gains in the signal-to-noise ratio for a steady sinusoidal signal strongly degraded by wind noise. Further, applications of the processors to field data have shown a number of systematic behaviors that so far have not been explained or understood quantitatively. This paper presents a theoretical analysis of the AWSUM(K) processors for a steady sinusoidal signal in the presence of exponential (Rayleigh) noise and intermittent (non-Rayleigh) noise. The theory quantitatively explains the observed systematic behaviors of the AWSUM(K) processors. In particular, it is shown that in the limit of large sample number, the AWSUM(K) gain in the (signal+noise)-to-noise ratio is independent of processor order (for $K \geq 2$). For a steady sinusoidal signal, the gain is determined solely by the shape of the noise probability density distribution near zero. For Rayleigh noise, for example, the gain is given by exp(SNR)/(SNR+1), where SNR is the usual linear signal-to-noise ratio (e.g., SNR = 1 corresponds to a signal-to-noise ratio of 0 dB). For wind noise, which is intermittent noise, the measured distribution function is very strongly peaked near zero, so that gains in approaching 20 dB are predicted, even for small values of SNR. The predictions are in accord with field data from an atmospheric sound propagation experiment.

1.0 INTRODUCTION

Detection of a narrowband acoustic signal in the presence of background noise is a common problem in defense applications and is usually done by means of spectral analysis. Namely, one computes the Fourier transform of the signal and looks for peaks in the resulting frequency spectrum. More specifically, if one has a pressure-versus-time signal, $P(t)$, the signal is first sampled from a time t to a time $t + \Delta t$, and the complex Fourier transform, $\tilde{P}(f)$, is computed. Generally, one calculates $\tilde{P}(f)$ for several hundred time intervals and computes the average "power" spectrum. That is, $\tilde{P}_j(f)$ is first computed, where the time sample is from t_j to $t_j + \Delta t$, and $j = 1,N$. Then the average power spectrum AVGPR(f) is computed as,

$$\mathrm{AVGPR}(f) = (1/N)\sum_{j=1}^{N} X_j(f). \tag{1}$$

where $X_j(f) = |\tilde{P}_j(f)|^2$ is the "power " density at a frequency f, on the jth time sample.

For outdoor sound propagation, if no acoustic signal is present, the spectrum given by Eq. (1) is simply the spectrum of the non-acoustic pressure fluctuations imposed on the microphone by the turbulent flow of the atmosphere over the microphone. The pressure fluctuations due to the atmosphere are commonly called "wind noise." If an acoustic signal is present that is significantly stronger than the wind noise, a discernable peak occurs at the frequency of the signal. Thus, for a given frequency "bin," if the increase in the average power in the bin is sufficiently greater than the average noise power in the bin, then we say a "detection" of an acoustic signal has been made. (Note: In the discussion that follows, we shall assume that the signal has been Fourier analyzed and generally will not explicitly write out the dependence on the frequency.)

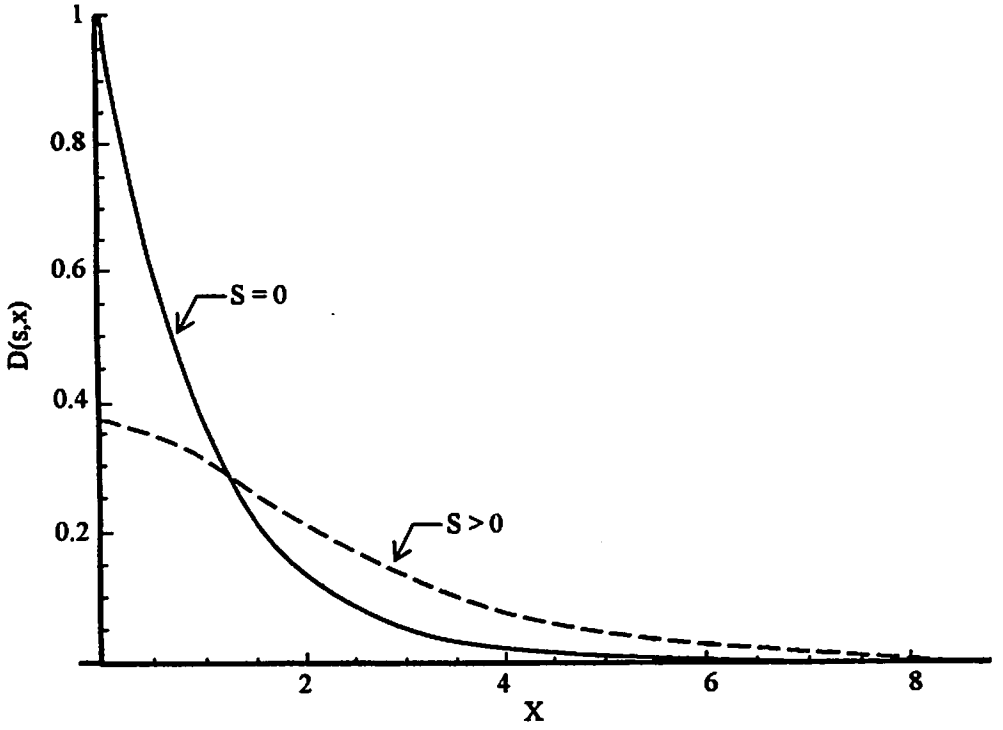

Figure 1. Power distribution function for Rayleigh noise (solid line) and a steady sinusoidal signal embedded in Rayleigh noise (dashed line). The signal power is equal to the average noise power, i.e., the signal-to-noise ratio is zero dB.

To further illustrate the points discussed above, consider the specific case of the K=1 (WISPR) processor:

$$\text{AWSUM(1)} = \left[\frac{1}{N}\sum_{j=1}^{N} X_j^{-1}\right]^{-1}$$

$$= \frac{1}{\frac{1}{N}\sum_{j=1}^{N}\frac{1}{X_j}} \quad . \tag{3}$$

Consider a frequency bin with no signal, so that the power fluctuations are governed by the noise-only distribution (solid line) in Fig. 1. There will be a certain number of very small values for X that will dominate the sum in Eq. (3) and consequently produce a small value for the harmonic mean given by AWSUM(1). Now suppose that a steady signal is added to the bin so that the power distribution is given by the dashed line in Fig. (1). As shown in Fig.1, the number of very small values for X will be dramatically reduced in the frequency bin containing the signal. As a result, for that frequency bin, the sum in Eq. (3) will be much smaller, and the value of the quantity AWSUM(1) will increase significantly. Experience has shown that in a plot of AWSUM(1) versus frequency, with realistic distributions for noise and signal-plus-noise, a frequency bin with a narrowband signal will usually stand out clearly, even in situations where the signal-to-noise ratio is small. Experience has further shown that the higher-order processors (e.g., K = 4) are generally more effective than the original K = 1 (i.e., WISPR) processor. Thus, the AWSUM(K) processors can produce a significant gain in the detection capability even in situations where wind noise is severe.

3.1. GENERAL THEORETICAL APPROACH

To proceed with the theoretical analysis, we consider a steady sinusoidal signal in the presence of stochastic noise. We assume that the summations over the sample index j for AVGPR in Eq. (1) and for AWSUM(K) in Eq. (2) can be approximated by dividing the X coordinate into bins and summing over the bins. For example, with summation over bins, the average power for noise plus a steady sinusoidal signal of power S is given by,

$$\mathrm{AVGPR}(S) = (1/N)\sum_{b=1}^{N_b} n_b X_b \quad , \tag{4}$$

where X_b is the value of X in the center of the b^{th} bin, n_b is the number of occurrences in the b^{th} bin, and N_b is the total number of bins. We further consider an ensemble average for AVGPR(S) which we denote as ⟨AVGPR(S)⟩. Taking the ensemble average of Eq. (4) gives

$$\langle \mathrm{AVGPR}(S) \rangle = (1/N)\sum_{b=1}^{N_b} \langle n_b \rangle X_b \quad , \tag{5}$$

It is assumed here that, for sufficiently small bin size, the summation in Eq. (5) accurately approximates the ensemble average of the direct sum in Eq. (1).

To achieve a tractable formulation, we write $\langle n_b \rangle / N$ in terms of a distribution function $D(S,X)$:

$$\begin{aligned} \langle n_b \rangle / N &= \int_{X_b - \Delta X/2}^{X_b + \Delta X/2} D(S,X)\,dX \\ &\approx D(S,X_b)\,\Delta X \quad , \end{aligned} \tag{6}$$

where ΔX is the bin size, which we assume is sufficiently small that the integral is well approximated by the product $D(S,X_b)\ \Delta X$. Hence we have

$$\langle \mathrm{AVGPR}(S) \rangle = \sum_{b=1}^{N_b} X_b D(S,X_b)\,\Delta X \quad , \tag{7}$$

For the sake of generality, it is convenient to define power variables normalized by the average noise power: $X/\langle \mathrm{AVGPR}(0) \rangle \equiv x$, $S/\langle \mathrm{AVGPR}(0) \rangle \equiv s$, and $\Delta X/\langle \mathrm{AVGPR}(0) \rangle \equiv \varepsilon$. Note that for a steady signal, the quantity s is simply the signal-to-noise ratio, which we have previously denoted as SNR. In terms of normalized variables, the distribution function $D(s,x)$ is dimensionless and is defined by $\langle \mathrm{AVGPR}(0) \rangle D(S,X) \equiv D(s,x)$. For example, for a steady sinusoidal signal embedded in Rayleigh noise, the signal-plus-noise distribution function we are considering can be written in as

$$D_{Rayleigh}(s,x) = \exp[-(x+s)]\,\mathrm{I}_0(2\sqrt{sx}) \tag{8}$$

where I_0 is the modified Bessel function of zero order. Since $\mathrm{I}_0(0) = 1$, the noise distribution for Rayleigh noise, $D_{Rayleigh}(0,x)$, is the familiar exponential distribution. (Note: Written in terms of pressure instead of pressure squared, the distribution in Eq. (8) would be the Rician distribution cited earlier. Since we use pressure squared throughout, the functional form is not that of a Rician distribution. Hence, we choose to retain the designation "Rayleigh " in order to minimize the number of labels.)

$$NS(K) \equiv AWSUM(K,0) / AVGPR(0)$$

$$= \left[2^K \varepsilon^{-K+1} e^{-\varepsilon/2} + \int_{\varepsilon}^{\infty} x^{-K} e^{-x} dx \right]^{-1/K} \tag{14}$$

where we have used $D(0,x) = \exp(-x)$. The integral in Eq.(14) is given by $\varepsilon^{-K+1}E_K(\varepsilon)$, where $E_K(\varepsilon)$ is the exponential integral [Abramowitz and Stegun, 1964]. Thus the noise suppression for Rayleigh noise can be written,

$$NS(K) = \varepsilon^{\frac{K-1}{K}} \left[2^K e^{-\varepsilon/2} + E_K(\varepsilon) \right]^{-1/K}, \tag{15}$$

where the lower integration limit, ε, is taken as a free parameter for now. As will be shown, ε is generally much less that one, so that the $NS(K)$ can be written using small-argument approximations ($\varepsilon << 1$) for $E_K(\varepsilon)$ [Abramowitz and Stegun, 1964]. Using the small-argument approximations and $\exp(-\varepsilon/2) \approx 1$, we have,

$$NS(K) = \varepsilon^{\frac{K}{K-1}} \begin{cases} [2 - \ln(\varepsilon) - 0.577]^{-1}, & K = 1 \\ \left[2^K + 1/(K-1) \right]^{-1/K}, & K \geq 2 \end{cases} . \tag{16}$$

Written in terms of decibels, the noise suppression is given by,

$$NS(K) = -\left(\frac{K-1}{K} \right) 10 \log_{10}(\varepsilon) + (1/K) 10 \log_{10} \begin{cases} 2 - \ln(\varepsilon) - 0.577, & K = 1 \\ 2^K + 1/(K-1), & K \geq 2 \end{cases} \tag{17}$$

Note that in Eq.(16) and Eq.(17), for $K \geq 2$ and $\varepsilon \to 0$, the contribution from the first bin dominates the noise suppression. In contrast, for $K = 1$, the contribution from the first bin is constant and the contribution from the integral dominates for $\varepsilon \to 0$.

To determine if Eq. (17) gives meaningful predictions for the noise suppression, we compare it with the experimental suppression of noise obtained by Wagstaff for ocean noise data. Specifically, we use the noise suppression shown in Fig. 4 of [Wagstaff, 1997] for $N = 800$. As shown in Table I, the measured noise suppression can be well fit as a function of K with a single value of ε, namely, $\varepsilon = 1.8 \times 10^{-3}$. The good agreement between Eq. (17) and Wagstaff's ocean noise suppression data indicates that the approach used for approximating the AWSUM(K) summation is physically meaningful. It further suggests that the noise power distribution for Wagstaff's data was, quite fortuitously, close to exponential (i.e., Rayleigh).

To further test Eq.(17), we compare the predicted and the measured suppression of wind noise for an atmospheric acoustic experiment conducted by this laboratory. For wind noise, a Rayleigh distribution (i.e., a single exponential) is a very poor approximation for the noise distribution function. The power distribution for the wind noise was measured, however, and can be empirically fit reasonably well with a sum of three exponentials. With the empirical fit to the noise distribution, the predicted noise suppression can be written analytically as a sum of terms similar to those given in Eqs. (16) and (17). However, it is more useful to generalize the Eqs.(16) and (17) to account for an arbitrary distribution function.

Table I. Comparison of predicted and measured noise suppression by the AWSUM(K) processors for ocean data. Rayleigh noise was assumed, i.e., D(0,0) = 1. A bin width of $\varepsilon = 1.18 \times 10^{-3}$ was used in Eq. (17), to fit the measured noise suppression for K=4.

Processor Order, K	Noise Suppression (dB)	
	Measured	Predicted
1	10	9.4
2	18	18.1
3	23	22.6

$$\approx D(0,0)\varepsilon. \tag{20}$$

The number of samples, N, can be chosen at will, and the noise distribution function $D(0,x)$ can be measured. Hence, there is an approximate, but definite, relationship between $\langle n_1 \rangle$ and ε,

$$\langle n_1 \rangle \approx ND(0,0)\varepsilon\,. \tag{21}$$

Recall that $\varepsilon_{ocean} = 1.18\text{x}10^{-3}$, and $\varepsilon_{atmosphere} = 1.19\text{x}10^{-4}$, which is a difference of over an order of magnitude. We can use the fitted values for ε, together with the associated values for N ($N_{ocean} = 800$, $N_{atmosphere} = 200$), and for $D(0,0)$ ($D_{ocean}(0,0) = 1$, $D_{atmosphere}(0,0) = 46$), and apply Eq. (21) to the ocean and atmospheric noise data discussed above. We then obtain, respectively, $\langle n_1 \rangle_{ocean} = .94$, and $\langle n_1 \rangle_{atmosphere} = 1.09$. The fact that $\langle n_1 \rangle \approx 1$ for two completely different noise mechanisms, with values of ε that differ by more than an order of magnitude, suggests that we can choose $\langle n_1 \rangle \equiv 1$, and thus arrive at a unique *a priori* choice for ε:

$$\varepsilon \equiv 1/ND(0,0) \tag{22}$$

The *a priori* value for ε given in Eq. (22) gives noise suppression predictions that differ by less than a decibel from the predicted values in Table I and Table II, where a fitted value of ε was used. We note, finally, that the above *a priori* choice for ε is also supported by numerical simulations of wind noise data which indicate that ε scales as $1/N$.

The variation of ε with N in Eq. (22) can be tested using Wagstaff's ocean data for noise suppression as a function of the number of sample intervals, N. Wagstaff has fitted regression curves to observed noise suppression for $K = 1$ [Wagstaff, 1998] and $K = 4$ [Wagstaff, 1997] as a function of N for a large number of ocean experiments. The regression equations for no overlap in the time samples, are given below in Eq. (23). (Note: The regression equation in [Wagstaff, 1997] apparently contains an error as it does not fit the zero time overlap result shown in Fig. 5 of that reference. The equation for K=4 given in Eq. (23) below is a modification of the K=4 regression curve of [Wagstaff, 1997] that does agree with the curve shown there for zero time overlap.)

$$\text{NS}_{\text{regression}}(K) = \begin{cases} 6[\log_{10}(N)]^{1/2}, & K = 1 \\ 2 + 8.33\log_{10}(N) - .16[\log_{10}(N)]^2, & K = 4 \end{cases} \tag{23}$$

Figure 3 shows a comparison between Wagstaff's regression equations (dashed lines) for K=1,4 and the predicted noise suppression (solid lines) for K=1,2,3,4. The predicted noise suppression is obtained using the expression for ε in Eq. (22) together with Eq. (17). The good agreement between the predictions and Wagstaff's regression equations provides strong support for the validity of Eq. (22) and further supports the notion that Wagstaff's ocean noise distributions were approximately exponential (i.e., Rayleigh).

Since we consider a steady sinusoidal signal, one can easily show that $D(s,0) = D(0,s)$. For example, consider Fig. 4, which shows schematically the distribution of the complex pressure values, $\tilde{P}_j$ (j = 1,N), in the complex plane. Figure 4(a) is for noise only ($s = 0$), and Fig. 4(b) is for noise plus a steady sinusoidal signal ($s > 0$). From the figure, it is clear that for $s > 0$, the value of the complex noise-plus-signal distribution function at the origin is just the value of the complex noise distribution evaluated a distance $\sqrt{s}$ from the center. Hence it follows that $D(s,0) = D(0,s)$. (For a mathematical analysis, see the Appendix.) Thus, for a steady sinusoidal signal and $N >> 1$, $\varepsilon(s,N)$ can be estimated using the number of samples, N, and the noise distribution curve, $D(0,x)$. Note that, since $D(s,0)=D(0,s)$, $D(0,s)$ decreases with increasing s. Hence the bin size $\varepsilon(s,N)$ increases with increasing s. The increase in $\varepsilon(s,N)$ with increasing s is because a larger first bin is needed to have $\langle n_1 \rangle = 1$ when $D(s,0)$ becomes smaller due to the presence of a signal.

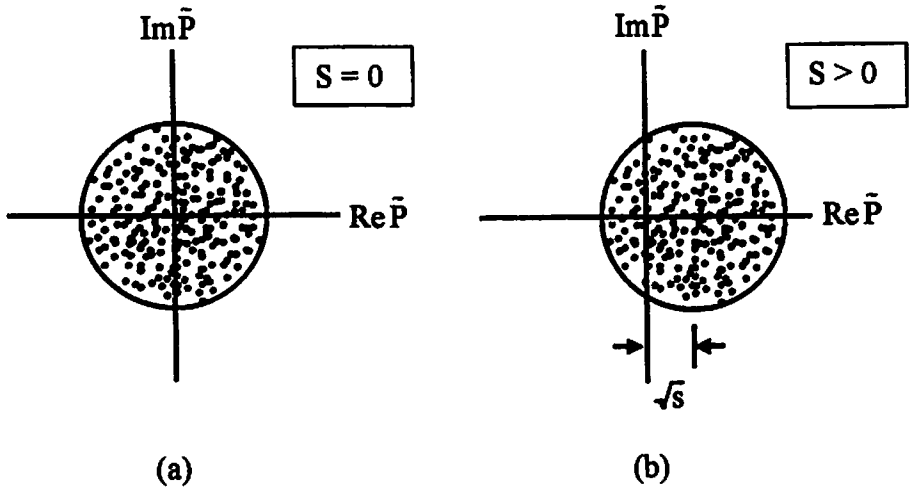

Figure 4. Schematic representation of the distribution of complex pressure values, $\tilde{P}_j$, in the complex plane, for j = 1,N, where $N >> 1$. Figure 4(a) shows the distribution for noise only (s = 0), and Fig. 4(b) shows the distribution for noise plus a steady sinusoidal signal with power equal s ($s > 0$), and a phase angle of zero degrees. Note that for $s > 0$, the value of the distribution at the origin is just that of the noise-only distribution evaluated at a distance $\sqrt{s}$ from the origin. This property leads to the result $D(s,0) = D(0,s)$ discussed in the text.

The signal-plus-noise suppression is defined as,

$$\mathrm{SS}(K,s) \equiv \mathrm{AWSUM}(K,s) / \mathrm{AVGPR}(s) = \frac{\mathrm{AVGPR}(0)}{\mathrm{AVGPR}(s)} \frac{\mathrm{AWSUM}(K,s)}{\mathrm{AVGPR}(0)} = \left(\frac{1}{s+1}\right) \frac{\mathrm{AWSUM}(K,s)}{\mathrm{AVGPR}(0)} \tag{26}$$

Using the above definition for $\mathrm{SS}(K,s)$, along with the generalized expression for ε, and Eq. (18) generalized for $s > 0$, we obtain,

$$\mathrm{SS}(K,s) = \left(\frac{1}{s+1}\right) D^{-1/K}(0,s)\varepsilon(s,N)^{\frac{K-1}{K}} \begin{cases} [2 - \ln\varepsilon(s,N)]^{-1}, & K = 1 \\ [2^K + 1/(K-1)]^{-1/K}, & K \geq 2 \end{cases} . \tag{27}$$

Using Eq.(25) for $\varepsilon(s,N)$ and Eq. (27) for $\mathrm{SS}(K,s)$, together with the measured noise distribution $D(0,x,)$, we can predict, with no adjustable parameters, the signal-plus-noise suppression given by the AWSUM(K) processors. Table III compares the predicted signal-plus-noise suppression to the values measured in the atmospheric sound propagation experiment discussed earlier. The predicted signal-plus-noise suppression values for $K \geq 2$ are too large by 6-7 dB. At present we have no explanation for the nearly constant 6-7 dB offset between the predicted and

signal, s. For example, suppose the wind noise distribution has been measured in an experiment and plotted in a histogram showing the frequency of occurrence of noise power values versus normalized power, x. Then, for a given value of $SNR^+ = s+1$, the predicted gain in SNR^+ can be read directly off the histogram. Alternatively, as done here, one could fit the measured noise distribution with a functional form and construct a normalized probability distribution function. With either approach, the predicted gain in SNR^+ is easily obtained.

Written in terms of decibels, the gain in signal-to-noise is,

$$SNR^+GAIN = 10\log_{10} D(0,0) - 10\log_{10} D(0,s) - 10\log_{10}(s+1) \tag{30}$$

To test the predicted gain given in Eq. (30), we compare with the measured values obtained in the outdoor sound experiment discussed earlier. We can use Fig. 2 to obtain a value for s. The value of $10\log_{10}SNR^+ = 10\log_{10}(s+1)$ in Fig. 2 is approximately 4 dB, which gives a $s \approx 1.5$. The values $D(0,0)$ and $D(0,1.5)$ can be obtained from the empirical expression for $D(0,x)$ obtained by fitting three exponentials to wind noise data or, equivalently, from the curve labeled "wind noise" in Fig. 5. Using the measured values for s, $D(0,0)$ and $D(0,1.5)$ in Eq. (30), we obtain a predicted value of SNR^+GAIN = 20.5 dB. The corresponding measured signal-to-noise gains are shown in Table IV. Because the signal-plus-noise suppression obtained earlier is over-predicted by 6-7 dB (see Table III), the SNR^+GAIN in Table IV is under-predicted by the same amount. (Recall that the SNR^+GAIN is the noise suppression in decibels minus the signal-plus-noise suppression in decibels.) Hence, the predicted values for SNR^+GAIN are uniformly too small by 6-7 dB. More important, however, the data show the predicted lack of dependence on the processor order. The comparison indicates that the simple result in Eq. (29) provides a useful estimate of the gain in SNR^+ provided by the AWSUM(K) processors. The implications of Eq. (29) are discussed in the next section.

Table IV. Comparison of predicted and measured gain in the (signal+noise)-to-noise ratio, SNR^+, for the AWSUM(K) processors. The gain prediction has no adjustable parameters.

Processor Order, K	Gain in (Signal-Noise)-to-Noise Ratio (dB)	
	Measured	Predicted
2	27	20.5
3	26	20.5
4	27	20.5
6	26	20.5
8	27	20.5
10	27	20.5

4.0 DISCUSSION OF RESULTS

The result in Eq. (29) has important implications for detecting sinusoidal signals embedded in severe wind noise. To motivate the discussion, consider Fig. 4 and Fig. 5. If the complex pressure values in Fig. 4 are uniformly distributed, then the probability distribution function, $D(0,x)$, will be the uniform distribution shown in Fig. 5. If the real and imaginary parts of the complex pressure are each independently distributed as a Gaussian, then the distribution function $D(0,x)$ will be an exponential, as shown by the curve denoted "Rayleigh" in Fig. 5. If the complex pressure values are distributed as observed in wind noise measurements, then $D(0,x)$ will be sharply peaked for small values of x, as shown by the curve labeled "wind noise" in Fig. 5. For the uniform distribution, for $x < 2$, the ratio $D(0,0)/D(0,s)$ is unity, so that $SNR^+GAIN=1/(s+1)=1/SNR^+$. Hence for a steady simusoidal signal embedded in noise that is uniformly distributed, the AWSUM(K) processors give no gain at all, and, in fact, make SNR^+GAIN decrease. For Rayleigh noise, the ratio $D(0,0)/D(0,s)$ is exp(SNR), so for linear SNR less than 1, (SNR < 0 dB), only minimal gain is given by the AWSUM(K) processors. In sharp contrast, for wind noise, which has a strong peak below about x =0.1, the AWSUM(K) processors give substantial gain, even for weak signals. For example, for linear SNR=.4 (SNR = -4 dB), Eq. (30) predicts a gain of 19.8 dB. Further, according to the wind noise curve in Fig. 5, gains approaching 20 dB should be possible down to SNR $\approx$ 0.1 (-10 dB), which is the value of x at the "break point" in the wind noise curve. Whether such large gains can always be realized in practice, for such weak signals, remains to be demonstrated.

One of the authors (K.E.G.) would like to thank R.A. Wagstaff for numerous helpful discussions and for providing analyzed data from an atmospheric propagation experiment. The research reported here was supported by the U.S. Army Space and Missile Defense Command (SMDC), under Contract No. DASG60-00-C-0061.

APPENDIX: SUPPRESSION OF NOISE AND SIGNAL-PLUS-NOISE FOR A GENERAL NOISE PROBABILITY DISTRIBUTION FUNCTION

For $N >> 1$ ($\varepsilon << 1$), estimates for the suppression of noise and signal-plus-noise can be derived for a general noise probability distribution function. Equation (13), for the suppression of noise and signal-plus-noise, contains the following expressions:

$$I(K,s,\varepsilon) = I_1(K,s,\varepsilon) + I_2(K,s,\varepsilon), \tag{A.1}$$

where

$$I_1(K,s,\varepsilon) = 2^K \varepsilon^{-K+1} D(s,\varepsilon/2), \tag{A.2}$$

and

$$I_2(K,s,\varepsilon) = \int_\varepsilon^\infty x^{-K} D(s,x)\,. \tag{A.3}$$

Since, in general, we have $\varepsilon << 1$, it is useful to write $I_1(K,s,\varepsilon)$ and $I_2(K,s,\varepsilon)$ in a form that involves a power series expansion of $D(s,x)$. For example, for $I_1(K,s,\varepsilon)$, we can write

$$I_1(K,s,\varepsilon) = 2^K \varepsilon^{-K+1}[D(s,0) + D_x(s,0)\varepsilon/2 + \Lambda]\,, \tag{A.4}$$

where $D_x(s,0)$ denotes first derivative of $D(s,x)$ with respect to x, evaluated at $x = 0$.

To obtain a similar expansion for $I_2(K,s,\varepsilon)$, we can apply integration by parts successively to Eq. (A.3). For example, for $K \geq 3$, we can write,

$$I_2(K,s,\varepsilon) = \varepsilon^{-K+1}\left[\frac{D(s,\varepsilon)}{K-1} + \frac{D_x(s,\varepsilon)}{K-2}\varepsilon + \otimes\right]. \tag{A.5}$$

Similarly, for K=1, 2, we can use integration by parts and write the following explicit expressions:

$$I_2(1,s,\varepsilon) = -\ln\varepsilon D(s,\varepsilon) + \varepsilon(\ln\varepsilon - 1)D_x(s,\varepsilon) + \Lambda \tag{A.6}$$

and

$$I_2(2,s,\varepsilon) = \varepsilon^{-1} D(s,\varepsilon) - \ln\varepsilon D_x(s,\varepsilon) + \Lambda \tag{A.7}$$

Expanding $D(s,\varepsilon)$ and $D_x(s,\varepsilon)$ in Eqs. (A.5)-(A.7) to first order in ε, and combining the results with Eq. (A.4), we have, to first-order in ε,

REFERENCES

Abramowitz, M. and Stegun, I.A., editors (1964). *Handbook of Mathematical Functions*, p. 229, U.S. Government Printing Office, Washington, D.C.

Rice, S. O. (1944). "Mathematical Analysis of a Random Noise," Bell System Tech. J., 23, 184-294. Reprinted in *Selected Papers on Noise and Stochastic Processes* (N. Wax, Editor), Dover Publications, Inc., New York, 1954.

Rice, S. O. (1945). "Mathematical Analysis of a Random Noise," Bell System Tech. J., 24, 133-183. Reprinted in *Selected Papers on Noise and Stochastic Processes* (N. Wax, Editor), Dover Publications, Inc., New York, 1954.

Rayleigh, Baron (1937). *Theory of Sound*, Vol. I, p. 41, Macmillan Co., London.

Wagstaff, R. A. (1997). "The AWSUM Filter: A 20-dB Gain Fluctuation-Based Processor," IEEE Journal of Oceanic Engineering, 22, 110-118.

Wagstaff, R. A. (1998). "The Wagstaff's integration silencing processor filter: A method for exploiting fluctuations to achieve improved sonar signal processor performance," J. Acoust. Soc. Am., 104, 2915-2924.

Wagstaff, R. A. (2002). "Using Amplitude Fluctuations to Improve Long Range Signal Detection," Tenth International Symposium on Long Range Sound Propagation, Grenoble, France, September 12-13, 2002.

A Modal Expansion for Low Frequency Acoustic Propagation in the Nocturnal Boundary Layer

Roger Waxler

The National Center for Physical Acoustics at the University of Mississippi

Sound propagation in the nocturnal boundary layer is characterized by downward refraction near the ground and upward refraction higher up in the atmosphere.[1] A model sound speed profile is depicted in Figure 1. Profile 1, $c_1(z)$, is the model used in the simulations presented here, profile 2, $c_2(z)$, is an asymptotically constant profile used as a starting point in the perturbative schemes described below. The sound's interaction with the ground is modeled here by an impedance Z written in the form

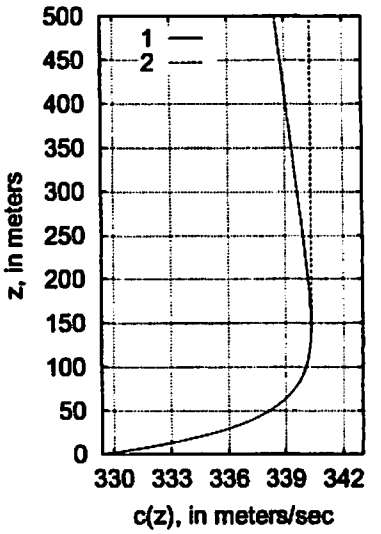

Figure 1: Model Sound Speed Profile

$$Z(\omega) = \frac{i\omega\rho_0}{A(\omega) + iB(\omega)}.$$

Here ω is the angular frequency. Note that if $B = 0$ then the impedance is pure imaginary and the interaction with the ground does not attenuate the sound field. In the simulations presented here the specific form chosen for $Z(\omega)$ is that one used in Ref. 2.

Physically, the downward refraction causes the sound to be ducted along the ground, but the upward refraction causes the duct to be imperfect, allowing sound to leak out of the duct into the upper atmosphere. In addition the propagation is effected by the sound's interaction with the ground which is both compliant and lossy, as reflected by the imaginary and real parts (respectively) of the impedance. It has been shown[3] that the attenuation of the sound field by the ground stabilizes the duct: the ducted part of the sound field attenuates more rapidly than the rate at which it leaks into the upper atmosphere.

The propagation of a monotone continuous wave of frequency ω is described by solving the Helmholtz equation

$$\Big(\nabla_H^2 + \frac{\partial^2}{\partial z^2} + \frac{\omega^2}{c(z)^2}\Big)P(\mathbf{x}_H, z) = 0$$

for the acoustic pressure amplitude P. Here $\mathbf{x}_H$ are the horizontal coordinates and ∇_H the corresponding Laplacian; z is the height from the ground. At the ground one has the impedance boundary condition

$$\frac{\partial P}{\partial z}|_{z=0} = -(A + iB)P(\mathbf{x}_H, 0).$$

A vertical eigenfunction expansion will be used to solve the Helmholtz equation. One considers

$$\Big(\frac{d^2}{dz^2} + \frac{\omega^2}{c(z)^2} - \epsilon\Big)\psi_\epsilon(z) = 0 \tag{1}$$

with the boundary condition

$$\psi_\epsilon'(0) = -(A + iB)\psi_\epsilon(0). \tag{2}$$

Then one has the modal expansion[2,3,4]

$$P(\mathbf{x}_h, z) = \sum_{j=1}^{N} p_{\epsilon_j}(\mathbf{x}_h)\psi_{\epsilon_j}(z) + \int_\Gamma p(\epsilon, \mathbf{x}_h)\psi_\epsilon(z)\, d\epsilon. \tag{3}$$

Here ψ_{ϵ_j} are the square integrable solutions of (1) subject to (2) and ψ_ϵ are the polynomially bounded solutions. The set of values $\{\epsilon_1, \ldots, \epsilon_N\}$ is called the point spectrum; the ϵ_j are generally complex valued. Γ is the continuous spectrum; for the asymptotically upward refracting profile, profile 1, $\Gamma = (-\infty, \infty)$ while for the asymptotically constant approximation, profile 2, $\Gamma = (-\infty, \frac{\omega^2}{c_2(\infty)^2})$. The functions $p(\epsilon, \mathbf{x}_h)$ satisfy the two dimensional Helmholz equation (with constant coefficients)

$$\Big(\nabla_H^2 + \epsilon\Big)p(\epsilon, \mathbf{x}_H) = 0$$

subject to appropriate (depending on the source and topography) boundary conditions. The ψ_ϵ are normalized so that[2,3]

$$\int_0^\infty \psi_{\epsilon_j}(z)\psi_{\epsilon_k}(z)\, dz = \delta_{jk}$$

and

$$\int_0^\infty \psi_\epsilon(z)\psi_{\epsilon'}(z)\,dz = \delta(\epsilon - \epsilon').$$

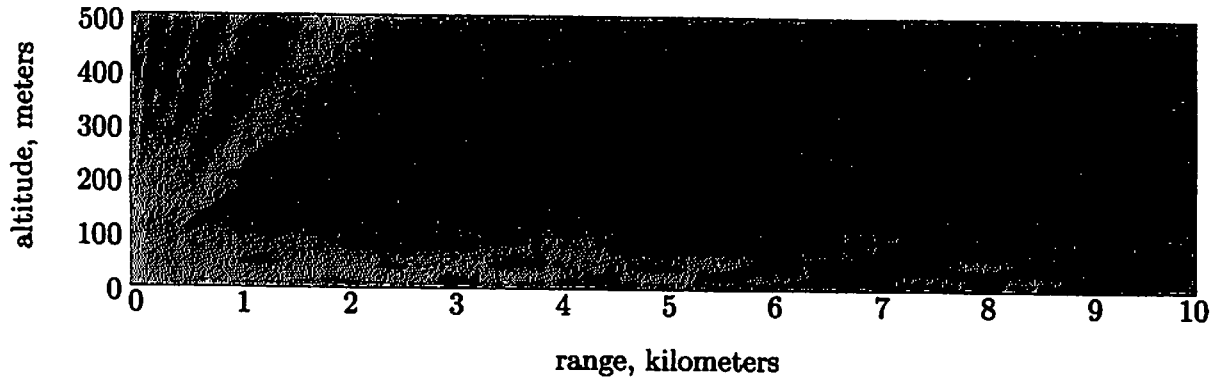

Figure 2: Magnitude of $\sqrt{r}P$. 50 Hz point source at 20 meters elevation.

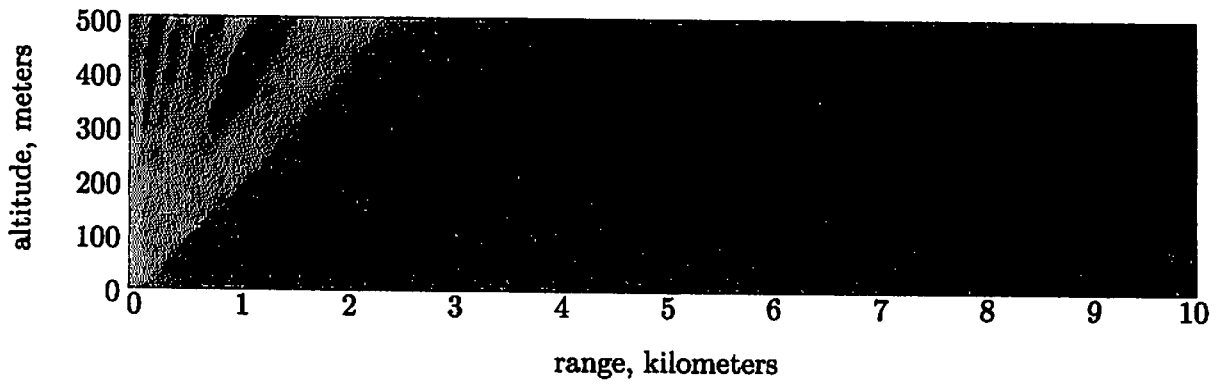

Figure 3: Magnitude of the continuum integral contribution to $\sqrt{r}P$. 50 Hz point source at 20 meters elevation.

The expansion (3) breaks the sound field into a ducted part and an upwardly propagating part. The discrete sum in (3) contains the ducted part of the field while the integral over the continuous spectrum contains the upwardly propagating part. This behavior is demonstrated in Figures 2 and 3 above. In Figure 2 the magnitude of the pressure field (with cylindrical spreading removed) produced by a 42 Hz point source 20 meters above the ground is presented. In Figure 3 the same quantity is presented, however with the discrete sum left out. The frequency 42 Hz was chosen because at this frequency (as will be shown below) the leaking of the sound field from the ducted to the upwardly diffracting part of the sound speed profile should be maximal. Despite this there is a relatively clean separation into ducted and

upwardly propagating parts.

It follows that if one is only interested in low angle, long range propagation then the continuum integral can be neglected. The main technical difficulty that remains is that of finding the point spectrum ϵ_j. Due to the complex boundary condition (2) ϵ_j are generally complex valued so that numerical searches must be done in the complex plane. In addition to the difficulties inherent in searching for roots in two dimensions the solutions to (1) can be poorly behaved for complex ϵ making blind numerical searches problematic.

The solution is to find analytical estimates for the point spectrum which are accurate enough so that standard numerical routines converge rapidly from the analytical estimate to the precise value. A two step procedure has been developed. One begins with the asymptotically constant approximation of profile 2 (see Figure 1). Here a technique has been developed which relates the complex point spectrum to the real spectrum one obtains by setting $B = 0$ in (2).[2] Then one obtains the point spectrum for the asymptotically upward refracting profile by treating the difference between profiles 1 and 2 as a perturbation.[3]

To produce the point spectrum for an asymptotically constant sound speed profile introduce the vertical Greens function $g(A, \epsilon, z_1, z_2)$ for the differential equation (1) subject to (2) with $B = 0$. It is shown in Ref. 2 that the point spectrum $\epsilon_j^{(1)}$ in the asymptotically constant approximation are the solutions η of

$$1 = -iBg(A, \eta, 0, 0).$$

Thus the point spectrum is given by the intersection of the curves along which the real part of $g(A, \eta, 0, 0)$ is zero with the curves along which the imaginary part of $g(A, \eta, 0, 0)$ is $\frac{1}{B}$. For small B a perturbative formula can be developed:

$$\epsilon_j^{(1)} = \epsilon_j^{(0)} + iB\psi^{(0)}_{\epsilon_j^{(0)}}(0)^2 + \ldots. \tag{4}$$

Here $\epsilon_j^{(0)}$ are the elements of the point spectrum for $B = 0$ and $\psi^{(0)}_{\epsilon_j^{(0)}}$ are the corresponding (normalized) solutions to (1). Note that for $B = 0$ the point spectrum is real valued so that standard numerical methods can be used to find it. In practice it has been found that the perturbative estimate (4) is quite accurate.

To estimate the point spectrum in the asymptotically upward refracting case the approach used in the asymptotically constant case can not be used because for asymptotically

upward refracting sound speed profiles there is no point spectrum if $B = 0$ in (2).[5] Rather, if $B = 0$ then sharp peaks arise in the integrand in (3) which contribute terms which mimic ducted behavior but which eventually leak into the upper atmosphere.

Rather than treating B as a perturbation one may treat the upward refraction perturbatively, using formal first order perturbation theory[5] as a starting point for numerical searches. One finds that the perturbative approximation is generally quite good. Except in some exceptional circumstances, the point spectrum for asymptotically upward refracting sound speed profiles is close to point spectrum of the asymptotically constant approximation. The exceptions occur near transition frequencies at which the number of elements in the point spectrum of the asymptotically constant approximation changes. At these transition frequencies an element of the point spectrum emerges from the continuous spectrum and can be strongly perturbed (even to the point of not existing) by the asymptotic upward refraction.[3]

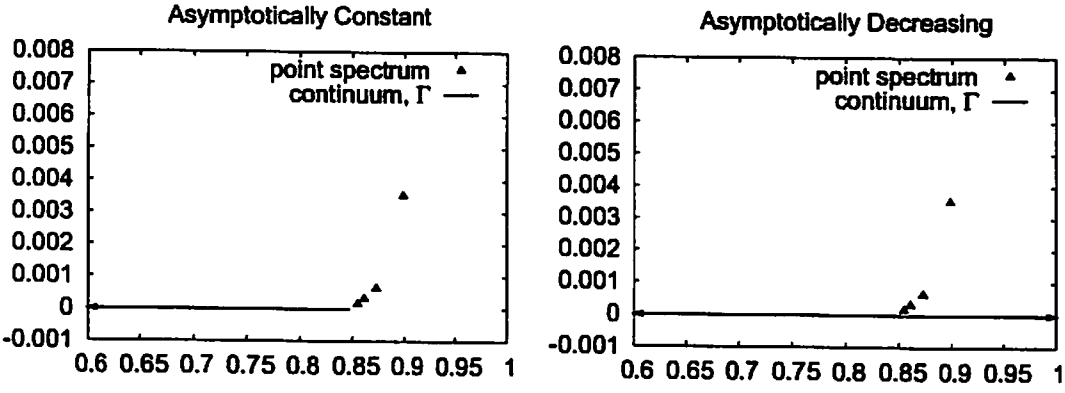

Figure 4: Point and continuous spectra for the model sound speed profiles at 50 Hz.

In Figure (4) the spectrum of the asymptotically constant approximation and of the asymptotically upward refracting model are shown at 50 Hz. In Figure (5) the (normalized) solutions of (1) at 50 Hz corresponding to the third and fourth elements of the point spectra are plotted superimposed on the vertical wave number profile $\frac{\omega^2}{c_1(z)^2}$. In Figure (6) the (normalized) solutions of (1) at 42 Hz corresponding to the third and fourth elements of the point spectra are plotted superimposed on the vertical wave number profile. For this model 42 Hz is near a transition frequency. This is reflected in the fourth mode's extending high into the atmosphere.

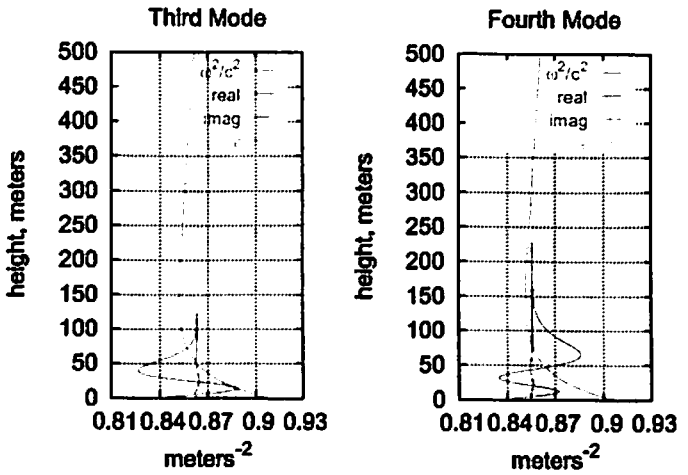

Figure 5: Some modes in the point spectrum at 50 Hz.

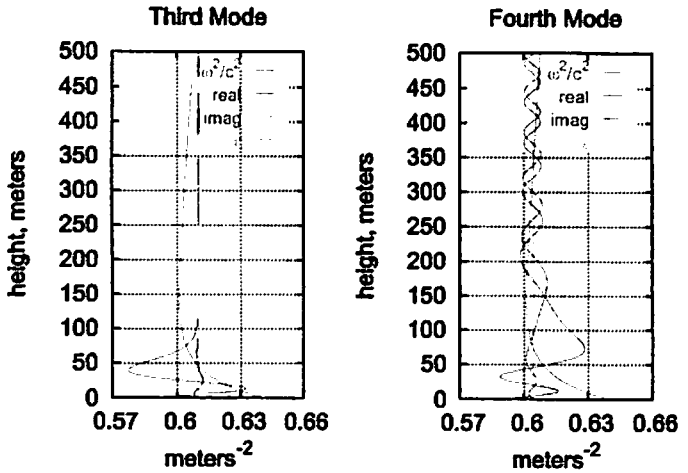

Figure 6: Some modes in the point spectrum at 42 Hz.

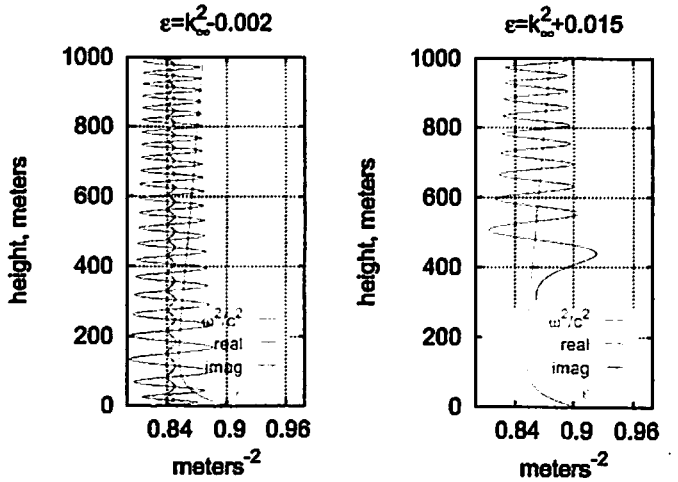

Figure 7: Some modes in the continuous spectrum at 50 Hz.

Finally, in Figure (7) some continuum modes at 50 Hz are plotted, again superimposed on the vertical wave number profile. Note that the part of the continuous spectrum greater than $\frac{\omega^2}{c_2(\infty)^2}$, the part that does not appear in the asymptotically constant approximation, contains a part of the sound field which remains in the upper atmosphere and never penetrates down to the ground. This reflects the fact that sound produced up high is refracted upwards away from the ground.

[1] D. Keith Wilson, John M. Noble and Mark A. Coleman, "Sound propagation in the nocturnal boundary layer", to appear in the Journal of the Atmospheric Sciences.

[2] Roger Waxler, "A vertical eigenfunction expansion for the propagation of sound in a downward-refracting atmosphere over a complex impedance plane," J. Acoust. Soc. Am. **112** (6), 2540-2552 (2002).

[3] Roger Waxler, "Modal expansions for sound propagation in the nocturnal boundary layer," submitted to J. Acoust. Soc. Am. June 2003.

[4] Finn B. Jensen, William A. Kuperman, Micheal B. Porter and Henrik Schmidt, *Computational Ocean Acoustics*, American Institute of Physics, N.Y. (1994).

[5] E. C. Titchmarsh, "Some theorems on perturbation theory," Proc. Roy. Soc. A **210**, 30-44 (1951).

Effect of Atmospheric Pressure Fluctuations on Low-Frequency and Infrasound Detection

Carrick L. Talmadge and Douglas Shields
The University of Mississippi, National Center for Physical Acoustics, Oxford MS 38677

ABSTRACT

A fundamental difficulty in low-frequency and infrasound detection is the so-called "wind noise" problem. At higher frequencies (> 50 Hz), this wind noise is usually associated with the obstruction formed by the pressure probe body. In this case, most of this wind noise can be adequately removed by the use of an appropriate windscreen. At lower frequencies (< 50 Hz), the magnitude of the intrinsic fluctuations appears to be much larger than the fluctuations induced by the sensor body. A new large-element (> 30 elements) pressure sensor array is used to quantify the relative magnitude of the intrinsic and induced pressure fluctuations. Signal processing algorithms are discussed which enhance the signal-to-noise ratio over that obtained using standard beam forming algorithms, by utilizing the localized nature of many of the fluctuations across the array. The effect of the height of the sensor above ground on the magnitude of the observed pressure fluctuations is also examined using a 3-axis linear pressure sensor array.

I. Introduction

The long-range detection of low- and infrasound from tactical (e.g., low-flying aircraft), strategic (e.g., nuclear weapon tests) and natural (e.g., bolide) sources represents an important frontier in atmospheric acoustics. These low frequencies are important because they propagate relatively larger distances with reduced atmospheric attenuation and are less scattered by topographic features.

The major challenge to directly measuring these low frequency sounds is the effect of temperature and wind fluctuations on the measurement. Wind fluctuations carry associated pressure fluctuations associated with these fluctuations. Airflow across a finite-sized microphone also induces pressure changes, which are indistinguishable from ordinary acoustic waves for single-sensor measurements

Fluctuations in wind also have associated temperature fluctuations, which produce a masking signal through the pyroelectric effect in solid-state sensors, by changes in the physical properties of the sensors, by thermal effects on the digitizing electronics (e..g., by a drift in the voltage reference of the DAQ system) and by bulk changes in the dimensions of the sensor (e.g., changes in the dimension of the back-volume). Because many infrasound signals are relatively small at the receiver location (~10 Pa), the influences of thermal effects become progressively more important as the frequency being probed decreases.

The scale of the turbulence can be related to its frequency using Taylor's "Frozen Turbulence" hypothesis, which states

$$k_1 = 2\pi/\lambda = 2\pi f/V \qquad (1)$$

where k_1 is the wavenumber associated with the turbulence, f is the frequency, and V is the mean wind speed. Note that Eq. (1) implies that the size of the turbules scales with the mean wind speed.

The power spectrum associated with turbulence is illustrated in the figure below (e.g., Panofsky and Dutton, 1984). Note that this spectrum is divided in three distinct regions: a source region where the turbulence is generated, an inertial sub-range, in which a cascade from large-scale to small-scale eddies occurs, and a dissipative sub-range, where the viscosity of the air damps out the turbulence. In the inertial sub-range, power-law relationships can be derived on dimensional grounds for wind, temperature and pressure (summarized in Lumley and Panofsky, 1964).

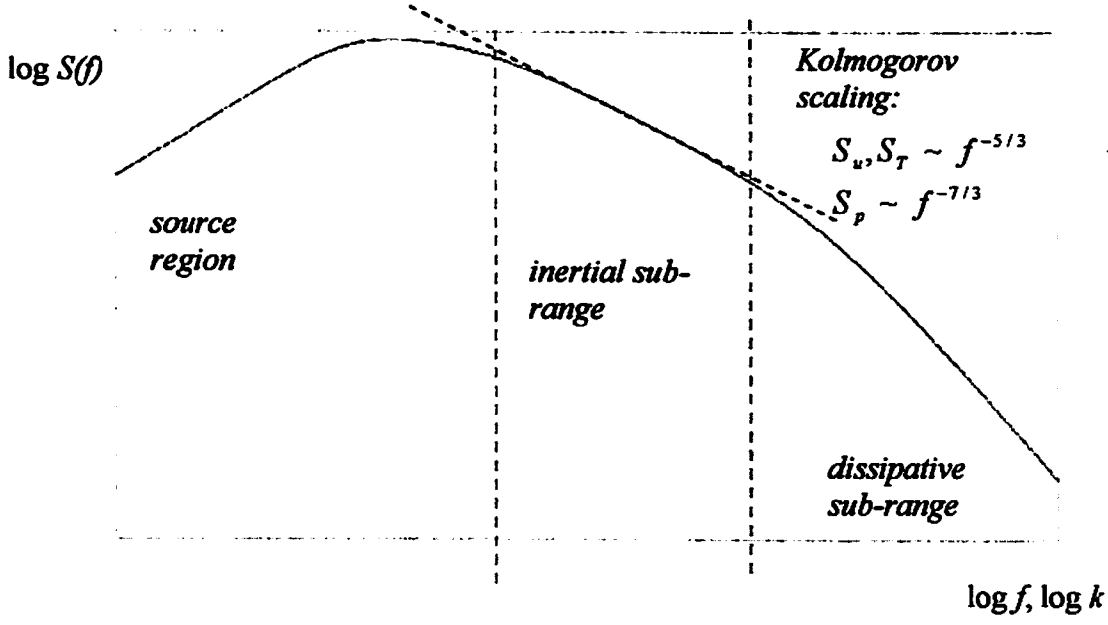

Figure 1: Illustration of the power-spectra associated with atmospheric turbulence. Note the existence of scaling laws for wind (S_u),, temperature (S_T) and pressure (S_p) in the inertial sub-range.

The scaling law associated with pressure fluctuations induced by air flowing across the sensor (often referred to as the pressure probe-body error) can be shown to correspond to a –5/3 exponent. *Note that this discussion implies that the dominant source of pressure*

fluctuations measured at the microphone can be inferred by measuring the power-law exponent in the inertial sub-range.

In this paper, we report on wind-noise large-element-array studies using a new innovative sensor based upon piezoceramic sensor technology. These sensors are low-cost, low-noise alternative to traditional sensors and make practicable a whole new range of outdoor and sound-propagation measurements. Existing sensor technologies that are low-cost enough to permit fielding large sensors arrays (e.g., electret microphones) generally suffer from a large variability in sensitivity at these low frequencies (both intrinsic and induced by thermal fluctuations), making them unsuitable for use in sensor arrays.

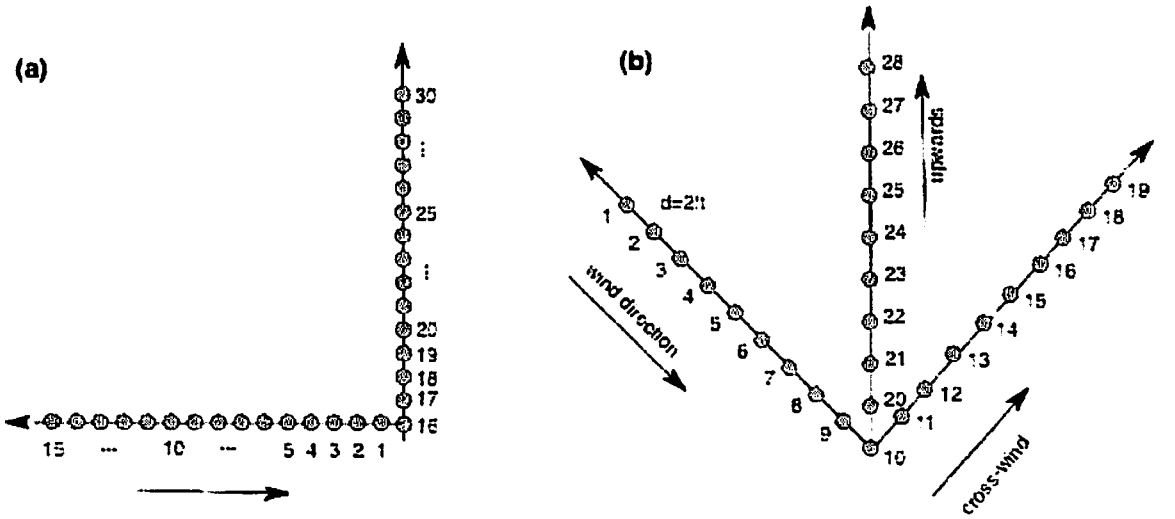

Figure 2: Configurations for (a) Yocona bottom experiment, and (b) for all other array measurements involving piezoceramics.

II. Methods

Pressure measurements were obtained using custom built 4-element pressure sensors. The sensors were configured in a dual-bimorph configuration to reduce the influence of temperature effects on the sensors. The resonance characteristics of these sensors have been previously studied by Warren (1993) and Dravida (2003). Dravida has also characterized their thermal sensitivity and linearity.

For one experiment (Oxford Airport), 6 B&K 4190 microphones were arranged in a linear array with a 3.414-m separation. The signals from these microphones were amplified then digitized onto a computer for later analysis. In all other experiments, the piezoceramic sensors were used, and were read directly by a National Instruments PCI-6031E multiplexing DAQ board. For one of these experiments ("Yocona River bottom", see Fig. 2a), the microphones were arranged in a 30-element L-shaped array (16 elements in each arm, see Fig. 2b) with a 1-ft spacing between elements. In the remainder of the array experiments, the sensors were arranged in a 28-element 3-axis array (10-elements along each arm). For most measurements, simultaneous wind-speed measurements were obtained using a Campbell Ultrasonic anemometer.

III. Results

A. Single Sensor Measurements

In Fig. 3, power spectra from individual microphones are compared against the horizontal wind-speed for the region identified with the inertial sub-range. These results are consistent with the dominant pressure fluctuations being associated with pressure fluctuations intrinsic to the atmosphere, as opposed to those induced by the presence of the finite-size of the sensor probe body. It should be noted that this result is expected to be true only for lower frequencies (larger-scaled eddies). We note that when the eddies become comparable or smaller than the characteristic dimension of the probe body, however, the probe-body error is expected to dominate.

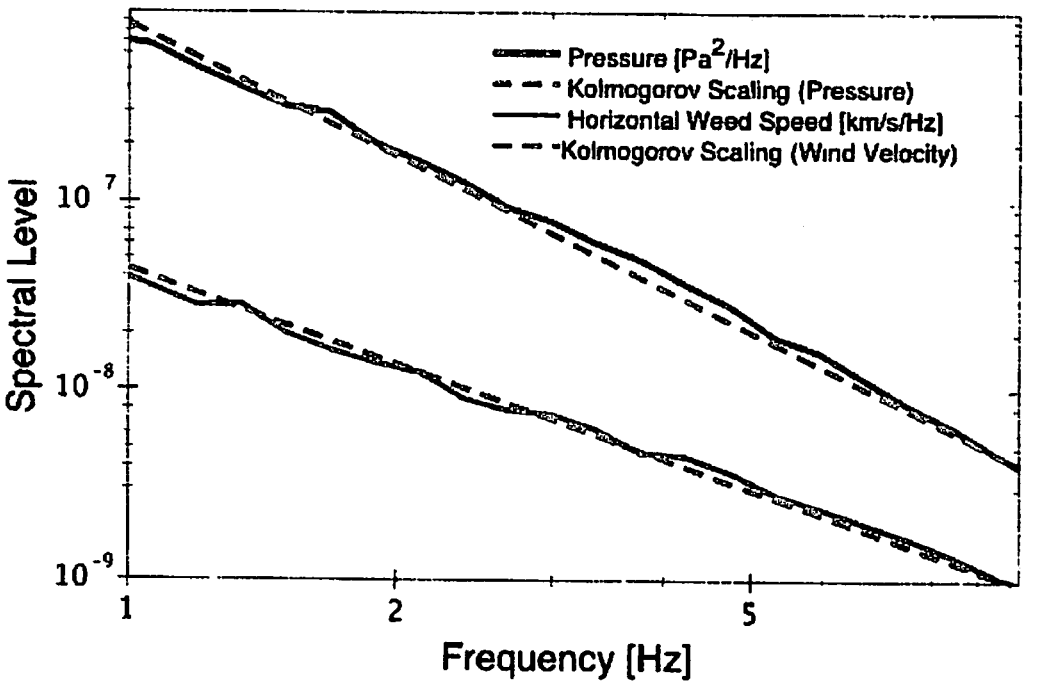

Figure 3: Comparison of pressure versus window-speed spectra. The dashed lines correspond to the predictions from the Kolmogorov theory.

B. Correlational Studies

The cross-correlations between sensors along and transverse to the direction of the wind are shown in Fig. 4 from the Yocona River bottom experiment. Note, as expected, the maximum correlation decreases with increasing separation. Also note that periodic structure, including regions with significant negative correction, is clearly observed at larger delays.

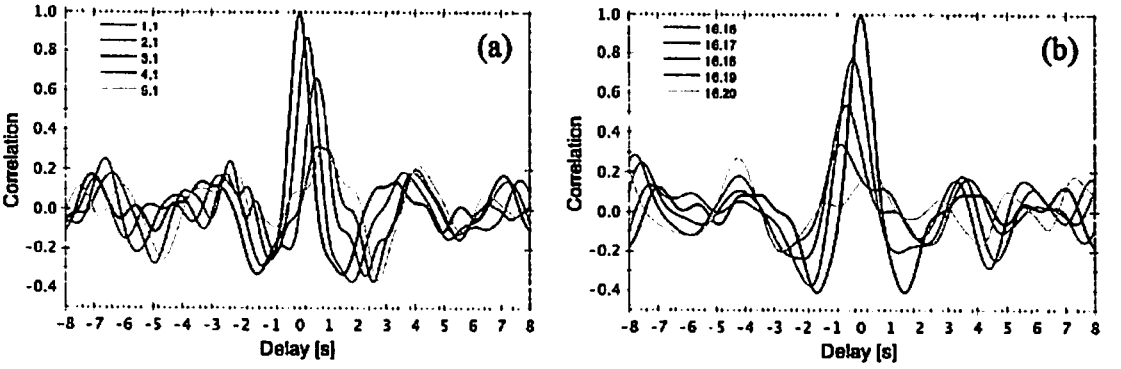

Figure 4: Cross-correlation between microphone elements as a function of delay for the Yocona River bottom experiment (see Fig. 2a) for (a) down-wind and (b) cross-wind directions.

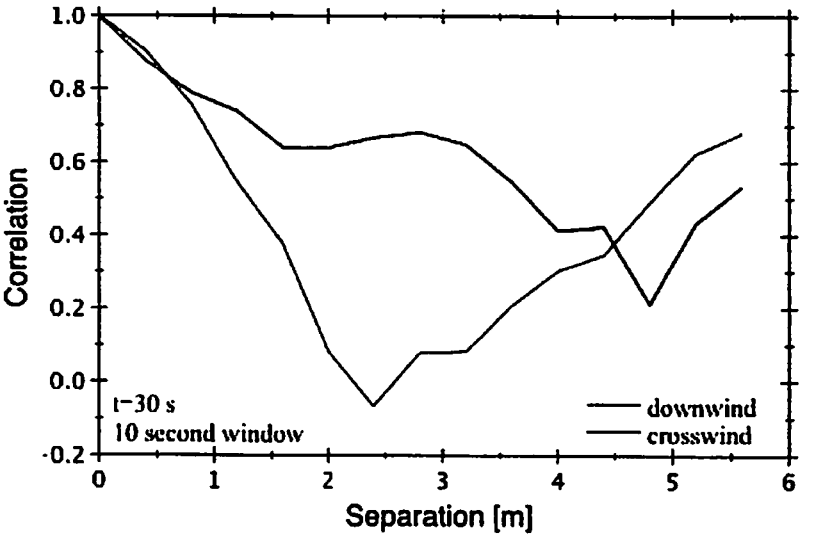

Figure 5: Cross-correlation (τ=0s) as a function of separation for the Yocona River bottom experiment.

An alternative way of interpreting this data are shown in Fig. 5, in which the cross-correlation is plotted as a function of separation of elements for zero lag (τ=0). As seen in Fig. 4, the decrease in the cross-correlation with distance for the downwind case can be partly understood as a consequence of shifting of the correlation peak away from τ=0 by the advection of the wind.

C. 2-Dimension Field Studies

The 2-dimensional pressure field can be reconstructed by generating an image map of the pressure as a function of time and position for the array elements on the arm perpendicular to the wind direction. Since the atmosphere is advecting across the array, then the time can be related to an equivalent spatial position $x' = V t$ where V is the mean wind speed. Hence such a 2-d image may be considered a reconstruction of the 2-d pressure field, as is illustrated in Fig. 6 below (top half of image, as indicated). For this image lighter colors correspond to positive incremental pressure and darker colors to negative ones. We note that this data indicates that the surface boundary layer contains a wave-like structure, which explains the correlations observed in Fig. 4.

Similarly, the arm parallel to the wind can be used to construct a similar image map (see Fig. 6, bottom half of image). The interpretation of this map is less straightforward, however, the same wavelike structure is seen in this data as well. Note that for the crosswind case, the dark streaks correspond to turbules striking the array broadside (i.e., each sensor is sampling a different portion of the wave). For the downwind arm, the dark streaks represent a single turbule traveling down the sensor arm and evolving over time. The larger "slant" of the structure is a result of the X = V T relationship for the turbules.

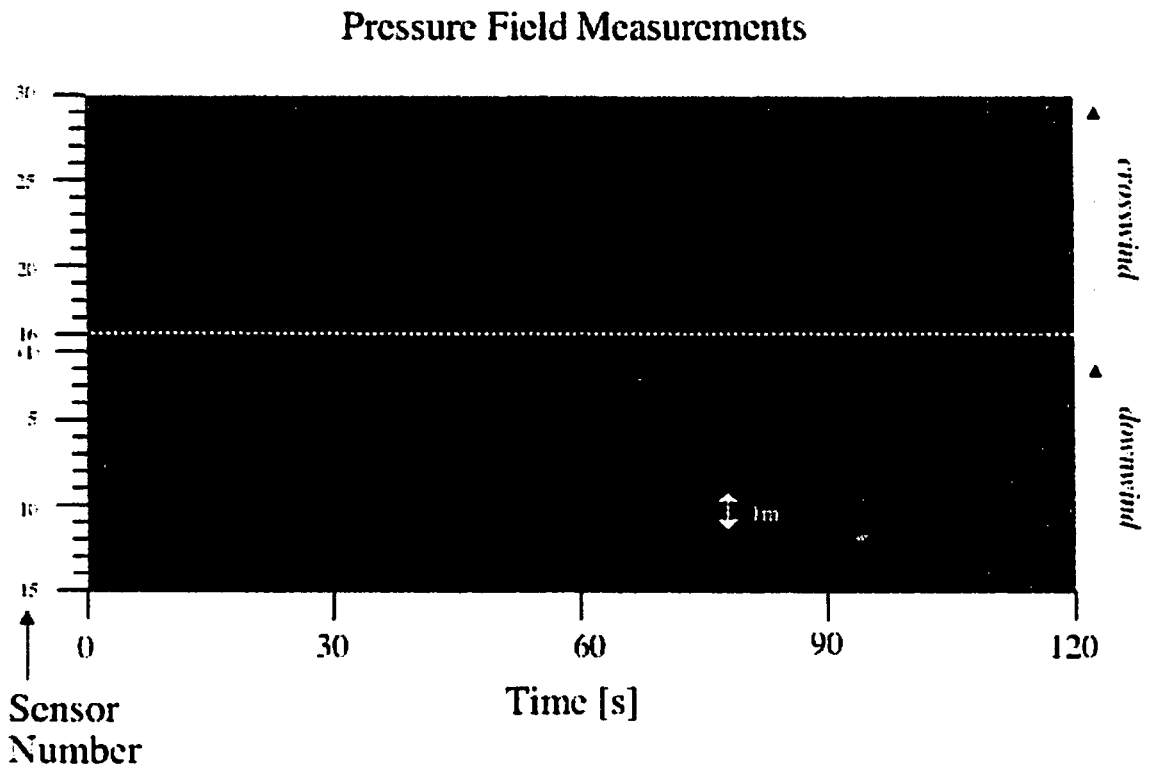

Figure 6: Reconstructed pressure field for Yocona River bottom experiment (black=negative pressure, gray = positive pressure).

D. Array Beam-Forming Studies

The array beam forming performance was evaluated by broadcasting a series of frequencies from 25 Hz to 60 Hz in 5 Hz steps. The volume of the sound was approximate 100 dB at 1-m from the source, which was placed 100-m broad side from the array. As shown in Fig. 7, the principal advantages of an array of microphones are *i*) the reduction of off-angle sound (note that when the beam is pointed 90° off the direction of the source), *ii*) reduction in the noise floor of the power spectrum by 1/N, and *iii*) reduction in broad-band noise which is off-angle from the signal of interest. In this experiment, the wind-generated sound was produced by rustling of leaves in a line of trees approximately 150 m from the array.

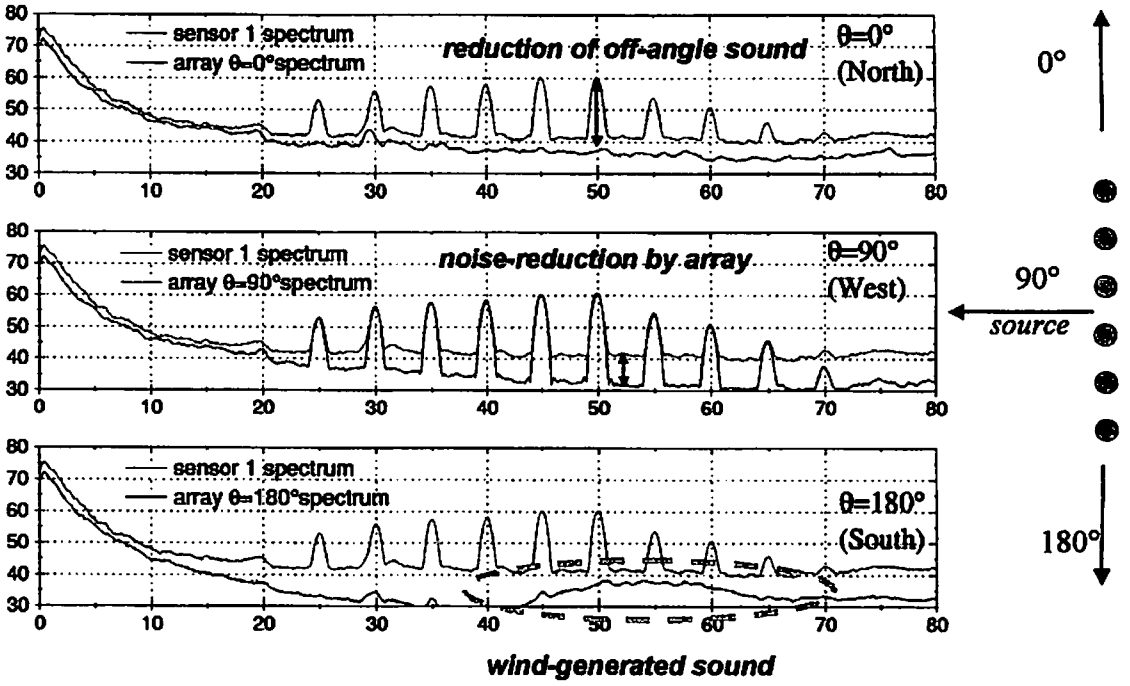

Figure 7: Array beam-forming performance at Oxford Airport for 6-element B&K 4190 microphones (circles). Shown are the spectra (level in dB versus frequency in Hz) for beam-forming in the direction of the source, and in the +/- 90° directions from the source. The wind was from the 135° direction in this experiment.

E. Suppression of Coherent Wind-Noise

Because the wind noise is often partially coherent at low and infrasound frequencies, the beam forming performance of an array can often exceed the signal-to-noise gain expected from random incoherent noise. An example of this is shown in Fig. 8 for the 10-element arm of the 3-axis array pointed into the wind.

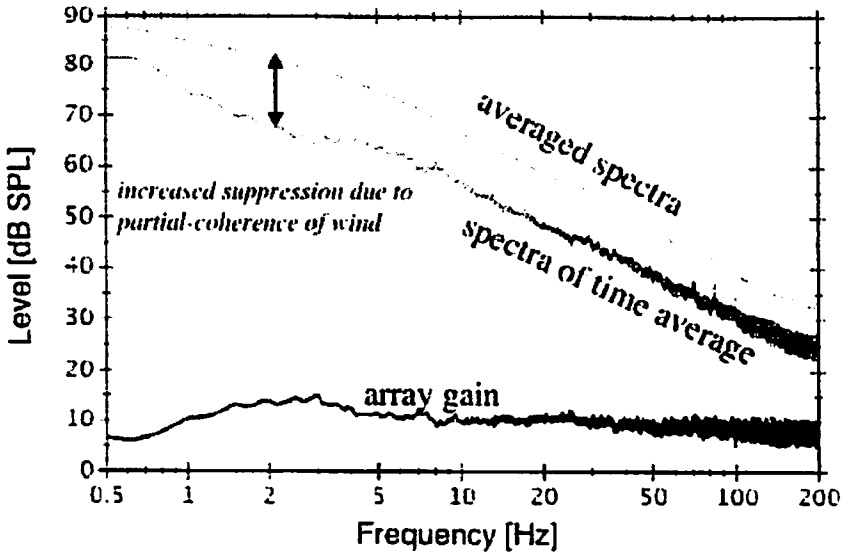

Figure 8: Effect of beam-former on partially-coherent wind noise.

IV. Conclusions

- For light- to moderate-wind *low-frequency* atmospheric measurements, static ("intrinsic") pressure variations are dominant. (Kolmogorov statistics can be used as a diagnostic.)
- Incoherent noise sources were found to be suppressed by 1/N. Coherenent sound sources *in bandwidth of array beamformer* can be further suppressed (40+ dB are possible).
- Coherent noise (correlated turbulent noise, wind-generated sound) can also be suppressed by more than 1/N.
- Low frequency coherent ("in phase") sound is a problem for any array.
- For "deep" ($f < 0.1$ Hz) infrasound arrays, there are many unknowns as to what the dominant sound and noise sources are.
- Similar large-scale array measurements to 0.003 Hz (possibly larger spacing) could prove important in the design of pipe arrays.

Acknowledgements

We would like to thank Kenneth E. Gilbert, Roger Waxler and John Wyngaard for helpful discussions. This work was supported by supported by contract DASG60-00-C-0061 with the United States Army.

References

Shantharam Dravida (2003), *Experimental Characterization of Modified and Thin Film Piezoceramic Sensors, MS. Thesis, 142 pages.*

J. L. Lumley and H. A Panofsky (1964). *The Structure of Atmospheric Turbulence*, Interscience (New York), 239 pages.

H. A. Panofsky and J. A. Dutton (1984). *Atmospheric Turbulence: Models and Methods for Engineering Applications*, John Wiley & Sons, 397 pages.

Daniel M. Warren (1993), *The Flexure of Asymmetrically Stacked Piezoelectric Laminate Disks*, Ph.D. Thesis, The University of Mississippi, 92 pages.

USING AMPLITUDE FLUCTUATIONS TO IMPROVE LONG-RANGE SIGNAL DETECTION

Ronald A. Wagstaff

National Center for Physical Acoustics, University of Mississippi
University, MS 38677
United States of America

ABSTRACT

A new signal processor is introduced, and a method is described that establishes a symbiotic relationship between it and a host processor to produce additional gains. This relationship enhances the performance of each processor and provides new capabilities that were not previously possessed. The new processor uses the power amplitude of the spectrum analyzed time history signal and noise data from the host and calculates normalized differential amplitudes. It utilizes the differential amplitudes to provide an additional independent source of processing gain. The differential amplitudes are sensitive to the amplitude fluctuations and the order in which they occur. As a result of this symbiotic relationship, the signal-to-noise ratio of the host is improved more than 10 dB. The minimum detectable level is improved more than 3 dB, and the resolution is improved more than 2X. This symbiotic relationship also provides a signal auto-detection capability. Results are presented for beamformer, single sensor, and microbarometer host processors.

INTRODUCTION

This paper presents a method for exploiting amplitude fluctuations to improve the performance of some signal processors. A brief background discussion of fluctuations with, emphasis on acoustic fluctuations, is included below. The background is followed by the equations for the new processor and the method of enhancing the host processor. The results are presented next, followed by observations and conclusions.

BACKGROUND

Fluctuations of signals and noise seem to be a universal phenomenon in nearly all propagation media. For example, Urick[1] gives a brief discussion of fluctuations of sound in the ocean and suggests that they may be the reason for longer signal detection ranges than expected. Simanin[2] includes amplitude fluctuations, when he states that the amplitude distribution of the signal can provide a clue to the depth of a source in the ocean. Sound propagating in air from a source to a

receiver will fluctuate as a result of large and small scale eddies due to winds and turbulence caused by diurnal heating and cooling of the ground[3]. The twinkling of a star is the fluctuation of light as it propagates through the atmosphere. This form of fluctuations is often referred to as scintillations. Similar examples could be given for many other propagation media such as magnetic, electromagnetic, electric field, infrared, and laser optic.

Fluctuations are such an important factor in confounding signal measurements that a single realization of a measured signal magnitude has a very small confidence level. The confidence level is usually increased to an acceptable level by averaging multiple realizations of power values (exponent of 2). The resulting average is biased toward the higher values and is relatively insensitive to the lower values. By this means, the power average reduces the influence of fluctuations. This is considered to be one of the average power processors' most beneficial characteristics. Yet in some important cases, the power average still falls short of satisfying the processing objectives.

METHOD

The average power processor (AVGPR) is one of the two host processors that will be used herein to illustrate the improvements resulting from the symbiotic relationship between processors, and it is also used as the benchmark standard for evaluating performance improvements. It is defined as:

$$\text{AVGPR}_f = \langle X_{f,n} \rangle \tag{1}$$

where $X_{f,n}$ = spectral power in frequency bin f for sample number n and,
$\langle\rangle$ means the average over a predetermined number of power samples.

The Wagstaff's Integration Silencing Processor IV (WISPR IV) is the self-normalized differential power:

$$\text{WISPR IV}_f = \left\langle \frac{X_{f,n} - X_{f,n-1}}{X_{f,n} + X_{f,n-1}} \right\rangle^2 \tag{2}$$

Unlike Eq. (1), which is order independent, Eq. (2) is order dependent. This is an important property that will be discussed later.

WISPR IV does not produce a spectrum similar to Eq. (1). Its role is to enhance the output of a processor that produces a spectrum. The result is designated a type "V" spectrum. In other words, an AVGPR spectrum modified by the WISPR IV processor is designated an AVGPR V spectrum. It does this modification in the following manner:

$$\text{AVGPR V} = \frac{AVGPR_f}{WISPRIV_f} = \frac{\langle X_{f,n} \rangle}{\left\langle \frac{X_{f,n} - X_{f,n-1}}{X_{f,n} + X_{f,n-1}} \right\rangle^2} \tag{3}$$

WISPR IV is also an auto-detector. When

$$\text{WISPR IV}_f \leq \varepsilon , \tag{4}$$

(ε is a data dependent small value) detection of a signal with small amplitude fluctuations is declared.

The most basic form of order independent fluctuation-based processors is the Wagstaff's Integration Silencing Processor (WISPR)[4]. It is the reciprocal of the average of reciprocals:

$$\text{WISPR}_f = \left\langle X_{f,n}^{-1} \right\rangle^{-1} \tag{5}$$

WISPR is also known as the Harmonic Mean. It produces a spectrum similar to the average power processor. It will be used with WIV in a similar manner to Eq. (3) to produce WISPR V, a variation of the order independent WISPR that is enhanced by the order dependence of WIV.

RESULTS AND DISCUSSION

Figure 1 illustrates the nature of the WISPR VI symbiotic relationship to another processor (WISPR in this case, Eq. (5)), the method of its implementation, and the gains that can be achieved as a result. Figure 1a is a plot of three narrow band frequency spectra. The top curve is the AVGPR spectrum. The arrows near the maximum level identify frequency bins of two signals. There is only one maximum in the AVGPR spectrum, because the signals are too close for the AVGPR processor to resolve them into separate local maxima. These results might lead one to the incorrect conclusion that there is only one signal present. The middle curve is the corresponding WISPR V spectrum, truncated at 20 dB. WISPR V is obtained by modifying the WISPR spectrum by WISPR IV in the same manner that is done in Eq. (3) to produce an AVGPR V spectrum from an AVGPR spectrum. WISPR V successfully separated the two signals, while attenuating the power in nearly all other bins to levels below the threshold of the plot (20 dB). Hence, the SNR and the resolution have been increased compared to the AVGPR processor. The bottom curve is the WISPR IV spectrum. It has been truncated at 19 dB to avoid interference with the WISPR V curve. This WISPR IV curve has two local minima that are below the predetermined detection threshold of 10 dB. Local minima that are below the detection threshold automatically identify frequency bins that have power amplitude fluctuations that are smaller than would be expected for noise, in this case bins 314 and 316. The implication is that signals are present in those bins. Identification of signal present/not present is made by WISPR IV independent of other processors. In other words, only WISPR IV is needed for signal detection, and it does it automatically according to the magnitude of the normalized differential amplitudes. The presence of two separate signals was verified by doubling the FFT size. This

reduced the width of the frequency bin sufficiently to clearly identify two separate local maxima. In this case, the WISPR IV processor is providing 2X enhancement in frequency resolution without the need to use a larger FFT size.

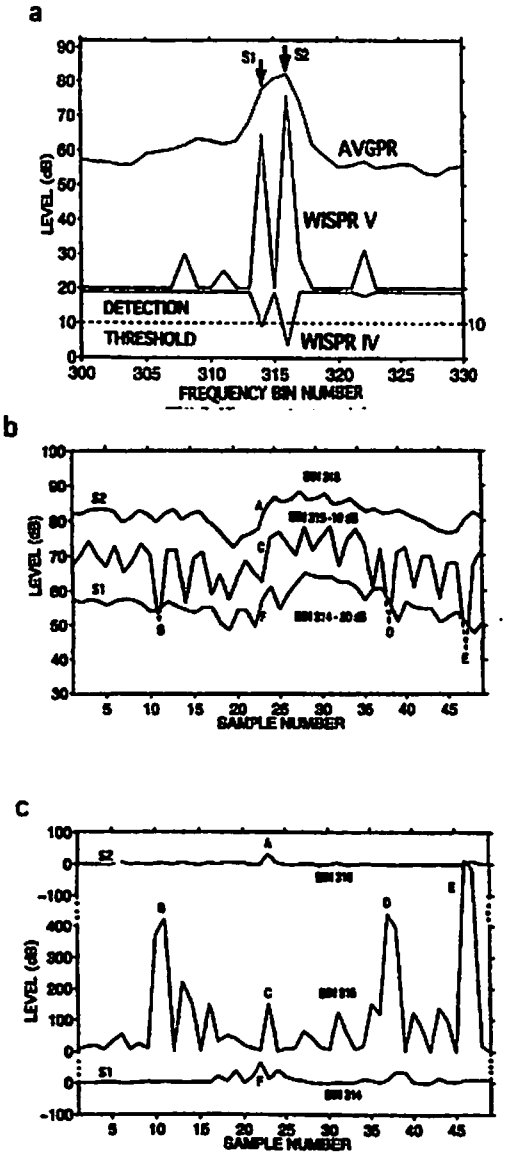

Fig. 1. a) AVGPR, WISPR V, and WISPR IV spectra, b) sequential power samples for frequency bins 314, 315, and 316, and c) normalized successive differential amplitudes.

Used together, Figs. 1b and 1c illustrate the manner in which WISPR IV is generated. The point-by-point successive power differences squared along each curve in Fig. 1b, are the time history values plotted in the corresponding curves of Fig. 1c. The average of the values along each of these curves in Fig. 1c is the corresponding WISPR IV value. The top and bottom curves for the

signal bins 316 and 314 in Fig. 1b have significantly smaller successive power differences than the middle curve for bin 315, which has the effects of the two interfering signals in adjacent frequency bins. Relatively small successive differences in the two signal bins and larger successive differences in the bin between them yield WISPR IV values of approximately 4, 101, and 9 dB for frequency bins 316, 315, and 314, respectively. When a host spectrum is divided by consecutive values, such as these, the power of the center bin will be severely attenuated relative to the power in the two surrounding bins. In many cases, this selective attenuation will be sufficient to create local maxima, indicating the presence of separate signals.

The plot in Fig. 2 illustrates a similar symbiotic relationship of the WISPR IV processor in the spatial domain, e.g., the beam space of a towed horizontal line array in the ocean. The results are presented as beam power level versus beam number at the frequency of a known signal of interest. There are four beam spatial spectra in this plot. The top curve is due to the AVGPR processor. The next two in order are the symbiotic results due to the AVGPR V and WISPR V processors, respectively. The bottom curve is the corresponding WISPR IV results, divided by 10 for display purposes. The location of a signal (S) is indicated by an arrow.

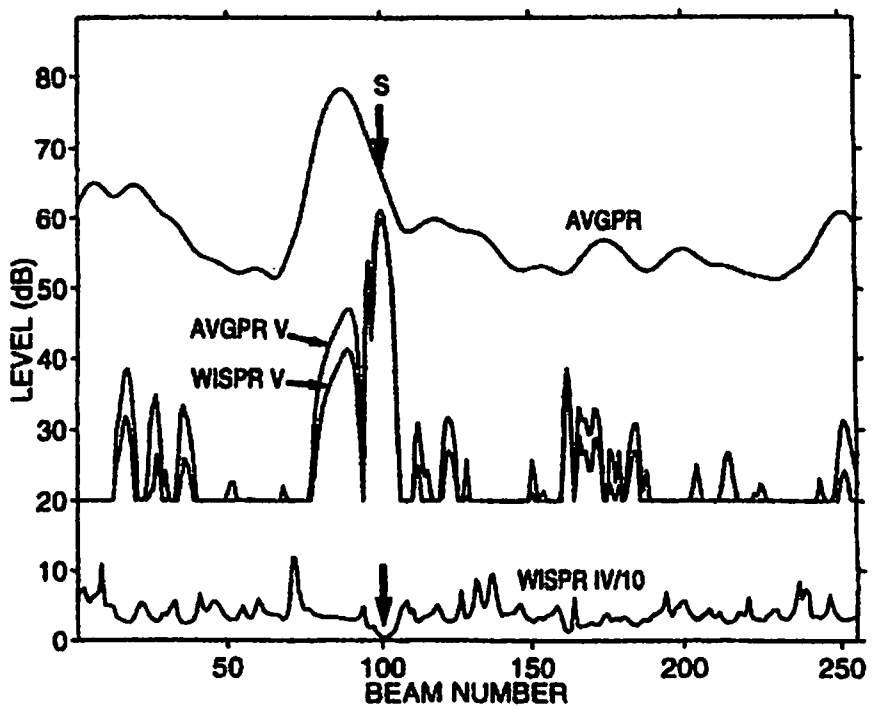

Fig. 2. Beamformer undersea ambient noise spatial spectra for AVGPR, AVGPR V, WISPR V, and WISPR IV (divided by 10).

There does not exist a local maximum in the AVGPR results to indicate the presence of a signal at the location of the arrow. There are maxima at other locations, but they are caused by noise from near and distant shipping traffic. However, in the case of the WISPR IV results at the bottom of the plot, there is a clear indication of a signal present near beam number 100. At that

location the WISPR IV curve (divided by 10) approaches 0 dB to identify the location of the signal in beam space. This signal is below the MDL of the AVGPR processor, but not below the MDL of the WISPR IV processor.

The AVGPR V and WISPR V results can be compared with the corresponding curve for the AVGPR results. The effective widths of their beam responses, measured 3 dB down from signal or noise peaks, are about one third as wide as the corresponding ones in the AVGPR results. This is indicative of previous results which suggest approximately 3X enhancement in resolution. This is due to dividing the outputs of the host processor (AVGPR and WISPR processors in this case) by the corresponding higher resolution WISPR IV processor outputs. The bins, or beams, dominated by small fluctuations (signal) will be preserved while those dominated by large fluctuations (noise) will be severely attenuated. This results is an increase in resolution.

There are many local maxima in the AVGPR and AVGPR V curves in Fig. 2. It is not possible to identify the signal among them based on magnitude, "SNR", or how narrow the peak is. The AVGPR results don't even have a local maximum at the signal location. With the exception that the AVGPR V and WISPR V results have their maximum levels at the signal location, there is no other feature in their results that would suggest a signal is present. Noise can also have a large magnitude. However, noise by its very nature can not have small fluctuations, as signal most often does. That is why WISPR IV correctly identifies the signal to be near beam 100 by crossing the detection threshold and noise everywhere else the threshold is not crossed.

The results in Fig. 2 are for one beam from a beamformer that is steered in the direction of a signal. There were two other sound projectors operating simultaneously at different ranges from the array, along different bearing angles, and at different frequencies. The purpose of the measurement exercise was to obtain data to evaluate the performance of signal processors that exploit the differences in the fluctuations of signals and noise to achieve additional gains. When complete sets of processed results are viewed for all beams and all frequencies simultaneously, a better perspective is achieved of the effectiveness of the WISPR IV and a host processor to provide additional gains. This includes enhancements in SNR, MDL, and resolution, and an automatic signal detection capability. These gains are illustrated in Fig. 3.

Figures 3a, 3b, and 3c display the AVGPR WISPR V, and WISPR IV power levels, respectively, on grids of frequency bin number versus beam number. The levels that are plotted in Fig. 2 for the AVGPR, WISPR V and WISPR IV processors constitute slices across the respective plots that are parallel to the beam number axes at frequency bin number 150. The signal in Fig. 2 has coordinates of frequency bin 150 and beam number 100 in the plots of Fig. 3.

The need to have other exploitable parameters for signal detection, in addition to magnitude, is illustrated by the AVGPR results in Fig. 3a. The acoustic space measured by the array was the complex arrangement of "hills" and "valleys" that is usually observed in processed results. There seems to be no end of local maxima and minima in such outputs. Detecting signals of unknown location (i.e., beam number and frequency not known in advance) and the time periods of signal presence in such "rugged acoustic terrain" is not easy. Detection is made even more difficult by the time evolving nature of the signal and noise fields, which this static plot fails to

reveal. The processing integration time was less than two minutes, and three sound sources were known to be projecting signals. However, the signal frequencies and the geographic locations of the three sources were not known in advance of the measurement. For all practical purposes they contributed unknown signals to the data, i.e., frequency bin and beam number locations.

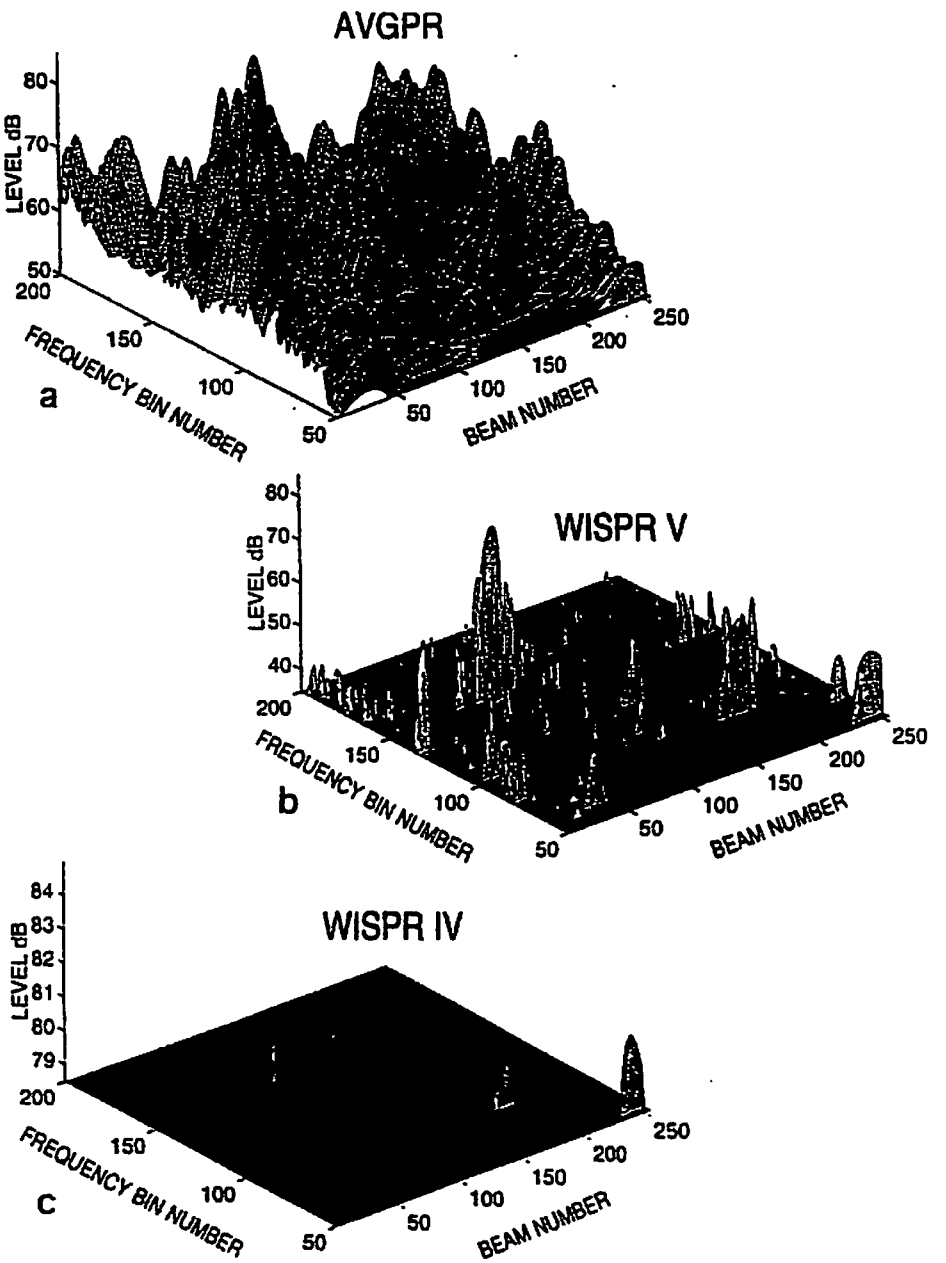

Fig. 3. AVGPR, WISPR V, and WISPR IV frequency bin number versus beam number surfaces illustrating a) AVGPR noise field variability, b) WISPR V noise suppression, and c) WISPR IV unalerted automatic detection of three signals.

The WISPR V results in Fig. 3b are displayed for all values that exceed an arbitrary threshold. The suppression of ambient noise and shipping clutter by the WISPR V processor has preferentially reduced most of the "hills" to the point that a small fraction of them protrude above the threshold of the plot. Less than a dozen could be considered major peaks. It would still be difficult to identify the three signals.

Figure 3c is the WISPR IV detection surface. In a similar manner that cuts across Fig. 3a and 3b give the same values plotted in Fig. 2 for AVGPR and WISPR V, respectively, the WISPR IV values are the same, with one exception. The values are inverted to appear above the detection surface instead of below. There are only three peaks (detections), in this surface, one for each signal that was projected. Only the amplitude time histories of the three signals projected had average normalized differential amplitudes sufficiently small to appear above the detection surface. Of the nearly 40,000 frequency bin-beam number cells, the three signals were detected automatically by the WISPR IV processor, and it did it from a consideration of the normalized differential amplitude. Once the differential amplitude is normalized, there is no longer a reference to, or a dependence upon, amplitude. This is not the case with the "V" type processors, such as AVGPR V, which retain the amplitude dependence of the host processor.

The spectra in Fig. 4 illustrate the robustness of the WISPR IV and the type "V" processors to transient high-level noise contamination. These results were obtained from data measured by a microphone located at an airport, about 50 m from the landing strip. There was a sound source at a distance of 200 m from the microphone projecting tonals from 25 to 50 Hz at 5 Hz spacing. During the measurements, small private aircraft were taking off and landing. The time span of the data for Fig. 4 includes a plane landing and passing by the microphone. This increased the background noise level by about 40 dB. Previous uncontaminated AVGPR results showed the projected group of tonals plus additional non-projected tonals at 55, 60, and 65 Hz. A second group of signals with 5 Hz spacing, and sufficient SNR to be unmistakable, were also present in the spectra. The three non-projeted signals in the first group and all of the signals is in the second group are due to sums of the projected tonals, i.e., sum-signals. For example, the 55 Hz signal is the sum of the 25 and 30 Hz tonals. The resulting sum-signals for various combinations of frequencies are at the sum frequencies, and they also have 5 Hz spacing. When they occur, they are easily recognized, because of the 5 Hz spacing.

The top spectrum in Fig. 4 is for the AVGPR processor. Only the presence of the signals projected at 30, 40, and 45 Hz and the sum-signal at 55 Hz (25 Hz + 30 Hz) are readily detected. On the other hand, the middle spectrum for AVGPR V shows an extended group of contiguous signals with 5 Hz spacing from 25 Hz to 75 Hz, and a second group composed of contiguous sum-signals from 95 Hz to 125 Hz. Unlike the results for the AVGPR processor, the AVGPR V processor provided enough SNR and MDL enhancements for all of the projected signals (25-50 Hz) and two groups of sum-signals, 55-75 Hz and 95-125 Hz, to be easily identified and detected in the presence of high level transient noise contamination. Only when the data were free of the contamination was the AVGPR processor able to detect most of the signals in both groups.

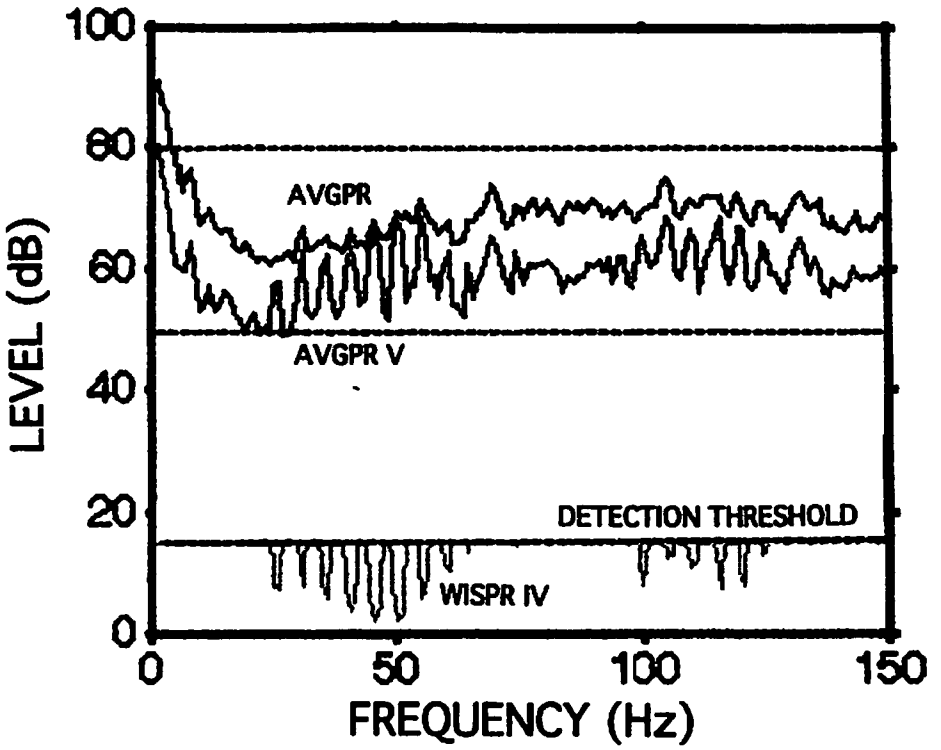

Fig. 4. AVGPR, AVGPR V, and WISPR IV microphone spectra for a time contaminated by high level transient noise due to an air plane landing nearby.

It is fortunate when the SNRs of signals are large and there is additional signal or source information available for aiding signal detection and identification purposes, as seen in the WISPR V results. However, there are other local maxima in the spectrum due to noise that have SNRs about the same as the real signals that were declared detected. These noise maxima were not declared detected, because they did not fit into a pattern with 5 Hz spacing. In fact, the WISPR V processor only provided the real signals with sufficient SNR to attract attention. High confidence detections could not be made on just SNR alone. Additional information had to be used, such as the projected frequencies of the signals and their spacings. It is common to not have enough information about the signal such as knowledge of signal presence, signal frequency and intelligence to reduce the bearing sector to search with an array, etc. In such cases, the unalerted auto-detection capability of the WISPR IV processor could be helpful.

The bottom spectrum in Fig. 4 is due to the WISPR IV processor. There are two groups of signals that extend below the detection threshold to be automatically detected by WISPR IV. There are nine signal detections from 25 Hz to 65 Hz in the first group of signals and six signal detections from 100 Hz to 125 Hz in the second group. The signals in each group have 5 Hz spacings, which confirms the automatic detection. There are local maxima in the WISPR V spectrum, related to the signal groups, that the WISPR IV processor did not detect. Some of

them could have been detected with a higher WISPR IV detection threshold, but it would have been at an increased probability of noise "detection".

By using knowledge of the special frequency relationship between the signals, more signals would be detected in the WISPR V results than in either the AVGPR or the WISPR IV results. However, without signal intelligence, WISPR IV detected the same signals that WISPR V detected using highly specific signal intelligence. The results in Fig. 3c are a more realistic example of the simplicity and the effectiveness of the WISPR IV unalerted automatic detection capability.

Figure 5. illustrates spectral results that are similar to the those in Fig. 4. However, in this case, the sensor is a microbarometer; the propagation medium is the atmosphere, and the measured phenomenon is atmospheric pressure. These data were provided by Dr. Michael A. H. Hedlin[5]. The sample rate of the data provided was 20 Hz. The FFT length used in processing the data was 1024 points, and the number for averaging was five. The resulting spectra are plotted on a log-frequency scale to stretch out the frequencies range of interest, below 1 Hz.

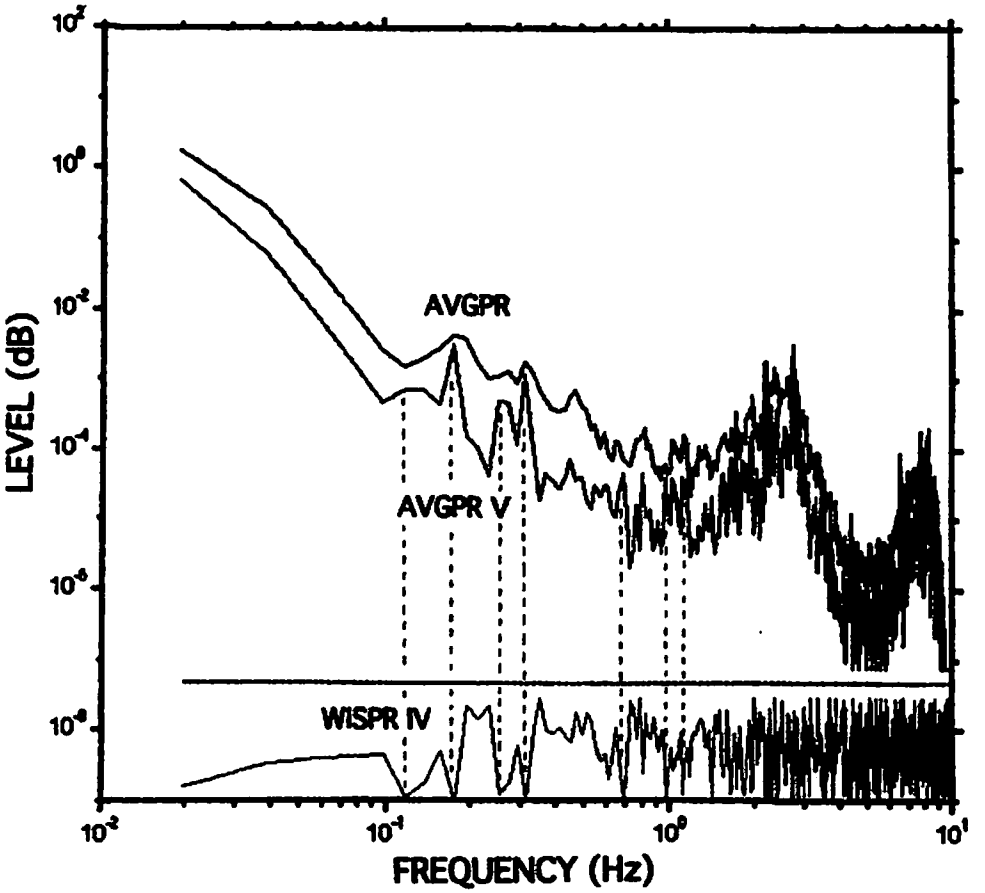

Fig. 5. AVGPR, AVGPR V, and WISPR IV microbarometer spectra showing enhancement and detection of 0.16 Hz signal due to standing ocean waves.

There are many local maxima in the AVGPR and WISPR V spectra that indicate the presence of signals. Unfortunately, their origins are unknown. The part of the spectrum that is of present interest is a small frequency range around 0.2 Hz. This is the frequency range where the pressure changes due to standing ocean waves interacting with the atmosphere can be measured by a microbarometer. These pressure changes are called microbaroms, and they are observed world-wide[6].

There is a local maximum in the AVGPR results in Fig. 5 at approximately 0.16 Hz. Its SNR is only a few decibels. The surrounding spectrum does not have the appearance that would suggest that a signal is present. This is not the case in either the WISPR V or the WISPR IV spectra. The WISPR V spectrum has a local maximum that is well defined at 0.16 Hz with a SNR of 8 dB. It has the appearance that suggests the presence of a signal at 0.16 Hz. Furthermore, it would be declared detected in the WISPR IV results for any reasonable detection threshold which one might choose. It can not be claimed that these microbarometer results can be considered typical of what should be expected for other microbarometer data. Only one data set was processed as an exploratory effort to see if additional gains could be achieved by exploiting the amplitude fluctuations in atmospheric pressure. The indications are that significant gains in SNR and MDL can be achieved, and some signals can be auto-detected.

CONCLUSIONS

The WISPR IV processor calculates the self-normalized differential amplitude from the spectral time histories in each frequency bin. The resulting spectral values are used to either automatically detect signals that have smaller amplitude fluctuations than noise or to enhance the SNR, MDL, and resolution of another processor such as the AVGPR. Resolution enhancement of 2X in the spectral domain was demonstrated. The cause was the presence of large amplitude fluctuations in a bin between the two signals that WISPR IV attenuated more than the smaller fluctuations in the signal bins. The capability for 3X resolution enhancement in the spatial domain was also indicated, based on decreased beam responses and agreement with previous results. The SNR of some signals below the MDL of the AVGPR processor have been increased sufficiently by WISPR IV processing to be easily identified, providing signal excesses greater than 10 dB. Furthermore, some of these signals were automatically detected, even when they were not visible in the AVGPR results. These processing gains due to the WISPR IV processor and related symbiotic processors were consistently achieved, whether the measurement apparatus was a microbarometer, a single microphone, or an array of hydrophones and when the propagation medium was the atmosphere or the ocean.

ACKNOWLEDGMENTS

The U.S. Army Space and Missile Defense Command (SMDC) funded this work. For that support, the author is grateful. The author also wishes to express his appreciation for the support provided by NCPA and Miltec researchers in conducting measurements and collecting some of

the data used to provide the results reported herein. Appreciation is also expressed to Dr. Michael A. H. Hedlin of the Scripps Institute of Geophysics and Planetary Physics, Scripps Institute of Oceanography, for providing the microbarometer data in a convenient format for us to use and for including reference spectra that allowed verification of the results.

REFERENCES

1. R. J. Urick, "Models of the Amplitude Fluctuations of Narrow-Band Signals in the Sea," J. Acoust. Soc. Am., **62**, pp. 878-887, 1977.
2. A. A. Simanin, "Possibility of classifying water and surface rays by amplitude fluctuations of the received signal," Sov. Phys. Acoust. **36**, 622-624 (1990).
3. Hubbard, H. H., editor, "Aeroacoustics of Flight Vehicles: Theory and Practice, vol. 2: Noise Control,"NASA Reference Publication 1258, vol. 2, WRDC technical report 90-3052, 1991, Ch. 12, Atmospheric Propagation, p. 81, Aug. 1991.
4. R. A. Wagstaff, "The Wagstaff's integration silencing processor filter: A method for exploiting fluctuations to achieve improved sonar signal processor performance," J. Acoust. Soc. Am., **104**, pp. 2915-2924, 1998.
5. Personal communication and source of microbarometer data, Dr. Michael A. H. Hedlin, Scripps Institute of Geophysics and Planetary Physics, Scripps Institute of Oceanography, University of California, San Diego.
6. J. V. Olson and C. A. L. Szuberla, "The Distribution of Wave Packet Sizes in Microbarom Wave Trains Observed in Alaska," draft submitted to: J. Atmospheric and Solar-Terrestrial Phys., Jun. 2001.

NGI

10th Long Range Sound Propagation Seminar, Grenoble 12–13, 2002

Air-ground Interaction in Long Range Propagation of Low Frequency Sound and Vibration – Field Tests and Model Verification

Christian Madshus[1)], Finn Løvholt[1)], Amir Kaynia[1)] and Lars Robert Hole[2)]

[1)] Norwegian Geotechnical Institute, Oslo, Norway
[2)] Norwegian Institute for Air Research, Oslo, Norway

ABSTRACT

An extensive program of intermediate and long range impulsive sound propagation field tests have been conducted. The test program and the performed measurements are presented. Particular focus is given on the air-ground interaction and its effect on low frequency sound and vibration propagation. It is found that the pressure wave interaction with the viscoelastic Rayleigh wave in the ground may have a significant effect on the ground impedance and the sound and vibration propagation. This introduces an important mechanism not covered in commonly used ground impedance models. Numerical simulation models have been developed and verified against the test data.

1. INTRODUCTION

Activities like blasts and heavy weapons shooting create low frequency impulsive sound waves which propagate over long distances, therefore creating a major environmental problem for military training fields. Such impulsive sound sources tend to disturb neighbours more through the vibration and rattling induced in buildings, than by the direct audible sound itself (/1/ and /2/). Human perception of whole body vibration includes frequencies down to 1 Hz /3/ and the fundamental natural frequencies of buildings are in the range 1-10 Hz. Planning tools to predict and control such activities must therefore be able to handle sound propagation down to these low frequencies. Meteorology, topography and ground conditions affect the propagation differently than at higher frequencies, and common propagation models fail at low frequencies. As a step towards the development of improved prediction models for low frequency sound and vibration, an extensive full scale field test program was performed in Norway. This paper focuses on the interaction between air pressure and ground response at low frequencies, with respect to how the ground effects the sound propagation and how the sound generates vibration in the ground. Firstly, the field tests are presented in general, and secondly results specific to the air-ground interaction are discussed in more detail. The major physical mechanisms which control the interaction are outlined and implemented in a numerical model which is verified against the experimental data. An accompanying paper /5/ elaborates on the modelling of ground influences on sound

propagation. The application of low frequency sound and vibration propagation models is not limited to the environmental issue of military training; they may be applied operationally for the detection, localisation and identification of intruders, or for other types of low frequency sound sources, such as sonic booms.

2. EXPERIMENTAL BASIS – FIELD TESTS

A series of large scale field tests to study the long range propagation of impulsive sound over forest terrain were performed in South-Eastern Norway during the years 1994 to 1996. The tests are termed the Norwegian Trials and were conducted by the Norwegian Defence Construction Service (now Norwegian Defence Estates Agency). In addition, teams from Cold Region Research and Engineering Lab, Civil Engineering Research Lab, Applied Research Associates, Jack W. Reed - all USA, University of Salford – UK, Institut für Lärmschutz – Germany, the University of Bergen, SINTEF, Kilde Akustikk, Norwegian Defence Research Establishment and the Norwegian Geotechnical Institute – all Norway, took part in the tests.

Two test sites were used; Haslemoen and Finnskogen. The Haslemoen site is entirely flat and consists of a deep fluvial silt deposit. Tests were made both through a dense coniferous forest and over open farmland, with source to receiver ranges from 200m up to 1500m. Finnskogen is a much larger site, with test ranges from 2km to 17km. The terrain is undulating, with a maximum elevation difference of 250m. The ground varies from exposed rock through, glacial till and fluvial sand deposits to marsh and smaller lakes. The vegetation consists of various types of coniferous forest, grassland, and moss cover. At both sites tests were made during both summer and winter (snow covered) conditions.

At Haslemoen, a test layout consisting of a straight line in the North-South (roughly) direction was used. At Finnskogen the layout had a North-South line and a perpendicular East-West line. Recording stations were placed near the ends of each line, and at Finnskogen also at the point where the lines crossed, as illustrated in Figure 1. Spherical charges of C4-explosive were used as impulsive sound sources throughout the entire test program. Detonation positions were placed at different positions along the two lines in-between the recording stations. Charge weights of 1, 8 and 64 kg were used, all detonated 2m above the ground. In total more than 800 charges were fired during the test programme. Using this scheme, a large variety of combinations of charge weights, ranges, directions and propagation paths to the various recording stations was obtained.

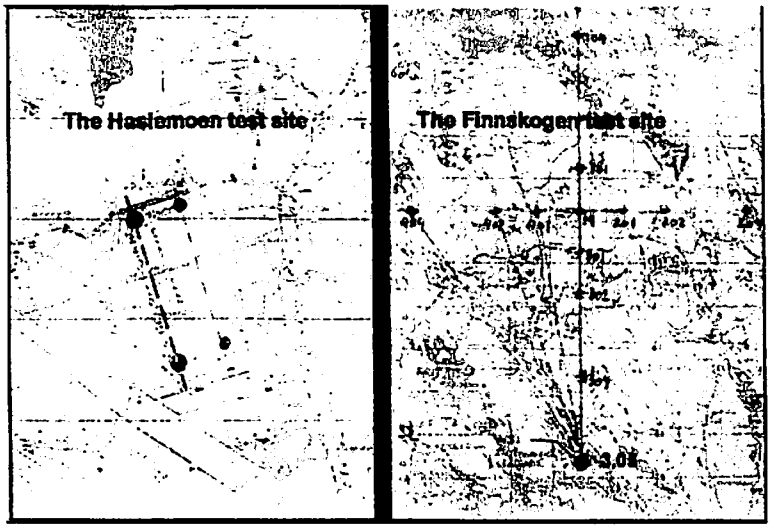

Figure 1 – Plan view and test layout for the Haslemoen and Finnskogen sites.

At all stations sound pressure time histories from each shot were recorded at various elevations from the ground level up to 8 m, and at some locations to 32 m height. In addition, ground response was recorded at the southernmost stations both at Haslemoen and Finnskogen. Separate teams, with their individual instrumentation operated the various stations. The frequency range from about 0.1Hz (1Hz for ground response) up to at least 250 Hz was maintained in all the recordings. Within each station all signals were recorded simultaneously. The time synchronisation among the stations was obtained through recording of the GPS time reference.

The ground response instrumentation at each sensing point comprised a seismometer (particle velocity sensor) slightly buried in the ground, a microphone at the ground level exactly above the seismometer, and a microphone one meter above, as illustrated in Figure 2. For most tests, the ground response recording station had two or three ground response sensing points, separated by some meters, in addition to the sound sensing. Most seismometers were 3-axial, but at some points only vertical ground response was recorded. During the winter tests, seismometers were placed both on top of the frozen ground crust and on top of the snow cover. During the Finnskogen winter tests, a more extensive array of five ground response sensing points was used, as shown in Figure 3.

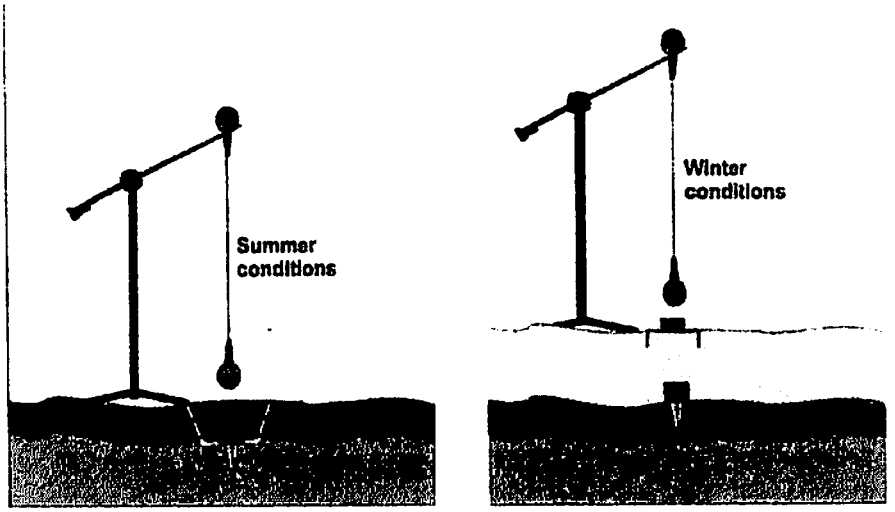

Figure 2 – Air-ground interaction instrumentation

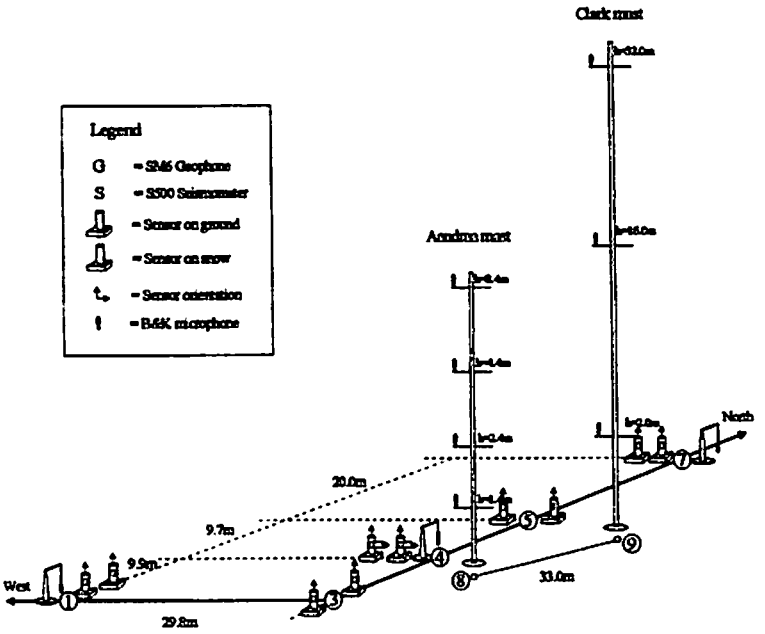

Figure 3 – Sound and ground response recording station during Finnskogen winter tests

Meteorological data were recorded frequently and regularly throughout the entire test program. Meteorological towers covered measurements within the forest, up to about 20 m above the ground. A tether sound near the centre of the test fields recorded up to 1000 m. Wind speed, wind direction, air temperature, air pressure and relative humidity were recorded by all systems. At the towers turbulence and thermal radiation was also recorded. More details and results are found in /7/. During the winter tests, snow cover profiles were taken at 11 pits at Haslemoen, and at 28 pits at Finnskogen. In addition, snow cover and the frozen ground were mapped along survey lines using a Ground

Penetrating Radar. Ground conditions were mapped around the ground response recording stations using sampling, seismic investigations and radioactive sounding. At a few locations the flow resistivity and impedance in the higher frequency range was determined by separate measurements, in tube samples, by reflection measurements /9/ and by pistol shot response measurements /9/. A more extensive description of the test program and data recording is found in /6/ and /7/.

3. TEST RESULTS OVERVIEW

The intention has been that all data from the tests should be made available to any institution who wants to use them in their research. For the purpose of data access an effort is made unify all the information into one common database. Even though most data are now collected, work still remains before the database is operative. Due to lack of funding, there is currently no progress.

So far, only a limited joint interpretation has been made on the data from all the recording stations. Most in-depth interpretation has up till now been made by the individual test teams on data from "their" stations (/11/, and /12/).

The remaining part of this paper will concentrate on an interpretation of sound and ground response data recorded by the Norwegian Geotechnical Institute, at their station termed 3.06, during the Finnskogen summer tests. (These tests were performed in late September).

3.1. Fundamental findings of air-ground interaction behaviour

Figure 4 plots the time histories representing a set of air-pressure and corresponding vertical ground response particle velocity, recorded at one observation point during one typical blast (8 kg charge at 16 km distance). The two traces illustrate some fundamental features which appear in the records from all shots and all points, and probably represents one essential physical mechanism on how air-pressure and ground interact at low frequency: The air-pressure appears to always be a reasonably short transient. For close-in blasts, it consists of a distinct pulse of one or two oscillations. At longer distances, the duration becomes longer and there are more oscillations, probably originating from interacting reflections and refractions from the atmosphere, the terrain and the ground. The first arrival however, always corresponds to the shortest source to receiver distance and the actual sound speed in air. The ground response is different. For almost all blasts it arrives at exactly the same instance as the air-pressure. Further, and also for mostly all blasts, it has a lead-in part that is more or less a "footprint" of the air-pressure wave as it propagates over the ground. Unlike the air-pressure however, the ground response has a long "tail" of oscillations following behind the lead-in.

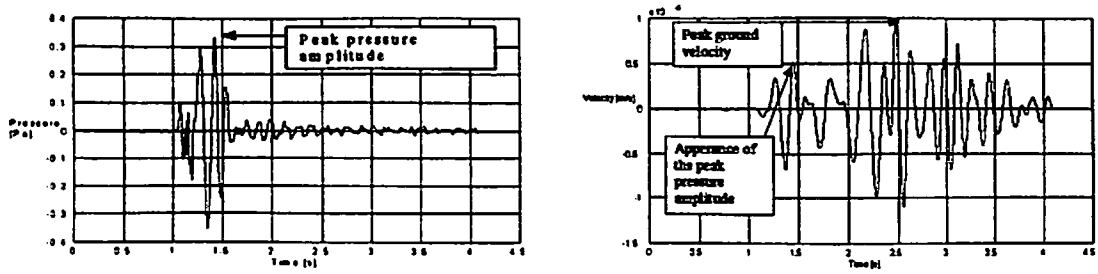

Figure 4 – Typically recorded air pressure and ground response traces from the Finnskogen summer tests.

Theoretically there are two different paths that can bring ground vibration from a blast position to an observation point; one seismic and one acoustic: Just around the source, the blast will set up powerful vibrations in the ground. These vibrations propagate through the ground as seismic waves. For close-in observations, or for partly or fully buried charges, arrivals of the compressional wave, the shear wave and the Rayleigh wave may be observed, at the instances corresponding to the travel distance and the seismic speed for the three wave-types in the ground. These are the seismically transmitted vibrations. The acoustically transmitted vibration, on the contrary, is the response of the ground to the air-pressure wave as it sweeps along the ground surface over the observation point. This is illustrated in Figure 5. The arrival of the acoustically transmitted vibration is controlled by the sound speed in air. The ground response plotted in Figure 4, is an acoustically transmitted vibration. Whether a seismically or acoustically transmitted vibration arrives first depends on the seismic speed of the ground, relative to the sound speed in air. However, it appears that the energy loss for seismic wave propagation is much higher than the loss for sound propagation in air. At some distance the seismically transmitted vibrations therefore vanish, compared to the acoustically transmitted vibration. This is always the case for above-ground, on-ground and slightly buried charges. For well buried charges, a dominant portion of the released energy goes into the ground, and the seismically transmitted vibration may dominate also at long distances. In neither the Haslemoen (distances larger than 100m) nor the Finnskogen recordings (distances larger than 2km) the seismically transmitted ground vibration was visible.

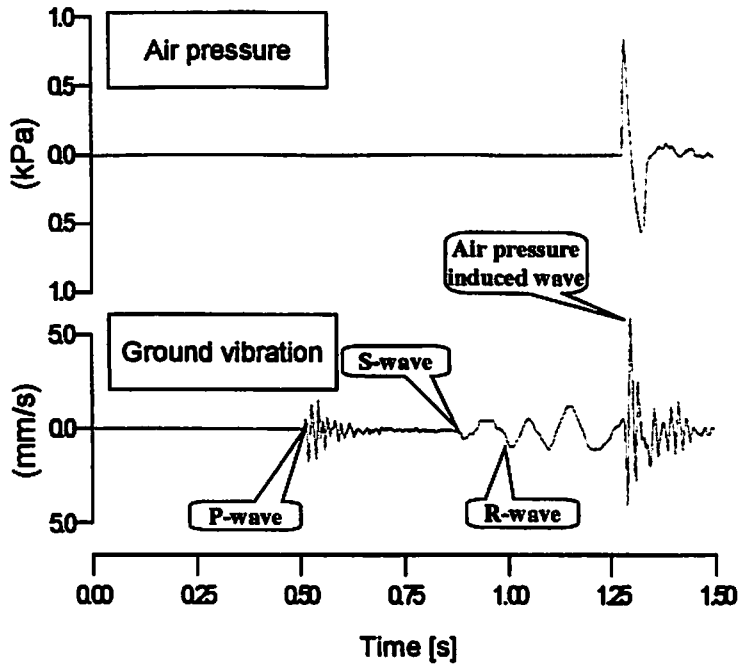

Figure 5 – Air pressure and ground response from a partly buried 50 kg charge, as recorded at 200 m on a stiff soil site./1/

The "tail" of ground response vibration observed for all the blasts, and as illustrated in Figure 4, has the following explanation: As the air pressure wave propagates along the ground surface from the source, towards the observation point, it continuously interacts with the ground at its instantaneous position, and there sets up vibration which propagate as seismic waves in the ground. For the case shown in Figure 4, the seismic speed for the dominant waves is lower than the sound speed in air. They therefore arrive at the observation point later than the direct acoustically generated response (the lead-in). The length of the tail tells something about the difference between the sound speed in air and the seismic speed, and about the seismic energy loss in the ground. I.e., to say; over how long distance in front of the observation point, the seismic waves have "memory" of the ground. It is obvious that the characteristics of the ground response must vitally depend on whether the seismic speed is lower (superseismic), the same (transseismic) or higher (subseismic) than the sound speed in air /17/. This interaction is complicated, and will be elaborated on further in the following chapters. There it will be demonstrated that the interaction mainly involves the Rayleigh waves in the ground. Plotting measured vertical ground response versus horizontal response indicates retrograde, elliptically shaped surface motion trajectories, which further supports the assumption of Rayleigh waves. The fact that these waves are usually dispersive (have freq uency dependent speed) adds to the complexity. The fact that the ground response at a given position also contains components generated by the air pressure at other positions is an obvious demonstration that the ground in this case is not locally reacting.

3.2. Overview based on peak values of air-pressure and ground response

The most obvious singe-vale parameter to characterise the recorded air pressures and ground responses is the peak value. The rest of this chapter focuses on giving an overview of the results from the tests, based on peak values from all the blasts. Figure 4 shows how the values are selected. The frequency content will also be discussed

Figure 6 shows recorded peak air pressure from all shots during the Finnskogen summer tests, plotted against the distance to the shot positions (i.e. the range). The pressure is recorded 1 m above ground level, and shots with insufficient data quality are dropped. To be able to compare data from shots with different charge weight, a Hopcinson-Cranz scaling has been applied (/13/ and /14/). The scaled range is $r = R/Q^{1/3}$, where R is the actual range in meters, and Q is the charge weight in kg. As a reference, the ANSI /15/ standard model for hemispherical propagation is also plotted (represents 22 dB attenuation per distance decade).

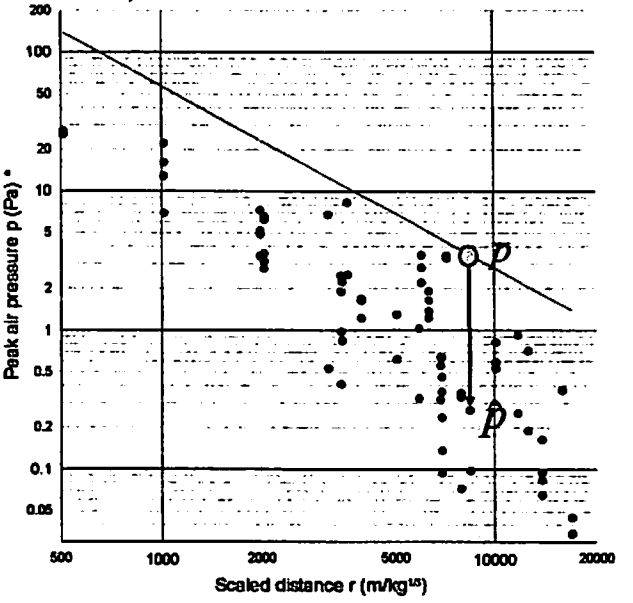

Figure 6 – Peak air pressure versus scaled distance for all processed blasts during the Finnskogen summer tests. The solid line (p) corresponds to the theoretical ANSI standard /15/. The measured peak pressures ($\hat{p}$) deviates up to 40dB from this standard.

The most obvious observation is the large scatter in the measured pressures, and the general tendency for the pressures to be lower and attenuate faster than the reference curve. A rough estimate on a lower envelope to the data, gives more than 40 dB attenuation per decade, and peak pressures about 40dB below the ANSI-curve at a scaled range of 10000 (e.g. 10 km from a 1 kg charge). The peak pressure is influenced by the meteorology, the terrain and the ground interaction. A first attempt to correlate the deviation in peak pressure with the sound speed gradient, the diffraction angle over

terrain features, charge weight (in case the scaling is not relevant) and whether the ground was frozen or not (part of the test period had night temperatures below zero, leaving a thin frozen crust on the ground), did not reveal any consistent trends. Hopefully more sophisticated, e.g. multi-variant correlation methods, where all controlling parameters and data from all measurement stations are being jointly processed, may do better. However, the data demonstrates the inherent large stochastic variability in long range sound propagation, and the immense challenge in making realistic propagation models. Models must be stochastically formulated to also predict the uncertainty. Present prediction models tend to overestimate the peak pressure at low frequency e.g /16/.

The way the field tests were performed may have introduced some hardly traceable randomness. Since the recording stations were kept stationary and the shot points were moved from blast to blast, the close-in ground conditions may therefore also have varied from blast to blast. The near-field ground interaction may influence on the air-blast as transmitted into the far-field, and produced variability in the source strength. A joint interpretation of data from all the recording stations has not yet been performed, but such an interpretation may partly resolve this.

Figure 7 plots vertical peak particle velocity of the ground response versus scaled range, for the same blasts as plotted in Figure 6. The scatter is slightly less than for the peak pressures. Correlation studies of the peak velocities gave similarly inconsistent trends. A best fit trend line for the peak particle velocity is $\hat{v} = 1.61 \cdot r^{-1.42}$ (i.e. 28 dB attenuation per scaled distance decade).

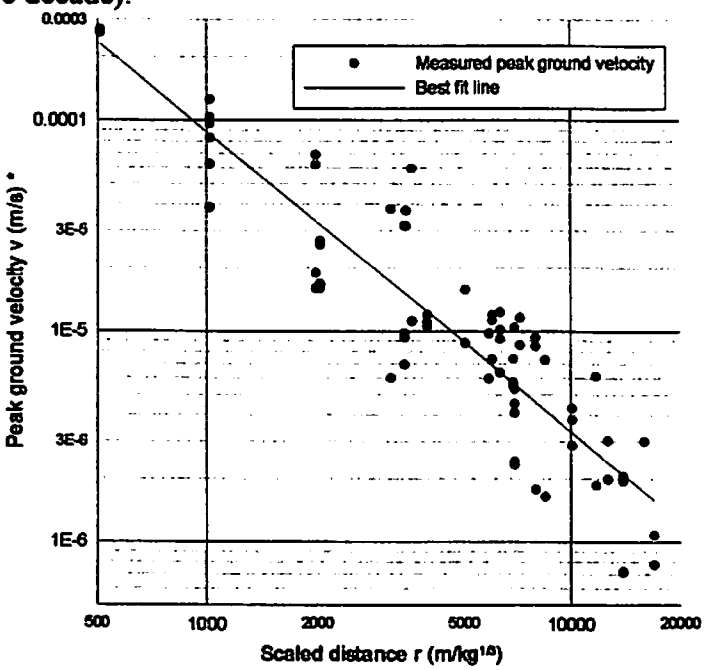

Figure 7 – Peak ground particle velocity versus scaled distance for all processed blasts during the Finnskogen summer tests

Figure 8 -a and -b plot the dominant frequency of air-pressure and ground vibration versus scaled range. In accordance with Hopcinson-Cranz, the scaled frequency is determined as: $\overline{f} = f \cdot Q^{1/3}$, where f is the actual frequency in Hz and Q is the charge weight. The frequency is taken at the maximum value of the power spectrum of the signals. Even though the scatter is high, particularly for the air pressure, there is a consistent trend towards decreased frequency as the distance increases. For most of the blasts the dominant frequency of the air-pressure and the ground response is about the same. However, there is a trend for the pressure frequency to be slightly lower than the ground frequency. For 1kg charges, the frequency axes can be read directly in Hz. It can be seen that frequencies of about 30Hz are typical at 500 m distance. At 10000 m the frequency is reduced to some few Hertz. The correlation study gave no consistent trends, except for a slight tendency for non-frozen ground give lower frequency than frozen ground.

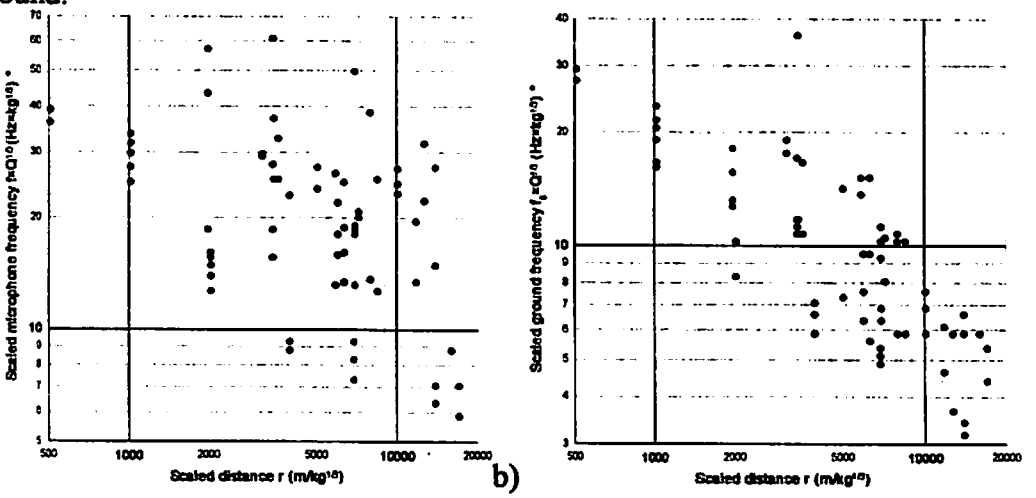

a) b)

Figure 8 – Scaled characteristic frequency of air pressure (a) and ground particle velocity (b) for all blasts from the Finnskogen summer tests

The ratio between the peak air pressure and the corresponding peak ground velocity can be used as a rough measure of the air-ground interaction. The ratio will here be termed the pseudo acousto-seismic Impedance: $\hat{Z}_{ag} = \hat{p}/\hat{v}$. Figure 9 plots peak ground velocity versus peak air pressure. The thin lines in the figure represent constant values of $\hat{Z}_{ag}$. The dotted reference line in the figure represents a typical value of the specific Rayleigh wave impedance of the ground at the site. ($\overline{z} = \overline{\rho} \cdot \overline{C}_R$, where $\overline{\rho}$ and $\overline{C}_R$ are typical values of, respectively, the mass density and the Rayleigh wave speed at the upper part of the soil profile). It can be seen from the plot that $\hat{Z}_{ag}$ is consistently close to, or lower than, $\overline{z}$. This means that the ground response to a given air pressure, is consistently the same or higher than $\hat{p}/\overline{z}$. The higher the value of $\hat{Z}_{ag}$, the "softer" is the ground response. $\hat{Z}_{ag}$ varies by a factor of more than 10 from one blast to another. The

correlation study gave no consistent trends. Initially one should expect $\hat{Z}_{ag}$ to be a constant from blast to blast, since the ground at the site is the same for all the blasts. Why this is not the fact is an issue that is elaborated on in the following chapters.

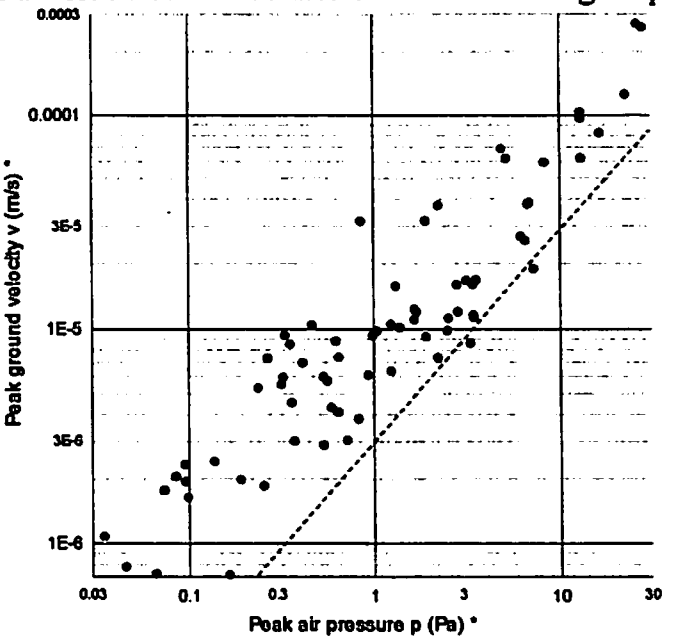

Figure 9 – Peak ground velocity versus peak air pressure – pseudo acousto-seismic impedance.

A normalized measure of the deviation in peak air pressure can be obtained by dividing the measured peak pressure, $\hat{p}$ by the value of the ANSI-line at the same scaled range, $\overline{p}$, i.e. $p_r = \hat{p}/\overline{p}$, as illustrated in Figure 6. If $p_r = 1$, it means that the peak pressure is on the ANSI-line, while $p_r = 0.1$ means it is 20 dB below etc. Figure 10 plots p_r versus $\hat{Z}_{ag}$. Even though there is scatter in the plot, there is a definite trend that p_r increases with increasing $\hat{Z}_{ag}$. The trend is far more consistent than that found in any of the other performed correlation studies. In other words, it shows the peak air pressure is attenuated more, the "softer" the ground response is. It may appear from this plot that the ground impedance has a dominant effect on the sound propagation. However, this is not a firm conclusion that should not be drawn right away. There may be other mechanisms that make the peak pressure and the ground impedance covariate. At this stage, the findings if Figure 10 is left as an observation, whose interpretation should be the subject for further studies. This is partly done in the following chapters.

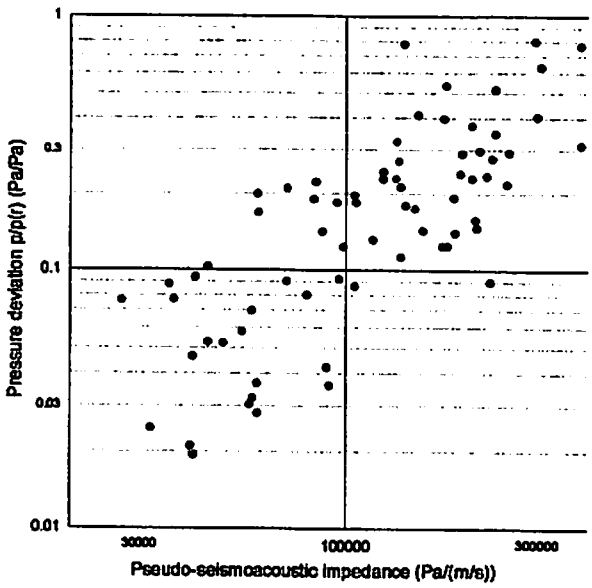

Figure 10 – Air pressure deviation versus pseudo ground impedance – indications on how the ground effects the sound pressure attenuation

3.3. Energy flux

Having measured the air pressure just above the ground surface; $p(t)$ and the vertical response of the ground at the same position, $v(t)$, as illustrated in Figure 9, it is possible to calculate the energy flux (energy per unit area) from the air pressure into the ground vibration, according to:

$$e_{air} = \int_0^T p(t) \cdot v(t) \cdot dt \qquad (1)$$

The integration starts from the arrival of the signal, and T is the duration of the signal. However, the integral will only gain contribution as long as there are air pressure fluctuations. The "tail" of ground vibration after that will not contribute. Similarly, it is possible to estimate the seismic energy per unit width which propagates along the ground in the form of the ground vibration, assuming the wave-mode resembles a Rayleigh wave:

$$E_{ground} = \int_0^T \Theta \cdot \overline{z}_R \cdot v(t)^2 \cdot dt \qquad (2)$$

Here, $\overline{z}_R$ is an average specific Rayleigh wave impedance of the ground (close to the shear wave impedance), and Θ is a factor, with dimension length, accounting for the mode shapes of the seismic waves and the layering of the ground. It is assumed that the ground vibration is in a steady state balance with the air pressure, which means that the energy gained by the seismic waves from the air pressure is balanced by the energy which

goes into the seismic loss mechanisms in the ground. The ratio between the two energy measures;

$$\ell_e = E_{ground} / e_{air} \tag{3}$$

represents a measure of the length in front of the observation point, over which the ground has accumulated seismic energy from the air pressure thus creating the present ground vibration. In other words, ℓ_e is the "memory length" of the ground at the site. Putting in representative values of $\overline{z}_R$ and Θ for the measurement site, and repeating the above calculations for a series of the recorded blasts, ends up with a typical value of $\ell_e \approx 500\,m$. This means that the air-ground response properties of the actual site, measured during these tests, actually reflects the ground properties of the area from the observation point and about 500 m towards the sound source. Property contrasts in the ground closer than this distance should be expected to effect the measurements, while changes further away should not give an effect. The actual measurement site was homogeneous to within this distance.

4. AIR-GROUND INTERACTION - GROUND SURFACE IMPEDANCE

4.1. Ground surface impedance definitions

The air interaction properties of a ground surface are controlled by the complex-valued, frequency dependent normal impedance of the surface. In a modeling and interpretational perspective the ground can be considered as a layered poro-elastic half space. The normal impedance of a surface is generally defined as the ratio between the air pressure p_a above the surface and the particle velocity normal to the surface. For a porous and elastic surface, there are more than one velocity that may be considered: (1) The air particle velocity just above the surface v_a, (2) the particle velocity of the grain skeleton of the ground at its surface v_g, and (3) the average vertical velocity of air particle flow in the pores at the ground surface v_p. See Figure 11 for further explanation. The three velocities are inter-related through the equation

$$v_a(t) = v_g(t)\cdot(1-\Phi) + v_p(t)\cdot\Phi \tag{4}$$

where Φ is the porosity of the ground.

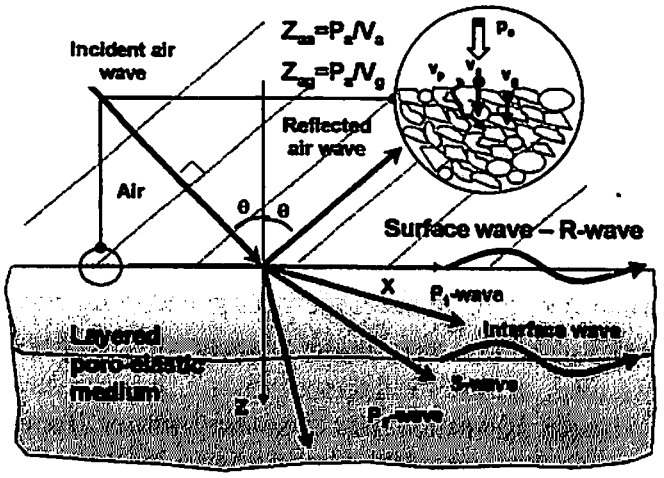

Figure 11 – Air-ground interaction – Definition of terms

Based on these velocities, two types of impedances have been considered here: The Acoustic Impedance; $Z_{aa}(f)$, measures the relation between the pressure p_a and v_a, and the acousto-seismic impedance; $Z_{ag}(f)$, measures the relation between the air pressure p_a and v_g . Attenborough et al. /18/ use the inverse of $Z_{ag}(f)$, and terms it the acoustic transfer function.

The surface impedance of this type of layered ground is determined by the first- and second (slow) compressional wave and the shear wave in the ground material, by the reflected and refracted components of these waves, and by the resulting surface and interface waves, as illustrated in Figure 11.

4.2. Impedance determined from the field measurements

The velocity sensed by the buried seismometers in the Norwegian Trials field tests is assumed to correspond to the particle velocity of the grain skeleton. From measured air pressure just above the ground and vertical ground particle velocity, the acousto-seismic impedance has been determined from each recorded blast according to the equation:

$$Z_{ag}(f) = P_a(f)/V_g(f) \tag{5}$$

where $P_a(f)$ and $V_g(f)$ are the Fourier transforms of $p_a(t)$ and $v_g(t)$ respectively. In this process $p_a(t)$ and $v_g(t)$ have been windowed, so that they only contain the part of the signals where the air-pressure exhibits significant oscillations, i.e. the "tail" of ground vibration is not included in the determination of $V_g(f)$. Each power spectrum of $P_a(f)$ and $V_g(f)$ from all the processed blasts turned out to have a well defined peak, with low signal levels outside the peak. The dominant frequencies plotted in Figure 8*a* and –*b* are found from these spectral peaks.

Figure 12 plots the magnitude of $Z_{ag}(f)$, determined according to the above equation, from all recorded blasts which had sufficient data quality to be processed. Each blast is presented in the plot by circles; determined at the frequency of the maximum power spectrum of the air-pressure, the ground response and the cross-spectrum respectively. In this way the impedance determination for each blast is made where the signal to noise ratio is at the highest. A total of 71 blasts are plotted in the figure. Since the dominant frequency varies from blast to blast according to distance, charge weight, meteorology etc, as demonstrated in Figure 8 -a and –b, the ensemble of impedance values in Figure 12 do cover the frequency range from about 3 Hz to 30 Hz.

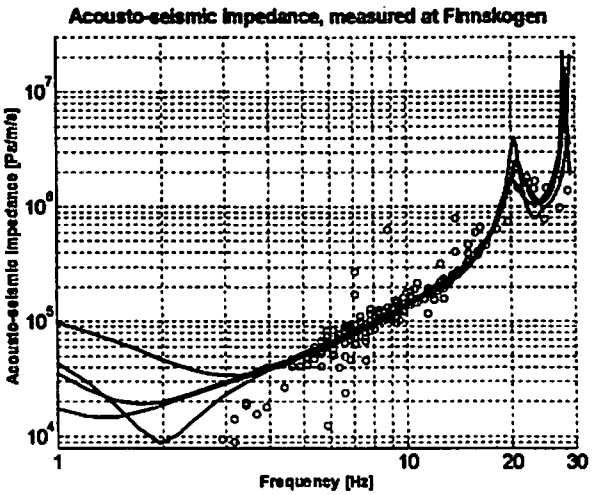

Figure 12 – Acousto-seismic impedance for the Finnskogen site, determined from the field measurements – Magnitude. The four solid lines represent the measured impedances at four different shots, while the circles are determined at the frequency of the maximum power spectrum of the air-pressure, the ground response and the cross-spectrum respectively.

Figure 12 shows that the impedance values determined from all the blasts line up in an amazingly consistent manner, and forms what appears to be a uniquely defined impedance function of the ground around the measurement site. The results do not contain any of the severe scatter found in the previously presented results. Furthermore, including the impedances determined for single blasts over the whole frequency range, frequencies where the signal level is extremely low, create a smooth impedance function in full agreement with the one defined by the assembly of dots from all the blasts. The thin solid lines in the figure represent such impedance functions determined from three selected blasts. In addition, these curves further confirm that the dots represent a unique, continuous impedance function. They also indicate that the impedance has a minimum value at about 2 Hz, and then starts to increase at lower frequencies.

The above confirms that the measurements define one unique impedance function for the measurement site. This is, in contradiction to what was observed for the Pseudo

Impedances as presented in Figure 9. It is now seen that what appeared in that plot as a random scatter from blast to blast actually is caused by the different Pseudo Impedances values being individual "samples" from this unique, continuous function taken at different incoming wave frequencies.

The shape of the impedance function presented in Figure 12, may appear unexpected. All familiar ground impedance models /19/ does tend to increase monotonically towards low frequency, while this impedance has a dramatic drop. This is elaborated on in the next section.

Figure 13 plots the real and imaginary parts of the same $Z_{ag}(f)$ as presented in Figure 12. Again the impedance values from all the blasts line nicely up, without substantial scatter. However, the points line up along two separate branches. When tracing back it is found that all points along the branch marked with solid symbols originate from shots taken when the ground was not frozen, while those along the branch with open symbols represent shots over frozen ground. The pattern appears fully consistent. During the second half of the test period night temperatures dropped below zero during the nights (-1 to -5 °C), leaving a thin crust of frozen water in the layer of the ground cover. One explanation may be that the frozen crust seals off the pore channels into the ground. However, the large effect it has on the impedance should be made subject for further investigation.

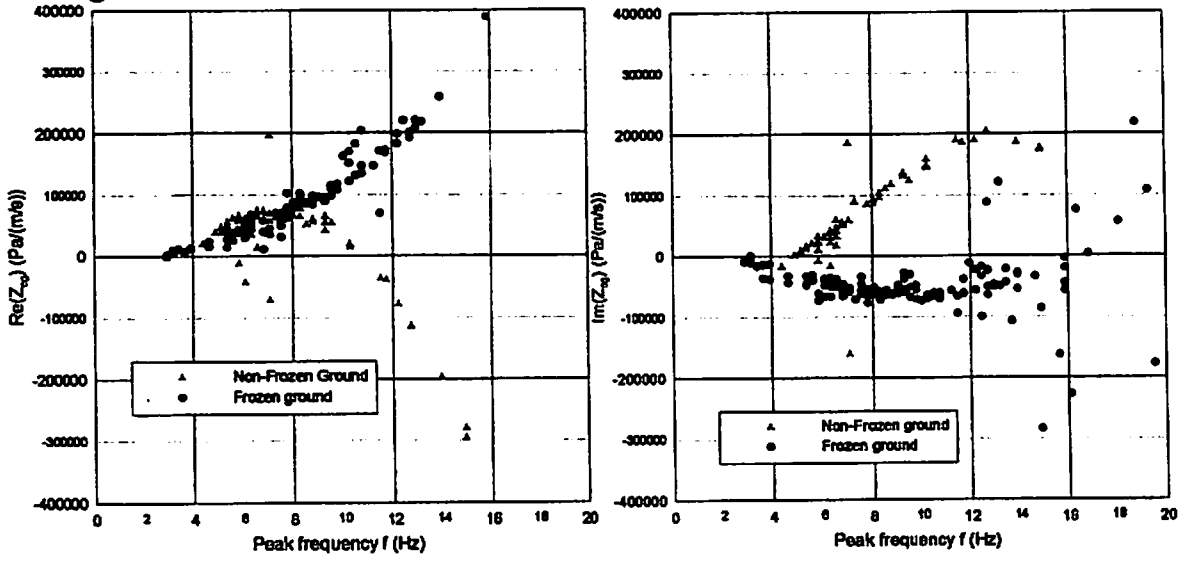

Figure 13 - Acousto-seismic impedance for the Finnskogen site, determined from the field measurements – Real and Imaginary part.

4.3. Findings from the theoretical impedance model

An analytically based and numerically implemented model has been developed to further study the nature of air-ground interaction at low frequency. The model is based on analytical discrete Greens-function solution of the wave equation in a layered poro-elastic half-space overlain by a fluid (air). It is implemented in the computer program MultiPor

/20/ and /21/. Plane waves are assumed, which is considered a reasonable approximation in the present context, where the distance to the source is long and the curvature of the wave front is marginal compared to the size of the area affecting the response.

Figure 14 shows an example of the absolute value of the Acousto-seismic impedance for a homogeneous poro-elastic ground, as predicted by MultiPor, for 90° angle of incidence of the air pressure. I.e., the air pressure wave is sweeping along the ground surface (grazing incidence). The impedance is plotted against frequency and shear wave velocity of the ground. More details are found in /21/ and /7/. The most characteristic feature of the plot is the striking dip in the impedance where the shear wave speed, C_s is about 340 m/s. This appears at all frequencies. With the present ground parameters, this C_s corresponds to a Rayleigh wave speed of the ground, C_R of about 340 m/s, e.g. C_R is exactly the same as the sound speed used for the air in the model. Parametric studies and further investigation of the numerical results confirm that an intense coupling between the air wave and the Rayleigh wave in the ground always appears when the speed of the two waves coincides. This confirms that the Rayleigh wave interaction is explanation of the air-ground response observed in the field tests and described in the previous chapters.

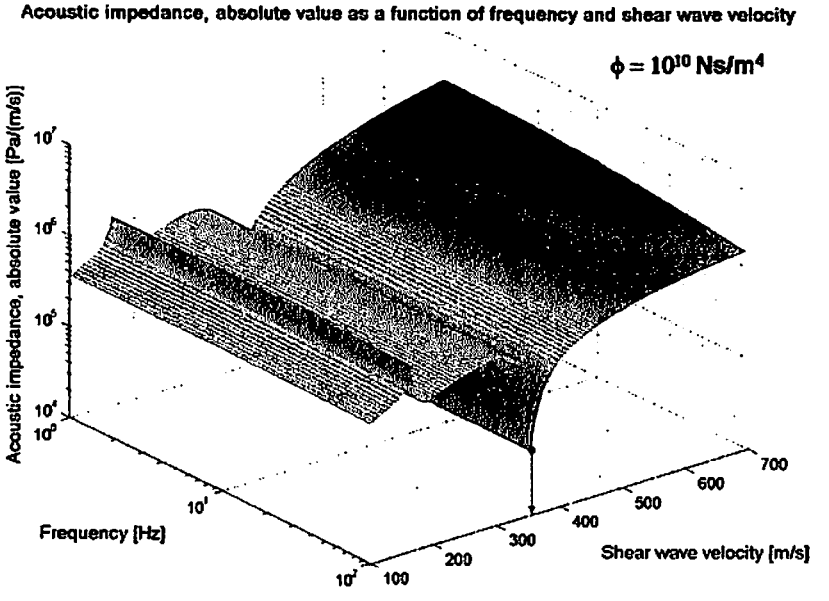

Figure 14 – Acoustic impedance of a visco-poro-elastic half space under air – magnitude versus frequency and shear wave velocity of ground – MultiPor simulation

Figure 15 plots together the acoustic- and acousto-seismic impedance functions for the same case as above. The impedances are taken at 10 Hz frequency, and are here plotted against flow resistivity and shear wave velocity of the ground. The flow resistivities in the plot cover the whole range from impermeable soils like saturated clays to extremely permeable ground like such as boulder fields. The distinct dip appears in both impedances, also at the sound speed – Rayleigh speed coincidence. It can be observed that at high flow resistivity (impermeable ground) the acoustic and acousto-seismic

impedances coincide. This is because the vertical (normal to the ground surface) air particle velocity just above the ground, which is what controls the acoustic impedance, equals the vertical particle velocity of the ground grain skeleton, since the flow velocity of air in and out of the pores in the ground will be small due to the low permeability. Both impedances may be said to be controlled by the viscoelastic properties of the ground. For lower flow resistivities, the acoustic impedance becomes consistently lower than the acousto-seismic. This is due to the fact that the velocity of flow in and out of the pores increases relative to the velocity of the grain skeleton as the permeability gets higher. For the most permeable grounds, the acoustic impedance seems completely controlled by the porous properties of the ground, while the acousto-seismic impedance is determined by the viscoelastic properties. The transition from viscoelastic to porous dependency varies with the frequency. The sandy soil at the field measurement site is in the range where the two impedances deviates substantially, while the viscoelastic properties, and thus the Rayleigh wave interaction, still has a significant effect also on the acoustic impedance.

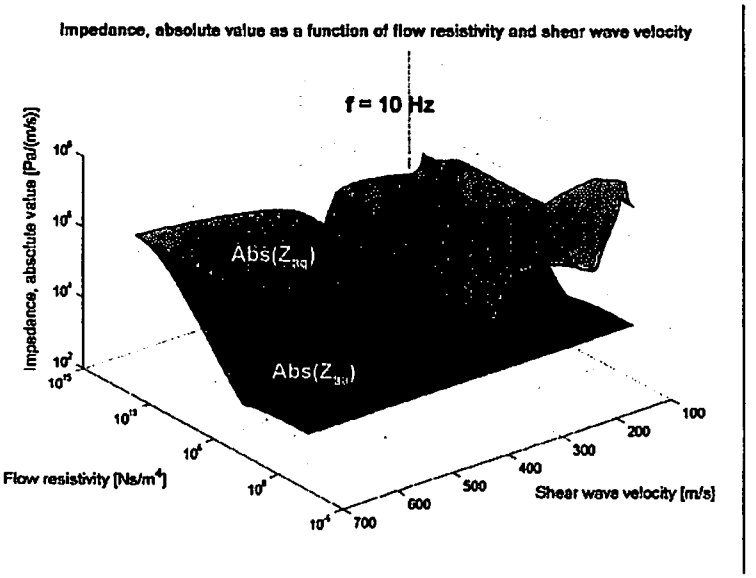

Figure 15 – Acoustic- and acousto-seismic impedance of a poro-elastic half space under air – magnitudes versus flow resistivity and shear wave velocity of ground at 10 Hz – MultiPor simulation.

Figure 16 shows the acoustic impedance estimated by MultiPor, plotted versus angle of incidence of the air pressure wave and the shear wave speed. The flow resistivity is typical for coarse sandy ground. The plot is for 3 Hz, however, the same general pattern also appears for other frequencies. The plot clearly demonstrates that the impedance depends on the angle of incidence. Another indicator of interaction with the viscoelastic waves is that the ground is not locally reacting. It is further seen that Rayleigh wave coincidence depends on the angle, because the horizontal slowness component of the air pressure wave must coincide with the Rayleigh wave speed slowness along the ground surface.

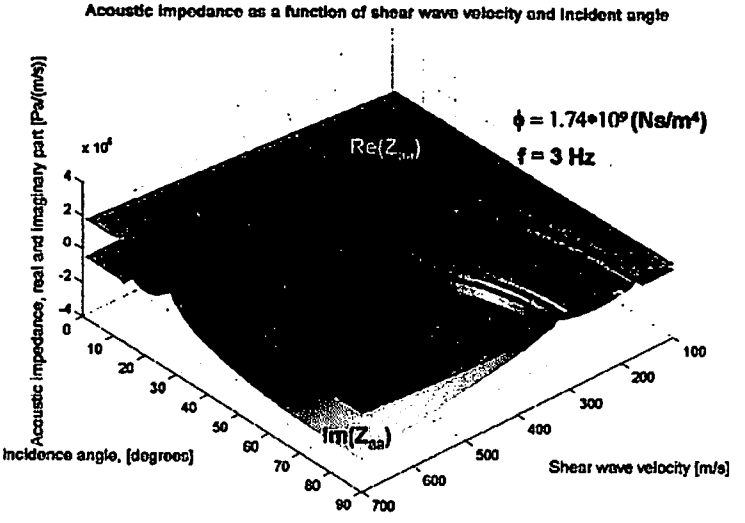

Figure 16 – Acoustic impedance of a visco-poro-elastic half space under air – magnitude versus angle of incidence and shear wave velocity of ground at 3 Hz – MultiPor simulation.

4.4. Comparisons for the actual measurement site - verification

So far, the assumed importance of the Rayleigh wave interaction on the ground impedance has been justified through simulations with the MultiPor model. However, the strong frequency dependency derived from the field test data has not been explained. The he above model results are based on a homogeneous ground, which is not a proper representation of the ground at the measurement site. The site is definitely layered, and there is a trend for overburden pressure to give increased shear wave velocity of soils /23/. Shear wave velocity will therefore vary with depth, leading to the Rayleigh waves being dispersive /24/ and thereby a frequency dependent propagation speed. The Rayleigh wave dispersion of the measurement site has been determined by means of the SASW seismic method (Spectral Analysis of Surface Waves). A string of geophones was placed on the ground surface and Rayleigh waves generated by impacting the surface. By analyzing the phase shift between the wave arrivals at the various sensors, the dispersion curve can be constructed. Through an inversion process, the corresponding shear wave versus depth profile of the site can be established. The method is further described in /24/.

The seismic profile from the SASW-measurements, and assumed values of flow resistivity and the other ground properties based on knowledge of the geology of the site were used as input to MultiPor simulation of the ground impedance if the site. The flow resistivity of the top layer agrees with the tabulated values for sand given by Bear /25/. Figure 17 presents the results. The bold solid line plots the magnitude of the acousto-seismic impedance versus frequency ($|Z_{ag}(f)|$), as determined by MultiPor. The dots and thin lines are the results from the field measurements as reproduced from Figure 12. As the figure demonstrates, there is an excellent agreement between the simulation and the

test results. This gives confidence in the assumptions behind the MultiPor solution of the poro-elastic layered ground, and the ability of such a model to represent a real ground. It particularly gives confidence to the assumption that interaction between pressure waves in the air and the dispersive Rayleigh waves in the ground has a dominant effect on the ground impedance.

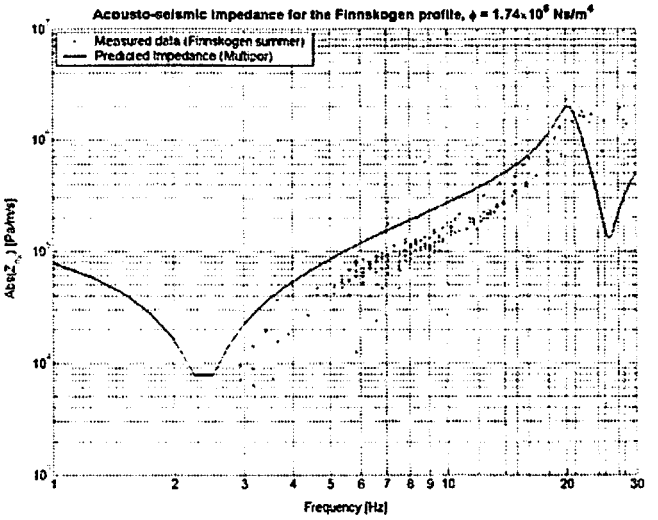

Figure 17 – Acousto-seismic impedance of test site at Finnskogen – magnitude: Comparison of field measurement and MultiPor simulation.

4.5. Implication of ground impedance of low frequency sound and vibration propagation

How a ground surface with an impedance controlled by Rayleigh wave interaction will effect the propagation of low frequency sound has been further studied by the use of the Fast Field program FFLAGS. This program simulates sound propagation from a point source, over a layered poro-elastic ground. Results are presented in an accompanying paper /5/. FFLAGS is shown to give very much the same simulated ground impedances as MultiPor, with similar agreement to the measured results. This indicates that the assumption of plane waves inherent in MultiPor does not conceal important features.

With respect to the effect on sound propagation, the FFLAGS simulations indicate a substantial drop (up to about 5dB) in excess attenuation around the frequency where the sound speed coincides with the (dispersive) Rayleigh wave speed. In a real case, the ground properties will vary along the sound propagation path from the source to the receiver point. Over which frequency range the excess attenuation will appear and how large it will be depends on the ground layering and thus the Rayleigh wave dispersion in the various sections of the propagation path, and of the extent of the sections.

To what extent the Rayleigh wave interaction effect is present and at which frequency it will appear may be highly sensitive to minor variations. Figure 18 plots the Rayleigh wave dispersion for the measurement location at Finnskogen, together with the sound speed in air. As can be seen from the plot, the shape of the dispersion curve makes the frequency coincidence extremely sensitive to even small variations in sound speed e.g. due to temperature changes. It also appears from the plot, which for a site with a slightly lower wave speed in the ground than the one presented, the Rayleigh wave interaction does not appear at all, and a slightly higher speed would gives interaction at substantially higher frequency. The shape of the dispersion curve for a given site may also vary over time, particularly from summer to winter, when a thick frozen crust can have significant effect. The figure highlights elements that may easily lead to apparently random variations in the air-ground interaction, the impedance of the ground and sound propagation attenuation.

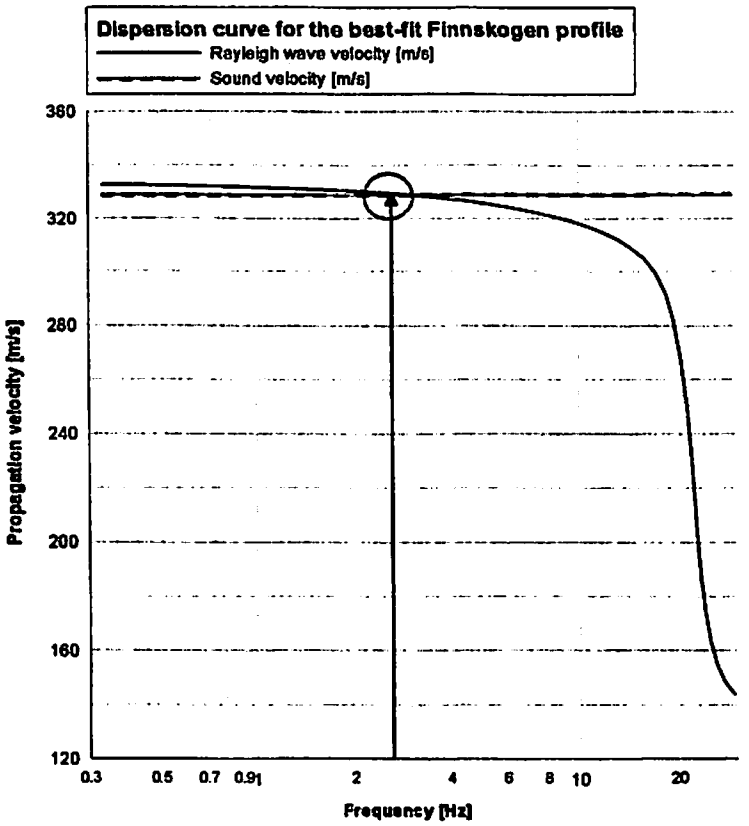

Figure 18 – Rayleigh wave dispersion for the Finnskogen test location: Sensitivity

The ground impedance does not only effect the sound pressure propagation. If acoustically induced ground vibration, or ground to building transmitted vibration are to be considered, the acousto-seismic impedance has a dramatic effect on the level of ground vibration induced by a given sound pressure. For a site where Rayleigh wave interaction appears at the dominant frequencies of the sound pressure, the ground vibration may be greater than a factor 100 (40dB) than at a site with ground conditions not making the interaction happen.

5. DISCUSSION, CONCLUSIONS AND FURTHER WORK

Based on data measured at the Finnskogen location during the Norwegian Trials impulsive sound propagation tests, major new phenomena of air-ground interaction related to acoustically coupled Rayleigh waves have been discovered. This introduces an additional mechanism in the ground effect on sound propagation; not contained in commonly used ground impedance models, which mainly focus on the porous effects of the ground. The mechanism may have a significant effect on the sound propagation attenuation, and a dominant effect on sound induced ground vibration.

Even though the discussion in this paper has been linked to the ground conditions at the measurement site, the major findings are considered generally valid. The excessive Rayleigh-coupled ground response can only take place where the wave speed in the ground at any relevant frequency coincides with the sound speed in air. This condition is fulfilled for a large variety of commonly appearing ground conditions.

The physical and numerical models presented in this paper basically explain the major findings on air-ground interaction, made from the field tests. However, there is far more that needs to be investigated, e.g. related wave modes, energy transfer, ground inhomogeneity and particularly on ground effect on sound propagation. Relevant parameters for ground classification need to be revised, and efficient methods for their determination must be developed.

What is presented in this paper is based on the interpretation of a minute fraction of the entire volume of data collected during the Norwegian Trials. The remaining data represents a large potential for further development and validation of sound and vibration prediction models. Meteorological, topographical and ground cover effects, including snow and frost, still need to be investigated. Joint interpretation of data from several recording stations provides a promising potential. The large amount of recordings available enables quantification of the stochastic elements that will always be present in this type of sound and vibration prediction.

6. ACKNOWLEDGEMENTS

The authors want to acknowledge the Norwegian Defence Construction Service (NDCS)/ Norwegian Defence Estates Agency (NDEA) for having initiated, conducted and largely funded the Norwegian Trials field test program, under which grant the presented research have been made possible. Their willingness to release all data from the tests for publication is appreciated. We also acknowledge funding from the Norwegian Research Council under the programs SIP 4 "Optimal fundamentering av bygningskonstruksjoner på land". The authors particularly want to emphasis on the vital role of Mr. Arnfinn Jenssen, now retired from NDCS/NDEA. His initiative, foresight, effort, driving force and leadership made the test program possible and successful. His insight, intuition and knowledge have given us the inspiration needed, and is highly acknowledged. We are also grateful for the constructive cooperation given by all the other test teams in the project.

NGI

7. REFERENCES

/1/ Madshus, C. and N.I. Nilsen (2000). Low frequency vibration and noise from military blast activity – prediction and evaluation of annoyance, Proc. InterNoise 2000, Nice, France.

/2/ Øhrstrøm, E. (1996). Community reaction to noise and vibrations from railway traffic. Proc. Internoise 1996, Liverpool U.K.

/3/ ISO 2631-2 (1998), Mechanical vibration and shock – Evaluation of human exposure to whole body vibration – Part 2: Vibration in buildings

/4/ Hole, L.R., Kayina, A.M., Madshus, C, (1998). Measurements and simulations of low frequency impulsive noise and ground vibration from airblast. J. Sound and Vib. Vol. 214, pp 309-324.

/5/ Attenborough, K., S. Taherzadeh and C. Madshus (2002). Preliminary results from comparisons of infrasonic acoustic-seismic coupling data with predictions using FFLAGS, Proc. LRSP-seminar 2002, Grenoble, France.

/6/ Guice,L.R., Hole,L.R., Jenssen,A., Kerry,G. (1998). Impulsive noise measurements in a forest during summer and winter conditions. Noise Control Engineering Journal Vol 46-5, pp. 185-189.

/7/ Kerry, G. An overview of the long range impulse sound propagation measurements made in Norway, Proc. Internoise 1996, Liverpool U.K.

/8/ Hole,L.R., Gjessing,Y, Lange,de T., Reed,J.W. (1998), Meteorological measurements and conditions during Norwegian trials, Noise Control Engineering Journal Vol 46-5, pp. 199-207.

/9/ Albert, D.G., Snow cover effects on impulsive noise propagation in forest. Proc. Internoise 1996, Liverpool U.K.

/10/ Storeheier, S.Å. (1998). Estimations of acoustic impedance of ground surfaces at Haslemoen and Finnskogen sites, during the Norwegian Trials 1994-1996. Main results-2. SINTEF Memo, 40-NO980231, 1998-11-05.

/11/ Hirsh, K. (1998) On the influence of local ground reflections on sound levels from distant blasts at large distances, Noise Control Engeneering Journal, Vol 46-5

/12/ Storeheier, S.Å. and T.E. Vigran (2000). Prediction of low frequency impulsive sound propagation. Proc. InterNoise 2000, Nice, France

/13/ Hopkinson, B. (1915), British Ordonance Board Minutes 1356

/14/ Cranz, C. (1926), Lehrbuch der Ballistik, Springer – Verlag , Berlin

/15/ ANSI S2.20-1983 American National Standard. Estimating Airblast Characteristics for Single Point Explosions in Air, With a Guide to Evaluation of Atmospheric Propagation and Effects

/16/ Delany,M.E.; Bazley,E.N. (1968) Acoustical Properties of Fibrous Absorbent Materials, Applied Acoustics, 3, pp. 105-116

/17/ de Barros, F.C.P., Luco, J.E. (1994), Response of a layered viscoelastic half-space to a moving point load. Wave motion 19, pp. 189-210

/18/ Attenborough,K.; Richards,T.L (1989), Solid particle motion induced by a point source above a poroelastic half-space, Jour. of the Acoust. Soc. of Am. Vol 86-3, pp. 1085-1092

/19/ Attenborough, K. (1985) Acoustical impedance models for outdoor ground surfaces, J. Sound Vib., Vol 99, pp. 521-544.

/20/ Løvholt, F. (2002) Acoustic-seismic coupling of low frequency sound waves over layered poro-elastic ground. Eur. Young Geotech. Eng. Conf. Dublin 2002

/21/ Kaynia, A.M., Løvholt, F. and Madshus C. (2003). Ground effects of sound and vibration propagation – Theoretical model and verification. Submitted for publication in Jour. of the Acoust. Soc. of Am.

/22/ Madshus, C., Numerical modelling of low-frequency sound propagation over poro-elastic ground, International Conference on Acoustics (ICA) in Rome 2001

/23/ Hardin, B.O. and V.P. Dnevich (1972) Shear modulus and damping of soils. Design equations and curves. Proc. ASCE, Vol. 98, SM7, pp. 667-692

/24/ Stokoe, K.H., Rix, G.J., Nazarian, S., (1989), Proc of the Int. conf, on soil mech. and found. eng., Rio de Janeiro, Brazil 1989, pp. 331-334

/25/ Bear, J.(1972) Dynamics of fluids in porous media. Dover publications, Inc.

Preliminary results from comparisons of infrasonic acoustic-seismic coupling data with predictions using FFLAGS.

Keith Attenborough, The University of Hull, Hull HU6 7RX, UK k.attenborough@hull.ac.uk
Shahram Taherzadeh, The Open University, Milton Keynes, MK7 6AA,UK
Christian Madshus, Norwegian Geotechnical Institute

Abstract
Predictions of propagation from a point source in a stratified fluid above a layered porous and elastic ground [Tooms, Taherzadeh and Attenborough, J. Acoust. Soc. Am. 93 173 (1993)] are compared with acoustic-to-seismic coupling spectra obtained from Norwegian blast propagation trials at low frequencies and long ranges. The predictions are found to be sensitive to the assumed sound speed in air as well as to the assumed seismic profile. Two features of the measured and predicted coupling spectra are noted and discussed. The feature below 5 Hz is found to be very angle-dependent. On the other hand that between 20 and 30 Hz is predicted to be independent of angle. Corresponding features are found in associated predictions of excess attenuation spectra. Although the feature between 20 and 30 Hz is predicted by an effective impedance approach, that below 5 Hz is not.

1. Introduction

A recent report [1] presents data for the ratio of air pressure 0.1 m above the ground to the vertical soil particle velocity measured at a collocated geophone buried just beneath the ground surface measured in response to C4 explosions. These data were obtained at ranges above 2 km at Finnskogen in Norway. The objective stated in the NGI report is to derive an improved impedance model for low frequencies that takes into account ground elasticity. The report calculates the impedance of a multi-layered poroelastic system at an angle of incidence of 90° (grazing incidence). A plane wave model (Multipor) for reflection at the surface of a multi-layered poro-elastic medium is used also to compute the acoustic-seismic coupling ratio (ASR) i.e. the ratio of incident pressure to the component of solid particle velocity normal to the surface (termed acousto-seismic impedance in the report). It is shown that the computed quantities are sensitive to ground elasticity. Moreover it is found possible, using the plane wave model, to match the computed acoustic-seismic coupling ratio to data measured at ranges of 2 km and above during blast propagation trials in Norway. The seismic profile deduced on site using the Spectral Analysis of Surface Waves (SASW) method (see Table 1) is altered to enable data fitting (Figure 21 of the report, see Figure 1).

Table 1 Seismic layering deduced from SASW at Finnskogen in Norway

Layer	Fl. Res. kPa s m^{-2}	porosity	thickness	P-wave speed m/s	S-wave speed m/s	Damping
1	1740	0.3	0.5	560	230	0.04
2	1740	0.3	1.0	220	90	0.02
3	1740000	0.1	3.0	415	170	0.002
4	1740000	0.01	3.0	1500	170	0.001
5	1740000	0.01	4.0	1500	200	0.001
6	1740000	0.01	5.0	1500	400	0.001
7	1740000	0.01	halfspace	1500	450	0.001

The plane wave predictions show a significant minimum in the acoustic-to-seismic coupling ratio at 2.5 Hz. The NGI Report points out that 2.5 Hz is the frequency at which the Rayleigh

wave speed predicted from the (presumably elastic) dispersion curve for the Figure 21 profile in the ground, coincides with the sound speed in air.

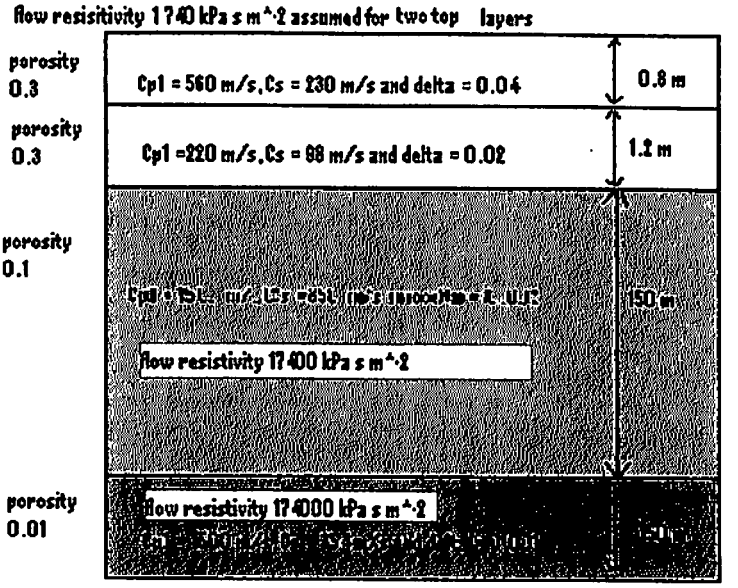

Figure 1 Ground profile used in the calculations.

It is noticeable that the data shown in Figure 23 of the report has a significant spread below 7 Hz. It is mentioned in the report that data have been obtained at horizontal ranges between 2 and 17 km. The different data series shown in Figure 23 are for different ranges between 6.3 and 12.6 km. It is noticeable also, that with one possible exception, the data in Figure 23 of the report do not show as sharp a minimum as predicted by Multipor. Moreover the minima in the ASR data appear to be over a range of frequencies between 1.5 Hz and 3 Hz.

2. Predictions of A/S ratios using FFLAGS

Calculations for propagation from a point source that take ground elasticity, porosity and layering into account may be made using FFLAGS (Fast Field program for Layered Air-Ground Systems). FFLAGS enables atmospheric refraction to be included also but for the calculations presented here the atmosphere is assumed to be homogeneous. Details of FFLAGS are given elsewhere [2]. The NGI report does not specify the flow resistivities and porosities that have been used for the individual layers. The values that have been used in the calculations reported here are shown in Table 1 and Figure 1. It should be noted that the assumed porosities are not consistent with the assumed densities but this inconsistency has little effect on the predictions.

Example comparisons between predicted and measured acoustic-seismic coupling ratios (i.e. the ratio of sound pressures at microphones divided by vertical soil particle velocities measured at collocated geophones, called the acousto-seismic impedance in the report) are shown in Figure 2. Points (circles, boxes and crosses) in Figure 2(a) represent data. Predictions by FFLAGS at ranges of 6.3, 7.2 km and 12.6 km for source height 2 m, receiver heights 0.1 m (microphone) and – 0.05 m (geophone) and the 4-layer ground profile (Figure 1) derived from the Finnskogen data are shown in Figures 2(b) and 2(c). Clearly FFLAGS predictions are in tolerable agreement with data, similar to Multipor but, unlike Multipor, show range dependence. The predictions are consistent with the differences between data at

different ranges. The main minimum in the acoustic-seismic coupling spectrum below 5 Hz is predicted to be relatively shallow and to depend on range.

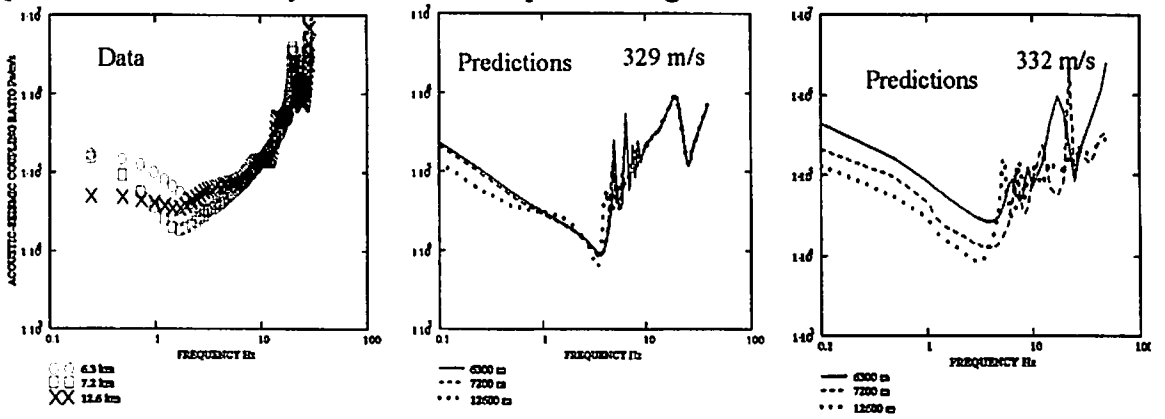

Figure 2 Acoustic-seismic coupling ratios deduced from measurements [1] and predicted by FFLAGS at ranges of 6300 m, 7200 and 12600 m for two different sound speeds in air; 332 m/s and 329 m/s.

Comparison of predictions in Figures 2(b) and 2(c) indicates that predictions have a significant dependence on the assumed sound speed in air. Figure 3 shows predictions obtained at 6300 m range with 4 different air sound speeds. Sound speeds in air of 329 m/s, 332 m/s, 335 m/s and 343 m/s correspond to temperatures of – 4°C, 1°C, 6°C and 20°C respectively at sea level.

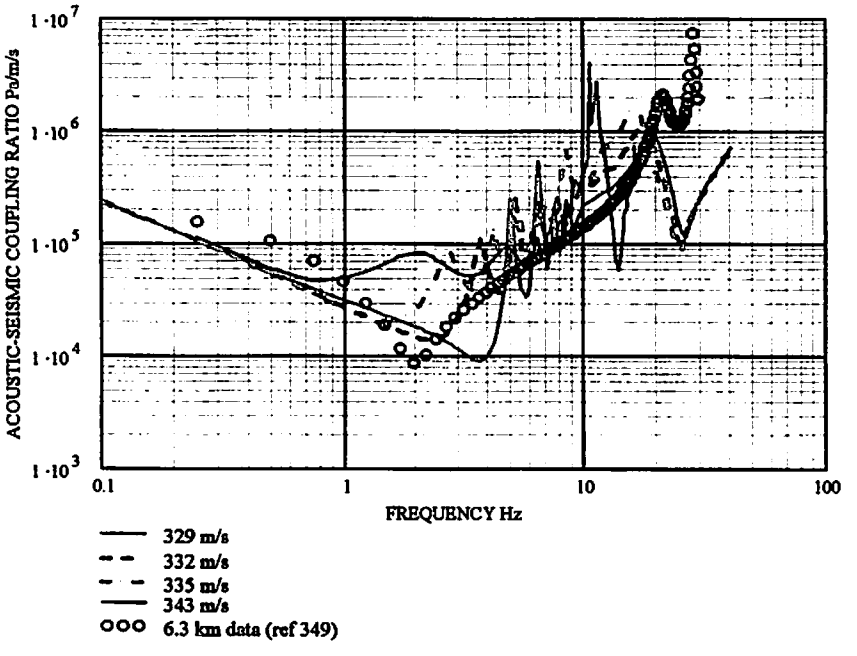

Figure 3 Predicted A/S ratio at 6300 m using sound speeds in air of 329 m/s, 332 m/s, 335 m/s and 343 m/s respectively.

In particular the predicted A/S ratio below 5 Hz is much altered by different air sound speed values. This is consistent with the interpretation that an air-coupled Rayleigh wave is involved below 5 Hz and the small slope of the predicted Rayleigh wave dispersion curve near 329 m/s [1].

It should be noted that the data at different ranges presented in the NGI report display some variability. Figure 4 shows this variability and indicates that it can be reproduced in the FFLAGS predictions by varying sound speed and third layer thickness.

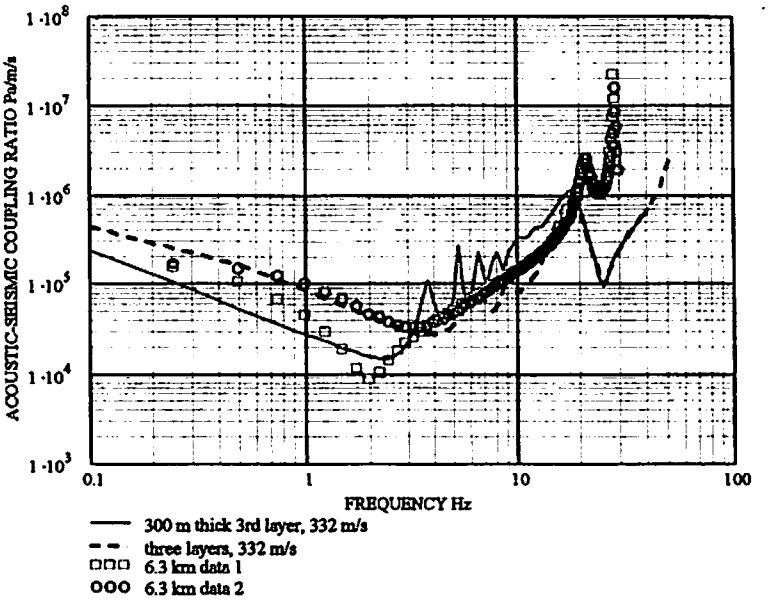

Figure 4 Two sets of 'data' at 6.3 km and FFLAGS predictions of acoustic-to-seismic coupling ratio assuming a sound speed in air of 332 m/s and for two different seismic profiles.

3 Predictions of surface impedance

The surface impedance predicted for a grazing angle of 0.018° (corresponding for example to a source height of 2 m and a range of 12.6 km is shown as a function of frequency in Figure 5. In this figure the predictions for the layered porous and elastic system are compared with those for a rigid porous ground with the same flow resistivity and porosity. The influence of ground elasticity is to reduce the magnitude of the impedance considerably below 50 Hz.

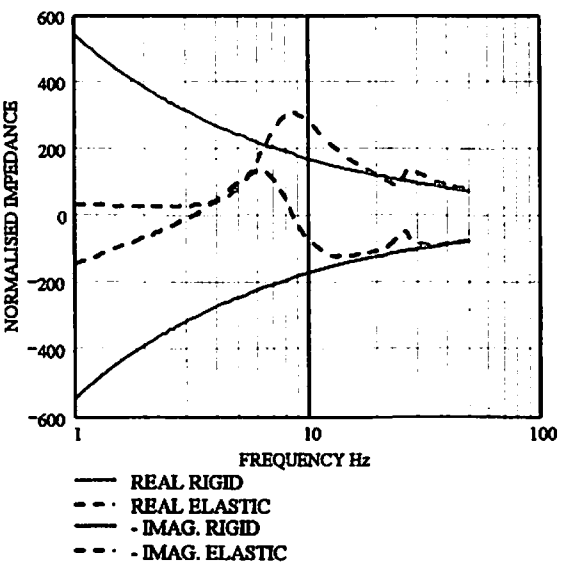

Figure 5 Predicted surface impedance at a grazing angle of 0.018° for poro-elastic and rigid porous ground (4-layer system).

Figure 6 shows that the surface impedance of the 4-layer poro-elastic system varies between grazing angles of 5.7° and 0.57° but remains more or less constant for smaller grazing angles.

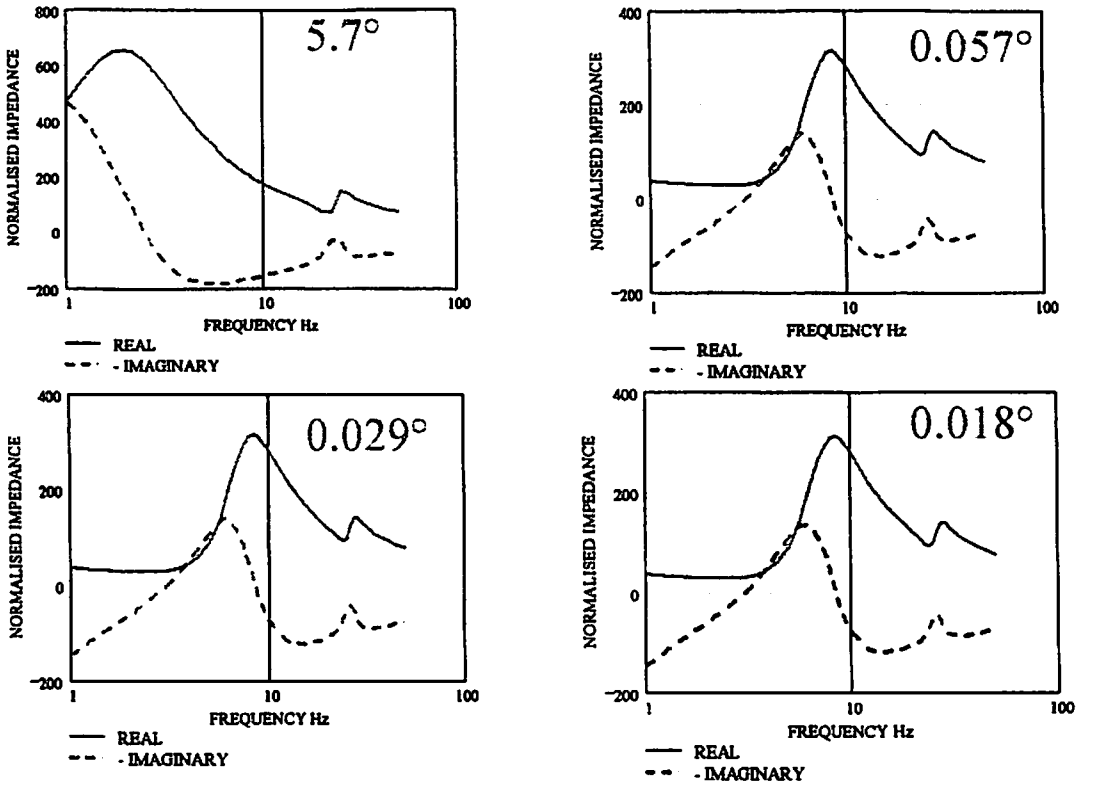

Figure 6. Normalised surface impedance predicted for the 4-layer structure, sound speed in air = 329 m/s. for grazing angles between 0.018 and 5.7 degrees.

The predictions in Figure 6 show two 'layer-type' resonances. The lowest frequency resonance is the most angle-dependent. The peak in the real part changes from 2Hz at 5.7 degrees to 8 Hz at 0.057 deg. On the other hand the higher frequency resonance peak near 25 Hz remains relatively unchanged with range.

4. Predictions of Excess Attenuation

As well as A/S ratios FFLAGS may be used to predict excess attenuation spectra (i.e. the sound pressure spectra relative to free field. The Excess attenuation spectrum at 20 m predicted by FFLAGS is shown in Figure 7. The most remarkable feature of this prediction is the region showing more than pressure doubling below 7 Hz. This suggests significant surface ducted energy. At longer ranges this type of behaviour is predicted to occur at lower frequencies still and may be worthy of further investigation. The 'normal' or flow-resistivity-associated dip in the excess attenuation spectrum is visible at 800 Hz in this prediction.

Figure 8 shows the corresponding excess attenuation predictions for 6.3, 7.2 and 12.6 km ranges. There are interesting dips in the EA spectrum. These represent maxima in the excess attenuation in the convention used here. The depths of the dips increase with range. The depth of the dip predicted at 3.5 Hz is 9 dB and shows a small frequency-dependence with changing range. The enhanced (above + 6dB) excess attenuation spectrum immediately before the 3.5 Hz dip is symptomatic of a surface wave.

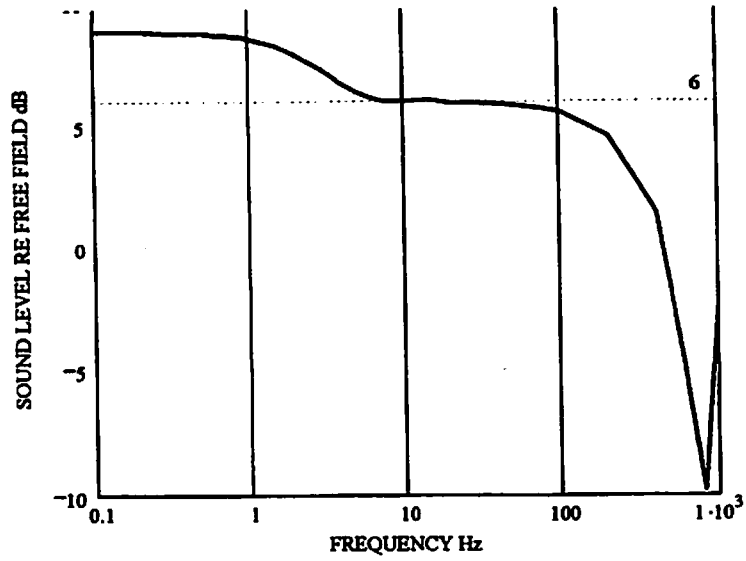

Figure 7 Excess attenuation predicted at 20 m range for source height at 2 m and receiver height 1 m

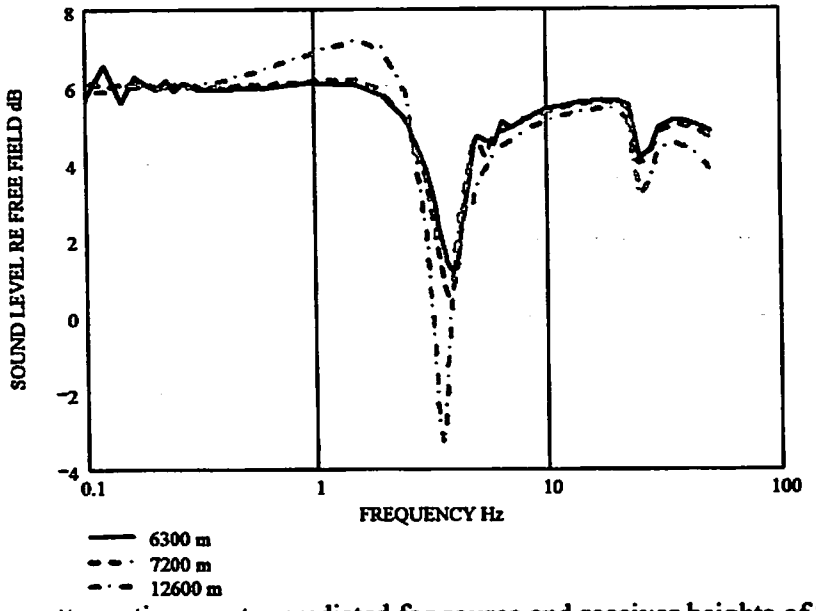

Figure 8 Excess attenuation spectra predicted for source and receiver heights of 2 m and 0.1 m and three ranges assuming a sound speed in air of 329 m/s.

As with the A/S ratio predictions, the Excess attenuation spectra predicted by FFLAGS for the 4-layer poro-elastic structure are rather dependent on the assumed sound speed in air. Figure 8 shows corresponding predictions with an assumed sound speed of 332 m/s.

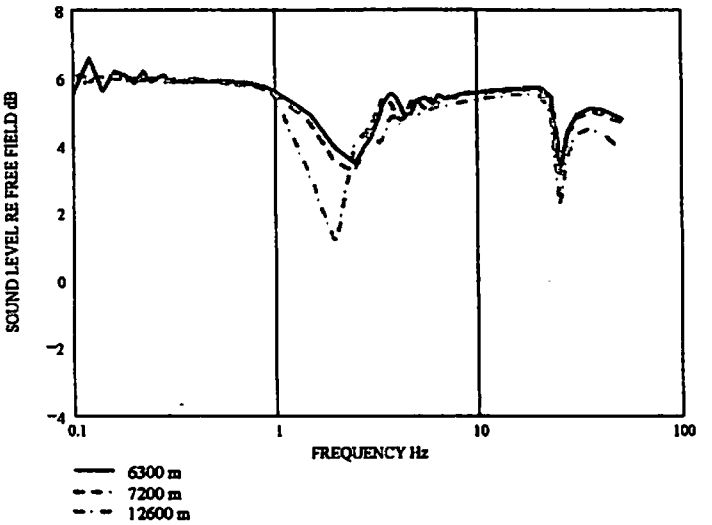

Figure 9 Excess attenuation spectra below 50 Hz predicted at ranges of 6300 m, 7200 m and 12600 m, source height 2.0 m, receiver height 1 m, with an assumed sound speed in air of 332 m/s

The low frequency dip is predicted to move to 2 Hz from 3.5 Hz and to become shallower. The dip between 20 and 30 Hz remains at the same frequency but becomes more pronounced.

5. Representation of the sound field by an effective impedance

A stated objective of the NGI report is to propose a form of impedance that will be more accurate than classical impedance model predictions at low frequencies. Figure 10 compares the excess attenuation predicted by FFLAGS for a range of 6300 km with that predicted by classical theory for a point source above an impedance plane using the impedance predicted for the same layered porous and elastic ground system at a grazing angle of 0.018 degrees. The predictions indicate that, for an assumed sound speed in air of 329 m/s, the excess attenuation is predicted fairly accurately in this way.

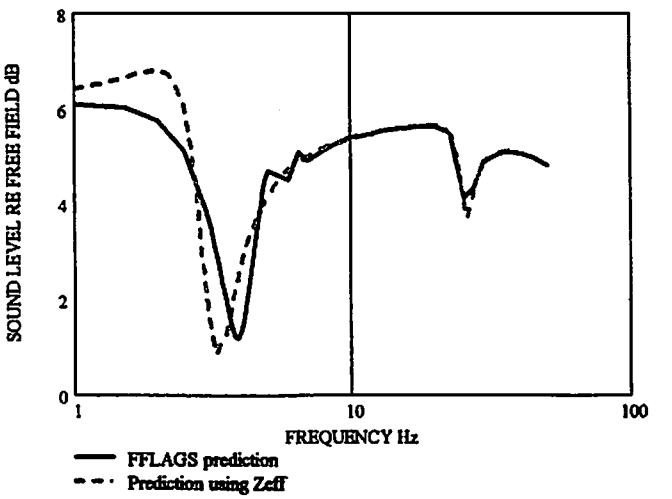

Figure 10 Excess attenuation spectra predicted for source height 2 m, receiver height 0.1 m and horizontal range of 6.3 km by FFLAGS (assumed sound speed in air of 329 m/s) and by classical theory using impedance calculated for 0.018 degrees grazing angle.

Figure 11 shows that this will not be true consistently for the low frequency dip. This Figure shows the same information but for an assumed sound speed of 332 m/s.

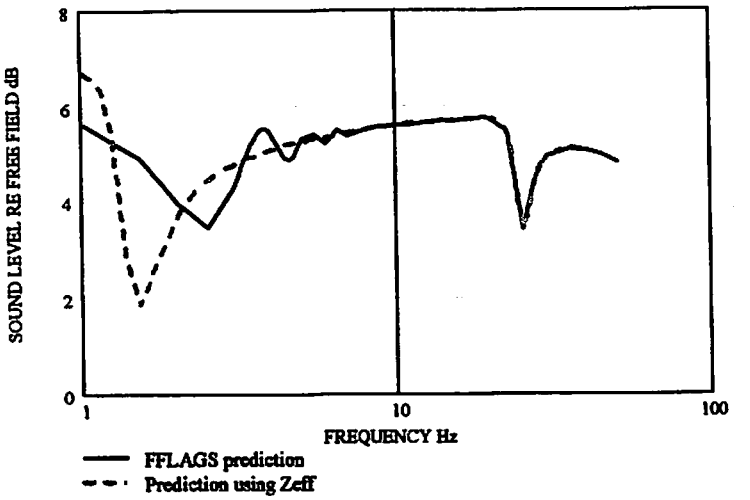

Figure 11 As for Figure 10 but with assumed sound speed 332 m/s.

Conclusions and discussion

Good agreement is achieved between predictions using FFLAGS and data for the acousto-seismic impedance at low frequencies and long range, obtained from blast trials in Norway, using a seismic structure derived from a SASW profile [1]. Predictions and data show shallower dips in the acoustic-seismic impedance spectrum than predicted by a plane wave analysis (Multipor [1]). The dips are predicted to be range dependent in accordance with the data. As with Multipor, FFLAGS predicts an impedance spectrum that differs considerably from that predicted for a rigid-porous medium.

FFLAGS predicts increased excess attenuation compared with a hard surface at two frequencies below 50 Hz. The effect below 10 Hz is consistent with an air-coupled Rayleigh wave in air and soil. It seems rather similar to the coincidence effect in building acoustics transmission loss and is not predictable consistently by classical theory using effective impedance. The effect between 20 and 30 Hz is consistent with the predicted (by FFLAGS and Multipor) and measured 'second' minimum in the acousto-seismic impedance and the predicted second resonance in the impedance spectrum. This 'second' minimum is independent of grazing angle and is consistent with such a resonance in the predicted impedance spectrum.

References

[1] C. Madshus and F. Lovholt, "Coupled vibration and Noise", Norwegian Geotechnical Institute Report No. 20021020 April 2002 (see also C. Madshus *et al* "Air-ground interaction in long range propagation of low frequency noise and vibration" Proc. 10th LRSPS, Grenoble)

[2] S Tooms, S Taherzadeh and K. Attenborough "Sound propagation in a refracting fluid above a layered porous and elastic medium" *J. Acoust. Soc. Amer.* **93**(1) 173-181 (1993).

ASPECTS OF PASSIVE SOURCE LOCATION IN THE ATMOSPHERE

Qiang Wang[a], Keith Attenborough[a] and Richard Brind[b]

[a]Department of Engineering, University of Hull, Hull HU6 7RX, UK
[b]DERA Winfrith Technology Centre, Dorchester, Dorset DT2 8XJ, UK

ABSTRACT

Data obtained from a nine-microphone array at a range of 250 m have been used to locate an elevated source at three different heights by a ground effect inversion and localization algorithm (GEILA) in turbulent and downward refracting atmospheric conditions. A matched field processing technique, i.e. the Bartlett processor developed for the underwater environment, has been adapted for this purpose. The statistical distributions of results from using the source location algorithm show some frequency dependence. The largest errors in the mean range and height are at frequencies corresponding to the dips in level difference spectra between vertically-separated microphones and seem to be related to the resultant variation in signal-to-noise ratio. The scatter in location results seems to be related to the effects of atmospheric turbulence. Although the accuracy of the results is limited by the lengths of the arrays, multi-frequency averaging improves the peak-to-sidelobe ratio in the ambiguity surfaces. Two numerical methods for frequency averaging are presented and compared. An alternative to conventional broadband coherent processing is found to give better performance.

I. INTRODUCTION

A ground effect inversion and location algorithm (GEILA) has been reported previously[1-4]. In the version of the algorithm used here a heuristic ray-trace model has been employed[1]. However, in principle, any propagation model can be used. The algorithm makes use of complex pressures received by a multi-element microphone array system, equivalent to three vertical arrays, each containing n microphones, z_{nj} ($n = 1,2,...N$; $j = 1,2,3$), placed at the corners of an arbitrary triangle, see Figure 1.

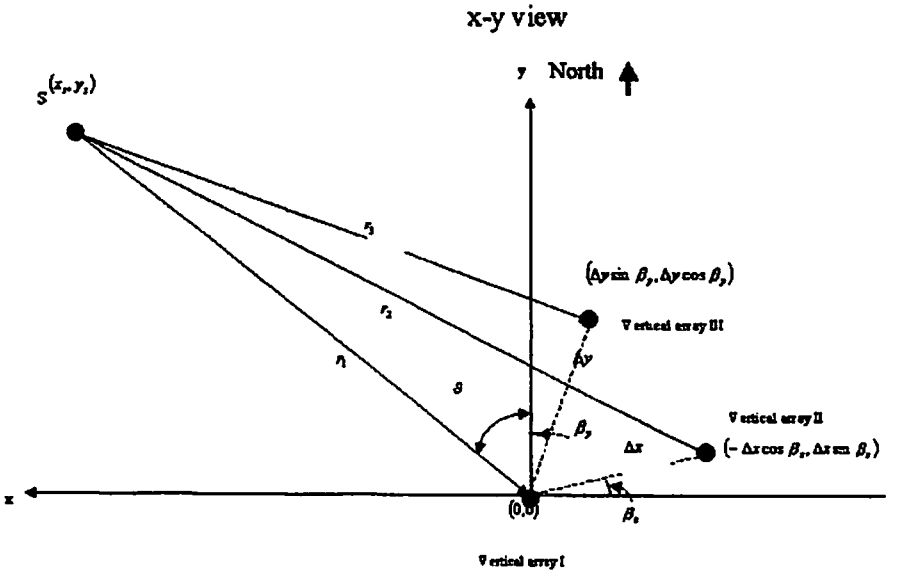

Figure 1. x-y view of the acoustic measurement system

Measurements have been made, over flat grassland at the University of Hull sports field (UH), using an elevated loudspeaker source and a nine-microphone array system at a horizontal range of 250 m. The resulting data have been used to test the algorithm in turbulent and refracting atmospheric conditions. Some aspects of the results, particularly the frequency-dependence, are investigated in this paper.

II. THE ALGORITHM

Given a fixed single source, the range and height ambiguity function, $A_j(r_j, z_s)$, is computed for each set of trial values of effective flow resistivity σ'_j, effective rate of change of porosity with depth α'^5_j, sound velocity gradient, a'_j

$$A_j(r_j, z_s) = 10\log\left|\frac{1}{M}\sum_{i=1}^{M}\frac{\left|\sum_{n=1}^{N} P_m(f_i, r_j, z_s, z_{nj}) P_e^*(f_i, r'_j, z'_s, z_{nj}, a'_j, \sigma'_j, \alpha'_j)\right|^2}{\sum_{n=1}^{N}|P_m|^2 \sum_{n=1}^{N}|P_e|^2}\right|^2, j = 1,2,3 \qquad (1)$$

where f_i is the ith single frequency. r_j is the horizontal range between the source and the jth vertical array

$$r_j = \sqrt{(x_j - x_s)^2 - (y_j - y_s)^2}\,. \qquad (2)$$

Equation (1) is the normalized sum over N microphones of the correlation between the measured and estimated fields. Equation (1) uses a coherent method of averaging over M frequencies. P_m denotes the measured pressure due to a source $S(r_j, z_s)$ at frequency f_i, and P_e represents the corresponding estimated pressure for a source $S'(r'_j, z'_s)$. The superscripts prime and asterisk denote trial value and complex conjugate respectively. In a correctly-matched environment, $P_e \approx P_m$, $r'_j \approx r_j$ and $z'_s \approx z_s$. GEILA determines the position of the source in the horizontal plane by finding the range from each of the three arrays. The source azimuth ϑ can be determined by solving the following equations numerically

$$\vartheta = \frac{\pi}{2} - \arctan\left(\frac{y_s}{x_s}\right), \tag{3}$$

$$\begin{cases} r_1^2 = x_s^2 + y_s^2, \\ r_2^2 = r_1^2 + \Delta r^2 + 2r_1 \Delta r \sin(\vartheta - \beta_x), \\ r_3^2 = r_1^2 + \Delta r^2 - 2r_1 \Delta r \cos(\vartheta + \beta_y), \end{cases} \tag{4}$$

where $\Delta r = \Delta x = \Delta y$ is the known separation between arrays. The values of Δx and Δy are not necessarily the same, but both of them should be sufficient large to give different lengths r_1, r_2 and r_3 for triangulating the azimuth ϑ.

III. THE FIELD EXPERIMENTS

Experiments were carried out over flat grassland at the University of Hull, UK. A nine-microphone array system was used, with $\Delta x = \Delta y = 20$ m and $\beta_x = \beta_y = 0$ (see Figure 1). The array system was composed of three sub-arrays each of which consisted of three microphones separated vertically at heights of 0.1, 1 and 3m. In consecutive experiments, an Electro-Voice loudspeaker broadcast white noise and thirty simultaneous pure tones between 100 Hz and 3000 Hz. The source was placed at heights of 10, 5 and 2 m respectively during the experiments. During the experiments, the speed and direction of wind together with temperature varied continuously. Meteorological measurements were made simultaneously with the acoustical measurements. The meteorological equipment mast was placed near array I. Wind speed and direction and temperature were measured simultaneously at heights of 2, 5 and 10m above the ground surface using sonic anemometers. To reduce the running time of the GEILA, initial trial values of ground impedance parameters were obtained from a short-range measurement at the propagation site using a local source and receivers. It should be noted that GEILA does not need prior

knowledge of ground impedance data, however the use of values based on the short-range measurement makes it possible to reduce the search ranges for ground impedance in the algorithm.

IV. ANALYSIS AND RESULTS

The meteorological data were logged every 2 minutes. According to the meteorological measurements, the normalized sound speed gradients in the direction of the sound propagation corresponded to conditions of downward refraction with values between 2×10^{-4} m^{-1} and 5×10^{-4} m^{-1}.

To extract frequency domain data, the time series of the received white noise signal and the pure tones have been sampled over ten consecutive periods of 2 minutes and 10 seconds respectively. These data were analyzed over narrow frequency bands between 100 Hz and 3000 Hz. For each tonal frequency f, GEILA has been used to estimate source locations by matching the complex acoustic pressure obtained simultaneously at each microphone of the arrays with the estimated ones using a ray-tracing model in the frequency range $f \pm \Delta f$, where $\Delta f = 5$ Hz. The source location results have been averaged over twenty-two frequency bins between 400 Hz and 2500 Hz. Each bin consists of results for eleven single frequencies in the band $f \pm \Delta f$. The signal-to-noise ratio was uniformly poor for the white noise and superior results have been obtained with pure tones. Nevertheless, with the source at 10 m height, the signal-to-noise ratio at 100 Hz, 200 Hz and 300 Hz was too poor for these data to be useful. Similarly for the lower two source heights only data above 800 Hz was used.

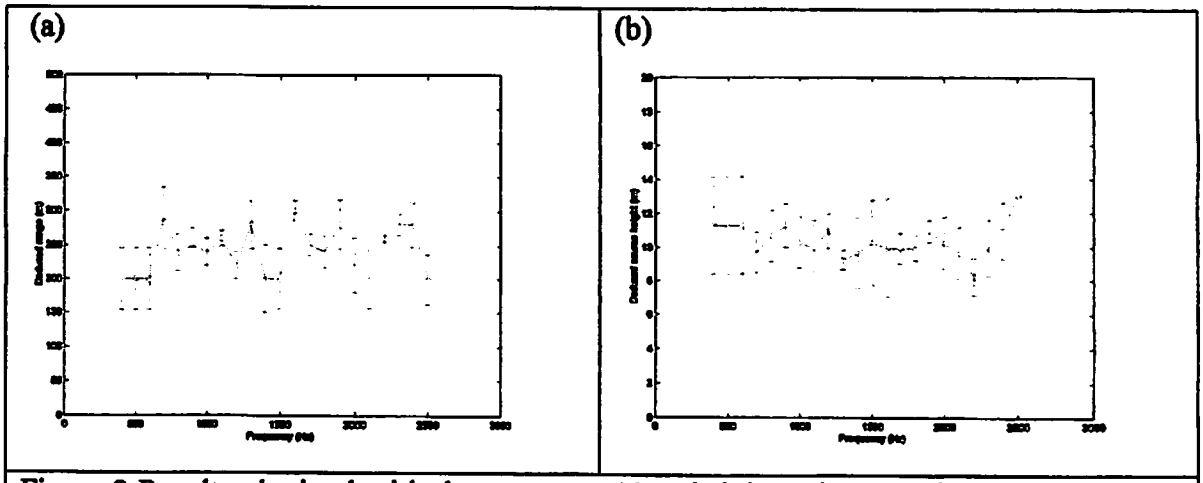

Figure 2 Results obtained with the source at 10 m height and 250 m from the receivers, using 2-minute data segments at each frequency (a) for range and (b) for height.

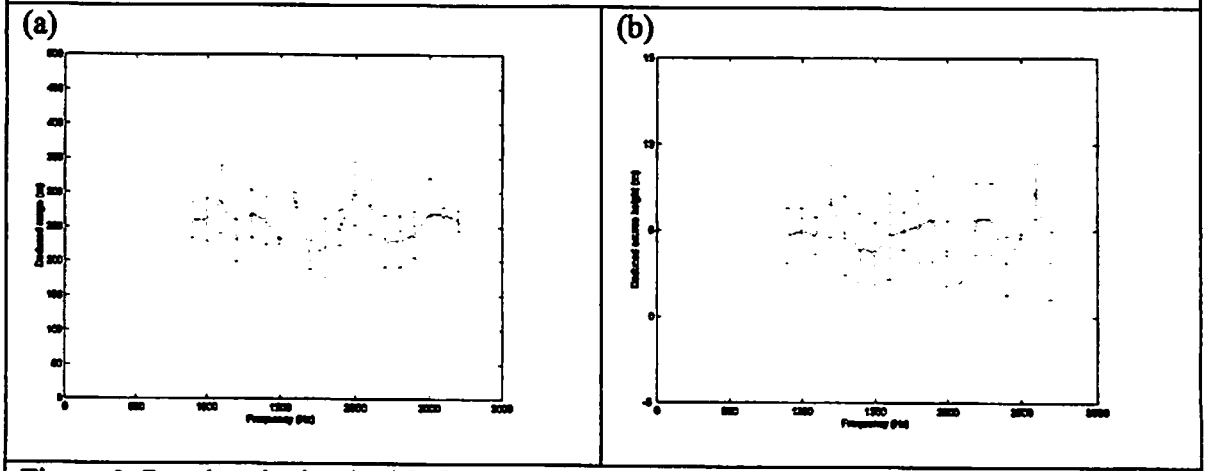

Figure 3. Results obtained with the Source at 5 m height and 250 m from the receivers, using 2-minute data segments at each frequency (a) for range and (b) for height.

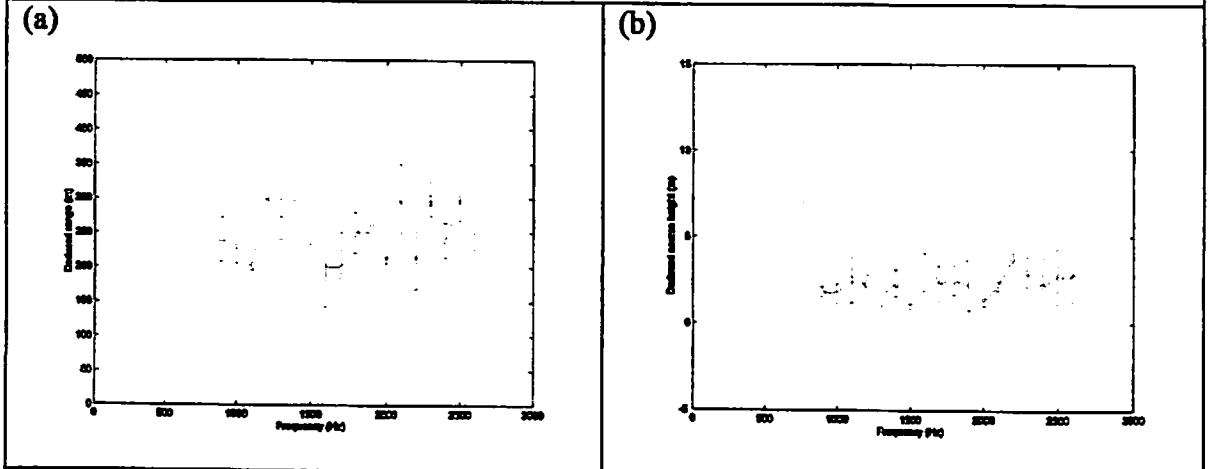

Figure 4. Results obtained with the source at 2 m height and 250 m from the receivers, using 2-minute data segments at each frequency (a) for range and (b) for height.

Figures 2-4 show the mean ranges and heights (open circles) deduced at each tonal frequency with error-bars of ± 1 S.D. indicating the uncertainty of estimation at each frequency. For a range of 250 m and source heights of 10, 5 and 2 m, respectively, the frequency-averaged source ranges, heights and bearings and corresponding standard deviations deduced from GEILA, using 2 minute segments of time series data, are $r_1' = 240 \pm 35\,\text{m}$, $255 \pm 25\,\text{m}$ and $246 \pm 39\,\text{m}$, $z_s' = 10.4 \pm 2.0\,\text{m}$, $4.5 \pm 3.0\,\text{m}$ and $2.4 \pm 1.2\,\text{m}$, $\vartheta' = 87 \pm 35°$, $78 \pm 36°$ and $74 \pm 42°$. Under rapidly changing atmospheric conditions, it might be preferable to use time series data sampled over shorter periods of time. In the trials reported here, slightly more accurate source locations and reduced standard deviations have been obtained using 10 second segments of time series data. With these shorter sampling periods the results are $r_1' = 240 \pm 30$, 242 ± 24 and $245 \pm 35\,\text{m}$, $z_s' = 10.4 \pm 1.5$, 4.4 ± 2.5 and $2.4 \pm 1.0\,\text{m}$, $\vartheta' = 87 \pm 25°$, $78 \pm 30°$ and $74 \pm 28°$. Figures 5-7 show the ranges and heights deduced at each tonal frequency with error-bars using 10 second segments of data.

It is noted from Figures 2-7 that the means and uncertainties vary with frequency. The large errors in the means near 1500 Hz and 2800 Hz correspond to the dips in the level difference spectra (see Figure 8). On the other hand, at frequencies near 900 Hz and 2 kHz, the peaks in the level difference spectra give rise to relatively accurate source location. The error bars tend to be largest for the highest source location. These variations of means and error bars with frequency suggest that both turbulence and signal-to-noise affect the performance of GEILA. Turbulence has most effect in the frequency ranges of the ground effect dips and for the highest source location. Furthermore, the signal-to-noise ratio is worst in the vicinity of the ground dips.

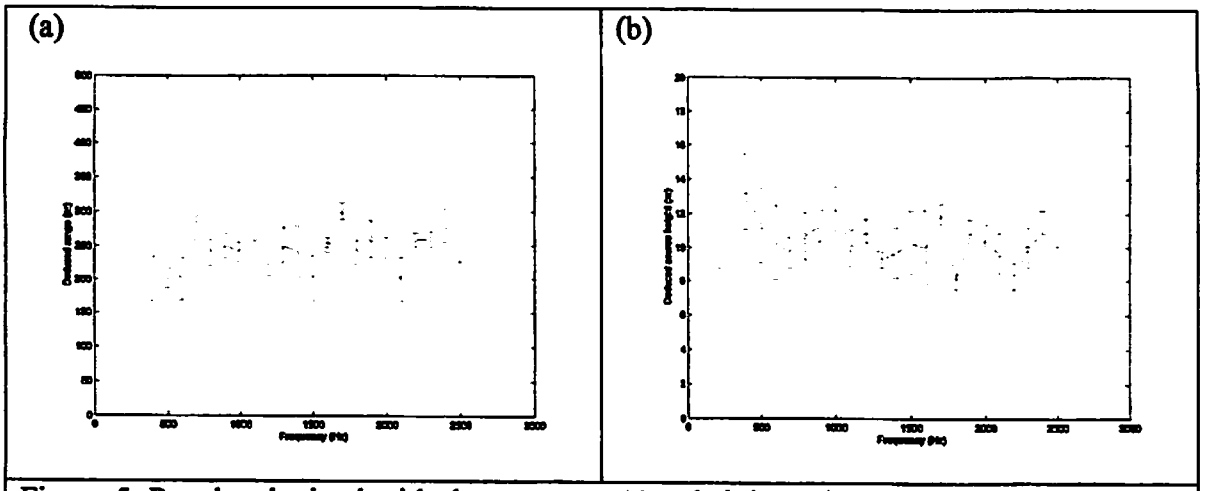

Figure 5. Results obtained with the source at 10 m height and 250 m from the receivers, using 10-second data segments at each frequency (a) for range and (b) for height.

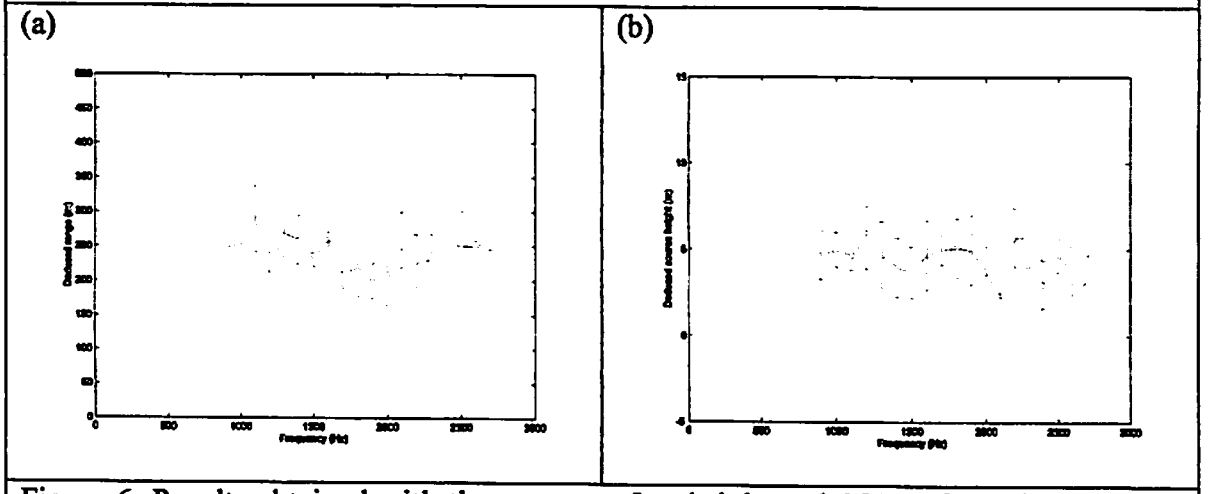

Figure 6. Results obtained with the source at 5 m height and 250 m from the receivers, using 10-second data segments at each frequency (a) for range and (b) for height.

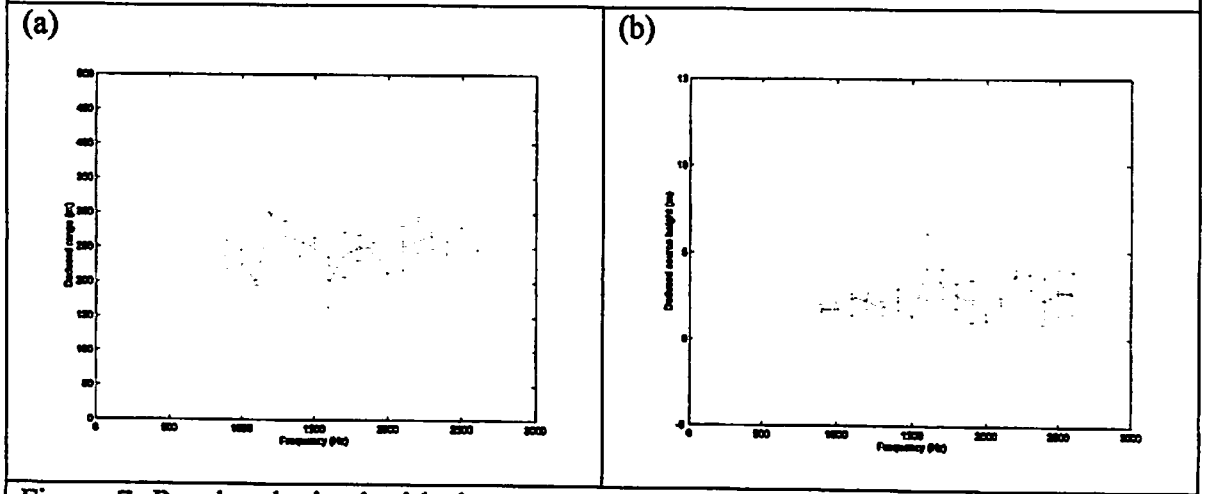

Figure 7. Results obtained with the source at 2 m height and 250 m from the receivers, using 10-second data segments at each frequency (a) for range and (b) for height.

Figure 8 shows example comparisons between measured the sound level difference spectra sampled over consecutive periods of 2 minutes and 10 seconds respectively and those predicted using the values deduced from GEILA. There is better agreement between predictions and data sampled over a period of 10 seconds than with data sampled over a period of 2 minutes. Nevertheless, if the atmosphere is relatively stable and the sound speed profiles in the direction of propagation are not varying rapidly, reasonable results are obtained with 2 minute segments of time series data.

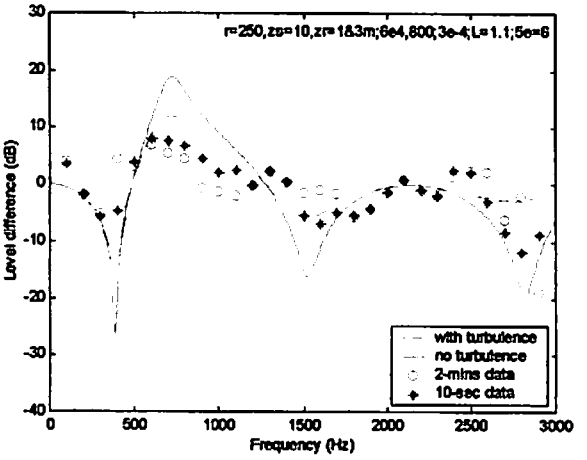

Figure 8. Comparison between the spectrum of the level difference between microphones at 1 and 3 m height predicted using the values deduced from GEILA and the UH data sampled over periods of 2 minutes (open circles) and 10 seconds (asterisks). The continuous and broken lines represent predictions without and with turbulence respectively.

The *effective* ground impedance parameters deduced from GEILA are a function of frequency and they lie in the ranges $\sigma_e' = 7\times10^3$ to 6.5×10^4 Pa s m^{-2} and $\alpha_e' = 800$ to 950 m^{-1} at frequencies between 100 Hz and 3000 Hz. The parameters deduced from short-range measurements were $\sigma_e' = 4.6\times10^4$ Pa s m^{-2} and $\alpha_e' = 960$ m^{-1}. The *effective*

normalized sound velocity gradients deduced from GEILA are between 1.4×10^{-4} and 4.4×10^{-4} m^{-1}.

These results, for *effective* sound velocity gradient deduced acoustically from GEILA, are comparable with those obtained independently from meteorological measurements.

IV. AMBIGUITY SURFACES

Multiple frequency averaging methods are required to improve the peak to side lobe ratio of the ambiguity surfaces especially where the arrays are relatively short. Conventionally a broadband coherent processing method[6] is used to generate ambiguity surfaces for a set of frequencies f_m. Figure 9(a-c) shows examples of the ambiguity surfaces obtained in this way from the UH trial data using twenty-one frequencies between 500 and 2500 Hz.

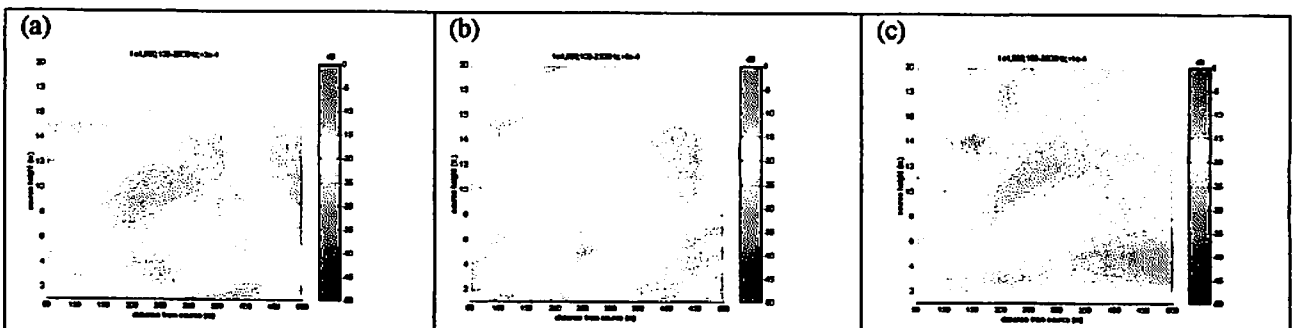

Figure 9 Ambiguity surfaces obtained from broadband coherent processing with a source at 250m range after averaging over 21 narrow bands between 500-2500Hz for source heights of (a) 2 m (b) 5 m and (c) 10m.

Alternatively, the source location results may be obtained using a two-stage frequency averaging method. First ambiguity surfaces are averaged for frequency bins of $f_m \pm \Delta f$, where $\Delta f = 5$ Hz. Each of the bins consists of eleven narrow bands with a

bandwidth of 1 Hz. Figure 10(a-c) shows examples of the ambiguity surfaces obtained from the UH trial data using this alternative averaging method. Figure 10 shows better peak to side lobe ratios than those presented in Figure 9. Then the source location results are averaged over twenty-two such frequency bins at 100 Hz intervals between 400 Hz and 2500 Hz.

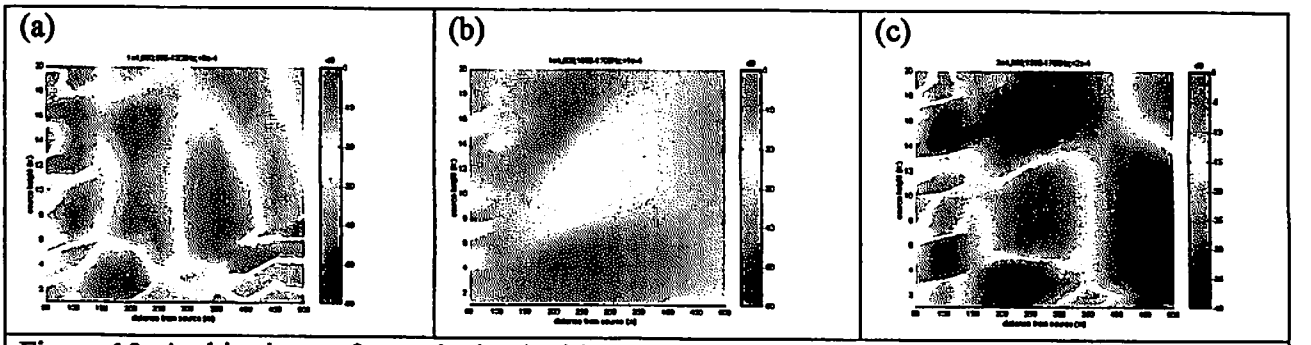

Figure 10. Ambiguity surfaces obtained with the source at 250m range (a) for 2m height and the frequency band 1000 ± 5 Hz (b) for 5m height and the frequency band 1700 ± 5 Hz (c) for 10m height and the frequency band 1700 ± 5 Hz.

V. SUMMARY

The performance of a ground effect inversion and location algorithm (GEILA), using a nine-element microphone array has been examined. For an elevated stationary source at ranges out to 250 m over flat grassland in turbulent atmospheric environments, the source locations deduced from the acoustical measurement data agree tolerably with the true source positions. The accuracy of the performance of the algorithm has been found to depend upon the length of the segments of time series data used in the processing. 10 second segments give more accurate results than 2 minute segments. The statistical distributions of source location results show some frequency dependence. The largest errors in the means have been found at frequencies that correspond to the dips in

level difference spectra and seem to be associated with signal-to-noise ratio. Atmospheric turbulence affects the standard deviations of the results particularly for the highest source locations. Two multi-frequency averaging methods have been examined and compared. Better peak to side lobe ratios in ambiguity surfaces have been found where an alternative to conventional broadband coherent processing is used.

ACKNOWLEDGMENT

This work was carried out as part of Technology Group 01 of the MoD Corporate Research Programme.

REFERENCES

1. Q. Wang, K. Attenborough and R. Brind, "Elevated source location in the atmosphere," Proceedings of the 9th LRSPS, (The University of Mississippi) 89-107 (2000).
2. Q. Wang, K. Attenborough and R. Brind, "Localization of elevated and ground sources in the atmosphere," Proceedings of the 8th ICSV, Hong Kong 1275-1280 (2001).
3. Q. Wang, K. Attenborough and R. Brind, "Source localization by ground effect," Proceedings of the 17th ICA, Rome, (2001).
4. Q. Wang, K. Attenborough and R. Brind, "Source localization in the presence of atmospheric turbulence," Proceedings of the IOA Spring Conference, Salford, Institute of Acoustics, St. Albans, UK, 2002.
5. K. Attenborough, "Acoustical impedance models for outdoor ground surfaces," J. Sound Vib. **99**, 512-544 (1985).
6. R. M. Hamson and M. A. Ainslie, "Broadband geoacoustic deduction," J. Computation Acoust., **6**, 45-59 (1998).

Secondary Sonic Boom in a Stratified Atmosphere and Related Issues

Kaouri K, Allwright D.J., Dallois L.[1]

Oxford Centre for Industrial and Applied Mathematics, Mathematical Institute,

Oxford University, 24-29 St Giles', Oxford OX1 3LB, UK.

kaouri@maths.ox.ac.uk

Introduction

Many studies have been done on sonic boom but still not much is known about *Secondary Sonic Boom* (SSB). In contrast to the primary boom, the SSB is caused by shock waves that travel for some time *above* the flight altitude,"reflect" under certain conditions and subsequently reach the ground. SSB is very different to primary boom: it is weaker and has lost most of the high frequency content but it is of longer duration and affecting a much larger ground area. The most likely reason for these differences is the long range involved in SSB propagation (at least $300km$), over which effects that are negligible over short ranges may become important. The SSB presence is affected by wind, inhomogeneity and/or other effects in the atmosphere. Without wind, the SSB can only be thermospheric, i.e. caused by a shock wave that reflects in the thermosphere (around or above $100km$). With wind, the shock wave can also reflect from lower stratospheric altitudes(at around $50km$). The limited literature on SSB is summarised on Slide 5. It is not conclusive and in places even contradictory; much more research on SSB is required.

In this work we consider still, stratified atmospheres, neglecting the wind presence. The calculations for obtaining the Mach surface (the surface of influence of the boom), where the aircraft is modelled as a point source and for arbitrary stratification, are presented in Slide 6. Since the SSB shocks are very weak, employing the linear potential flow theory leads to a good approximation of the SSB geometry.

Steady Flight: Aerodynamic frame

We first assume a constant aircraft velocity. It is therefore natural to use the aerodynamic frame, moving with the aircraft (see Slide 7 for the relevant calculations). In this frame the Prandtl-Glauert parameter $B = \sqrt{V^2/c^2 - 1}$ is defined. We also define the bicharacteristics (BICHs): these are curves on the Mach surface on which the boom propagates (for a schematic see Slide 7). In Slide 8, we outline that we parametrize BICHs by their azimuthal angle ϕ and a parameter s, a function of distance along them. We first consider a typical atmospheric sound speed profile (see Slide 9, left picture). We determine numerically the bicharacteristics, assuming perfect reflection of the boom at the ground. In Slide 9, the right picture displays four of the bicharacteristics in our calculations. Two of them enter the

thermosphere, reflect there, and then reach the ground. At the reflection height we see cusps. Such cusps indicate places of strong focusing. The other two bicharacteristics shown are trapped in the stratosphere, due to the waveguide nature of the atmospheric profile, and never reach the ground. In Slide 10, we present the boom carpet, obtained by locating the trace of the bicharacteristics on the ground. The leftmost curve corresponds to the primary boom carpet formed by bicharacteristics, which started from the aircraft downwards and went directly to the ground. The first curve to the right of the primary boom carpet is the "direct" SSB carpet, formed by bicharacteristics which were emitted upwards from the aircraft, reflected in the thermosphere, and subsequently reached the ground. The rightmost curve is the "indirect" SSB carpet, formed by the primary carpet bicharacteristics that reflected off the ground, propagated upwards and reflected also in the thermosphere. We see that the SSB carpet is disjoint from the primary carpet as we expect from the existence of trapped bicharacteristics (the same feature leads to all carpets having finite extent), and of much larger extent.

We then consider the model stratified profile $c(z) = c_0\sqrt{1/(1-bz)}$, where z is the altitude. With $c_0 = 1, b = 1/2$, this profile corresponds to the Prandlt-Glauert parameter $B^2 = 1 - z$ (see Slide 11), which is linear in z. The bicharacteristics, the Mach surface (and hence the carpet) can be determined analytically (after long calculations). In Slide 12, we plot many BICHs so that the Mach surface is outlined, and use our analytical expression to plot the corresponding carpet. Interesting features appear, such as caustics and cusps. Our analytical results shed light on the results found for the typical atmospheric profile. In particular, in Slide 13 we look into the $y = 0$ section of the Mach surface in more detail. For $B^2 = 1 - z$, the linear potential equation (Slide 7) is a mixed-type Tricomi equation; it is elliptic for the subsonic region $z > 1$ ($\Rightarrow B^2 < 0$), parabolic at the sonic line $z = 1$ ($\Rightarrow B^2 = 0$) and hyperbolic in the supersonic region $z < 1$ ($\Rightarrow B^2 > 0$). The boom reflects off the sonic line, passing through a Tricomi type cusp. Therefore, our analytical paradigm illuminates the local behaviour at the reflection height in the typical atmosphere case where a linear approximation can be taken for B^2.

Unsteady Flight: Aeroacoustic frame

However, the aerodynamic frame can be employed only in the case of steady flight. For unsteady flight the aeroacoustic frame has to be used and the Mach surface is obtained as the envelope of wavefronts. It can alternatively be obtained as the locus of boomrays, the special rays emitted at an angle to the flight path that is equal to the complement of the Mach angle $\theta_M = \arcsin(c_0/M)$ (see Slide 3). Considering first a stationary source, for the profile $c^2 = 2/(2-z)$ above, the ray conoid, the surface of influence of the source, is immediately obtained through the coordinate transformation $X \to t/2, y \to \sqrt{x^2+y^2}/2, z \to z/2$ applied to the Mach surface expression in the $B^2 = 1 - z$ case. For clarity, we

concentrate on the $y = 0$ section of the ray conoid, and we plot selected wavefronts in Slide 14, right picture. We see cusps; their locus is a caustic. We stress that these cusps and the Tricomi cusp in Slide 13 are of different nature. The former cusps are purely a consequence of the stratification, whereas the Tricomi cusp is intimately related to the focusing and reflection of the boom on the sonic line. In Slide 15, considering a steady flight, we see the Tricomi cusp forming from a coalescence of wavefronts; the stratification cusps form a locus unrelated to the boom. In the same slide, we refer to our analytical calculations that demonstrate the validity of the aeroacoustic framework by calculating the envelope of the wavefronts, and finding it in agreement with the Mach surface in Slide 11.

Amplitudes

For the same model profile with $c_0 = b = 1$, we also present some preliminary calculations on amplitudes in two space dimensions (x, z). We consider a monochromatic, stationary, point source and employing methods of linear wave propagation, we show that the wave field can be obtained everywhere mainly analytically (Slide 16) and that the effect of diffraction renders the amplitude on the caustic finite as expected. A picture of the wavefield where these features are clearly visible is found in Slide 17. For this model profile our method is a more accurate alternative to the existing methods coupling ray theory away from the caustic to an asymptotic treatment of diffraction, in the vicinity of caustics.

Curvature and Coriolis effects

Finally, since SSB is a long-range phenomenon, it is probable that coriolis and curvature effects, rightly neglected in primary boom studies, may become significant. It is easy to see that Coriolis effects are not important; the time of SSB travel is significantly smaller than 1 day, the period of earth rotation. However, curvature effects do become significant for SSB. We propose a simple way that will account for these effects to first order (see also Slides 18 and 19): if a "flat-earth" ray-propagation code is used then the sound speed profile should be taken as $c_{\text{flat}}(z) = \dfrac{c(z)}{1 + z/R}$, where $c(z)$ is the actual profile as a function of the altitude z (as measured above the earth's surface), R is the radius of the earth.

Acknowledgements: Dr P.J. Dellar and Dr J.R. Ockendon (F.R.S.), both at Oxford University, for valuable discussions. *The research of the first and third author has been supported by the Sonic Boom European Research Programme (SOBER).*

---

[1] currently at Ecole Centrale Lyon, 36 Avenue G. Collongue, 69134, Ecully, France

Secondary Sonic Boom in a Stratified Atmosphere and Related Issues

K. Kaouri, D.J. Allwright, L. Dallois

Acknowledgements:

P.J. Dellar, J.R. Ockendon

Centre for Industrial and Applied Mathematics, Oxford University

24-29 St Giles', Oxford, OX1 3LB, UK.

kaouri@maths.ox.ac.uk

Research partially supported by the Sonic Boom European Research Programme (SOBER).

Project leader: F. Coulouvrat

Introduction

Sonic Boom: Shock wave generated by any object moving faster than the sound it generates (and reaching the ground).

- Sonic Boom research motivated by supersonic aviation.
- 1969-to date: UK-France Concorde (uneconomical)
- Feasibility studies for Concorde successor

Research Challenges

Modelling of Sonic Boom for precise understanding of propagation in the atmosphere leading to accurate prediction of position and strength on the ground.

Secondary Sonic Boom (SSB)

SSB very different to primary boom

- Upward propagating shock waves
- shock waves "reflect" due to atmospheric inhomogeneity, wind and other effects and reach the ground.
- No wind: SSB from thermosphere (~180km)
- With wind: SSB can also come from stratosphere (~50km)

Outline of this work

---investigate thermospheric SSB geometry

---investigate some aspects of amplitude

---discuss Coriolis and curvature effects

Secondary Sonic Boom Literature

- 1978: Donn, W.L (Amer.Sci.)
- 1978: Liszka, L. (JASA)
- 1979: George and Kim (J. Aircraft)
- 1980: Rickley, E.J. and Pierce, A.D. (FAA)
- 1980: Rogers, P.H. and Gardner, J.H (JASA)
- 1991: Robinson, L.D.: (PhD thesis, Texas Austin)
- 1995: Haglund, G.T. and Poling, H.W. (Boeing)
- 2002: Allwright, D.J., Dallois, L., Kaouri, K (SOBER Report)

not sufficient and in places contradictory

Secondary Boom(SB) Geometry

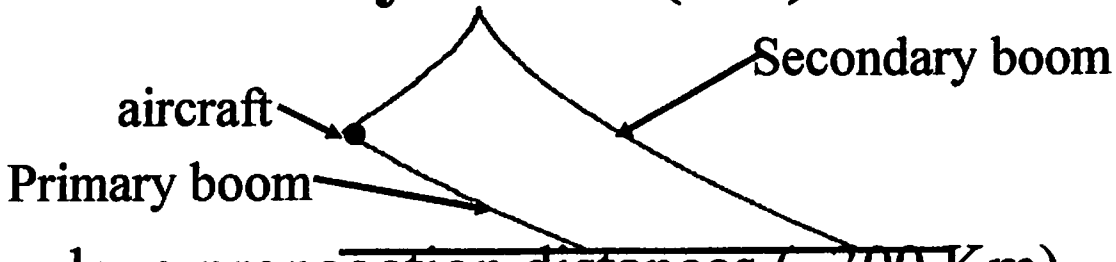

•SB involves long propagation distances (~300 Km).

•Sonic Boom is weak shock:

shock position ~ linear theory characteristics

•Euler equations reduce to the linear potential equation

$$\phi_{tt} = c^2(\phi_{xx} + \phi_{yy} + \phi_{zz}) + \delta(x - x_0(\tau))\delta(y - y_0(\tau))\delta(z - z_0(\tau))\delta(t - \tau)$$

The characteristic surface $\Gamma = 0$ obeys the eikonal PDE

$$\Gamma_t^2 = c^2(\Gamma_x^2 + \Gamma_y^2 + \Gamma_z^2)$$

•When we solve the eikonal (Charpit's method), we get rays, boomrays and (by "gluing") ray conoids (wavefronts)

•**Envelope of Wavefronts is the Mach surface**

Carpet: intersection of Mach surface with the ground

Bicharacteristics

- parametrised by the initial azimuthal angle ϕ

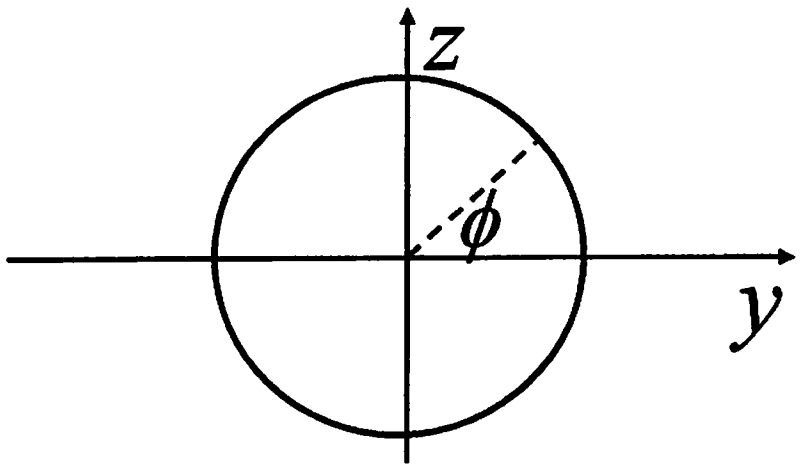

- and s, for distance along the characteristic

Note: Same Mach angle for all bicharacteristics

The secondary sonic boom carpet is

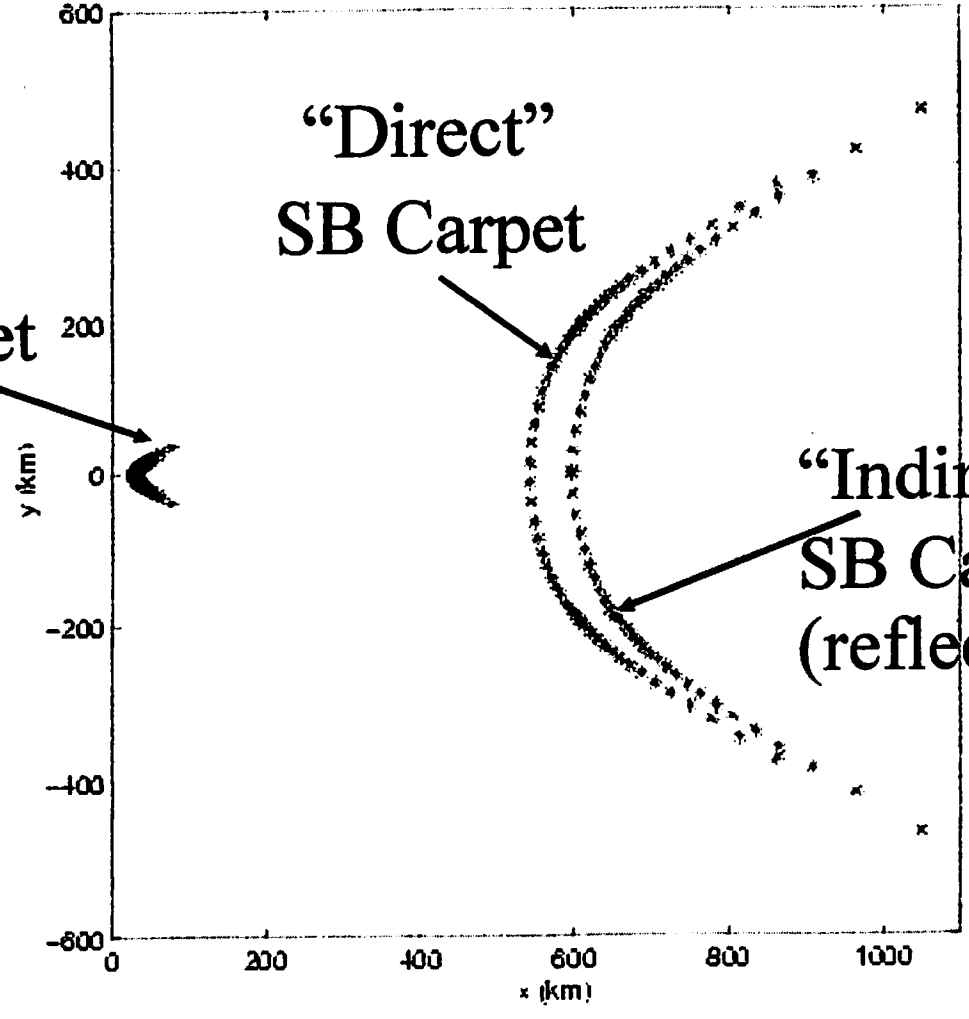

- Secondary and Primary Boom are disjoint due to trapped bicharacteristics
- SSB carpet much larger

Model atmosphere: $B^2 = 1 - z$

Sound speed profile : $c = \sqrt{2/(2-z)}$, Velocity : $V = \sqrt{2}$

Analytical expression for bicharacteristics (s parameter along them):

$$X(s,\phi;\theta_M) = \frac{2}{3} p_0^3 s^3 + 2 r_0 p_0 s^2 - 2 p_0 s$$

$$y(s,\phi;\theta_M) = -2 q_o s$$

$$z(s,\phi;\theta_M) = -p_0^2 s^2 - 2 r_0 s$$

where $(p_0, q_0, r_0) = (\cos\theta_M, \sin\theta_M \cos\phi, \sin\theta_M \sin\phi)$

Eliminate s, ϕ and θ_M and obtain (long analysis):

Mach surface $9X^2 = (2-z)(4-4z+4z^2+3y^2) \pm 8(1-z-y^2/4)^{3/2}$

Note **positive** and **negative** branches, 3/2 typical power

Unsteady flight: need Aeroacoustics frame

$c = \sqrt{2/(2-z)}$: Stationary source

Using the transformation $X \to Pt,\ z \to Qz,\ y \to \sqrt{(Qx)^2 + (Qy)^2}$

in the Mach surface expression (Slide 11), the ray conoids are

$$9(Pt)^2 = (2-Qz)(4-4Qz+4(Qz)^2+3(Qx)^2) \pm 8(1-Qz-((Qx)^2+(Qy)^2)/4)^{3/2}, P=Q=1/2$$

Wavefronts, y=0 cut

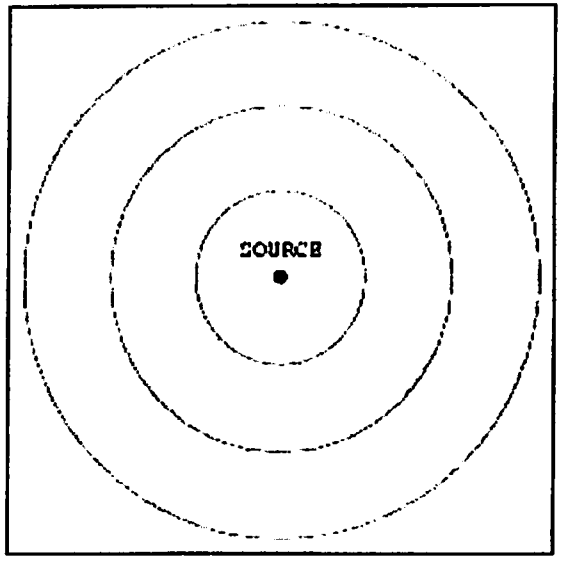

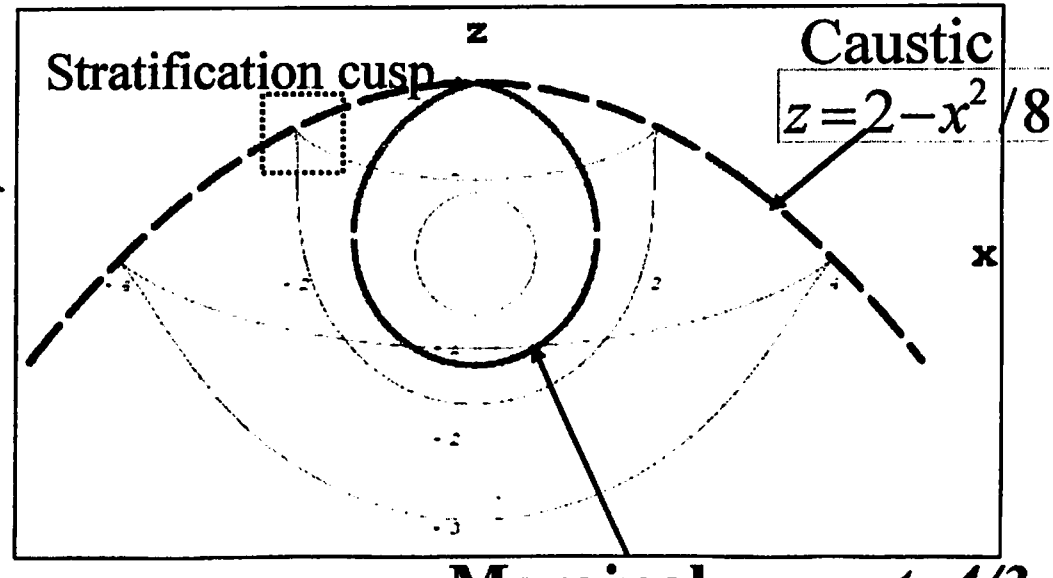

Marginal curve *t=4/3*

Amplitude: Caustic, Diffraction effects

$$\phi_{tt} = c^2(\phi_{xx} + \phi_{zz}) - \delta(x)\delta(z)e^{i\omega t}, \quad c = 1/\sqrt{1-z}$$

Monochromatic dependence $\phi = e^{i\omega t}U(x,z)$ (linearity)

- Helmholtz's equation:

$$U_{xx} + U_{zz} + \frac{\omega^2}{c^2}U = \delta(x)\delta(z)$$

P=Fourier Transform of U w.r.t x

- Airy equation:

$$\frac{d^2P}{ds^2} = sP + \delta(z)$$

$$\text{where } s = \omega^{2/3}(z - 1 + \alpha^2/\omega^2)$$

- The solution is a linear combination of Airy functions Ai, Bi

- Impose B.Cs:

1) $P \to 0$ as $s \to \infty$

2) P outgoing wave as $s \to -\infty$

3) P continuous at $s = s_{\text{SOURCE}}$

4) $\left[\frac{dP}{ds}\right] = 1$ at $s = s_{\text{SOURCE}}$

Primary Sonic Boom

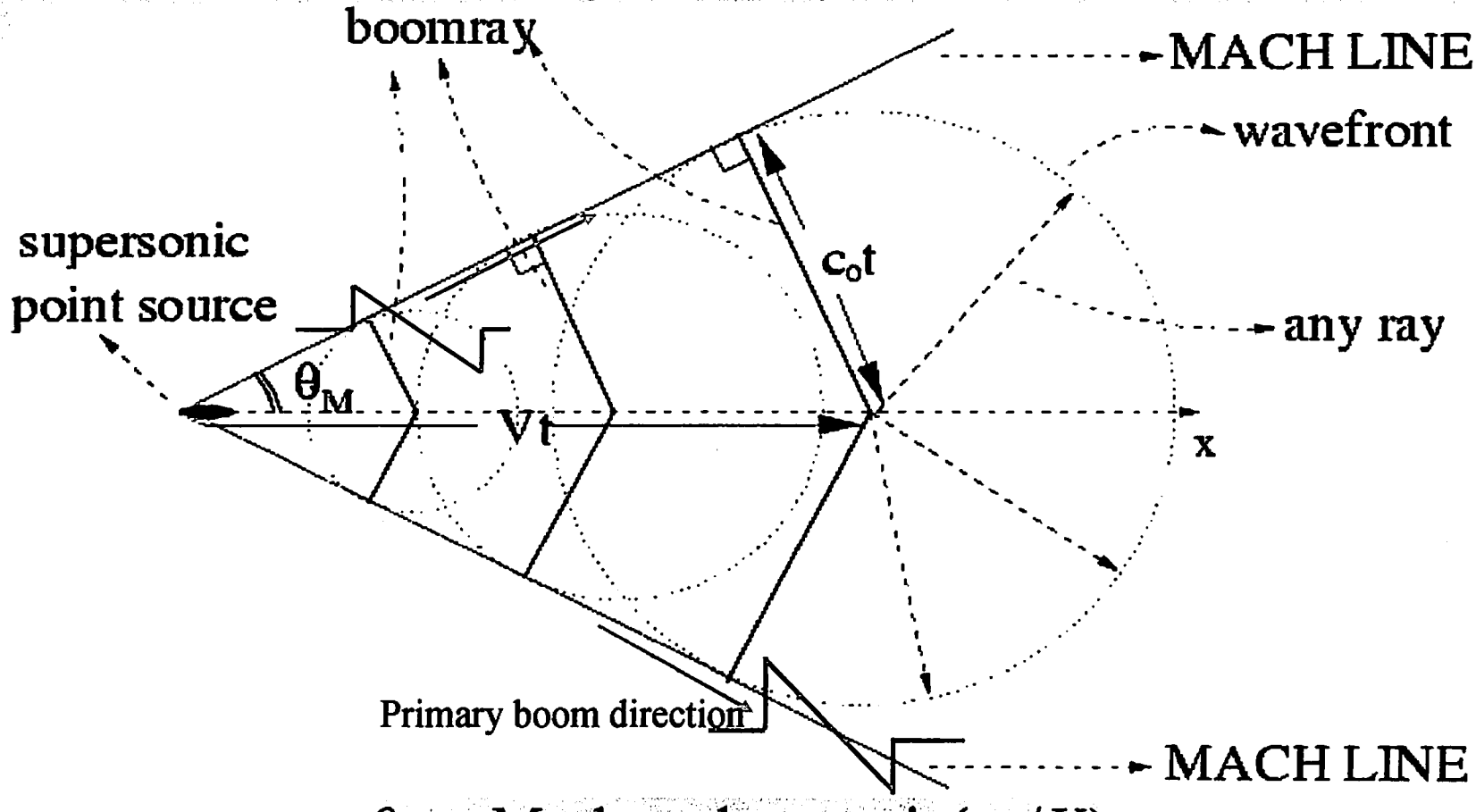

θ_M = Mach angle = $\arcsin(c_0 / V)$

- Any ray carries sound BUT only boomrays make up the boom.
- Mach lines are envelopes of (the circular) wavefronts.
- These concepts generalise to unsteady flight, nonuniform media.

Steady Flight: Aerodynamic frame

$$(x, y, z, t) \rightarrow (X = x + Vt, y, z)$$

- Frame moving with aircraft

$$B^2 \Phi_{XX} = \Phi_{yy} + \Phi_{zz} + \delta(X)\delta(y)\delta(z)$$

where $B^2 = V^2 / c^2 - 1, \Phi(X, y, z) = \int_0^\infty \phi(\tau; x, z, t) d\tau$

- The characteristic surface, $\Psi = 0$ *is* the Mach surface and obeys the eikonal PDE $B^2 \Psi_X^2 = (\Psi_y^2 + \Psi_z^2)$
- Bicharacteristics (BICHs) lie *on* the Mach surface.
- Boom propagates along bicharacteristics.

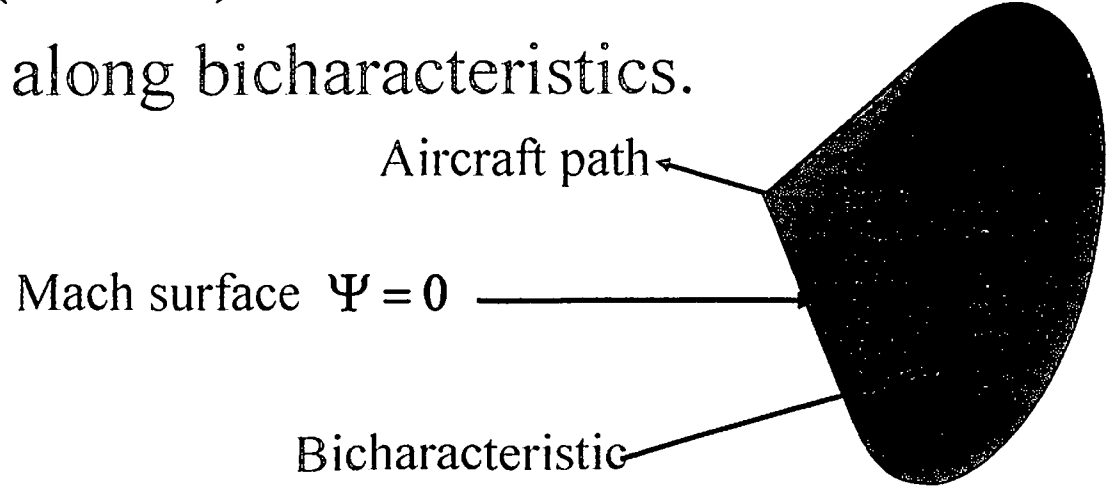

Apply to a typical atmospheric profile (no wind):

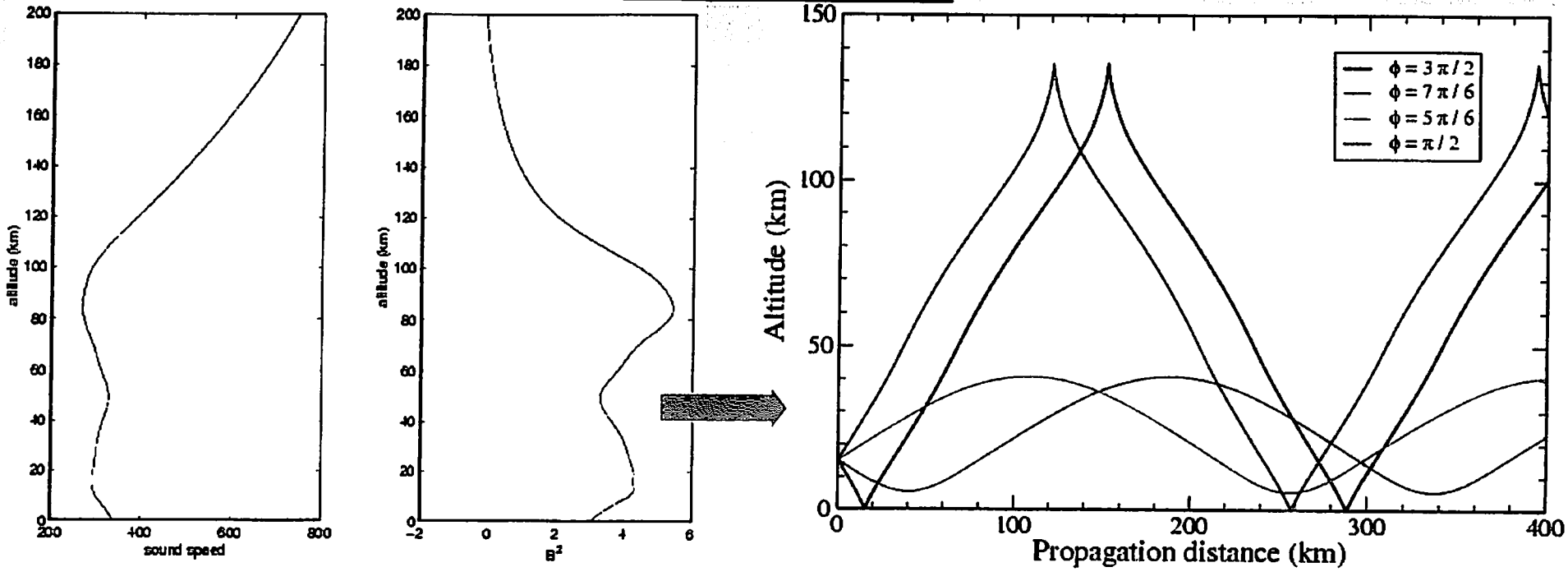

- Cusps at "reflection" height

- Waveguide nature of sound speed profile: there are trapped bicharacteristics that do not leave any trace at the ground

Recall: In windless atmosphere the secondary carpets can only be "thermospheric" (see reflection at ~170km)

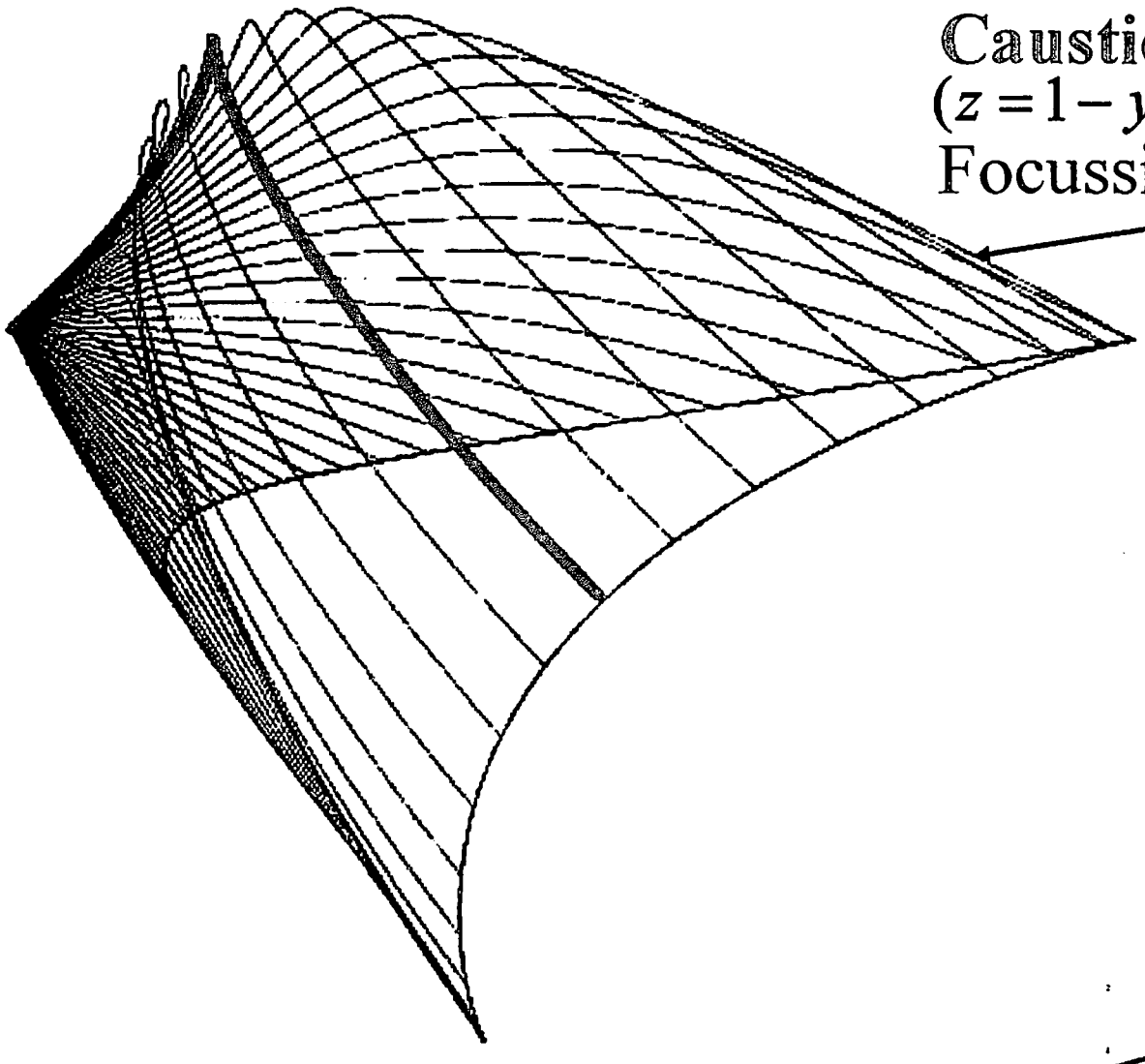

Caustic,
$(z = 1 - y^2/4)$
Focussing, bending of BICHs

Carpet

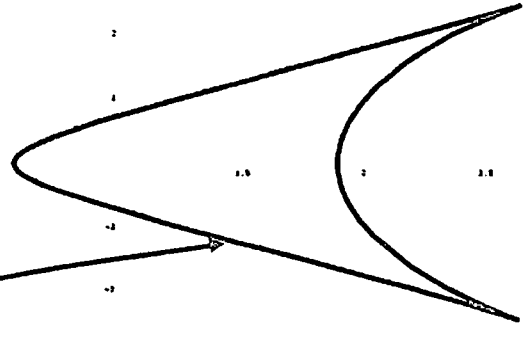

Note: Primary and Secondary Carpet joined due to downward refracting atmosphere (no waveguide)

Look details: $y=0$ section of Mach surface

Get (mixed-type) Tricomi equation: $B^2\Phi_{XX} = \Phi_{zz} + \delta(X)\delta(z)$

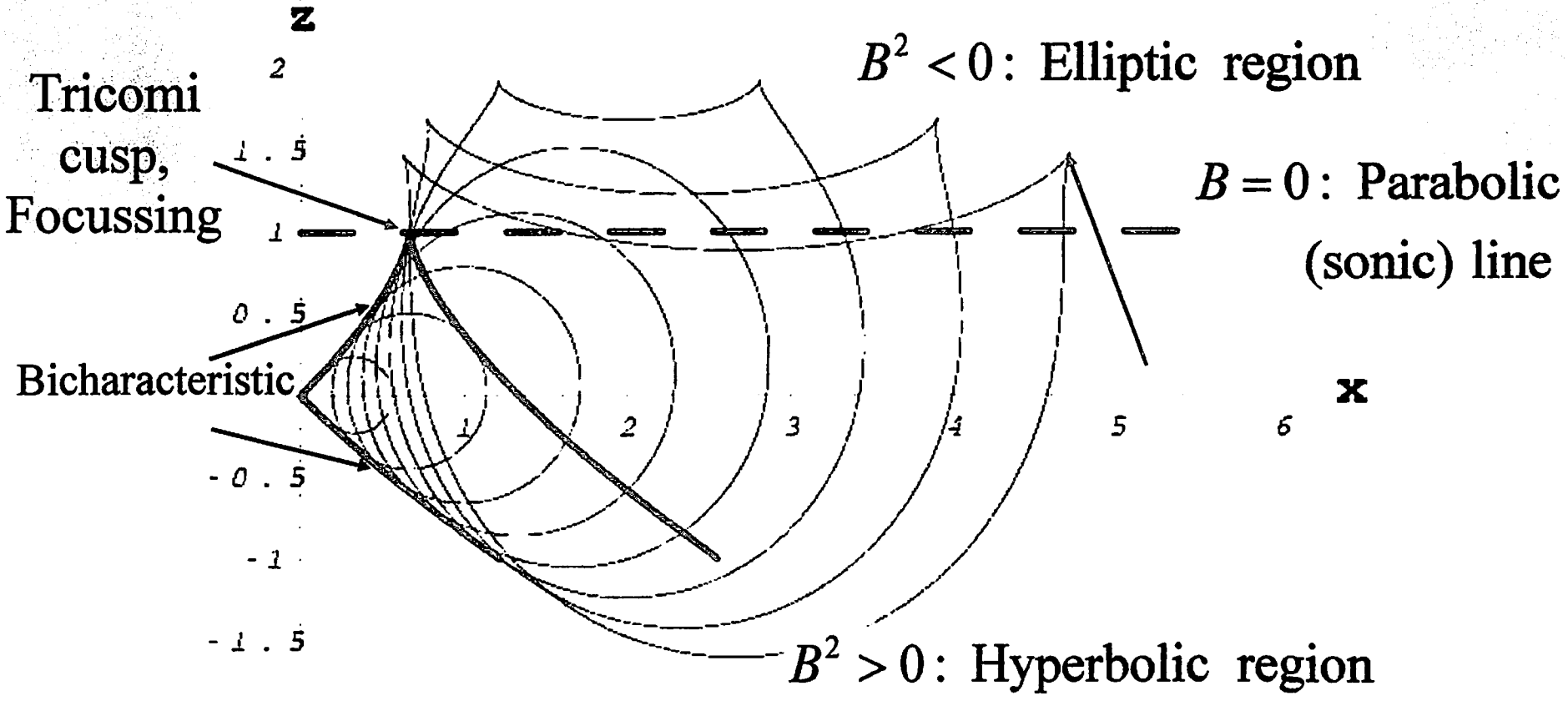

(Bi)Characteristic of Tricomi equation is Mach curve

$$9X^2 = (2-z)(4-4z+4z^2) \pm 8(1-z)^{3/2}$$

Steadily moving source

Verify Slide 11 result through aeroacoustics by taking envelope of wavefronts: indeed get

$$9(x+Vt)^2 = (2-z)(4-4z+4z^2) \pm 8(1-z-y^2/4)^{3/2}$$

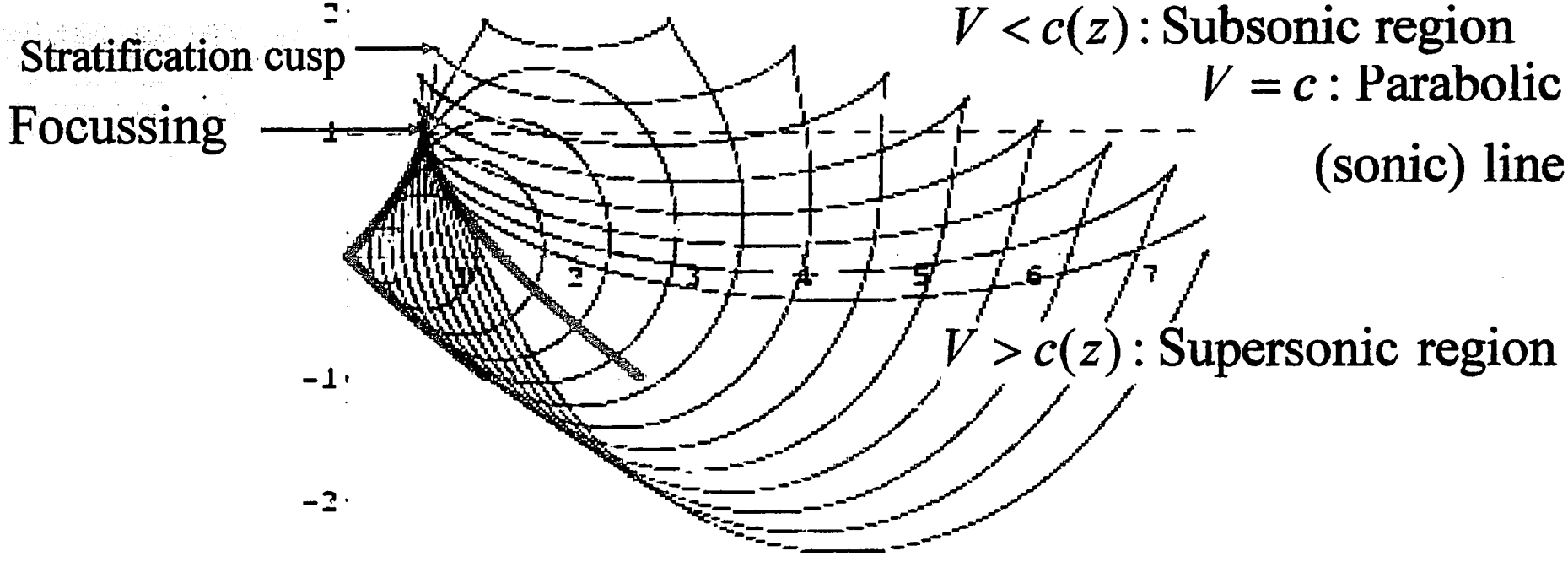

- Tricomi cusp different from stratification cusps

$$U(x,z) = \frac{1}{2\pi}\int_0^\infty P_{\text{UP}}(s, s_{\text{SOURCE}})\cos(\alpha x)d\alpha, \quad s \geq s_{\text{SOURCE}}$$

$$\frac{1}{2\pi}\int_0^\infty P_{\text{DOWN}}(s, s_{\text{SOURCE}})\cos(\alpha x)d\alpha, \quad s \leq s_{\text{SOURCE}}$$

1D Numerical Integration (Fortran) yields:

$|U|$

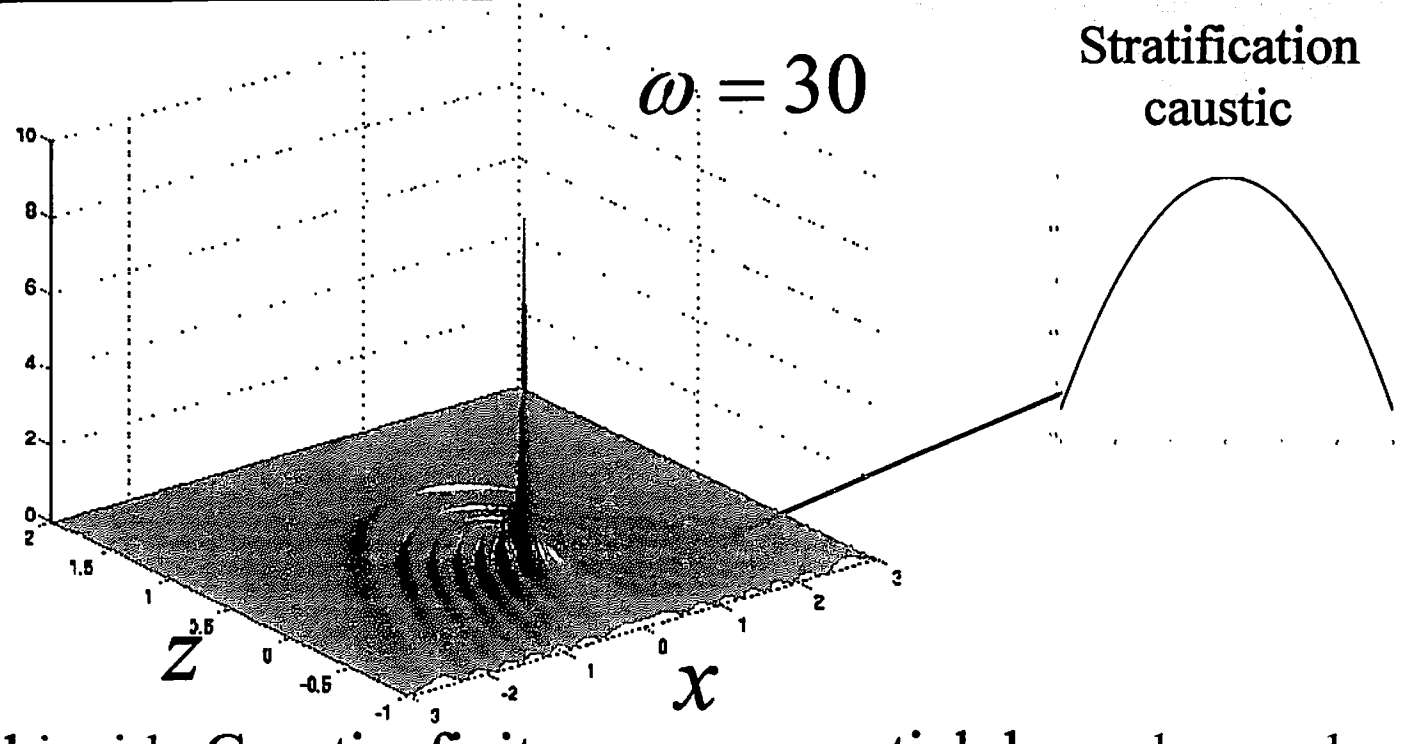

- **Wavelike wavefield** inside **Caustic, finite** on, **exponential decay** beyond
- **This corresponds to real rays** inside, **complex rays** beyond **caustic** (steepest descents analysis).

Earth Curvature

The exact curved-earth problem

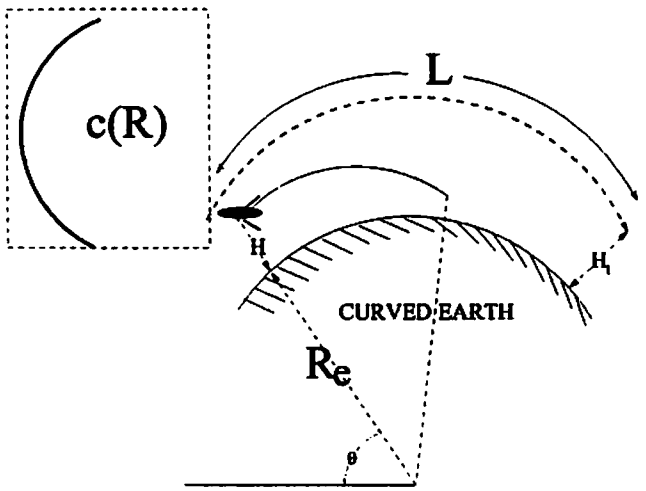

is approximated with the flat-earth problem

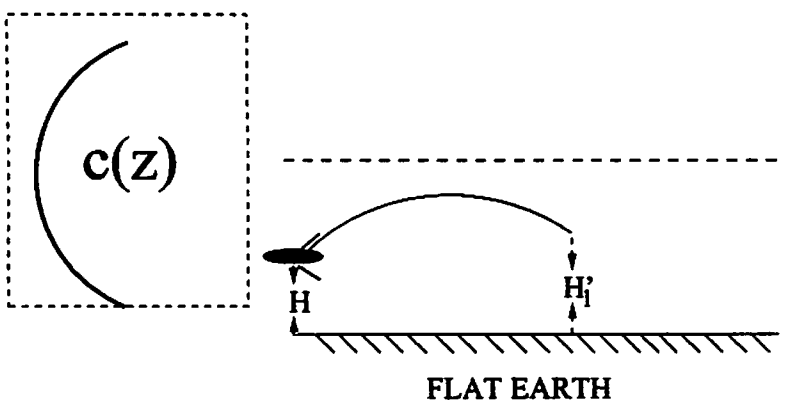

$1/R_e \longrightarrow 0$

Long-Range Propagation

Approximation not sufficient: in a homogeneous atmosphere hit horizon after $L_0 = \sqrt{(2R_eH)} \sim$ 300Km

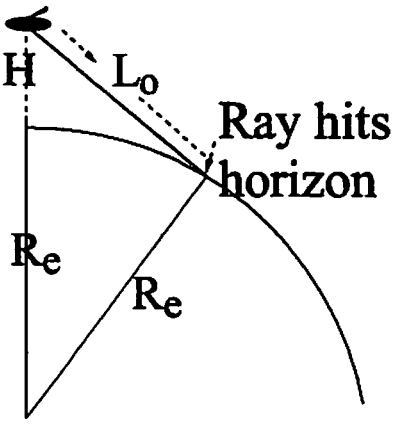

- Used 2D Ray Theory to find first correction:

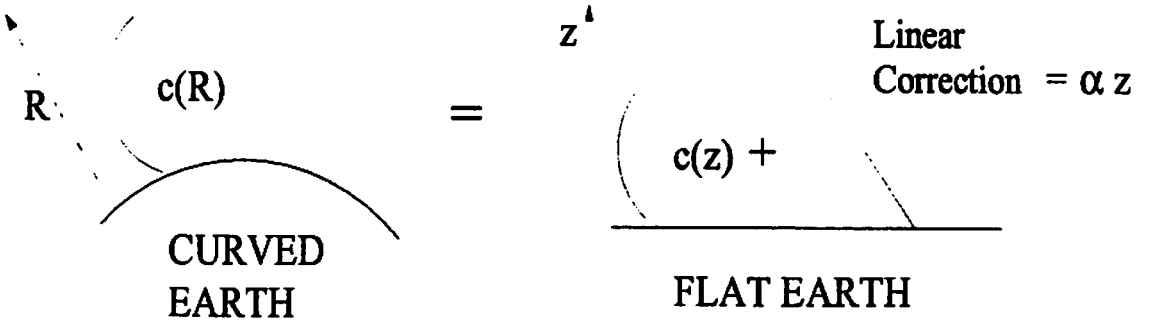

SUMMARY

- **Geometry of Secondary Sonic Boom**

(real and model atmospheres)

(linear waves theory)

- **Amplitude**:

$c = 1/\sqrt{1-z}$, diffraction effects at caustic, stationary source

(linear waves)

- Curvature and Coriolis effects discussion

10th International Symposium on Long Range Sound Propagation
Grenoble, 12-13 September 2002

SOUND PROPAGATION THROUGH FORESTS WITH REALISTIC METEOROLOGICAL CONDITIONS: THEORY AND EXPERIMENT

Jérôme DEFRANCE, Nicolas BARRIERE and Eric PREMAT

Centre Scientifique et Technique du Bâtiment
24, rue Joseph Fourier
38400 Saint Martin d'Hères – France
Tel. +33 (0)4 7676 2525 Fax. +33 (0)4 7644 2046

j.defrance@cstb.fr

Abstract

Recent studies have shown that a forest strip along a road or a railway could be a good solution to reduce noise for residents located at the other side of the forest strip - especially at night when a temperature inversion occurs. In this paper results from numerical calculations and outdoor measurements are compared for different meteorological situations. The numerical method is based on the Green's Function Parabolic Equation in which an equivalent wavenumber is considered for the propagation under the canopy in order to take into account the diffusion by the trunks. The experimental values have been achieved during an important measurement campaign in a pine forest. For different range dependent sound speed profiles (downward, homogeneous or upward situations), the acoustic attenuation due to the forest (compared to a plain configuration) is discussed depending on the receiver location behind the trees strip.

1. Theoretical approach

1.1. Propagation with the GFPE

In order to precisely bring to the fore the effect of meteorology on sound propagation through forests, a 2D GFPE code has been developed [1] and adapted to road traffic noise situations [2] where road line sources are modeled as series of equivalent point sources of height 0.5 m. In the case of non-uniform wind conditions, GFPE calculations are made for each equivalent source by projecting the wind profile on the source-receiver direction. For each equivalent source, the acoustic field is initialized by an analytical expression [3] on a vertical axis containing the source point, and then propagated step by step to the receiver.

The expression of the propagation equation is given by [2, 3, 20]:

$$\Psi(r+\Delta r,z)=\left\{\frac{1}{2\pi}\left[\int_{-\infty}^{+\infty}\left(\tilde{\Psi}(r,k_z)+R(k_z)\tilde{\Psi}(r,-k_z)\right)\times e^{i\Delta r\left(\sqrt{k_0^2-k_z^2}-k_0\right)}e^{ik_z z}dk_z\right]\right\}$$
$$+2i\beta\times\tilde{\Psi}(r,\beta)\times e^{i\Delta r\left(\sqrt{k_0^2-\beta^2}-k_0\right)}e^{-i\beta z}\Bigg\}e^{i\frac{\Delta r\,dk^2(z)}{2k_0}} \quad (1)$$

where:

Ψ is the acoustic field, z is the altitude,

r is the horizontal distance between source and receiver, Δr the calculation step,

$\beta = \frac{-k_0}{Z_g}$ is the surface wave pole in the plane wave reflection coefficient $R(k') = (k' Z_g - k_0)/(k' Z_g + k_0)$,

$\tilde{\Psi}(r,k_z) = \int_0^\infty \exp(-ik_z z')\Psi(r,z')dz'$ is the Fourier transform of Ψ,

$k(z)$ is the wavenumber at altitude z and k_0 the reference one (corresponding to the homogeneous atmosphere case).

Equation 1 is composed of three terms which represent respectively the direct wave, the ground reflected wave and the surface wave.

1.2. Multi-diffusion model

The effect of sound diffusion by a tree trunk may be represented by the scattering from an infinite rigid cylinder [4]. The diffusion by an incident plane wave is characterized by the radius a of the cylinder and the wavenumber k. The directivity and the intensity of the diffused energy depends on the value of ka. Embleton approach [5] derived from Twersky's theory of diffraction [6] consists in assessing analytically the mean energy diffused by an infinite strip of depth d of infinite parallel cylinders. The total acoustic field is calculated as the sum of the incident plane wave and the mean diffused field neglecting the phenomenon of multiple-diffusion between cylinders.

Embleton assumes that the diffused field is identical as the one obtained in the case of a mean homogeneous medium composed of rigid isolated cylinders whose radius is the average of the trees radii and whose density is the average trees density in the strip.

The heuristic attenuation Att_{heur} of a plane wave of wavenumber k by an infinitely wide strip of depth d of infinitely long cylinders of mean radius a is given by, in dB:

$$Att_{heur} = 20d \times \mathrm{Im}(k_{eq})/\ln(10) \tag{2}$$

with:

$$k_{eq} = \sqrt{k^2 - 4jNg + (g_1^2 - g^2) \times (2N/k)^2} \tag{3}$$

where N is the number of cylinder per m^2, Im is the imaginary part, and:

$$g = \sum_{n=-\infty}^{+\infty} A_n, \quad g_1 = \sum_{n=-\infty}^{+\infty} (-1)^n A_n \tag{4}$$

with:

$$A_n = \frac{i J_n(ka) + Z J'_n(ka)}{i H_n(ka) + Z H'_n(ka)} \quad (5)$$

Z is here the cylinders normalised impedance, J_n and J'_n are the Bessel functions of order n and their derivative, respectively, and , H_n and H'_n are the Hankel functions with positive imaginary part of order n and their derivative.

1.3. Heuristic approach

In the previous statistical approach, the infinite cylinders strip is represented by a material of fixed width with a given density of obstacles. This theory allows to describe only the energy of the square mean of the transmitted sound field $\left|\langle\psi\rangle^2\right|$ instead of the quadratic mean of the transmitted energy $\left\langle|\psi|^2\right\rangle$ which is the value of interest since it characterizes the global attenuation. The statistical approach neglects the incoherent diffusion between cylinders and thus introduces an error which is of importance only at high frequency. This error has been empirically estimated by Price [7] by comparing to scale model measurements results. It appears that this model is in agreement with the experiments for a cylinder density artificially reduced by 60%, the frequency dependence being the same. Equation 2 can finally be rewritten as follows:

$$Att_{heur} = 20d \times \mathrm{Im}(k_{heur})/\ln(10) \quad (6)$$

with:

$$\mathrm{Im}(k_{heur}) = 0.4 \times \mathrm{Im}(k_{eq}) \quad (7)$$

1.4. Ground effect

The ground impedance has been evaluated from impulse measurements with an iterative method. Attenborough's two-parameter impedance model [8] has been used here with a flow resistivity σ_e of *200 and 7.5 kPa s* m^{-2}, and a rate of exponential change of porosity of σ_e of *0* and *25* m^{-1}, for the plain ground and the forest ground, respectively. The ground impedance Z_g is given by:

$$Z_g = 13.79(\sigma_e/f)^{1/2}(1+j) + 9.74j(\alpha_e/f) \quad (8)$$

where f is the frequency.

In Figure 1 is shown the comparison of Excess Attenuation obtained from Attenborough's model calculation and measurements above forest ground for source and receiver heights of 4 m and an horizontal source-receiver distance of 8 m.

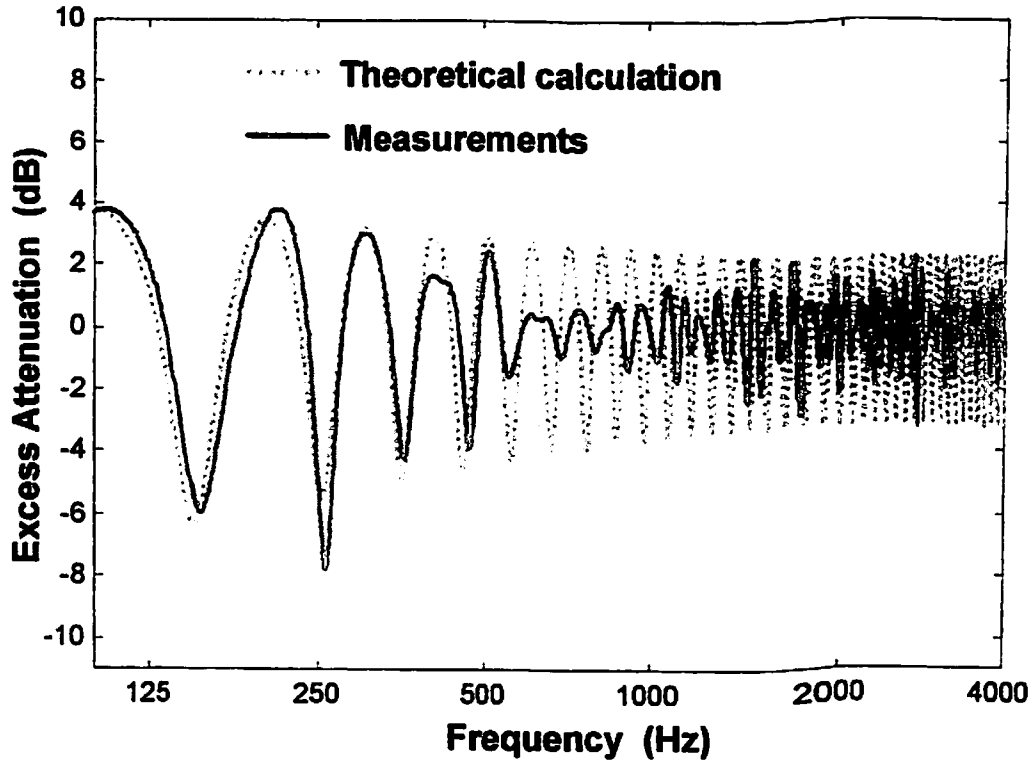

Fig. 1. Comparison of Excess attenuation in dB as a function of frequency measured in situ from impulse response and predicted using Attenborough's ground impedance model. Source an receiver heights: 4 m; source-receiver distance: 8 m

2. Simulations

2.1. Geometrical configuration

The omnidirectional point source is located 0.5 m high above a rigid surface (for asphalt) and 20 m away from a 100 m deep and 10.5 m high forest strip. The trees have an average circumference of 0.16 m and their density is of 0.14 trunks/m^2. In the case of the reference plain situation, the forest region is replaced by the plain ground (meadow) without any tree (see Fig. 2).

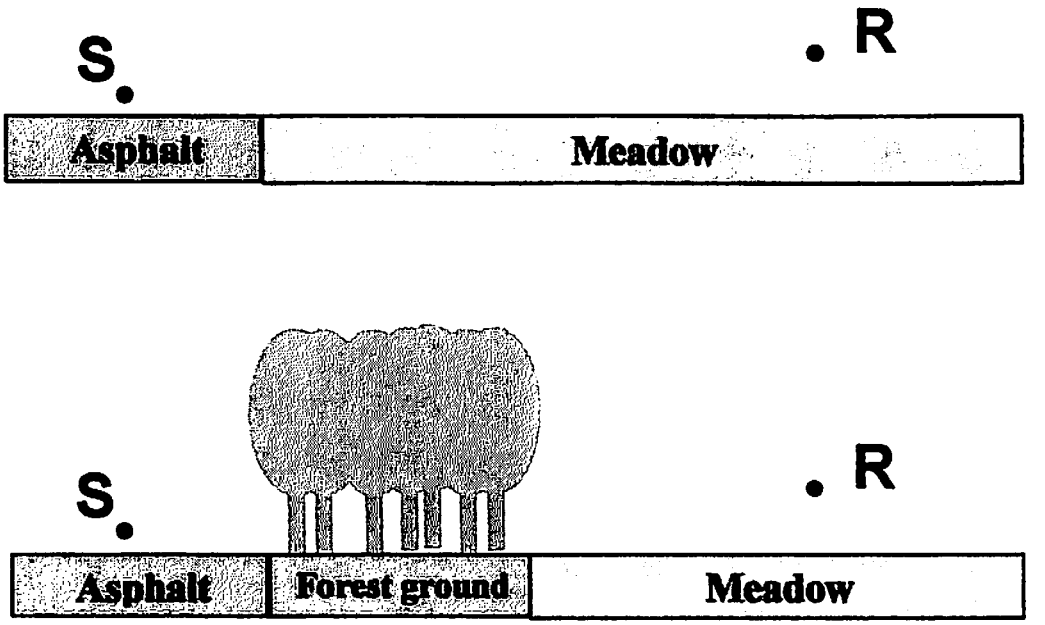

Fig. 2. Geometries of the plain situation (top) and forest one (bottom)

2.2. Meteorological sound speed profiles

Temperature profiles used in the following calculations are obtained from Raynor [9]. Figure 3 shows daytime and night profiles interpolated up to 50 m high for both the forest and the plain situations.

The PE method requires the knowledge of the sound speed profiles between the ground and a top limit depending on the frequency. Knowing the characteristics of wind speed profiles at some particular points above the plain and within the forest, it is necessary to determine their evolution inside the forest and after it. Accoprding to Liu's works [10], the wind profile inside the forest is considered to be constant after 100 m of propagation. Moreover, it is assumed that the wind profile after the end of the forest strip becomes similar to the plain situation one at a distance of 20 times the mean height of the trees. Wind speed profiles used in the following calculations are given in Figure 4.

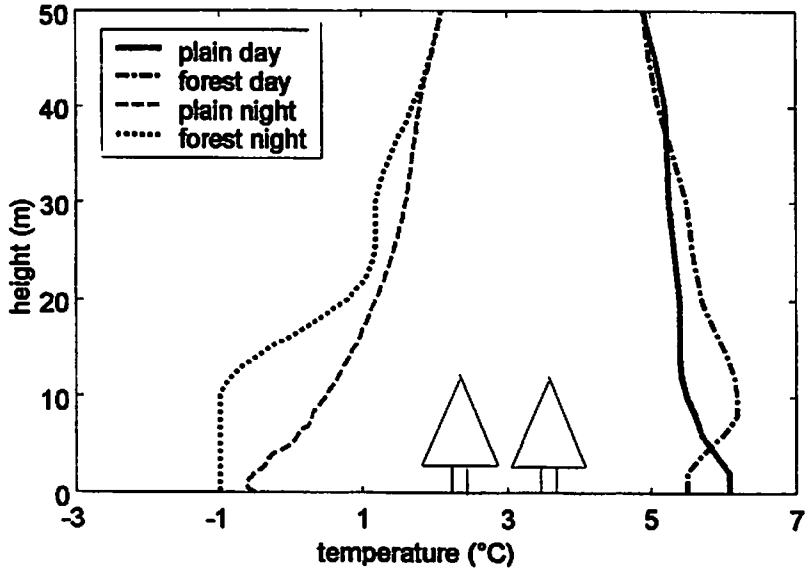

Fig. 3. Temperature profiles used in the simulations

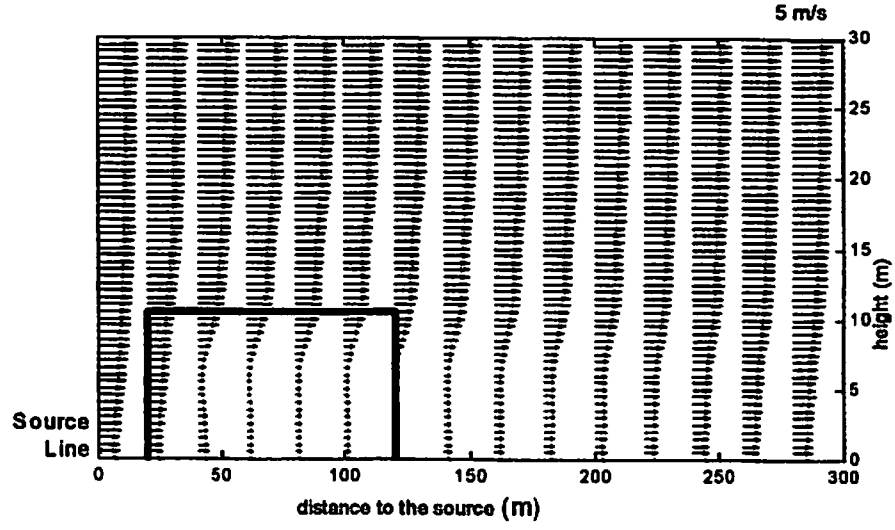

Fig. 4. Wind speed profiles used in the simulations (the forest is within the thick rectangle)

2.3. "3D" calculation principle

Figure 5 shows the calculation principle which allows to take into account the road as a line source splitting it up into a series of point sources. For each specific point source-to-receiver propagation, the wind speed vectors (given in Fig. 4) are "projected" onto the specific vertical plane seen under angle θ, when temperature profiles (Fig. 3) remain constant.

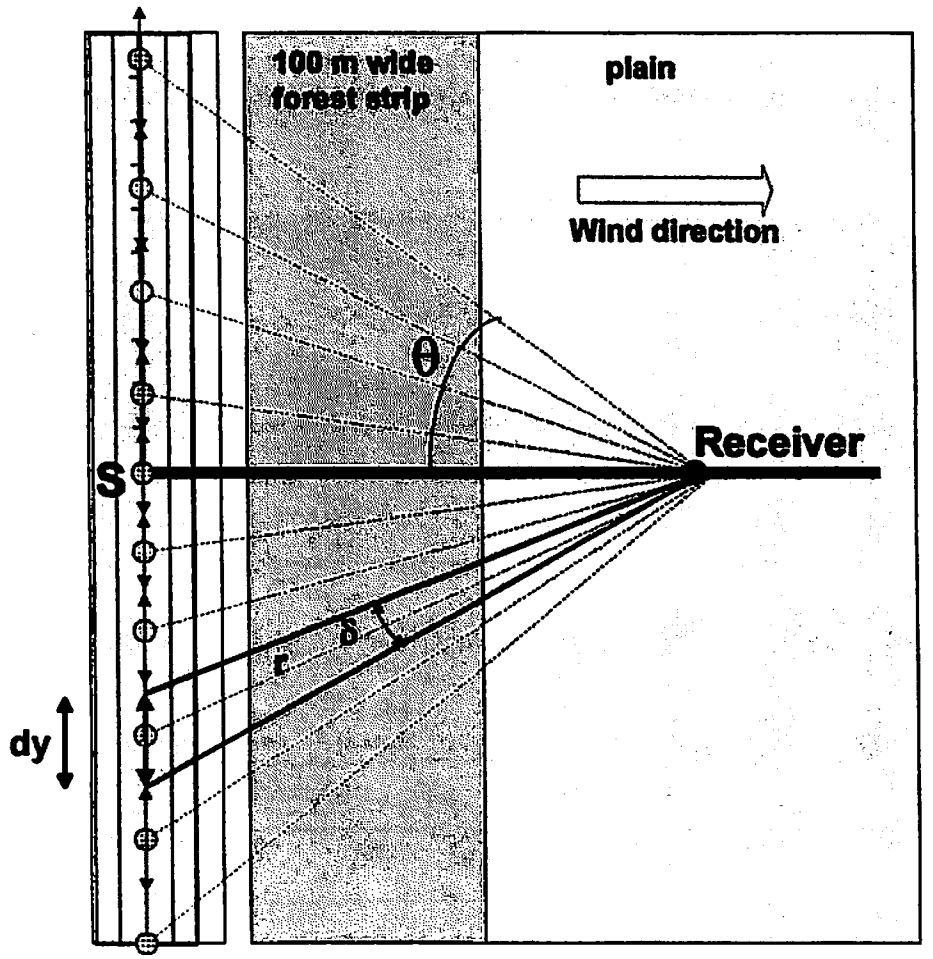

Fig. 5. Principle of the "3D" calculations

A total of 19 sources are considered with $-75° \leq \theta \leq +75°$. The calculations are led from 125 to 4000 Hz with 10 frequencies per octave band. The acoustic power of each specific point source is proportional to the corresponding cut length *dy* [2] (see Fig. 5). Traffic noise spectrum is determined from European standard EN 1793-3:1995 when air absorption is calculated from ISO 9613-1 formula (15°C and 70%RH).

The global dB(A) result is then obtain for one receiver point of the vertical noise map (perpendicular to the road line, such as those shown hereafter in Fig. 6) by summing the 19 calculated sound levels over the 6 octave bands. This is achieved for both forest and plain situations.

2.4. Results and discussion

Figure 6 shows three maps of iso-efficiencies calculated in a vertical plane perpendicular to the road (thick line between S and R in Fig. 5) and corresponding to three different typical meteorological conditions: negative temperature gradient (unfavorable condition to propagation), positive temperature gradient and downwind (favorable conditions).

In favorable conditions, the attenuation brought by the forest is between 2 and 6 dB(A) with the receiver at least 100 m away from the road. In unfavorable conditions, the forest may increase somewhat the received sound levels at large distances but it is of less importance

since levels are there quite low. In homogeneous conditions, sound propagation through the forest is not significantly affected by meteorology anymore but only by the scattering by trunks and foliage. A forest strip of at least 100 m wide appears thus to be an efficient natural acoustic barrier.

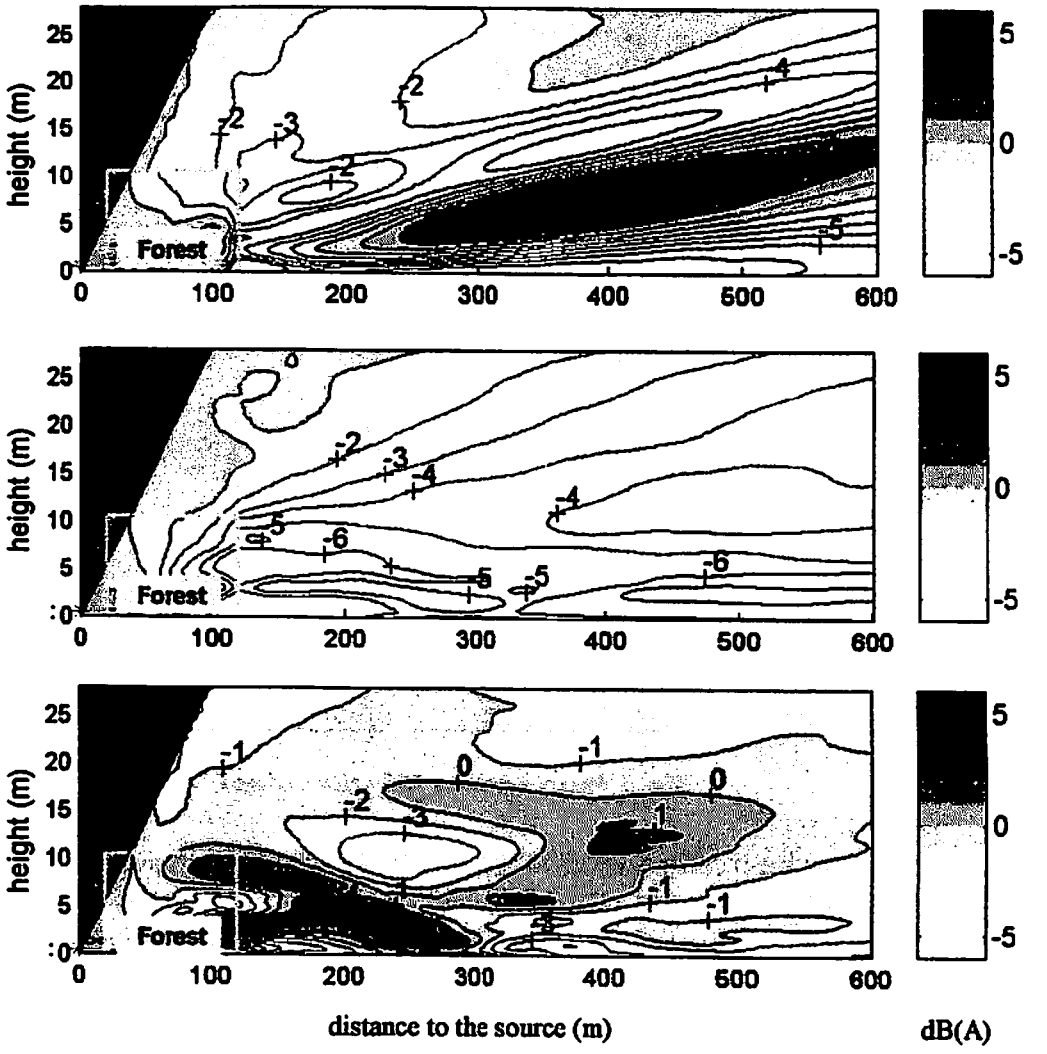

Fig. 6. Acoustical efficiency of a 100 m wide and 10.5 m high pine forest referred to the plain situation, in dB(A), in the case of: (a) typical day temperature profile (unfavorable to propagation), (b) typical night temperature profile (favorable) and (c) typical downward situation for a positive gradient wind speed profile (favorable)

However, in the case of a typical downward wind situation (favorable to propagation), zones of negative acoustical effects exist (the darkest areas in Fig. 6c). In this class of meteorological situations, the forest is acoustically efficient only for receivers sufficiently close to the strip of trunks. A strong sound level increase is noticeable in this latter case in Fig. 6c 200 m away from the road at a height of 5 m.

3. Experimental approach

3.1. Description of the site

The site is along the national road RN10 (2 lanes) 30 km Southwest from Bordeaux, France. The measurement area is composed of a wooded zone and an adjacent deforested zone (called plain hereafter). The road is straight and oriented NNE/SSW with dominant east-west winds. The wooded part is made of pine trees with an average height of 11.83 m, an average circumference of 53.1 cm and a density of 0.1078 trunks/m^2. First row of trees is about 40 m from the road. Measurements zones are east from the road.

3.2. Description of the measurements

The period of measurements was 16-29 June 1999. Four microphones were located 2 m high on the plain 150 m from the forest at different distances from the road: 50, 100, 150 and 300 m. On the other hand, a set of four microphones were positioned 2 m high within the forest, at the same 4 distances. These 4 positions correspond to a forest depth of 10, 60, 110 and 260 m respectively. At these 8 measurement points were recording every second, day and night, the LAeq (1s) as well as the 3rd octave band SPL spectrum.

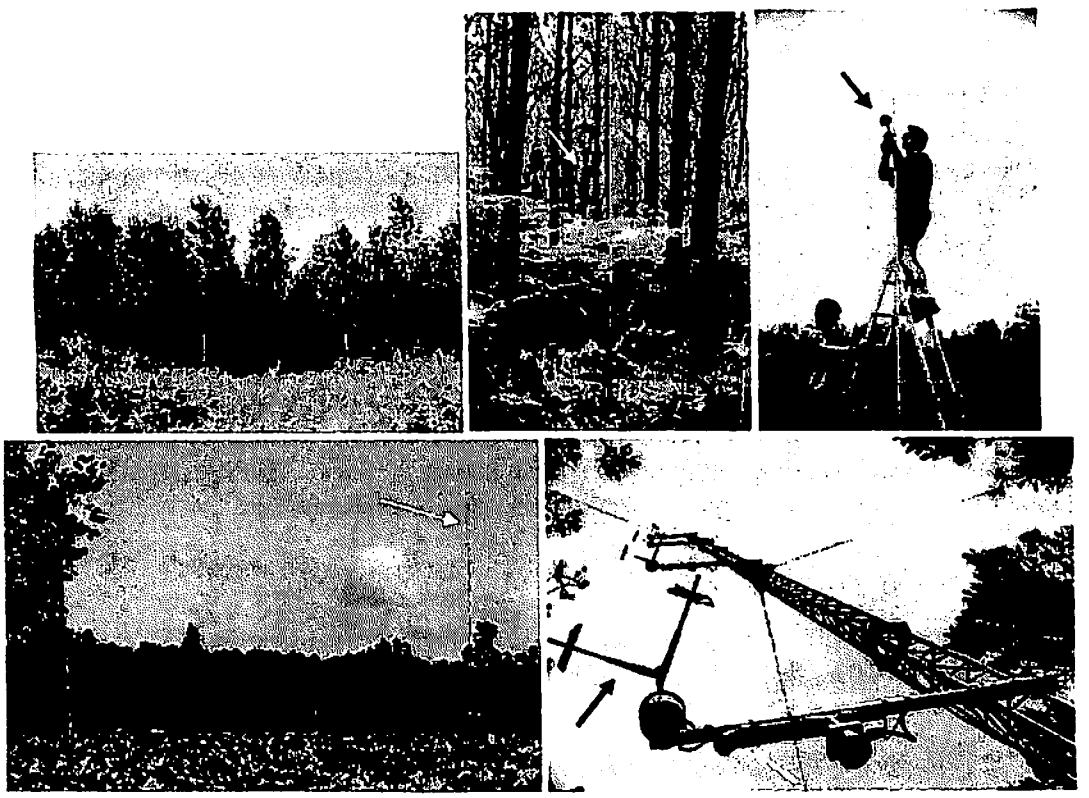

Fig. 7. Some pictures of the experiment: (a) the forest from the plain zone, (b) a 2 m high mike within the forest, and (c) a 4 m high one above the plain, (d) the plain 20 m high meteo mast and (e) the forest one seen from below (in the foreground a temperature probe and a bi-directional anemometer)

In order to get wind speed and temperature vertical profiles in simultaneity with acoustic measurements, two 20 m high meteorological masts have been installed 150 m inside the forest and inside the plain (Fig. 7). The masts were equipped with 3 bi-directional anemometers located 3.7, 9.7 and 20.7 m high, and 4 temperature probes installed 1.5, 3, 9 and 20 m high. The measurement frequency was 1 second but the recording of data was achieved every 2 minutes (mean wind speeds, mean wind directions, standard deviations and mean temperatures).

Road traffic was measured by means of a counting loop on the road. During the measurement period, the mean flow was 2200 vehicles per day, for each of the two lanes, with 5% of heavy trucks. The mean speed of light vehicles was 85 km/h.

4. Measurements results

4.1. Meteorological classification

In order to underline the influence of mean meteorological parameters, the meteo-acoustical conditions have been determined from a criterion corresponding to a wind speed of ±1 m/s 10 m high with no temperature gradient. First, from the temperature and wind measured data, a mean logarithmic-type sound celerity profile [19] have been determined every 2 minutes and the calculation of theoretical sound level have been led for each 150 and 300 m away receiver. The conditions of propagation have then been classified as:

- favourable (to acoustic propagation) if the calculated level was greater than the one calculated with the criterion 1 m/s 10 m high for a fair wind,
- unfavourable (to acoustic propagation) if the calculated level was greater than the one calculated with the criterion 1 m/s 10 m high for an adverse wind,
- homogeneous otherwise.

Globally, at daytime (0600-2200), occurrences were 52.6% for favourable conditions, 8.7% for homogeneous and 38.7% for unfavourable ones. At night (2200-0600), we got 93.3% favourable and 6.7% homogeneous (no unfavourable conditions). These values are close to those given by the NMPB French method [13] where they have been calculated from an average over 10 years of meteorological data (Bordeaux region, direction source-receiver 260°: 41% favourable at daytime and 95% favourable at night). Though this measurements campaign is of short time, it represents quite well a long term situation.

4.2. Attenuation due to the forest

The efficiency $\Delta_{d\,m}$ of the forest strip compared to the plain situation for a receiver located at $d = 100, 150$ or $300\ m$ from the road is referred to the measurements at $50\ m$ and is given by:

$$\Delta_{d\,m} = (LAeq_{forest\,d\,m} - LAeq_{forest\,50\,m}) - (LAeq_{plain\,d\,m} - LAeq_{plain\,50\,m}) \qquad (9)$$

The first observation is that in favourable conditions, the mean measured forest efficiency is about –2 dB(A) at 100 and 300 m, and –3 dB(A) at 150 m. This phenomenon is mainly due to the decreasing or cancellation of the positive temperature gradient inside the forest, especially at night. As expected, the efficiency seems to increase with the width of the forest strip; however, the value at 300 m is lower than the one at 150 m for two main reasons: first, a distortion due to a too high electronic background noise (cable length > 100 m) and second, a

too small acoustic signal-to-noise ratio observed at this large distance from the road. Noise from the forest (as bird songs, foliage noise) have also to be taken into account.

In homogeneous conditions, the mean efficiency is –2 dB(A) at 150 m. However, this meteorological situation being rarely encountered, the data generally correspond to only something like 20 minutes of data making somewhat difficult the interpretation of results.

In unfavourable conditions, the mean efficiency is –1 dB(A) at 150 m. This negative value does not correspond to the expected one; indeed, the GFPE calculation predicted a positive value of the efficiency, that is an increasing of sound level in a forest situation compared to a plain one. Again, a small signal-to-noise ratio made difficult the acoustic analysis.

Figure 8 gives an example of results for the receivers located 150 m from the road and for the 3 meteorological conditions (average efficiencies on 120 consecutive minutes for the favourable and unfavourable situations, and on 20 minutes for the homogeneous one).

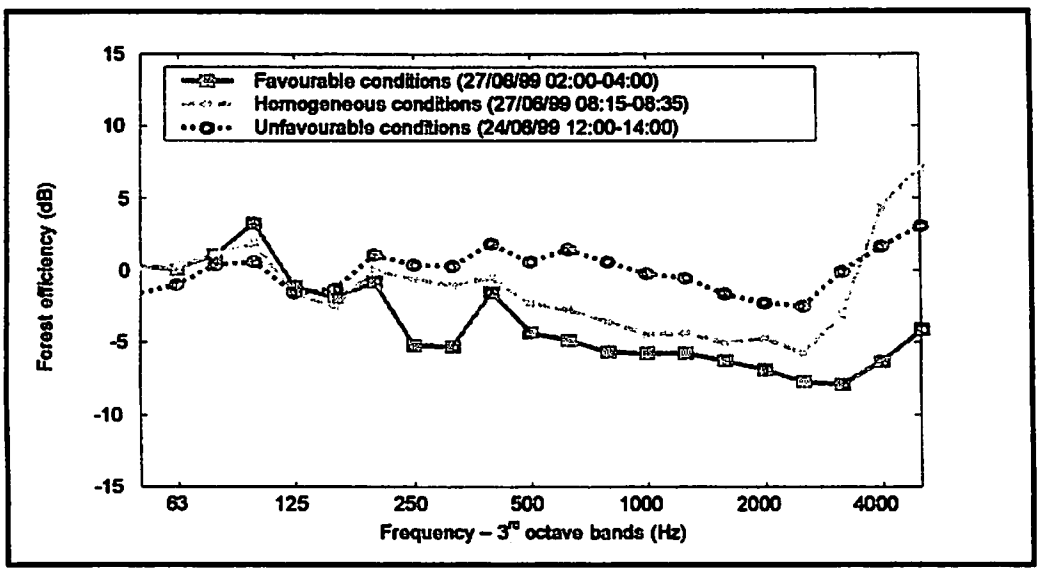

Fig. 8. Comparison of mean SPL 3rd octave bands spectra for the 3 different meteorological conditions and for the receivers 150 m from the road

It is of importance to notice that $\Delta_{150\ m}$ has been calculated in reference with the plain situation where the ground is very absorptive (recent deforested zone). If the comparisons were achieved with a harder plain ground, an increasing of the efficiency might be expected.

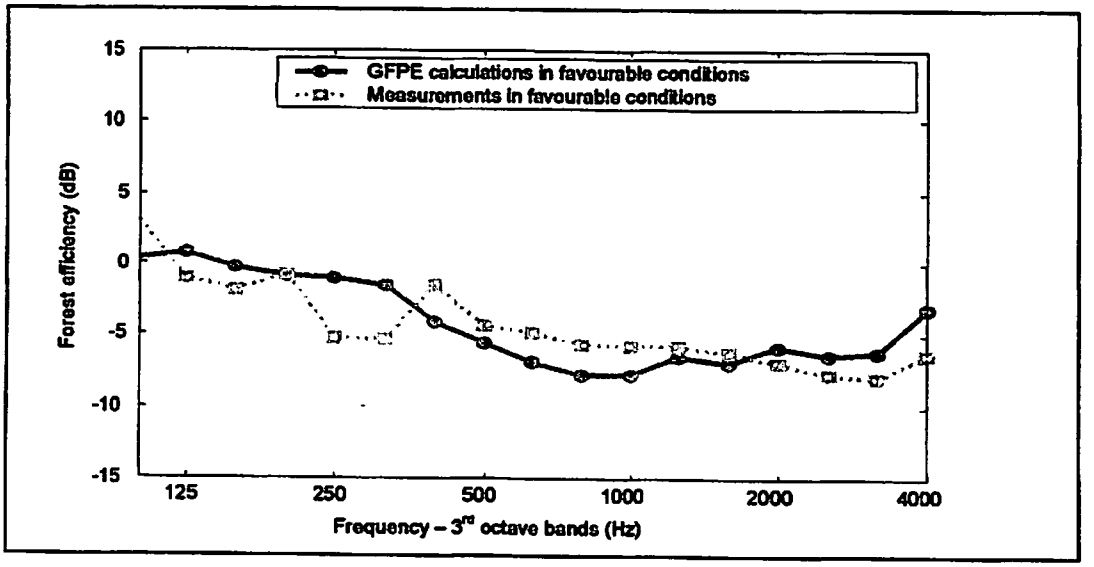

Fig. 9. Comparison between measurements and GFPE calculations in favourable conditions (receivers 150 m from the road, 27/06/99 02:00-04:00)

4.3. Global results

Table 1 sums up the measurements/calculations comparisons for the meteorological situations presented in Fig. 9. Agreement is good, except for the unfavourable condition.

	GFPE calculations	Measurements
Favourable	-5.5	-5.8
Homogeneous	-2.2	-3.6
Unfavourable	4.7	-0.2

Table 1. Comparison of forest efficiencies $\Delta_{150\,m}$ in dB(A) for the 3 different meteorological conditions corresponding to the situations presented in Fig. 9

5. Concluding remarks

In order to study the effect of the sound diffusion by trunks in the presence of meteorological effects, the forest has been considered as an equivalent homogeneous medium characterized by a single mean complex wavenumber whose value is obtained from an heuristic approach. The calculation is quite complex since the medium is range dependent but the use of the GFPE approach allows one to overcome this problem.

It has been shown that in favorable conditions, the gain brought by the forest may theoretically rise up to 5 dB(A) with the receiver at least 100 m away from the road. This meteorological situation occurs very often at night due to a temperature inversion phenomenon. It is of most interest since it corresponds to the periods when the annoyance due to the road in a plain situation is the highest. In homogeneous conditions, the maximum expected gain is of 3 dB(A).

From vertical noise maps calculation, it has been pointed out that in the case of a typical day temperature profile (unfavorable to propagation) as well as a typical downward situation for a positive gradient wind speed profile (favorable to propagation), areas of negative acoustical effects exist. For these two meteorological classes, the forest brings efficiency only for receivers sufficiently close to the strip of trunks.

A measurement campaign achieved in the French Landes pine forest has also been presented and results have been analysed. In favourable conditions, the gain brought by the forest is between 3 and 5 dB(A) with the receiver at least 100 m away from the road. In unfavourable conditions, the forest may increase somewhat the received sound level at large distances but it is of less importance since levels are quite low. In homogeneous conditions, the sound propagation through the forest is not appreciably affected by meteorology anymore but only by the scattering by trunks and foliage.

A forest strip of at least 100 m wide appears thus to be an efficient natural anti-noise "climatic" barrier. Lastly, the comparison of these results to those from a new method of forest attenuation prediction based on a fast implementation of the Parabolic Equation has shown a good agreement.

Work is still in progress in order to develop approximate expressions of the attenuation due to forests to be included in an analytical prediction model [12] such as the French NMPB noise prediction method [13-15]. At the same time theoretical investigations are led to derive advanced numerical models based on BEM formulations [16-18] accounting for forest effects.

Acknowledgements

The authors would like to thank the following French Institutions: the Agence de L'Environnement et de la Maîtrise de l'Energie (ADEME), the Ministère de l'Aménagement du Territoire et de l'Environnement and the Institut National de la Recherche Agronomique (INRA) for their financial support.

References

[1] **N. Barrière, Y. Gabillet**, Acta Acustica, **85**, 325-334 (1999)

[2] **N. Barrière**, "Theoretical and experimental study of traffic noise propagation through forest", PhD (1999)

[3] **E. Salomons**, J. Acoust. Soc. Am., **104**, 100-111 (1998)

[4] **P. Morse, K.U. Ingard**, Theoretical Acoustics, Ed. M.G. Hill (1968)

[5] **T.F.W. Embleton**, J. Acoust. Soc. Am., **40**, 667-670 (1966)

[6] **V. Twersky**, J. Acoust. Soc. Am., **36**, 1314-1329 (1964)

[7] **M.A. Price, K. Attenborough**, "Sound attenuation in woodland", Open University (1988)

[8] **K. Attenborough**, J. Sound Vib., **99**, 521-544 (1985)

[9] **G.S. Raynor**, Forest Science, **17**(3), 351-363 (1971)

[10] **J. Liu et al.**, Boundary Layer Meteorology, **77**, 21-44 (1996)

[11] **N. Barrière, J. Defrance et al.**, Proc. InterNoise 2000 (Nice)

[12] **J. Defrance, Y. Gabillet**, Applied Acoustics, **57**(2), 109-127 (1999)

[13] **J. Defrance, Y. Gabillet et al.**, "Road traffic noise. Calculation method including meteorological effects", Ed. CERTU (1997) (available in English)

[14] **J. Defrance, Y. Gabillet et al.**, Proc. InterNoise 2000 (Nice)

[15] **J. Defrance, M. Bérengier, J.-F. Rondeau**, Proc. InterNoise 2001 (The Hague)

[16] **P. Jean, J. Defrance, Y. Gabillet**, Journal of Sound and Vibration, **226**(2), 201-216 (1999)

[17] **E. Premat, Y. Gabillet**, J. Acoust. Soc. Am., **108**(6), 2775-2783 (2000)

[18] **E. Premat, Y. Gabillet, J. Defrance**, 9th Symposium on Long Range Sound Propagation, 154-164 (2000)

[19] **H. Panosky, J. Dutton**, Atmospheric turbulences; models and methods for engineering applications

[20] **K. E. Gilbert, X. Di**, J. Acoust. Soc. Am., **94**, 2343-2352 (1993)

An Equivalent Sources Method Solution to the 2D City Canyon Problem

Mikael Ögren, Wolfgang Kropp
Applied Acoustics, Chalmers University of Technology
SE-412 96 Gothenburg, Sweden

November 18, 2002

Abstract

A common situation in an urban traffic environment is straight roads with high buildings on both sides, forming a city canyon. This problem can be simplified into a two dimensional situation where the road traffic is included as a line source. The sound pressure level inside the canyon and above it can be predicted with a FEM or FDTD method, but a more numerically effective solution can be obtained with the ESM (Equivalent Sources Method). The problem can be divided into two domains, a room-like cavity and a free field above it. The two domains are then coupled by a set of sources. The strength of these sources can be determined by the boundary condition between the two domains, and the source strengths can then be used to calculate the pressure at any receiver position. The model can be extended to situations with arbitrary impedances on the surfaces at a cost of an increased computational time.

1 Introduction

The sound level on the noisy side of a building in a city environment, including reflections from nearby façades, can be predicted with many standardized methods, for example [1]. The level at shielded courtyards is however more difficult to predict. Ray based methods are difficult to apply, and often give too low levels at such positions [2]. Therefore some effort have been put into finding a better method for such positions. This paper presents a different approach based on the method of equivalent sources, which might be more reliable.

The approach of using equivalent sources to couple two domains have been used for similar problems earlier by e.g. Kropp [3] and Cummings [5]. However, due to the size of the geometries considered here in 3D it could only be used for low frequencies due to the computational effort. Using a 2D model is therefore a natural first step in order to deal with problems where the dimensions (5–20 m) correspond to many wavelengths at the most important frequencies (500 Hz–1kHz).

The geometry considered in this paper is outlined in figure 1, where Γ denotes the boundary between the canyon and the free half-space above it.

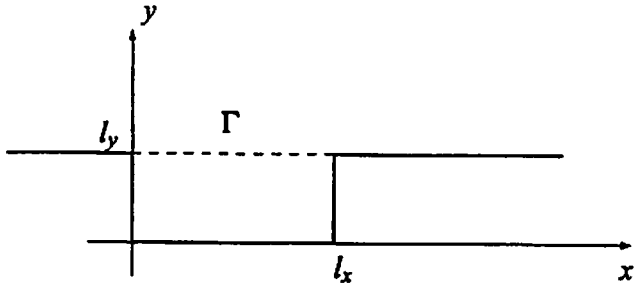

Figure 1: Coordinate system of the 2D city canyon.

2 Theory

2.1 The Green functions

The main idea of the method of equivalent source is to describe the unknown impedance at the interface between canyon and half-space (Γ) by a set of monopoles which are adjusted in such a way that continuity of the sound field at the interface is maintained. This demands so-called Green functions for the radiation from the interface into the half-space and into the canyon, which in this case can be considered as a cavity with rigid walls.

The following assumes a harmonic time dependence described by $e^{j\omega t}$. The geometry is divided into two domains, the canyon itself and a half space above it. The intersection between the two domains is denoted Γ. In the domains the Green functions are

$$G_1(\mathbf{r}|\mathbf{r}_0,\omega) = \frac{c^2}{l_x l_y}\sum_n\sum_m \frac{\Psi_{n,m}(\mathbf{r})\Psi_{n,m}(\mathbf{r}_0)}{\Lambda_{n,m}(\omega_{n,m}^2(1+j\eta)-\omega^2)} \tag{1}$$

$$G_2(\mathbf{r}|\mathbf{r}_0,\omega) = \frac{-j}{4}H_0^{(2)}(k|\mathbf{r}-\mathbf{r}_0|). \tag{2}$$

Equation (1) is valid in a 2D rectangular cavity with rigid walls, and (2) in a 2D free field. The room like Green function (1) is a summations of modes, where the resonance frequencies, mode shapes and modal weights are described by

$$\omega_{n,m} = \pi c\sqrt{\left(\frac{n}{l_x}\right)^2+\left(\frac{m}{l_y}\right)^2} \tag{3}$$

$$\Psi_{n,m}(\mathbf{r}) = \cos\left(\frac{n\pi r_x}{l_x}\right)\cos\left(\frac{m\pi r_y}{l_y}\right) \tag{4}$$

$$\Lambda_{n,m} = \int_S \Psi_{n,m}^2 dS. \tag{5}$$

The mode summation extends over all modes in theory, but in practice only a finite amount can be included. In this paper modes with resonance frequencies up to three times the frequency of interest are included in the summation. The damping is very important for the final result, and it is included as the factor η. The actual values used in this paper are described in section 2.3 below.

2.2 Matrix formulation

In order to calculate the sound pressure at any point the two domains must be coupled together. Here a brief description is included on how that is accomplished. For a more detailed description see [3].

The first step is to formulate the pressure in the two domains as a function of the pressure contribution from sources located in the respective domains together with a contribution from the boundary Γ, which is seen as a source distribution. The pressure can be calculated using

$$p = QG_1 + \int_\Gamma qG_1 dx \tag{6}$$

inside the canyon, where Q denotes the primary source (e.g. due to the traffic), and

$$p = -2\int_\Gamma qG_2 dx \tag{7}$$

above it. For simplicity only one primary source is included in the formulas above, but the model can handle any number of (coherent) sources located in one or both domains. $q(x)$ denotes the source distribution over the boundary Γ. The factor 2 in (7) is due to the image source in the boundary which is considered to be rigid.

The next step is to divide the boundary into elements where q is constant over each element. Then the integrals in equation (6) and (7) can be split up into into a sum of integrals over each element. The width of the elements were set to $\lambda/10$. Finally the pressure at the center point of each element is expressed both using (6) and (7), and since they must be equal the following matrix equation is formed,

$$\mathbf{Aq} = \mathbf{b} \tag{8}$$

where

$$A_{i,j} = \int_{\Gamma_j} G_1(\mathbf{r}_j|\mathbf{r}_i)dx + 2\int_{\Gamma_j} G_2(\mathbf{r}_j|\mathbf{r}_i)dx \tag{9}$$

$$b_i = Q\int_{\Gamma_i} G_1(\mathbf{r}_0|\mathbf{r}_i)dx. \tag{10}$$

Solving this equation system for the unknown source strengths $\mathbf{q}$ is straight forward, but the integrals of the exterior Green function must be dealt with carefully. Here a numerical integration technique known as Gauss quadrature was used [4]. The integrals of the room like Green function can be performed analytically, so no numerical method is needed.

Finally the pressure at any position can be calculated using (6) or (7) depending on whether the receiver is inside the canyon or above it.

This approach could be improved by assuming a higher order for the elements, for instance a linear or quadratic dependence of $q(x)$ on each element. Another improvement would be to introduce elements which length depends on the position, with smaller elements close to the corners. Both approaches are interesting, but have not been investigated so far.

2.3 Damping in the canyon

The assumption of damping is essential for the sound levels inside the cavity. Assuming rigid walls and only including air absorption leads to surprisingly high values at interior resonances. A more realistic approach would be to include the reflection factors of typical façades and other materials normally present, but for the purpose of validating the model as such a simpler way is to use measured values from rooms.

In this paper the damping measured in a reverberation chamber at Chalmers is used. A logarithmic curve fitting of measured values gave

$$\eta(f) = 10^{-0.94} f^{-0.42} \tag{11}$$

within the frequency range 100 Hz – 1 kHz. However, preliminary measurements of damping in courtyards indicate that these values are too low.

Note that the use of the Green function (1) assumes that the damping is evenly distributed throughout the medium. The method can also be modified to include the effect of patches with nonzero absorption at the boundaries at the cost of an increased computational effort, see [3].

3 Calculation examples

3.1 Single canyon

For the initial tests a canyon from Söder in Stockholm, Sweden, was chosen. The distance between the façades is about 11 m and the height of the nearby buildings around 18 m. One line source was positioned at the floor of the canyon ($y = 0$), slightly of center at $x = 5$ in order to excite modes with both odd and even n. The sound pressure level relative to free field was calculated using the above method in a grid of points, and the results are presented for two third octave bands in figure 2.

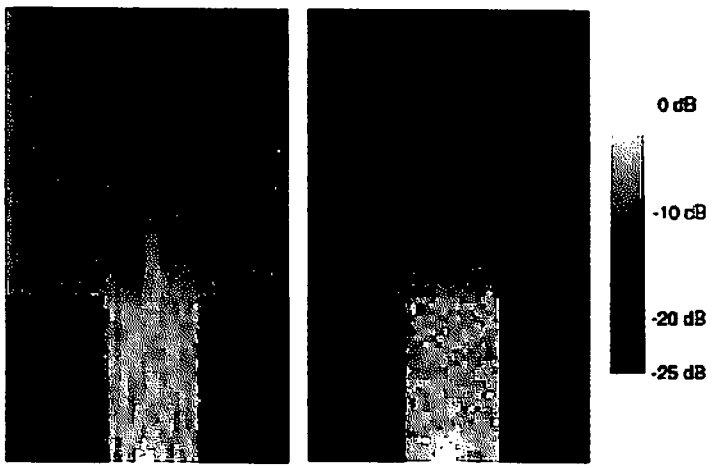

Figure 2: Color plot of the sound pressure level (uncal.) averaged over the third octave bands 125 Hz and 500 Hz.

3.2 Two canyons

The shielded courtyard was added to the model as a second canyon beyond the first. The width of the houses between the two canyons was set to 14 m, and the second canyon was 20 m wide, see figure 3. First the geometry without the second canyon was solved, and then the sources from the boundary were used as the primary sources for a second calculation, where only the second canyon was included. This approach will not take into account a possible interaction between the canyons, which is assumed to be weak.

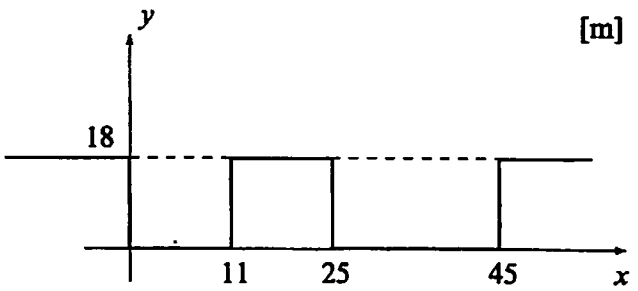

Figure 3: Sketch of the geometry for two canyons.

The calculations are displayed as color plots for the sound pressure level in figure 4 and 5 for the third octave bands 125 Hz and 500 Hz. The levels very close to the primary source have been truncated, since the level theoretically goes to infinity at that point.

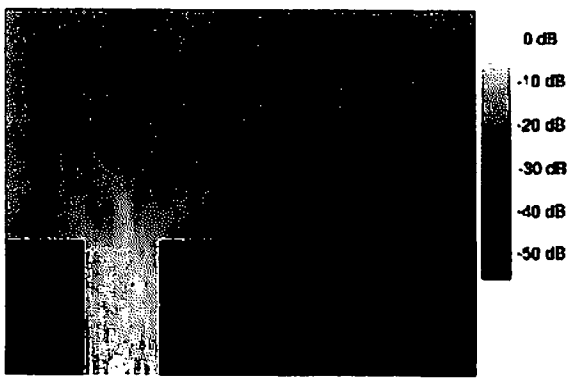

Figure 4: Results for two canyons, third octave band 125 Hz.

4 Conclusions

The level is relatively constant in both canyons, the variation with height and position within respective canyon is small. This is consistent with measurements from courtyards.

The level in the shielded canyon is not strongly dependent of the height of the shielding building. This is in contradiction to results obtained when a simplified diffraction theory is applied.

5 Acknowledgements

This paper is based on a study performed within the research programme "soundscape support to health", sponsored by the Swedish Foundation for Strategic Environmental Research (MISTRA), the Swedish Agency for Innovation Systems (Vinnova) and the Swedish National Road Administration (VV).

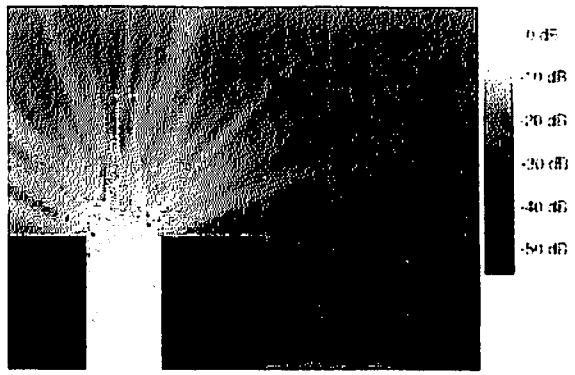

Figure 5: Results for two canyons, third octave band 500 Hz.

References

[1] Jonasson H. and Nielsen H. L., Road Traffic Noise – Nordic Prediction Method, ISBN 92 9120 836 1, TemaNord 1996:525, Nordic Council of Ministers

[2] Ögren M., Forssén J., Prediction of noise levels in shielded urban areas, Internoise 2001, paper 157, The Hague

[3] Bérillon J., Kropp W., A Theoretical Model to Consider the Influence of Absorbing Surfaces Inside the Cavity of Balconies, Acustica–Acta Acustica, Vol. 86, 2000, pp. 485-494

[4] Bécot F., Thorsson P., Kropp W., An Efficient Application of Equivalent Sources to Noise Propagation Over Inhomogeneous Ground, Submitted to Acustica–Acta Acustica

[5] Cummings A., The Effects of a Resonator Array on the Sound Field in a Cavity, J. of Sound and Vibration, 154 (1), 1992, pp. 25-44

Finite element application of linear transport to sound propagation in cities

Pontus J. Thorsson

Department of Applied Acoustics, Chalmers University of Technology, Göteborg, Sweden

Abstract

Sound propagation in complex acoustic environments such as cities is in this paper studied by using a linear transport equation. The relationship between the used equation and the wave equation is also given. The equation is solved using a finite element approach, where the city is divided into its relevant parts such as roads, different building structures and recreational areas. Each part is characterized through its mean building size, mean absorption properties and the density and frequency spectrum of the sources present. The results from this method are not pointwise exact, but instead intended as a mean value of the background noise level.

1 Introduction

A multitude of models exist for calculating the noise levels from point sources or sets of point sources (see for example [1]). The models include different grades of complexity, e.g., diffraction over rooftops or around houses, finite ground impedance or a varying ground profile. However, the major part of these models only include a single source. In principle it is possible to add the fields from several sources, but this can be a tedious assignment, since the geometry must be given in relation to each source.

There are a large amount of sources in a real city, e.g., different kinds of fans and sources related to vehicle transportation. This paper's focus is on vehicle transportation noise, but the method described here is not limited to those sources.

Previous studies have shown that common prediction methods can give substantial errors in shielded situations [2]. This is probably caused by the fact that only the nearest road is normally assumed to contribute to the noise level. Especially in strongly shielded situations, like in closed backyards, this hypothesis would be incorrect.

It is not feasible to handle this large number of individual sources separately with analytical methods. Numerical methods, like the Finite Element Method (FEM), are better adapted to this situation. However, when considering noise propagation in cities the important sources are distributed over a large area. Thus, a numerical model based on the wave equation gets very large in terms of storage and solution time, since the element size in the discretization must be a fraction of the wavelength to get reasonable results. A possible alternative is then to treat the noise propagation in terms of linear transport [3]. This approach is explained in this paper and its connection to the wave equation is also given. In some cases the transport equation can be simplified to the well-known diffusion equation. Finally, some application examples are given.

2 Theoretical basis of the method

Linear transport equations are normally used for calculation of molecular or particle dynamics, e. g. evolution of a perfect gas or neutron transport inside nuclear reactors. A general form of the transport equation can be written as:

$$\frac{\partial f}{\partial t} + \mathbf{v} \cdot \frac{\partial f}{\partial \mathbf{r}} + \frac{1}{m}\mathbf{F} \cdot \frac{\partial f}{\partial \mathbf{v}} = J_{gain} - J_{loss}. \tag{1}$$

This equation describes the dynamics of the particles inside the control volume $\mathrm{d}\mathbf{r}\mathrm{d}\mathbf{v}$ in phase space, where $\mathbf{r} = (x, y, z)$ and $\mathbf{v} = (v_x, v_y, v_z)$ are the position and the velocity respectively. The distribution function f describes the density of particles in phase space. The vector $\mathbf{F}$ describes any forces acting on the particles, and in most acoustical problems it can be set to zero. The value on the right hand side is the net flow of particle densities in and out of the control volume. In transport applications sound is assumed to be transported in small packages of equal energy called sound particles or phonons.

2.1 Twersky's theory for multiple scattering

The following presentation of the multiple scattering theory by Twersky follows mainly Ishimaru [4], who studied the propagation of electromagnetic waves in random media. Consider a random distribution of N particles located at $\mathbf{r}_1, \mathbf{r}_2, \ldots, \mathbf{r}_N$ in a volume V. The particles need not have identical size and shape. The scalar field ϕ at the point $\mathbf{r}_a$ between the scatterers satisfies the wave equation

$$\nabla^2\phi + k^2\phi = 0, \tag{2}$$

where $k = 2\pi/\lambda$ is the wavenumber in the medium between the particles. Now, ϕ_i is the incident field in the absence of any particles. The total field can then be written as a sum of the incident field and the fields scattered from the N particles.

$$\phi(\mathbf{r}_a) = \phi_i(\mathbf{r}_a) + \sum_{s=1}^{N} U_s^a. \tag{3}$$

U_s^a is the contribution at $\mathbf{r}_a$ from the scatterer at $\mathbf{r}_s$. This contribution can be expressed in terms of the the total field incident upon the scatterer at $\mathbf{r}_s$, $\phi(\mathbf{r}_s)$, and the scattering characteristic of this scatterer, u_s^a:

$$U_s^a = u_s^a \phi(\mathbf{r}_s). \tag{4}$$

It is important to note that $u_s^a\phi(\mathbf{r}_s)$ does in general not mean a product of u_s^a and $\phi(\mathbf{r}_s)$. Instead, u_s^a is an operator and $u_s^a\phi(\mathbf{r}_s)$ means the field at $\mathbf{r}_a$ due to the scatterer at $\mathbf{r}_s$ when the field $\phi(\mathbf{r}_s)$ is incident upon it.

The total field at $\mathbf{r}_s$ can be written as a sum of the incident field in absence of any scatterer and the field scattered from all the scatterers except the one at $\mathbf{r}_s$.

$$\phi(\mathbf{r}_s) = \phi_i(\mathbf{r}_s) + \sum_{t=1, t\neq s}^{N} u_t^s \phi(\mathbf{r}_t). \tag{5}$$

Through combining Equation 3 with Equation 5 in an iterative manner it is possible to eliminate the total field at the positions of the scatterers and hence it is possible to write the total field at $\mathbf{r}_a$ in terms of the field incident on the scatterers ϕ_i.

$$\begin{aligned}
\phi(\mathbf{r}_a) &= \phi_i(\mathbf{r}_a) + \sum_{s=1}^{N} u_s^a \left(\phi_i(\mathbf{r}_s) + \sum_{t=1, t\neq s}^{N} u_t^s \phi(\mathbf{r}_t) \right) \\
&= \phi_i(\mathbf{r}_a) + \sum_{s=1}^{N} u_s^a \phi_i(\mathbf{r}_s) + \sum_{s=1}^{N} \sum_{t=1, t\neq s}^{N} u_s^a u_t^s \phi_i(\mathbf{r}_t) \\
&\quad + \sum_{s=1}^{N} \sum_{t=1, t\neq s}^{N} \sum_{m=1, m\neq t}^{N} u_s^a u_t^s u_m^t \phi_i(\mathbf{r}_m) + \cdots .
\end{aligned} \tag{6}$$

The first term in this series is the incident wave. The second term is the singly scattered waves and the third term represents all the double scattering with the term $t = s$ excluded, since a wave cannot be scattered in the same particle two times without being scattered from another particle. The third term in the series represents triple scattering with the terms $t = s$ and $m = t$ excluded for the same reason. The term $m = s$ have not been excluded since it means that the wave have first been scattered from the particle at $\mathbf{r}_s$, then at $\mathbf{r}_t$ and then at $\mathbf{r}_s$ again.

The complete field at $\mathbf{r}_a$, which consists of the incident wave and all the mulitple scattered waves, can be divided into two groups:

(1) One group which is composed of the multiple scattered waves which involve chains of successive scatterings going through different particles.
(2) The other group is composed of the multiple scattered waves that have passed a scatterer more than once.

Twersky's theory includes all the terms belonging to the first group but neglects the terms from the second group. Obviously, Twersky's theory should give good results when the backscattering is small compared to the scattering in other directions. If the backscattering is small it is possible to write the total field as:

$$\phi(\mathbf{r}_a) = \phi_i(\mathbf{r}_a) + \sum_{s=1}^{N} u_s^a \phi_i(\mathbf{r}_s) + \sum_{s=1}^{N} \sum_{t=1, t\neq s}^{N} u_s^a u_t^s \phi_i(\mathbf{r}_t) + \sum_{s=1}^{N} \sum_{t=1, t\neq s}^{N} \sum_{m=1, m\neq t, m\neq s}^{N} u_s^a u_t^s u_m^t \phi_i(\mathbf{r}_m) + \cdots . \tag{7}$$

As N becomes large the difference between Twersky's theory and the exact theory becomes very small [4]. The expression above is useful in understanding the scattering processes, but it is impractical for practical calculations. It is better to use Foldy-Twersky's integral equations which are presented in the following section.

2.2 *Integral representation of multiple scattering*

Since the locations of the scatterers are random, the total field $\phi(\mathbf{r}_a)$ is a random function of the receiving position $\mathbf{r}_a$ and time. This random function can be divided into the average field $\langle\phi(\mathbf{r}_a)\rangle$ and the fluctuating field $\phi_f(\mathbf{r}_a)$. The average field is also called the coherent field and the square of its magnitude $|\langle\phi(\mathbf{r}_a)\rangle|^2$ is called the coherent intensity. The fluctuating field is called the incoherent intensity and the average of its squared magnitude $\langle|\phi_f(\mathbf{r}_a)|^2\rangle$ is called the incoherent intensity. The total intensity is then the average of the squared magnitude of the total field $\langle|\phi(\mathbf{r}_a)|^2\rangle$ and is equal to the sum of the coherent and the incoherent intensity.

$$\langle|\phi(\mathbf{r}_a)|^2\rangle = \langle|\langle\phi(\mathbf{r}_a)\rangle + \phi_f(\mathbf{r}_a)|^2\rangle = |\langle\phi(\mathbf{r}_a)\rangle|^2 + \langle|\phi_f(\mathbf{r}_a)|^2\rangle. \tag{8}$$

The coherent field can now be written as:

$$\langle\phi(\mathbf{r}_a)\rangle = \phi_i(\mathbf{r}_a) + \sum_{s=1}^{N} \langle u_s^a \phi_i(\mathbf{r}_s)\rangle + \sum_{s=1}^{N} \sum_{t=1, t\neq s}^{N} \langle u_s^a u_t^s \phi_i(\mathbf{r}_t)\rangle$$

$$+\sum_{s=1}^{N}\sum_{t=1,t\neq s}^{N}\sum_{m=1,m\neq t,m\neq s}^{N}\langle u_s^a u_t^s u_m^t \phi_i(\mathbf{r}_m)\rangle + \cdots . \tag{9}$$

Provided that the scatterers are independent of eachother and that their scattering characteristics are equal it is possible to show that

$$\sum_{s=1}^{N}\langle u_s^a \phi_i(\mathbf{r}_s)\rangle = \sum_{s=1}^{N}\int u_s^a \phi_i(\mathbf{r}_s)\frac{\rho(\mathbf{r}_s)}{N}\,d\mathbf{r}_s = \int u_s^a \phi_i(\mathbf{r}_s)\rho(\mathbf{r}_s)\,d\mathbf{r}_s, \tag{10}$$

and that

$$\begin{aligned}\sum_{s=1}^{N}\sum_{t=1,t\neq s}^{N}\langle u_s^a u_t^s \phi_i(\mathbf{r}_t)\rangle &= \sum_{s=1}^{N}\sum_{t=1,t\neq s}^{N}\int\int u_s^a u_t^s \phi_i(\mathbf{r}_t)\frac{\rho(\mathbf{r}_s)\rho(\mathbf{r}_t)}{N^2}\,d\mathbf{r}_s\,d\mathbf{r}_t \\ &= \frac{N-1}{N}\int\int u_s^a u_t^s \phi_i(\mathbf{r}_t)\rho(\mathbf{r}_s)\rho(\mathbf{r}_t)\,d\mathbf{r}_s\,d\mathbf{r}_t. \end{aligned}\tag{11}$$

In these expressions $\rho(\mathbf{r}_s)$ is the number density of scatterers, i. e., the number of scatterers per unit volume. In the limit $N \to \infty$ this leaves

$$\sum_{s=1}^{N}\sum_{t=1,t\neq s}^{N}\langle u_s^a u_t^s \phi_i(\mathbf{r}_t)\rangle = \int\int u_s^a u_t^s \phi_i(\mathbf{r}_t)\rho(\mathbf{r}_s)\rho(\mathbf{r}_t)\,d\mathbf{r}_s\,d\mathbf{r}_t. \tag{12}$$

Similar expressions can be derived for any number of scatterers. The sums in Eq. 9 can now be replaced by the integrals above. The resulting expression can be written as:

$$\langle\phi(\mathbf{r}_a)\rangle = \phi(\mathbf{r}_a) + \int u_s^a\langle\phi(\mathbf{r}_s)\rangle\rho(\mathbf{r}_s)\,d\mathbf{r}_s. \tag{13}$$

The equivalence between Eq. 9 and the above expression can be shown by iteration. Twersky also derived a similar expression for the intensity. This formulation reads (from [4]):

$$\langle\phi(\mathbf{r}_a)\phi^*(\mathbf{r}_b)\rangle = \langle phi(\mathbf{r}_a)\rangle\langle\phi^*(\mathbf{r}_b)\rangle + \int v_s^a v_s^{b*}\langle|\phi(\mathbf{r}_s)|^2\rangle\rho(\mathbf{r}_s)\,d\mathbf{r}_s, \tag{14}$$

where v_s^a satisfies the equation

$$v_s^a = u_s^a + \int u_t^a v_s^t \rho(\mathbf{r}_t)\,d\mathbf{r}_t. \tag{15}$$

The total intensity at one point can be written as:

$$\langle|\phi(\mathbf{r}_a)|^2\rangle = |\langle phi(\mathbf{r}_a)\rangle|^2 + \int |v_s^a|^2\langle|\phi(\mathbf{r}_s)|^2\rangle\rho(\mathbf{r}_s)\,d\mathbf{r}_s, \tag{16}$$

The former two equations constitute the basic equations for the correlation function $\langle\phi(\mathbf{r}_a)\phi^*(\mathbf{r}_b)\rangle$. The physical meaning of these equations can be established through expanding it iteratively and examine each term. The resulting terms will represent the contribution to the correlation function from single, double and further increasing orders of scattering.

2.3 Far-field approximation

In the preceding section it was assumed that the scatterers were independent of each other. This assumption is fulfilled if the density of scatterers is low, i. e., if each scatterer is in the far-field of the other scatterers. In this case it is possible to write the scattering operator u as:

$$u_t^a = h(\hat{\mathbf{i}}_{at}, \hat{\mathbf{i}}_{ts}) \frac{e^{jk|\mathbf{r}_a - \mathbf{r}_t|}}{|\mathbf{r}_a - \mathbf{r}_t|}, \tag{17}$$

where $\hat{\mathbf{i}}_{at}$ is the unit vector in the direction from $\mathbf{r}_t$ to $\mathbf{r}_a$ and $\hat{\mathbf{i}}_{ts}$ is the unit vector from $\mathbf{r}_s$ to $\mathbf{r}_t$. The function $h(\hat{\mathbf{i}}_{at}, \hat{\mathbf{i}}_{ts})$ is the scattering strength in the $\hat{\mathbf{i}}_{at}$-direction due to an incident plane wave in the $\hat{\mathbf{i}}_{ts}$-direction.

With this approximate scattering operator it is possible to derive

$$v_s^a = h(\hat{\mathbf{i}}_{as}, \hat{\mathbf{i}}_i) \frac{e^{jK|\mathbf{r}_a - \mathbf{r}_s|}}{|\mathbf{r}_a - \mathbf{r}_s|}, \tag{18}$$

where $\hat{\mathbf{i}}_{as}$ is the unit vector in the direction from $\mathbf{r}_s$ to $\mathbf{r}_a$ and $\hat{\mathbf{i}}_i$ is the direction of the incident wave. The wave number K for the propagation through the scattering medium can be deduced for constant scatterer density and as:

$$K = k + \frac{2\pi h(\hat{\mathbf{i}}_{as}, \hat{\mathbf{i}}_{as})}{k} + j\frac{\rho\sigma_t}{2}, \tag{19}$$

where σ_t is the total scattering cross section for a scatterer. The total scattering cross section is the sum of the scattering cross section σ_s and the absorption cross section σ_a.

Since Eq. 18 is an operator, $|v_s^a|^2(|\phi(\mathbf{r}_s)|^2)$ should represent the scattered field from all incident directions $\hat{\mathbf{i}}_i$. This can also be expressed using the specific intensity $I(\mathbf{r}, \hat{\mathbf{i}}_i)$ (see /citeishimaru for a description of the specific intensity):

$$\langle\phi(\mathbf{r}_a)\phi^*(\mathbf{r}_b)\rangle = \Gamma(\mathbf{r}_a, \mathbf{r}_b) = \Gamma(\mathbf{r}, \mathbf{r}_d) = \int I(\mathbf{r}, \hat{\mathbf{i}}_i) e^{j\mathrm{Re}\{K\}\hat{\mathbf{i}}_i \cdot \mathbf{r}_d} \, d\omega. \tag{20}$$

Here $d\omega$ is the infinitesimal solid angle in the direction of $\hat{\mathbf{i}}_i$. Furthermore, $\mathbf{r} = (\mathbf{r}_a + \mathbf{r}_b)/2$ and $\mathbf{r}_d = \mathbf{r}_a - \mathbf{r}_b$. This equation is valid when the correlation function $\Gamma(\mathbf{r}, \mathbf{r}_d)$ is a slowly varying function of $\mathbf{r}$. The intensity $\langle|\phi(\mathbf{r})|^2\rangle$ can now be written as:

$$\langle|\phi(\mathbf{r})|^2\rangle = \Gamma(\mathbf{r}, 0) = \int I(\mathbf{r}, \hat{\mathbf{i}}_i)\, d\omega. \tag{21}$$

The part $\langle|\phi(\mathbf{r}_s)|^2\rangle$ in the integral in Eq. 16 can now be decomposed in the same manner. Each intensity component should produce scattering according to Eq. 18. This gives:

$$|v_s^a|^2\langle|\phi(\mathbf{r}_s)|^2\rangle = \int |h(\hat{\mathbf{s}}, \hat{\mathbf{s}}')|^2 \frac{e^{-\rho\sigma_t|\mathbf{r}_a - \mathbf{r}_s|}}{|\mathbf{r}_a - \mathbf{r}_s|^2} I(\mathbf{r}_s, \hat{\mathbf{s}}')\, d\omega', \tag{22}$$

where $\hat{\mathbf{i}}_{a_s}$ and $\hat{\mathbf{i}}_i$ is replaced by $\hat{\mathbf{s}}$ and $\hat{\mathbf{s}}'$ respectively. Using the phase function $p(\hat{\mathbf{s}}, \hat{\mathbf{s}}')$:

$$p(\hat{\mathbf{s}}, \hat{\mathbf{s}}') = \frac{4\pi}{\sigma_t}|h(\hat{\mathbf{s}}, \hat{\mathbf{s}}')|^2, \tag{23}$$

and the average intensity

$$U(\mathbf{r}) = \frac{1}{4\pi}\int_{4\pi} I(\mathbf{r}, \hat{\mathbf{s}})\, d\omega \tag{24}$$

it is possible to write Eq. 16 as:

$$U(\mathbf{r}) = U_{ri}(\mathbf{r}) + \int_V \left[\frac{\rho\sigma_t}{4\pi}\int_{4\pi} p(\hat{\mathbf{s}}, \hat{\mathbf{s}}') I(\mathbf{r}_s, \hat{\mathbf{s}}')\, d\omega'\right] \frac{e^{-\rho\sigma_t|\mathbf{r} - \mathbf{r}_s|}}{|\mathbf{r} - \mathbf{r}_s|^2}\, d\mathbf{r}_s, \tag{25}$$

where U_{ri} is the average intensity due to the direct path from source to receiver only, i. e., without the scattering from other particles in the volume. The integral represent the contribution from scattering from all other particles in the volume.

2.4 Transport theory

The general Boltzmann equation (Eq. 1) can be derived in different ways. One way is presented in [5], but here the derivation comes from [4]. Consider the specific intensity $I(\mathbf{r}, \hat{\mathbf{s}})$ incident upon a cylindrical elementary volume with unit cross section and length ds. The volume ds contains ρds particles (scatterers), where ρ is the

particle density, i. e., the number of particles in a unit volume. Now, each particle absorbs the power $\sigma_a I$ and scatters the power $\sigma_s I$, where σ_a and σ_s is the absorbing and scattering cross section respectively. Therefore, the decrease of the specific intensity in the volume $\mathrm{d}s$ is

$$\mathrm{d}I = -\rho \mathrm{d}s\,(\sigma_a + \sigma_s)I = -\rho \mathrm{d}s\,\sigma_t I. \tag{26}$$

At the same time there is also an increase in the specific intensity due to scattering from other points in the volume V containing all scatterers. Through adding the incident flux from all directions $\hat{\mathrm{s}}'$ the specific intensity scattered into the direction $\hat{\mathrm{s}}$ is given by

$$\mathrm{d}I = \int_{4\pi} \rho \mathrm{d}s\,|h(\hat{\mathrm{s}}, \hat{\mathrm{s}}')|^2 I(\mathrm{r}, \hat{\mathrm{s}}')\,\mathrm{d}\omega', \tag{27}$$

where $h(\hat{\mathrm{s}}, \hat{\mathrm{s}}')$ is the scattering amplitude as defined before. This integral can also be expressed using the phase function $p(\hat{\mathrm{s}}, \hat{\mathrm{s}}')$:

$$p(\hat{\mathrm{s}}, \hat{\mathrm{s}}') = \frac{4\pi}{\sigma_t}|h(\hat{\mathrm{s}}, \hat{\mathrm{s}}')|^2. \tag{28}$$

The specific intensity may also increase due to a source inside the volume $\mathrm{d}s$. The radiated power from the source is $\epsilon(\mathrm{r}, \hat{\mathrm{s}})$ which gives the increase

$$\mathrm{d}I = \mathrm{d}s\,\epsilon(\mathrm{r}, \hat{\mathrm{s}}) \tag{29}$$

Through adding the specific intensity changes in Eqs. 26, 27 and 29 a steady-state differential equation of the specific intensity is obtained.

$$\frac{\mathrm{d}I(\mathrm{r}, \hat{\mathrm{s}})}{\mathrm{d}s} = -\rho\sigma_t I(\mathrm{r}, \hat{\mathrm{s}}) + \frac{\rho\sigma_t}{4\pi}\int_{4\pi} p(\hat{\mathrm{s}}, \hat{\mathrm{s}}')I(\mathrm{r}, \hat{\mathrm{s}}')\,\mathrm{d}\omega' + \epsilon(\mathrm{r}, \hat{\mathrm{s}}). \tag{30}$$

Assume now that the intensity flow is a flow of particles, like photons for electromagnetic wave propagation. All particles travel with the speed of sound and they all carry an equal amount of specific intensity. Then $I(\mathrm{r}, \hat{\mathrm{s}}) = \mathrm{v}f(\mathrm{r}, \hat{\mathrm{s}})$ and the transfer equation in Eq. 30 can be written in the form

$$\mathrm{v} \cdot \nabla f(\mathrm{r}, \hat{\mathrm{s}}) = \frac{\rho\sigma_t}{4\pi}\int_{4\pi} f(\mathrm{r}, \hat{\mathrm{s}})\,\mathrm{d}\omega' - \rho\sigma_t f(\mathrm{r}, \hat{\mathrm{s}}), \tag{31}$$

where the source term has been neglected. This equation is actually a steady-state version of the general Boltzmann equation (Eq. 1) given in the beginning of this

chapter. Thus a transport equation can be written in terms of a distribution function or in terms of specific intensity.

In general there are two different ways to formulate a problem. The first way is to start with a differential equation and obtain a general solution to it with unknown parameters. The values of these unknown parameters are then determined from the boundary conditions. The second way is to combine the differential equation and the boundary conditions into an integral equation for unknown functions. The latter method is used in many FEM applications. The differential equation in Eq. 31 can be formulated as an integral equation. Following [4], the resulting integral equation can be written as:

$$U(\mathbf{r}) = U_{ri}(\mathbf{r}) + \int_V \left[\frac{\rho\sigma_t}{4\pi} \int_{4\pi} p(\hat{\mathbf{s}}, \hat{\mathbf{s}}') I(\mathbf{r}_s, \hat{\mathbf{s}}') \, \mathrm{d}\omega' \right] \frac{\mathrm{e}^{-\rho\sigma_t|\mathbf{r}-\mathbf{r}_s|}}{|\mathbf{r}-\mathbf{r}_s|^2} \, \mathrm{d}\mathbf{r}_s. \tag{32}$$

This formulation is equal to the result from the multiple scattering theory which can be seen in Eq. 25. Since the multiple scattering theory is deduced from the wave equation, this means that it is also possible to use linear transport theory for sound propagation calculations under certain assumptions. During the derivation a number of approximations are taken into account. The most important one is that the scatterers must be in the far-field of eachother. This assumption is probably fulfilled in many suburban or even urban environments. For more dense environments it is possible to use the diffusion approximation [4], and it is hence possible to calculate sound propagation in dense environments using the diffusion equation. However, if the environment is not very sparse and not very dense it is possible to use linear transport theory.

A simple diffusion model can be achieved through applying the heat equation

$$\frac{\partial u}{\partial t} - D\Delta u + \sigma_a u = 0 \ , \tag{33}$$

to the propagation problem. D is here the diffusion parameter dependent on the building environment. This approach has been used by Picaut [6], who has shown that it is possible to deduce a diffusion equation from a transport equation.

3 Application outline

The Boltzmann equation for noise transport with isotropic scattering can be derived as (from [3]):

$$\frac{\partial f}{\partial t} + \mathbf{v} \cdot \nabla f + \frac{c}{\lambda} f = \frac{1-\alpha}{4\pi\lambda} \int f \, \mathrm{dv}. \tag{34}$$

In this equation $|\mathbf{v}| = c$ is the speed of sound and λ is the mean free path length of the sound particles. In the derivation of this equation, the propagation distance for the phonons without colliding with an obstacle is assumed to obey a negative exponential distribution. The mean free path length for the phonons can be calculated as

$$\lambda = \frac{1}{\rho \sigma_s}, \tag{35}$$

where ρ is the density of obstacles, i.e., houses or trees, and σ_s is the scattering cross section for the obstacles.

The phonons are assumed to propagate over a flat plane loosely built with houses. The houses are assumed to be random in position, orientation and size, but the probability distributions for these parameters should still give a meaningful average inside a given domain. A city can be thought of as a set of domains with different parameters. Each domain represents an area of specialized building density or building size and can be used to characterize different kinds of urban or suburban city environments, including parks or recreation areas. However, the house concentration is restricted to be relatively low. This restriction comes from the definition of the infinitesimal element in phase space (drdv) that has been used in the derivation of the Boltzmann equation (see [5] for details).

The concept of mean free path length is relying on constant statistical parameters for the whole domain, i.e., the city. Thus Eq. 34 is not exact for varying parameters, but since the distance involved in sound propagation through cities often is large compared to the value of the mean free path length it is possible to use this approach as a first approximation. Certainly the results close to the boundaries of the subdomains will be inaccurate, but since the aim of the present model is to achieve an average background noise level this drawback is not judged to be of critical importance. The validity of this approach will be studied in further work with the present model.

Eq. 34 can be further simplified by assuming the geometry to be two-dimensional, by assuming steady-state condition, and by replacing the velocities in x- and y-direction with polar representations. All sound particles travel with the speed of sound c and only the direction of propagation ϕ is hence of importance. This leads to the simplified equation:

$$\frac{\partial f}{\partial x}\cos\varphi + \frac{\partial f}{\partial y}\sin\varphi + \frac{f}{\lambda(\mathbf{r})} = \frac{1-\sigma_a(\mathbf{r})}{2\pi\lambda(\mathbf{r})}\int_0^{2\pi} f \, \mathrm{d}\varphi. \tag{36}$$

In this equation $f = f(\mathbf{r}, \varphi)$ where $\mathbf{r} = (x, y)$, and σ_a is the absorption cross section. Interesting is that this equation is not dependent on the speed of sound.

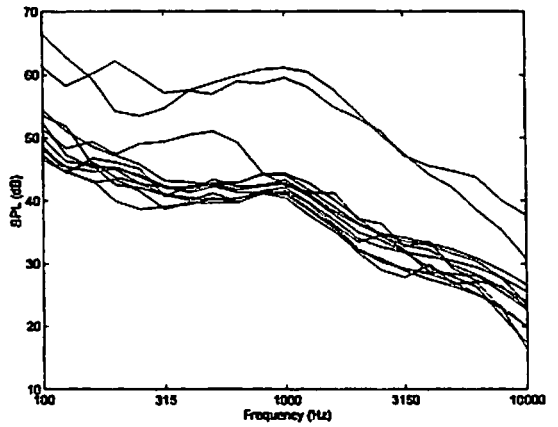

Fig. 1. Sound pressure level as a function of frequency at Hägerstensvägen, Stockholm. The two upper curves correspond to directly exposed positions, while the other curves represent positions with varying degrees of shielding.

The present model can be used to calculate the average noise levels in a part of a city. The boundary conditions for the region of interest should be adapted to that situation. Homogeneous Neumann boundary conditions are used in the x- and y-direction, since the calculation domain boundaries have no fixed noise levels. This does however not mean that the energy flow over the boundary is zero. In linear transport theory the energy flow is not proportional to the spatial derivative of the distribution function, like in the wave equation or in the diffusion equation. Because of the definition of φ as an angular direction, cyclic boundary conditions ($f(\mathrm{r}, 2\pi) = f(\mathrm{r}, 0)$) are used in the φ-direction.

There is no direct dependency on frequency in Eq. 36, but the frequency can affect the results indirectly through the parameters λ and σ_a. However, noise levels measured close to roads and in shielded areas have shown relatively constant frequency contents. Figure 1 shows measured results for various degrees of shielding, from directly exposed positions to positions inside closed courtyards, at Hägerstensvägen in Stockholm. The frequency spectrum indicates that it may be possible to calculate noise levels in cities without regarding frequency dependency. The possibility of this assumption will be studied in further work.

4 Solution method

In this section a solution method for Eq. 36 based on the variational finite element method will be outlined. The used method is often referred to as continuous Galerkin method of order 1 (cG1) [7]. Both sides of Eq. 36 are multiplied with a known continuous test function $\Phi(\mathrm{r}, \varphi)$ and integrated over the whole domain of interest Ω. The domain Ω is now discretized in a three-dimensional mesh. For

simplicity, the 3D mesh is derived from a 2D mesh by translation in the third dimension. By using a fixed discretization in the third dimension, the volume is built up from prism-shaped elements like in Figure 2. It is also possible to achieve tetrahedral elements by using a translation procedure, but this is more cumbersome. An example of a 2D mesh for a part of the city of Stockholm is shown in Figure 3. The area is roughly 2.2 × 3.2 km and the final 3D mesh holds 5901 nodes and 9702 prism elements. The test functions used here are first order polynomials which are adapted to the used elements. For one single node (x_j, y_j, φ_j) the test function can be written as:

$$\Phi_j(x,y,\varphi) = \left(1 - \frac{|x-x_j|}{h_x} - \frac{|y-y_j|}{h_y}\right)\left(1 - \frac{|\varphi-\varphi_j|}{h_\varphi}\right) \quad . \tag{37}$$

The parameters h_x, h_y and h_φ are the dimensions of the reference element in Figure 2. Each element is built up from six test functions:

$$\Phi(\mathrm{r},\varphi) = \sum_{j=1}^{6} \Phi_j(\mathrm{r},\varphi) \quad . \tag{38}$$

Using the test functions in Eq. 37 it is possible to write a discretized version of Eq. 36:

$$\sum_{i=1}^{N}\left[\int_{\Omega_i}\frac{\partial f}{\partial x}\cos\varphi\;\Phi\;\mathrm{d}\Omega_i + \int_{\Omega_i}\frac{\partial f}{\partial y}\sin\varphi\;\Phi\;\mathrm{d}\Omega_i + \int_{\Omega_i}\frac{f}{\lambda}\;\Phi\;\mathrm{d}\Omega_i\right]$$
$$= \sum_{i=1}^{N}\int_{\Omega_i}\frac{1-\alpha}{2\pi\lambda}\int_{\varphi=0}^{2\pi} f\;\mathrm{d}\varphi\;\Phi\;\mathrm{d}\Omega_i \quad . \tag{39}$$

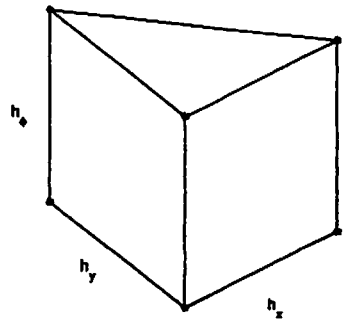

Fig. 2. A prism-shaped reference element built up through a translation of a 2D mesh.

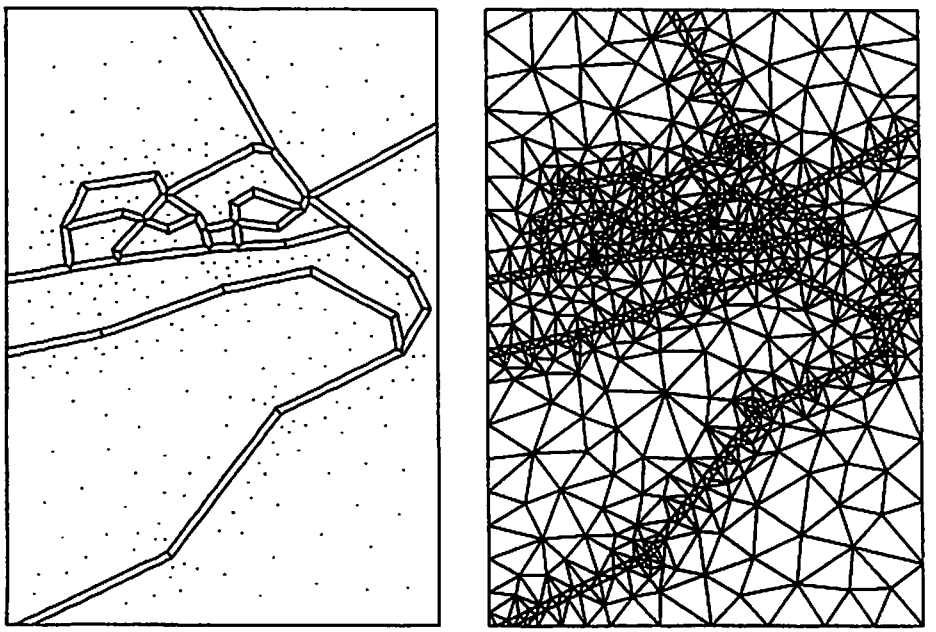

Fig. 3. Left: A simplified figure of the roads important for the traffic noise around Hägerstensvägen in Stockholm. Right: A 2D mesh of the area (843 nodes and 1617 triangular elements).

The distribution function can now be replaced by its interpolant. The interpolant is built from basis functions like in Eq. 37:

$$f(\mathrm{r},\varphi) = \sum_{j=1}^{6} f_j \, \Phi_j(\mathrm{r},\varphi) \ , \tag{40}$$

where f_j is the value of the solution at node j. By inserting the expressions for the test functions (Eq. 37) and the interpolant for f (Eq. 40) an expression suitable for numerical evaluation is achieved:

$$\sum_{i=1}^{N}\sum_{j=1}^{6}\sum_{k=1}^{6} f_j \left[A_{i,j,k} + B_{i,j,k} + E_{i,j,k} - F_{i,j,k}\right] = 0 \ . \tag{41}$$

Here,

$$A_{i,j,k} = \int_{\Omega_i} \frac{\partial \Phi_j}{\partial x} \, \Phi_k \cos\varphi \, \mathrm{d}\Omega_i \ ,$$

$$B_{i,j,k} = \int_{\Omega_i} \frac{\partial \Phi_j}{\partial y} \, \Phi_k \sin\varphi \, \mathrm{d}\Omega_i \ ,$$

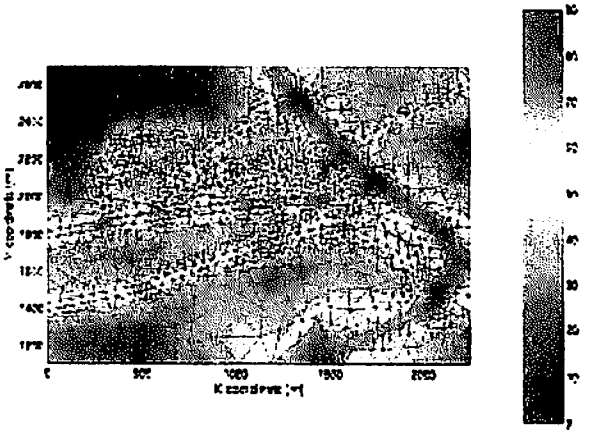

Fig. 4. Results from a test calculation on the Hägersten area in Stockholm.

$$E_{i,j,k} = \frac{1}{\lambda} \int_{\Omega_i} \Phi_j \, \Phi_k \, \mathrm{d}\Omega_i \ ,$$

$$F_{i,j,k} = \frac{1-\alpha}{2\pi\lambda} \int_{\Omega_i} \Phi_k \int_{\varphi=0}^{2\pi} \Phi_j \mathrm{d}\varphi \, \mathrm{d}\Omega_i \ .$$

The integrals in Eq. 42 can now be evaluated analytically. The evaluations must be done by integrating for all different combinations of i,j and k. The contribution from each prism element in Eq. 39 can thus be interpreted as a 6×6 matrix of contributions to nodes. An efficient way do this numerically is to evaluate the integrals on a reference element and then map the reference element onto each element. The final equation system is assembled element by element using the submatrices described above. The equation system can easily be solved with standard methods.

The development of the present model is not finished, but initial tests have shown promising results and the calculation times are fairly short. For the test mesh shown above the calculation time is roughly 3 minutes on a standard PC. The results for the sound pressure level can be seen in Fig. 4, where it can be seen that the distribution function correspond to sound pressure levels that are reasonable.

5 Conclusions

Twersky's theory for multiple scattering have been presented here. By using Foldy-Twersky's integral equations it was possible to deduce an expression which was equal to an integral form of Boltzmann's collision equation. Some assumptions were made during the derivation, the most important being that the scatterers must

be in each others far-field and that the back-scattering from a scatterer must be small. If these assumptions are fulfilled it is possible to use linear transport theory for sound propagation calculations.

By using linear transport models it is possible to use a coarser discretization, and hence it is possible to calculate over larger areas. A simple FEM solution method has been presented here that gives promising results. The method is still under development and the accuracy can therefore not be given at this time.

The results from the present models are however not pointwise exact, they are more intended as a value for the background noise level. This model needs to be used together with a diffraction model to give accurate results in all positions.

Acknowledgements

This paper is based on a study performed within the research programme "Soundscape support to health", sponsored by the Swedish Foundation for Strategic Environmental Research (MISTRA), the Swedish Agency for Innovation Systems (Vinnova) and the Swedish National Road Administration (VV).

References

[1] Jonasson H. and Nielsen H. L. (1996). Road Traffic Noise – Nordic Prediction Method. ISBN 92 9120 836 1. TemaNord 1996:525, Nordic Council of Ministers.

[2] Ögren, M. and Forssén, J. (2001). Prediction of noise levels in shielded urban areas, Proceedings of Inter-Noise 2001, The Hague, Netherlands.

[3] Kuttruff, H. (1982). A mathematical model for noise propagation between buildings. Journal of Sound and Vibration **85(1)**, pp. 115–128.

[4] Ishimaru, A. (1997). Wave propagation and scattering in random media. IEEE Press and Oxford University Press, New York.

[5] Sommerfeld, A. (1971). Thermodynamics and statistical mechanics. Academic Press, London.

[6] Picaut, J., XX (2002). Sound propagation in cities using the diffusion equation Applied Acoustics

[7] Eriksson, K., Estep, D., Hansbo, P. and Johnson, C. (1996). Computational differential equations. Studentlitteratur, Lund, Sweden.

REPORT DOCUMENTATION PAGE

Form Approved
OMB No. 0704-0188

1. AGENCY USE ONLY (*Leave Blank*)	2. REPORT DATE	3. REPORT DYPE AND DATES COVERED
	04 Nov 03	Conference Proceedings

4. TITLE AND SUBTITLE
Tenth International Symposium on Long-Range Sound Propagation

5. FUNDING NUMBERS
DAAD19-02-1-0406
E-43869-EV-CFO-02240-1

6. AUTHOR(S)
James P. Chambers and Henry E. Bass

7. PERFORMING ORGANIZATION NAME(S) AND ADDRESS(ES)
University of Mississippi
Jamie L. Whitten, National Center for Physical Acoustics
Coliseum Drive
University, MS 38677

CSTB
24 rue Joseph Fourier
F-38400
St-Martin d'Heres
Grenoble, France

8. PERFORMING ORGANIZATION REPORT NUMBER
University of Mississippi, Jamie L. Whitten, National Center for Physical Acoustics

300211970A

9. SPONSORING / MONITORING AGENCY NAME(S) AND ADDRESS(ES)
U. S. Army Research Office
P.O. Box 12211
Research Triangle Park, NC 27709-2211

10. SPONSORING / MONITORING AGENCY REPORT NUMBER

11. SUPPLEMENTARY NOTES
The views, opinions and/or findings contained in this report are those of the author(s) and should not be construed as an official Department of the Army position, policy or decision, unless so designated by other documentation

12a. DISTRIBUTION / AVAILABILITY STATEMENT
Approved for public release; Distribution unlimited

12b. DISTRIBUTION CODE

13. ABSTRACT *(Maximum 200 words)*

The 10th Long Range Sound Propagation Symposium (LRSP) was held on September 12-13, 2002 in Grenoble France and was hosted by Drs. Jerome Defrance and Eric Premat of the CSTB. The meeting had 29 presentations (as well as group discussions). The presentations were separated into 4 categories: Ground and Meteorological Effects (9); Turbulence (6); Infrasound, Signal Processing and Experimental Techniques (8); Computational Issues (6). There was a continued consensus that the state of the art for long range sound propagation has grown from 100's of meters (from the early symposia) to kilometers and beyond now - especially with the growing emphasis on infrasound. The 11th symposia is slated for the Fall of 2004 and the venue chosen was the Cold Regions Research Lab (CRRL) in New Hampshire. The event is to be hosted by Dr. Keith Wilson.

14. SUBJECT TERMS: Physical Acoustics, Acoustic Propagation, Infrasound, Symposia	15. NUMBER OF PAGES 418
	16. PRICE CODE

17. SECURITY CLASSIFICATION OF REPORT	18. SECURITY CLASSIFICATION OF THIS PAGE	19. SECURITY CLASSIFICATION OF ABSTRACT	20. LIMITATION OF ABSTRACT
UNCLASSIFIED	UNCLASSIFIED	UNCLASSIFIED	UL

NSN 7540-01-280-5500

Standard Form 298 (Rev. 2-89)
Prescribed by ANSI Std. Z39-1
298-102